Christian Klein-Bösing

Study of the Quark-Gluon Plasma with Hard and Electromagnetic Probes

— 2013 —

Experimentelle Physik

Study of the Quark-Gluon Plasma with Hard and Electromagnetic Probes

als Habilitationsschrift
dem Fachbereich Physik
der Westfälischen Wilhelms-Universität

vorgelegt von

Dr. rer. nat. Christian Klein-Bösing

— 2013 —

FÜR MELA UND MARIA

Contents

Introduction

The quest for the fundamental building blocks of matter and the understanding of the forces between them has been the subject of philosophical discussions for over 2400 years. But our modern understanding of elementary constituents did not start until the end of the nineteenth century, when the discovery of radioactivity initiated the development of the new concepts of *Nuclear and Elementary Particle Physics* in a mutual inspiration of theoretical and experimental advances. In the latter case, the development has been driven to a large part by the construction of increasingly powerful particle accelerators.

The current understanding of the structure of matter is that the atomic nucleus consists of protons and neutrons. These in turn consist of elementary quarks which are confined in the nucleons by the *strong interaction* mediated by massless *gluons* which couple to the *color charge* carried by quarks, as well as by themselves. Their interaction is described in the theory of *Quantum Chromodynamics* (QCD), the quantum field theory of the strong interaction.

In practice, the calculation of processes involving the strong interaction suffers from the fact that the coupling constant is usually large, i.e. of the order of unity. Thus, well established approximation methods, such as the expansion in orders of the coupling, do not converge. In QCD, the regime of small coupling, and thereby applicability of perturbative methods, is reached for large momentum transfer or small distances. Here, the quarks and gluons act as asymptotically free particles.

These reactions with large momentum transfer can be reached in nuclear collisions, where the individual partons (quarks and gluons) can scatter off each other at high collision energy. However, these hard scattered partons cannot be observed as free particles. This property of QCD is known as *confinement*. Instead, the quarks and gluons fragment into sprays of color neutral hadrons, which are observed as *jets* of particles in the original parton direction. In the last 30 years, the production of jets has been the major tool to investigate the properties of the strong interaction and provided stringent tests of QCD predictions in the perturbative regime.

For a deeper understanding of the ground state of strongly interacting matter, or more

general the properties of QCD at large distances and small momentum transfer, a different approach is needed. Here, the goal should not be to study the strong interaction for asymptotically free, single partons, but in a system of many particles that can be described by its thermodynamic properties. In nuclear matter at normal conditions, the strong interaction is only apparent as a residual interaction between constituting quarks. This leads to the van-der-Waals-like, short range binding between the protons and neutrons. In order to study the strong interaction over distances larger than the size of a nucleon in a collective medium of quarks and gluons, their confinement into hadrons must be overcome. This is potentially achieved at extreme temperatures and densities.

On the one hand, theoretical guidance on the phase transition from hadronic matter to this *Quark-Gluon Plasma* (QGP) is provided by phenomenological models. On the other hand, by numerical methods to solve QCD on discrete lattices of space-time. Both approaches suggest critical temperatures of the order of 10^{12} K. Similar conditions are assumed to have existed a few microseconds after the Big Bang. It is the main objective of ultra-relativistic heavy-ion collisions to create such conditions for a short time in the laboratory and to study the imprint of the fleeting existence of the QGP on the colorless objects detectable by the experiment.

The experimental effort in the study of ultra-relativistic heavy-ion collisions is currently concentrated at two accelerators: the Relativistic Heavy Ion Collider (RHIC) at Brookhaven National Laboratory (BNL), which began operating in 2000, and at the Large Hadron Collider (LHC) at CERN, where first heavy-ion collisions were measured in the fall of 2010. The experiments located at these colliders are operated and maintained by large international collaborations with hundreds of scientists and engineers, and the individual contribution cannot be evaluated from the author list. The aim of this thesis is to summarize the main results of selected publications by the PHENIX and ALICE experiments, in which the author made essential contributions to the analysis and the preparation of the paper.

The particular research focus of the author in the study of the QGP are jets, as a *hard probe* of the created medium. They have provided an invaluable tool for the discovery of the QGP and a more in-depth investigation of its properties. The initial hard (large momentum transfer) parton scattering is well controlled and calculable in perturbative QCD, which can be compared to the same measurements in proton-proton collisions. In heavy-ion collisions, the hard scattered partons are created in the initial stage of the reaction and then propagate through the medium. Here, their fragmentation into observable jets of hadrons is expected to be modified relative to the vacuum case by interactions with the medium. One

observable consequence of this medium interaction is the suppression of particle production at large transverse momentum in heavy-ion collisions compared to the expectation from pp reactions. This effect, known as *jet quenching*, was first observed in 2001 in Au + Au collisions at RHIC and has been investigated in more detail in the following years at RHIC and at the LHC with more differential hadron measurements and with the transition from single particle measurements to the reconstruction of jets in heavy-ion collisions. The text of this habilitation thesis puts these detailed investigations into context, highlights the significant contribution of the author in [CKB01 – CKB10] to this effort, and provides an insight into recent experimental studies with the ALICE experiment based on preliminary results, in which the author is actively involved.

1. Quarks, Gluons, and the Quark-Gluon Plasma

The historical development of the theory of the strong interaction can be separated into three phases, starting with the era of hadron spectroscopy: at the beginning of the 1960s, the originally simple picture of only few strongly interacting, elementary particles had completely changed. In addition to the proton, the neutron, and the π-mesons as short range force carriers between the nucleons, a *zoo* of different particle species had been observed at increasingly powerful particle accelerators. At that point, new quantum numbers, such as isospin, baryon number and strangeness, had already been introduced to group the strongly interacting particles (*hadrons*) according to their decay and production properties. The most successful approach to quantify the emerging structure was independently put forward in 1964 by Gell-Mann and Zweig. They showed that the hadrons can be classified in group-theoretical terms as multiplets of the SU(3) symmetry group [GM64, Zwe64]. This picture was confirmed shortly thereafter, when the vacant positions in the multiplets were filled by newly discovered particles, most notably the Ω^- [Bar64]. Gell-Mann and Zweig also postulated the existence of the fundamental representation of this SU(3) group consisting of three particles (u,d,s) with spin-$^1/_2$ and fractional charges ($+^2/_3$,$-^1/_3$,$-^1/_3$). Following Gell-Mann, these particles were called *quarks*. Baryons are constructed from three quarks, while mesons consist of a quark-antiquark combination. In this constituent-quark model, all hadrons known at that time could be constructed in a systematic way, though experimental evidence for the existence of quarks was still lacking.

The further increase in the available particle energy at accelerators initiated the second phase towards our current understanding of the strong interaction: the parton model. When the momentum of beam particles exceeded 1 GeV/c, structures smaller than the size of a proton could be resolved for the first time, and the charge distribution inside the nucleon could be probed via deep inelastic electron-nucleon scattering. It was found that after proper choice of variables the structure functions in these scatterings did not show any dependence on the four momentum transfer Q^2 exchanged by a virtual photon between the electron and

the nucleon. They appeared only to depend on one additional dimensionless parameter, the Bjorken-x, or x_{B}. A conceptually simple picture emerged under the assumption that the inelastic electron-nucleon cross sections can be described as an incoherent sum of elastic scatterings with point-like constituents (*partons*). Then x_{B} gives the fraction of the total nucleon momentum carried by a parton in the nucleon. In addition, the observed connection between the magnetic and electric form factors of the nucleon revealed that the partons probed via deep inelastic scattering carry spin $^1/_2$. The comparison of the form factors obtained in electron- and neutrino-nucleon scattering showed that the nucleons contain a rich substructure of point-like, fractionally charged partons. The connection with the static quark model is then directly given by the separation of the measured parton distribution function (PDF) into the contribution from a sea of virtual quark-antiquark pairs and three valence quarks with the quantum numbers predicted by the constituent quark model.

Despite the success of the combined Quark-Parton Model, it left open a couple of questions that pointed the way to the formulation of Quantum Chromodynamics. One is the spin-statistics problem in the static quark model, which is most easily seen for baryons consisting of quarks of only one flavor and with $J = {}^3/_2$, e.g. the $\Omega^- = |s\uparrow\rangle\,|s\uparrow\rangle\,|s\uparrow\rangle$. The spatial wave function, as well as the spin and flavor wave functions are fully symmetric. This would yield a symmetric total wave function for identical fermions in contradiction to the Pauli principle. The contradiction can be resolved by the introduction of a new internal quantum number that has three distinct values and a wave function that is completely anti-symmetric. This new degree of freedom was called *color* and its three values are usually denoted *red*, *green* and *blue*. The choice is inspired by the fact that the superposition of equal amounts of three ordinary basic colors yield *white*, and the wave function to describe the color part of the baryon is a SU(3) singlet, i.e. baryons do not carry any net color. The experimental fact that no free quarks have been observed can then be reformulated to the condition that net color charge is always confined inside hadrons.

One further observation was that the integration of the momentum distributions of quarks and antiquarks in the nucleon, measured in deep inelastic scattering, accounts only for about one half of the total nucleon momentum. In addition, a violation of the aforementioned scaling behavior was found with a magnitude that could not be explained by the expected violation due to vacuum fluctuations with quark-antiquark annihilation into a photon. Both findings suggested a further parton, that neither couples to electrons nor neutrinos, but strongly couples to quarks. This parton was later identified with the gauge boson of the quantum field theory of the strong interaction, the gluon.

1.1. Quantum Chromodynamics

The first simplification of the classical distinction between forces, particles, and waves has been achieved in quantum theory, where particles and waves become unified in a sense that they appear complementary. A further generalization under the inclusion of special relativity was found in quantum field theory, where the distinction between forces and the particles that these forces act upon is removed: a force is described as the exchange of an intermediate particle that carries the force (the *gauge boson*). Quantum Electrodynamics (QED), the quantum field theory of the electromagnetic interaction, was developed shortly after the Second World War and tested to extreme accuracy [Fey72]. It describes the coupling of the gauge boson of QED, the photon, to electrical charges. It is illustrative to compare the properties of QED to Quantum Chromodynamics (QCD), the field theory of the strong interaction, with the gluons as gauge bosons coupling to color charge.

Some properties of QED and QCD are listed in Table 1.1 and are explained in more detail in the following. In QED, the photon couples to the electric charge, which is expressed in units of the positron charge. The photon itself carries no charge. Thus, photons cannot interact with each other. This yields a basic set of three Feynman-Diagrams that is needed to construct all motions and interactions in QED: a propagating charge, a real photon, and the charge-photon vertex. The diagrams are shown in Figure 1.1 and find their correspondence in the Lagrangian of QED. The charge-photon vertex can be interpreted from different perspectives. Depending on the time direction it is: the emission of a photon from a charge, the scattering from a photon off a charge, or the conversion of a photon into a particle-antiparticle pair. The strength of the electromagnetic force at this vertex is proportional to the coupling constant g (where $\alpha = g^2/4\pi$) and the charge of the particle. In general, the coupling constant can depend on the scale, e.g. the momentum transfer Q^2, of the process. This scale dependence is rather weak in QED, as shown for two cases in Table 1.1. It can be understood in a way that each electric charge is partially shielded by a cloud of virtual e^+e^- pairs. The cloud is penetrated at higher momentum transfer, and more of the *bare* charge is exposed, thus the coupling becomes stronger. For all relevant scales, the coupling in QED stays below unity. This means that perturbative techniques that employ power-series in g or α converge.

In contrast to the electrically neutral photon, the gluons in QCD carry net color-charge, a combination of color and anticolor. This yields nine independent combinations for the three colors: one is a color neutral combination and not realized in nature while the remaining eight different gluons act color-specific and couple to each other. In QCD, two additional diagrams need to be considered in the theoretical description (see Figure 1.1): the three- and four-gluon

	QED	QCD
Symmetry group	U(1)	SU(3)
Charge	1 electric (e)	3 colors (r, g, b)
Gauge bosons	1 Photon (γ) neutral	8 Gluons (g) color charged
Scale dependence of coupling		
$Q^2 = (\ 0\,\mathrm{GeV}/c)^2$	$\alpha \approx 1/137$	$\alpha_\mathrm{S} \approx O(1)$
$Q^2 = (92\,\mathrm{GeV}/c)^2$	$\alpha \approx 1/127$	$\alpha_\mathrm{S} \approx 0.12$
		no free color charge (confinement)
		asymptotic freedom

Table 1.1.: Basic properties of QED and QCD compared.

vertices. They represent the self-coupling of the gauge bosons. These self couplings are characteristic of a gauge theory based on a non-Abelian group. The gauge group chosen in the Lagrangian also defines the relative strength of the coupling, i.e. in the case of quarks and gluons the effective color charge C_R. For SU(3) the gluon has a color charge that is larger than that of a quark by a factor $C_\mathrm{A}/C_\mathrm{F} = 9/4$. This value has been experimentally verified by measuring the gluon emission off a quark compared to the emission off a gluon, which is more than twice as probable.

The scale dependence of the coupling is much more pronounced and opposite in QCD compared to QED. In QCD, due to the contributions of the gluon-self coupling, anti-shielding terms dominate at low momentum transfer. Thus, coupling becomes smaller with increasing Q^2. This characteristic is known as the *asymptotic freedom* of QCD and can be derived in perturbation theory. At leading order, the running coupling in QCD is:

$$\alpha_\mathrm{S}(Q^2) = \frac{12\pi}{(33 - 2N_\mathrm{f}) \ln \frac{Q^2}{\lambda^2}}, \tag{1.1}$$

where N_f is the number of relevant quark flavors for the momentum scale Q^2, and λ is the QCD scale parameter. It corresponds to the scale where the perturbatively defined coupling would diverge, i.e. where the non-perturbative regime of QCD begins. Depending on the

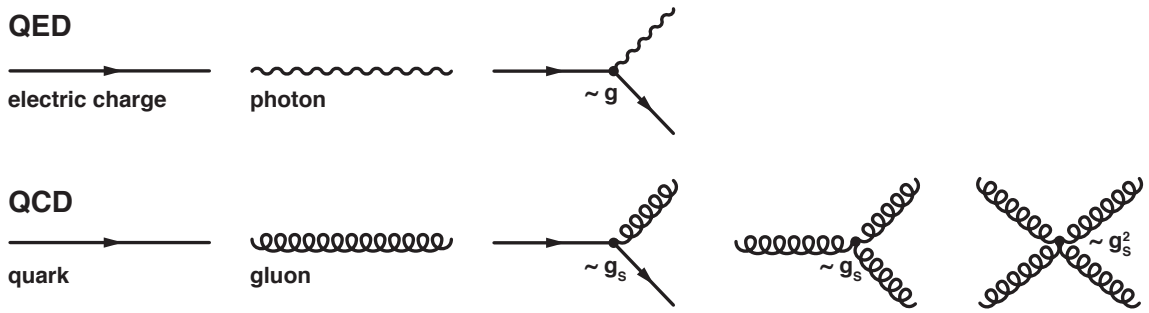

Figure 1.1.: Elementary QED and QCD Feynman graphs: free particles/fields and interaction vertices.

number of active quark flavors, its numerical value varies between approximately 210 and 340 MeV [Ber12].

1.2. QCD Phase Diagram

Even though the complete physics of the strong interaction is encoded in the well known Lagrangian of QCD, it can be only solved analytically in certain limits. As discussed above, perturbative expansions in particular rely on the fact that the coupling is much smaller than unity.

For the understanding of QCD matter in the non-perturbative regime, one can resort to phenomenological models that mimic the behavior of QCD in a regime of low momentum transfer. Here, the dominant feature of QCD is the confinement of quarks and gluons into hadrons, which is sometimes called the *infrared slavery* of the quarks and gluons as an antipole to their asymptotic (ultraviolet) freedom. A useful phenomenological description of confinement is provided by *bag models*. In the simplest case, the quarks are treated as massless particles within a bag of finite dimensions and infinitely heavy outside [Won94]. The confinement in the bag is reached by the balance between the kinetic stress of the ideal gas of quarks and the bag pressure B that is directed inward. The bag pressure encodes the non-perturbative effects of QCD in a single constant. Its numerical value of $B^{1/4} \approx 210\,\mathrm{MeV}$ can be derived from the minimization of the total energy of a bag with radius R, using a confinement radius of about 0.8 fm in a three quark system:

$$E = \frac{2.04 \cdot n_q}{R} + \frac{4\pi}{3} \cdot R^3 \cdot B. \tag{1.2}$$

Here, the first term corresponds to the zero-point energy of a system of n_q relativistic, distinguishable fermions in a spherical cavity. The second term accounts for the higher energy density inside the bag due to the perturbed QCD vacuum.

In the bag model, a new phase of matter of deconfined quarks and gluons, the QGP, can be formed in case the kinetic energy of the quarks is larger than the bag pressure. Here, two extreme scenarios can be considered: a phase transition at large temperature, where the kinetic energy of quarks and gluons with corresponding pressure P exceeds the bag pressure, or a phase transition at $T = 0$ but large baryon density or baryo-chemical potential μ_B. In the latter case, the degenerative pressure of the quarks may exceed the bag pressure.

Knowing the phenomenological bag constant, the critical temperature can be estimated e.g. for the transition of a pion gas to a gas of free quarks and gluons with no net baryon number, that is the baryo-chemical potential $\mu_B = 0$. At the phase transition the two phases co-exist at the same temperature. The pressure in the hadron gas and the QGP phase is identical:

$$\overbrace{3 \cdot \frac{\pi^2}{90} \cdot T_C^4}^{P_{HG}} = \overbrace{(16 + \frac{7}{8} \cdot 24) \cdot \frac{\pi^2}{90} \cdot T_C^4 - B}^{P_{QGP}}. \tag{1.3}$$

The different pre-factors reflect the change in the number of the effective degrees of freedom: three for the pion gas, 16 for the eight gluons and their spin in the QGP, while for two active quark flavors one has to take into account particles and anti-particles, spin and color degrees of freedom, as well as their fermionic character by the factor 7/8. It follows that the critical temperature is:

$$T_C = \left(\frac{90}{34\pi}\right)^{1/4} \cdot B^{1/4} \approx 150\,\mathrm{MeV}. \tag{1.4}$$

This temperature corresponds to a critical energy density in the QGP of:

$$\varepsilon_C = \frac{37 \cdot \pi^2}{30} \cdot T_C + B \approx 1\,\mathrm{GeV/fm^3}. \tag{1.5}$$

Here, the phase transition is by construction a first order phase transition. In this simple model the energy density rapidly changes at the critical temperature since the number of degrees of freedom jumps from the pion gas to the QGP. A more realistic picture of the hadronic phase close to the critical temperature is provided by a hadron-resonance gas instead of a pion gas. Here, the experimental observation is used that the density of accessible hadronic states increases exponentially going to higher masses $\mathrm{d}N/\mathrm{d}m \propto m^a e^{m/T_H}$. Folded with the Boltzmann probability distribution for the occupation of a given mass state this leads

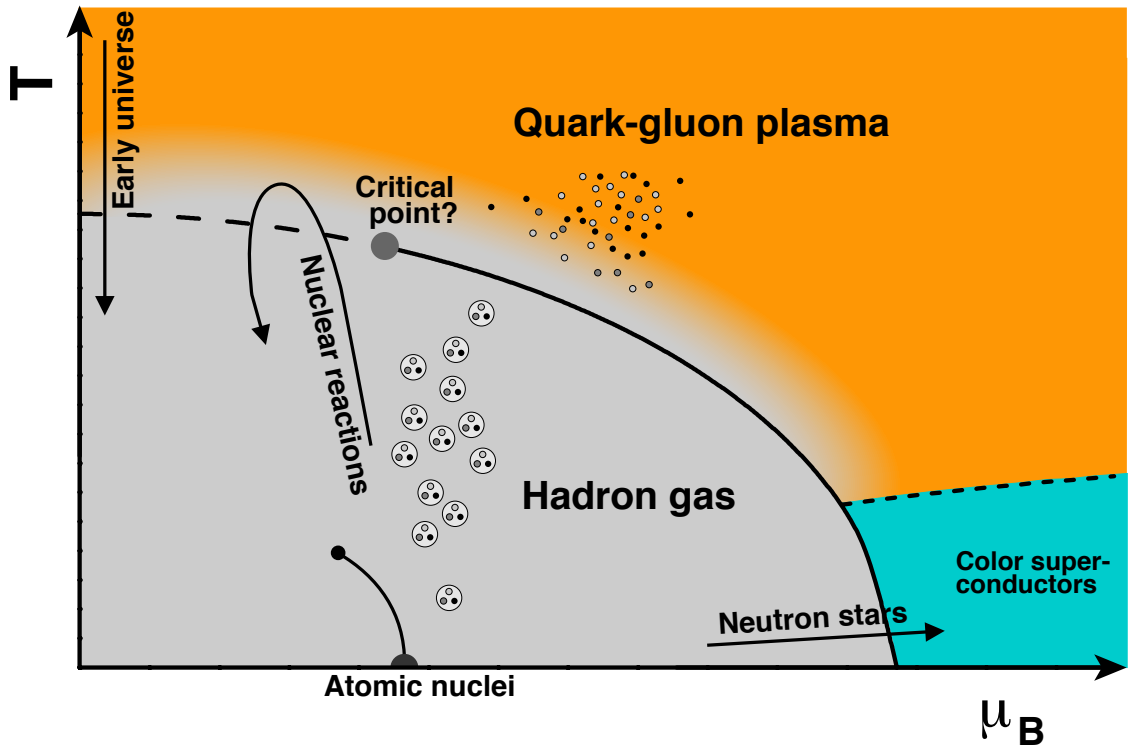

Figure 1.2.: Conjectured phase diagram of strongly interacting matter.

to more degrees of freedom with increasing temperature. The energy density of the hadron resonance gas increases rapidly and diverges at the *Hagedorn temperature* $T_{\mathrm{H}} \approx 170\,\mathrm{MeV}$. This divergence of the energy density in the thermodynamic treatment of hadronic matter was discovered in 1965 by Hagedorn well before the advent of QCD and provided an early indication of new physics in the region of T_{H} [Hag65, Hag71].

A more fundamental theoretical study of the QCD phase transition is possible via the formulation of QCD on a discrete lattice of space-time, *lattice QCD*, and its numerical solution [Wil74]. This approach avoids divergences that occur at small momentum transfer in the continuous formulation, while preserving the fundamental characteristics of the gauge theory. The extrapolation to the continuum limit of vanishing lattice spacing and physical quark masses allows one to derive e.g. the properties of bound quark systems or the thermodynamic equation of state of strongly interacting matter based on first principles. Already in early lattice QCD calculation, using only gluons, a phase transition of QCD matter was observed at similar temperatures as obtained in the simplistic bag models [Kut81].

The nature of the transition to the QGP at vanishing net baryon density $\mu_{\mathrm{B}} = 0$ crucially

depends on the used masses for u, d and s quarks (see e.g. [Kar03]). For realistic values it is not a phase transition, but a smooth crossover transition. Thus, the definition of a critical temperature is no longer unique. Nevertheless, the thermodynamic properties change rapidly, which makes it possible to extract a transition temperature: a recent calculation of the pseudo-critical temperature yields $T_C = 154 \pm 9$ MeV [Baz12]. Whether the transition becomes a first order phase transition at higher μ_B, implying the existence of a critical point, is still an open question in lattice QCD [dF08]. Here, it is difficult to obtain results for $\mu_B > 0$ and one has to rely on extrapolation techniques using derivatives at $\mu_B = 0$.

For large net baryon densities, the bag model can again provide guidance on the location of the phase-transition. Here, the phase transition at $T = 0$ is estimated at a baryon density of approximately $0.72/\text{fm}^3$, about five times the baryon density of normal, cold nuclear matter [Won94]. Furthermore, effective theories can be used to model the low temperature behavior of quarks in QCD. They predict the dynamical formation of various quark condensates from Fermi interactions, similar to the formation of Cooper pairs from electrons in superconductors [Nam61, Raj00].

A sketch of the phase diagram of QCD is shown in Figure 1.2. The phase transition from a hadron gas along the ordinate or abscissa of the phase diagram covers two extremes that are also interesting for cosmology and astrophysics. On the one hand, about 1 μs after the Big Bang, the initial hadrons were produced in the freeze-out from a QGP phase with high temperature and low baryon density. On the other hand, the conditions for a phase transition at low temperature may today still be reached in the core of neutron stars [Alf01, Sch10].

2. Experimental Search for the QGP

The study of nuclear matter under extreme conditions is facilitated in the laboratory by ultra-relativistic heavy-ion collisions, meaning in collision between heavy nuclei with center of mass energies per nucleon pair ($\sqrt{s_{\mathrm{NN}}}$) above 10 GeV. In these reactions the initial temperature and density may be sufficient to create a quark-gluon plasma for a short time, and it is the experimental challenge to separate the signatures of its fleeting existence from the signals of the later phase of hot hadronic matter and to disentangle the effects of cold and hot nuclear matter. There is no single indisputable signature for the creation of a quark-gluon plasma. Indeed, in the experimental programs of the SPS/CERN, RHIC/BNL, and LHC/CERN, an increasing number of various observables shows a behavior that is distinctly different from usual nuclear matter and can be consistently described with the creation of a new, partonic phase of matter created in heavy-ion collisions [CER00, BNL05, CER10].

2.1. Experimental Program

The experimental search for the quark-gluon plasma started in the mid-eighties using existing facilities (the Alternating Gradient Synchrotron (AGS) at Brookhaven National Laboratory (BNL) and the Super Proton Synchrotron (SPS) at CERN) to accelerate moderately heavy ions (e.g. Si) instead of protons and to collide them with a *fixed target* at rest. In the following years, many dedicated heavy-ion experiments have been carried out at the SPS and AGS using nuclei as heavy as lead as projectile. The center-of-mass energy per colliding nucleon pair reached in these fixed-target experiments was limited to $\sqrt{s_{\mathrm{NN}}} \approx 17$ GeV, and they were followed by the next generation of heavy-ion experiments at hadron colliders. Since 2000 these involve experiments at the Relativistic Heavy Ion Collider (RHIC) and at the Large Hadron Collider (LHC) since 2010. The leap in the available center of mass energy in each generation has been more than an order of magnitude (see Table 2.1). The consequences of this increase for the created medium are discussed further below. First, the setup of the two experiments that provided the main data for the author's work is described: the PHENIX and the ALICE experiment.

Year	Accelerator	Main Projectile	$\sqrt{s_{\mathrm{NN}}}$
1985	AGS (BNL)	Si	5.4 GeV
1985	SPS (CERN)	S	20 GeV
1993	AGS (BNL)	Au	4.8 GeV
since 1994	SPS (CERN)	Pb	17 GeV
since 2000	RHIC (BNL)	Au	200 GeV
since 2010	LHC (CERN)	Pb	2760 GeV

Table 2.1.: Selected heavy-ion accelerators and their center of mass energy. At design energy the LHC will reach $\sqrt{s_{\mathrm{NN}}} = 5500\,\mathrm{GeV}$ in Pb + Pb reactions.

2.1.1. RHIC and PHENIX

RHIC started its operation with colliding gold nuclei at $\sqrt{s_{\mathrm{NN}}} = 130\,\mathrm{GeV}$. The collider consists of two rings which accelerate the colliding species in opposite directions. The energy range covered per nucleon in each ring is from 5 to 100 GeV/nucleon for heavy ions and up to 250 GeV for protons [Hah03].

The various acceleration steps of the RHIC complex are shown in Figure 2.1, heavy ions are injected in a Tandem van de Graaf accelerator and further accelerated in the Booster and the AGS before being injected in either of the two RHIC rings. At the beginning of RHIC operation four experiments were active: PHENIX and the second, large experiment STAR, as well as the two smaller ones in terms of size of cost of construction, PHOBOS and BRAHMS. The latter two completed operation in 2006 and 2005, respectively, while PHENIX and STAR continue to operate. They take advantage of the versatility of RHIC in the choice of asymmetric colliding species and its large range of beam energies. The various heavy-ion collision systems, energies, and integrated luminosities inspected at RHIC so far are listed in Table 2.2. The integrated luminosity $\mathscr{L}_{\mathrm{int}} = \int \mathscr{L}(t)\mathrm{d}t$ relates the accumulated data to the expected number of observable events for a process with given cross section σ:

$$N = \mathscr{L}_{\mathrm{int}} \cdot \sigma. \tag{2.1}$$

In particular, the number of inspected collisions can be determined using the total inelastic cross section of the collision. For example $\sigma^{\mathrm{inel}} \approx 6.8\,\mathrm{b}$ for Au + Au collisions at top RHIC energies.

The setup of the PHENIX experiment is shown in Figure 2.2. It can be subdivided into the inner detectors close to the beam pipe and four spectrometer arms: two muon arms at forward

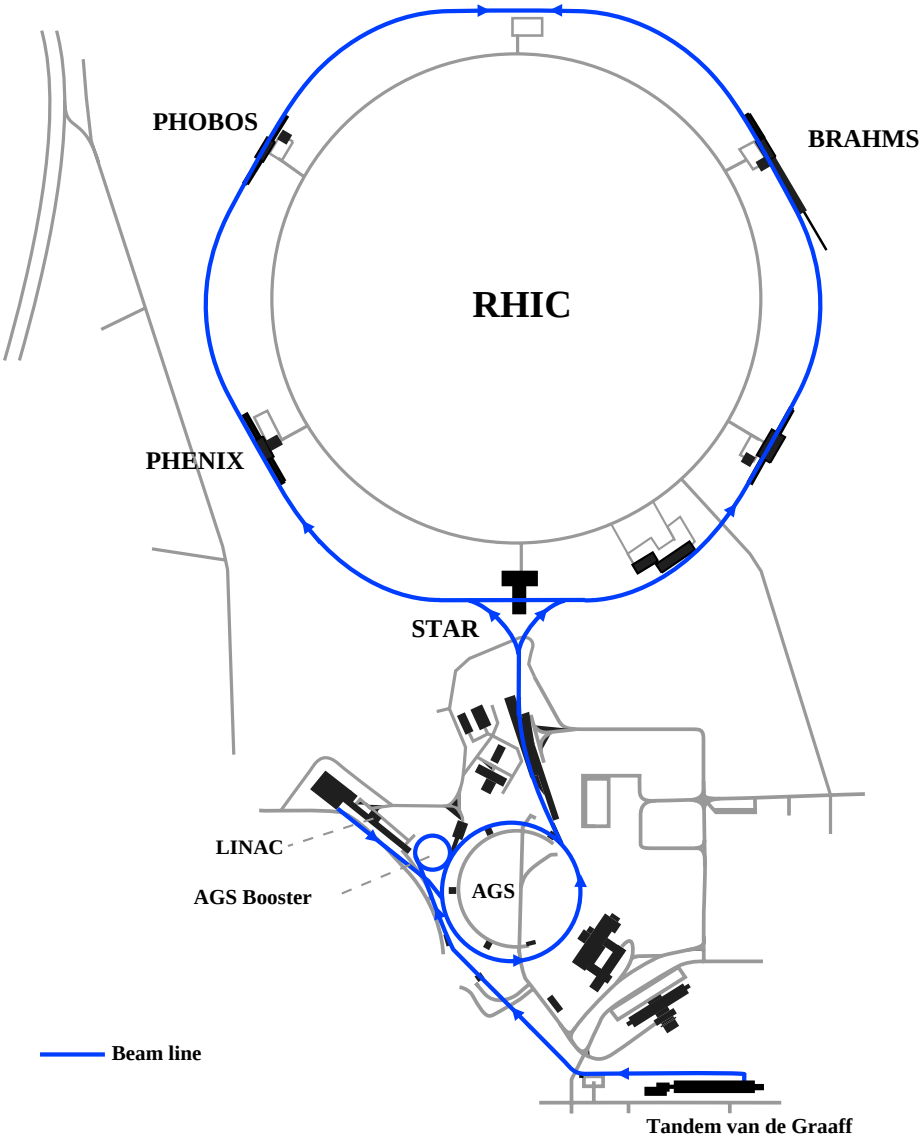

Figure 2.1.: Map of the RHIC complex with its four experiments and the different acceleration stages. The RHIC ring has a circumference of 3.8 km. The PHOBOS and BRAHMS experiments are no longer active.

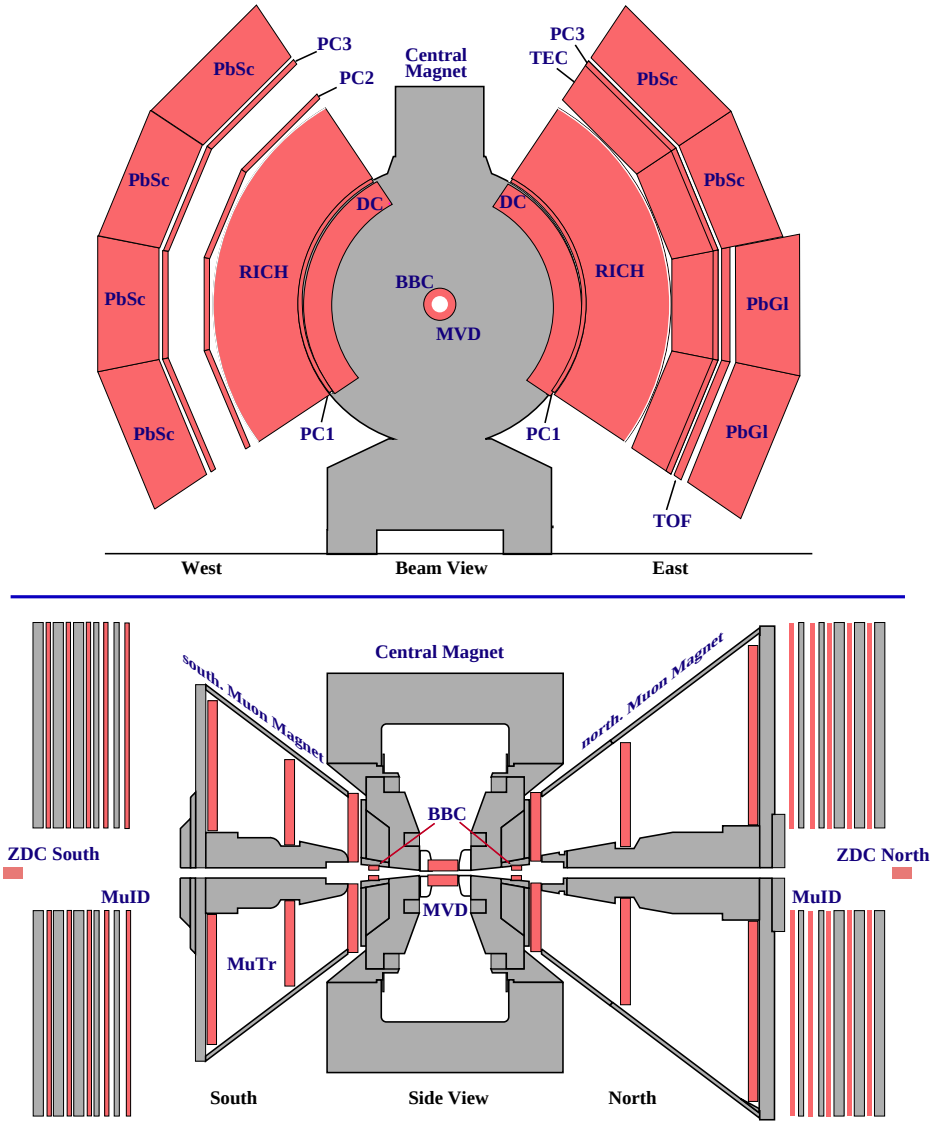

Figure 2.2.: PHENIX setup during the third RHIC beam period (2002/03).

(north) and backward (south) rapidity, and the two central spectrometer arms at mid-rapidity.[1] The detectors of the east and west arm cover the pseudo-rapidity interval $-0.35 < \eta < 0.35$ and $2 \times 90^\circ$ in azimuth.

In the PHENIX experiment, the Beam-Beam Counters (BBC) and the Zero Degree Calorimeters (ZDC) are the main trigger detectors. They are also used to determine the primary collisions vertex and the *centrality* of a heavy-ion reaction, i.e. the displacement of the two colliding nuclei. It is usually provided in fractions of the total cross section. The major source of information are the BBCs that measure the multiplicity and arrival time of charged particles in the pseudo-rapidity region of $3.1 < |\eta| < 3.5$.

The main detector employed for the analyses presented in this work is the Electromagnetic Calorimeter (EMCal) [Aph03]. It is the outermost detector of the central arms, with a radial distance of more than five meters, which consists of six sectors of lead-scintillator sandwich calorimeter (PbSc) and two sectors of lead-glass Cherenkov calorimeter (PbGl) [Aph03]. Each sector covers 22.5° in azimuth. With their fine segmentation of $\Delta\eta \times \Delta\varphi = 0.01 \times 0.01$ both calorimeters provide a good energy and position resolution for the detection of photons and electrons, and the reconstruction of neutral mesons via their decay into two photons, e.g. $\pi^0 \rightarrow \gamma\gamma$.

2.1.2. LHC and ALICE

The first Pb + Pb collisions at the LHC in the fall of 2010 with $\sqrt{s_{\mathrm{NN}}} = 2760\,\mathrm{GeV}$ exceeded the energy of RHIC by more than an order of magnitude. This is achieved by the acceleration steps illustrated in Figure 2.3: lead ions are produced from vaporized, highly purified lead and selected for the Pb^{+29} state. These are accelerated to 4.2 MeV/u (energy per nucleon) by a linear accelerator (LINAC 3). At exit they are stripped by a carbon foil to Pb^{+54} and accumulated in the Low Energy Ion Ring (LEIR). It accelerates the ions to 72 MeV/u and transfers them to the Proton Synchrotron (PS). After the PS, the beam has an energy of 5.9 GeV/u and passes a second foil, which fully strips the ions to Pb^{+82}. The SPS accelerates to 177 GeV/u, before the beam is transferred to the LHC and injected in either of the two beam pipes, where it is further accelerated. In the operation scheme of the Pb + Pb runs until 2011, the Pb ions have been accelerated to the energy of $Z/A \cdot 3500\,\mathrm{GeV} \approx 1380\,\mathrm{GeV/u}$.

The LHC has been installed in the existing 26.7 km tunnel constructed for the Large Electron Positron collider (LEP). This tunnel consists of eight arcs and eight straight sections. LEP started operation in 1989 and was shut down in 2000 to start construction of the LHC.

[1] For the definition of the rapidity and other kinematic variables refer to Appendix A.

PHENIX/RHIC

Year	System	$\sqrt{s_{\mathrm{NN}}}$ (GeV)	$\mathscr{L}_{\mathrm{int}}$ ($\mu\mathrm{b}^{-1}$)
2000	Au + Au	130	7
2001/02	Au + Au	200	93
2002/03	d + Au	200	24200
2003/04	Au + Au	200	1260
	Au + Au	62.4	22
2004/05	Cu + Cu	200	15200
	Cu + Cu	62.4	520
	Cu + Cu	22.4	6
2006/07	Au + Au	200	3270
2007/08	d + Au	200	238000
2009/10	Au + Au	200	5000
	Au + Au	62.4	281
	Au + Au	39	107
	Au + Au	7.7	2
2010/11	Au + Au	19.6	16
	Au + Au	200	4970
	Au + Au	27	33
2011/12	U + U	193	13500
	Cu + Au	200	368

ALICE/LHC

Year	System	$\sqrt{s_{\mathrm{NN}}}$ (GeV)	$\mathscr{L}_{\mathrm{int}}$ ($\mu\mathrm{b}^{-1}$)
2010	Pb + Pb	2760	10
2011	Pb + Pb	2760	100

Table 2.2.: Integrated luminosities sampled at PHENIX and ALICE in selected RHIC and LHC heavy-ion runs.

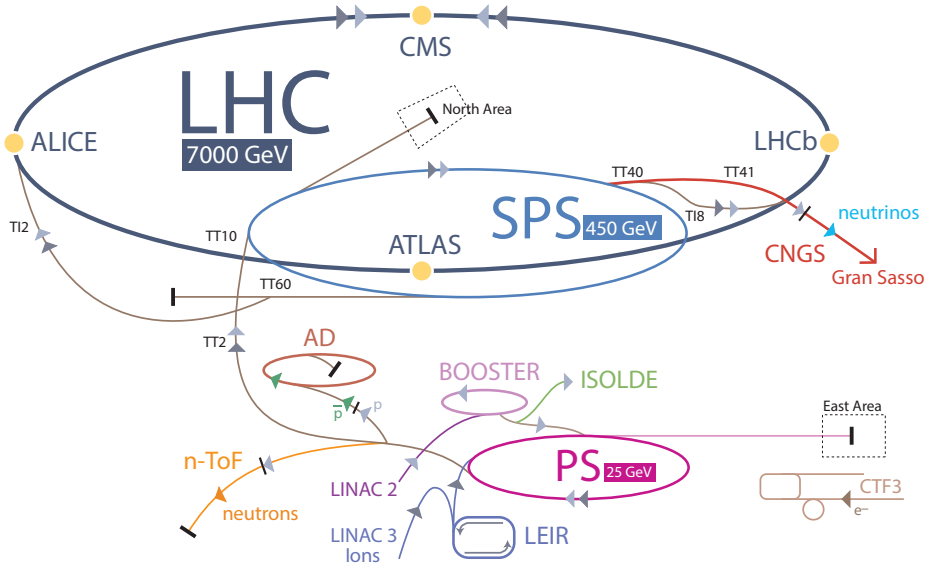

Figure 2.3.: Schematic view of the CERN accelerator complex. The maximum beam energy in the main accelerators PS, SPS, and LHC is given for protons. 7000 GeV is the LHC design energy. In case of heavy ions the values need to be corrected for the ratio Z/A (based on [CER06]).

The re-usage of the LEP tunnel and some of the underground caverns, L3/LEP for ALICE/LHC and OPAL/LEP for LHCb/LHC, was chosen for cost and time effectiveness. However, the infra-structure optimized for the electron-positron machine added extra constraints to the LHC design. Due to the limited size of the tunnel in the arcs, it has been easier to use a compact magnet design for the bending dipoles. They house the two rings of the LHC in one superconducting magnet with design field strength of 8.33 T. One disadvantage of this design is that, unlike at RHIC, the two rings are magnetically coupled and cannot be operated independently.

One of the main physics objectives of the LHC is the study of proton-proton collisions to discover the last missing elementary particle of the Standard Model, the Higgs boson, and to search for physics beyond the Standard Model. The two largest experiments at the LHC, ATLAS and CMS, have been specifically designed for this purpose. In 2012, they reported evidence for the discovery of a new boson at a mass of 125 GeV/c^2 consistent with a Standard Model Higgs [CER12, Aad12, Cha12c].

During standard LHC running, about one month per year is dedicated to heavy-ion operation. The integrated luminosities recorded by the ALICE experiment in the first two running

periods with Pb + Pb collisions are listed in Table 2.2.

The experimental setup of ALICE is shown in Figure 2.4. It can be subdivided into the detectors of the central barrel and the muon arm. The detectors of the central barrel are located inside the L3 solenoid magnet with a 0.5 T field, they are shown in a cross sectional (beam) view in Figure 2.5 a).

The deflection of charged particles in the magnetic field facilitates the momentum measurement in the tracking system of the central barrel. It is divided into the Inner Tracking System (ITS), the Time Projection Chamber (TPC), and the Transition Radiation Detector (TRD). The ITS consists of six cylindrical layers of silicon detectors, with distances from the beam axis between $r = 3.9\,\text{cm}$ and $r = 43\,\text{cm}$ and provides track points close to the primary vertex. The two innermost layers are Silicon Pixel Detectors (SPD), followed by two layers of Silicon Drift Detectors (SDD) and two layers Silicon Strip Detectors (SDD). The digital SPD information provides a precise measurement of the primary vertex position and of secondary vertices from heavy flavor decays. The four outer detectors of the ITS have analog readout for particle identification via specific energy loss ($\mathrm{d}E/\mathrm{d}x$) in the detector. The TPC, a cylindrical drift detector surrounding the ITS, is the main tracking detector in ALICE. The TPC inner radius is 85 cm, and the outer radius is 247 cm, with longitudinal coverage $-250 < z < 250\,\text{cm}$. It has been optimized for reliable performance at highest particle densities, of the order of 10 000 particles in the acceptance, and provides a uniformly high tracking efficiency for charged particles in the pseudo-rapidity region of $|\eta| < 0.9$ and full azimuth. Furthermore, the TPC can serve as a detector for particle identification with a $\mathrm{d}E/\mathrm{d}x$ resolution of better than 7% [Abe12b]. The high precision of the ITS and the large radial lever arm of the TPC provide a good momentum resolution for combined (*global*) tracks, that is further improved at high momentum by the outermost TRD. The tracking capabilities of the ALICE detector are exemplified in Figure 2.5 b), where the invariant mass of two electron-positron pairs is shown. These pairs originate from photon conversions in the detector material and are selected via their displaced vertex, pointing angle to the primary vertex, and electron identification cuts. The high efficiency and good mass resolution for the reconstruction of neutral mesons through the four conversion particles is enabled by the uniformly high efficiency for single particles, excellent momentum resolution and particle identification of the ALICE tracking detectors.

In addition to the specific energy loss measurements in the ITS and TPC, particles in the central barrel can be identified via time-of-flight measurements in the TOF detector and Cherenkov radiation in the HMPID. In the TRD, electrons are separated from pions via the

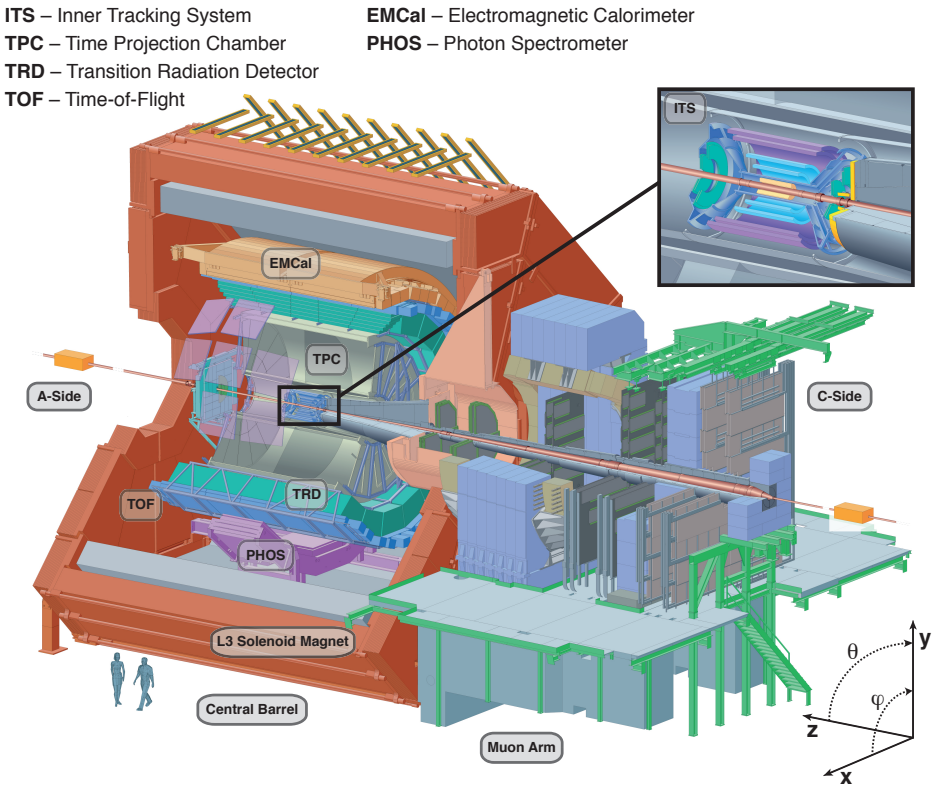

Figure 2.4.: Perspective view of the ALICE experiment and definition of the ALICE coordinate system. It is centered at the nominal collision point in the ITS, with the Muon arm in the negative z-direction (Based on [Aam08]).

characteristic *transition radiation*, in addition to their energy loss via ionization. Electrons can also be identified via energy-momentum matching of tracks and clusters reconstructed in the calorimeters PHOS and EMCal. The PHOS detector is a high granularity electromagnetic spectrometer at a distance of 4.6 m. It uses cooled lead-tungstate crystals with a $2 \times 2\,\mathrm{cm}$ cross sections and extends over $|\eta| < 0.12$. The installed three modules cover $\Delta\varphi \approx 60^\circ$ as shown in Figure 2.5. The EMCal is a Pb-scintillator sampling calorimeter with projective cells ($\Delta\eta \times \Delta\varphi \approx 0.025 \times 0.025$). It covers a pseudo-rapidity of $|\eta| < 0.7$ and $\Delta\varphi \approx 107^\circ$ and has been proposed as an addition to ALICE in 2006 [Cor06]. With its large acceptance compared to PHOS, it facilitates the measurement of the electromagnetic component of jets.

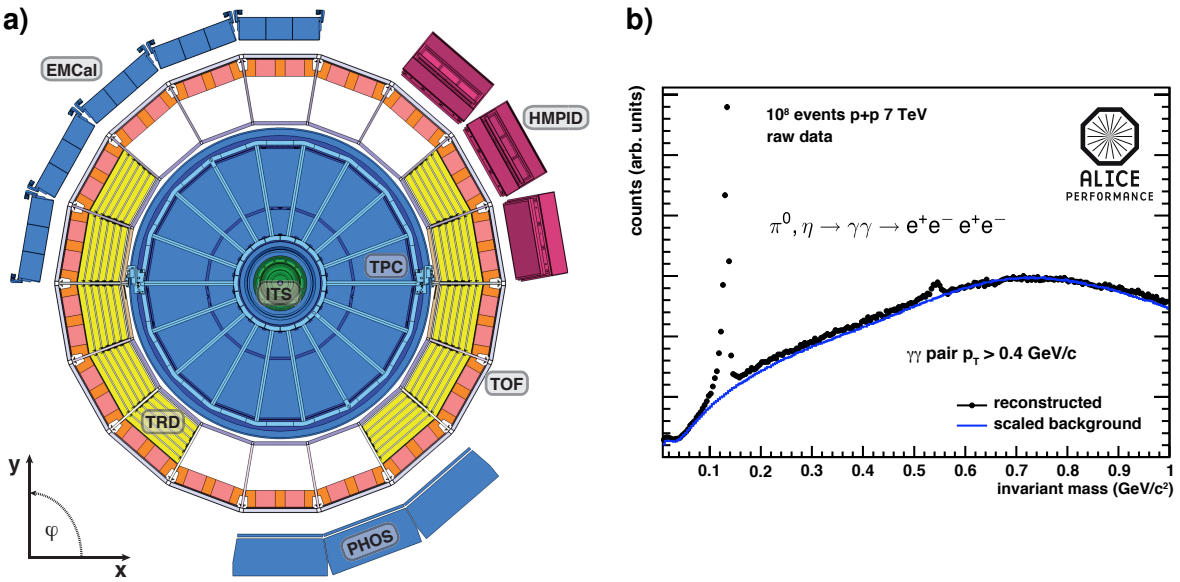

Figure 2.5.: a) Cross section of the ALICE central barrel viewed from the A-side. The detectors correspond to the installed systems during data taking in 2011. b) Example for ALICE tracking capabilities in the measurement of neutral mesons via the tracking of photon conversion pairs.

2.2. QCD Vacuum

The discovery of a new state of matter created in heavy-ion collisions relies on the detailed understanding of the baseline measurement; nuclear reactions where it is not expected that a partonic medium will be formed (QCD *vacuum*). The most important reference measurements in this context are obtained in proton-proton collisions. They need to be scaled appropriately to account for the increased number of individual nucleon-nucleon reactions in a heavy-ion collision.

2.2.1. Particle Production

Particles are produced in nuclear collisions via inelastic reactions of the incoming nucleons. For inelastic pp and $\mathrm{p\bar{p}}$ reactions, the total cross-section changes only slowly above $\sqrt{s} \approx 10\,\mathrm{GeV}$: over almost three orders of magnitude in collision energy it increases by little more than a factor of two from $\sigma_{\mathrm{inel}} \approx 32\,\mathrm{mb}$ to $\sigma_{\mathrm{inel}} \approx 73\,\mathrm{mb}$ at 7000 GeV [Ant13].

The energy lost by the incoming nucleons in the reaction is transformed into the production of particles (mostly pions). These produced particles are characterized via their rest mass m_0

and momentum $\vec{p}$, which can be separated into a transverse component p_{T}, perpendicular to the direction of the incoming particles, and a longitudinal component p_{L}. Instead of p_{L}, it is convenient to introduce the rapidity y as described in Appendix A. It is a measure of the longitudinal momentum for a given particle mass and additive under Lorentz transformation. In the limit $p \gg m_0$, the rapidity can be approximated by the pseudo-rapidity η, which only depends on the angle with respect to the beam-axis.

The transverse momentum is by definition invariant with respect to Lorentz transformation along the beam axis and is a direct measure for the momentum transfer Q^2 in a reaction. Based on this, particles produced in nuclear collisions can be separated via their p_{T} into two regimes: *hard* particles with large transverse momentum originate from reactions with a large $Q^2 > (2\,\mathrm{GeV}/c)^2$, sufficient to resolve the partonic structure of the nucleons. *Soft* particles with significantly lower transverse momentum dominate the total number of produced particles, as seen in Figure 2.6 for the p_{T}-differential invariant cross section of pion production in pp collisions measured by PHENIX and ALICE at different collision energies.

The average multiplicity of particles produced at central rapidity $\mathrm{d}N/\mathrm{d}\eta|_{\eta=0}$ increases by a factor of two going from $\sqrt{s} = 10\,\mathrm{GeV}$ to 7000 GeV. The combined effect of the increase in total cross section and produced particles leads to the modest separation of the spectra at low p_{T} visible in Figure 2.6.

The particle production at low transverse momentum shows an exponential shape that is very similar for all energies. It can be described empirically with:

$$E\frac{\mathrm{d}^3\sigma}{dp^3} \propto e^{-\alpha p_{\mathrm{T}}}, \tag{2.2}$$

where the slope parameter $\alpha \approx 6/(\mathrm{GeV}/c)$ varies only little with the collision energy. The interactions in this region are characterized by momentum transfers of the order of the QCD scale parameter λ, and one has to resort to phenomenological models to describe the particle production. E.g. via longitudinal excitation of the protons in form of a quark-diquark string. The energy stored in the string increases with the separation and is converted into hadrons via creation of quark-antiquark pairs. While the longitudinal momentum of such a string increases with $\sqrt{s}$, resulting in a broader rapidity distribution, the transverse momentum is limited by the radius of the flux tube and the small initial momentum transfer.

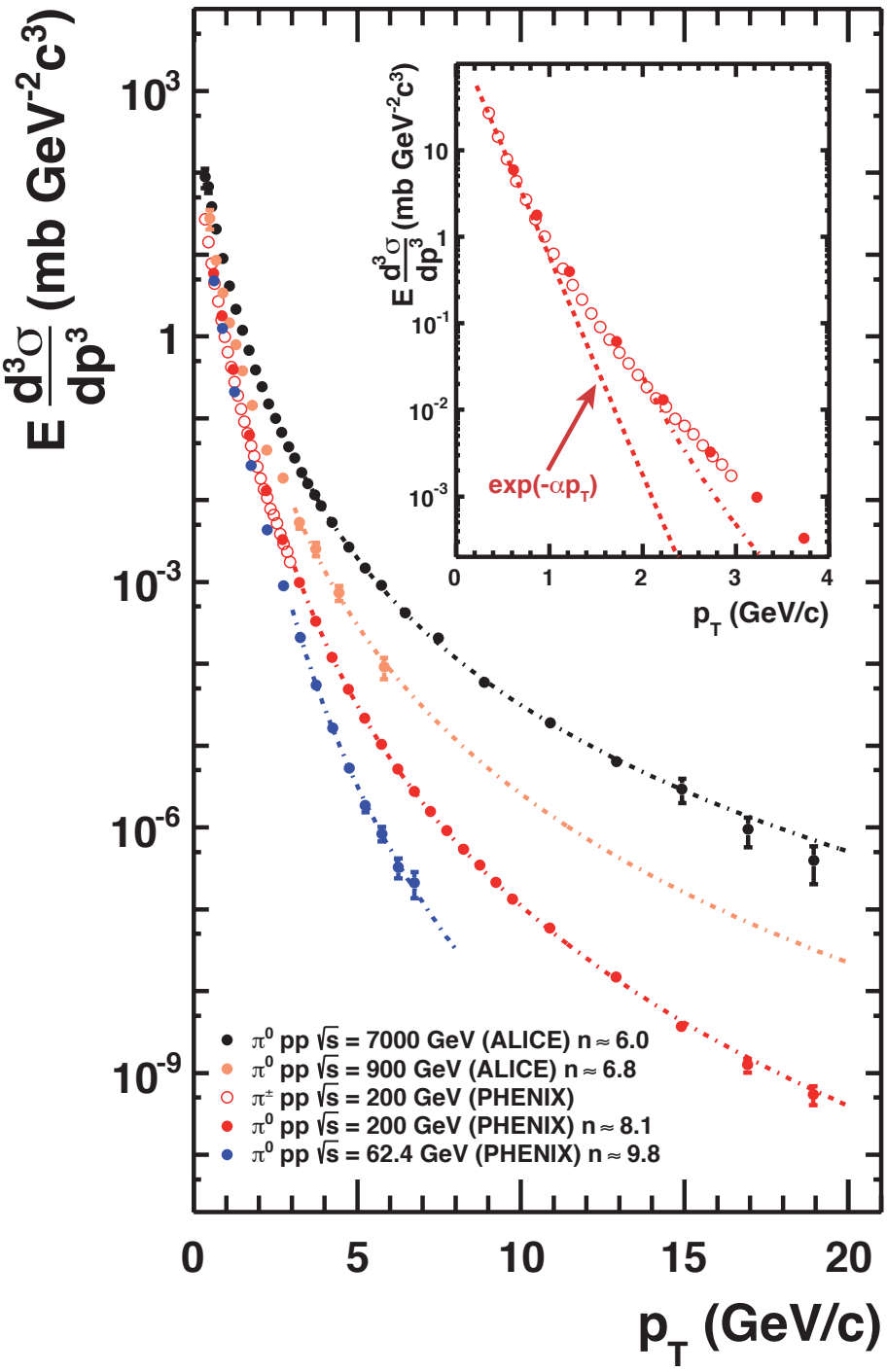

Figure 2.6.: Invariant cross section of pions produced in pp collisions at $\sqrt{s}$ =62.4, 200, 900 and 7000 GeV [Ada07b, Ada09, Ada11, Abe12a]. All data are fit to a power law p_{T}^{-n} above 2 GeV/c. The data at 200 GeV are also fit to an exponential for $p_{\mathrm{T}} < 1\,\mathrm{GeV}/c$ according to Equation (2.2) with $\alpha = 6/(\mathrm{GeV}/c)$ (see inset).

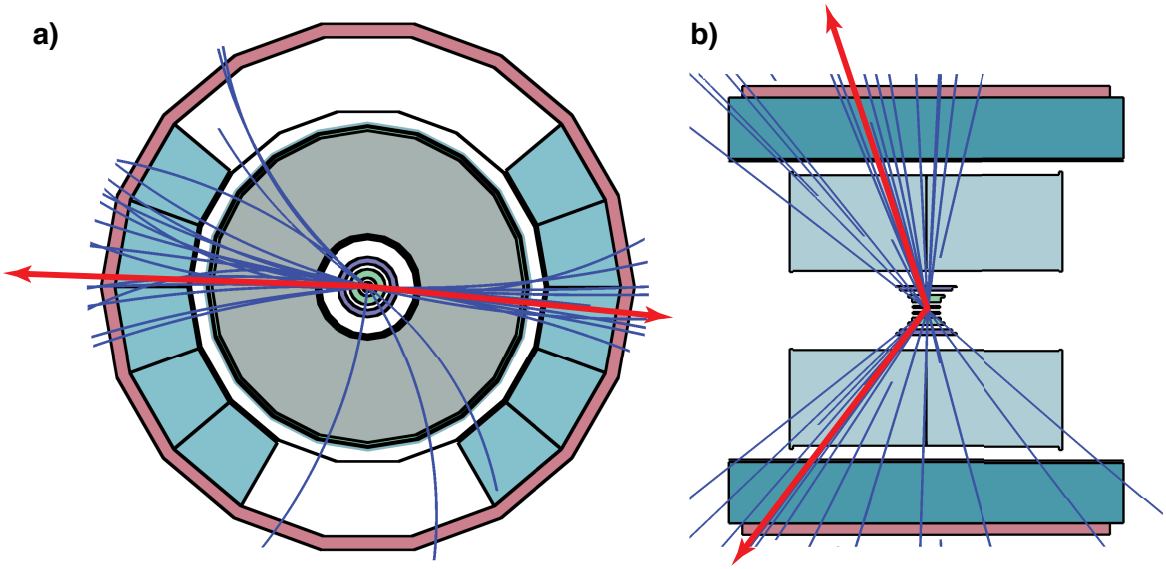

Figure 2.7.: Event display of tracks measured by ALICE in a pp collision at 7000 GeV. Reconstructed tracks are shown with their curvature in the magnetic field which is perpendicular to the *xy*-plane. The directions of two reconstructed jets are indicated by the red arrows. a) projection in *xy* as viewed from the A-side. b) Cross sectional view along the beam axis with tracks projected into the *rz*-plane.

2.2.2. Hard Processes

The momentum region above $p_{\mathrm{T}} > 2\,\mathrm{GeV}/c$ in Figure 2.6 shows a clear deviation from the exponential fall-off and the spectral shape is better characterized by a power law:

$$E\frac{\mathrm{d}^3\sigma}{dp^3} \propto p_{\mathrm{T}}^{-n}. \tag{2.3}$$

At large p_{T} ($\gtrsim 2\,\mathrm{GeV}/c$) the momentum transfer in the reaction is at least of the same magnitude and thus sufficiently large to resolve the partonic substructure of the nucleons. Here, the inelastic scattering of the nucleons can be described in the framework of perturbative QCD in terms of the scattering of the pointlike, asymptotically free partons (quarks and gluons) inside the nucleons that lead to *jets* of observable, color-neutral particles produced along the direction of the scattered partons as seen in Figure 2.7. The characteristic time and length scales of the parton-parton interaction, $\tau \propto \hbar/\sqrt{Q^2} \ll 0.1\,\mathrm{fm}/c$, are short compared to those of the soft interactions between the bound partons in the initial state and of the fragmentation process of the scattered partons in the final state. Therefore the hard inelastic cross

section for the production of a given hadron h can be factorized [Col85]:

$$E\frac{\mathrm{d}^3\sigma^{\mathrm{hard}}_{\mathrm{NN}\to\mathrm{h}}}{\mathrm{d}p^3} = \sum_{a,b,c} f_a(x,Q^2)\otimes f_b(x,Q^2) \otimes\frac{\mathrm{d}\hat{\sigma}^{\mathrm{hard}}_{ab\to c+X}}{\mathrm{d}^3\hat{p}}\otimes D_{c/h}\,(z,Q^2). \tag{2.4}$$

The different factors are:

- The non-perturbative distribution functions (**PDFs**) $f(x,Q^2)$ of partons in the two colliding nucleons. They only depend on the momentum transfer and the parton momentum fraction x in the nucleon and can be determined in deep-inelastic electron-nucleus reactions as shown in Figure 2.8;
- The short-distance, **partonic cross section** for the production of parton c, $ab\to c+X$. Since the coupling is small at large momentum transfer cross section it is calculable perturbatively up to a given order in α_{S};
- The universal but non-perturbative fragmentation function (**FF**) $D_{c/h}(z,Q^2)$ of the scattered parton c into hadron h that carries the fraction $z=p^h/\hat{p}^c$ of the parton momentum. They also need to be determined experimentally. If a photon is produced at leading order, the fragmentation function reduces to a $\delta(1-z)$ function.

Parton Distribution Functions

The increase of the differential cross section by several orders of magnitude at high p_{T} as seen in Figure 2.6 can be understood with the larger band-width of incoming parton p_{T} for increasing $\sqrt{s}$. For a fixed available energy in the partonic system, $\sqrt{\hat{s}}=x_1x_2\sqrt{s}$, smaller x with higher parton density contribute, as seen in the parton distribution functions of Figure 2.8. This is tantamount to an increase of the effective parton luminosity.

The parton distribution functions can change when a nucleon is bound in a nucleus. This nuclear modification of the initial state can have a direct impact on the yield of observable final state particles and has been measured in deep-inelastic scattering by comparison of nuclear structure functions for deuterium to heavier ions. The largest variation is a depletion by up to $\approx 20\%$ in the region of $0.5<x<0.8$ (EMC-Effect) [Aub83]. In the x-region below 0.1, also a depletion has been observed which is generally called *shadowing*. The latter may be an indication for saturation effects in the nucleus. As seen in Figure 2.8 b), the gluon density at a given x rises rapidly with increasing resolution Q^2 of the virtual photons.

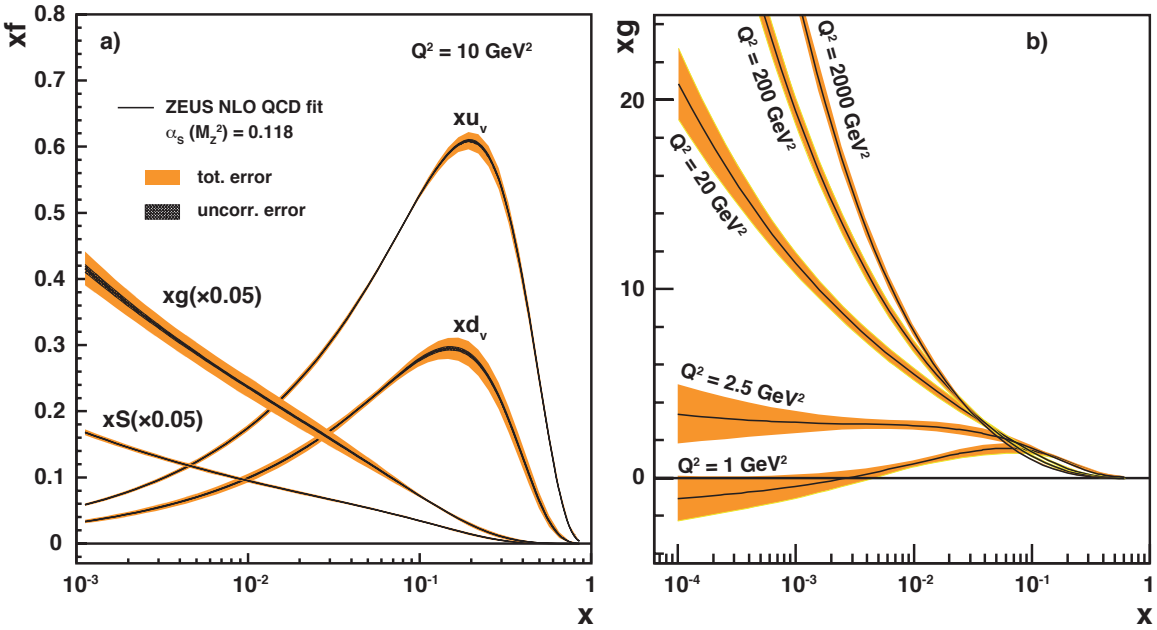

Figure 2.8.: The parton densities $x \cdot f$ determined by a NLO QCD fit to ZEUS data from deep-inelastic electron-proton scattering [Che03]. a) Densities of valence u- and d-quarks (u_v and d_v), gluons (g), and sea quarks (S) for a fixed Q^2 b) gluon densities for different resolution of the virtual photon or momentum transfer Q^2.

For increasing $\sqrt{s}$ this would cause a more rapid increase of the total cross section than allowed by very general arguments invoking unitarity (Froissart bound [Fro61]). A solution is provided in the framework of gluon saturation models, e.g. the *Color-Glass Condensate* (CGC) [Ian03]. Its basic idea is that at sufficiently large gluon densities, the separation between the gluons is so small that they can fuse ($gg \rightarrow g$), which leads to a saturation of gluon densities at small x. These saturation effects become more important for heavy-nuclei since the saturation scale Q_S depends on the number of gluons seen by a probe traversing a nucleus A, i.e. the gluon density per transverse area, which is proportional to $A^{1/3}$. In the limit that Q_S becomes much larger than the QCD scale parameter, weak coupling techniques can be applied again to calculate the distribution of gluons in the initial state.

The relevant, probed x-region in the nucleus can be estimated by the transverse momentum of the *leading* hadron, carrying the largest momentum fraction of the original scattered parton:

$$x_\mathrm{T} = \frac{2p_\mathrm{T}}{\sqrt{s}}. \tag{2.5}$$

Thus, saturation effects are more relevant at low particle p_{T}, which dominate the total number of produced particles. Initially, saturation effects had been proposed also as a possible explanation for the suppressed production of hadrons at higher p_{T} observed in heavy-ion collisions. This assumption of a strongly modified initial state, or cold nuclear matter effect can be tested by the measurement of hadron production in proton– or deuteron–nucleus collisions and has been ruled out at RHIC in [CKB02]. These findings represent one of the major accomplishments of the author's research work during and shortly after his PhD thesis.

Parton Scattering

The combination of the incoming parton flux and the partonic cross sections yields the hard scattered partons in the outgoing channel. As already mentioned above, the effective parton flux for given parton energy increases with $\sqrt{s}$. At the same time, the relevant scattering processes change since the dominant incoming parton type changes from (valence)-quarks to gluons, which have a stronger coupling to color charges than quarks and a different angular dependence.

However, when considering fixed x_{T} and rapidity, one expects that the parton production cross section is constant in the parton model as the energy is varied, and the differential cross section changes as:

$$E\frac{\mathrm{d}\hat{\sigma}^{c}}{\mathrm{d}\hat{p}_{\mathrm{T}}\mathrm{d}\hat{y}} = \frac{1}{\hat{p}_{\mathrm{T}}^{n}} \cdot F(x_{\mathrm{T}}), \tag{2.6}$$

where $n = 4$ for scattering via exchange of a vector boson, such as in the classical Rutherford scattering [Ber71]. This separation into a momentum scale independent function $F(x_{\mathrm{T}})$ and a generic power law is referred to as x_{T}-scaling. Scaling violations occur in QCD due to the running of the coupling constant α_{S}, scaling violations in the parton distributions, and intrinsic transverse momentum of the partons in the nucleon.

Momentum conservation dictates that in the case of $2 \rightarrow 2$ processes, the outgoing partons are separated in φ by 180° and are balanced in transverse momentum. This leads to the characteristic correlation of particles in a di-jet event as seen in Figure 2.7. The exact symmetry is modified at the parton level due to intrinsic transverse momentum of the incoming partons and higher order effects, such as additional initial and final state radiation. In the longitudinal direction, the parton system is boosted with respect to the center-of-mass system of the colliding nucleons by $y = \ln(x_1/x_2)$, so the recoiling jet is not fixed opposite in rapidity as can also be seen in the reconstructed jet directions in Figure 2.7.

Hadronic Cross Section

The scattered outgoing partons fragment into observable, color neutral objects. This process is summarized effectively in the fragmentation function. It can be described in part via the perturbative evolution of a *parton shower*, that is the subsequent splitting of the initial parton into partons of successively lower energy; down to a point where perturbative techniques are no longer applicable. The strong scale dependence of the coupling ensures that large angle splittings (high Q^2) are suppressed compared to partons radiated under a small angle, leading to the strong collimation of hadrons in jets as visible in Figure 2.7. Phenomenological models such as string models, can be used again to describe the parton shower in the non-perturbative regime and the recombination of the partons into color neutral objects.

Jet algorithms take advantage of the collimated nature of particles in the parton fragmentation and use the information available at a certain stage of this process to reconstruct the momentum vector of the original parton. In the experiment this of course can only involve final state particles, while in theoretical calculations and Monte Carlo generators, such as PYTHIA [Sjo06], jet algorithms can also be applied at parton level. Jet (or parton) properties can also be studied on the single particle level, e.g. by the momentum spectrum at high p_{T} or the angular correlation of particles as visible in Figure 2.7.

A simplifying assumption in this context is the complete scaling of the fragmentation process of partons into observable hadrons. I.e. the number density $F(z)$ of fragments with fractional momentum z does not depend explicitly on the total jet momentum. In this case, the inclusive cross section for hadron production at large p_{T} is:

$$\frac{\mathrm{d}\sigma}{\mathrm{d}p_{\mathrm{T}}} = \int_{\hat{p}_{\mathrm{T}}>p_{\mathrm{T}}} \mathrm{d}\hat{p}_{\mathrm{T}} \frac{\mathrm{d}\hat{\sigma}}{\mathrm{d}\hat{p}_{\mathrm{T}}} \int_0^1 \mathrm{d}z F(z) \delta(p_{\mathrm{T}} - z\hat{p}_{\mathrm{T}}). \tag{2.7}$$

As discussed above, the parton cross section follows a power law and can be parameterized as $\mathrm{d}\hat{\sigma}/\mathrm{d}\hat{p}_{\mathrm{T}} = A/\hat{p}_{\mathrm{T}}^{n-1}$. When at a given center-of-mass energy the small $\hat{p}_{\mathrm{T}}$ dependence of A and n is neglected, Equation (2.7) simplifies to:

$$\frac{\mathrm{d}\sigma}{\mathrm{d}p_{\mathrm{T}}} = \frac{A}{p_{\mathrm{T}}^{n-1}} \int_0^1 \mathrm{d}z z^{n-2} F(z). \tag{2.8}$$

This formula exhibits two basic features of particle production originating from hard scattered partons. First, the single particle cross section has the same power law dependence as the parton cross section, this is also known as Bjorken's *parent-child relationship* [Bjo73]. The power law behavior at high p_{T} is clearly seen in Figure 2.6. Second, the factor z^{n-2} under

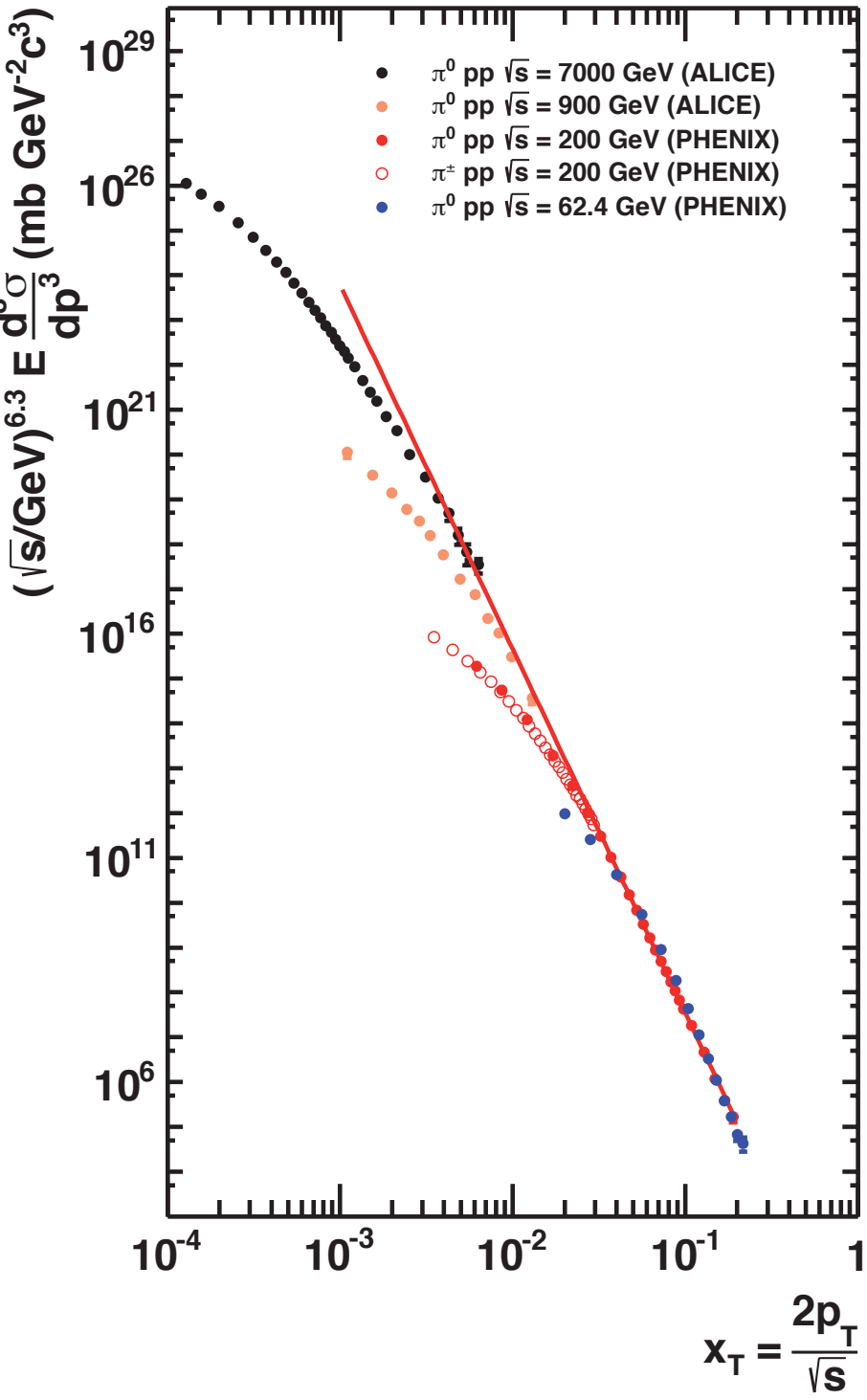

Figure 2.9.: Invariant cross section of pions as function of x_T and multiplied by $\sqrt{s}^{6.3}$ (data from [Ada07b, Ada09, Ada11, Abe12a]). The data at 200 GeV are fitted to a power law for $0.01 < x_T < 0.2$. The resulting curve is shown here over a larger range.

the integral implies that larger values of z contribute most to the single particle cross section at a given p_{T}. This is one example of a *trigger bias* [Jac76], where in this case the single particle spectrum is dominated by fragments that carry a large fraction of the original parton p_{T}: the larger the value of n the more pronounced is this bias. Thus, as seen in Figure 2.6, it is more relevant at lower $\sqrt{s}$. This kind of bias is of particular importance in the study of particle correlations and needs to be evaluated carefully in full Monte Carlo studies, which also account for violations of the simplifying assumptions above.

The parent child-relation allows one to also introduce x_{T}-scaling on the single particle level. Scaling violations can be taken into account explicitly in the exponent $n(x_{\mathrm{T}}, \sqrt{s})$ so that Equation (2.6) for single high p_{T} particles can be rewritten:

$$E\frac{\mathrm{d}\sigma^c}{\mathrm{d}p_{\mathrm{T}}\mathrm{d}y} = \frac{1}{\sqrt{s}^{n(x_{\mathrm{T}},\sqrt{s})}} \cdot G(x_{\mathrm{T}}). \tag{2.9}$$

The scaled cross section for pion production in pp is shown in Figure 2.9 using a fixed exponent, determined by comparison of spectra at $\sqrt{s} = 62.4$ and 200 GeV. The spectra approach a common curve, though it is seen that the power law is less steep for the higher collision energy.

2.3. QCD Medium

At high energies, when going from elementary nucleon-nucleon collisions to reactions of heavy nuclei, it is a good approximation to consider the individual nucleons of the incoming ions as independent due to their small de-Broglie wavelength. This implies that only the nucleons in the geometric overlap region of the nuclei interact as illustrated in Figure 2.10. These are called *participants*. In this geometric picture, their number relates directly to the impact parameter b of the collision. The nucleons outside the overlap are called *spectators* and are basically unaffected by the collision.

The interaction of the participants leads to the formation of a hot and dense region between the outgoing nuclei. As will be discussed later, the number of participants N_{part} can be directly related to the number of produced particles in a collision and is often used as a measure for centrality or size of the overlap region for comparison across different experiments or colliding systems. Depending on the degree the incoming nucleons are stopped, there are two scenarios. For large stopping, the complete kinetic energy is deposited and a baryon-rich fireball is formed. At energies $\sqrt{s_{\mathrm{NN}}} \gtrsim 10$ GeV, the stopping is limited and the nucleons become transparent. They interpenetrate each other and the baryon number remains concen-

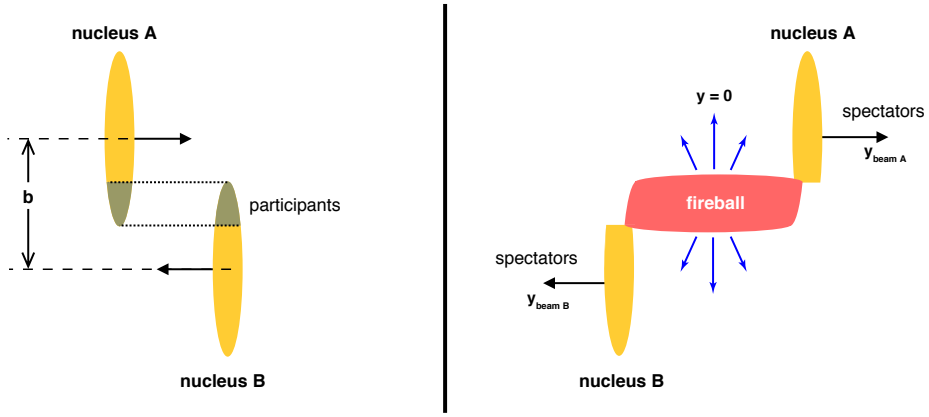

Figure 2.10.: Schematic view of the collision of two Lorentz-contracted nuclei in the geometric participant spectator model. The distance between the two centers is the impact parameter b.

trated close to beam rapidity. This *Bjorken-McLerran scenario* leads to a fireball with small baryo-chemical potential, i.e. small net-baryon density, resembling the situation shortly after the Big-Bang. The multiplicity distribution in this case is flat around mid-rapidity ($y = 0$ at colliders).

It is still one of the open question in the study of the quark-gluon plasma how exactly the initial energy is deposited and distributed in the reaction zone and how a thermal equilibration is achieved after that on time-scales smaller than 1 fm/c.

2.3.1. Medium Evolution

The models used to describe the evolution of a heavy-ion reaction can be divided into microscopic and macroscopic models. Microscopic models try to incorporate the individual interactions between all particles in the reaction. Most of these start with the description of the elementary nucleon-nucleon reaction, which is extended to large nuclei via incoherent superposition of the elementary reactions followed by the evolution of the outgoing partons and excited strings. For example in the AMPT model [Lin05], all outgoing partons are followed in a parton cascade till they reach a momentum scale where the partons need to be effectively described by strings. These freeze out into hadrons, which can further interact with each other.

Macroscopic models treat the evolution of the fireball via relativistic hydrodynamics and describe the complete system at a given point in time with a set of parameters such as tem-

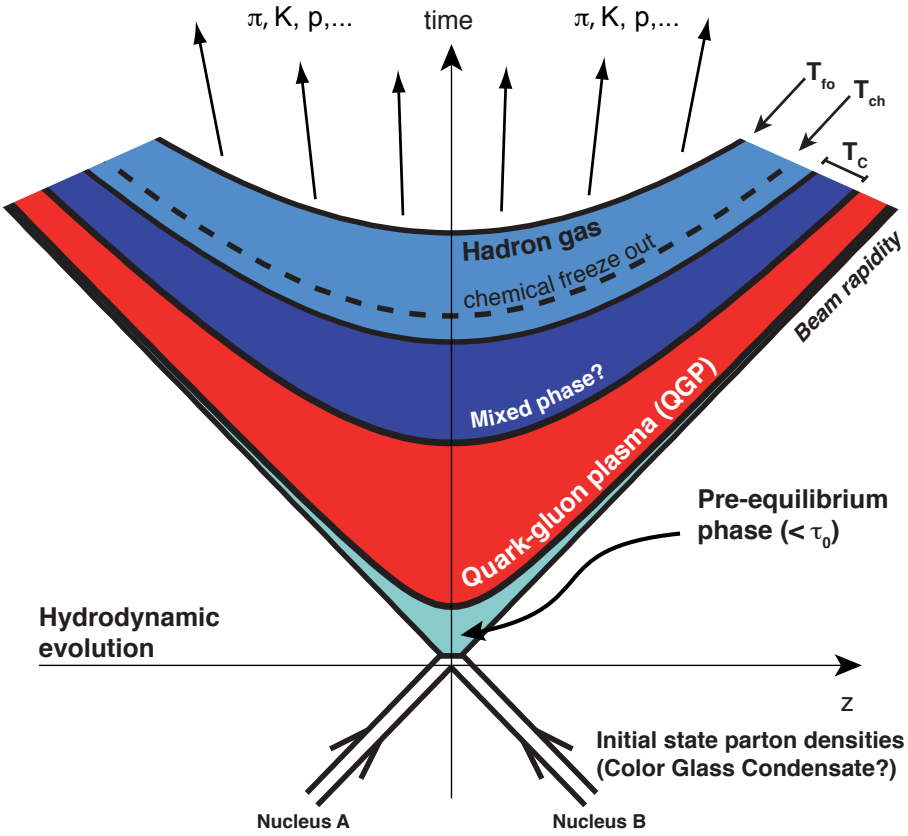

Figure 2.11.: Space time evolution of a heavy-ion collision. The different phases are separated by curves of constant proper time $\tau = \sqrt{t^2 - z^2}$.

perature T, pressure P, and baryo-chemical potential μ_B, as already discussed in the context of the critical parameters in Chapter 1.2. The evolution of the system is dictated by the initial conditions at thermal equilibration, the hydrodynamic equations of motions, and the equations of state (EOSs) of the following partonic and hadronic fluids. In the EOS, pressure, energy density, and chemical potential are related and different scenarios, e.g. with or without a partonic phase, can be tested and compared to experimental data.

In the simplest case, that of a relativistic gas of massless quarks and gluons in the bag model, the EOS of the QGP is:

$$\varepsilon_{\mathrm{QGP}} = 3P_{\mathrm{QGP}} + 4B, \tag{2.10}$$

with the bag pressure $B \approx (210\,\mathrm{MeV})^4$ as discussed in Chapter 1.2. For an ideal gas of free

massless pions it is:

$$\varepsilon_{\mathrm{HG}} = 3P_{\mathrm{HG}}. \tag{2.11}$$

The EOS can also be calculated in lattice QCD; here it is usually provided over the full temperature range in form of the *trace anomaly* $I(T) = \varepsilon - 3P$, i.e. the deviation from the ideal gas of massless particles. This deviation is also present for the QGP phase in the Bag model as seen in Equation (2.10), however it dies out quickly with increasing temperature, while recent lattice calculations indicate that the trace anomaly is sizable even at at $T = 1000\,\mathrm{MeV}$, far above the critical temperature [Bor10].

The results of hydrodynamic models depend strongly on the choice of the initial conditions, inclusion of dissipative effects, and the dimension of the evolution model. E.g. in the most simple hydrodynamic picture (Bjorken or (1+1)D evolution) only the expansion of an ideal fluid in longitudinal direction is considered. Furthermore, it is currently still an open question how the initial energy deposit in the overlap region is distributed. I.e. whether the density profile is driven by the density of the incoming nucleons (*Glauber* initial conditions) or by the saturated gluon density profile of a color-glass condensate.

The space time evolution of two colliding nuclei is illustrated in Figure 2.11. In the initial interaction of the nuclei, the same hard scatterings occur as in elementary pp-reactions, but the majority of energy is deposited in the reaction zone via soft processes and the reaction zone contains highly excited matter far off thermal equilibrium. After thermalization of the system at a time τ_0 and for a high enough initial temperature, a quark-gluon plasma is formed. The combination of EOS and the hydrodynamic equations of motion for the partonic or hadronic system then describes the evolution of the medium. The system expands into the QCD vacuum and cools down until the partons recombine into hadrons. In case of a first order phase transition this hadronic freeze-out at the critical temperature T_{C} is connected with a latent heat and goes via a mixed phase into a hot hadronic gas. In the hadronic phase, the chemical composition, that is the abundance of different hadron species, is not changed after a certain energy density is reached at the chemical freeze-out temperature T_{ch}.

The conditions at the chemical freeze-out are accessible via the measured ratios of various identified particle species. These can be compared to the expectations from a thermal, statistical model. It uses the partition function of a Grand-Canonical ensemble with only the temperature and the (baryo)-chemical potential μ_{B} as free parameters [BM03]. For heavy-ion collisions at RHIC, the extracted chemical freeze-out conditions approach the phase boundary $T_{\mathrm{ch}} \approx 160\,\mathrm{MeV}$ at vanishing net-baryon number [And06]. The chemical freeze-out temperature cannot exceed the critical temperature for a phase transition, since it is determined

in the hadronic phase. This can be compared to a temperature measurement in the liquid phase of water, which cannot exceed 100 °C under normal conditions.

The final step in the reaction is the complete decoupling (*freeze-out*) of hadrons, when the system is diluted by the expansion such that also elastic scattering between the hadrons ceases and it can no longer be described in terms of macroscopic parameters. The temperature for this kinetical freeze-out can be determined with the transverse momentum spectra of identified particles at low p_{T} via *blast wave* fits [Sch93]. Here, the particles are assumed to originate from a thermal source in a common, radial velocity field (see Chapter 3.3.1).

2.3.2. Particle Production and Initial Energy Density

One of the most basic questions to answer in the study of heavy-ion collisions is whether the necessary condition for the creation of a quark-gluon plasma is fulfilled: an initial energy density ε_0 that exceeds the critical density of $\varepsilon_{\mathrm{C}} \approx 1\,\mathrm{GeV/fm^3}$ predicted via simplistic bag models as well as in lattice QCD calculations [Kar03].

Following the prescription of Bjorken [Bjo83], the initial energy density can directly be related to the rapidity-density of produced particles or the transverse energy deposited at mid-rapidity:

$$\varepsilon_{\mathrm{Bj}} = \frac{\langle m_{\mathrm{T}} \rangle}{A \cdot \tau_0} \cdot \left.\frac{\mathrm{d}N}{\mathrm{d}y}\right|_{y=0} = \frac{1}{A \cdot \tau_0} \cdot \left.\frac{\mathrm{d}E_{\mathrm{T}}}{\mathrm{d}y}\right|_{y=0}, \tag{2.12}$$

where τ_0 is the formation time of the medium after the energy deposit of the incoming nuclei and A their overlap area. Equation (2.12) is derived using the correspondence between rapidity and spatial coordinate $z = \tau \sinh y$ ($\mathrm{d}z/\mathrm{d}y = \tau \cosh y$). This relation indicates that for a given proper time a small value of rapidity corresponds to a small value of z (see also Figure 2.11). Thus it connects the measured rapidity density at mid-rapidity to the density around $z = 0$ at τ_0 in the spatial volume $A\mathrm{d}z$. Finally, the relation to the energy density is made assuming that the energy deposit of all quanta in this volume is additive and that the energy of a particle at a given rapidity is $E = m_{\mathrm{T}} \cosh y$.

It needs to be emphasized that the parameter τ_0, the proper time at which the system is thermalized, is a-priori unknown. It can be constrained e.g. from generic considerations, based on the uncertainty principle, using the time needed to form initial quanta of average transverse mass $\langle m_{\mathrm{T}} \rangle$. A confirmation whether the system achieved thermalisation at all is provided by hydrodynamic models that describe the collective behavior of particles observed in heavy-ion collisions as will be discussed later. These require typical formation times of $0.2 - 1\,\mathrm{fm}/c$ where $1\,\mathrm{fm}/c$ is often used as a conservative upper bound and common value to

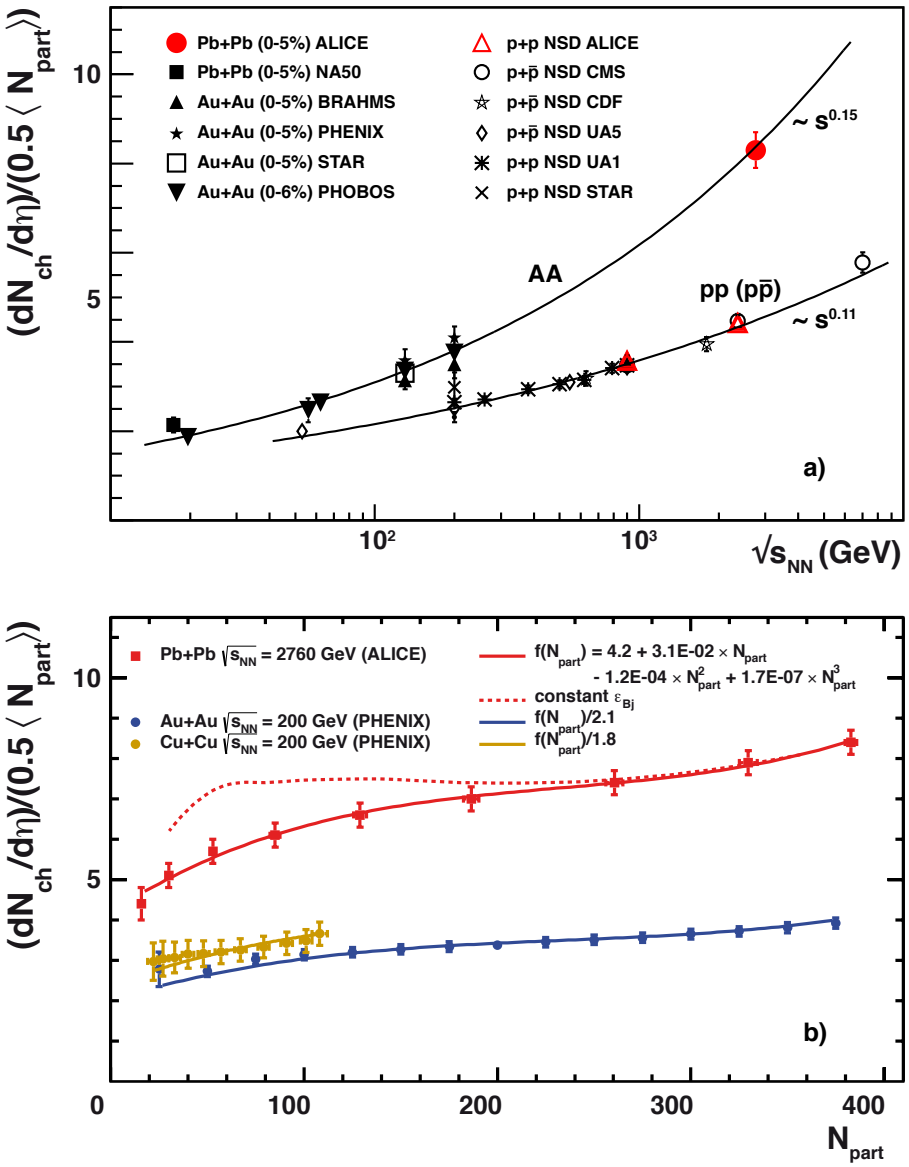

Figure 2.12.: a) Charged particle multiplicity density per participant pair in nucleon-nucleon and central heavy-ion collisions for different energies. b) Comparison of the centralitiy dependence in $\mathrm{Pb}+\mathrm{Pb}$ collisions at the LHC [Aam11a] and in $\mathrm{Cu}+\mathrm{Cu}$ and $\mathrm{Au}+\mathrm{Au}$ collisions at RHIC [Adl05c, Alv11]. The function $f(N_{\mathrm{part}})$ is fit to the $\mathrm{Pb}+\mathrm{Pb}$ data and scaled to the lower energy data. The dashed line indicates the N_{part} dependence for a constant energy density (fixed in central collisions) according to Equation (2.12), the relation is determined by the change of the overlap area A.

estimate the increase of energy density between different experiments and colliding energies. However, at energies $\sqrt{s_{\mathrm{NN}}} \lesssim 20\,\mathrm{GeV}$, the Lorentz contracted nuclei still overlap for this value at $z = 0$, which further complicates the interpretation at low energies.

The rapidity density of transverse energy and charged particles has been measured by PHENIX at energies from 19.6 to 200 GeV [Adl05c]. At the maximum RHIC energy of $\sqrt{s_{\mathrm{NN}}} = 200\,\mathrm{GeV}$, the energy density in central $\mathrm{Au} + \mathrm{Au}$ collisions can be estimated to:

$$\varepsilon_{\mathrm{Bj}}(\tau_0 = 1\,\mathrm{fm}/c) = 5.4 \pm 0.6\,\frac{\mathrm{GeV}}{\mathrm{fm}^3}. \tag{2.13}$$

This lower limit on the initial energy density significantly exceeds the critical energy density. Thus, the necessary condition for the creation of a quark-gluon plasma is fulfilled. Based on similar measurement by the CMS experiment at the LHC, the energy density in central $\mathrm{Pb} + \mathrm{Pb}$ collision at $\sqrt{s_{\mathrm{NN}}} = 2760\,\mathrm{GeV}$ increases to $\varepsilon_{\mathrm{Bj}}(\tau_0 = 1\,\mathrm{fm}/c) = 14\,\frac{\mathrm{GeV}}{\mathrm{fm}^3}$ [Cha12b]. Assuming the temperature dependence of an ideal relativistic gas $\varepsilon \propto T^4$, this corresponds to a 30% increase of the initial temperature. Thus, the system created at the LHC is expected to remain in the QGP phase significantly longer.

Compared to pp collisions the total particle production in heavy-ion reaction is expected to increase roughly with the number of wounded, or participating nucleons N_{part} [Bia76]. Since the total number of produced particles in elementary nucleon-nucleon collisions as well as in heavy-ion collisions is dominated by the particles at low transverse momentum, this scaling behavior is in general assumed for soft processes. This linear dependence of the particle production on N_{part} implies that for more central collisions the number of produced particles is significantly larger than in peripheral. In the determination of the energy density, this increase is canceled to some extent by the larger overlap area. However, the particle production mechanisms are also expected to change when going from elementary pp to central heavy-ion collisions. In the latter case, the particle production can be affected e.g. by thermal sources. Furthermore, the energy deposition at mid-rapidity is presumably more effective. As discussed above, at the same time, the saturation of initial state gluons or shadowing of nuclear PDFs, respectively, is more pronounced in heavy ions, which may limit the increase.

The particle production in different systems and for different centralities is often compared by taking out the presumed linear dependence on N_{part}. The different production mechanisms and intial state effects for proton-proton and central heavy-ion reactions are reflected in the different energy dependence of particle multiplicity per participant pair as shown in Figure 2.12 a). The particle production in heavy-ion collision is generally more effective at a given energy and the separation increases with higher energy. The centrality dependence

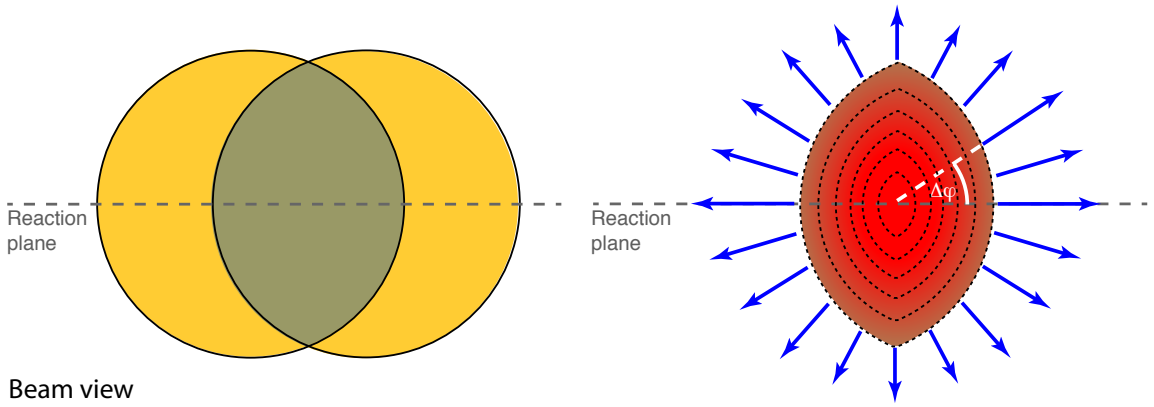

Figure 2.13.: Spatial anisotropy in the geometric picture of a non-central collision and illustration of the resulting anistropy in momentum space due a larger pressure gradient in direction of the reaction plane (dashed lines indicate isobars).

of charged particle production in heavy-ion collisions at RHIC and LHC is shown in Figure 2.12 b). It is remarkable that both can be described by the same functional form and are related by a simple scaling factor. This observation points to similar processes dominating the particle production at the same N_{part}. The decrease towards peripheral events in both cases is interpreted as the decrease in energy density. Thus, the selection of a given collision centrality allows, to some extent, for the variation of the initial temperature of the system.

2.3.3. Collective Flow

The estimate of the initial energy density presumes that the system created in heavy-ion collisions can be described via an expanding relativistic fluid. To validate this hydrodynamic picture of the medium evolution, the observation of collective dynamics is essential. The first indication of collective behavior is the observation of radial flow: the isotropic boost of particles from a thermal source in a common radial velocity field. It leads to a characteristic mass ordering of particle spectra at low p_{T}. It is discussed in more detail in the context of nuclear modification of momentum spectra in Chapter 3.3.

More sensitive observables to the hydrodynamic properties of the medium are provided by its response to pressure gradients induced by initial asymmetries of the deposited energy. These are e.g. reflected in the *elliptic flow* of produced particles in off-central heavy-ion collisions. As seen in Figure 2.13, an impact parameter $b > 0$ leads to an asymmetric, almond-shaped, overlap region. In a thermalized medium a pressure builds up in the center, which

falls off to zero at the edges. This gives rise to pressure gradients that are largest in direction of the *reaction plane* spanned by the impact parameter vector and the beam axis. The pressure gradient transforms the initial spatial anisotropy to an anisotropy in momentum space; during the collective expansion of the medium particles in-plane experience a larger boost than perpendicular to it (out-of-plane). The magnitude of this elliptic flow is characterized by the second Fourier coefficient v_2 of the azimuthal modulation of the particle momentum distribution with respect to the reaction plane:

$$\frac{\mathrm{d}^2N}{\mathrm{d}(\Delta\varphi)\mathrm{d}p_\mathrm{T}\mathrm{d}y} = \frac{\mathrm{d}N}{\mathrm{d}p_\mathrm{T}\mathrm{d}y} \cdot (1 + 2 \cdot v_2(p_\mathrm{T}) \cdot \cos(2\Delta\varphi)) \,. \tag{2.14}$$

At RHIC energies, the measured elliptic flow below $p_\mathrm{T} \approx 2\,\mathrm{GeV}/c$ reaches a value that is compatible with predictions from hydrodynamic calculations for a nearly perfect fluid with minimal shear viscosity. Dissipative effects are characterized by the dimensionless ratio of shear viscosity to entropy density η/s which has an extremely small value, with current estimates of $1 < 4\pi\eta/s < 2.5\pi$ [Son11]. Such a small value is close to the universal quantum bound of $\eta/s \geq 1/(4\pi)$ conjectured in *gauge/gravity dual models* [Pol01, Kov05]. This duality allows one to solve specific problems of strongly coupled conformal field theories in weakly coupled gravity Anti-de-Sitter Space (*AdS/CFT correspondence*, see review in [Aha00]).

Such a small viscosity requires a short mean free path among the interacting quanta, which can only be reached in a strongly coupled quark-gluon plasma (sQGP), which is in contrast to the simplified initial picture of the QGP as an ideal gas of non-interaction quarks and gluons [BNL05]. This non-ideal behavior of the QGP is also seen in lattice QCD and perturbative calculations as finite trace anomaly and the deviation from the Stefan-Boltzmann limit of the energy density even at temperatures well beyond 1000 MeV [Fod07, Bor10].

Higher Flow Coefficients

For a smooth distribution of matter as suggested by the purely geometric picture of a heavy-ion collision in Figure 2.13, the symmetry of the system and the resulting angular dependence are solely defined by the direction of the reaction plane ψ_RP. Here, only higher odd harmonics of the second moment with respect to this plane would be observable. However, on an event-by-event basis the symmetry is not fulfilled; e.g. the finite number of participating nucleons as seen in Figure 2.14 may lead to independent, odd and even symmetry planes of higher order, with corresponding variations of the pressure gradients. One can define corresponding

flow coefficients for each symmetry plane:

$$v_n = \langle \cos [n \cdot (\varphi - \psi_n)] \rangle \tag{2.15}$$

where n is the order of the harmonic, φ is the azimuthal angle of the particle and ψ_n the angle of the n-symmetry plane of the initial state, e.g. $n = 3$ for triangular symmetry. The centrality dependence of these additional flow components provides further constraints on the EOS of the system, the value of η/s, and the initial conditions of the hydrodynamic evolution. This is of particular importance, since the mechanisms with which the initial energy deposit is converted into a thermalized medium remain uncertain, e.g. if nuclear densities or a color-glass condensate drive the initial energy deposit.

An independent method to test the evolution and properties of the medium is provided by hard probes. These are produced early in the collisions and can be attenuated by the strongly coupled QGP as discussed in the following.

2.4. Probing the QCD Medium

In heavy-ion collisions, hard scattering of partons occurs in the initial stage of the reaction ($\tau \approx 1/\sqrt{Q^2} < 0.1\,\text{fm}/c$), before a thermalized medium is established as sketched in Figure 2.11. These scattered partons provide a self-generated, color-charged probe of the QGP. This probe is well calibrated since the initial hard scattering cross section is calculable in perturbative QCD and can be verified to high precision with measurements in (vacuum) pp reactions.

The presence of a strongly interacting medium is expected to modify the structure and correlation of the colorless particles that originate from the initially scattered parton. In particular, the energy loss of the scattered parton in the medium is expected to lead to a suppression of the particle production at high p_T compared to pp-reactions, the *jet quenching*.

2.4.1. Nuclear Modification Factor

The main observable to study the phenomenon of jet quenching starting with its discovery has been the nuclear modification factor (R_{AA}) of single particles at high transverse momentum. As discussed in the context of particle production in pp, these particles can be considered as proxies for the leading partons in the jet fragmentation, which are affected most by the energy loss in the medium. R_{AA} compares the particle production in pp and AA and is a measure for

the transmission of hard probes through nuclear or partonic matter. Above $p_{\mathrm{T}} \approx 2\,\mathrm{GeV}/c$ it is expected to be unity in the absence of nuclear effects.

The nuclear modification factor is defined under the assumption that an AA collision is an independent superposition of nucleon-nucleon collisions and the particle production at high p_{T} is related to the pp case via a simple scaling factor that accounts for the larger number of nucleons in AA:

$$R_{AA} = \frac{\mathrm{d}^2 N^h_{AA}/\mathrm{d}p_{\mathrm{T}}\mathrm{d}y}{\langle T_{AA}\rangle_f \mathrm{d}^2\sigma^h_{pp}/\mathrm{d}p_{\mathrm{T}}\mathrm{d}y}. \tag{2.16}$$

Here, the scaling factor is the average *nuclear thickness* $\langle T_{AA}\rangle$ for a given centrality class f. It can be viewed as an integrated *nucleon luminosity* for the range of impact parameters b sampled by the centrality selection as illustrated in Figure 2.14. The distribution of impact parameters for the experimental centrality measure, as well as the nuclear thickness function $T_{AA}(b)$ for a fixed impact parameter, can be calculated in a *Glauber Model*.

2.4.2. Glauber Calculations

In the geometric Glauber Model, nucleons are distributed according to the measured nuclear density profile and considered to travel on straight line trajectories (eikonal approximation) as illustrated in Figure 2.14. The nuclear thickness and the number of inelastic, binary collisions N_{coll} are related via the effective size of the nucleon given by the inelastic nucleon-nucleon cross section σ_{NN}:

$$\begin{aligned} \langle T_{AA}\rangle_f &= \frac{\int_f T_{AA}(b)\mathrm{d}^2 b}{\int_f \left(1 - e^{-\sigma_{\mathrm{NN}} T_{AA}(b)}\right)\mathrm{d}^2 b} \\ &= \frac{\langle N_{\mathrm{coll}}\rangle_f}{\sigma_{\mathrm{NN}}}. \end{aligned} \tag{2.17}$$

In addition, Glauber calculations provide the number of participating nucleons N_{part}, i.e. the number of nucleons that suffered at least one inelastic collisions, and other parameters related to the geometry of the collision, e.g. the average eccentricity of the nuclear overlap region. The advantage of a Monte Carlo approach compared to analytical determination of (average) geometric properties is that event-wise fluctuations present in real collisions can also be modelled. The Glauber Model is reviewed in detail in [Mil07].

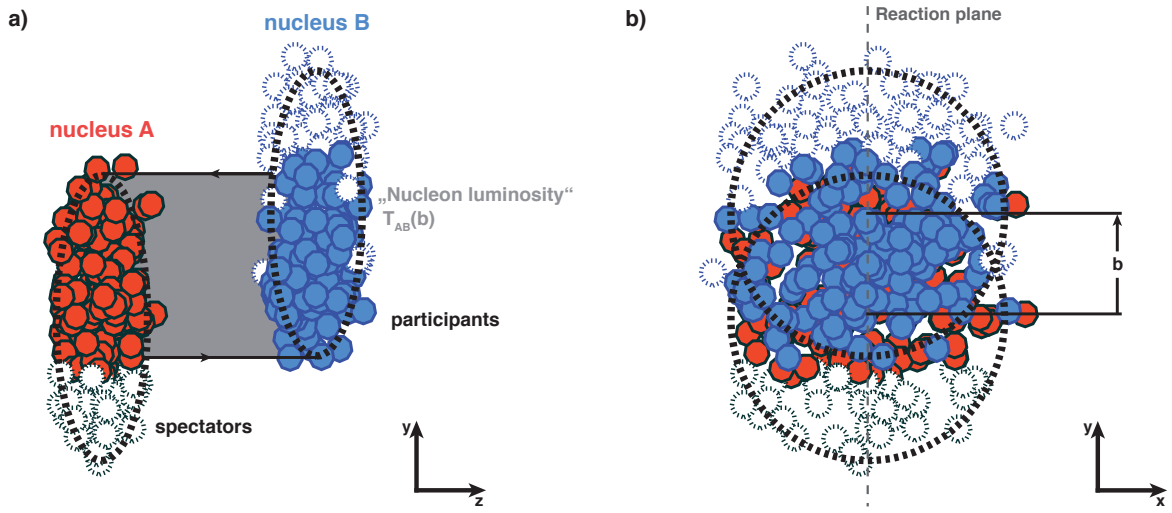

Figure 2.14.: The concept of binary scaling and its implementation in a Glauber MC: A heavy-ion collisions as incoherent superposition of nucleon-nucleon collisions on straight line trajectories. Participating nucleons are shown as filled circles.

2.4.3. Discovery of Jet Quenching

The first measurements of hadron production at RHIC in central Au + Au collisions at $\sqrt{s_{\mathrm{NN}}} = 130\,\mathrm{GeV}$ already showed a suppressed hadron production in the accessible p_{T} region up to $4.5\,\mathrm{GeV}/c$, with respect to the scaled expectation from pp collisions [Adc02]. This observation has been confirmed with better precision at the maximum RHIC energy of $\sqrt{s_{\mathrm{NN}}} = 200\,\mathrm{GeV}$ and is supported by a set of crucial reference measurements [KB05, Adl03b, Adl03a, Adl05a]:

- vacuum reference: π^0 production in pp collisions at $\sqrt{s} = 200\,\mathrm{GeV}$,
- cold nuclear matter reference: π^0 production in d + Au collisions at $\sqrt{s_{\mathrm{NN}}} = 200\,\mathrm{GeV}$,
- in-situ control of hard-scattering: direct photons in Au + Au collisions at $\sqrt{s_{\mathrm{NN}}} = 200\,\mathrm{GeV}$.

The production of neutral pions is suppressed by a factor of five in central Au + Au collisions at $\sqrt{s_{\mathrm{NN}}} = 200\,\mathrm{GeV}$ compared to the same measurement in pp reactions as seen with the nuclear modification factor in Figure 2.15. At the same time, direct photons that are also produced in initial hard scatterings but do not interact strongly are not suppressed and show a R_{AA} consistent with unity. This observation demonstrates that the rate of hard scatterings is

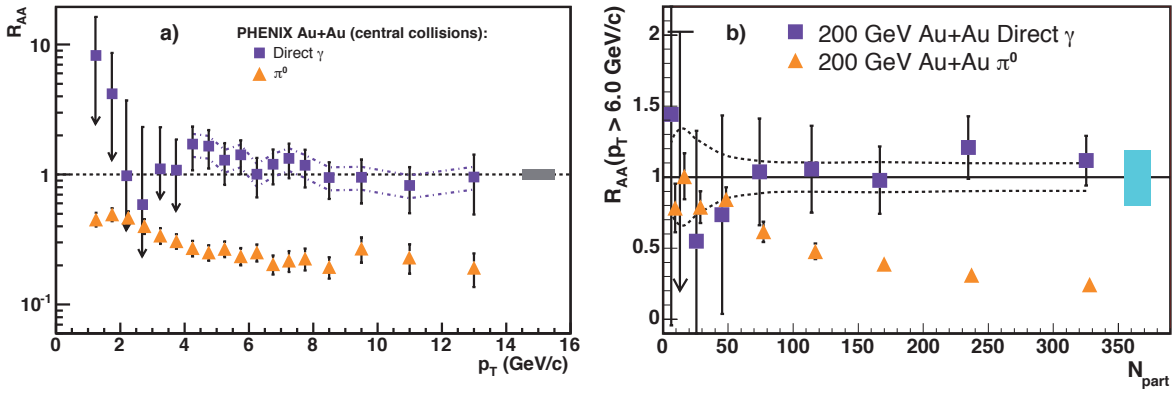

Figure 2.15.: The nuclear modification factor for neutral pions and direct photons in Au + Au at $\sqrt{s_{\mathrm{NN}}} = 200\,\mathrm{GeV}$ a) in central collisions b) integrated above 6 GeV/c for different centralities. Neutral pions are increasingly suppressed for more central collisions, direct photons are unaffected by the medium [KB05, Adl05a].

not modified and a strong final state effect is needed to account for the observed suppression [KB05, Adl05a]. It marks the essential first step in the author's research work of the past years towards a deeper understanding of the medium created in central heavy ion collisions at RHIC and the LHC.

Cold Nuclear Matter Effects

As mentioned before, the nuclear modification factor in cold nuclear matter that has been measured in d + Au collisions at the same energy does not show a large suppression at high p_{T} [CKB02]. It provides further confirmation that neither a change in the initial distribution of partons, nor an attenuation of hard scattered partons in cold nuclear matter are sufficient to explain the observed deficit of high p_{T} hadrons in central Au + Au collisions. As seen in Figure 2.16, the nuclear modification factor is consistent with unity within the uncertainties for η and π^0 mesons in minimum-bias (all impact parameters) and a central impact of the deuteron on the Au-nucleus.

However, in [CKB02], a slight centrality dependence of the nuclear modification factor of neutral pions and η mesons is observed, which is not fully accounted for by recent impact parameter dependent nuclear PDFs [Hel12]. The high-p_{T} yield per N_{coll} is larger in peripheral than in central events by about 50%. This observation is confirmed by recent preliminary PHENIX results on π^0s with an extended p_{T} reach and reconstructed jets [Sah12]. It is currently still an open question whether this observation constitutes a true impact pa-

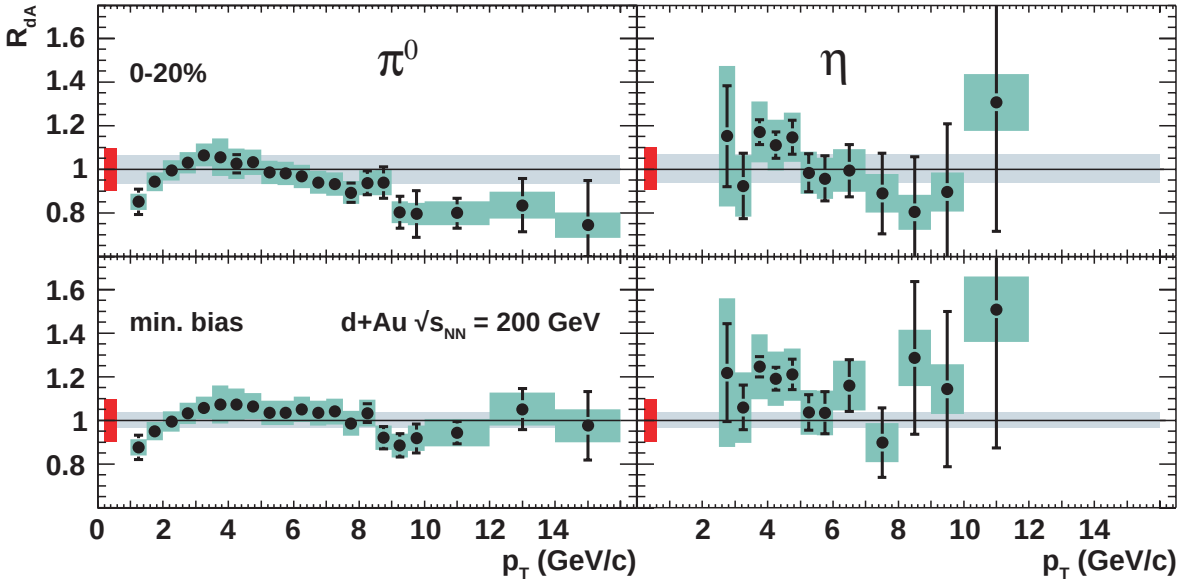

Figure 2.16.: The nuclear modification factor for neutral pions and η mesons in central and minimum bias d + Au collision [CKB02]. The particle yield is not strongly suppressed, but a decrease at high p_{T} for central collisions is not ruled out. It should be noted that this observation is closely related to the experimental centrality definition in these collisions.

rameter dependence of particle production at high p_{T} in d + Au collisions, or is an artefact of the poorly constrained relation between impact parameter and the employed centrality estimation.

Jet Tomography

The study of jet quenching is often motivated via the goal of a tomographic study of matter in analogy to the attenuation of X-rays for medical imaging. This analogy is useful to introduce the concept of the nuclear modification factor but is certainly an over-simplification. The nuclear modification factor has to be understood as an integral measurement that averages over varying initial conditions, medium evolution, origin, momentum, and type of the parton. In the following sections it will be discussed how these limitations can be partially overcome and the medium properties can be constrained via the measurement of single particle R_{AA}.

3. Parton Energy Loss and Nuclear Modification Factor

The observation of jet quenching via the suppression of single particle production in heavy-ion collisions at high p_{T} is one of the major discoveries at RHIC. It provides strong support for the creation of a dense partonic final state in heavy-ion collisions in which the traversing partons lose energy. It also prompted the first extraction of medium parameters in the framework of perturbative models that describe the energy loss via medium induced gluon radiation [Vit02, Wan02]. However, the extracted parameters vary strongly between models, due to specific assumptions and simplifications for the connection between medium evolution and the parton energy loss implementation.

The focus of the author's research is to provide precision, differential measurement of particle production in heavy-ion collisions at large transverse momentum, in order to constrain the properties of the underlying parton energy loss mechanism. This will be discussed in more detail in the following chapters. Here, the different classes of energy loss mechanisms and their generic dependence on path length and medium parameters are briefly introduced. Furthermore, the general sensitivity of the nuclear modification factor to the modified particle production mechanisms in heavy-ion collisions is investigated based on a simplified model.

3.1. Energy Loss Mechanisms

The basis for each model description of parton energy loss observables is the assumption on the parton-medium interaction process. It introduces the characteristic length, mass, and flavor dependence of the energy loss. Similar to the QED energy loss of a charged particle in ordinary matter one can consider two classes of interaction with the medium: collisional and radiative energy loss. They are sketched in Figure 3.1 and are concurrent processes. Their relative contribution to the total energy loss depends on the properties of the medium and the probe. Similar to the energy loss of charged particles, collisional energy loss is most important for lower particle momentum or small $\beta\gamma = p/m_0$, respectively. The following

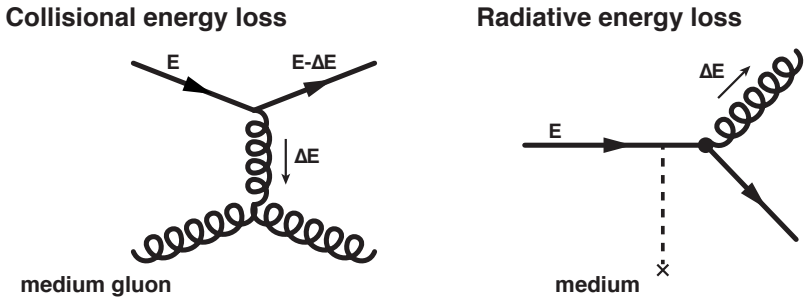

Figure 3.1.: Elementary diagrams for collisional and radiative energy loss of a quark traversing the QGP with energy E.

discussion is limited to the qualitative features of different classes of models, with some examples on their implementation for the calculation of observables. A broader account on model implementations and limitations is provided in [d'E10, Maj11, Ren12, Arm12].

3.1.1. Collisional Energy Loss

The transfer of energy from the hard scattered parton via elastic QCD collisions with the thermal partons of the medium is the simplest process for partonic energy loss. It was first discussed in [Bjo82] in analogy to the energy loss via ionization of charged particles passing through ordinary matter, which is described via the Bethe equation. Elastic scatterings are incoherent and as such, the total amount of lost energy is given by the average energy lost in a single scattering $\langle \Delta E \rangle$ and the number of elastic scatters N along the path length L:

$$\langle \Delta E \rangle_{\text{coll}} = \overbrace{\sigma \rho L}^{N} \langle \Delta E \rangle \propto L. \tag{3.1}$$

Here, the number of scatterings is defined by the density of scattering centers in the medium, ρ, and the elastic scattering cross section σ. The linear path-length dependence holds as long as the single energy loss and the cross section can be considered independent of the incident parton energy E. It is tantamount to a constant specific energy loss $\mathrm{d}E/\mathrm{d}x$.

The details of the underlying processes are encoded in the parameters of Equation 3.1. First, the cross section σ for elastic scattering is larger for gluons than for quarks due to their larger effective color charge C_R. It also needs to take into account the running of the coupling constant $\alpha_{\text{S}}(Q^2)$. Second, the single energy transfer depends on the masses of the parton and the properties of the medium, in particular on the *Debye mass* $m_{\text{D}}(T)$, where

$m_D^2 = 4\pi\alpha_S T^2(1+n_f/6)$ for n_f active quark flavors. It characterizes the typical momentum exchange with the plasma and provides the order of magnitude for the *thermal mass* of the medium constituents. The detailed dependence of the specific energy loss via elastic collisions for fast, light partons is given e.g. in [Pei08a]:

$$\left.\frac{dE}{dx}\right|_{q,g} \approx C_R \cdot \pi \cdot \alpha_S(m_D^2) \cdot \alpha_S(ET) \cdot T^2 \cdot \left(1+\frac{n_f}{6}\right) \cdot \ln\frac{ET}{m_D^2}. \tag{3.2}$$

For light quarks and gluons, collisional energy loss is not considered as the main mechanism of energy transfer to the medium. They are expected to lose energy dominantly via bremsstrahlung, similar to relativistic electrons in ordinary matter. For heavy quarks, where radiative energy loss is expected to be suppressed, elastic scatterings may contribute significantly. It may be responsible for the observed large suppression of electrons from heavy flavor decays [Ada07a, Pei08b].

3.1.2. Radiative Energy Loss

The expected, dominant mechanism for partonic energy loss at high parton momentum is given by medium induced gluon radiation, or bremsstrahlung. As illustrated in Figure 3.1, the underlying idea is that a parton traversing the QGP acquires momentum, or *virtuality*, via medium interaction. The momentum acquired per unit path length dQ^2/dx is measured by the *transport coefficient* $\hat{q} = m_D^2\rho\sigma$. The total virtuality of the parton is thus proportional to the path length. The virtuality can be reduced again via the emission of a real gluon. The probability for the formation of this gluon is also proportional to the path length resulting in a radiated energy of:

$$\langle\Delta E\rangle_{\text{rad}} \propto \hat{q}L^2 \propto T^3L^2. \tag{3.3}$$

The additional power in the path-length dependence is one of the main reasons that the radiative energy loss is considered to dominate over collisional energy loss.

In practice, two limiting scenarios need to be considered: *thin* and *thick* media. In a thin medium the total path length L is much smaller than the mean free path $\lambda = 1/\rho\sigma$ and no interference effects between successive scatterings need to be considered. In this *Bethe-Heitler* regime holds [d'E10]:

$$\langle\Delta E\rangle_{\text{rad}}^{\text{BH}} \approx \alpha_S\hat{q}L^2 \ln\frac{E}{m_D^2 L}. \tag{3.4}$$

Thus, the initial L^2 dependence is reduced by the logarithm.

For a thick medium ($L \gg \lambda$) interference effects, similar to the Landau-Pomeranchuk-Migdal (LPM) effect in QED, need to be taken into account. This case is further differentiated into the regime of hard and soft emission with respect to the characteristic radiated gluon energy $\omega_C = \hat{q}L^2/2$:

$$\langle \Delta E \rangle_{\text{rad}}^{\text{LPM}} \approx \alpha_S \hat{q} L^2 \cdot \begin{cases} 1 & \text{if } \omega < \omega_C, \\ \ln \frac{E}{\hat{q}L^2} & \text{if } \omega > \omega_C. \end{cases} \tag{3.5}$$

It can be seen that the radiation of soft gluons ($\omega < \omega_C$) is suppressed compared to the independent emission in Equation (3.4).

Compared to massless partons, the radiation off a heavy quark with mass m_Q is suppressed already in the vacuum at angles smaller than $\theta = m_Q/E$ with respect to the direction of the heavy quark. This so called *dead cone* effect should also lead to a suppression of the induced radiation in the QGP compared to the radiation from light quarks. Combined with the color charge dependence of the cross section, and thereby $\hat{q}$, the radiative energy loss in the QGP is expected to be largest for gluons and then follow the mass ordering of the quarks, with bottom quarks showing the smallest energy loss.

Strong Coupling Limit

Based on the idea that a QCD medium can be described in the strong coupling limit via the AdS/CFT correspondence [Aha00], which has been also used to derive a lower bound on dissipative effects in a strongly coupled plasma, the energy loss of partons can be calculated in an alternative way. Within this framework, a parametrically different dependence of the radiated energy on the path length as well as on temperature is obtained [Ren12]:

$$\langle \Delta E \rangle_{\text{rad}}^{\text{AdS/CFT}} \propto T^4 L^3. \tag{3.6}$$

Furthermore, it is found that in this approach, particles from b quarks are strongly suppressed. This may provide an alternative explanation for the similarity of the nuclear modification factor of light and heavy quarks. It also predicts a more drastic variation than pQCD based calculations when comparing the nuclear modification factor for particles originating from c and b quarks as discussed in [Hor08].

3.2. Model Implementation with Medium Evolution: Jet Tomography?

The energy loss descriptions as provided above reflect the ideal situation of a uniform and static QGP, viewed from a single parton. Up to this point the comparison to conventional tomographic studies in medical imaging is evident. However, the situation for partonic probes in a realistic, expanding QGP is far more complex, the most important differences are:

- The **medium expands** with velocities $\beta > 0.5$. This introduces a time dependence of the medium density that needs to be modeled correctly. The expansion velocity in addition depends on initial spatial asymmetries of the system.

- The **origin of the probe** is not known on an event-by-event basis, neither is the flavor of the leading parton and the momentum, which is sampled from a steeply falling power law spectrum.

- The **initial conditions** are not well constrained and fluctuate event-by-event. In particular the relation between the density profile of hard scatterings and initial density profile of the medium is not known. Currently two different assumptions are in use: the N_{part} density from a Glauber model and the expected energy deposit of a color-glass condensate.

- The probe is not observed as single particle with a well defined energy loss. Instead it evolves as a **parton shower**, which in itself may be modified by the presence of the medium.

The experimental observables have to be understood as averages for many events over these characteristics and coordinates.

In addition to the modeling of medium properties, the methods for analytical pQCD calculations of the energy loss vary for different models. Popular classes of models that incorporate the radiative QCD energy loss are the path integral formalism (BDMPS, ASW [Bai95, Sal03]), opacity expansion (GLV, WHDG [Gyu00, Wic07]), and Higher Twist (HT [Guo00, Maj08]).

In the path integral method, the energy loss in the medium is computed in a multiple soft-scattering approximation, where a gluon is radiated from the traversing parton after it accumulated virtuality along the path via scattering with the static medium constituents. The main parameter in these models is the transport coefficient $\hat{q}$ of the medium. It defines the

gluon emission spectrum at a given point in space time. Similar to the path-integral approach, the opacity expansion assumes static scattering centers. Here, the gluon emission spectrum is calculated starting from the single-hard radiation spectrum and employs diagrams that are ordered in *opacity* L/λ_g, where λ_g is the mean free path of the radiated gluon. The main parameter of the model is the density of scattering centers in the medium, or the gluon density.

Both approaches allow a probabilistic interpretation in which the propagating parton loses a fraction of the energy due to n gluon emissions and then fragments into the vacuum. In this case the effect of the leading parton energy loss can be conveniently cast into a medium modified fragmentation function at reduced parton energy that factorizes into an energy loss probability $P(\Delta E, E, \mathscr{M})$ and the vacuum fragmentation function:

$$D_{i/h}^{\mathrm{med}}(z, E, Q^2, \hat{q}(\mathbf{r})) \approx \int_0^E \mathrm{d}(\Delta E)\, P(\Delta E, E, \mathscr{M}) D_{i,h}^{\mathrm{vac}}(z - \frac{\Delta E}{E}, Q^2). \tag{3.7}$$

Where $\mathscr{M}$ has to be taken as the generic argument for the medium properties. It has to encode e.g. the medium expansion and the average over the production points.

One important consequence of the medium expansion can be illustrated starting from the longitudinal (Bjorken) expansion. In this case the medium density drops as $1/\tau$. For a probe propagating in the transverse plane, this will reduce the medium density such that one power of the length dependence is cancelled. When a transverse expansion of the system is also considered, the time spent in the (co-moving) medium increases and partially compensates the decreasing medium density. For the transport coefficient this is tantamount to a rescaling according to an effective average:

$$\langle \hat{q} \rangle = \frac{2}{L^2} \int_{\tau_0}^{\tau_0 + L} \mathrm{d}\tau \cdot (\tau - \tau_0) \cdot \hat{q}(\tau_0) \left(\frac{\tau_0}{\tau} \right)^{\alpha}, \tag{3.8}$$

with $\alpha \leq 1$ ($= 1$ for Bjorken expansion).

In the GLV model, the main medium parameter is usually provided as the *initial* gluon density $\mathrm{d}N_g/\mathrm{d}y$ after accounting for the expansion of the plasma. An often used approximation for the energy loss after a (1+1)D expansion is [Vit06b]:

$$\frac{\Delta E}{E} \approx 9\pi \alpha_{\mathrm{S}}^3 C_{\mathrm{R}} \frac{1}{A} \frac{\mathrm{d}N_g}{\mathrm{d}y} \frac{L}{E} \ln \frac{2E}{\mu_{\mathrm{D}}^2 L}. \tag{3.9}$$

Again, the quadratic length dependence of radiative energy loss is reduced to a linear one. Equation (3.9) can be further simplified using the generic approximations: length $L \propto N_{\mathrm{part}}^{1/3}$,

overlap area $A \propto N_{\text{part}}^{2/3}$, gluon density $\mathrm{d}N_g/\mathrm{d}y \propto N_{\text{part}}$:

$$\frac{\Delta E}{E} \propto N_{\text{part}}^{2/3} \propto \frac{1}{E} \ln \frac{2E}{\mu_{\text{D}}^2 L}. \tag{3.10}$$

So, the centrality dependence of the fractional energy loss should scale up to logarithmic corrections as $N_{\text{part}}^{2/3}$ for a parton of fixed energy.

Higher Twist Calculations

The approach of higher twist calculations has originally been applied to calculate medium corrections to the total cross section in deep inelastic electron-nucleus scattering due to multiple scattering from partons still confined in the nucleons [Qiu91a, Qiu91b]. These lead to corrections, which are suppressed by powers of the hard scale Q^2 and increase proportionally with the length L. The corrections can be cast into a medium modified fragmentation function with an additional medium contribution to the vacuum fragmentation due to modified splitting probabilities in the parton shower [Wan01, d'E10]. Thus, the production of additional particles within the parton shower and their correlations is intrinsically accounted for.

3.2.1. Jet Quenching Monte Carlos

From the experimental point of view, the description of jet quenching within a Monte Carlo simulation has the clear advantage that it can be studied on an event-by-event basis, similar to a real measurement. Furthermore, the sensitivity of experimental observables to jet quenching and the modified fragmentation can be tested in full simulations of the experimental setup, including a realistic detector response.

Compared to the pure energy-rescaling of the fragmentation function, modern jet quenching Monte Carlos modify the parton shower, which is governed by the DGLAP (Q^2) evolution of the fragmentation function. The probabilistic implementation of these parton showers via *splitting functions* describes the amplitudes of individual branching processes. It forms the basis for event generators such as PYTHIA [Sjo01] or HERWIG [Cor02], which are well tested against a wealth of pp data on jet production at various energies. Medium effects are then easily included by modifying the splitting functions. E.g. the JEWEL [Zap13] and YAJEM Monte Carlos are based on the PYTHIA fragmentation implementation. JEWEL modifies the splitting functions via an additional factor in the infrared part, while YAJEM increases the virtuality of the traversing partons according to the medium transport coefficient

$\hat{q}$ and by that their probability to radiate a gluon. The validity of these implementations can be tested with more differential observables than the single particle R_{AA} that are e.g. sensitive to the energy flow within jets.

3.3. Shape of Single Particle R_{AA}: A Simple Model

The nuclear modification factor for neutral pions, as introduced in Chapter 2.4.1, has been measured by PHENIX with increasing precision for central Au + Au collisions at $\sqrt{s_{\mathrm{NN}}} = 200\,\mathrm{GeV}$ [CKB04, CKB06]. It is shown together with the measurement of charged pions and protons [Ada11] in Figure 3.2. The pion R_{AA} exhibits only a mild variation with p_{T} and shows an almost constant suppression by a factor of five at high p_{T}, while the proton measurement approaches unity in the accessible, limited p_{T} reach up to $6\,\mathrm{GeV}/c$. In the following, Figure 3.2 is used to discuss the different mechanisms that affect the shape of the nuclear modification factor in the low, intermediate, and high p_{T} region. As demonstrated with the control measurements of direct photons in central Au + Au collisions [KB05, Adl05a] and neutral pions in d + Au reactions [CKB02], a possible modification of the initial state parton distributions has no sizable effect on the nuclear modification factor of hadrons. This knowledge is the premise for all following studies of the final state parton energy loss via the nuclear modification factor.

The particle production via hard processes, which dominates at high p_{T}, is in AA expected to scale with the number of binary collisions N_{coll} in the absence of any nuclear modification. This would result in a nuclear modification factor of unity. These hard processes dominate above $p_{\mathrm{T}} \gtrsim 2\,\mathrm{GeV}/c$ in pp as seen in Figure 2.6. In order to understand the nuclear modification factor at lower transverse momentum one has to recall that this region dominates the total particle multiplicity as discussed in Chapter 2.3.2 Here, the particle production in AA does not scale with N_{coll}. It rather exhibits an approximate scaling with the number of wounded nucleons or participants N_{part}. As a consequence of this alone, the nuclear modification should increase from approximately $N_{\mathrm{part}}/N_{\mathrm{coll}}$ to unity in the absence of any other medium effects, as illustrated in Figure 3.3.

3.3.1. Soft Final State Effects

In case a hot and dense medium is created, it affects the particle production in the full p_{T} range, not only where hard scattering is dominant. E.g. for a purely thermal source of particles in AA, the momentum spectrum follows a Boltzmann distribution determined by the

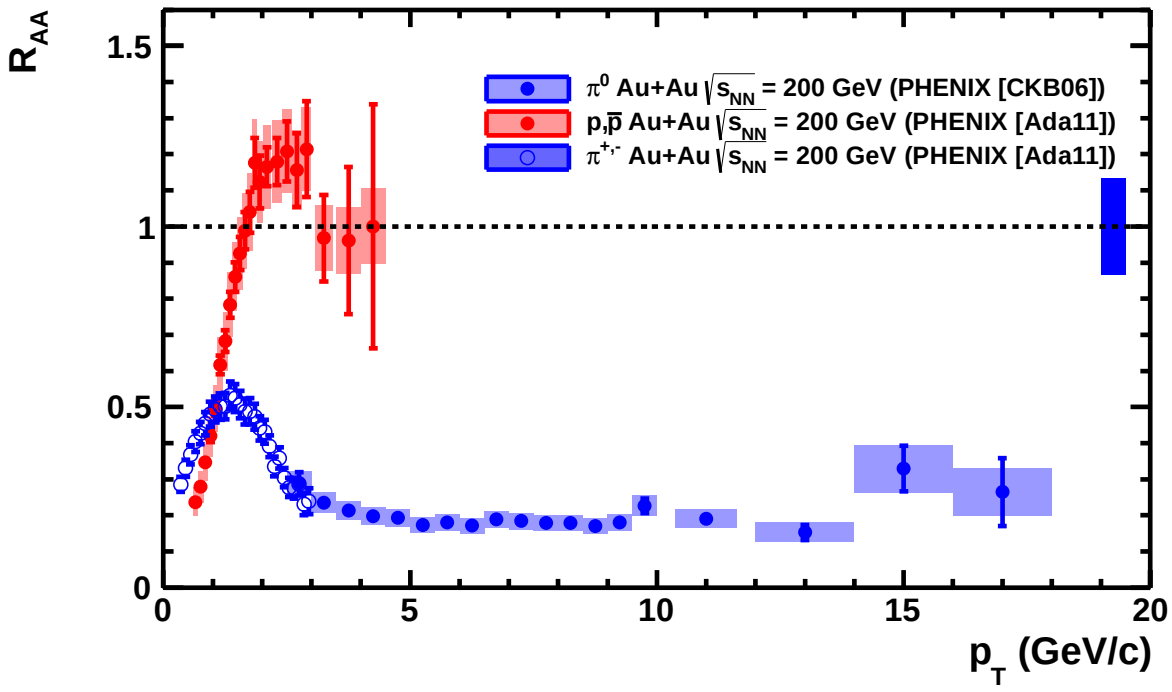

Figure 3.2.: Nuclear modification factor in central $\mathrm{Au}+\mathrm{Au}$ collisions at $\sqrt{s_{\mathrm{NN}}} = 200\,\mathrm{GeV}$ for neutral pions [CKB06], charged pions, and protons [Ada11].

temperature of the system. Integrated over rapidity and expressed in terms of the transverse mass $m_{\mathrm{T}} = \sqrt{p_{\mathrm{T}}^2 + m_0^2}$ this yields [Sch93]:

$$\begin{aligned} \frac{\mathrm{d}N}{m_{\mathrm{T}}\mathrm{d}m_{\mathrm{T}}} &\propto m_{\mathrm{T}} K_1\left(\frac{m_{\mathrm{T}}}{T}\right) \\ &\overset{m_{\mathrm{T}} \gg T}{\longrightarrow} \sqrt{m_{\mathrm{T}}} e^{-m_{\mathrm{T}}/T}, \end{aligned} \tag{3.11}$$

where the modified Bessel function of second kind K_1 decreases asymptotically as an exponential. The thermal spectrum is further modified in the common velocity field of the radial medium expansion. It leads to a boost of the thermal sources, which can be parameterized as [Sch93]:

$$\begin{aligned} \frac{\mathrm{d}N}{m_{\mathrm{T}}\mathrm{d}m_{\mathrm{T}}} \propto\ & m_{\mathrm{T}} K_1\left(\frac{m_{\mathrm{T}} \cdot \cosh\rho}{T}\right) \\ & \times I_0\left(\frac{p_{\mathrm{T}} \cdot \sinh\rho}{T}\right), \end{aligned} \tag{3.12}$$

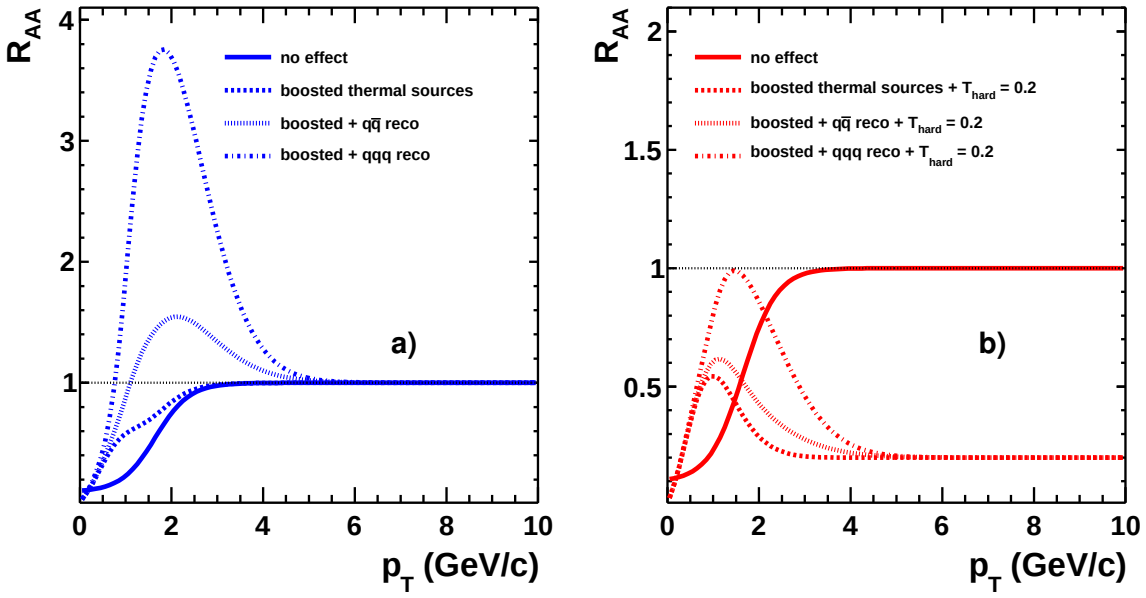

Figure 3.3.: Sketch of the different low and intermediate p_T effects on the nuclear modification factor (based on the spectral shape in pp collisions at RHIC): a) without high p_T suppression b) with high p_T suppression under the assumption that 20% of all jet particles are not absorbed ($T_{\mathrm{hard}} = 0.2$), the soft part of the spectrum is not modified with respect to a).

where I_0 is the modified Bessel function of first kind and ρ corresponds to the transverse rapidity:

$$\rho = \mathrm{athanh}(\beta_r), \tag{3.13}$$

with the average transverse or radial expansion velocity β_r. The boosted thermal distribution also approaches an exponential in m_T with a slope that can be considered as effective temperature:

$$T_{\mathrm{eff}} \approx T_0 \cdot \sqrt{\frac{1+\beta_r}{1-\beta_r}}. \tag{3.14}$$

For central $\mathrm{Au}+\mathrm{Au}$ collisions at $\sqrt{s_{\mathrm{NN}}} = 200\,\mathrm{GeV}$, typical values obtained via a common fit to identified particle spectra are $T_0 \approx 95\,\mathrm{MeV}$ and $\beta_r \approx 0.55$ [Ada05]. The temperature T_0 can be interpreted as kinetic freeze-out temperature T_{fo} of the hot hadron gas, the temperature when the hadrons cease to interact.

The effect of the boosted thermal sources is a (blue)shift of particles to higher transverse

momentum and a smaller slope than in the generic exponential drop observed in pp collisions (cf. Figure 2.6). This leads to an enhanced nuclear modification factor as illustrated in Figure 3.3, depending on the mass of the final state particle. It has to be emphasized that this effect does not a-priori require the creation of a partonic phase.

As seen in Figure 3.2, a distinct difference between protons and pions persists, even as one moves beyond $2\,\mathrm{GeV}/c$, which is the transition region to hard processes in pp reactions. At RHIC, it was observed that this is a systematic difference between baryons and mesons which appears not to be related to the mass but rather to the number of valence quarks [Adl05b]. This is also sketched in Figure 3.3 and interpreted as the dominance of quark recombination from a thermal source in a densely populated phase space over hadron production via pure fragmentation. The former leads to a larger momentum gain in case of three valence quarks [Vol03, Fri03], while in the latter case the meson production is favored over baryon production at a given p_{T}. The observation that these medium effects not related to hard processes appear to reach farther in p_{T} for baryons makes mesons a better tool to study jet quenching over a broad p_{T} range, in addition to their larger production cross section.

3.3.2. Hard Final State Effects, Jet Quenching

For the qualitative understanding of the shape of the single particle nuclear modification factor at high p_{T} ($\gtrsim 6\,\mathrm{GeV}/c$) one can use a simple model, which only considers the energy loss of the leading parton (LP) from the initial hard scattering. In fact, the concept of energy *loss* is only well defined in this picture, where the medium modification of the parton shower is neglected. The direct connection to single particle observables is given by the large trigger bias in the single particle spectrum, where the measured yield is dominated by hadrons with large z (see Chapter 2.2.2).

The nuclear modification factor is given by the probability density function for a given energy loss $P(\Delta E, E)$ convoluted with the steeply falling parton production spectrum. The former can be divided into two parts. First, the probability for no energy loss, or transmission T. This includes e.g. partons produced close to the surface or in the corona of the reaction zone. Second, the continuous part $P(\Delta E, E)$ that represents the shift and smearing of the partonic energy E and encodes the basic features of the energy loss model. The modified leading parton yield can then be approximated taking $E \approx p_{\mathrm{T}} c$ for light quarks at mid-rapidity:

$$\frac{\mathrm{d}N_{AA}^{\mathrm{LP}}}{\mathrm{d}p_{\mathrm{T}}}(p_{\mathrm{T}}) \approx N_{\mathrm{coll}} \cdot T \cdot \frac{\mathrm{d}N_{\mathrm{pp}}^{\mathrm{LP}}}{\mathrm{d}p_{\mathrm{T}}}(p_{\mathrm{T}}) + N_{\mathrm{coll}} \cdot \int_0^{E_{\mathrm{max}}} \mathrm{d}(\Delta E) \cdot P(\Delta E) \cdot \frac{\mathrm{d}N_{\mathrm{pp}}^{\mathrm{LP}}}{\mathrm{d}p_{\mathrm{T}}'}\left(p_{\mathrm{T}}'\right). \qquad (3.15)$$

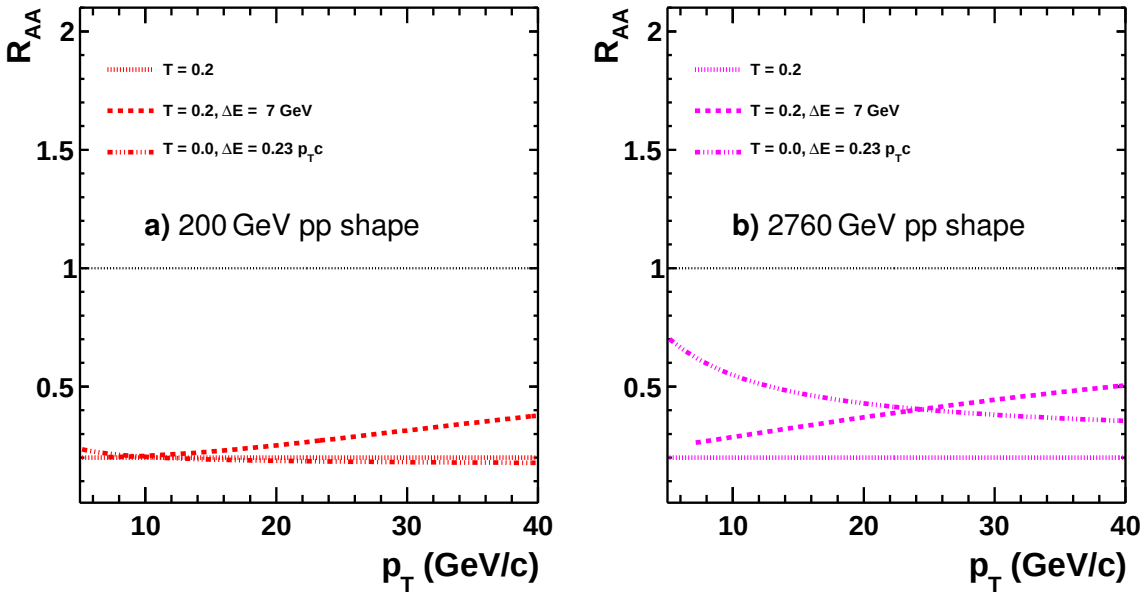

Figure 3.4.: Sketch of the nuclear modification factor at high p_{T} for different simplified parton energy loss scenarios. The shape of the underlying leading parton spectrum is approximated a) with the measured spectrum π^0 ($n \approx 8.1$) in pp collisions at $\sqrt{s} = 200\,\mathrm{GeV}$ and b) with the charged particle reference spectrum at $\sqrt{s} = 2760\,\mathrm{GeV}$ ($n \approx 6.5$).

It consists at a given p_{T} of the number of partons that escape without energy loss and the partons that feed down from the spectrum at $p_{\mathrm{T}}{}' = p_{\mathrm{T}} + \Delta E/c$ due to energy loss in the medium. For $\Delta E > p_{\mathrm{T}} \cdot c$ the parton is considered as lost, with all its energy thermalized in the medium.

As discussed in Chapter 2.2.2, the invariant cross section of the scattered partons has a power law shape ($\propto p_{\mathrm{T}}^{-n}$), which is also reflected in the single inclusive particle spectrum (see Figure 2.6). At top RHIC energy of $\sqrt{s} = 200\,\mathrm{GeV}$, the slope parameter in pp-collisions is $n \approx 8.1$, while at $\sqrt{s} = 2760\,\mathrm{GeV}$ it is $n \approx 6.5$. One now can consider two generic cases where the parton energy loss is approximated by an average behavior: constant energy loss and fractional energy loss.

For a constant energy loss $\Delta E_{\mathrm{const}}$ and a pure power law, the energy loss as reflected in the

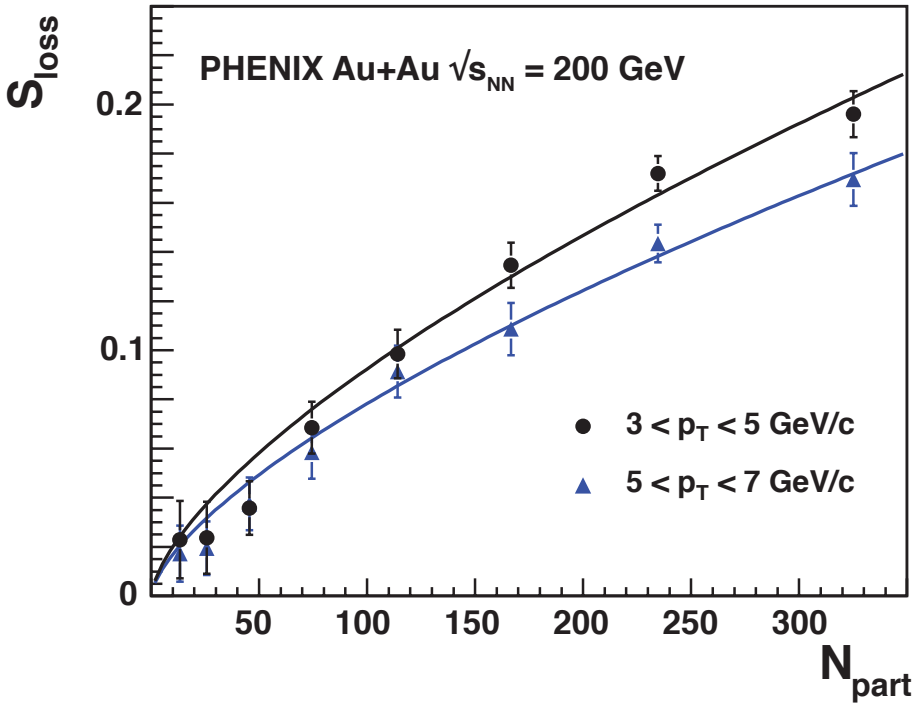

Figure 3.5.: Centrality dependence of the fractional energy S_{loss} obtained from Equation (3.18) using the nuclear modification factor of π^0s at $\sqrt{s_{\mathrm{NN}}} = 200\,\mathrm{GeV}$ evaluated in two p_{T} ranges. The centrality is given by the number of participating nucleons N_{part}, the two lines are a fit to a $N_{\mathrm{part}}^{2/3}$ dependence [CKB04].

nuclear modification factor is amplified by the steepness of the spectrum:

$$R_{AA} \approx T + \left(\frac{1}{1 + \frac{\Delta E_{\mathrm{const}}}{p_{\mathrm{T}} c}} \right)^{n-1} . \tag{3.16}$$

Here, the exponent $n-1$ is due to the fact that the relevant distribution is the differential yield $\mathrm{d}N/\mathrm{d}p_{\mathrm{T}}$ and not the differential invariant yield $(1/p_{\mathrm{T}} \cdot \mathrm{d}N/\mathrm{d}p_{\mathrm{T}})$. As seen in Equation (3.16) for a constant energy loss, there is a natural increase of R_{AA} with transverse momentum. This is illustrated in Figure 3.4 for a constant energy loss of 7 GeV and two different shapes of the input spectrum roughly representing the situation at $\sqrt{s_{\mathrm{NN}}} = 200\,\mathrm{GeV}$ and 2760 GeV, respectively. For the steeper input spectrum at RHIC used in Figure 3.4 a), the increase above the constant transmission is less pronounced illustrating the small sensitivity of R_{AA} to the partonic energy loss in this p_{T} region.

For constant, fractional energy loss $S_{\text{loss}} = \Delta E_{\text{frac}}/p_{\text{T}}c$ the nuclear modification factor is given by:

$$R_{AA} \approx T + (1 + S_{\text{loss}}) \cdot \left(\frac{1}{1 + S_{\text{loss}}}\right)^{n-1}, \tag{3.17}$$

where the additional factor is due to the Jacobian $\mathrm{d}p_{\text{T}}'/\mathrm{d}p_{\text{T}}$. A fractional energy loss in conjunction with a pure power-law spectrum leads to a constant R_{AA}. This is shown in Figure 3.4; the deviation from a constant in the LHC scenario is due to the a steeper local slope parameter of the employed spectrum at low p_{T}, the constant is approached for higher p_{T}.

These examples illustrate two important points in the interpretation of R_{AA} with respect to parton energy loss. First, the measurement of R_{AA} alone at a given $\sqrt{s_{\text{NN}}}$ does not provide strong constraints on the details of parton energy loss. In particular, a flat p_{T} dependence can be reproduced under very different assumptions, a dominance of surface emission or a spectrum shift by fractional energy loss. A modest energy loss of the order of a few GeV is already sufficient to reach the limit of an opaque medium. Second, the sensitivity to the details of parton energy loss strongly varies with the steepness of the parton spectrum, where characteristic features are more suppressed for steeper spectra or larger n.

This is of particular importance when comparing the nuclear modification factors at different $\sqrt{s_{\text{NN}}}$ or for particles originating from the fragmentation of different parton flavors, e.g. gluons, light or heavy quarks. In this context, the calculation of the effective fractional energy loss S_{loss} as it can be defined via Equation (3.17) for $T = 0$ provides a useful measure in which the dependence on the slope has been reduced as proposed in [CKB04]:

$$S_{\text{loss}} = 1 - R_{AA}^{1/(n-2)}. \tag{3.18}$$

This is illustrated in Figure 3.5, where S_{loss} has been calculated according to the measured R_{AA} and shape of the π^0 spectrum for different p_{T} ranges and for different centralities. The derived fractional energy loss increases strongly with centrality and reaches up to 20%. The generic centrality dependence of the fractional energy loss ($\propto N_{\text{part}}^{2/3}$) as predicted by the GLV energy loss model reproduces well the data. It is remarkable that there is also a qualitative agreement with the expectation of a reduced fractional energy loss for higher energy probes as given in Equation (3.10).

In the following chapters, the parton energy loss models will be compared to more differential measurements and over a broad range of medium properties to test their basic assumptions and the region of applicability.

4. Testing Parton Energy Loss I: Single Particles from $\sqrt{s_{NN}}$ = 22 to 2760 GeV

In the experimental study of (light) parton energy loss, the PHENIX results on neutral pion production currently provide the richest source of information on identified particles at high transverse momentum at various energies. These measurements have been the research focus of the author immediately following his PhD work [CKB01, CKB02, CKB04, CKB05, CKB06]. Neutral pions can be cleanly reconstructed via their decay into two photons ($\pi^0 \rightarrow \gamma\gamma$), where the π^0 yield is extracted on a statistical basis from the invariant mass distribution of photon pairs. The calorimetric measurement of the two photons has the advantage that the energy resolution improves with increasing particle energy. It also facilitates the selection of events with high p_{T} photons via specific triggers in order to enrich these rare, large Q^2 processes in the recorded data sample.

A natural extension of the measurement is provided by the reconstruction of η-mesons via their two-photon decay channel. The electromagnetic decays of π^0 and η mesons also constitute the main source of background in the reconstruction of direct photons. The latter serve as an important control measurement for the rate of hard scatterings in heavy-ion collision, since they do not interact strongly with the medium. The unmodified direct photon production at large transverse momentum confirms the strong parton energy loss as explanation for the observed suppression of the production of high p_{T} hadrons in central $\mathrm{Au}+\mathrm{Au}$ reaction at RHIC. Furthermore, the measurement of direct photons at low p_{T} constrains the thermal evolution of the medium.

After the effect of jet quenching was established, more differential measurements were needed to test the assumptions and predictions of various energy loss models. These are provided by the PHENIX measurements presented here. The models that have been newly developed and refined with the constraints imposed by the PHENIX data have been put to a rigorous test at the LHC by the first ALICE measurements of particle production at high p_{T}, Here, a novel kinematic range is accessible in the measurement of hard probes.

4.1. Fragmentation Properties of Neutral Mesons

For transverse momenta below approximately $6\,\mathrm{GeV}/c$, the nuclear modification factor differs systematically for baryons and mesons in central Au + Au collisions at RHIC as seen in Figure 3.2. This behavior can be explained with particle production processes in heavy-ion collisions that dominate over the hard production out to higher p_T for baryons than for mesons, e.g. the recombination of quarks from thermal sources. The observation that inclusive charged hadrons and neutral pions at higher p_T show the same suppression pattern again supports the interpretation that beyond $6\,\mathrm{GeV}/c$ the particle production follows the same production probabilities as in elementary reactions [Adl04]. This behavior is expected in the case that the particle production is dominated by the fragmentation of the leading parton outside of the medium. An assumption that is also made in many energy loss models. They consider the attenuation of the leading parton as the dominating effect and treat its energy loss via an energy-rescaled vacuum fragmentation function, as discussed in Chapter 3.2.1. However, the comparison of neutral pions and unidentified hadrons at large transverse momentum does not provide a stringent constraint on the behavior of different particle species, since the latter is dominated by charged pions, the isospin partners of the neutral pion.

Information on identified particles at high p_T has been obtained by the PHENIX experiment with the extension of the invariant mass analysis of photon pairs from $\pi^0 s$ to the region of the η meson ($m_\eta = 547.853 \pm 0.024\,\mathrm{MeV}/c^2$ [Ber12]). The comparison of the nuclear modification factor of π^0 and η mesons in Au + Au collisions at $\sqrt{s_\mathrm{NN}} = 200\,\mathrm{GeV}$ as presented in [CKB01] does not reveal a significant difference in the centrality- and p_T-dependence of the two light flavored mesons, despite a difference of close to a factor of four in their mass. The comparison for the most central collisions is shown in Figure 4.1 a). Over the full measured range, the suppression of the η meson is consistent with the observed pattern for neutral pions.

An alternative way to investigate the effects on the final state hadron production is to compare the ratio η/π^0 for different colliding systems and centralities as shown in Figure 4.1 b) together with the expectation in pp reactions at this energy from the PYTHIA event generator. The η/π^0 ratio has a larger sensitivity to the fragmentation pattern of neutral mesons since common uncertainties between the measurements are significantly reduced. From the theoretical perspective, the effect of different initial parton distributions is also reduced, since they are shared in the π^0 and η measurement for the same collision system. As seen in Figure 4.1 b) the ratio increases from low p_T and approaches an asymptotic value of ≈ 0.5. The rise is governed by the difference in the transverse mass m_T at a given p_T for the heavier η. A

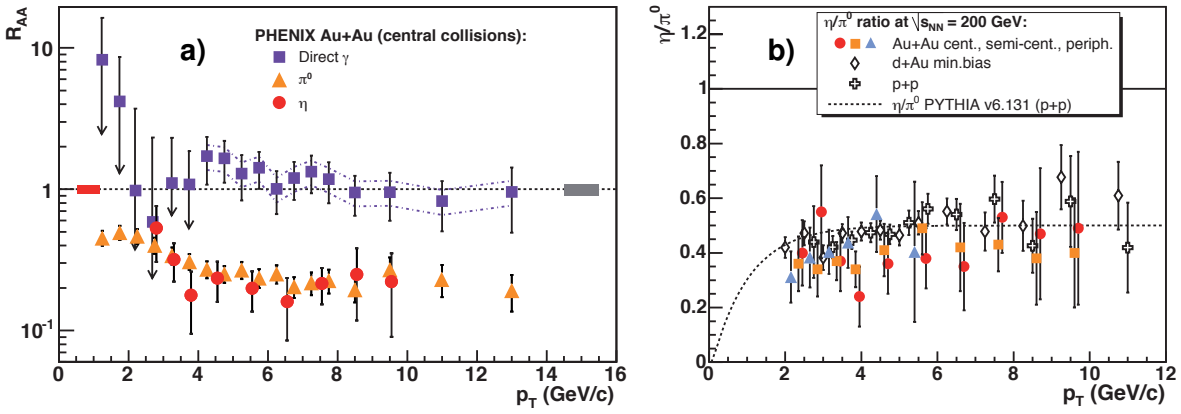

Figure 4.1.: a) The nuclear modification factor for η, π^0, and direct photons measured in central Au + Au collisions at $\sqrt{s_{\mathrm{NN}}} = 200\,\mathrm{GeV}$ [CKB01]. The reference in case of the direct photon measurement is a NLO calculation for pp $\rightarrow \gamma + X$, which has been verified in [CKB03]. b) Comparison of the η/π^0 ratio, for different colliding systems and centralities at $\sqrt{s_{\mathrm{NN}}} = 200\,\mathrm{GeV}$ and for a PYTHIA simulation for the same energy [CKB01].

constant fit to the plateau above $2\,\mathrm{GeV}/c$ yields an agreement within one standard deviation between the values of elementary collisions (pp: $C = 0.48 \pm 0.03$), the control measurement in cold nuclear matter (d + Au: $C = 0.48 \pm 0.03$), and central heavy-ion collisions (0-20% Au + Au: $C = 0.40 \pm 0.04$). These results suggest that the effects of the medium on the production of the two light flavored mesons is similar at high p_{T}. This is in agreement with the picture that hard scattered parent partons first lose energy in the QGP and then fragment in vacuum into leading hadrons following the same probabilities as in the high p_{T} production of hadrons in elementary collisions. I.e. the factorization approach made in many energy loss models that the medium modification for single hadrons can be separated into energy loss probability and vacuum fragmentation function at a rescaled energy appears to be justified at RHIC energies.

4.2. Energy Dependence: Onset of Jet Quenching

The measurement of the excitation function of parton energy loss and the search for the onset of hadron suppression has been one goal of the RHIC program in the measurement of Cu + Cu collisions at different collision energies: $\sqrt{s_{\mathrm{NN}}} = 22$, 62.4 and 200 GeV. The choice of the lower energies was motivated by the available reference data on π^0 and charged hadron

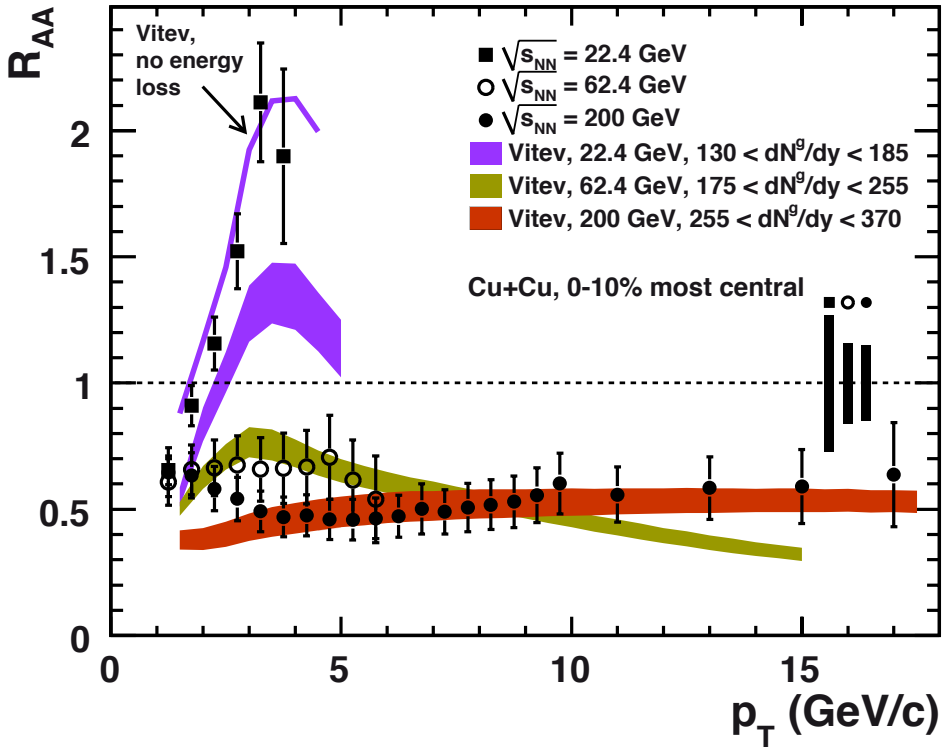

Figure 4.2.: Energy dependence of the nuclear modification factor in Cu + Cu from $\sqrt{s_{\mathrm{NN}}}$ = 22 GeV to 200 GeV [CKB05] compared to an energy loss calculation based on [Vit06b]. In case of the lowest energy, the impact of jet quenching is illustrated via an additional calculation that does not contain energy loss.

production at similar energies. While the reference for 22.4 GeV uses a scaled average of the world data in the range $21.7 \leq \sqrt{s} \leq 23.8$ GeV, the reference data obtained at the CERN-ISR at 62 GeV could be replaced by the PHENIX measurement of pp reaction at the same energy [CKB05].

The nuclear modification factor for central collisions is shown for the three energies in Figure 4.2. The neutral pion production at $\sqrt{s_{\mathrm{NN}}} = 62.4$ and 200 GeV is clearly already suppressed in the lighter collision system with ^{63}Cu instead of ^{197}Au. The nuclear modification factor at 62.4 GeV is slightly above the measurement at the higher energy. R_{AA} at 22.4 GeV is clearly above unity. It shows an enhancement of approximately 1.5 as observed in p + A collisions at similar energies and referred to as *Cronin* enhancement [Cro75].

In addition, the prediction of a parton energy-loss model based on the GLV approach for radiative energy loss and a (1+1)D (Bjorken) expansion [Vit06b] is compared to the data in Figure 4.2. It is able to reproduce the observed energy and p_{T} dependence. The main

medium characteristic in the model, the initial gluon rapidity density $\mathrm{d}N^g/\mathrm{d}y$, has not been fitted to the measured R_{AA}. Instead, it has been constrained by the measured charged particle multiplicity density assuming the same linear dependence for all energies: $\mathrm{d}N^g/\mathrm{d}y = k \cdot \mathrm{d}N^{\mathrm{ch}}/\mathrm{d}\eta$. Furthermore, the model incorporates initial and final state cold nuclear matter effects such as the Cronin enhancement. These effects are needed to describe the data at $\sqrt{s_{\mathrm{NN}}} = 22.4\,\mathrm{GeV}$. While the inclusion of parton energy loss reduces the nuclear modification factor, it is not necessary in this case to describe the data. On the other hand, the data at higher $\sqrt{s_{\mathrm{NN}}}$ can only be described with the inclusion of parton energy loss.

In the comparison of the two energies, one should keep in mind the rather different slope of the parton spectra, which is also reflected in the reference distribution of π^0 production in pp (see Figure 2.6). Despite the rather similar magnitude of R_{AA}, the effective spectrum shift $S_{\mathrm{loss}} = \Delta p_{\mathrm{T}}/p_{\mathrm{T}}$ as defined by Equation (3.18) differs by a factor of about 1.3. For $\sqrt{s_{\mathrm{NN}}} = 62.4$ and 200 GeV it is $S_{\mathrm{loss}} \approx 8.5\%$ and 11%, respectively. These empirical values take into account only the spectral shift and also contain the contribution of unmodified partons. In the employed energy loss model, the average fractional energy loss $\Delta E/E$ for quarks (gluons) at 6 GeV are $16-20\%$ $(35-44\%)$ and $20-28\%$ $(44-63\%)$, respectively. Between the two energies they change by a similar factor as the S_{loss} estimate.

The comparison of the data at the three different energies suggests that the parton energy loss starts to prevail over the Cronin enhancement observed for cold nuclear matter between $\sqrt{s_{\mathrm{NN}}} = 22.4$ and 62.4 GeV.

4.3. System-Size Dependence

The study of the system-size dependence of single particle suppression provides a first handle on the path-length dependence of parton energy loss. For a larger system, the average path-length through the medium increases. The system size, i.e. the size of the created medium can be varied by the choice of centrality or by using different sizes of colliding nuclei.

The use of a lighter collision system compared to gold ($^{197}_{79}$Au) has the advantage that for a fixed number of participants, the surface-to-volume ratio is smaller. In addition, it provides a better experimental centrality resolution for smaller N_{part}, where the parton energy loss sets on. At RHIC this has been done with copper ($^{63}_{29}$Cu) collisions. Here, the 10% most central Cu + Cu collisions correspond roughly to the $50-60\%$ centrality class in Au + Au in terms of the number of participants. The measured nuclear modification factor of π^0s in Cu + Cu and Au + Au collisions at the same average N_{part} is shown in Figure 4.3 a).

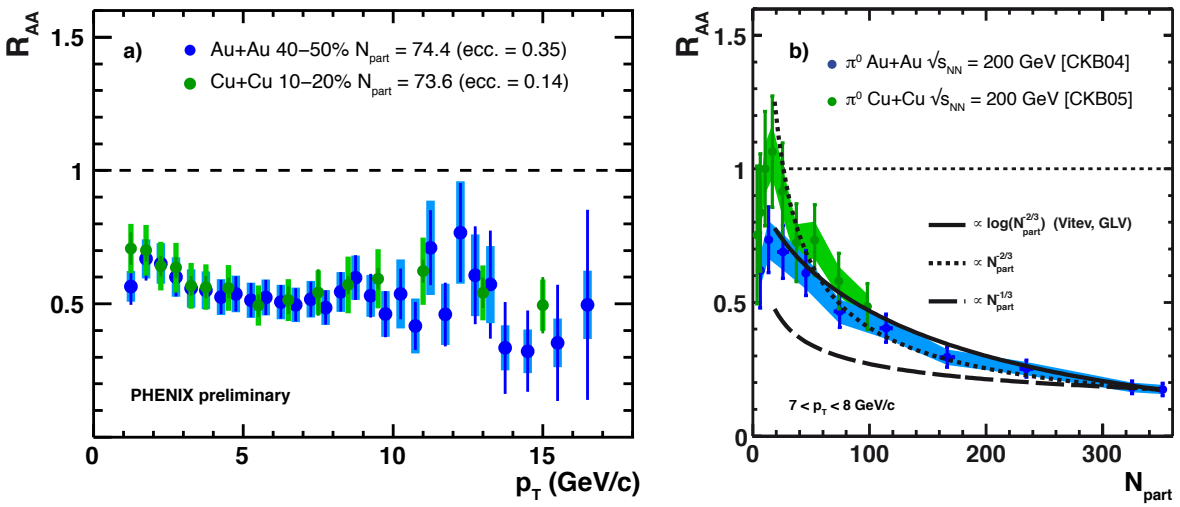

Figure 4.3.: a) The nuclear modification factor for neutral pions in Au + Au and Cu + Cu collisions at $\sqrt{s_{\mathrm{NN}}} = 200\,\mathrm{GeV}$ at the same N_{part} [KB06]. b) The nuclear modification factor at a selected p_{T} for the two colliding systems [CKB04, CKB05]. The solid line indicates the behavior expected from the radiative energy loss model in [Vit06a] (GLV and (1+1)D expansion), the dashed lines show two generic N_{part} dependences. All curves are fixed to the most central point in Au + Au.

The two measurements show a remarkable agreement. It strongly suggests that the overall magnitude of suppression at a fixed collision energy is mainly driven by the system size, i.e. the combination of similar (average) path-length and energy density. In this measurement, no strong effects of the different spatial eccentricity of the overlapping Cu and Au nuclei are observed. This is tantamount to a small impact of the different surface-to-volume ratio of the created medium at this N_{part}. It shows that the basic features of parton energy loss can be compared across different colliding species. The suitable reference scale for the comparison is the number of participating nucleons, which also drives the total number of produced particles (see Chapter 2.3.2).

The comparison of the centrality dependence of the suppression in the two systems is done via the magnitude of the nuclear modification factor in a fixed p_{T} range. As seen in Figure 4.3 b), the data for the smaller collision system follows the suppression pattern in Au + Au for all N_{part}. The expected system-size dependence of the parton energy loss model discussed above (radiative GLV energy loss and (1+1)D hydrodynamic evolution) is also shown for comparison. It is normalized to the R_{AA} at the largest N_{part} and found to be in good agreement with the measurement.

Two additional, generic dependences are considered as well in the context of this thesis:

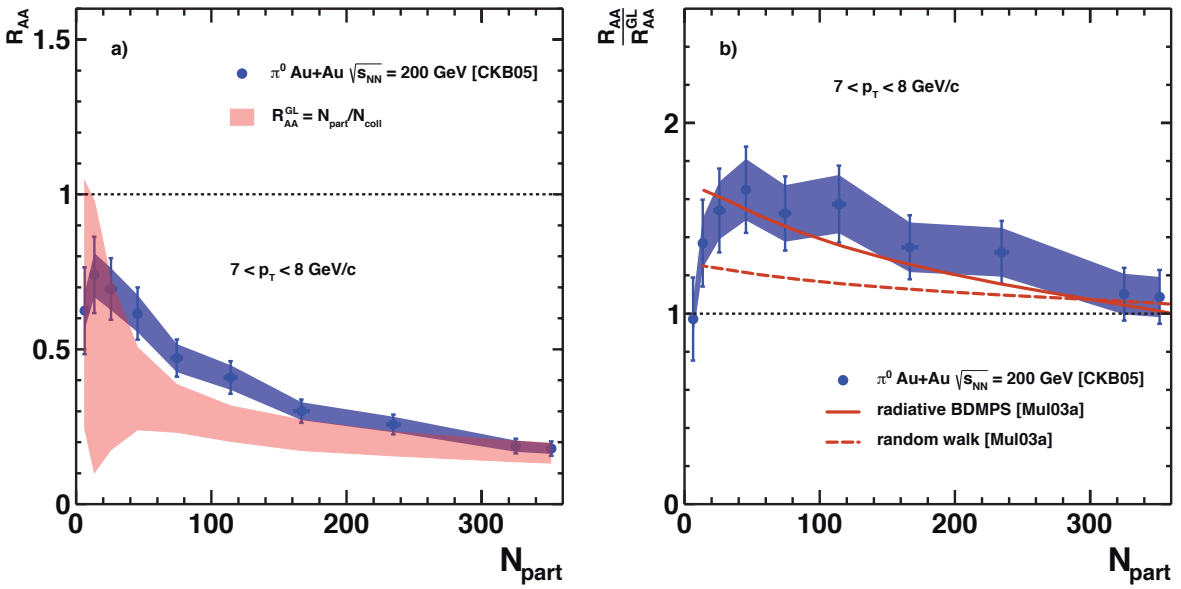

Figure 4.4.: a) Centrality dependence of the nuclear modification factor for neutral pions in Au + Au at $\sqrt{s_{\mathrm{NN}}} = 200\,\mathrm{GeV}$ compared to the geometric limit from Equation (4.1). b) Deviation from the geometric limit due to path length and energy density dependence of radiative energy loss and a random walk in p_{T} [Mue03]. The calculation is for parton p_{T} of $10\,\mathrm{GeV}/c$, due to the trigger bias in the leading particle spectrum this corresponds to the selected single particle p_{T}.

$R_{AA} \propto N_{\mathrm{part}}^{-2/3}$ and $R_{AA} \propto N_{\mathrm{part}}^{-1/3}$. However, some care has to be taken in the comparison to these scaling approaches. The $N_{\mathrm{part}}^{-2/3}$ ($N_{\mathrm{part}}^{-1/3}$) dependence does not represent the L^2 (L) dependence, since in the R_{AA} measurement, the particle production has already been normalized to the expected increase from hard scatterings, $N_{\mathrm{coll}} \propto N_{\mathrm{part}}^{4/3}$.

In the case of $R_{AA} \propto N_{\mathrm{part}}^{-2/3}$, as seen in Figure 4.3, the assumption is well compatible with the data. The observation of such a dependence can be phrased in two ways: a scaling of the particle production at high p_{T} with the surface of the overlap region ($R_{AA} \propto N_{\mathrm{part}}^{2/3}/N_{\mathrm{coll}}$) or a transmission that scales with the radius-to-volume ratio $N_{\mathrm{part}}^{1/3}/N_{\mathrm{part}}$. The scaling with $N_{\mathrm{part}}^{-1/3}$ does not describe the data well. Such a dependence could be either expected for a particle production that scales with N_{part} or a suppression that is driven by the surface-to-volume ratio. The latter scaling approach corresponds to a popular scenario for surface dominated production of hard particles and an basically opaque medium: a *black-and-white* picture of the energy loss. Here, only partons from the surface or a thin skin of the fireball are not absorbed. This view is compatible with the observed flat R_{AA} at high p_{T} as discussed in

Chapter 3.3. It is often considered in the context of a lower bound on the numerical value of the nuclear modification factor, which should approach a geometric limit (GL):

$$R_{AA}^{\mathrm{GL}} = k \cdot \frac{N_{\mathrm{part}}}{2 \cdot N_{\mathrm{coll}}} \propto N_{\mathrm{part}}^{-1/3}. \tag{4.1}$$

The additional constant factor k can be used to account for a certain *skin-depth* of the surface or a corona of vacuum nucleon-nucleon collisions. Close to this bound the magnitude of R_{AA} should exhibit only little dependence on the characteristics of parton energy loss. This offers a possible explanation for the observed similarity of R_{AA} for particles originating from heavy quarks to the R_{AA} of light flavored hadrons [Kha09]. In case the limit of a complete surface domination is already reached for heavy quarks, no difference in R_{AA} between various parton flavors is expected. As seen in Figure 4.4 a), the overall magnitude of R_{AA} in central collisions matches the geometric limit, but the centrality dependence is clearly underestimated, as already expected from the $N_{\mathrm{part}}^{-1/3}$ scaling.

A more detailed, phenomenological investigation of a geometry driven R_{AA} has been presented in [Mue03]. It takes into account the distribution of hard scatterings, the expansion of the medium, and the central value of the density to calculate an effective length in the medium for a given centrality. The resulting centrality dependence with respect to the naïve scaling assumption of Equation (4.1) is compared to the data for two scenarios in Figure 4.4 b): radiative energy loss (BDMPS) and a *random walk* in p_{T} with some interactions leading to an energy loss and some with a gain during the passage through the QGP ($\Delta E \propto \sqrt{L}$). In both cases, the geometric limit is reached in central collisions, but the centrality modulation is better reproduced with the path-length and density dependence of the radiative energy loss model. This observation demonstrates that in particular the R_{AA} in central collisions at RHIC has a reduced sensitivity to details of the energy loss model. Its magnitude is possibly determined by surface emission at these transverse momenta.

For a deeper understanding of the path-length dependence of parton energy loss one needs to separate effects of path length and density. This can be achieved by varying the effective path length for a fixed centrality using the spatial asymmetry of the overlap region.

4.4. Path-Length Dependence

At small transverse momentum, the initial spatial anisotropy in non-central heavy-ion collisions leads to an observable anisotropy in momentum space due the varying pressure gradients and the collective expansion of the system: the elliptic flow (cf. Chapter 2.3.3). For

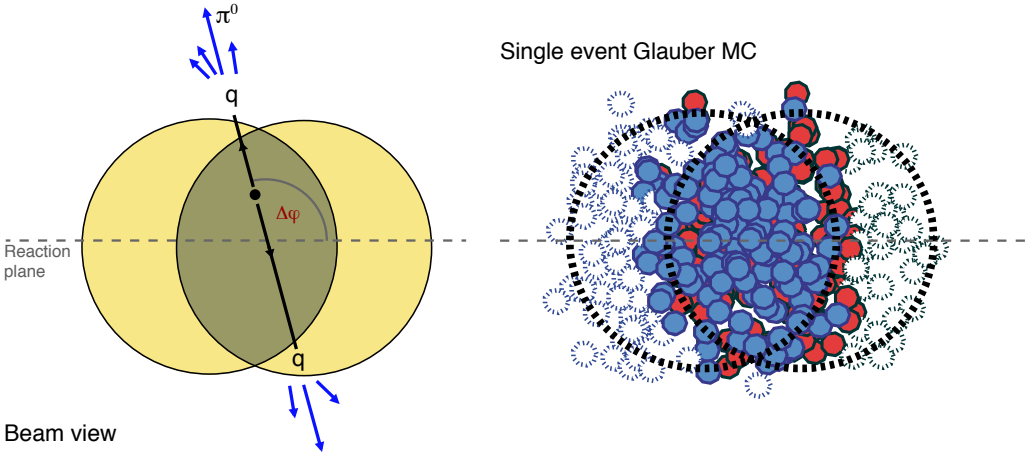

Figure 4.5.: Left: Path length traversed by the scattered parton depending on the orientation of the initial hard scattering to the event reaction plane and the position in the overlap region. Right: Distribution of participants and spectators for a single event in a Glauber MC of Au + Au collisions at $\sqrt{s_{\mathrm{NN}}} = 200$ GeV with $b = 4.7$ fm (centrality $\approx 11\%$).

high-p_{T} hadron production, the spatial anisotropy is tantamount to a different (average) path-length in the medium for the hard scattered parton depending on its orientation with respect to the event reaction plane as illustrated in Figure 4.5. In principle this allows one to differentiate the measurement of the nuclear modification factor at the same initial energy density (centrality) for different path lengths traversed in the medium and thereby test the L dependence of partonic energy loss.

As seen in Figure 4.6, the particle production at high transverse momentum exhibits a clear dependence on the orientation with respect to the event reaction plane: for in-plane emission ($\Delta\varphi = 0°$) the nuclear modification factor is larger by almost a factor of two compared to the out-of-plane direction ($\Delta\varphi = 90°$) [CKB04]. This is in qualitative agreement with the expectation of a stronger parton energy loss for a larger average path length. For a more quantitative analysis of the path length dependence of parton energy loss, different estimations for the effective path length have been studied as a function of centrality and $\Delta\varphi$ in [CKB04]. Two descriptions have been found that exhibit a universal development of the nuclear modification factor R_{AA} and the fractional energy loss S_{loss}, these are shown in Figure 4.7.

The dependence on the first definition of an effective path length L_ε is shown in Figure 4.7 a) and c). The overlap region of the two nuclei is estimated on average for each

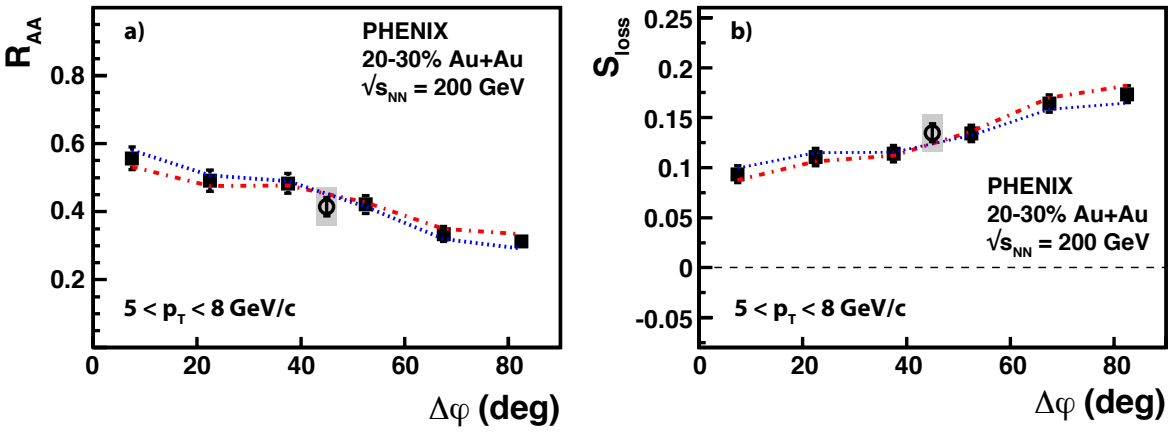

Figure 4.6.: Nuclear modification factor and derived fractional energy loss according to Equation (3.18) for semi-central Au + Au collisions [CKB04]. The lines show the bin-to-bin uncertainty of values. The open symbol represent the value for the $\Delta\varphi$-integrated measurement, and the shaded band represents the overall uncertainty.

centrality by an ellipse with eccentricity ε. The magnitude of L_ε is then given by the distance from the center of the ellipse to the edge for a given $\Delta\varphi$. For $L_\varepsilon < 2$ fm there are no observable effects of partonic energy loss. Since this observation also holds true for other transverse momenta than presented here, it suggests the presence of a surface emission zone as discussed already in the context of the simple model approach in Chapter 3.3 and the centrality evolution of R_{AA}.

The universality observed in L_ε is surprising, since it neglects the dependence on the local variation of the density of the traversed medium. It is expected to change with the location of the hard scattering in the transverse plane and the emission angle. To take this into account, linear (ρL) and quadratic (ρL^2) effective path length estimators have been calculated by weighting with the participant density along the path, e.g.:

$$\rho L = \int_0^\infty \mathrm{d}r \rho_{\mathrm{part}}(r, \Delta\varphi). \tag{4.2}$$

In both cases, no universal behavior has been observed, neither in R_{AA} nor in S_{loss}. In a last refinement, the production points of the jet in the transverse plane have also been incorporated in the effective path length (ρL_{xy}), again with no apparent universality. The latter is recovered when the length estimator is rescaled with the central value of the participant density for a given centrality $\rho(0,0) = \rho_{\mathrm{cent}}$ as shown in Figure 4.7 b) and d). This suggests that

		Parton-medium interaction model		
		elastic L	radiative L^2	AdS L^3
Medium model	3+1d ideal	fails	**works**	fails
	(2+1)D ideal	fails	fails	marginal
	(2+1)D viscous CGC	fails	marginal	**works**
	(2+1)D viscous Glauber	fails	marginal	**works**

Table 4.1.: Validity of different combinations of medium model and parton-medium interaction model in comparison to the PHENIX data for the reaction plane dependent R_{AA} [CKB04]. Table based on [Ren12].

simple geometry may indeed be more important than the details of the participant or medium density along the path.

These measurements provide strong constraints on the path-length dependence of the nuclear modification factor at high transverse momentum and connect directly to low p_{T} elliptic flow measurement via the common dependence on the intial geometry. This puts additional boundary conditions on the implementation of hydrodynamic medium evolution in various energy loss calculations. This has been done comprehensively e.g. in [Ren12] using the PHENIX data on the reaction-plane- and p_{T}-dependent nuclear modification factor. The work comprises a systematic study of different parton energy loss mechanisms within a common framework for the medium evolution. This enables the direct comparison of the medium interaction mechanisms for different expansions models and initial conditions. The results are summarized in Table 4.1. It is found that regardless of the employed mechanism, an ideal (2+1)D hydrodynamic medium evolution cannot be reconciled with the PHENIX data presented here, while the ideal (3+1)D description in combination with a radiative energy loss (L^2 dependence) agrees within the current theoretical uncertainties. A similar agreement is seen with the models using the L^3 dependence of strong coupling in combination with a viscous (2+1)D evolution. A pure linear path-length dependence in the energy loss model is ruled out.

4.5. Constraining Medium Evolution Parameters with Direct Photons

Direct photons, defined as all photons not originating from decays of hadrons (such as $\pi^0 \rightarrow \gamma\gamma$), provide an important complementary tool to identified hadrons in the study of

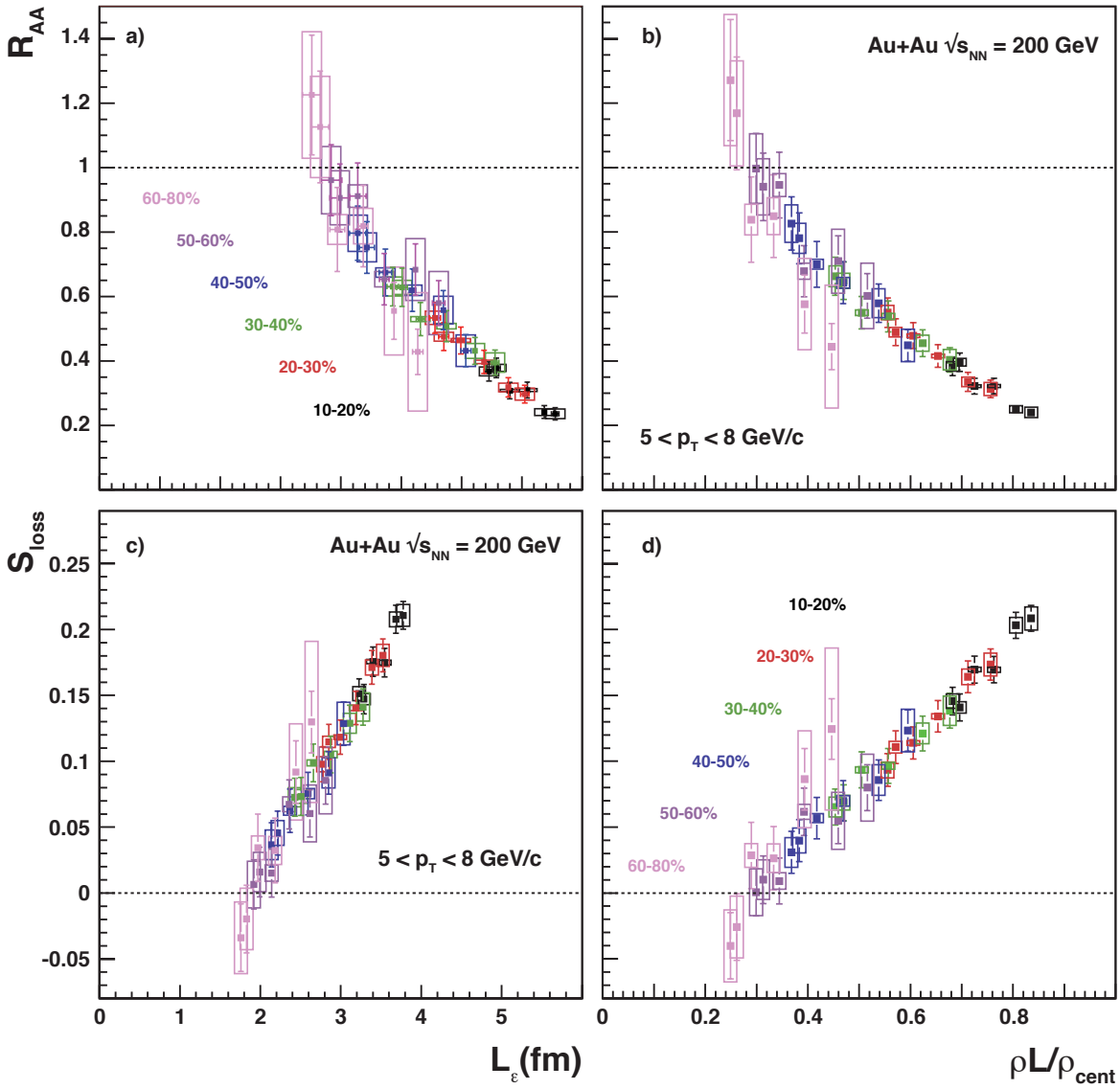

Figure 4.7.: Dependence of the magnitude of R_{AA} and S_{loss} on two effective length scales L_ε and $\rho L/\rho_{\mathrm{cent}}$ that show a universal behavior for all reaction plane bins and centralities [CKB04].

the medium created in heavy-ion collision. Once produced, they escape unaffected by the strong interaction and thus provide an integrated measurement over all stages of the reaction. In this context, the momentum of the direct photon is a measure for the production time. High-p_{T} photons are produced early in initial hard scatterings, while the low p_{T} production is dominated by thermal production in the dense partonic phase and the hot hadron gas.

The major challenge in the measurement of direct photons is their separation from the background of decay photons, which is dominated by π^0 and η decays. The extraction of the direct photon signal is often done on a statistical basis, e.g. by comparing the yield of inclusive photons, γ_{incl}, to the expectation from a hadronic decay cocktail, γ_{decay}. Since π^0s provide the largest contribution to the decay background and also share many systematic uncertainties with the inclusive photon measurement, the measured inclusive and calculated decay photon yields are conveniently normalized to the π^0 yield in the double ratio:

$$R^{\gamma} = \frac{N^{\gamma}/N^{\pi^0}\Big|_{\mathrm{meas}}}{N^{\gamma}/N^{\pi^0}\Big|_{\mathrm{cocktail}}}. \tag{4.3}$$

A direct photon signal is seen as an excess of R^{γ} above unity. $(R^{\gamma}-1)$ directly provides the signal-to-background ratio. It is also the essential input for statistical measurements of direct photon observables, e.g. for the separation of the direct γ–hadron correlation function [Ada10b, Gra11].

In the following, the same major observables as used for the hadron production are discussed for direct photons. On the one hand, the p_{T}-differential production yield and its nuclear modification. On the other hand, the azimuthal asymmetry with respect to the reaction plane of the event. The latter is expressed as the magnitude of in- and out-of-plane yield asymmetry v_2, instead of a $\Delta\varphi$-differential R_{AA}.

4.5.1. Direct Photon Yield

The measurement of direct photons at high p_{T} provides a direct control for the rate of the initial hard scatterings in heavy-ion collisions. The observation of no nuclear modification of photons for $p_{\mathrm{T}} > 4\,\mathrm{GeV}/c$ by the PHENIX experiment has been a key component to establish the strong final state effect in central Au + Au collisions at $\sqrt{s_{\mathrm{NN}}} = 200\,\mathrm{GeV}$. In this case, the direct photon signal R_{γ} has been extracted via the calorimetric measurement of photons and the statistical comparison to the expected decay background [KB05, Adl05a]. This observation has been further strengthened by the reference measurement of direct photons at high p_{T} in pp collisions [CKB03], where the agreement with NLO pQCD predictions has

been shown. Furthermore, the pp reference measurement demonstrated that at high p_T the majority of photons occurs isolated and is not produced in a late fragmentation process of a parton. A large fraction of these fragmentation photons would have resulted in a nuclear modification factor smaller than unity in central Au + Au reactions.

For the yield of direct photons at low p_T, the production from thermalized sources, i.e. the QGP or the hot hadron gas, is expected to become the dominant mechanism. They are emitted throughout the lifetime of the thermalized system and escape the medium unaffected. Thus, these direct photons provide valuable information on the properties of the medium, beyond the test of initial hard scattering rates. In the region $p_T < 4\,\mathrm{GeV}/c$, direct photons have been observed by PHENIX in Au + Au collisions at $\sqrt{s_{NN}} = 200\,\mathrm{GeV}$ [Ada10a] via the measurement of *internal conversions*. It is an indirect approach where the increased production of e^+e^- pairs (*virtual photons* with $m > 0$) for $1 < p_T < 5\,\mathrm{GeV}/c$ is used to deduce the excess of real photons ($m = 0$). As shown in Figure 4.8, an enhancement above the scaled expectation from pp reactions is observed below $3\,\mathrm{GeV}/c$. It can be parameterized with an exponential with $T = 221 \pm 27\,\mathrm{MeV}$. This can be interpreted as a temperature averaged over the evolution of the system. It is well above the critical temperature for the phase transition to the QGP. It provides a direct constraint on the initial conditions in the QGP for hydrodynamic models. These reach a qualitative agreement with the data for initial temperatures $T_0 = 300 - 600\,\mathrm{MeV}$ and formation times $\tau_0 = 0.6 - 0.15\,\mathrm{fm}/c$.

The first preliminary results on direct photon production in heavy-ion collisions at the LHC for $p_T < 10\,\mathrm{GeV}/c$ have been presented for ALICE in [CKB09] using the reconstructed e^+e^- pairs from *external conversions*. These are conversions of real photons in the detector material. The advantage of this method compared to a calorimetric measurement is the excellent momentum resolution at low p_T and the high purity of the inclusive photon measurement. The result for the 0-40% most central Pb + Pb collisions at $\sqrt{s_{NN}} = 2760\,\mathrm{GeV}$ is also shown in Figure 4.8. For $p_T > 5\,\mathrm{GeV}/c$ the measured direct photon yield agrees with the expectation from a pp (vacuum) NLO pQCD calculation scaled by the number of binary collisions. The agreement demonstrates that also at the LHC the initial hard scatterings occur at the expected rate. There is no indication for a large contribution of suppressed fragmentation photons or a strong modification of the parton distribution in the initial state. The latter is confirmed at higher p_T (larger x) via the measurement of the nuclear modification factor of isolated direct photons [Cha12a] and other color neutral probes such as the Z^0 [Aad11, Cha11].

At low p_T, ALICE observes a similar exponential behavior in the direct photon measurement as seen by PHENIX at RHIC. The slope is visibly flatter at the higher energy, indicating

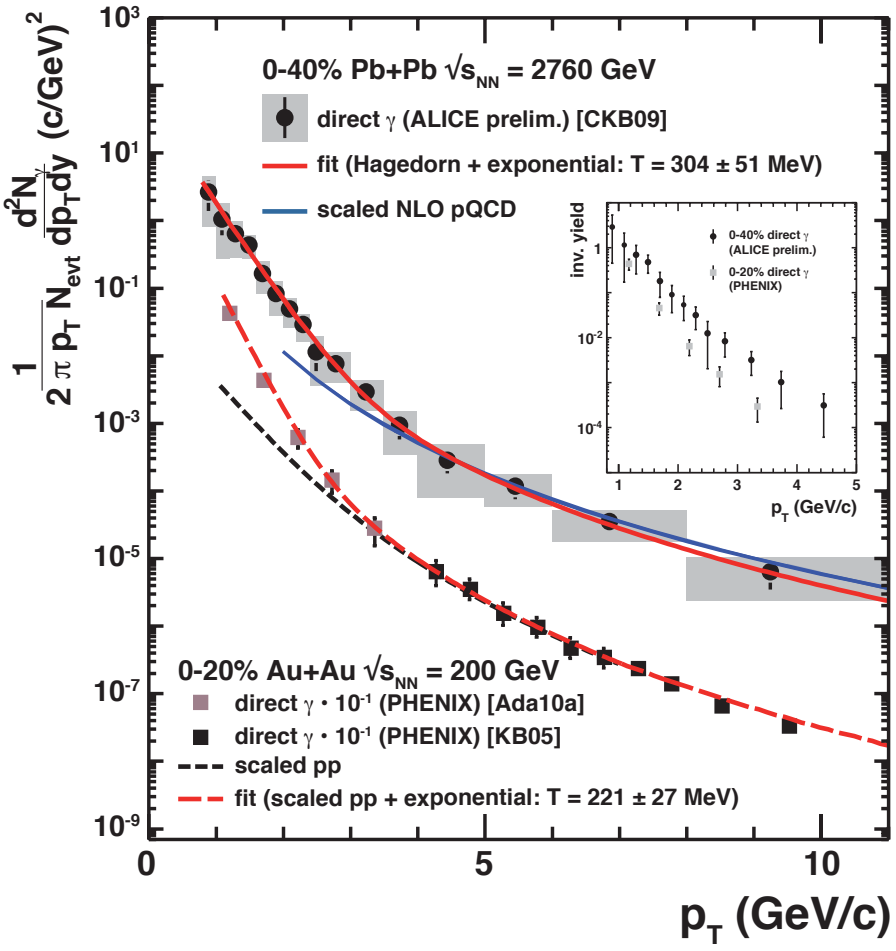

Figure 4.8.: Direct photon yield measured in central Pb+Pb [CKB09] and Au+Au collisions [KB05, Ada10a]. A clear enhancement at low p_{T} is seen in both cases above the scaled pp measurement and the high-p_{T} NLO trend. It can be parameterized by an exponential with slope $T_{200} = 221 \pm 27\,\mathrm{MeV}$ and $T_{2760} = 304 \pm 51\,\mathrm{MeV}$, respectively. The inset shows the direct comparison of the direct photon yield RHIC ad LHC at low p_{T} without the offset factor of 10^{-1}.

a higher effective temperature. A combined fit to the full spectrum yields $T = 305 \pm 51\,\mathrm{MeV}$, which is about 35% higher than in Au + Au collisions at $\sqrt{s_{\mathrm{NN}}} = 200\,\mathrm{GeV}$. This increase is similar to the approximately 30% change of the initial temperature estimated from the comparison of charged particle production as a proxy for the initial energy density (see Chapter 2.3.2).

4.5.2. Direct Photon v_2

A more differential test of the medium properties is provided by the measurement of the direct photon production with respect to the initial geometric asymmetry of the overlap region. Again, the momentum region $p_T > 6\,\mathrm{GeV}/c$ reflects the particles or partons produced in early hard scattering. For $p_T < 3\,\mathrm{GeV}/c$, the asymmetry of direct photon production with respect to the event reaction plane is sensitive to collective motion (flow) of the thermalized constituents of the QGP and the hot hadron gas.

The direct photon flow coefficient $v_2^{\gamma,\mathrm{dir}}$ is obtained by comparing the expected momentum asymmetry of the hadron decay background, $v_2^{\gamma,\mathrm{bg}}$, to the inclusive photon v_2 [CKB07]:

$$v_2^{\gamma,\mathrm{dir}} = v_2^{\gamma,\mathrm{inc}} + \frac{v_2^{\gamma,\mathrm{inc}} - v_2^{\gamma,\mathrm{bg}}}{R_\gamma - 1}. \tag{4.4}$$

The inclusive photon v_2 is reduced or enhanced by a direct photon v_2 that is smaller or larger than $v_2^{\gamma,\mathrm{bg}}$, respectively. Thus, it is corrected by the difference between the measured inclusive and expected background v_2 and weighted by the direct photon signal strength as given by $R_\gamma - 1$ in a certain p_T bin. When $v_2^{\gamma,\mathrm{dir}}$ is similar to $v_2^{\gamma,\mathrm{bg}}$, this term is only a small correction.

Two detectors have been employed at PHENIX to determine the reaction plane, the BBC, and the reaction plane detector RXN. The latter provides a better resolution of the event plane but is closer to mid-rapidity, which makes it more sensitive to a jet induced bias in the reaction plane determination. The v_2 measurement using the BBC is shown in Figure 4.9 for inclusive photons and neutral pions together with the extracted direct photon flow coefficient. At low p_T, where $R_\gamma \approx 20\%$, the values inclusive for photons and π^0s are very similar, which already points to a significant flow of direct photons. The magnitude of the extracted direct photon flow shown in the right panels of Figure 4.9 is surprising. While in a hydrodynamic picture hadronic flow is built up during the full evolution of the fireball down to the kinetic freeze out at $T_{\mathrm{fo}} \approx 100\,\mathrm{MeV}$, direct photons decouple from the medium evolution at all temperatures once they are produced. In this case, a large direct photon flow points to a late production, which obscures the interpretation of the observed slope parameter as effective temperature, dominated by early thermal production in the QGP. This is also illustrated by the comparison to two hydrodynamic calculations in Figure 4.9 for different formation times τ_0 [Cha09]. The later formation leads to a smaller contribution from the QGP phase, which has a smaller v_2. Even with a large formation time of $\tau_0 = 0.6\,\mathrm{fm}/c$ the trend observed in the data is not fully reproduced. The ALICE experiment has presented preliminary results that confirm the large elliptic flow of direct photons also at the LHC [Loh12], providing

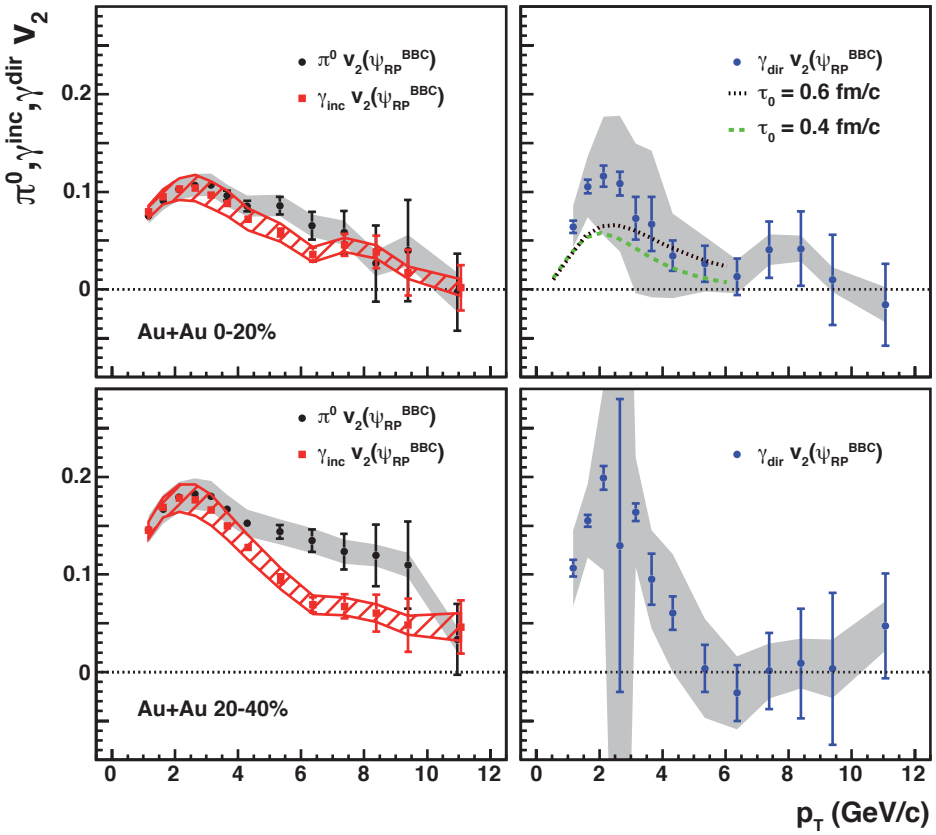

Figure 4.9.: Azimuthal asymmetry v_2 of neutral pions, inclusive and direct photons for central and semi-central Au + Au collisions at $\sqrt{s_{NN}} = 200\,\text{GeV}$ [CKB07]. In addition, the upper right panel also shows two hydrodynamic calculations from [Cha09] using different initial formation times.

additional input to the further development and tuning of hydrodynamic models, which are vital for the quantitative interpretation of the observables of partonic energy loss. Using a fireball description with a more violent transverse expansion, a recent study in [vH11] found a consistent hydrodynamic description of the v_2 and low p_T production spectra for hadrons and direct photons at RHIC. The large effective temperature extracted from the direct photon yield is explained by the blueshift of photons produced in the hadronic phase (compare Equation (3.14)). The larger fraction of photons from the hadronic phase can then account for the large v_2, as discussed above. In addition to this conventional approach, more exotic sources of a large direct photons v_2 are currently discussed, such as the photon emission due to strong electromagnetic fields in heavy-ion collisions [Bas12] or from the pre-equlibrium phase in the transition from a color-glass condensate initial state to a thermalized QGP [Chi13].

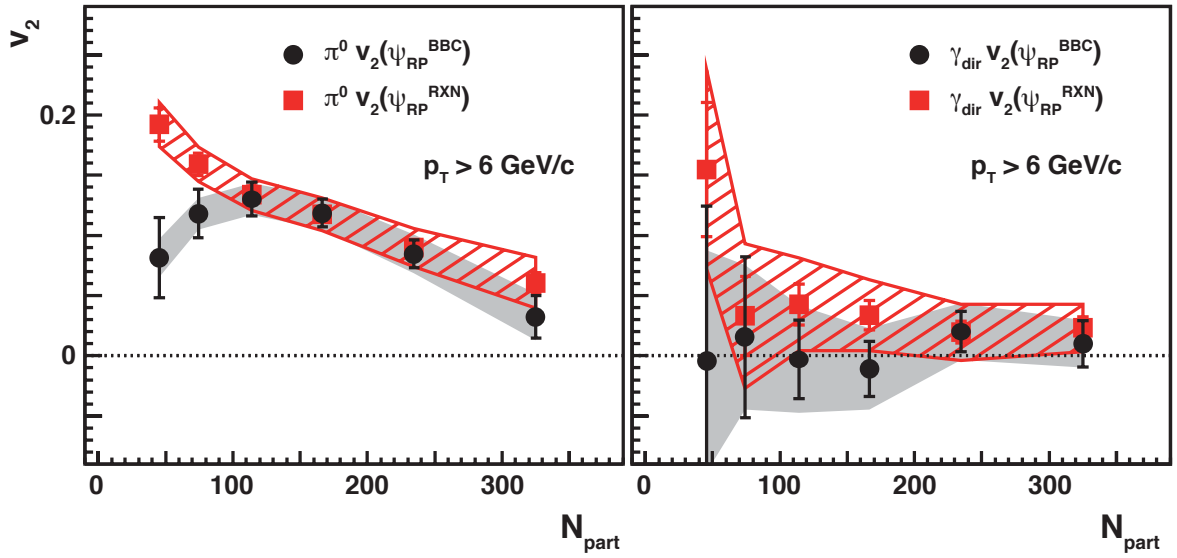

Figure 4.10.: Centrality evolution of the integrated v_2 above 6 GeV/c for neutral pions and direct photons using two different detectors for the determination of the event plane [CKB07].

At high p_T, the direct photon v_2 is dominated by the production in hard processes. In this regime, different mechanisms influence the azimuthal asymmetry of direct photons. At leading order, hard direct photons are pre-dominantly produced by quark-gluon Compton scattering ($qg \rightarrow \gamma q$). Direct photons produced in LO processes do not exhibit any dependence on the orientation to the reaction plane. I.e. the nuclear modification factor is expected to be unity for all cases in a $\Delta\varphi$-differential measurement. Expressed as the magnitude of in- and out-of-plane yield asymmetry, this is tantamount to $v_2 = 0$. Photons produced directly in the fragmentation of a parton have positive v_2 since the energy loss of the originating parton is smaller in the reaction plane. Jet-conversion photons, where a hard-scattered quark interacts with a thermal gluon in the medium and converts into a photon with almost equal p_T are expected to have negative v_2 because the conversion probability is larger along the larger path length out of the reaction plane than within. Similarly, photon bremsstrahlung induced from the large density of electric charges in the medium is emitted preferentially in the direction where the medium is thicker.

The finite v_2 of π^0s at high p_T, as seen in Figure 4.9, is caused by the path-length dependence of energy loss as discussed in the previous section. The asymmetry is larger

for the more eccentric system in the centrality class $20-40\%$. The direct photon v_2 for $p_{\mathrm{T}} \gtrsim 4\,\mathrm{GeV}/c$ is consistent with zero. The centrality dependence of the integrated v_2 above $p_{\mathrm{T}} = 6\,\mathrm{GeV}/c$ is shown in Figure 4.10. The behavior in peripheral events (low N_{part}) is strongly influenced by the pseudo-rapidity window covered by the reaction plane detector. The π^0 v_2 is comparable to other hadrons and shows a clear evolution with centrality. It is smallest for the almost symmetric overlap region in central events. The two direct photon v_2 measurements are both consistent with zero. This corresponds to the expected behavior if the leading order production of photons is the dominant source of photons. The measurement is currently not sensitive to the typical contributions from jet-conversion and fragmentation photons, which are expected to be at the level of $v_2 \approx 0.02$ and $v_2 \lesssim 0.01$ [Tur06, Gal10].

4.6. Constraining Energy Loss Parameters

For the nuclear modification factor the comparison of different dependences, e.g. on geometry and energy density, is a valuable tool for discerning various model assumptions for parton energy loss. However, to reach the goal of a tomographic picture of the medium, one must consider one further aspect: The quantitative determination of the medium parameters that govern the parton energy loss.

Here, the most important input to models are the overall magnitude of the suppression and its evolution with p_{T} in a momentum region that is dominated by particles produced in parton fragmentation, so beyond $6\,\mathrm{GeV}/c$. For quantitative constraints not only the experimental data has to cover a broad p_{T} range; the effects of the different systematic uncertainties on the overall normalization and the shape of R_{AA} need to be quantified for the model comparison. This has been done in [CKB06], using a high statistics measurement of neutral pions and employing a refined χ^2 minimization approach that takes into account normalization, p_{T}-correlated, and p_{T}-uncorrelated uncertainties in the experimental data. Exemplarily, the comparison to the PQM model [Dai05] is shown in Figure 4.11. The refined χ^2 value, $\tilde{\chi}^2$, is calculated for a model curve with given medium parameter, here the average effective transport coefficient $\langle\hat{q}\rangle$, and the best match is provided via the minimal $\tilde{\chi}^2$. The data constrain the value of $\langle\hat{q}\rangle$ to $13.2^{+2.1}_{-3.2}\,\mathrm{GeV}^2/\mathrm{fm}$ at one-standard deviation level and confirms the view that the created matter in heavy-ion collisions consists of strongly coupled partons. As seen in Figure 4.11, the precision data on neutral pion production provides a strong constraint on the magnitude of partonic energy loss in a given model.

However, the procedure does not take into account the large model dependent uncertain-

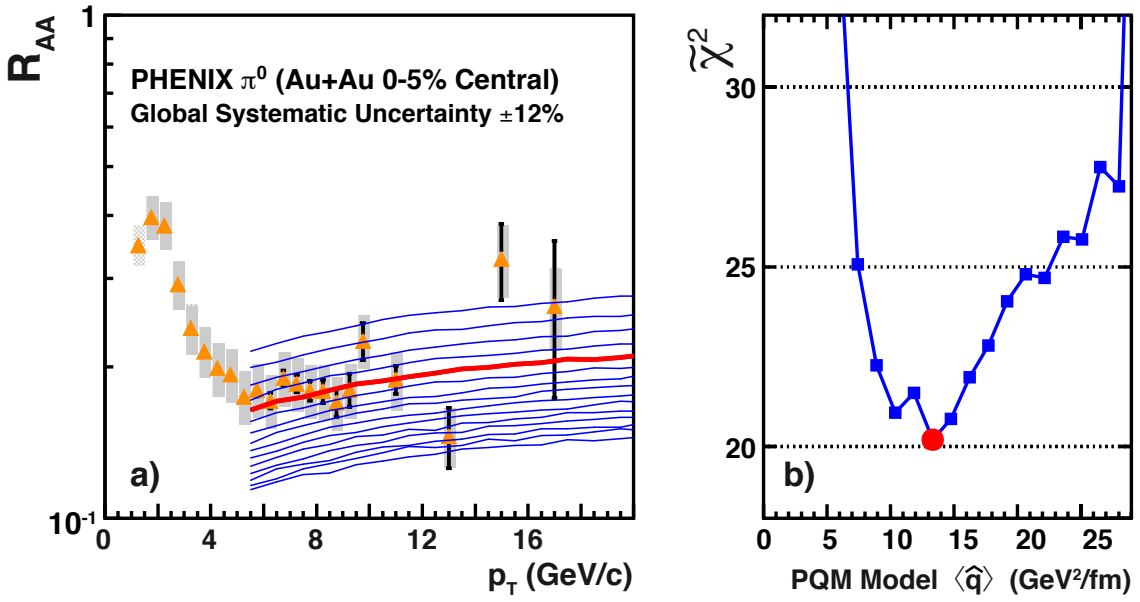

Figure 4.11.: Nuclear modification factor compared to the expectation from the PQM model for different medium parameters $\langle\hat{q}\rangle$ [CKB06]: a) direct comparison b) χ^2 with respect to the measured R_{AA} for different $\langle\hat{q}\rangle$.

Model Name	Model Parameter	One Standard Deviation Uncertainty	Maximum p-value
PQM	$\langle\hat{q}\rangle = 13.2\,\mathrm{GeV}^2/\mathrm{fm}$	$+2.1\ -3.2$	9.0%
GLV	$\mathrm{d}N^g/\mathrm{d}y = 1400$	$+270\ -150$	5.5%
WHDG	$\mathrm{d}N^g/\mathrm{d}y = 1400$	$+200\ -375$	1.3%
ZOWW	$\varepsilon_0 = 1.9\,\mathrm{GeV/fm}$	$+0.2\ -0.5$	7.8%
Linear	b (intercept) = 0.168	$+0.033\ -0.032$	11.6%
	m (slope) = 0.0017 (c/GeV)	$+0.0035\ -0.0039$	

Table 4.2.: Quantitative constraints on the parameters from different models: PQM [Dai05], GLV [Vit06b], WHDG [Wic07], and ZOWW [Zha07] parton energy loss models and a linear fit.

ties in the quenching scenario, the model simplifications, and the description of the medium and its evolution. A direct comparison between models is also complicated by the fact that the medium properties are expressed in terms of different variables, such as the initial gluon density, the average medium transport coefficient, or the initial temperature. Table 4.2 shows these relevant energy loss parameter for various model. They are constrained to the PHENIX data with the procedure as described above. The parameters are closely related to each other via the thermodynamic properties and the evolution of the medium as well as the fundamental cross sections for parton-parton interactions in the medium. Once compared on the same grounds, it is seen that the medium parameters from different models only agree within a factor of 3–4 [d'E10]. This lead to concentrated theoretical efforts in the last years to separate the possible sources of differences, e.g. via a unified implementation of the hydrodynamic evolution coupled to the energy loss calculation [Bas09, Ren12], and the comparison of pure energy loss descriptions in a generic setup: the passage of partons through a static *brick* of QCD matter of finite length [Arm12]. It has been found that the major sources of discrepancies between models for the predicted radiated energy within the brick are related to model simplifications and approximations, but not to fundamental differences in the respective assumptions.

The hypothesis of a constant nuclear modification factor has also been tested with the PHENIX data. As seen in Table 4.2, a slope parameter of $0.0017^{+0.0035}_{-0.0039}\,c$/GeV was found in the region between 5 and 20 GeV/c, consistent with a flat R_{AA}. The negligible variation of R_{AA} at RHIC remains the major obstacle in the separation of energy loss scenarios. As discussed in the context of the toy model R_{AA} in Chapter 3.3, such behavior can be caused by three generic assumptions: a black-and-white picture, where only unquenched partons from the surface of the fireball contribute to the particle yield at high p_{T}, a constant fractional energy loss, and a moderately large constant energy loss.

However, after tight constraints on the individual model parameters have been extracted based on the author's work with PHENIX, the increase in collision energy at the LHC provides a more stringent test. In particular, the flatter parton spectrum provides an increased sensitivity to generic model assumptions as seen already in the toy model R_{AA} Figure 3.4.

4.7. Single Particles at the LHC: A Large Lever Arm

With the first measurement of Pb + Pb collisions at the LHC, it was possible to test parton energy loss models over more than one order of magnitude in collision energy. In particular,

the study of single particle suppression offers several qualitatively new aspects compared to RHIC: the flatter parton spectrum provides a higher sensitivity to the medium parameters, the increased cross section for high-p_{T} particle production allows for the study over a broader p_{T} range, and the large increase in energy allows to test the temperature dependence of model parameters constraint at RHIC energies.

The nuclear modification factor for charged particles in central Pb + Pb collisions at $\sqrt{s_{\mathrm{NN}}} = 2760\,\mathrm{GeV}$ has been measured by the ALICE experiment with the tracking system of the central barrel. With this measurement ALICE has established the expected suppression of hadron production at high p_{T} for LHC energies [Aam11b], and the magnitude of R_{AA} provided the first benchmark of the models validated at lower energy. The R_{AA} for the 5% most central collisions is shown in Figure 4.12. It reaches a minimum of approximately 0.14 around $6\,\mathrm{GeV}/c$. This value is lower than in any previous measurement of the nuclear modification factor. For the first time, a clear increase of the nuclear modification factor is observed for higher p_{T}. This feature is contained in any energy loss calculation as long as the limit of constant fractional energy loss is not reached as discussed in Chapter 3.3. This clearly demonstrates that it is no longer possible to explain the evolution of R_{AA} with p_{T} within a simple black-and-white picture. R_{AA} appears to saturate above $40\,\mathrm{GeV}/c$ at about $0.4 - 0.5$, a trend that is supported by charged particle measurements of CMS that extend to $100\,\mathrm{GeV}/c$ [Cha12d]. The data in peripheral collisions (not shown here) is consistent with only little energy loss. It exhibits no pronounced minimum and R_{AA} is constant at high p_{T}.

A selection of different parton energy loss models is compared to the data in Figure 4.12. The comparison compiled here includes all major energy loss scenarios with model implementations from different authors. For most of these models the absolute magnitude of the suppression was calibrated at RHIC and for the prediction only the increase in energy density at LHC was taken into account. Figure 4.12 a) shows models based on a leading parton energy loss description for elastic energy loss ($\propto L$), radiative energy loss ($\propto T^3L^2$ WHDG, ASW), and strong coupling ($\propto T^4L^3$, AdS/CFT). They all show a similar increase from low to high p_{T} as also seen in the data, but fail to match the overall magnitude of the suppression. Radiative and strong coupling models show too large suppression, while the elastic energy loss is too small at low p_{T}. So while the energy dependence of R_{AA} going from RHIC to LHC favors a parametric dependence L^n with $1 < n < 2$, the reaction plane dependent R_{AA} measured by PHENIX prefers $2 \leq n < 3$ as discussed above. This supports once more the view that radiative energy loss is the dominant mechanism for in-medium energy loss, with some room for contributions from QCD elastic scattering. Exotic models that only contain

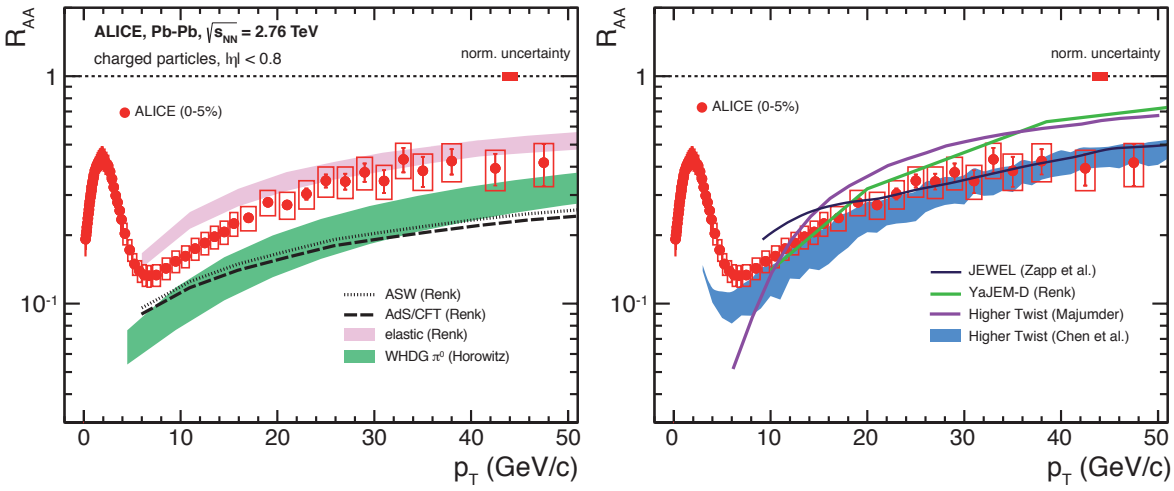

Figure 4.12.: The nuclear modification factor in central Pb + Pb collisions at $\sqrt{s_{\mathrm{NN}}} = 2760\,\mathrm{GeV}$ [Abe13a] compared to various model predictions. a) Leading parton energy loss models [Hor11, Sal03, Ren12] b) (Radiative) QCD-energy loss models with full shower evolution [Che11, Maj08, Ren11, Zap13]. All models from Renk share the same (2+1)D medium evolution model. JEWEL also incorporates elastic energy loss.

higher powers in the length dependence are ruled out by the combination of RHIC and LHC data.

The models that are compared to the data in Figure 4.12 b) take a different approach to the modeling of high p_{T} parton suppression. Their major mechanism also is QCD radiative energy loss, but rather than a leading parton effect, they model the full in-medium shower evolution. This leads to an additive component to the fragmentation function, which explicitly keeps track of low z hadron production from the medium induced soft gluon radiation. The sensitivity of R_{AA} to this radiation is suppressed at RHIC energies due to the steeper parton spectrum, and it has been sufficient to account only for the leading parton energy loss. As seen in Figure 4.12 b), full in-medium evolution models provide a better description of R_{AA}, but clearly further improvements will be facilitated with more differential suppression measurements, such as the reaction plane dependent R_{AA}, and advances in the hydrodynamic evolution model.

An additional field where leading parton energy loss models are bound to fail is the description of the modification of full jets in a QGP. Here, the full shower evolution is tested by definition. The sensitivity of jet observables to the medium modified shower beyond the

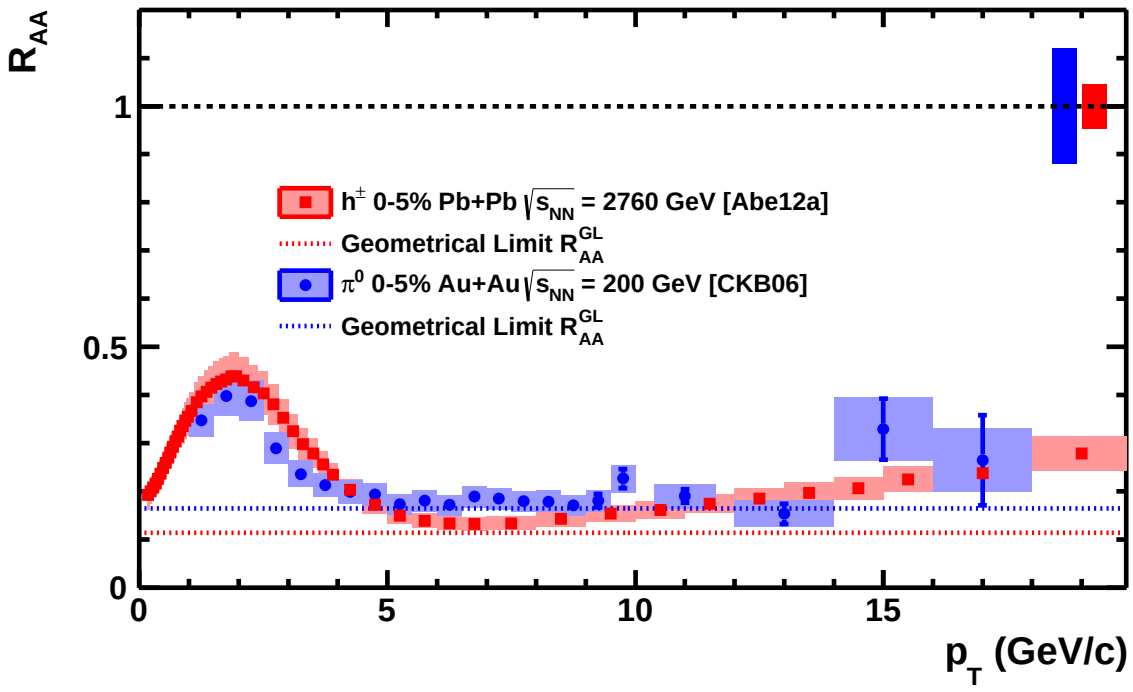

Figure 4.13.: Nuclear modification factor in central collisions at RHIC [CKB06] and LHC [Abe13a] compared to the geometric limit from surface emission as given by Equation (4.1) with $k = 1$.

leading parton energy loss will be discussed in Chapter 5 together with the first preliminary results on reconstructed jets measured with ALICE, which have been the author's primary research interest during the last years.

Surface Emission Limit in Central Collisions

The basically p_{T}-independent R_{AA} in central Au + Au collisions at RHIC is consistent with a surface dominated emission and the overall magnitude is reproduced via the estimated surface-to-volume ratio as given by Equation (4.1). In this extreme case, only particles originating from partons produced close to the surface of the medium contribute to the particle yield at high p_{T}. All other partons are completely absorbed, i.e. their energy is redistributed to low momentum such that the produced hadrons do not exhibit any jet-like properties and cannot be separated from the (thermal) background.

The strong p_{T} dependence of R_{AA} observed in central Pb + Pb collisions at the LHC does no longer support this picture. However, it may still hold in a finite kinematical range. In that case, the sensitivity of R_{AA} in this regime to the details of parton energy loss is very limited.

In Figure 4.13, the nuclear modification factor for neutral pions at $\sqrt{s_{\mathrm{NN}}} = 200\,\mathrm{GeV}$ and for charged hadrons at $\sqrt{s_{\mathrm{NN}}} = 2760\,\mathrm{GeV}$ is shown for the 5% most central collisions. The two can be compared directly above a transverse momentum of $p_{\mathrm{T}} \gtrsim 6\,\mathrm{GeV}/c$ since here the p/π-ratio in heavy-ion collisions returns to the value in proton-proton reactions. The geometric limit following Equation (4.1) is indicated as a dotted line for each collision system. It is reached in both cases at intermediate transverse momentum of $6-8\,\mathrm{GeV}/c$. While the data at $\sqrt{s_{\mathrm{NN}}} = 2760\,\mathrm{GeV}$ show a clear increase towards larger p_{T} the PHENIX measurement is compatible with an increase, as well as with a flat p_{T}-dependence. It is remarkable that the simple estimate reproduces the overall difference of the minimum observed R_{AA} at both energies. This points to the small sensitivity of the nuclear modification factor in this p_{T} range to the details of partonic energy loss and the slope of the parton spectrum. In case the particle production is driven only by jets from the surface, a stronger partonic energy loss will not lead to a modification of the spectral shape of single particles. It is also interesting to note that in the case of particles originating from heavy quark fragmentation, such as non-photonic electrons [Adl06] and reconstructed D-mesons [Abe12c], the observed nuclear modification factor is very similar to the one of hadrons from the fragmentation of light quarks/gluons. This can be interpreted such that the geometric limit has already been reached for the heavy quarks. Then, R_{AA} in this region is not sensitive to the mass dependence of the radiative energy loss, where heavy quarks are expected to lose less energy via induced gluon radiation than light quarks and gluons.

5. Testing Parton Energy Loss II: Jet Measurements in ALICE

The study of the parton energy loss in heavy-ion collision via reconstructed jets has been the main focus of the author's research work at the ALICE experiment during the last years. It is the natural continuation of the single particle measurements at high p_{T} presented in the previous chapter. A reconstructed jet covers a certain angular region, which is determined by the distance parameter or radius R of the algorithm as illustrated in Figure 5.1. Thus, by definition the four momentum of the reconstructed jet is closer to the original parton momentum and sensitive to the angular distribution of shower fragments beyond the leading particle in the fragmentation. When in heavy-ion collisions the energy lost by the leading parton is radiated within the jet radius it can be recovered and the jet nuclear modification factor is unity. In this case, the parton-medium interaction must should only be seen in the modification of the longitudinal and transverse structure of the jet, i.e. the change of the fragmentation pattern compared to elementary pp reactions.

However, the angular region covered by a jet can also contain particles from other sources than the parton fragmentation. These particles are usually considered as background. In the context of heavy-ion collisions, this underlying event (UE) of particles not related to the hard scattering significantly contributes to the reconstructed jet momentum. The background can be reduced e.g. by a minimum p_{T} threshold on particles used as input for the jet finding procedure or by choice of a smaller radius R. Both options lead to an increased bias on the fragmentation pattern of the reconstructed jets and a loss of information, in particular on the redistribution of momentum below the threshold and to larger angles.

The ability of ALICE to reconstruct charged particles with high and uniform efficiency down to low p_{T} is a pre-requisite for the measurement of jet constituents over a broad kinematic range. It enables the necessary characterization of the background momentum density in the events and its local variation. These can be measured and then employed directly in the correction of the reconstructed jet observables. The main effects of the heavy-ion background on jet reconstruction and the corrections to the inclusive reconstructed jet spectra are

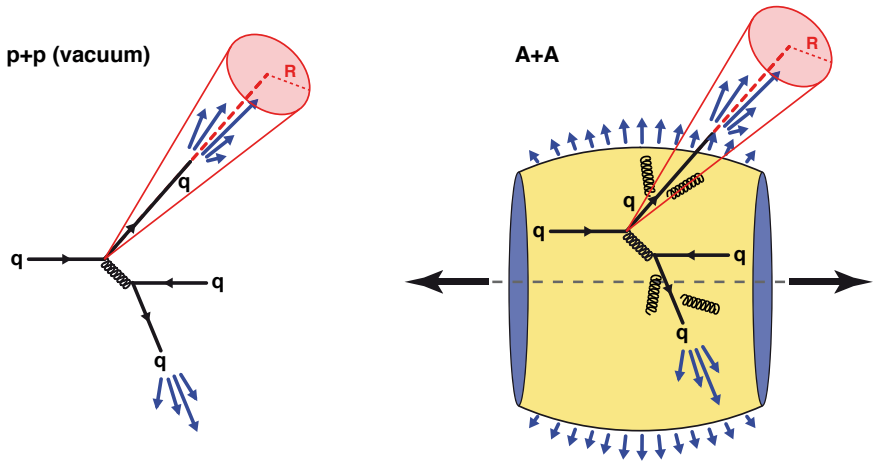

Figure 5.1.: Illustration of jet reconstruction from the fragments of a single hard scattered quark in pp and *AA* collision. The observable particles are collected in an angular region around the original parton direction, e.g. a cone with given radius R in (η, φ). In *AA* reactions a significant amount of uncorrelated background falls into this cone, as discussed in the text. The background contribution from the underlying in pp reaction is negligible and not shown in this sketch.

discussed below. Finally, the nuclear modification of different reconstructed jets measured with ALICE at the LHC is compared to the measurement of single hadrons. In the comparison, the latter provides the limiting case of a jet measurement with $R \to 0$. It is free of underlying event contamination but highly biased in terms of the selected fragmentation pattern and the origin of the hard scattered parton, which is expected to be closer to the surface of the collision region as discussed in the previous chapter.

5.1. Jet Reconstruction

The visual impression of a jet, as a collimated spray of hadrons in the direction of the originally produced parton with a large momentum, is instructive. However, it is not the precise definition that is needed to enable quantitative comparisons of experimental jet observations and perturbative QCD calculations. A jet definition is given by the procedure how to recombine the observed particles into a single four momentum vector or in theoretical calculations by phase space (angular) cuts in the integration of partonic cross sections beyond leading order. One of the first jet definitions has been used in [Ste77] for the calculation of the probability to observe two jets in an e^+e^- annihilation. Two-jet events have been defined by the

requirement to observe a fraction $(1-\varepsilon)$ of the total event energy $\sqrt{s}$ in two opposing cones of opening angle θ. The choice of the two parameters θ and ε is arbitrary and has a direct impact on the observed and calculated cross sections, respectively. This already illustrates the fact that jets are not uniquely identifiable objects. Instead, they are defined via a certain algorithm and its parameters.

The jet algorithms used in the following are the sequential recombination algorithms k_{T} and anti-k_{T} [Cat93, Cac08]. Both are insensitive to divergences that occur in QCD beyond leading order. The reconstructed jet properties do not change if one parton is replaced by two in the same direction that share the energy (*collinear safety*) and if a very soft gluon is added to the event (*infrared safety*).

The algorithms start with a list of clusters (e.g. particles, partons, or calorimeter cells) and calculate

$$\begin{aligned} d_i &= p_{\mathrm{T},i}^{2m}, \\ d_{ij} &= \min(p_{\mathrm{T},i}^{2m}, p_{\mathrm{T},i}^{2m}) \cdot \frac{R_{ij}^2}{D^2} \end{aligned} \tag{5.1}$$

for each cluster i and all pair combinations ij. The distance measure d_{ij} as well as d_i use $m = 1$ for the k_{T}-algorithm and $m = -1$ in case of the anti-k_{T} algorithm. $R_{ij}^2 = (\eta_i - \eta_j)^2 + (\varphi_i - \varphi_j)^2$ is the squared distance in (η, φ), which is weighted with the distance parameter D, the free parameter of the algorithm [Sal10]. If the minimum of all d_i, d_{ij} belongs to a pair ij, then the two clusters are merged and the new cluster is inserted in the list. In the case the minimum is single cluster i, it is removed from the list and called a jet. This procedure is repeated until the list is exhausted and all initial clusters are associated with a jet object.

The different exponent m in Equation (5.1) for the two algorithms directly affects the order of how particles are recombined into the jets. In the anti-k_{T} algorithm, high-p_{T} particles are combined first, while k_{T} starts with low-p_{T} particles. The latter mimics the inversion of the branching in a parton shower and collects particles from rather irregular areas. In Figure 5.2 (left), the shape and constituents of jets reconstructed from charged particles in one pp event can be compared for the two algorithms. It is clearly seen that all particles in the event are contained in reconstructed jet objects. The majority of these should not be interpreted as belonging to a hard scattered parton, since their reconstructed momentum is very low. Both algorithms clearly identify the two leading jets in the event, back-to-back in φ ($\Delta\varphi \approx \pi$) and with $p_{\mathrm{T}}^{\mathrm{jet}} > 25\,\mathrm{GeV}/c$. Some reconstructed properties of the two leading jets are summarized in Table 5.1. The main difference between the two algorithms is that the

k_T jets exhibit large areas and a rather irregular shape, while anti-k_T prefers a circular area $A \approx \pi R^2$ with radius $R = D$ for high-p_T jets.

In the following a further experiment specific distinction of jet types is done. Since ALICE features a tracking system that covers the full azimuth and calorimetry is only installed for a smaller acceptance (roughly 10% of the tracking coverage), two types of reconstructed jets will be distinguished depending on their input. *Charged jets* only use reconstructed tracks as input, so ideally contain all charged particles. *Full jets* combine the momentum information of the ALICE tracking system with the neutral energy measurements in the EMCal.

	k_T algorithm			anti-k_T algorithm		
	$p_T^{jet,rec}$	area	index	$p_T^{jet,rec}$	area	index
Jet A	66.8 GeV/c	1.21	1	61.6 GeV/c	0.50	1
Jet B	27.1 GeV/c	0.60	2	27.1 GeV/c	0.50	2

Table 5.1.: Properties of the two jets with largest momentum (leading and sub-leading) reconstructed with the k_T and anti-k_T algorithm for the same simulated pp event at $\sqrt{s} = 2760$ GeV. The corresponding event displays are shown in Figure 5.2 (left).

5.2. Jet Event Background and Fluctuations

5.2.1. Background Momentum Density

In central heavy-ion collisions, the particle occupancy in the detector is so large that the acceptance of the ALICE tracking system is filled with reconstructed charged jets as seen in Figure 5.2 (center). The increase in charged particle multiplicity compared to pp reactions at the same energy leads to several jets with reconstructed momentum in the region of 60–90 GeV/c, and the momentum is clearly no longer sufficient to attribute a reconstructed jet to a hard scattering. The reconstructed momentum of background jets depends basically on the area. This is seen in the rather uniform color distribution of the circular anti-k_T jets in Figure 5.2 (middle). It is useful to define a background transverse momentum density ρ for each event, i.e. the p_T per unit area in (η, φ), under the premise that the majority of reconstructed objects is due to the soft background in the event.

For this, the median of all momentum densities p_T/A for the jet objects as reconstructed by the k_T algorithm is calculated, after exclusion of the two clusters with the highest p_T.

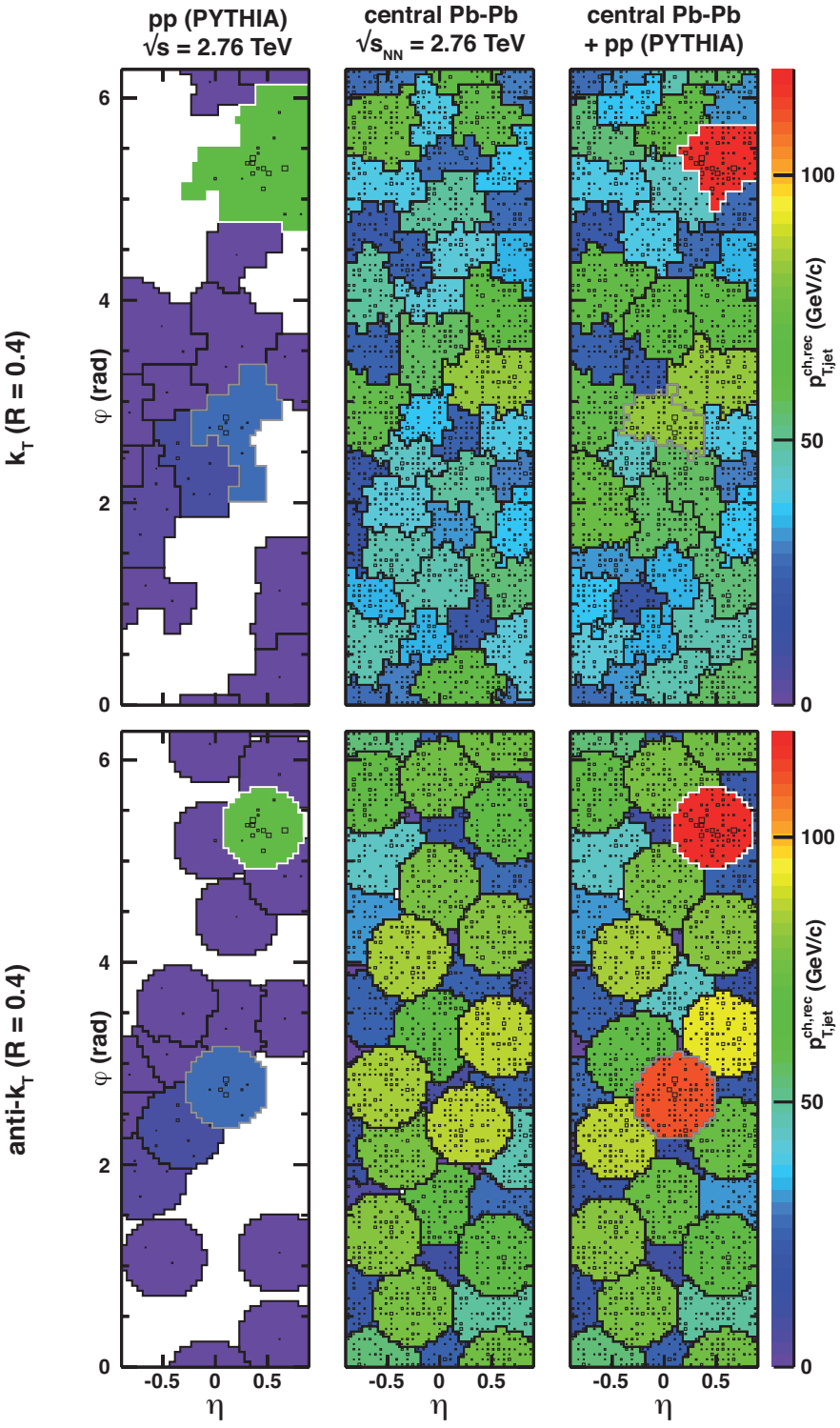

Figure 5.2.: Contours of jets reconstructed with the k_{T} and anti-k_{T} algorithm and $R = 0.4$ from charged particles reconstructed with the ALICE tracking system. Left: Simulated pp event with two high-p_{T} jets. Middle: measured heavy-ion event. Right: Combined event, the matched leading (sub-leading) jet from the pp event is shown by the white (grey) border. Some reconstructed jet properties are given in Tables 5.1 and 5.2.

The irregular shapes are advantageous for a more uniform sampling of the $p_{\mathrm{T}}$and a possible medium response to the traversing parton. density in the event and further suppresses high-p_{T} outliers. The correlation of ρ with the number of particles used as input in the jet finding, $N_{\mathrm{input}}^{\mathrm{raw}}$, is shown in Figure 5.3. The linear increase of the centroids is evident and demonstrates that the background density is driven by the same (soft) processes that also dominate the total particle production. For a typical jet cone with $R = 0.4$ (as for the circular jets in Figure 5.2), the event background $\pi R^2 \rho$ of charged particle tracks in the 10% most central events amounts to $\approx 70\,\mathrm{GeV}/c$ with an event-by-event variance of $9.25\,\mathrm{GeV}/c$ [CKB08]. In case also neutral particles are taken into account, which is needed for the analysis of full jets, the background is expected to increase by about 50%.

The reconstructed anti-k_{T} jets form the basis for the jet signal extraction. They are corrected on average for the event background via:

$$p_{\mathrm{T}}^{\mathrm{jet}} = p_{\mathrm{T}}^{\mathrm{jet,rec}} - \rho \cdot A^{\mathrm{jet,rec}}, \tag{5.2}$$

where $p_{\mathrm{T}}^{\mathrm{jet,rec}}$ is the uncorrected jet momentum, $A^{\mathrm{jet,rec}}$ its area, and ρ is the momentum density determined in the same event as the reconstructed jet in question.

In Figure 5.2 (right), the heavy-ion event and the pp jet event have been combined and reconstructed with the k_{T} and anti-k_{T} jet algorithm, respectively. The performance of the two jet algorithms in the presence of the heavy-ion event background is rather different. While in the case of anti-k_{T} the matched pp jets basically cover the same region, the area in the case of the k_{T} jet finder is strongly modified (*back reaction*). Hence, it is very difficult in the case of k_{T} jet objects to interpret jet modifications for different distance parameters and to compare to the same measurement in pp reactions. In addition, the k_{T}-algorithm does not allow to separate background jet objects based on the area and it has an increased chance for *jet splitting*, i.e. dividing the original pp jet momentum into more than one jet object. Thus, jets reconstructed with the anti-k_{T} algorithm are preferred over k_{T} jets for the extraction of the jet signal in heavy-ion events. k_{T} jets are mostly employed for the extraction of the background density.

Table 5.2 lists the properties of the reconstructed, embedded jets and the effect of background subtraction following Equation (5.2). Due to the strongly reduced area for the leading k_{T} jet in the combined event, not all particles of the leading pp jet are part of the reconstructed jet in the merged event. The background corrected transverse momentum of the matched reconstructed jets deviate from the vacuum case for all jet finders. This is expected due to local variation of the background with respect to the estimated event average.

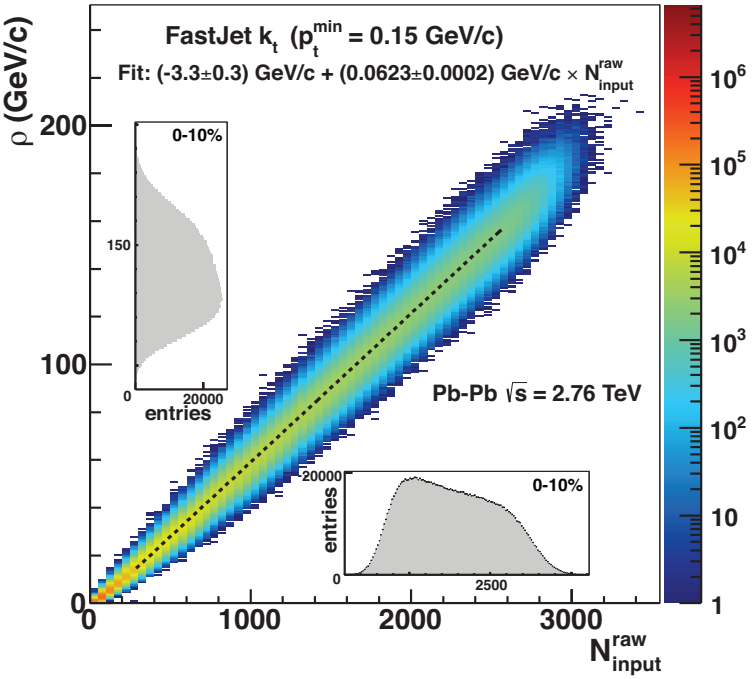

Figure 5.3.: Correlation of charged particle background p_{T}-density ρ with the uncorrected multiplicity of tracks used for jet finding ($|\eta| < 0.9$). The dotted line is a linear fit to the centroids in each multiplicity bin. The insets show the projected distributions of ρ and raw multiplicity for the 10% most central events [CKB08].

	k_{T} algorithm			anti-k_{T} algorithm		
	$p_{\mathrm{T}}^{\mathrm{jet,rec}}$	area	index	$p_{\mathrm{T}}^{\mathrm{jet,rec}}$	area	index
Jet A	$124.9\,\mathrm{GeV}/c$	0.43	1	$119.6\,\mathrm{GeV}/c$	0.50	1
Jet B	$82.2\,\mathrm{GeV}/c$	0.34	3	$110.5\,\mathrm{GeV}/c$	0.53	2

	$p_{\mathrm{T}}^{\mathrm{jet,rec}} - \rho \cdot A$	included pp $p_{\mathrm{T}}^{\mathrm{track}}$	$p_{\mathrm{T}}^{\mathrm{jet,rec}} - \rho \cdot A$	included pp $p_{\mathrm{T}}^{\mathrm{track}}$
Jet A	$60.9\,\mathrm{GeV}/c$	92%	$45.2\,\mathrm{GeV}/c$	100%
Jet B	$31.6\,\mathrm{GeV}/c$	100%	$31.6\,\mathrm{GeV}/c$	100%

Table 5.2.: Jet properties of matched pp jets after embedding into a measured, central heavy-ion collisions ($\rho = 148.8\,\mathrm{GeV}/c$). The corresponding event displays are shown in Figure 5.2 (right).

5.2.2. Event Background Fluctuations

In addition to the global shift of the reconstructed jet momentum scale, which is corrected via Equation (5.2), the soft event background also induces fluctuations that cannot be accounted for on a jet-by-jet basis. These fluctuations are basically an over- and underestimation of the local momentum density caused by statistical fluctuations and correlated region-to-region variations of the underlying event. The importance of these fluctuations has been recognized early [Ale06] and should be illustrated for two cases:

- the energy asymmetry of a reconstructed jet pair from the same hard scattering: $A_{\mathrm{j}} = (E_1 - E_2)/(E_1 + E_2)$,
- the ratio of jet cross-sections for different jet radii.

In the first case, the energy of a measured leading jet is compared to the energy of the reconstructed recoiling jet at $\Delta\varphi \approx \pi$. Both energies should balance at leading order. It is evident that any fluctuation on the jet energy scale will lead to an increased asymmetry since an upward fluctuation may trigger the selection of the leading jet and tends to separate the balanced energies of the leading and sub-leading jets. This is qualitatively similar to the behavior expected from parton energy loss, where the increased imbalance is caused by less energy recovered in the recoiling jet and needs to be separated for the quantitative interpretation of measured di-jet asymmetries that have been observed in the first evidence for parton energy loss of fully reconstructed jets at the LHC [Aad10, Cac11].

The second case can be used to study to what extent radiation is still correlated with the jet axis; the increase of the jet size should recover a larger fraction of the original parton energy, i.e. the nuclear modification factor should be closer to unity for larger cone radii, and the ratio of two cross sections with two different radii should differ in Pb + Pb and pp. However, statistical fluctuations also increase with the radius due to the larger average number of background particles in a typical jet area, $N_A \propto R^2$. This enhances the reconstructed jet yield for large radii as illustrated in Figure 5.4 for increasing Gaussian fluctuations of the jet momentum.

Thus, the quantification of background fluctuations is on the one hand essential for the correction of the inclusive jet spectrum as discussed below. On the other hand, it is crucial for the interpretation of observables that are selected in bins of jet energy. Each selection naturally biases towards increased fluctuations and can lead to similar modification patterns as expected from parton energy loss. The results of the ALICE experiment are presented in

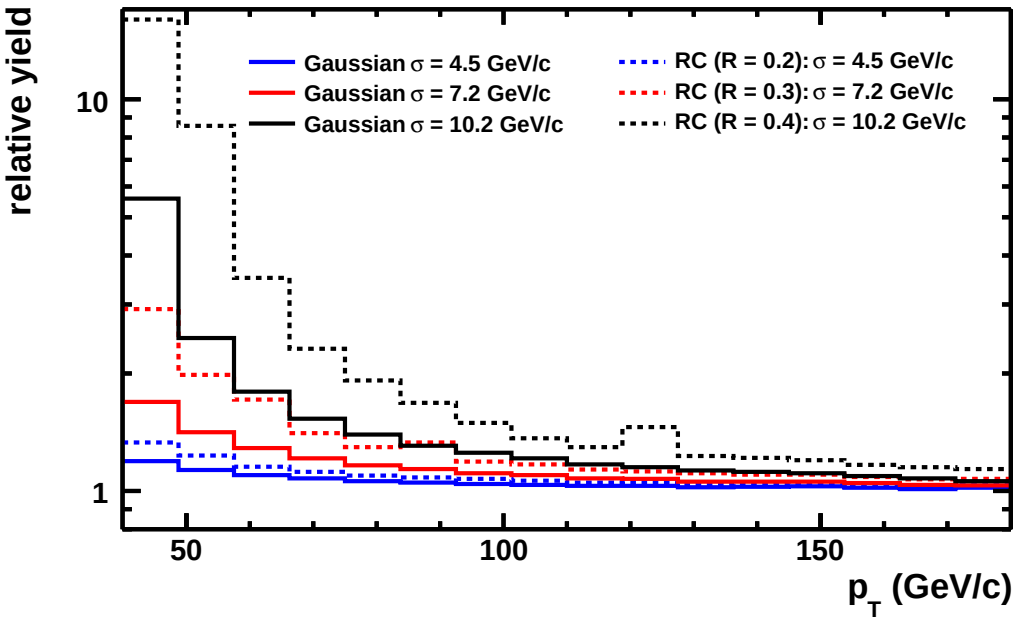

Figure 5.4.: Illustration of the impact of fluctuations on the reconstructed jet p_{T} spectrum. The charged jet spectrum above 5 GeV/c from a simulation of pp-collisions at $\sqrt{s} = 2760$ GeV is smeared and compared to the original distribution to quantify the relative yield increase. The smearing is done via folding with a Gaussian (full lines) and the δp_{T} response determined via embedding of random cones (RC) in central Pb + Pb collisions (dashed lines).

[CKB08] provided the first experimental assessment of these fluctuations and classifies their different sources.

A local variation of the measurable background particle density in heavy-ion events can be divided into two major components:

(i) Random, uncorrelated (Poissonian) fluctuations of the particle number and average momentum,

(ii) region-to-region correlated variations of the momentum density.

The latter can be induced by detector effects, e.g. a non-uniform efficiency, and by the heavy-ion collision itself, e.g. collective expansion of the asymmetric nuclear overlap region (flow) that induces a φ-dependent momentum distribution (see Chapter 2.3.3). Fluctuations are quantified by embedding well defined probes into the measured heavy-ion events and

calculating the residuals after background correction:

$$\delta p_{\mathrm{T}} = p_{\mathrm{T}}^{\mathrm{rec}} - A^{\mathrm{rec}} \cdot \rho - p_{\mathrm{T}}^{\mathrm{probe}}. \tag{5.3}$$

Different probes are used to evaluate the influence of the fluctuations on the jet finding itself. For example, the distribution of the background under the jet fragments can modify the shape and size of the reconstructed jet area as seen already in the example given in Figure 5.2 above. The different probes involve:

(i) random cones (RC) of fixed area placed into the acceptance ($p_{\mathrm{T}}^{\mathrm{probe}} = 0\,\mathrm{GeV}/c$),

(ii) isolated high-p_{T} particles acting as effective seeds for jet finding at this position ($p_{\mathrm{T}}^{\mathrm{probe}} = p_{\mathrm{T}}^{\mathrm{part}}$),

(iii) jets from a full GEANT simulation of the ALICE detector response to PYTHIA generated pp events ($p_{\mathrm{T}}^{\mathrm{probe}} = p_{\mathrm{T}}^{\mathrm{jet,pp}}$).

While the first case only samples the event track population in angular regions at the scale of a typical jet cone with radius R, the latter two cases reveal the sensitivity of the jet finding process to the background and the structure of the jet. Here, the focus shall be on the fluctuations that are independent of the jet finding procedure and probed via random cones.

Figure 5.5 a) shows the distribution of residuals δp_{T}, using reconstructed tracks above $p_{\mathrm{T}}^{\mathrm{min}} = 0.15\,\mathrm{GeV}/c$ measured with ALICE in central Pb + Pb collisions. The distribution can be characterized by the total width (σ) and a Gaussian fit to the left side of the distribution. The most probable value is located at zero, which demonstrates the validity of the employed background subtraction scheme, though a clear deviation from a Gaussian shape is observed. This is studied in more detail by either avoiding the overlap with the leading reconstructed jets, to reduce upward fluctuations due to hard correlations in the event, or by randomizing the directions of the input particles in (η, φ) in order to destroy all correlations in the heavy-ion event. The latter case represents the limit of purely random fluctuations.

Even in the case of fully randomized particle directions the distribution is not Gaussian. This is due to the asymmetric underlying single particle p_{T}-distribution. The finite number of samplings with about 140 charged particles within $R = 0.4$ for a central heavy-ion collision is not enough to compensate this asymmetry and reach the central limit of a Gaussian distribution. The distribution is well described by a Γ function shifted to zero. It represents the independent emission from a given number of sources and its parameters are closely related to the properties of the single particle p_{T} spectrum [Pop11].

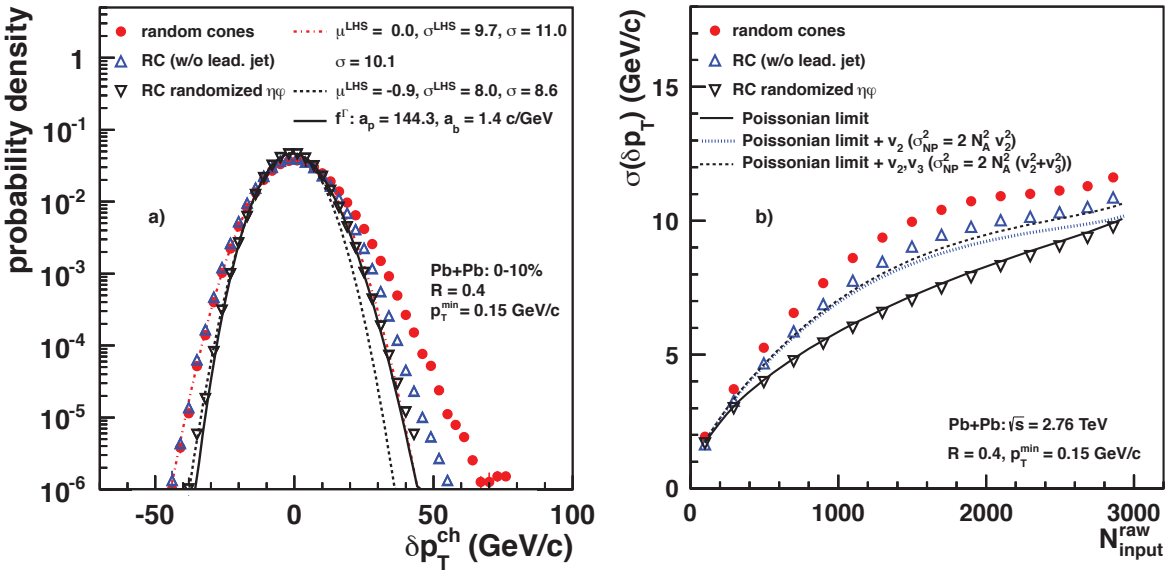

Figure 5.5.: Background fluctuations in jet reconstruction probed via the embedding of random cones in Pb + Pb collisions at $\sqrt{s_{\mathrm{NN}}} = 2760$ GeV. a) δp_{T} distribution in the 10% most central Pb + Pb events for three types of random cone. A Gaussian fit to the left-hand side and its extrapolation to positive δp_{T} are shown for measured Pb + Pb events and for randomized Pb + Pb events (μ^{LHS} and σ^{LHS} in GeV/c). The solid line is a fit to the δp_{T} distribution for the randomized events with a Γ distribution shifted to zero as approximation for the shape in the case of independent particle emission. b) Multiplicity dependence of the standard deviation of the δp_{T} distribution compared to the Poissonian limit derived from the measured track p_{T} spectrum and with additional elliptic and triangular flow contributions following Equation (5.4) [CKB08].

The evolution of the overall width of the fluctuations with centrality or particle number in the event is shown in Figure 5.5 b) and can be parameterized as found in [CKB08]:

$$\sigma(\delta p_{\mathrm{T}}) = \sqrt{N_A \cdot \sigma^2(p_{\mathrm{T}}) + \left(N_A + \sigma^2_{\mathrm{NP}}(N_A)\right) \cdot \langle p_{\mathrm{T}} \rangle^2}. \tag{5.4}$$

Here, N_A is the expected number of tracks in the cone area A for a given event centrality or multiplicity class, $\langle p_{\mathrm{T}} \rangle$ is the average p_{T}, and $\sigma(p_{\mathrm{T}})$ the standard deviation of the track p_{T}-spectrum. The purely statistical fluctuations increase as $\sqrt{N_A}$, which is clearly seen in the comparison to the measured width for randomized events in Figure 5.5 b).

Local variations of the average multiplicity, average p_{T}, or $\sigma(p_{\mathrm{T}})$, lead to additional fluctuations. These region-to-region variations can be induced e.g. by (mini-)jets, where the par-

ticle p_{T} spectrum is considerably harder than for the global event average, and by collective flow. The uncorrelated non-Poissonian (NP) fluctuations from elliptic and triangular flow are considered in Equation (5.4) with $\sigma^2_{\mathrm{NP}}(N_A) \approx 2{N_A}^2(v_2^2 + v_3^2)$, they lead to a fluctuation term that exhibits a stronger multiplicity dependence ($\propto N_A$). Thus it is more important for larger cone radii ($\propto R^2$). Using the centrality dependence of the measured ALICE v_2 and v_3 values accounts well for the strong deviation from the $\sqrt{N_A}$ increase as shown in Figure 5.5 b) after reducing the influence of the hard component.

In addition, it was demonstrated in [CKB08] that the main effects of fluctuations on the jet spectrum are in the case of the anti-k_{T} jet finder well reproduced by random cones. In particular, the role of the right-hand-side tail is decisive in the correction of jet measurements. Due to the steeply falling spectrum, these additional upward fluctuations have a large impact on the reconstructed jet spectrum compared to Gaussian fluctuations of the same width as illustrated in Figure 5.4. The data-driven determination of the fluctuation distribution provides the major ingredient for the correction of inclusive jet spectra, while the parameterization via Equation (5.4) allows for an intuitive understanding of the effects of varying cone size and p_{T} cuts solely based on the properties of the single particle p_{T} spectrum. It facilitates to estimate the effect of background fluctuations in energy loss simulations without the computing-time expensive generation of heavy-ion background events.

5.3. Nuclear Modification of Reconstructed Jets in ALICE

The measured background fluctuations are combined with the detector response matrix, which encodes the detector specific modification of the jet momentum scale mainly due to track finding efficiency and momentum resolution. The latter are determined via a full detector simulation of unmodified pp jets. The combined response matrix R transforms a given input jet ($p_{\mathrm{T}}^{\mathrm{gen}}$) spectrum to a measured jet ($p_{\mathrm{T}}^{\mathrm{rec}}$) spectrum:

$$\mathbf{m}(p_{\mathrm{T}}^{\mathrm{rec}}) = \mathbf{R}(p_{\mathrm{T}}^{\mathrm{rec}}, p_{\mathrm{T}}^{\mathrm{gen}}) \cdot \mathbf{j}(p_{\mathrm{T}}^{\mathrm{gen}}). \tag{5.5}$$

The reconstructed jet spectra for various centrality selections are corrected for their respective background fluctuations and the detector effects on a statistical basis via different unfolding techniques that try to invert Equation (5.5). Here, the basic idea is to find a solution $\mathbf{j}^{\mathrm{unfolded}}$ that produces a refolded vector $\mathbf{m}$ close to the measured jet momentum distribution. The principal difficulty in the unfolding procedure is to avoid unphysical but mathematically valid solutions, which can be induced for example by statistical fluctuations of the measured data.

In the χ^2 unfolding, the following expression is minimized to obtain the unfolded solution:

$$\chi^2 = \sum_{\text{refolded}} \left(\frac{y_{\text{refolded}} - y_{\text{measured}}}{\sigma_{\text{measured}}} \right)^2 + \beta \sum_{\text{unfolded}} \left(\frac{\mathrm{d}^2 \log y_{\text{unfolded}}}{\mathrm{d} \log p_{\mathrm{T}}^2} \right)^2 . \tag{5.6}$$

Here, y denotes the jet yield in the measured and refolded spectrum, σ_{measured} the statistical uncertainty of the measured value. The first term in the expression is the χ^2 value between the measured and refolded spectra, and the second is the *regularization term*, which prefers a certain shape of the unfolded distribution, here a local power law. The regularization strength is tuned via the factor β.

One additional complication, which occurs due to the finite size of reconstructed jets, is that Equation (5.5) cannot hold down to low p_{T}. It implies a one-to-one relation between reconstructed and true jet and does not contain the effect of overlapping jets in which one jet needs to be counted as background to the other and considered as lost. The measured δp_{T} distribution shown in Figure 5.5 a) for charged particles, does contain this effect in the tail to the right-hand side, which has a similar slope as the reconstructed jet p_{T} spectrum. The loss of jets can also not be incorporated directly via a detection efficiency, since this requires a precise separation of background and signal. Instead, it can be incorporated in the unfolding process by starting the unfolding above a certain threshold and allowing (background) jets to be lost below the threshold. This procedure effectively uses the knowledge of the background fluctuations as given by the δp_{T} distribution to determine the fraction of signal jets, while the total number of reconstructed jets in the event is still bound by the radius parameter and the acceptance of the detector.

The resulting, fully corrected charged jet spectra allow for a comparison of the modification of jet production when going from peripheral to central Pb + Pb collisions. This is shown in Figure 5.6 a) using the most peripheral bin (P = 50 − 80%) as reference in R_{CP}, the ratio of invariant yields scaled by the appropriate number of binary collisions:

$$R_{\mathrm{CP}} = \frac{N_{\mathrm{coll}}^{\mathrm{P}} \cdot \frac{\mathrm{d}N^{\mathrm{C}}}{\mathrm{d}p_{\mathrm{T}}}}{N_{\mathrm{coll}}^{\mathrm{C}} \cdot \frac{\mathrm{d}N^{\mathrm{P}}}{\mathrm{d}p_{\mathrm{T}}}} . \tag{5.7}$$

The production of charged jets reconstructed with $R = 0.2$ in central collisions is suppressed by more than 50% compared to the scaled expectation, consistent with the behavior of single particle production at large transverse momentum. The suppression decreases for more peripheral collisions, a similar behavior is observed for larger jets with $R = 0.3$ (not shown). The direct comparison of jet yields obtained with $R = 0.3$ and 0.2 is shown in Figure 5.6 b).

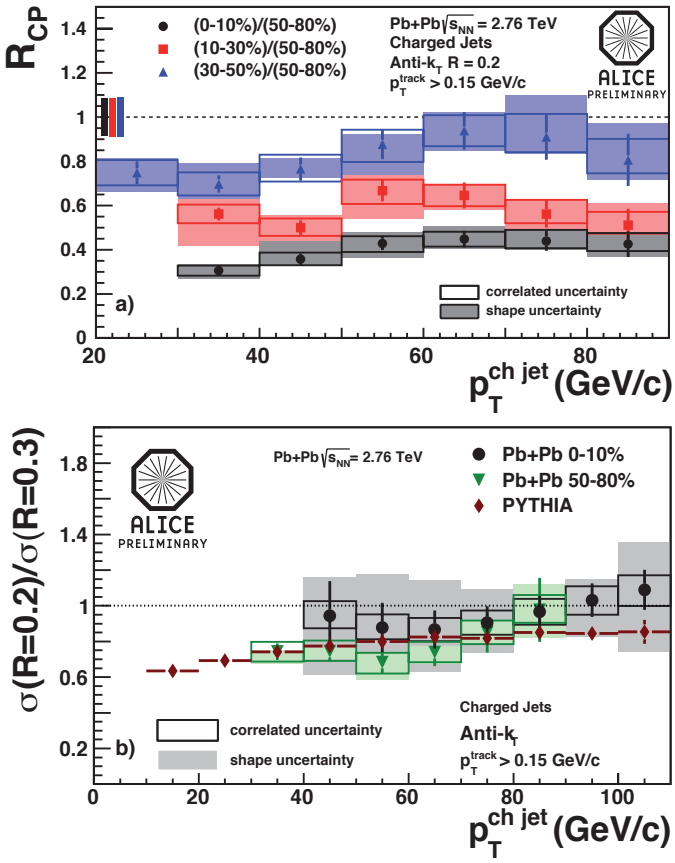

Figure 5.6.: a) Nuclear modification factor R_{CP} for jets reconstructed from charged particles with $R = 0.2$. b) Ratio of charged jet cross sections for two radii in central and peripheral Pb + Pb-collisions, as well as for simulated jets in pp collisions at $\sqrt{s} = 2760\,\mathrm{GeV}$ [CKB10].

In this ratio, a part of the uncertainties cancels out, but no significant modification compared to a PYTHIA simulation of pp reaction is observed for central collisions. The increase of the ratio towards higher p_{T} is due to the stronger collimation of high energy jets and is already present in elementary pp collisions. This means that the reconstructed charged jets do not show a strong modification of their structure at the scale up to $R = 0.3$, despite the usage of a very low p_{T} cut off in the jet reconstruction of $p_{\mathrm{T}}^{\mathrm{min}} = 0.15\,\mathrm{GeV}/c$.

The reconstruction of jets from charged particles has the advantage that the jet finding process can start on the individual particle level and does not depend on the detector granularity, which is typically of the order of $\Delta\varphi \times \Delta\eta = 0.1 \times 0.1$ for hadronic calorimeters. In addition, the precise characterization of the event background and its fluctuation has only been possible in the context of a measurement of individual particles over full azimuth. Nevertheless,

the relation to the initial parton p_{T} is limited by the unmeasured neutral component of the charged jet.

5.3.1. Full Jets in ALICE

In order to also recover the neutral fraction of the jet momentum in ALICE, the Electromagnetic Calorimeter is used. It covers a pseudo-rapidity interval $|\eta| < 0.7$ and $\Delta\varphi = 100°$. Compared to classical jet measurements, which also employ full hadronic calorimetry, the hadronic component in ALICE is measured via the tracking of charged particles. Double counting of hadrons that also deposit energy in the EMCal, e.g. as minimum-ionizing particles, needs to be avoided. Thus calorimeter clusters are corrected for the momentum of a matched track.

The feasibility of full jet reconstruction in ALICE with this combination of tracking and electromagnetic calorimeter has been demonstrated in [Abe13b], with the first measurement of the jet production cross section in pp-collisions at the reference energy of $\sqrt{s} = 2760\,\mathrm{GeV}$. The measured cross section agrees with the expectation from NLO pQCD calculations and the evolution of the jet cross section with the radius parameter is also well reproduced by state-of-the-art NLO calculations that incorporate the effects of the hadronization process on the jet structure.

Before turning to the measurement of full jets reconstructed in heavy ion collisions, the relation between single inclusive hadrons, charged jets, and full jets in pp reactions shall be briefly investigated. All three can be viewed as a generic, particle-like observable for which an effective fragmentation function $F(z)$ can be constructed. The function describes the probability to reconstruct a fragment with a certain fraction of the original parton momentum. In that sense, a reconstructed jet of given radius just represents a particle with a harder fragmentation, closer to the original parton p_{T}. This is illustrated in Figure 5.7 with a simulation of pp collisions at $\sqrt{s} = 2760\,\mathrm{GeV}$. The distribution of momentum fractions z' is shown for a fixed bin in reconstructed p_{T} and the momentum of the corresponding full jet reconstructed with $R = 0.4$ chosen as reference. A charged particle between 40 and 60 GeV/c carries on average about 60% of the reference jet momentum, charged particle jets recover about 75% with $R = 0.2$ and full jets with small radius 90% of the full jet with larger radius. As discussed in the context of trigger biases, these values strongly depend on the steepness of the underlying parton spectra. The slope of the parton spectra can be evaluated from the measured particle or jet spectra, since in all three cases the parent-child relation (see Chapter 2.2.2) results in a similar shape at high transverse momentum as seen in Figure 5.7 b). Thus, for a known

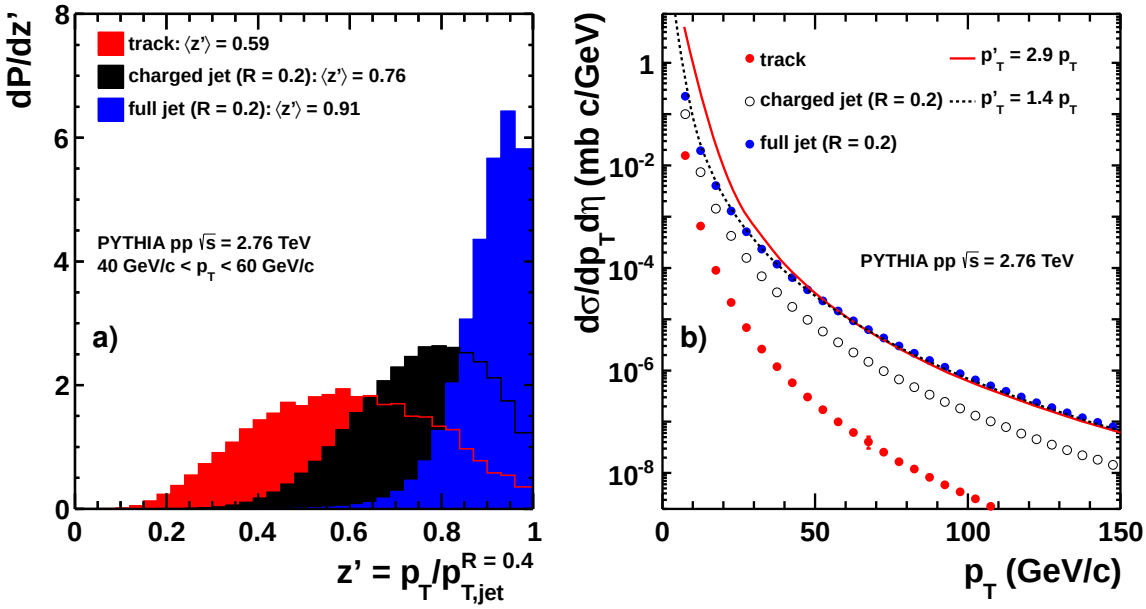

Figure 5.7.: Relation between reconstructed p_{T} for single charged particles, charged jets, and full jets in a PYTHIA simulation (pp at $\sqrt{s} = 2760\,\mathrm{GeV}$). a) Distribution of momentum fractions contributing to one reconstructed p_{T} bin. b) Rescaling of p_{T} spectra to the full jet momentum.

fragmentation pattern it is in principle possible to correct or unfold the measured particle or jet cross-section to the full jet cross section at a larger radius. Here, the scaling of the cross sections can be viewed as a shift of the observed p_{T} to the original jet p_{T} or a folding with the distribution in $1/z'$. As seen in Figure 5.7 b) the rescaling of the momentum with an effective correction $p_{\mathrm{T}} \rightarrow k \cdot p_{\mathrm{T}}$ ($\mathrm{d}p_{\mathrm{T}} \rightarrow \mathrm{d}p_{\mathrm{T}}/k$) is sufficient to match the spectra at high transverse momentum. As for the trigger bias, these factors strongly depend on the spectral shape and in addition, on the width of the $1/z'$ distribution, i.e. broader distributions lead to a stronger migration and larger effective corrections.

The measurement of fully reconstructed jets with ALICE in the context of heavy-ion collisions follows a similar approach as for the charged jets, the main ingredients being the evaluation and subtraction of the event-wise background and the determination of the residual fluctuations on the jet momentum scale. The former is particularly hindered by the relatively small acceptance of the EMCal (approximately 10% of the TPC coverage), which is reduced even further by the necessary cut on the jet direction to be at least a distance R away from the edge of the detector. In order to avoid a strong impact of the reconstructed jet in the EMCal

acceptance on the estimate of the background density, a scaling approach is chosen. Here, the background density obtained over the full azimuth with charged tracks is scaled with a pre-determined factor to the equivalent full jet background. This factor depends on centrality and can also deviate from the naïve expectation of 1.5 due to intrinsic thresholds of the EMCal clustering, π^0 decay kinematics, and additional sources of photons and electrons. E.g. the low p_{T} photon yield in central collisions increases by about 30% due to direct photons compared to only decay photons. The correction factor increases from 1.4 in peripheral to approximately 1.8 for the 0-10% most central collisions.

The inclusion of neutral particles further increases background fluctuations in the reconstructed full jet, which makes additional measures necessary to reduce the impact of pure background jets at low p_{T}. This is needed to enable unfolding with a sufficient number of signal dominated measured points. Two approaches are used simultaneously. First, the focus on jet reconstruction with a small radius ($R = 0.2$). Second, the requirement of a minimum leading track $p_{\mathrm{T}} > 5\,\mathrm{GeV}/c$ in the reconstructed jet.

In the reconstruction of full jets in pp collisions, the leading track requirement selects about 90% of all jets at 20 GeV/c, a relatively small effect which cancels in the ratio R_{AA} of equally biased pp and Pb + Pb spectra to the extent that the fragmentation patterns for leading particles in the jets are similar. The nuclear modification factor for fully reconstructed jets can be seen in Figure 5.8. It employs the ALICE pp reference measurement obtained with the same detector setup [Abe13b]. It features a similar rise from low to high p_{T} as the single charged particles and the charged particle jets. The latter is normalized to a PYTHIA reference. All measurements appear to approach a common limiting value of $60-50\%$ suppression, a view that is supported by jet measurements of the ATLAS experiment that cover the region beyond 100 GeV/c [Aad13]. Since reconstructed jets and single hadrons originate from the same underlying partons, the common emission spectrum seems to result in the same asymptotic behavior in central events. A prediction of the charged jet R_{AA} from the JEWEL energy loss Monte Carlo is also shown in Figure 5.8. Though it describes the single charged R_{AA} well, it appears to under-predict the magnitude and the rise of the nuclear modification factor of charged jets at high p_{T}. It is still compatible within the large uncertainties of the measurement.

The similarity in the shape of the nuclear modification factor for the different jet observables is even more remarkable in Figure 5.8 b), where for this work the p_{T} of the single charged particle and the charged jet measurement is rescaled by the same factors as used above in Figure 5.7 b) to match the spectra in pp to the full jet measurement.

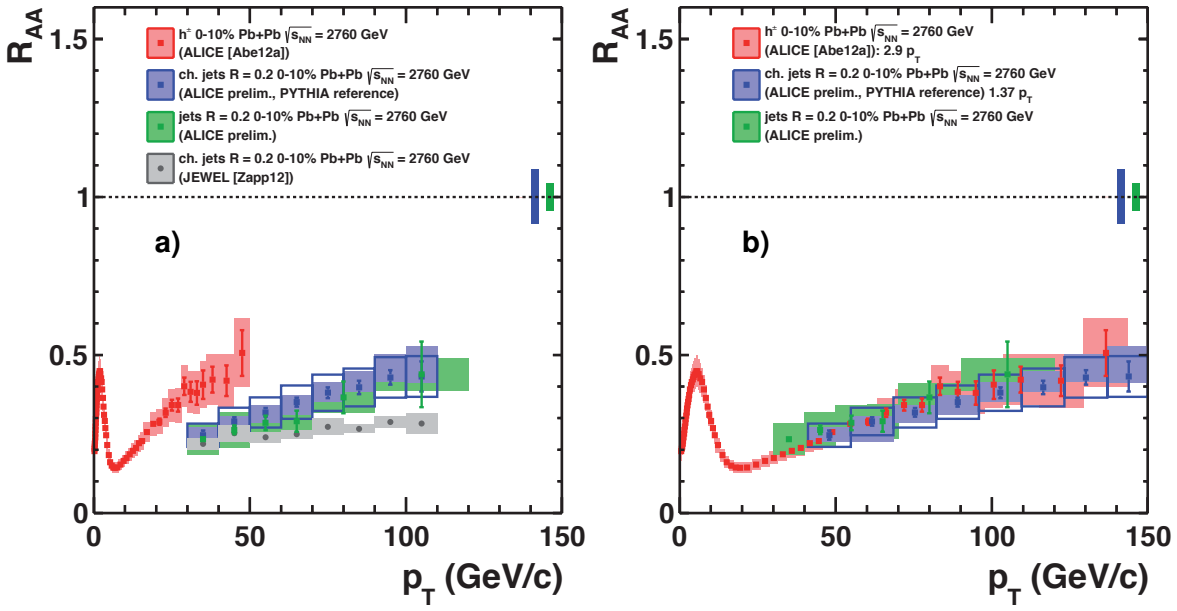

Figure 5.8.: Comparison of the nuclear modification factor in central Pb + Pb collisions for single charged particles, charged jets, and full jets. For the charged jet R_{AA} a PYTHIA reference has been used, which has been updated with respect to [CKB10]. In addition, a prediction from JEWEL is shown [Zap13]. In b) the p_{T} of the single particles and the charged jets is rescaled to the full jets with a factor determined in pp simulations.

These observations can be summarized in the simplified model interpretation of Chapter 3.3.2:

- All R_{AA} show an increase, which can be interpreted as the transition from a surface dominated emission given by the transmission coefficient T to a true energy loss measurement.
- The constant limiting value at high p_{T} of approximately 0.5 suggests in conjunction with the power law shape of the initial parton spectrum a constant fractional energy loss at high p_{T}, $S_{\mathrm{loss}}(n = 6.5) \approx 14\%\,(20\%)$ for $T = 0\,(0.12)$.
- The observation that full jet, charged jet, and single particle R_{AA} can be rescaled such that they overlay using factors determined in pp reactions, points to an unmodified fragmentation pattern for the observed jets compared to pp and that the lost energy is not recovered in the jet reconstruction with $R = 0.2$.

5.4. Recoil Jets

The suppression effect on jets and single particle is striking. However, the tests of the jet fragmentation patterns provided above do not show a modification compared to the vacuum case. This can be interpreted in a way that the parton energy is lost via large angle radiation leaving a hard parton that fragments in the vacuum. Measurements at larger radii are needed to better test the structure of jets and potentially recover the lost energy.

The main challenge of jet reconstruction with large radii is the large impact of background fluctuations. They potentially create jet objects in the sense of the algorithm that do not originate from a hard scattering. To improve the signal-to-background in the single full jet measurement, a particle above a high p_{T} threshold has already been required in the reconstructed jets. The main idea of the method discussed in the following is to apply this tagging procedure not on the jet itself, but instead use the reconstructed jets opposite in azimuth ($\Delta\varphi \approx 180^{\circ}$) from a high-$p_{\mathrm{T}}$ particle: *recoil jets*. The trigger track p_{T} than sets the minimum Q^2 of the parton scattering. Furthermore, a high-p_{T} hadron trigger induces a geometric bias towards jets generated close the surface of the fireball and directed outward. Thus, the jets recoiling from such a trigger are biased towards larger in-medium path length compared to the inclusive jet population. Due to the limited azimuthal acceptance of the EMCal, this procedure can currently only be applied to charged particles.

The semi-inclusive distribution of these hadron-jet coincidence measurements is shown in Figure 5.9 a) for anti-k_{T} jets reconstructed with $R = 0.4$ opposite of the trigger hadron, $\Delta\varphi = 180^{\circ} \pm 35^{\circ}$. As seen, the right-hand-side tail of the distribution increases with increasing trigger p_{T}. On the one hand, this is due to an improved jet signal selection. On the other hand, the Q^2 of the hard scattering increases as a larger trigger p_{T} is required, and a flatter parton p_{T} spectrum contributes to the spectrum. The left-hand side of the distribution contains the jet objects uncorrelated to the hard scattering and is completely driven by event background fluctuations. It does not change with the trigger p_{T} and shows the same features as the δp_{T} distribution discussed above. This uncorrelated behavior can be exploited in a novel purely data-driven method to eliminate the contribution of combinatorial jets in the measurement by taking the difference of distributions with hadron triggers in a *signal* and a *reference* p_{T} interval, $]p_{\mathrm{T}}^{\mathrm{sig,1}}, p_{\mathrm{T}}^{\mathrm{sig,2}}[$ and $]p_{\mathrm{T}}^{\mathrm{ref,1}}, p_{\mathrm{T}}^{\mathrm{ref,2}}[$ respectively, [Cun13]:

$$\Delta_{\mathrm{recoil}} = \frac{1}{N_{\mathrm{trig}}} \frac{\mathrm{d}N}{\mathrm{d}p_{\mathrm{T,jet}}^{\mathrm{ch}}} (p_{\mathrm{T}}^{\mathrm{sig,1}} < p_{\mathrm{T}}^{\mathrm{trig}} < p_{\mathrm{T}}^{\mathrm{sig,2}}) - c \cdot \frac{1}{N_{\mathrm{trig}}} \frac{\mathrm{d}N}{\mathrm{d}p_{\mathrm{T,jet}}^{\mathrm{ch}}} (p_{\mathrm{T}}^{\mathrm{ref,1}} < p_{\mathrm{T}}^{\mathrm{trig}} < p_{\mathrm{T}}^{\mathrm{ref,2}}). \quad (5.8)$$

Here, the scaling of the reference distribution is needed to take into account the strict con-

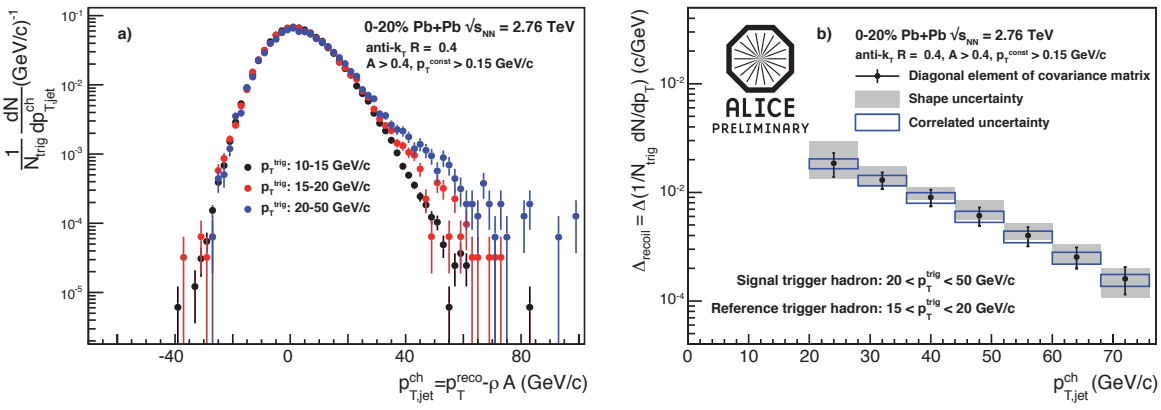

Figure 5.9.: a) Raw semi-inclusive charged spectra for jet recoiling from a high p_{T} trigger particle ($\Delta\varphi = \pi \pm 0.6$). b) Fully corrected difference of semi inclusive spectra.

servation of the number of jets in the acceptance. For higher $p_{\mathrm{T}}^{\mathrm{trig}}$, more combinatorial jets are displaced by signal jets and by construction the factor is smaller than unity, typically $c \approx 0.95$. The remaining distribution is free of combinatorial jets and only affected by the jet reconstruction efficiency and jet momentum scale fluctuations. For the correction of the Δ_{recoil} distribution the same techniques can be applied as for the correction of the charged jet spectrum, though the result itself is less sensitive to background fluctuations due to the a-priori flatter input spectrum. The fully corrected difference of the conditional charged jet yields represents the evolution of the true recoil charged jet spectrum from the reference to the signal trigger-interval. It is perturbatively well defined and does not impose any additional bias on the jet fragmentation. It is shown in Figure 5.9 b) for $R = 0.4$ and reaches down to $20\,\mathrm{GeV}/c$.

To study the possible energy redistribution within these jets with increased radius and potentially larger in-medium path length, a vacuum reference distribution is calculated using the PYTHIA event generator: $\Delta_{\mathrm{recoil}}^{\mathrm{PYTHIA}}$. The ratio ΔI_{AA} of the measured distribution to the vacuum reference is shown in Figure 5.10 for two jet radii. Unlike the nuclear modification factor, this observable does not exhibit a strong suppression. This can be understood qualitatively since the leading particle jet suppression is already factorized out to some extend due to the requirement of a high-p_{T} particle. This is also seen in single particle correlation measurements by ALICE [Aam12]. Here, the conditional away-side jet yield extracted on a statistical basis from the association with a $8 < p_{\mathrm{T}} < 15\,\mathrm{GeV}/c$ trigger particle is suppressed by 40% ($I_{AA} \approx 0.6$). There is no significant change within the uncertainties of going from

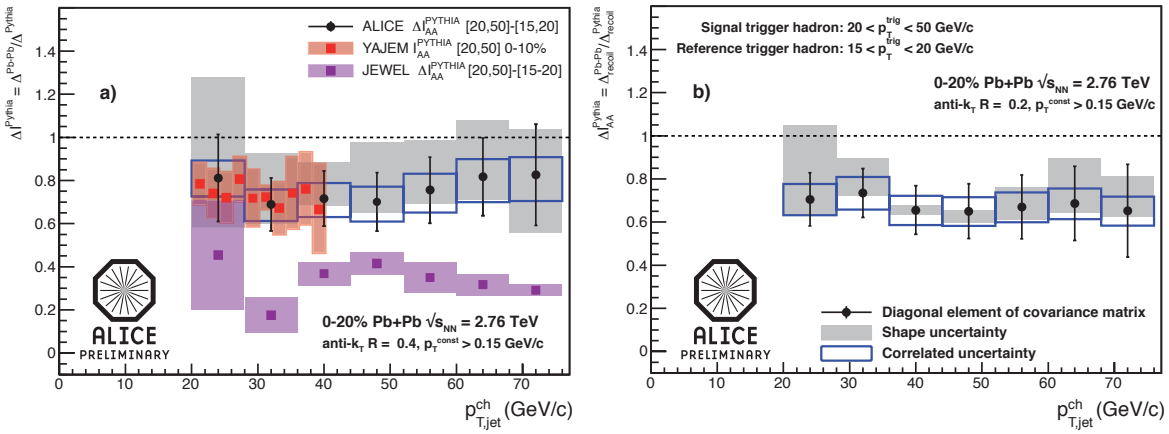

Figure 5.10.: Ratio of difference distributions from Pb + Pb collisions and PYTHIA simulations for two radii: $R = 0.4$ and $R = 0.2$. Figure a) includes a comparison to a preliminary study of this observable within YAJEM and the JEWEL MC.

$R = 0.4$ to $R = 0.2$ for the ratio of conditional yield in the recoil jet measurement. Thus, no conclusive statement of the broadening of the jet profile in heavy-ion collisions is currently possible.

The comparison of this observable to theoretical calculations puts stringent limits on the modeling of the recoil (quenched) jet structure. In addition to the perturbative scattering process and the complex medium evolution of the parton shower, the accurate theoretical description of the inclusive particle production is needed to model the trigger. Two preliminary studies using this novel observable have been performed with the jet quenching Monte Carlo simulations JEWEL and YAJEM. Both use a full evolution of the parton shower within the medium and successfully describe the single hadron R_{AA}. While YAJEM shows a good agreement with the data, JEWEL currently fails to describe it. ΔI_{AA} in JEWEL shows a larger suppression than compatible with the data. This may point to a too strong energy redistribution outside of the cone as already indicated by the JEWEL results on the inclusive jet R_{AA} shown in Figure 5.8. It should be noted, that even though JEWEL supports the coupling to various medium evolution models, here only a variant of the Bjorken model for the 1D longitudinal expansion is employed, a better agreement is expected for more realistic scenarios of hydrodynamic evolution of the medium. In any case, further studies are needed to discern the reason for the observed disagreement and map out the phase space of the incorporated processes and medium models. The comparison clearly demonstrates the discriminative power of this new observable beyond the abilities of single jet and hadron measurements.

Summary

This habilitation thesis summarizes the author's attempts to characterize nuclear matter under extreme conditions with the PHENIX and the ALICE experiment. The main objective of these experiments is the creation and study of a new state of matter, the Quark-Gluon Plasma (QGP), in the collision of heavy nuclei at ultra-relativistic energies. In this state, the fundamental constituents of strongly interacting particles, the quarks and gluons, are not confined into hadrons. Thus, the non-perturbative aspects of the strong interaction can be studied in a system where color charges are the relevant degrees of freedom. Important reference measurements for the creation of such a state are provided in elementary proton-proton reactions (QCD vacuum) and proton- or deuteron-nucleus collisions (cold nuclear matter).

The creation of this new state of matter in central Au + Au collisions at $\sqrt{s_{\mathrm{NN}}} = 200\,\mathrm{GeV}$ is supported by a set of observations: the energy density deposited in the reaction zone is well above the critical value for a phase transition, the created medium rapidly thermalizes, and its collective expansion can be described using relativistic hydrodynamics with a partonic equation-of-state in the early stage. However, one of the most direct pieces of evidence is provided by the observed suppression of particles with large transverse momentum, p_{T}, compared to the expectation from appropriately scaled proton-proton reactions. The production of these particles is dominated by *hard processes*, parton-parton interactions with large momentum transfer, and the subsequent fragmentation of the scattered partons into jets of observable particles. Since these hard scatterings occur in the early reaction phase and are calculable in perturbative QCD, they provide an ideal probe of the hot and dense medium created in the later stages of a central heavy-ion collision. In the QGP with its large color-charge density, the hard-scattered partons can lose energy prior to their fragmentation e.g. via *gluon bremstrahlung*. The observed magnitude of the suppression of high-p_{T} particle production, the so called *jet quenching* which is observed via the nuclear modification factor R_{AA}, can so far only be explained by this strong final state interaction of the scattered partons. Further support is provided by the measurement of direct photons at high p_{T}, which act as electromagnetic probe of the medium. They remain unaffected by the strong interaction in their passage through the QGP.

The focus of the author's research is the detailed investigation of the properties of the QGP and the fundamental processes of the parton-medium interaction using these hard and electromagnetic probes. The major advances in this field connected to the author's work are summarized in this thesis. Several dependences of the parton energy loss are mapped out experimentally. The comparison of the neutral pion production in Au + Au collisions to that of the heavier η meson does not show a significant difference between the nuclear modification of the two. This is consistent with the assumption that the nuclear modification of the measured production cross section already occurs at the parton level, prior to the fragmentation into hadrons. The measurement of the nuclear modification factor in central Cu + Cu collisions at $\sqrt{s_{\mathrm{NN}}} = 22.4, 62.4$, and 200 GeV demonstrates that parton energy loss starts to dominate over cold nuclear matter effects between 22.4 and 62.4 GeV. The energy, transverse momentum, and centrality dependence of the nuclear modification in these reactions, as well as in Au + Au collisions, is well reproduced by models based on radiative energy loss of the leading parton in the QGP. However, the sensitivity of R_{AA} is found to be limited in this kinematic regime, due to the steepness of the parton spectrum and the dominance of geometric effects in the centrality evolution.

The path-length dependence of parton energy loss is better constrained for a fixed centrality selection, exploiting the spatial asymmetry of the overlap region of the two nuclei in non-central heavy-ion collisions. The measurement of the nuclear modification factor with respect to the symmetry plane of the overlap region allows to select different effective path lengths of the parton through the medium. The observed dependence of R_{AA} for π^0s on the orientation to the symmetry plane clearly rules out (light) parton energy loss models with a linear path-length dependence, e.g. due to simple elastic scattering. Furthermore, the increased data sample collected by the PHENIX experiment in the Au + Au runs at $\sqrt{s_{\mathrm{NN}}} = 200$ GeV following the discovery of jet quenching allows for a precision constraint of the main energy loss parameters in different models. Once compared on the same ground, these parameters can differ significantly between models due to their varying underlying assumptions. Nevertheless, the models constraint this way can form the basis for the extrapolation from top RHIC energies to $\sqrt{s_{\mathrm{NN}}} = 2760$ GeV reached in the first Pb + Pb collisions measured at the LHC.

The measurement of direct photons provides a further independent constraint on the properties of the medium when going from RHIC to LHC. Since direct photons can leave the medium basically unaffected once they are produced, they carry more direct information on the early stages of the heavy-ion reaction. In particular, their effective temperature derived

from the observed excess above the vacuum sources in central heavy-ion collisions points already at $\sqrt{s_{\mathrm{NN}}} = 200\,\mathrm{GeV}$ to an initial temperature that is significantly larger than the phase transition temperature. The observed change of the effective temperature from 200 GeV to 2760 GeV is of the order of 30%. Interpreted as the increase in initial temperature this is tantamount to an increase of the initial energy density by approximately $(1.3)^4$ and a significantly longer lived QGP phase at the LHC.

A similar power dependence on the temperature is also found in various parton energy loss mechanisms. Thus, the leap in collision energy by one order of magnitude enables the test of the temperature dependence of parton energy loss. In addition, the flatter parton production spectrum provides a higher sensitivity to the medium parameters and the increased cross section for high-p_{T} particle and jet production allows for the study over a broader p_{T} range. Indeed, the nuclear modification factor of charged particles exhibits a qualitatively new behaviour compared to RHIC. It shows a minimum below the value obtained at RHIC and increases towards high p_{T}, where it levels off. This behaviour is generic in all parton energy loss models where the nuclear modification factor is not dominated by the emission from the surface of the medium. Models that have been tuned to describe the R_{AA} at RHIC and only consider the attenuation of the leading parton in the medium fail to describe the magnitude of R_{AA} observed at the LHC. A better agreement is reached with models that incorporate the full medium evolution of the parton shower and thus take also into account contributions of sub-leading partons in the fragmentation process.

The reconstruction of jets in heavy-ion collisions with ALICE has been the author's research focus following the study of parton energy loss with single particles at RHIC. Jets offer the possibility to study the modification of the fragmentation process and the role of sub-leading partons in the medium evolution of the parton shower in more detail. However, the reconstruction of jets is hindered in the context of heavy-ion collisions by the background of particles not related to the hard scattering. This background is collected in the angular acceptance, or jet area, which is connected to each jet definition. The effects of this background and its fluctuation on jet reconstruction have been quantified in detail, exploiting the capabilities of the ALICE detector to reconstruct charged particles down to very low transverse momentum. For the extraction of the jet production and jet fragmentation properties in heavy-ion collisions the quantification of these background effects is imperative.

For the currently employed jet resolution parameters ($R = 0.2$ and 0.3) no significant modification of the jet profile has been observed with ALICE. It has been shown in this work that the same nuclear modification factor is observed for all cases, once the different under-

lying parton p_{T} scale related to the momentum of single charged particles, jets reconstructed from charged particles, and full jets is accounted for. This observation in itself constrains the implementation of parton shower modifications in jet quenching models. For further constraints, a new jet observable has been introduced. It allows for a data-driven removal of background contributions and enables the reconstruction of jets with larger cone radii. The observable makes use of the angular correlation between jets and high-p_{T} particle production on the opposite side. The comparison to preliminary jet Monte Carlo studies of this observable clearly demonstrates the ability to discriminate between different Monte Carlo model implementations that affect the details of the parton shower evolution and the angular correlation with recoiling high-p_{T} particles.

In summary, the work by the author that is presented in this thesis provided the experimental data that helped to guide the transition from the discovery of jet quenching as a strong final state effect to a detailed understanding of the underlying mechanisms of parton energy loss. All reported investigations are compatible with a dominantly radiative energy loss via gluon bremsstrahlung for light partons. For RHIC energies $\sqrt{s_{\mathrm{NN}}} \leq 200\,\mathrm{GeV}$, the suppression observed in the nuclear modification factor can be described as an effect of leading parton energy loss. The qualitatively different sensitivity of hard scattering observables for the higher energies reached at the LHC shows the significance of the parton shower evolution to achieve a consistent picture across all reported measurements.

From the theoretical side, the implementation of QCD parton energy loss in Monte Carlo generators with event-by-event medium evolution and fluctuations of the initial conditions should provide the next advance in the interpretation of the experimental results. The use of Monte Carlo generators is of particular importance, since it eases the comparison to new experimental observables and allows testing their sensitivity to variations of the medium properties.

Future jet measurements using the ALICE experiment aim to verify a modified jet structure in heavy-ion collisions and to connect the observation of distorted jet shapes in hadron correlation measurements to the in-medium fragmentation of partons via reconstructed jets. This will be achieved with larger cone radii for jets tagged via a recoiling high-p_{T} hadron. A more differential picture will be achieved with the study of the jet composition via identified particles, and the discrimination of jet flavors and parton masses e.g. by using photon–jet correlations to identify quarks jets and by tagging heavy flavor jets via the decay properties of D and B mesons.

A. Kinematic Variables

When studying ultra-relativistic heavy-ion collisions it is useful to choose the kinematic variables in a way that they are subject to simple transformations when changing the reference frame. According to the rules of special relativity a particle is characterized by its *four-momentum*[1]:

$$P^{\mu} = (E, \vec{p}) = (E, p_x, p_y . p_z), \tag{A.1}$$

with the energy E and the usual three-momentum of the particle $\vec{p}$. The absolute value of the four-momentum, called invariant mass m_{inv}, is the same in all reference frames or invariant under Lorentz transformation:

$$m_{\text{inv}}^2 = P^2 = P^{\mu} P_{\mu} = E^2 - \vec{p} \cdot \vec{p}. \tag{A.2}$$

For a free particle the invariant mass is identical to its rest mass m_0 and Equation (A.2) becomes the well-known relativistic energy-momentum relation.
In high energy physics the sum of the four-momenta of two colliding particles leads to the definition of the *Mandelstam* variable s:

$$s = (P_1 + P_2)^2, \tag{A.3}$$

with $\sqrt{s}$ determining the center of mass energy of the reaction.
The beam is usually considered to point into the z-directions. Thus the transverse momentum component p_{T} and the longitudinal component p_{L} can be written as:

$$p_{\text{T}} = p \cdot \sin(\vartheta), \tag{A.4}$$

$$p_{\text{L}} = p \cdot \cos(\vartheta), \tag{A.5}$$

where p is the absolute value of the momentum $|\vec{p}|$ and ϑ is the angle with respect to the beam axis.

[1] Here, as well as in the following the convention $\hbar = c = 1$ is used.

The transverse momentum p_{T} is invariant under Lorentz transformation in z-direction, while p_{L} is not invariant. Therefore the dimensionless rapidity y is defined. It is directly related to the transverse velocity $\beta_{\mathrm{L}} = p_{\mathrm{L}}/E$ of a particle:

$$\begin{aligned} y &= \operatorname{atanh}\beta_{\mathrm{L}} \\ &= \frac{1}{2}\ln\left(\frac{E+p_{\mathrm{L}}}{E-p_{\mathrm{L}}}\right). \end{aligned} \tag{A.6}$$

It has the advantage to be additive under Lorentz transformation into a reference frame that moves at a velocity β with respect to the old reference frame in longitudinal direction:

$$y' = y + \operatorname{atanh}(\beta). \tag{A.7}$$

For this reason the shape of a distribution is independent of the reference frame when it is given in units of the rapidity. The rapidity is connected to the energy of a particle and to its longitudinal momentum via the transverse mass $m_{\mathrm{T}} = \sqrt{p_{\mathrm{T}}^2 + m_0^2}$:

$$E = m_{\mathrm{T}} \cdot \cosh(y), \tag{A.8}$$

$$p_{\mathrm{L}} = m_{\mathrm{T}} \cdot \sinh(y). \tag{A.9}$$

In the limit $E \gg m_0$ the rapidity can be approximated by the *pseudo-rapidity* η:

$$\eta = \frac{1}{2}\ln\left(\frac{p+p_{\mathrm{L}}}{p-p_{\mathrm{L}}}\right) \tag{A.10}$$

$$= -\ln\left[\tan\left(\frac{\vartheta}{2}\right)\right]. \tag{A.11}$$

The pseudo-rapidity is only determined by the angle of the particle direction of motion with respect to the beam axis. For this reason it is usually easier to determine the pseudo-rapidity than the rapidity of a particle. Similar to Equation (A.8) and (A.9) holds:

$$E = p_{\mathrm{T}} \cdot \cosh(\eta), \tag{A.12}$$

$$p_{\mathrm{L}} = p_{\mathrm{T}} \cdot \sinh(\eta). \tag{A.13}$$

In many jet algorithms the distance between objects, e.g. a particle and the jet axis, is measured in (η, φ). This has the advantage that the distance does not change (for massless objects) under Lorentz transformation. In particular, the angular region defined by a cone in

(η, φ) with radios R around the jet axis:

$$R = \sqrt{(\varphi - \varphi_{\text{jet}})^2 + (\eta - \eta_{\text{jet}})^2} \tag{A.14}$$

retains its circular contour in all reference systems.

Selection of Most Important Publications

[CKB01] S. S. Adler *et al.*, "Common suppression pattern of η and π^0 mesons at high transverse momentum in Au+Au collisions at $\sqrt{s_{NN}}$ = 200 GeV", *Phys. Rev. Lett.* **96**, 202301, 2006.

[CKB02] S. S. Adler *et al.*, "Centrality dependence of π^0 and η production at large transverse momentum in $\sqrt{s_{NN}}$ = 200 GeV d+Au collisions", *Phys. Rev. Lett.* **98**, 172302, 2007.

[CKB03] S. S. Adler *et al.*, "Measurement of direct photon production in p+p collisions at $\sqrt{s_{NN}}$ = 200 GeV", *Phys. Rev. Lett.* **98**, 012002, 2007.

[CKB04] S. S. Adler *et al.*, "A detailed study of high-p_T neutral pion suppression and azimuthal anisotropy in Au+Au collisions at $\sqrt{s_{NN}}$ = 200 GeV", *Phys. Rev.* **C76**, 034904, 2007.

[CKB05] A. Adare *et al.*, "Onset of π^0 Suppression Studied in Cu+Cu Collisions at $\sqrt{s_{NN}}$ = 22.4, 62.4, and 200 GeV", *Phys. Rev. Lett.* **101**, 162301, 2008.

[CKB06] A. Adare *et al.*, "Suppression pattern of neutral pions at high transverse momentum in Au+Au collisions at $\sqrt{s_{NN}}$ = 200 GeV and constraints on medium transport coefficients", *Phys. Rev. Lett.* **101**, 232301, 2008.

[CKB07] A. Adare *et al.*, "Measurement of direct photon v_2 in $\sqrt{s_{NN}} = 200$ GeV Au+Au collisions", *Phys. Rev. Lett.* **109**, 122302, 2012.

[CKB08] B. Abelev *et al.*, "Measurement of Event Background Fluctuations for Charged Particle Jet Reconstruction in Pb-Pb collisions at $\sqrt{s_{NN}} = 2.76$ TeV", *JHEP* **1203**, 053, 2012.

[CKB09] M. Wilde *et al.*, "Measurement of Direct Photons in pp and Pb-Pb Collisions with ALICE", *Nucl. Phys.* **A904-905C**, 573–576, 2013.

[CKB10] A. Morsch *et al.*, "Results on Jet Spectra and Structure from ALICE", *Nucl. Phys.* **A904-905C**, 138–145, 2012.

Bibliography

[Aad10] G. Aad *et al.*, "Observation of a Centrality-Dependent Dijet Asymmetry in Lead-Lead Collisions at $\sqrt{s_{NN}}$= 2.76 TeV with the ATLAS Detector at the LHC", *Phys. Rev. Lett.* **105**, 252303, 2010.

[Aad11] G. Aad *et al.*, "Measurement of the centrality dependence of J/ψ yields and observation of Z production in lead-lead collisions with the ATLAS detector at the LHC", *Phys. Lett.* **B697**, 294–312, 2011.

[Aad12] G. Aad *et al.*, "Observation of a new particle in the search for the Standard Model Higgs boson with the ATLAS detector at the LHC", *Phys.Lett.* **B716**, 1–29, 2012.

[Aad13] G. Aad *et al.*, "Measurement of the jet radius and transverse momentum dependence of inclusive jet suppression in lead-lead collisions at $\sqrt{s_{NN}} = 2.76$ TeV with the ATLAS detector", *Phys. Lett.* **B719**, 220–241, 2013.

[Aam08] K. Aamodt *et al.*, "The ALICE experiment at the CERN LHC", *JINST* **0803**, S08002, 2008.

[Aam11a] K. Aamodt *et al.*, "Centrality dependence of the charged-particle multiplicity density at mid-rapidity in Pb-Pb collisions at $\sqrt{s_{NN}}$ = 2.76 TeV", *Phys. Rev. Lett.* **106**, 032301, 2011.

[Aam11b] K. Aamodt *et al.*, "Suppression of Charged Particle Production at Large Transverse Momentum in Central Pb–Pb Collisions at $\sqrt{s_{NN}} = 2.76$ TeV", *Phys. Lett.* **B696**, 30–39, 2011.

[Aam12] K. Aamodt *et al.*, "Particle-yield modification in jet-like azimuthal di-hadron correlations in Pb-Pb collisions at $\sqrt{s_{NN}} = 2.76$ TeV", *Phys. Rev. Lett.* **108**, 092301, 2012.

[Abe12a] B. Abelev *et al.*, "Neutral pion and η meson production in proton-proton collisions at $\sqrt{s} = 0.9$ TeV and $\sqrt{s} = 7$ TeV", *Phys. Lett.* **B717**, 162–172, 2012.

[Abe12b] B. Abelev *et al.*, "Pion, Kaon, and Proton Production in Central Pb–Pb Collisions at $\sqrt{s_{NN}} = 2.76$ TeV", *Phys. Rev. Lett.* **109**, 252301, 2012.

[Abe12c] B. Abelev *et al.*, "Suppression of high transverse momentum D mesons in central Pb–Pb collisions at $\sqrt{s_{NN}} = 2.76$ TeV", *JHEP* **1209**, 112, 2012.

[Abe13a] B. Abelev *et al.*, "Centrality Dependence of Charged Particle Production at Large Transverse Momentum in Pb–Pb Collisions at $\sqrt{s_{\rm NN}} = 2.76$ TeV", *Phys. Lett.* **B720**, 52–62, 2013.

[Abe13b] B. Abelev *et al.*, "Measurement of the inclusive differential jet cross section in pp collisions at $\sqrt{s} = 2.76$ TeV", 2013, arxiv:1301.3475, submitted to Phys. Lett. B.

[Ada05] J. Adams *et al.*, "Experimental and theoretical challenges in the search for the quark gluon plasma: The STAR collaboration's critical assessment of the evidence from RHIC collisions", *Nucl. Phys.* **A757**, 102–183, 2005.

[Ada07a] A. Adare *et al.*, "Energy Loss and Flow of Heavy Quarks in Au+Au Collisions at $\sqrt{s_{NN}} = 200$ GeV", *Phys. Rev. Lett.* **98**, 172301, 2007.

[Ada07b] A. Adare *et al.*, "Inclusive cross section and double helicity asymmetry for π^0 production in p+p collisions at $\sqrt{s} = 200$ GeV: Implications for the polarized gluon distribution in the proton", *Phys. Rev.* **D76**, 051106, 2007.

[Ada09] A. Adare *et al.*, "Inclusive cross section and double helicity asymmetry for π^0 production in p+p collisions at $\sqrt{s} = 62.4$ GeV", *Phys. Rev.* **D79**, 012003, 2009.

[Ada10a] A. Adare *et al.*, "Enhanced production of direct photons in Au+Au collisions at $\sqrt{s_{NN}} = 200$ GeV", *Phys. Rev. Lett.* **104**, 132301, 2010.

[Ada10b] A. Adare *et al.*, "High p_T direct photon and π^0 triggered azimuthal jet correlations and measurement of k_T for isolated direct photons in $p+p$ collisions at $\sqrt{s} = 200$ GeV", *Phys. Rev.* **D82**, 072001, 2010.

[Ada11] A. Adare *et al.*, "Identified charged hadron production in p+p collisions at $\sqrt{s} = 200$ and 62.4 GeV", *Phys. Rev.* **C83**, 064903, 2011.

[Adc02] K. Adcox *et al.*, "Suppression of Hadrons with Large Transverse Momentum in Central Au+Au Collisions at $\sqrt{s_{NN}} = 130$ GeV", *Phys. Rev. Lett.* **88**, 022301, 2002.

[Adl03a] S. S. Adler *et al.*, "Absence of suppression in particle production at large transverse momentum in $\sqrt{s_{NN}}$ = 200 GeV d+Au collisions", *Phys. Rev. Lett.* **91**, 072303, 2003.

[Adl03b] S. S. Adler *et al.*, "Suppressed π^0 Production at Large Transverse Momentum in Central Au+Au Collisions at $\sqrt{s_{NN}} = 200$ GeV", *Phys. Rev. Lett.* **91**, 072301, 2003.

[Adl04] S. S. Adler *et al.*, "High p_T charged hadron suppression in Au+Au collisions at $\sqrt{s_{NN}} = 200$ GeV", *Phys. Rev.* **C69**, 034910, 2004.

[Adl05a] S. S. Adler *et al.*, "Centrality Dependence of Direct Photon Production in $\sqrt{s_{NN}} =$ 200 GeV Au+Au collisions", *Phys. Rev. Lett.* **94**, 232301, 2005.

[Adl05b] S. S. Adler *et al.*, "Production of ϕ mesons at mid-rapidity in $\sqrt{s_{NN}}$ = 200 GeV Au+Au collisions at RHIC", *Phys. Rev.* **C72**, 014903, 2005.

[Adl05c] S. S. Adler *et al.*, "Systematic studies of the centrality and $\sqrt{s_{NN}}$ dependence of $dE_T/d\eta$ and $dN_{ch}/d\eta$ in heavy ion collisions at mid-rapidity", *Phys. Rev.* **C71**, 034908, 2005.

[Adl06] S. S. Adler *et al.*, "Nuclear modification of electron spectra and implications for heavy quark energy loss in Au+Au collisions at $\sqrt{s_{NN}}$ = 200 GeV", *Phys. Rev. Lett.* **96**, 032301, 2006.

[Aha00] O. Aharony *et al.*, "Large N field theories, string theory and gravity", *Phys. Rept.* **323**, 183–386, 2000.

[Ale06] B. Alessandro *et al.*, "ALICE: Physics performance report, volume II", *J. Phys.* **G32**, 1295–2040, 2006.

[Alf01] M. G. Alford, "Color superconducting quark matter", *Ann. Rev. Nucl. Part. Sci.* **51**, 131–160, 2001.

[Alv11] B. Alver *et al.*, "Phobos results on charged particle multiplicity and pseudorapidity distributions in Au+Au, Cu+Cu, d+Au, and p+p collisions at ultra-relativistic energies", *Phys. Rev.* **C83**, 024913, 2011.

[And06] A. Andronic *et al.*, "Hadron production in central nucleus-nucleus collisions at chemical freeze-out", *Nucl. Phys.* **A772**, 167–199, 2006.

[Ant13] G. Antchev *et al.*, "Luminosity-independent measurements of total, elastic and inelastic cross-sections at $\sqrt{s} = 7$ TeV", *Europhys. Lett.* **101**, 21004, 2013.

[Aph03] L. Aphecetche *et al.*, "PHENIX calorimeter", *Nucl. Instrum. Meth.* **A499**, 521–536, 2003.

[Arm12] N. Armesto *et al.*, "Comparison of Jet Quenching Formalisms for a Quark-Gluon Plasma Brick", *Phys. Rev.* **C86**, 064904, 2012.

[Aub83] J. J. Aubert *et al.*, "The Ratio of the Nucleon Structure Functions $F_2(N)$ for Iron and Deuterium", *Phys. Lett.* **B123**, 275, 1983.

[Bai95] R. Baier *et al.*, "Induced gluon radiation in a QCD medium", *Phys. Lett.* **B345**, 277–286, 1995.

[Bar64] V. E. Barnes *et al.*, "Observation of a Hyperon with Strangeness Minus Three", *Phys. Rev. Lett.* **12**, 204–206, 1964.

[Bas09] S. A. Bass *et al.*, "Systematic Comparison of Jet Energy-Loss Schemes in a realistic hydrodynamic medium", *Phys. Rev.* **C79**, 024901, 2009.

[Bas12] G. Basar *et al.*, "Conformal anomaly as a source of soft photons in heavy ion collisions", *Phys. Rev. Lett.* **109**, 202303, 2012.

[Baz12] A. Bazavov *et al.*, "The chiral and deconfinement aspects of the QCD transition", *Phys. Rev.* **D85**, 054503, 2012.

[Ber71] S. M. Berman *et al.*, "Inclusive Processes at High Transverse Momentum", *Phys. Rev.* **D4**, 3388, 1971.

[Ber12] J. Beringer *et al.*, "Review of Particle Physics (RPP)", *Phys. Rev.* **D86**, 010001, 2012.

[Bia76] A. Bialas *et al.*, "Multiplicity Distributions in Nucleus-Nucleus Collisions at High-Energies", *Nucl. Phys.* **B111**, 461, 1976.

[Bjo73] J. D. Bjorken, "Can We Measure Parton Parton Cross-Sections?", *Phys. Rev.* **D8**, 4098, 1973.

[Bjo82] J. D. Bjorken, “Energy Loss of Energetic Partons in Quark - Gluon Plasma: Possible Extinction of High p_T Jets in Hadron - Hadron Collisions”, 1982, FERMILAB-PUB-82-059-THY.

[Bjo83] J. D. Bjorken, “Highly Relativistic Nucleus-Nucleus Collisions: The central rapidity Region”, *Phys. Rev.* **D27**, 140–151, 1983.

[BM03] P. Braun-Munzinger *et al.*, “Particle production in heavy ion collisions”, in R. C. Hwa, editor, “Quark-Gluon Plasma 3”, pages 491–599, World Scientific, 2003.

[BNL05] BNL, “RHIC Scientists Serve Up "Perfect" Liquid”, Press Release, 2005.

[Bor10] S. Borsanyi *et al.*, “The QCD equation of state with dynamical quarks”, *JHEP* **1011**, 077, 2010.

[Cac08] M. Cacciari *et al.*, “The Anti-k_t jet clustering algorithm”, *JHEP* **0804**, 063, 2008.

[Cac11] M. Cacciari *et al.*, “Fluctuations and asymmetric jet events in PbPb collisions at the LHC”, *Eur. Phys. J.* **C71**, 1692, 2011.

[Cat93] S. Catani *et al.*, “Longitudinally invariant k_t clustering algorithms for hadron hadron collisions”, *Nucl. Phys.* **B406**, 187–224, 1993.

[CER00] CERN, “New State of Matter created at CERN”, Press Release, 2000.

[CER06] CERN Communication Group, “CERN LHC: The Guide. FAQ Frequently Asked Questions”, CERN Brochure http://cdsweb.cern.ch/record/999421, Geneva, 2006.

[CER10] CERN, “LHC experiments bring new insight into primordial universe”, Press Release, 2010.

[CER12] CERN, “CERN experiments observe particle consistent with long-sought Higgs boson”, Press Release, 2012.

[Cha09] R. Chatterjee and D. K. Srivastava, “Elliptic flow of thermal photons and formation time of quark gluon plasma at RHIC”, *Phys. Rev.* **C79**, 021901, 2009.

[Cha11] S. Chatrchyan *et al.*, “Study of Z boson production in PbPb collisions at nucleon-nucleon centre of mass energy = 2.76 TeV”, *Phys. Rev. Lett.* **106**, 212301, 2011.

[Cha12a] S. Chatrchyan *et al.*, "Measurement of isolated photon production in pp and PbPb collisions at $\sqrt{s_{NN}} = 2.76$ TeV", *Phys. Lett.* **B710**, 256–277, 2012.

[Cha12b] S. Chatrchyan *et al.*, "Measurement of the pseudorapidity and centrality dependence of the transverse energy density in PbPb collisions at $\sqrt{s_{NN}} = 2.76$ TeV", *Phys. Rev. Lett.* **109**, 152303, 2012.

[Cha12c] S. Chatrchyan *et al.*, "Observation of a new boson at a mass of 125 GeV with the CMS experiment at the LHC", *Phys. Lett.* **B716**, 30–61, 2012.

[Cha12d] S. Chatrchyan *et al.*, "Study of high-p_T charged particle suppression in PbPb compared to pp collisions at $\sqrt{s_{NN}}$ =2.76 TeV", *Eur. Phys. J.* **C72**, 1945, 2012.

[Che03] S. Chekanov *et al.*, "A ZEUS next-to-leading-order QCD analysis of data on deep inelastic scattering", *Phys. Rev.* **D67**, 012007, 2003.

[Che11] X.-F. Chen *et al.*, "Suppression of high p_T hadrons in $Pb+Pb$ Collisions at LHC", *Phys. Rev.* **C84**, 034902, 2011.

[Chi13] M. Chiu *et al.*, "Production of Photons and Dileptons in the Glasma", *Nucl. Phys.* **A900**, 16–37, 2013.

[Col85] J. C. Collins *et al.*, "Factorization for Short Distance Hadron-Hadron Scattering", *Nucl. Phys.* **B261**, 104, 1985.

[Cor02] G. Corcella *et al.*, "HERWIG 6.5 release note", 2002, CERN-TH-2002-270.

[Cor06] T. Cormier *et al.*, "ALICE electromagnetic calorimeter: addendum to the ALICE technical proposal", 2006, cERN-LHCC-2006-014.

[Cro75] J. W. Cronin *et al.*, "PRODUCTION OF HADRONS WITH LARGE TRANSVERSE MOMENTUM AT 200 GeV, 300 GeV, AND 400 GeV", *Phys. Rev.* **D11**, 3105, 1975.

[Cun13] L. Cunqueiro *et al.*, "Jet structure in 2.76 TeV Pb Pb collisions at ALICE", *Nucl. Phys.* **A904-905C**, 728–731, 2013.

[Dai05] A. Dainese *et al.*, "Leading-particle suppression in high energy nucleus-nucleus collisions", *Eur. Phys. J.* **C38**, 461–474, 2005.

[d'E10] D. d'Enterria, "Jet quenching", in "Relativistic Heavy Ion Physics", volume 23 of *Landolt-Börnstein*, pages 471–520, Springer, Berlin, 2010.

[dF08] P. de Forcrand and O. Philipsen, "The Chiral critical point of $N(f) = 3$ QCD at finite density to the order $(\mu/T)^4$", *JHEP* **0811**, 012, 2008.

[Fey72] R. P. Feynman, "The Development of the Space-Time View of Quantum Electrodynamics", in "Nobel Lectures, Physics 1963 - 1970", Elsevier Publishing Company, Amsterdam, 1972.

[Fod07] Z. Fodor, "QCD Thermodynamics", *PoS* **LAT2007**, 011, 2007.

[Fri03] R. J. Fries *et al.*, "Hadronization in heavy ion collisions: Recombination and fragmentation of partons", *Phys. Rev. Lett.* **90**, 202303, 2003.

[Fro61] M. Froissart, "Asymptotic behavior and subtractions in the Mandelstam representation", *Phys. Rev.* **123**, 1053–1057, 1961.

[Gal10] C. Gale, "Photon Production in Hot and Dense Strongly Interacting Matter", in "Relativistic Heavy Ion Physics", volume 23 of *Landolt-Börnstein*, Springer, Berlin, 2010.

[GM64] M. Gell-Mann, "A Schematic model of baryons and mesons", *Phys. Lett.* **8**, 214–215, 1964.

[Gra11] N. Grau, "Probing nuclear matter with jets and gamma-hadron correlations: Results from PHENIX", *J. Phys.* **G38**, 124090, 2011.

[Guo00] X.-F. Guo and X.-N. Wang, "Multiple scattering, parton energy loss and modified fragmentation functions in deeply inelastic e A scattering", *Phys. Rev. Lett.* **85**, 3591–3594, 2000.

[Gyu00] M. Gyulassy, *et al.*, "Non-Abelian energy loss at finite opacity", *Phys. Rev. Lett.* **85**, 5535–5538, 2000.

[Hag65] R. Hagedorn, "Statistical thermodynamics of strong interactions at high-energies", *Nuovo Cim. Suppl.* **3**, 147–186, 1965.

[Hag71] R. Hagedorn, "Thermodynamics of strong interactions", 1971, CERN Note CERN-71-12.

[Hah03] H. Hahn *et al.*, "The RHIC design overview", *Nucl. Instrum. Meth.* **A499**, 245–263, 2003.

[Hel12] I. Helenius *et al.*, "Impact-Parameter Dependent Nuclear Parton Distribution Functions: EPS09s and EKS98s and Their Applications in Nuclear Hard Processes", *JHEP* **1207**, 073, 2012.

[Hop04] M. Hoppe, Aufbau und Inbetriebnahme einer Funkenkammer, Diplomarbeit, Institut für Kernphysik, Münster, 2004.

[Hor08] W. Horowitz and M. Gyulassy, "Heavy quark jet tomography of Pb + Pb at LHC: AdS/CFT drag or pQCD energy loss?", *Phys. Lett.* **B666**, 320–323, 2008.

[Hor11] W. Horowitz and M. Gyulassy, "The Surprising Transparency of the sQGP at LHC", *Nucl. Phys.* **A872**, 265–285, 2011.

[Ian03] E. Iancu and R. Venugopalan, "The Color Glass Condensate and High Energy Scattering in QCD", in R. C. Hwa, editor, "Quark-Gluon Plasma 3", pages 249–363, World Scientific, 2003.

[Jac76] M. Jacob and P. Landshoff, "Trigger Bias in Large p(T) Reactions", *Nucl. Phys.* **B113**, 395, 1976.

[Kar03] F. Karsch and E. Laermann, "Thermodynamics and in-medium hadron properties from lattice QCD", in R. C. Hwa, editor, "Quark-Gluon Plasma 3", pages 1–59, World Scientific, 2003.

[KB04] C. Klein-Bösing, "PHENIX measurement of high p_T particles in Au+Au and d+Au collisions at $\sqrt{s_{NN}}$ = 200 GeV", *J. Phys.* **G30**, S975–S978, 2004.

[KB05] C. Klein-Bösing, Production of Neutral Pions and Direct Photons in Ultra-Relativistic Au + Au Collisions, Ph.D. thesis, Institut für Kernphysik, Münster, 2005.

[KB06] C. Klein-Bösing, "Systematic study of particle production at high p_T with the PHENIX experiment", *Proc. 22nd Winter Workshop on Nuclear Dynamics 55* 2006.

[KB08] C. Klein-Bösing, "Systematic study of high-p_T hadron and photon production with the PHENIX experiment", *J. Phys.* **G35**, 044026, 2008.

[KB11a] C. Klein-Bösing, "First Jet and High p_T Measurements with the ALICE Experiment at the LHC", *Nuovo Cimento C* **034** 02, 41–47, 2011.

[KB11b] C. Klein-Bösing, "Jet and High p_T Measurement with the ALICE Experiment", *Int. J. Mod. Phys.* **E20** 7, 1533–1538, 2011.

[KB11c] C. Klein-Bösing, "Jet reconstruction and jet background classification with the ALICE experiment in PbPb collisions at the LHC", *J. Phys.* **G38**, 124088, 2011.

[KB12] C. Klein-Bösing, "Reconstruction of Jet Properties in Pb-Pb Collisions with the ALICE-Experiment", *AIP Conf. Proc.* **1441** 1, 841, 2012.

[Kha09] D. E. Kharzeev, "Parton energy loss at strong coupling and the universal bound", *Eur. Phys. J.* **C61**, 675–682, 2009.

[Kov05] P. Kovtun, *et al.*, "Viscosity in strongly interacting quantum field theories from black hole physics", *Phys. Rev. Lett.* **94**, 111601, 2005.

[Kut81] J. Kuti *et al.*, "Monte Carlo Study of SU(2) Gauge Theory at Finite Temperature", *Phys. Lett.* **B98**, 199, 1981.

[Lin05] Z.-W. Lin *et al.*, "A Multi-phase transport model for relativistic heavy ion collisions", *Phys. Rev.* **C72**, 064901, 2005.

[Loh12] D. Lohner, "Measurement of Direct-Photon Elliptic Flow in Pb-Pb Collisions at $\sqrt{s_{NN}} = 2.76$ TeV", 2012, arxiv:1212.3995, Submitted to Nucl. Phys. A.

[Maj08] A. Majumder and B. Muller, "Higher twist jet broadening and classical propagation", *Phys. Rev.* **C77**, 054903, 2008.

[Maj11] A. Majumder and M. Van Leeuwen, "The theory and phenomenology of perturbative QCD based jet quenching", *Prog. Part. Nucl. Phys.* **66**, 41–92, 2011.

[Mil07] M. L. Miller, *et al.*, "Glauber modeling in high energy nuclear collisions", *Ann. Rev. Nucl. Part. Sci.* **57**, 205–243, 2007.

[Mue03] B. Mueller, "Phenomenology of jet quenching in heavy ion collisions", *Phys. Rev.* **C67**, 061901, 2003.

[Nam61] Y. Nambu and G. Jona-Lasinio, "Dynamical Model of Elementary Particles Based on an Analogy with Superconductivity. I", *Phys. Rev.* **122**, 345–358, 1961.

[Pei08a] S. Peigne, “Collisional Energy Loss of a Fast Parton in a QGP”, *AIP Conf. Proc.* **1038**, 139–148, 2008.

[Pei08b] S. Peigne and A. Peshier, “Collisional energy loss of a fast heavy quark in a quark-gluon plasma”, *Phys. Rev.* **D77**, 114017, 2008.

[Pol01] G. Policastro *et al.*, “The Shear viscosity of strongly coupled N=4 supersymmetric Yang-Mills plasma”, *Phys. Rev. Lett.* **87**, 081601, 2001.

[Pop11] H. Poppenborg, Characterization of Heavy-Ion-Background in Jet-Reconstruction, Bachelorarbeit, Institut für Kernphysik, University of Münster, 2011.

[Qiu91a] J.-W. Qiu and G. F. Sterman, “Power corrections in hadronic scattering. 1. Leading $1/Q^2$ corrections to the Drell-Yan cross-section”, *Nucl. Phys.* **B353**, 105–136, 1991.

[Qiu91b] J.-W. Qiu and G. F. Sterman, “Power corrections to hadronic scattering. 2. Factorization”, *Nucl. Phys.* **B353**, 137–164, 1991.

[Raj00] K. Rajagopal and F. Wilczek, “The Condensed matter physics of QCD”, in M. Shifman, editor, “At the frontier of particle physics”, volume 3, pages 2061–2151, World Scientific, Singapore, 2000.

[Ren11] T. Renk, *et al.*, “Systematics of the charged-hadron p_T spectrum and the nuclear suppression factor in heavy-ion collisions from $\sqrt{s} = 200$ GeV to $\sqrt{s} = 2.76$ TeV”, *Phys. Rev.* **C84**, 014906, 2011.

[Ren12] T. Renk, “Constraining the Physics of Jet Quenching”, *Phys. Rev.* **C85**, 044903, 2012.

[Sah12] B. Sahlmueller, “Cold Nuclear Matter Effects in d+Au Collisions at PHENIX”, 2012, arxiv:1210.5547, Submitted to Nucl. Phys. A.

[Sal03] C. A. Salgado and U. A. Wiedemann, “Calculating quenching weights”, *Phys. Rev.* **D68**, 014008, 2003.

[Sal10] G. P. Salam, “Towards Jetography”, *Eur.Phys.J.* **C67**, 637–686, 2010.

[Sch93] E. Schnedermann *et al.*, “Thermal phenomenology of hadrons from 200 GeV S+S collisions”, *Phys. Rev.* **C48**, 2462–2475, 1993.

[Sch10] A. Schmitt, "Dense matter in compact stars: A pedagogical introduction", *Lect. Notes Phys.* **811**, 1–111, 2010.

[Sjo01] T. Sjostrand *et al.*, "High-energy-physics event generation with PYTHIA 6.1", *Comput. Phys. Commun.* **135**, 238–259, 2001.

[Sjo06] T. Sjostrand *et al.*, "PYTHIA 6.4 physics and manual", *JHEP* **05**, 026, 2006.

[Son11] H. Song *et al.*, "200 GeV Au+Au collisions serve a nearly perfect quark-gluon liquid", *Phys. Rev. Lett.* **106**, 192301, 2011.

[Ste77] G. Sterman and S. Weinberg, "Jets from Quantum Chromodynamics", *Phys. Rev. Lett.* **39**, 1436, 1977.

[Tur06] S. Turbide *et al.*, "Azimuthal Asymmetry of Direct Photons in High Energy Nuclear Collisions", *Phys. Rev. Lett.* **96**, 032303, 2006.

[vH11] H. van Hees *et al.*, "Thermal Photons and Collective Flow at the Relativistic Heavy-Ion Collider", *Phys. Rev.* **C84**, 054906, 2011.

[Vit02] I. Vitev and M. Gyulassy, "Jet quenching and the anti-p greater than or equal to pi-anomaly at RHIC", *Phys. Rev.* **C65**, 041902, 2002.

[Vit06a] I. Vitev, "Testing the mechanism of QGP-induced energy loss", *Acta Phys. Hung.* **A27**, 281–286, 2006.

[Vit06b] I. Vitev, "Testing the theory of QGP-induced energy loss at RHIC and the LHC", *Phys. Lett.* **B639**, 38–45, 2006.

[Vol03] S. Voloshin, "Anisotropic flow", *Nucl. Phys.* **A715**, 379–388, 2003.

[Wan01] X.-N. Wang and X.-f. Guo, "Multiple parton scattering in nuclei: Parton energy loss", *Nucl.Phys.* **A696**, 788–832, 2001.

[Wan02] E. Wang and X.-N. Wang, "Jet tomography of dense and nuclear matter", *Phys. Rev. Lett.* **89**, 162301, 2002.

[Wic07] S. Wicks, *et al.*, "Elastic, Inelastic, and Path Length Fluctuations in Jet Tomography", *Nucl. Phys.* **A784**, 426–442, 2007.

[Wil74] K. G. Wilson, "Confinement of Quarks", *Phys. Rev.* **D10**, 2445–2459, 1974.

[Won94] C.-Y. Wong, Introduction to High-Energy Heavy-Ion Collisions, World Scientific, Singapore, 1994.

[Zap13] K. C. Zapp, *et al.*, "A perturbative framework for jet quenching", *JHEP* **1303**, 080, 2013.

[Zha07] H. Zhang, *et al.*, "Dihadron tomography of high-energy nuclear collisions in NLO pQCD", *Phys. Rev. Lett.* **98**, 212301, 2007.

[Zwe64] G. Zweig, "An SU(3) model for strong interaction symmetry and its breaking", CERN Report CERN-TH-401, 1964.

Danksagung

Abschließend möchte ich mich allen bedanken, die zum Gelingen dieser Arbeit beigetragen haben.

Mein besonderer Dank gilt Prof. Dr. J. P. Wessels für seine langjährige Unterstützung, seine guten Ratschläge und viele hilfreiche Diskussionen.

Forschungsvorhaben wie das PHENIX- und das ALICE-Experiment können nur mit einer großen Zahl engagierter Personen erfolgreich vorbereitet und betrieben werden. Ich möchte mich daher bei allen Mitgliedern der PHENIX- und ALICE-Kollaboration bedanken. Insbesondere gilt mein Dank für zahlreiche anregende Diskussionen und die fruchtbare Zusammenarbeit bei verschiedenen Publikationen und Analysen: Dr. Bastian Bathen, Prof. Dr. Stefan Bathe, Dr. Oliver Busch, Prof. Dr. Henner Büsching, Dr. Gabor David, Dr. Tom Dietel, Dr. Leticia Cunqueiro, Dr. Jan Fiete Große-Oetringhaus, Dr. Marco van Leeuwen, Dr. Andreas Morsch, PD Dr. Klaus Reygers, Dr. Marta Verweij und Martin Wilde.

Für die angenehme Arbeitsatmosphäre und die große Unterstützung gilt mein Dank allen aktuellen und ehemaligen Mitgliedern des Instituts für Kernphysik in Münster, sowie dem ALICE CERN-Team.

Für die persönliche Förderung während der letzten Jahre im Rahmen des Helmholtz-Allianz Programmes HA216/EMMI *Extremes of Density and Temperature: Cosmic Matter in the Laboratory* gebührt mein Dank der Helmholtz Gemeinschaft. Des Weiteren bedanke ich mich für die großzügige Unterstützung der Arbeit der gesamten Münsteraner Gruppe im PHENIX- und ALICE-Experiment durch das BMBF.

Für die genaue und kritische Durchsicht dieser Arbeit und viele hilfreiche Anregungen danke ich Dr. Bastian Bathen, Dr. Melanie Klein-Bösing, Prof. Dr. R. Santo, PD Dr. Klaus Reygers und Prof. Dr. J. P. Wessels.

Ein ganz großes Dankeschön geht an all jene, die mich während der letzten Jahre außerhalb der Arbeit begleitet und unterstützt haben.

An meine beiden wichtigsten Konstanten: Danke M&m!

REPRINTS OF SELECTED PUBLICATIONS

Common Suppression Pattern of η and π^0 Mesons at High Transverse Momentum in Au + Au Collisions at $\sqrt{s_{NN}} = 200$ GeV

S. S. Adler,[5] S. Afanasiev,[18] C. Aidala,[5] N. N. Ajitanand,[44] Y. Akiba,[21,39] J. Alexander,[44] R. Amirikas,[12] L. Aphecetche,[46] S. H. Aronson,[5] R. Averbeck,[45] T. C. Awes,[36] R. Azmoun,[45] V. Babintsev,[15] A. Baldisseri,[10] K. N. Barish,[6] P. D. Barnes,[28] B. Bassalleck,[34] S. Bathe,[31] S. Batsouli,[9] V. Baublis,[38] A. Bazilevsky,[40,15] S. Belikov,[17,15] Y. Berdnikov,[41] S. Bhagavatula,[17] J. G. Boissevain,[28] H. Borel,[10] S. Borenstein,[26] M. L. Brooks,[28] D. S. Brown,[35] N. Bruner,[34] D. Bucher,[31] H. Buesching,[31] V. Bumazhnov,[15] G. Bunce,[5,40] J. M. Burward-Hoy,[27,45] S. Butsyk,[45] X. Camard,[46] J.-S. Chai,[19] P. Chand,[4] W. C. Chang,[2] S. Chernichenko,[15] C. Y. Chi,[9] J. Chiba,[21] M. Chiu,[9] I. J. Choi,[53] J. Choi,[20] R. K. Choudhury,[4] T. Chujo,[5] V. Cianciolo,[36] Y. Cobigo,[10] B. A. Cole,[9] P. Constantin,[17] D. d'Enterria,[46] G. David,[5] H. Delagrange,[46] A. Denisov,[15] A. Deshpande,[40] E. J. Desmond,[5] A. Devismes,[45] O. Dietzsch,[42] O. Drapier,[26] A. Drees,[45] R. du Rietz,[30] A. Durum,[15] D. Dutta,[4] Y. V. Efremenko,[36] K. El Chenawi,[50] A. Enokizono,[14] H. En'yo,[39,40] S. Esumi,[49] L. Ewell,[5] D. E. Fields,[34,40] F. Fleuret,[26] S. L. Fokin,[24] B. D. Fox,[40] Z. Fraenkel,[52] J. E. Frantz,[9] A. Franz,[5] A. D. Frawley,[12] S.-Y. Fung,[6] S. Garpman,[30,*] T. K. Ghosh,[50] A. Glenn,[47] G. Gogiberidze,[47] M. Gonin,[26] J. Gosset,[10] Y. Goto,[40] R. Granier de Cassagnac,[26] N. Grau,[17] S. V. Greene,[50] M. Grosse Perdekamp,[40] W. Guryn,[5] H.-Å. Gustafsson,[30] T. Hachiya,[14] J. S. Haggerty,[5] H. Hamagaki,[8] A. G. Hansen,[28] E. P. Hartouni,[27] M. Harvey,[5] R. Hayano,[8] N. Hayashi,[39] X. He,[13] M. Heffner,[27] T. K. Hemmick,[45] J. M. Heuser,[45] M. Hibino,[51] H. Hiejima,[16] J. C. Hill,[17] W. Holzmann,[44] K. Homma,[14] B. Hong,[23] A. Hoover,[35] T. Ichihara,[39,40] V. V. Ikonnikov,[24] K. Imai,[25,39] D. Isenhower,[1] M. Ishihara,[39] M. Issah,[44] A. Isupov,[18] B. V. Jacak,[45] W. Y. Jang,[23] Y. Jeong,[20] J. Jia,[45] O. Jinnouchi,[39] B. M. Johnson,[5] S. C. Johnson,[27] K. S. Joo,[32] D. Jouan,[37] S. Kametani,[8,51] N. Kamihara,[48,39] J. H. Kang,[53] S. S. Kapoor,[4] K. Katou,[51] S. Kelly,[9] B. Khachaturov,[52] A. Khanzadeev,[38] J. Kikuchi,[51] D. H. Kim,[32] D. J. Kim,[53] D. W. Kim,[20] E. Kim,[43] G.-B. Kim,[26] H. J. Kim,[53] E. Kistenev,[5] A. Kiyomichi,[49] K. Kiyoyama,[33] C. Klein-Boesing,[31] H. Kobayashi,[39,40] L. Kochenda,[38] V. Kochetkov,[15] D. Koehler,[34] T. Kohama,[14] M. Kopytine,[45] D. Kotchetkov,[6] A. Kozlov,[52] P. J. Kroon,[5] C. H. Kuberg,[1,28,*] K. Kurita,[40] Y. Kuroki,[49] M. J. Kweon,[23] Y. Kwon,[53] G. S. Kyle,[35] R. Lacey,[44] V. Ladygin,[18] J. G. Lajoie,[17] A. Lebedev,[17,24] S. Leckey,[45] D. M. Lee,[28] S. Lee,[20] M. J. Leitch,[28] X. H. Li,[6] H. Lim,[43] A. Litvinenko,[18] M. X. Liu,[28] Y. Liu,[37] C. F. Maguire,[50] Y. I. Makdisi,[5] A. Malakhov,[18] V. I. Manko,[24] Y. Mao,[7,39] G. Martinez,[46] M. D. Marx,[45] H. Masui,[49] F. Matathias,[45] T. Matsumoto,[8,51] P. L. McGaughey,[28] E. Melnikov,[15] F. Messer,[45] Y. Miake,[49] J. Milan,[44] T. E. Miller,[50] A. Milov,[45,52] S. Mioduszewski,[5] R. E. Mischke,[28] G. C. Mishra,[13] J. T. Mitchell,[5] A. K. Mohanty,[4] D. P. Morrison,[5] J. M. Moss,[28] F. Mühlbacher,[45] D. Mukhopadhyay,[52] M. Muniruzzaman,[6] J. Murata,[39,40] S. Nagamiya,[21] J. L. Nagle,[9] T. Nakamura,[14] B. K. Nandi,[6] M. Nara,[49] J. Newby,[47] P. Nilsson,[30] A. S. Nyanin,[24] J. Nystrand,[30] E. O'Brien,[5] C. A. Ogilvie,[17] H. Ohnishi,[5,39] I. D. Ojha,[50,3] K. Okada,[39] M. Ono,[49] V. Onuchin,[15] A. Oskarsson,[30] I. Otterlund,[30] K. Oyama,[8] K. Ozawa,[8] D. Pal,[52] A. P. T. Palounek,[28] V. Pantuev,[45] V. Papavassiliou,[35] J. Park,[43] A. Parmar,[34] S. F. Pate,[35] T. Peitzmann,[31] J.-C. Peng,[28] V. Peresedov,[18] C. Pinkenburg,[5] R. P. Pisani,[5] F. Plasil,[36] M. L. Purschke,[5] A. K. Purwar,[45] J. Rak,[17] I. Ravinovich,[52] K. F. Read,[36,47] M. Reuter,[45] K. Reygers,[31] V. Riabov,[38,41] Y. Riabov,[38] G. Roche,[29] A. Romana,[26,*] M. Rosati,[17] P. Rosnet,[29] S. S. Ryu,[53] M. E. Sadler,[1] B. Sahlmueller,[31] N. Saito,[39,40] T. Sakaguchi,[8,51] M. Sakai,[33] S. Sakai,[49] V. Samsonov,[38] L. Sanfratello,[34] R. Santo,[31] H. D. Sato,[25,39] S. Sato,[5,49] S. Sawada,[21] Y. Schutz,[46] V. Semenov,[15] R. Seto,[6] M. R. Shaw,[1,28] T. K. Shea,[5] T.-A. Shibata,[48,39] K. Shigaki,[14,21] T. Shiina,[28] C. L. Silva,[42] D. Silvermyr,[28,30] K. S. Sim,[23] C. P. Singh,[3] V. Singh,[3] M. Sivertz,[5] A. Soldatov,[15] R. A. Soltz,[27] W. E. Sondheim,[28] S. P. Sorensen,[47] I. V. Sourikova,[5] F. Staley,[10] P. W. Stankus,[36] E. Stenlund,[30] M. Stepanov,[35] A. Ster,[22] S. P. Stoll,[5] T. Sugitate,[14] J. P. Sullivan,[28] E. M. Takagui,[42] A. Taketani,[39,40] M. Tamai,[51] K. H. Tanaka,[21] Y. Tanaka,[33] K. Tanida,[39] M. J. Tannenbaum,[5] P. Tarján,[11] J. D. Tepe,[1,28] T. L. Thomas,[34] J. Tojo,[25,39] H. Torii,[25,39] R. S. Towell,[1] I. Tserruya,[52] H. Tsuruoka,[49] S. K. Tuli,[3] H. Tydesjö,[30] N. Tyurin,[15] H. W. van Hecke,[28] J. Velkovska,[5,45] M. Velkovsky,[45] V. Veszprémi,[11] L. Villatte,[47] A. A. Vinogradov,[24] M. A. Volkov,[24] E. Vznuzdaev,[38] X. R. Wang,[13] Y. Watanabe,[39,40] S. N. White,[5] F. K. Wohn,[17] C. L. Woody,[5] W. Xie,[6] Y. Yang,[7] A. Yanovich,[15] S. Yokkaichi,[39,40] G. R. Young,[36] I. E. Yushmanov,[24] W. A. Zajc,[9,†] C. Zhang,[9] S. Zhou,[7] S. J. Zhou,[52] and L. Zolin[18]

(PHENIX Collaboration)

[1]*Abilene Christian University, Abilene, Texas 79699, USA*
[2]*Institute of Physics, Academia Sinica, Taipei 11529, Taiwan*
[3]*Department of Physics, Banaras Hindu University, Varanasi 221005, India*

[4]Bhabha Atomic Research Centre, Bombay 400 085, India
[5]Brookhaven National Laboratory, Upton, New York 11973-5000, USA
[6]University of California - Riverside, Riverside, California 92521, USA
[7]China Institute of Atomic Energy (CIAE), Beijing, People's Republic of China
[8]Center for Nuclear Study, Graduate School of Science, University of Tokyo, 7-3-1 Hongo, Bunkyo, Tokyo 113-0033, Japan
[9]Columbia University, New York, New York 10027, USA and Nevis Laboratories, Irvington, New York 10533, USA
[10]Dapnia, CEA Saclay, F-91191, Gif-sur-Yvette, France
[11]Debrecen University, H-4010 Debrecen, Egyetem tér 1, Hungary
[12]Florida State University, Tallahassee, Florida 32306, USA
[13]Georgia State University, Atlanta, Georgia 30303, USA
[14]Hiroshima University, Kagamiyama, Higashi-Hiroshima 739-8526, Japan
[15]IHEP Protvino, State Research Center of Russian Federation, Institute for High Energy Physics, Protvino, 142281, Russia
[16]University of Illinois at Urbana-Champaign, Urbana, Illinois 61801, USA
[17]Iowa State University, Ames, Iowa 50011, USA
[18]Joint Institute for Nuclear Research, 141980 Dubna, Moscow Region, Russia
[19]KAERI, Cyclotron Application Laboratory, Seoul, South Korea
[20]Kangnung National University, Kangnung 210-702, South Korea
[21]KEK, High Energy Accelerator Research Organization, Tsukuba, Ibaraki 305-0801, Japan
[22]KFKI Research Institute for Particle and Nuclear Physics of the Hungarian Academy of Sciences (MTA KFKI RMKI), H-1525 Budapest 114, PO Box 49, Budapest, Hungary
[23]Korea University, Seoul, 136-701, Korea
[24]Russian Research Center "Kurchatov Institute," Moscow, Russia
[25]Kyoto University, Kyoto 606-8502, Japan
[26]Laboratoire Leprince-Ringuet, Ecole Polytechnique, CNRS-IN2P3, Route de Saclay, F-91128, Palaiseau, France
[27]Lawrence Livermore National Laboratory, Livermore, California 94550, USA
[28]Los Alamos National Laboratory, Los Alamos, New Mexico 87545, USA
[29]LPC, Université Blaise Pascal, CNRS-IN2P3, Clermont-Fd, 63177 Aubiere Cedex, France
[30]Department of Physics, Lund University, Box 118, SE-221 00 Lund, Sweden
[31]Institut für Kernphysik, University of Muenster, D-48149 Muenster, Germany
[32]Myongji University, Yongin, Kyonggido 449-728, Korea
[33]Nagasaki Institute of Applied Science, Nagasaki-shi, Nagasaki 851-0193, Japan
[34]University of New Mexico, Albuquerque, New Mexico 87131, USA
[35]New Mexico State University, Las Cruces, New Mexico 88003, USA
[36]Oak Ridge National Laboratory, Oak Ridge, Tennessee 37831, USA
[37]IPN-Orsay, Universite Paris Sud, CNRS-IN2P3, BP1, F-91406, Orsay, France
[38]PNPI, Petersburg Nuclear Physics Institute, Gatchina, Leningrad Region, 188300, Russia
[39]RIKEN, The Institute of Physical and Chemical Research, Wako, Saitama 351-0198, Japan
[40]RIKEN BNL Research Center, Brookhaven National Laboratory, Upton, New York 11973-5000, USA
[41]Saint Petersburg State Polytechnic University, St. Petersburg, Russia
[42]Instituto de Física, Universidade de São Paulo, Caixa Postal 66318, São Paulo CEP05315-970, Brazil
[43]System Electronics Laboratory, Seoul National University, Seoul, South Korea
[44]Chemistry Department, Stony Brook University, SUNY, Stony Brook, New York 11794-3400, USA
[45]Department of Physics and Astronomy, Stony Brook University, SUNY, Stony Brook, New York 11794, USA
[46]SUBATECH (Ecole des Mines de Nantes, CNRS-IN2P3, Université de Nantes) BP 20722 - 44307, Nantes, France
[47]University of Tennessee, Knoxville, Tennessee 37996, USA
[48]Department of Physics, Tokyo Institute of Technology, Oh-okayama, Meguro, Tokyo, 152-8551, Japan
[49]Institute of Physics, University of Tsukuba, Tsukuba, Ibaraki 305, Japan
[50]Vanderbilt University, Nashville, Tennessee 37235, USA
[51]Waseda University, Advanced Research Institute for Science and Engineering, 17 Kikui-cho, Shinjuku-ku, Tokyo 162-0044, Japan
[52]Weizmann Institute, Rehovot 76100, Israel
[53]Yonsei University, IPAP, Seoul 120-749, Korea

(Received 26 January 2006; published 22 May 2006)

Inclusive transverse momentum spectra of η mesons have been measured within $p_T = 2$–10 GeV/c at midrapidity by the PHENIX experiment in Au + Au collisions at $\sqrt{s_{NN}} = 200$ GeV. In central Au + Au the η yields are significantly suppressed compared to peripheral Au + Au, d + Au, and $p + p$ yields scaled by the corresponding number of nucleon-nucleon collisions. The magnitude, centrality, and p_T dependence of the suppression is common, within errors, for η and π^0. The ratio of η to π^0 spectra at high p_T amounts to $0.40 < R_{\eta/\pi^0} < 0.48$ for the three systems, in agreement with the world average measured in hadronic and nuclear reactions and, at large scaled momentum, in e^+e^- collisions.

DOI: 10.1103/PhysRevLett.96.202301 PACS numbers: 25.75.Dw

The major motivation for the study of high energy nucleus-nucleus ($A + A$) collisions is the opportunity to probe strongly interacting matter at extremely high energy densities. Of particular interest are energy densities well above the expected transition from normal hadronic matter to a deconfined system of quarks and gluons. Lattice quantum chromodynamics (QCD) calculations [1] predict that this transition will occur at a temperature of $T \approx 170$ MeV $\approx 10^{12}$ K. The formation of a quark-gluon plasma (QGP) in $A + A$ reactions should manifest itself in a variety of experimental signatures [2].

At center-of-mass energies reached by the Relativistic Heavy Ion Collider (RHIC), arguably the most exciting experimental results so far are connected with the predicted "jet quenching" phenomenon [3–5] due to energy loss of hard-scattered partons as they traverse the dense medium formed in the reaction. Since (leading) hadrons with $p_T > 4$ GeV/c at RHIC carry a large fraction of the momentum of the parent quark or gluon [$\langle z \rangle = p_{\mathrm{hadron}}/p_{\mathrm{parton}} \approx 0.5$–$0.7$ [6,7]], parton energy loss results in a significantly suppressed production of high-p_T hadrons [4]. The inclusive spectra of high-p_T neutral pions [8,9] and charged hadrons [10,11] in Au + Au at $\sqrt{s_{NN}} = 200$ GeV are indeed suppressed by as much as a factor of 5 compared to the corresponding yields in $p + p$ [12] and $d +$ Au [13,14], scaled by the number of incoherent nucleon-nucleon (NN) collisions. The centrality [15], p_T [16–18] and center-of-mass energy [19] dependences of the observed quenching are consistent with theoretical calculations of QCD energy loss due to multiple gluon emission in a dense medium. Assuming a thermalized parton system, the magnitude of the suppression for central Au + Au at $\sqrt{s_{NN}} = 200$ GeV implies initial energy densities above 15 GeV/fm^3, ~100 times larger than normal nuclear matter [20].

The equal amount of suppression for π^0 and $h^{\pm}$ observed above $p_T \approx 5$ GeV/c for the same Au + Au centrality seems to indicate that the mechanism of quenching is independent of the identity of the high-p_T light-quark hadron. This is expected if the suppression takes place at the parton level *prior* to its fragmentation into a given hadron. Indeed, in this case the high-p_T deficit depends only on the energy lost in the medium by the parent (u, d, s) quark or gluon and not on the nature of the final leading hadron which will be produced with the same *universal* probabilities (fragmentation functions) which govern hadron production in the vacuum in more elementary systems. The partons involved in high-p_T hadroproduction considered in this work have typical momenta $\gtrsim 5$ GeV/c, 10 times larger than the "bulk" average momenta $\langle p_T \rangle \approx 0.55$ GeV/c of the system [21]. Such energetic partons are then supposed to traverse (and lose energy in) the medium and hadronize in the *vacuum* a few tens of fm/c later [15]. The equal suppression of $h^{\pm}$ and π^0 does not by itself provide a conclusive argument for parton energy loss *before* fragmentation in the vacuum because above $p_T \approx 5$ GeV/c, unidentified charged hadron yields are dominated by $\pi^{\pm}$ [11]. Measurement of the yields of an additional light-quark species like the η meson at large enough p_T allows a confirmation of the independence of the quenching with respect to the nature of the produced hadron, and tests the consistency of the data with medium-induced *partonic* energy loss prior to vacuum hadronization. Besides its interest as a *signal* in its own right, the η meson constitutes, after the π^0, the second most important source of decay $e^{\pm}$ and γ. Reliable knowledge of their production cross sections is thus required in order to eliminate the *background* of secondary $e^{\pm}$ and γ in single electron [22], dielectron [23], and direct γ [24] measurements.

This Letter presents measurements of the η meson by the PHENIX experiment [25] in Au + Au collisions at $\sqrt{s_{NN}} = 200$ GeV during the second RHIC run (2001–2002) and compares them to η from $p + p$ and $d +$ Au [26] and to π^0 [8,9] and direct γ [24] from Au + Au, all measured in the same experiment at the same $\sqrt{s_{NN}}$. The η measurement reaches the second largest p_T for identified hadrons at RHIC, after the π^0. The analysis reported here uses beam-beam counters (BBC, $3.0 < |\eta| < 3.9$) plus the zero degree calorimeters (ZDC) for trigger and global event characterization. For each collision, the reaction centrality is obtained by cuts in the correlated distribution of the charge detected in the BBC and the energy measured in the ZDC [27]. A Glauber Monte Carlo model combined with a simulation of BBC and ZDC responses is used to determine the corresponding nuclear overlap function $\langle T_{AA} \rangle$ for each centrality [8]. The η mesons are reconstructed at midrapidity in the lead-scintillator (PbSc) electromagnetic calorimeter [28] via their $\gamma\gamma$ decay mode (BR = 39.43%). The PbSc consists of 15 552 individual lead-scintillator sandwich modules (5.54 cm × 5.54 cm × 37.5 cm, 18 X_0), grouped in six sectors located at a radial distance of 5.1 m from the beam line, covering a total solid angle of $\Delta\eta \approx 0.7$ and $\Delta\phi \approx 3\pi/4$ rad. The energy calibration of the PbSc modules is obtained from the beam-test values and confirmed with the measured position of the π^0 mass peak, the energy deposited by minimum ionizing particles traversing the calorimeter, as well as with the expected $E_{\mathrm{PbSc}}/p_{\mathrm{tracking}} \sim 1$ value for $e^{\pm}$ identified by the Ring-Imaging Čerenkov detector. The systematic error on the absolute energy scale is less than 1.5%, which translates into a maximum 8% uncertainty in the final η yields.

For this analysis a minimum bias (MB) trigger sample of 34×10^6 events, also used for the previously published π^0 analysis [8], is combined with a Level-2 trigger event sample for centralities 0%–60%, equivalent to an additional 30×10^6 minimum bias events. The Level-2 trigger sample is obtained with a software trigger on highly energetic particles (3.5 GeV threshold). The resulting trigger reaches a 50% (100%) efficiency for η above $p_T = 5(7)$ GeV/c. The normalization of the Level-2 data sample

relative to the MB data sample is accurate to 2%. Both sets of events are required to have a vertex position $|z| < 30$ cm along the beam axis. Photon candidates are identified in the PbSc by applying particle identification (PID) cuts based on the time-of-flight and shower profile [8,26]. The systematic uncertainty on the yields related to the applied PID cuts is ~8%. The η yields are determined by an invariant mass analysis of photon pairs with asymmetries $|E_{\gamma 1} - E_{\gamma 2}|/(E_{\gamma 1} + E_{\gamma 2}) < 0.5$. The combinatorial background is obtained by combining uncorrelated photon pairs from different events with similar centrality and vertex, and by normalizing the distribution in a region below ($m_{\rm inv} = 400$–450 MeV$/c^2$) and above ($m_{\rm inv} = 750$–1000 MeV$/c^2$) the η mass peak. The resulting distribution is fit to a Gaussian plus an exponential to account for the residual background not described by the mixed-event background (inset of Fig. 1). The open (solid) symbols depict the η signal after mixed (plus residual) background subtraction. To estimate the uncertainty in the subtraction procedure, different pair asymmetries and an alternative linear parametrization of the residual background are used. The signal-to-background ratio in peripheral (central) collisions is approximately 1.3 (1.5) for the highest p_T and 0.05 (0.002) for the lowest p_T.

The raw spectra are normalized to one unit of rapidity and full azimuth. This purely geometrical acceptance factor amounts to ~4 at large p_T. The spectra are further corrected for the detector response (energy resolution, dead areas), the reconstruction efficiency (analysis cuts), and occupancy effects (cluster overlaps). These corrections are quantified by embedding simulated single η from a full PHENIX GEANT [29] simulation into real events, and analyzing the merged events with the same analysis cuts used to obtain the real yields. The total η yield efficiency correction is ~3 and rises $\lesssim 20\%$ with centrality. The losses are dominated by fiducial and asymmetry cuts. The nominal energy resolution is adjusted in the simulation by adding a p_T-independent energy smearing of 3% for each PbSc tower. The shape, position, and width of the η peak measured for all p_T's and centralities are well reproduced by the embedded data.

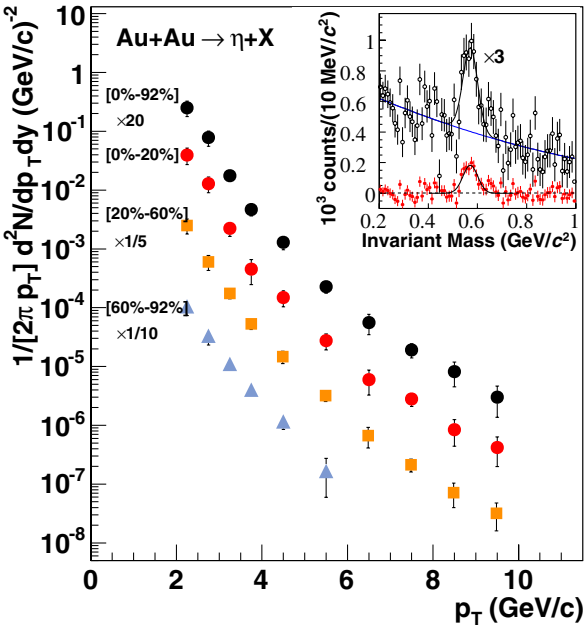

FIG. 1 (color online). Invariant η yields as a function of transverse momentum for 3 centralities and MB Au + Au at $\sqrt{s_{NN}} = 200$ GeV scaled by the factors indicated in the plot. Inset: invariant mass distribution of γ pairs with $p_T = 4$–5 GeV$/c$ measured in MB Au + Au, after mixed-event (black open circles) plus residual (red solid circles) background subtraction.

The main sources of systematic errors in the measurement are the uncertainties in the yield extraction (10%–30%), the yield correction (10%), and the energy scale (a maximum of 8%). The final combined systematic errors on the spectra are at the level of 10%–30% (point-to-point) and 10%–20% (p_T-correlated) depending on the p_T and centrality bin [26]. A correction in the yield to account for the true mean value of each p_T bin is applied to the steeply falling spectra. The fully corrected p_T distributions are shown in Fig. 1 for MB and 3 centrality bins (0%–20%, 20%–60%, and 60%–92%) scaled for clarity by the factors indicated. The error bars are the quadratic sum of statistical and systematic errors.

Medium effects in $A + A$ collisions are quantitatively determined using the *nuclear modification factor* given as the ratio of the measured $A + A$ invariant yield over the $p + p$ cross section scaled by the Glauber nuclear overlap function $\langle T_{AA} \rangle$ in the centrality bin under consideration:

$$R_{AA}(p_T) = \frac{d^2N_{AA}/dp_T dy}{\langle T_{AA} \rangle d^2\sigma_{pp}/dp_T dy}. \quad (1)$$

Deviations from $R_{AA}(p_T) = 1$ quantify the degree of departure of the hard $A + A$ yields from an incoherent superposition of NN collisions. Figure 2 compares the nuclear modification factor for η in central (0%–20%), semicentral (20%–60%), and peripheral (60%–92%) Au + Au reactions using the reference $d^2\sigma_{pp}/dp_T dy$ spectrum measured in $p + p$ collisions [26]. As observed for high-p_T π^0 [8,9], the η yields are consistent with the expectation of independent NN scatterings in peripheral reactions ($R_{AA} \approx 1$) but are increasingly reduced for smaller centralities. The p_T dependence of R_{AA} is flat above 4 GeV$/c$ as seen also for the π^0.

Figure 3 compares the $R_{AA}(p_T)$ measured in Au + Au at $\sqrt{s_{NN}} = 200$ GeV for η (0%–20% centrality), π^0 [8,9], and γ [24] (0%–10% centralities). Whereas direct γ are unsuppressed compared to the T_{AA}-scaled reference given here by a next-to-leading-order (NLO) calculation [24,30] that reproduces the PHENIX $p + p$ photon data well [31], π^0 and η are suppressed by a similar factor of ~5 compared to the corresponding $p + p$ cross sections [9,26]. Within the current uncertainties, light-quark mesons at

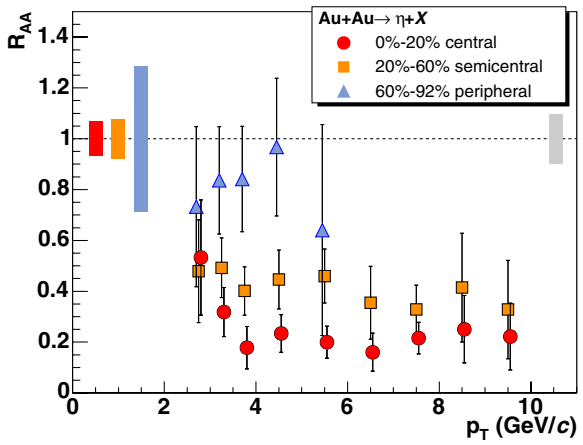

FIG. 2 (color online). Nuclear modification factors for η in Au + Au centralities: 0%–20%, 20%–60%, 60%–92%. The error bars show point-to-point uncertainties. The absolute normalization error bands at $R_{AA} = 1$ show the uncertainties in $\langle T_{AA} \rangle$ for decreasing centralities. The error box on the right indicates the 9.7% $p + p$ cross-section uncertainty [14].

RHIC show a flat suppression in the range $p_T = 4$–14 GeV/c, independent of their mass (note that the η is 4 times heavier than the π^0). The results are in agreement with expectations of in-medium non-Abelian energy loss of the parent parton prior to its fragmentation in the vacuum. The initial gluon densities needed to quench the high-p_T hadrons by such an amount are of the order of $dN^g/dy = 1100$ (solid curve in Fig. 3) [16].

An additional way to determine possible differences in the suppression pattern of π^0 and η is to study the centrality dependence of the η/π^0 ratio in Au + Au collisions and compare it with the ratio in more elementary systems (e^+e^-, $p + p$, d + Au). The η/π^0 ratio in hadron-hadron, hadron-nucleus, and nucleus-nucleus collisions is seen to increase rapidly with p_T and flatten out above $p_T \approx 2.5$ GeV/c at an asymptotically constant $R_{\eta/\pi^0} \approx 0.5$ for all systems [26]. Likewise, in e^+e^- at the Z pole ($\sqrt{s} = 91.2$ GeV) one also finds $R_{\eta/\pi^0} \approx 0.5$ for η and π^0 at large scaled momenta $x_p = p_{\text{hadron}}/p_{\text{beam}} \gtrsim 0.3$–$0.7$ [26] consistent with the range of fractional momenta $\langle z \rangle$ relevant for high-p_T production discussed here. It is interesting to test if this ratio is modified in any way by final- and/or initial-state medium effects in Au + Au collisions at RHIC.

Figure 4 shows $R_{\eta/\pi^0}(p_T)$ for three Au + Au centrality selections and for $p + p$ and d + Au collisions [26]. A fit to a constant for $p_T > 2$ GeV/c gives $R_{\eta/\pi^0}^{\text{AuAu0\%–20\%}} = 0.40 \pm 0.04$, $R_{\eta/\pi^0}^{d\text{AuMB}} = 0.47 \pm 0.03$, and $R_{\eta/\pi^0}^{pp} = 0.48 \pm 0.03$, where the quoted errors are the quadratic sum of statistical and systematic uncertainties. The Au + Au ratio is consistent within $\sim 1\sigma$ with both the essentially identical d + Au and $p + p$ ratios. The R_{η/π^0} ratio shows thus no apparent collision system, centrality, or p_T dependence. The dotted curve is the predicted PYTHIA [32] result for the $p + p$ ratio at $\sqrt{s} = 200$ GeV which is also coincident with the world data measured in the same momentum range in hadronic, nuclear, and e^+e^- collisions in a wide range of energies ($\sqrt{s} \approx$ 3–1800 GeV) [26].

In summary, the transverse momentum spectra of η mesons have been measured at midrapidity in the range $p_T = 2$–10 GeV/c in Au + Au at $\sqrt{s_{NN}} = 200$ GeV. The invariant yields per nucleon-nucleon collision are increasingly depleted with centrality in comparison to $p + p$ results at the same center-of-mass energy. The maximum

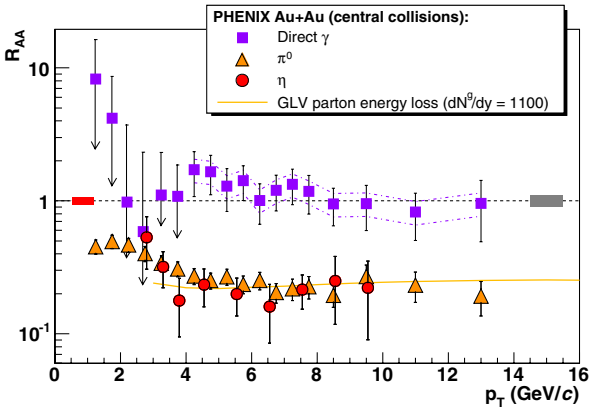

FIG. 3 (color online). $R_{AA}(p_T)$ measured in central Au + Au at $\sqrt{s_{NN}} = 200$ GeV for η, π^0 [8,9], and direct γ [24]. The error bars include all point-to-point errors. The error bands at $R_{AA} = 1$ have the same meaning as in Fig. 2. The baseline $p + p \rightarrow \gamma + X$ reference used is a NLO calculation [24,30], that reproduces our own data well [31], with theoretical uncertainties indicated by the dash-dotted lines around the points. The solid yellow curve is a parton energy loss prediction for a medium with density $dN^g/dy = 1100$ [16].

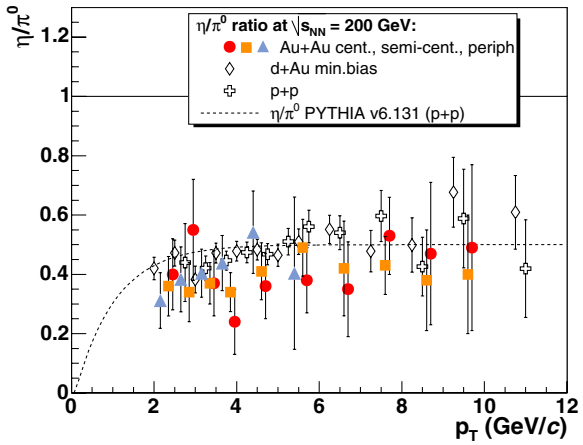

FIG. 4 (color online). η/π^0 ratio in Au + Au (centralities: 0%–20%, 20%–60%, 60%–92%) compared to the ratio in $p + p$ and d + Au [26] at $\sqrt{s_{NN}} = 200$ GeV. The error bars include all point-to-point errors that do not cancel in the ratio of yields. The dashed curve is the PYTHIA [32] prediction for $p + p$ at $\sqrt{s} = 200$ GeV consistent with the asymptotic $R_{\eta/\pi^0} \approx 0.5$ measured in hadronic and e^+e^- collisions in a wide range of c.m. energies [26].

suppression factor is ~5 in central Au + Au. The magnitude, p_T, and centrality dependences of the suppression are the same for η and π^0 suggesting that the production of light neutral mesons at large p_T in nuclear collisions at RHIC is affected by the medium in the same way. The measured η/π^0 ratio is flat with p_T and amounts to $R_{\eta/\pi^0} = 0.40 \pm 0.04$. This value is consistent with the world value at high p_T in hadronic and nuclear reactions and, at high x_p, in e^+e^- collisions. We conclude that all these observations are in agreement with a scenario where the parent parton first loses energy in the produced dense medium and then fragments into a leading meson in the vacuum according to the same probabilities that govern high-p_T hadroproduction in more elementary systems ($p + p$, e^+e^-).

We thank the staff of the Collider-Accelerator and Physics Departments at BNL for their vital contributions. We acknowledge support from the Department of Energy and NSF (USA), MEXT and JSPS (Japan), CNPq and FAPESP (Brazil), NSFC (China), CNRS-IN2P3 and CEA (France), BMBF, DAAD, and AvH (Germany), OTKA (Hungary), DAE and DST (India), ISF (Israel), KRF and CHEP (Korea), RMIST, RAS, and RMAE (Russia), VR and KAW (Sweden), US CRDF for the FSU, US-Hungarian NSF-OTKA-MTA, and US-Israel BSF.

*Deceased.
†PHENIX Spokesperson.
Email address: zajc@nevis.columbia.edu

[1] F. Karsch, Lect. Notes Phys. **583**, 209 (2002).
[2] J. W. Harris and B. Müller, Annu. Rev. Nucl. Part. Sci. **46**, 71 (1996).
[3] J. D. Bjorken, Fermilab Report No. FERMILAB-PUB-82-059-THY, 1982 (unpublished).
[4] M. Gyulassy and M. Plümer, Phys. Lett. B **243**, 432 (1990); X. N. Wang and M. Gyulassy, Phys. Rev. Lett. **68**, 1480 (1992).
[5] R. Baier, Y. L. Dokshitzer, A. H. Mueller, S. Peigné, and D. Schiff, Nucl. Phys. **B484**, 265 (1997); R. Baier, D. Schiff, and B. G. Zakharov, Annu. Rev. Nucl. Part. Sci. **50**, 37 (2000); U. Wiedemann, Nucl. Phys. **B588**, 303 (2000).
[6] S. S. Adler *et al.* (PHENIX Collaboration), hep-ex/0605039 (to be published).
[7] S. Kretzer, Acta Phys. Pol. B **36**, 179 (2005).
[8] S. S. Adler *et al.* (PHENIX Collaboration), Phys. Rev. Lett. **91**, 072301 (2003).
[9] S. S. Adler *et al.* (PHENIX Collaboration) (to be published).
[10] J. Adams *et al.* (STAR Collaboration), Phys. Rev. Lett. **91**, 172302 (2003).
[11] S. S. Adler *et al.* (PHENIX Collaboration), Phys. Rev. C **69**, 034910 (2004).
[12] S. S. Adler *et al.* (PHENIX Collaboration), Phys. Rev. Lett. **91**, 241803 (2003).
[13] S. S. Adler *et al.* (PHENIX Collaboration), Phys. Rev. Lett. **91**, 072303 (2003).
[14] S. S. Adler *et al.* (PHENIX Collaboration) (to be published).
[15] X. N. Wang, Phys. Lett. B **579**, 299 (2004).
[16] I. Vitev and M. Gyulassy, Phys. Rev. Lett. **89**, 252301 (2002); I. Vitev, J. Phys. G **30**, S791 (2004).
[17] K. J. Eskola, H. Honkanen, C. A. Salgado, and U. A. Wiedemann, Nucl. Phys. **A747**, 511 (2005).
[18] S. Jeon and G. D. Moore, Phys. Rev. C **71**, 034901 (2005).
[19] D. d'Enterria, Eur. Phys. J. C **43**, 295 (2005).
[20] K. Adcox *et al.* (PHENIX Collaboration), Nucl. Phys. **A757**, 184 (2005).
[21] S. S. Adler *et al.* (PHENIX Collaboration), Phys. Rev. C **69**, 034909 (2004).
[22] K. Adcox *et al.* (PHENIX Collaboration), Phys. Rev. Lett. **88**, 192303 (2002); S. S. Adler *et al.* (PHENIX Collaboration), Phys. Rev. C **72**, 024901 (2005); Phys. Rev. Lett. **96**, 032301 (2006).
[23] A. Toia (PHENIX Collaboration), *Proceedings of the QM'05*, nucl-ex/0510006.
[24] S. S. Adler *et al.* (PHENIX Collaboration), Phys. Rev. Lett. **94**, 232301 (2005).
[25] K. Adcox *et al.* (PHENIX Collaboration), Nucl. Instrum. Methods Phys. Res., Sect. A **499**, 469 (2003).
[26] S. S. Adler *et al.* (PHENIX Collaboration) (to be published).
[27] K. Adcox *et al.* (PHENIX Collaboration), Phys. Rev. Lett. **86**, 3500 (2001).
[28] L. Aphecetche *et al.* (PHENIX Collaboration), Nucl. Instrum. Methods Phys. Res., Sect. A **499**, 521 (2003).
[29] F. Carminati *et al.*, *GEANT 3.21: Detector Description and Simulation Tool*, CERN Program Library Long Writeup No. W5013, 1993 (unpublished).
[30] L. E. Gordon and W. Vogelsang, Phys. Rev. D **48**, 3136 (1993); Phys. Rev. D **50**, 1901 (1994).
[31] S. S. Adler *et al.* (PHENIX Collaboration), Phys. Rev. D **71**, 071102 (2005); K. Okada (PHENIX Collaboration), *Proceedings of SPIN04*, hep-ex/0501066.
[32] T. Sjöstrand, Comput. Phys. Commun. **82**, 74 (1994); computer code PYTHIA v6.131 with default parameters.

Centrality Dependence of π^0 and η Production at Large Transverse Momentum in $\sqrt{s_{NN}} = 200$ GeV d + Au Collisions

S. S. Adler,[5] S. Afanasiev,[20] C. Aidala,[10] N. N. Ajitanand,[44] Y. Akiba,[21,40] A. Al-Jamel,[35] J. Alexander,[44] K. Aoki,[25] L. Aphecetche,[46] R. Armendariz,[35] S. H. Aronson,[5] R. Averbeck,[45] T. C. Awes,[36] V. Babintsev,[17] A. Baldisseri,[11] K. N. Barish,[6] P. D. Barnes,[28] B. Bassalleck,[34] S. Bathe,[6,31] S. Batsouli,[10] V. Baublis,[39] F. Bauer,[6] A. Bazilevsky,[5,41] S. Belikov,[19,17] M. T. Bjorndal,[10] J. G. Boissevain,[28] H. Borel,[11] M. L. Brooks,[28] D. S. Brown,[35] N. Bruner,[34] D. Bucher,[31] H. Buesching,[5,31] V. Bumazhnov,[17] G. Bunce,[5,41] J. M. Burward-Hoy,[28,27] S. Butsyk,[45] X. Camard,[46] P. Chand,[4] W. C. Chang,[2] S. Chernichenko,[17] C. Y. Chi,[10] J. Chiba,[21] M. Chiu,[10] I. J. Choi,[53] R. K. Choudhury,[4] T. Chujo,[5] V. Cianciolo,[36] Y. Cobigo,[11] B. A. Cole,[10] M. P. Comets,[37] P. Constantin,[19] M. Csanád,[13] T. Csörgő,[22] J. P. Cussonneau,[46] D. d'Enterria,[10] K. Das,[14] G. David,[5] F. Deák,[13] H. Delagrange,[46] A. Denisov,[17] A. Deshpande,[41] E. J. Desmond,[5] A. Devismes,[45] O. Dietzsch,[42] J. L. Drachenberg,[1] O. Drapier,[26] A. Drees,[45] A. Durum,[17] D. Dutta,[4] V. Dzhordzhadze,[47] Y. V. Efremenko,[36] H. En'yo,[40,41] B. Espagnon,[37] S. Esumi,[49] D. E. Fields,[34,41] C. Finck,[46] F. Fleuret,[26] S. L. Fokin,[24] B. D. Fox,[41] Z. Fraenkel,[52] J. E. Frantz,[10] A. Franz,[5] A. D. Frawley,[14] Y. Fukao,[25,40,41] S.-Y. Fung,[6] S. Gadrat,[29] M. Germain,[46] A. Glenn,[47] M. Gonin,[26] J. Gosset,[11] Y. Goto,[40,41] R. Granier de Cassagnac,[26] N. Grau,[19] S. V. Greene,[50] M. Grosse Perdekamp,[18,41] H.-Å. Gustafsson,[30] T. Hachiya,[16] J. S. Haggerty,[5] H. Hamagaki,[8] A. G. Hansen,[28] E. P. Hartouni,[27] M. Harvey,[5] K. Hasuko,[40] R. Hayano,[8] X. He,[15] M. Heffner,[27] T. K. Hemmick,[45] J. M. Heuser,[40] P. Hidas,[22] H. Hiejima,[18] J. C. Hill,[19] R. Hobbs,[34] W. Holzmann,[44] K. Homma,[16] B. Hong,[23] A. Hoover,[35] T. Horaguchi,[40,41,48] T. Ichihara,[40,41] V. V. Ikonnikov,[24] K. Imai,[25,40] M. Inaba,[49] M. Inuzuka,[8] D. Isenhower,[1] L. Isenhower,[1] M. Ishihara,[40] M. Issah,[44] A. Isupov,[20] B. V. Jacak,[45] J. Jia,[45] O. Jinnouchi,[40,41] B. M. Johnson,[5] S. C. Johnson,[27] K. S. Joo,[32] D. Jouan,[37] F. Kajihara,[8] S. Kametani,[8,51] N. Kamihara,[40,48] M. Kaneta,[41] J. H. Kang,[53] K. Katou,[51] T. Kawabata,[8] A. V. Kazantsev,[24] S. Kelly,[9,10] B. Khachaturov,[52] A. Khanzadeev,[39] J. Kikuchi,[51] D. J. Kim,[53] E. Kim,[43] G.-B. Kim,[26] H. J. Kim,[53] E. Kinney,[9] A. Kiss,[13] E. Kistenev,[5] A. Kiyomichi,[40] C. Klein-Boesing,[31] H. Kobayashi,[41] L. Kochenda,[39] V. Kochetkov,[17] R. Kohara,[16] B. Komkov,[39] M. Konno,[49] D. Kotchetkov,[6] A. Kozlov,[52] P. J. Kroon,[5] C. H. Kuberg,[1,*] G. J. Kunde,[28] K. Kurita,[40] M. J. Kweon,[23] Y. Kwon,[53] G. S. Kyle,[35] R. Lacey,[44] J. G. Lajoie,[19] Y. Le Bornec,[37] A. Lebedev,[19,24] S. Leckey,[45] D. M. Lee,[28] M. J. Leitch,[28] M. A. L. Leite,[42] X. H. Li,[6] H. Lim,[43] A. Litvinenko,[20] M. X. Liu,[28] C. F. Maguire,[50] Y. I. Makdisi,[5] A. Malakhov,[20] V. I. Manko,[24] Y. Mao,[38,40] G. Martinez,[46] H. Masui,[49] F. Matathias,[45] T. Matsumoto,[8,51] M. C. McCain,[1] P. L. McGaughey,[28] Y. Miake,[49] T. E. Miller,[50] A. Milov,[45] S. Mioduszewski,[5] G. C. Mishra,[15] J. T. Mitchell,[5] A. K. Mohanty,[4] D. P. Morrison,[5] J. M. Moss,[28] D. Mukhopadhyay,[52] M. Muniruzzaman,[6] S. Nagamiya,[21] J. L. Nagle,[9,10] T. Nakamura,[16] J. Newby,[47] A. S. Nyanin,[24] J. Nystrand,[30] E. O'Brien,[5] C. A. Ogilvie,[19] H. Ohnishi,[40] I. D. Ojha,[3,50] H. Okada,[25,40] K. Okada,[40,41] A. Oskarsson,[30] I. Otterlund,[30] K. Oyama,[8] K. Ozawa,[8] D. Pal,[52] A. P. T. Palounek,[28] V. Pantuev,[45] V. Papavassiliou,[35] J. Park,[43] W. J. Park,[23] S. F. Pate,[35] H. Pei,[19] V. Penev,[20] J.-C. Peng,[18] H. Pereira,[11] V. Peresedov,[20] A. Pierson,[34] C. Pinkenburg,[5] R. P. Pisani,[5] M. L. Purschke,[5] A. K. Purwar,[45] J. M. Qualls,[1] J. Rak,[19] I. Ravinovich,[52] K. F. Read,[36,47] M. Reuter,[45] K. Reygers,[31] V. Riabov,[39] Y. Riabov,[39] G. Roche,[29] A. Romana,[26,*] M. Rosati,[19] S. S. E. Rosendahl,[30] P. Rosnet,[29] V. L. Rykov,[40] S. S. Ryu,[53] B. Sahlmueller,[31] N. Saito,[25,40,41] T. Sakaguchi,[8,51] S. Sakai,[49] V. Samsonov,[39] L. Sanfratello,[34] R. Santo,[31] H. D. Sato,[25,40] S. Sato,[5,49] S. Sawada,[21] Y. Schutz,[46] V. Semenov,[17] R. Seto,[6] T. K. Shea,[5] I. Shein,[17] T.-A. Shibata,[40,48] K. Shigaki,[16] M. Shimomura,[49] A. Sickles,[45] C. L. Silva,[42] D. Silvermyr,[28] K. S. Sim,[23] A. Soldatov,[17] R. A. Soltz,[27] W. E. Sondheim,[28] S. P. Sorensen,[47] I. V. Sourikova,[5] F. Staley,[11] P. W. Stankus,[36] E. Stenlund,[30] M. Stepanov,[35] A. Ster,[22] S. P. Stoll,[5] T. Sugitate,[16] J. P. Sullivan,[28] S. Takagi,[49] E. M. Takagui,[42] A. Taketani,[40,41] K. H. Tanaka,[21] Y. Tanaka,[33] K. Tanida,[40] M. J. Tannenbaum,[5] A. Taranenko,[44] P. Tarján,[12] T. L. Thomas,[34] M. Togawa,[25,40] J. Tojo,[40] H. Torii,[25,41] R. S. Towell,[1] V-N. Tram,[26] I. Tserruya,[52] Y. Tsuchimoto,[16] H. Tydesjö,[30] N. Tyurin,[17] T. J. Uam,[32] J. Velkovska,[5] M. Velkovsky,[45] V. Veszprémi,[12] A. A. Vinogradov,[24] M. A. Volkov,[24] E. Vznuzdaev,[39] X. R. Wang,[15] Y. Watanabe,[40,41] S. N. White,[5] N. Willis,[37] F. K. Wohn,[19] C. L. Woody,[5] W. Xie,[6] A. Yanovich,[17] S. Yokkaichi,[40,41] G. R. Young,[36] I. E. Yushmanov,[24] W. A. Zajc,[10,†] O. Zaudtke,[31] C. Zhang,[10] S. Zhou,[7] J. Zimányi,[22,*] L. Zolin,[20] X. Zong,[19] and H. W. vanHecke[28]

(PHENIX Collaboration)

[1]*Abilene Christian University, Abilene, Texas 79699, USA*
[2]*Institute of Physics, Academia Sinica, Taipei 11529, Taiwan*

[3]Department of Physics, Banaras Hindu University, Varanasi 221005, India
[4]Bhabha Atomic Research Centre, Bombay 400 085, India
[5]Brookhaven National Laboratory, Upton, New York 11973-5000, USA
[6]University of California-Riverside, Riverside, California 92521, USA
[7]China Institute of Atomic Energy (CIAE), Beijing, People's Republic of China
[8]Center for Nuclear Study, Graduate School of Science, University of Tokyo, 7-3-1 Hongo, Bunkyo, Tokyo 113-0033, Japan
[9]University of Colorado, Boulder, Colorado 80309, USA
[10]Columbia University, New York, New York 10027 and Nevis Laboratories, Irvington, New York 10533, USA
[11]Dapnia, CEA Saclay, F-91191, Gif-sur-Yvette, France
[12]Debrecen University, H-4010 Debrecen, Egyetem tér 1, Hungary
[13]ELTE, Eötvös Loránd University, H-1117 Budapest, Pázmány P. s. 1/A, Hungary
[14]Florida State University, Tallahassee, Florida 32306, USA
[15]Georgia State University, Atlanta, Georgia 30303, USA
[16]Hiroshima University, Kagamiyama, Higashi-Hiroshima 739-8526, Japan
[17]IHEP Protvino, State Research Center of Russian Federation, Institute for High Energy Physics, Protvino, 142281, Russia
[18]University of Illinois at Urbana-Champaign, Urbana, Illinois 61801, USA
[19]Iowa State University, Ames, Iowa 50011, USA
[20]Joint Institute for Nuclear Research, 141980 Dubna, Moscow Region, Russia
[21]KEK, High Energy Accelerator Research Organization, Tsukuba, Ibaraki 305-0801, Japan
[22]KFKI Research Institute for Particle and Nuclear Physics of the Hungarian Academy of Sciences (MTA KFKI RMKI), H-1525 Budapest 114, POBox 49, Budapest, Hungary
[23]Korea University, Seoul, 136-701, Korea
[24]Russian Research Center "Kurchatov Institute", Moscow, Russia
[25]Kyoto University, Kyoto 606-8502, Japan
[26]Laboratoire Leprince-Ringuet, Ecole Polytechnique, CNRS-IN2P3, Route de Saclay, F-91128, Palaiseau, France
[27]Lawrence Livermore National Laboratory, Livermore, California 94550, USA
[28]Los Alamos National Laboratory, Los Alamos, New Mexico 87545, USA
[29]LPC, Université Blaise Pascal, CNRS-IN2P3, Clermont-Fd, 63177 Aubiere Cedex, France
[30]Department of Physics, Lund University, Box 118, SE-221 00 Lund, Sweden
[31]Institut für Kernphysik, University of Muenster, D-48149 Muenster, Germany
[32]Myongji University, Yongin, Kyonggido 449-728, Korea
[33]Nagasaki Institute of Applied Science, Nagasaki-shi, Nagasaki 851-0193, Japan
[34]University of New Mexico, Albuquerque, New Mexico 87131, USA
[35]New Mexico State University, Las Cruces, New Mexico 88003, USA
[36]Oak Ridge National Laboratory, Oak Ridge, Tennessee 37831, USA
[37]IPN-Orsay, Universite Paris Sud, CNRS-IN2P3, BP1, F-91406, Orsay, France
[38]Peking University, Beijing, People's Republic of China
[39]PNPI, Petersburg Nuclear Physics Institute, Gatchina, Leningrad region, 188300, Russia
[40]RIKEN (The Institute of Physical and Chemical Research), Wako, Saitama 351-0198, JAPAN
[41]RIKEN BNL Research Center, Brookhaven National Laboratory, Upton, New York 11973-5000, USA
[42]Universidade de São Paulo, Instituto de Física, Caixa Postal 66318, São Paulo CEP05315-970, Brazil
[43]System Electronics Laboratory, Seoul National University, Seoul, South Korea
[44]Chemistry Department, Stony Brook University, Stony Brook, SUNY, New York 11794-3400, USA
[45]Department of Physics and Astronomy, Stony Brook University, SUNY, Stony Brook, New York 11794, USA
[46]SUBATECH (Ecole des Mines de Nantes, CNRS-IN2P3, Université de Nantes) BP 20722-44307, Nantes, France
[47]University of Tennessee, Knoxville, Tennessee 37996, USA
[48]Department of Physics, Tokyo Institute of Technology, Oh-okayama, Meguro, Tokyo 152-8551, Japan
[49]Institute of Physics, University of Tsukuba, Tsukuba, Ibaraki 305, Japan
[50]Vanderbilt University, Nashville, Tennessee 37235, USA
[51]Waseda University, Advanced Research Institute for Science and Engineering, 17 Kikui-cho, Shinjuku-ku, Tokyo 162-0044, Japan
[52]Weizmann Institute, Rehovot 76100, Israel
[53]Yonsei University, IPAP, Seoul 120-749, Korea

(Received 23 October 2006; published 24 April 2007)

The dependence of transverse momentum spectra of neutral pions and η mesons with $p_T < 16$ GeV/c and $p_T < 12$ GeV/c, respectively, on the centrality of the collision has been measured at midrapidity by the PHENIX experiment at the BNL Relativistic Heavy Ion Collider (RHIC) in d + Au collisions at $\sqrt{s_{NN}} = 200$ GeV. The measured yields are compared to those in $p + p$ collisions at the same $\sqrt{s_{NN}}$ scaled by the number of underlying nucleon-nucleon collisions in d + Au. At all centralities, the yield ratios show no suppression, in contrast to the strong suppression seen for central Au + Au collisions at RHIC. Only a weak p_T and centrality dependence can be observed.

DOI: 10.1103/PhysRevLett.98.172302 PACS numbers: 25.75.Dw

High-energy nucleus-nucleus collisions provide the opportunity to study strongly interacting matter at very high energy densities where Quantum Chromodynamics (QCD) predicts a transition from normal nuclear matter to a deconfined system of quarks and gluons, the Quark-Gluon Plasma (QGP) [1]. At the Relativistic Heavy Ion Collider (RHIC), the energy density is well in excess of the critical energy density that is expected for this transition [2]. One of the most intriguing results observed at RHIC so far is the suppression of hadrons with high transverse momentum (p_T) in central (head-on) Au + Au collisions. The hadron yield at high p_T is a factor of 5 less than expected from $p + p$ collisions scaled by the number of corresponding nucleon-nucleon collisions [3]. Such suppression was predicted as an effect of parton energy loss in the medium generated in the collisions [4,5]. A control experiment of d + Au collisions, where no medium is produced in the final state of the collision, showed no indication of hadron suppression at midrapidity [6], ruling out strong initial-state effects (final-state energy loss in the cold nucleus is generally expected to be small) as the cause for the suppression in Au + Au. For a better understanding of the medium effects at work in Au + Au, however, it is crucial to explore the exact role initial-state effects play in the modification of high-p_T particle production at RHIC.

Initial-state nuclear effects include p_T broadening, shadowing, and gluon saturation. The p_T broadening, often called Cronin effect [7], is an enhancement of the particle yield at intermediate p_T, which is often attributed to multiple soft parton scatterings before a hard interaction of the parton [8,9]. Shadowing is an apparent depletion of the structure function in the nucleus at small Bjorken x ($x \leq 10^{-2}$) [10] with (in some models) a corresponding enhancement at intermediate x ($x \sim 5 \times 10^{-2}$) called antishadowing. This is not well understood, but usually attributed to coherence effects or to gluon saturation. Gluon saturation refers to the nonlinear dynamics of gluons at small x where, due to the large densities, they tend to fuse rather than split. The Color Glass Condensate (CGC) model is a classical description of this saturation effect. In this picture, particle production at moderate p_T originally was predicted to be suppressed in central d + Au collisions at RHIC [11]. In recent CGC models, a Cronin enhancement can also be reproduced with a suitable choice of initial-state parameters [12].

One established way to test the contribution of different initial- and final-state nuclear effects is the study of the centrality dependence of particle production at high p_T. Initial state and medium effects are strongest in central collisions. In Au + Au collisions, a strong dependence of the suppression of high-p_T hadrons on the centrality of the collision has been observed [13–15]; the suppression weakens going to peripheral collisions and finally disappears. This can be compared to the centrality dependence of (initial-state) hadron production in d + Au. The yield of nonidentified charged hadrons in d + Au collisions with $p_T < 6$ GeV/c was found to be increasingly enhanced going from peripheral to central collisions [16], mainly attributed to the influence of (anti)protons [17]. At high p_T, the baryon contribution to the yield of unidentified charged hadrons is expected to become small, and instead the yield is dominated by charged pions [2]. All this sparks paramount interest in the centrality dependence of neutral pion (π^0) production especially as it can be measured up to very high p_T where particle production is truly perturbative. Furthermore, the high-p_T measurement of an additional identified particle like the eta meson (η), with 4 times the mass of the pion, may shed light on the question to what extent the particle-species dependence of the suppression (enhancement) observed in Au + Au (d + Au) depends on the number of constituent quarks rather than on the mass of the particle [18,19].

In this Letter, we present measurements by the PHENIX experiment [20] on the production of π^0 and η in $p + p$ and d + Au collisions at $\sqrt{s_{NN}} = 200$ GeV. The data provide the first measurement of neutral mesons in d + Au collisions at midrapidity as a function of the centrality of the collision. The π^0 measurements described in this Letter are similar to the analysis of minimum bias d + Au data in [6] but are based on an improved data set that allows the study of the particle production for different selections of the centrality of the collision. A more detailed description of the η analysis can be found in [21].

π^0 and η are measured by the PHENIX electromagnetic calorimeter (EMCal) via the $\pi^0 \rightarrow \gamma\gamma$ and $\eta \rightarrow \gamma\gamma$ decay. The EMCal consists of six lead scintillator (PbSc) and two lead glass (PbGl) sectors, each located at a radial distance of ~5 m from the beam axis. The detector covers a pseudorapidity range of $|\eta| \leq 0.35$ and an azimuthal angle of $\Delta\phi = \pi$. The EMCal granularity is $\Delta\eta \times \Delta\phi \approx 0.011 \times 0.011$ for the PbSc and 0.008×0.008 for the PbGl. The data sets from PbSc and PbGl are analyzed separately and combined for the final results. The energy calibration for the EMCal is obtained from beam tests, cosmic rays, and minimum ionizing energy peaks of charged hadrons. In a recent improvement of the calibration, the EMCal is calibrated by the invariant mass distribution of neutral pions for each of the 24768 readout channels separately. The uncertainty on the energy scale is 1.2%.

The data used in this analysis were recorded in 2002-2003 (RHIC Run-3) under two different trigger conditions. 25.2×10^6 and 58.3×10^6 minimum bias events were analyzed for $p + p$ and d + Au collisions, respectively. Minimum bias (MB) events are triggered by the Beam-Beam Counters (BBC) [20] ($|\eta| = 3.0$–3.9) and require a vertex position along the beam axis within $|z| < 30$ cm.

The minimum bias trigger accepts $(88 \pm 4)\%$ of all inelastic $d + \mathrm{Au}$ collisions that satisfy the vertex condition. This corresponds to 1.99 b $\pm 5.2\%$, the measured fraction of the total $d + \mathrm{Au}$ inelastic cross section, determined using photo-dissociation of the deuteron [22]. In $p + p$, this trigger measures 23.0 mb $\pm 9.7\%$ of the $p + p$ inelastic cross section. The measured particle yields are corrected for the $p + p$ MB trigger bias [23]: the MB trigger measures only $(79 \pm 2)\%$ of high-p_T particles. In $d + \mathrm{Au}$ collisions, this fraction varies from 85% to 100% from peripheral to central collisions; here the uncertainty is $\sim 3\%$. The second data sample was collected with a high-p_T photon trigger in the EMCal in addition to the MB trigger requirement in order to extend the measurement to higher p_T. This trigger requires a photon of $p_T > 1.4(1.4)$ GeV and $p_T > 2.5(3.5)$ GeV for PbSc (PbGl) and for $p + p$ and $d + \mathrm{Au}$ collisions, respectively. We analyzed 45.1×10^6 (19.5×10^6) events in $p + p$ $(d + \mathrm{Au})$ under this trigger condition. The sampled integrated luminosity was 216 nb^{-1} for $p + p$ and 1.5 nb^{-1} for $d + \mathrm{Au}$. (In $d + \mathrm{Au}$, that corresponds to an integrated nucleon-nucleon luminosity of 590 nb^{-1}).

The division of $d + \mathrm{Au}$ collisions in different centrality classes is based on the charge deposited in the backward BBC ($-3.9 < \eta < -3.0$), i.e., in the Au beam direction. For each centrality class, the corresponding average nuclear overlap function $\langle T_{AB} \rangle$ (compare Eq. (1)) is calculated using a Glauber Monte Carlo model and simulations of the BBC, taking into account its limited efficiency for peripheral collisions. For the four centrality classes (0–20%, 20–40%, 40–60%, and 60–88%) used in this analysis, the $\langle T_{AB} \rangle$ values are (0.365 ± 0.024), (0.252 ± 0.017), (0.165 ± 0.014), and (0.073 ± 0.007) mb^{-1}. The corresponding number of collisions can be calculated as $\langle N_{\mathrm{coll}} \rangle = \sigma_{\mathrm{inel}}^{pp} \times \langle T_{AB} \rangle$ with $\sigma_{\mathrm{inel}}^{\mathrm{pp}} = 42.2$ mb.

Photon candidates in the EMCal are selected by applying particle identification (PID) cuts based on the shower profile in the detector. To determine the yields of π^0 and η, the invariant mass of all photon pairs with an energy asymmetry $|E_1 - E_2|/(E_1 + E_2) < 0.7$ in a given p_T bin is calculated. After subtraction of the combinatorial background, the invariant mass distribution is integrated around the particle mass peak [13]; the integration window reflects thereby the p_T dependence of the mass peak position and width. The combinatorial background is determined by pairing photons from different events with similar centrality (for $d + \mathrm{Au}$) and vertex. In this analysis, the signal-to-background ratio for high-p_T π^0 is about 25 and 13 at $p_T = 4$ GeV/c in $p + p$ and central $d + \mathrm{Au}$ collisions, respectively. It decreases to 7 and 2 at $p_T = 2$ GeV/c. For η, this ratio is about 2 at $p_T = 8$ GeV/c, decreasing to 0.3 $(p + p)$ and 0.2 (central $d + \mathrm{Au}$) at $p_T = 3$ GeV/c. The raw spectra are corrected for trigger efficiency, acceptance, and reconstruction efficiency. This includes dead areas, the influence of energy resolution, analysis cuts, the peak extraction window, and photon conversion. The corrections are determined using Monte Carlo simulations. Because of the fine granularity of the calorimeter, occupancy effects are negligible. Furthermore, the π^0 spectra are corrected at $p_T > 10$ GeV/c (15 GeV/c) for two-photon merging effects in the PbSc (PbGl), studied in Monte Carlo simulations and confirmed with test beam data [24]. Finally, a correction in the π^0 and η yields to account for the true mean value of each p_T bin is applied to the steeply falling spectra. For $p_T < 3.5(3.0)$ GeV/c, the $p + p$ π^0 (η) spectrum is calculated from the minimum bias data sample; above this threshold, the high-p_T triggered sample is used. In $d + \mathrm{Au}$, this transition is made at $p_T = 4.5$ and 3.5 GeV/c for π^0 and η, respectively.

The main contributions to the systematic uncertainty on the $p + p$ and $d + \mathrm{Au}$ spectra are given in Table I for π^0 and η. Most uncertainties are identical for $p + p$ and $d + \mathrm{Au}$; only the uncertainty on the peak extraction is slightly larger in $d + \mathrm{Au}$. Category (d) includes uncertainties on the EMCal global energy scale and nonlinearity. The uncertainties in (d) and (e) are partially correlated. All others are uncorrelated and added in quadrature to get the total uncertainty.

The fully corrected p_T distributions of π^0 and η are shown in Fig. 1. The top panels show the invariant yield in $d + \mathrm{Au}$ collisions for four centrality bins scaled for clarity by the factors indicated. The bottom panels show the

TABLE I. Main systematic uncertainties in % on π^0 and η spectra. The uncertainties are given for PbSc (PbGl). The normalization uncertainties of 9.7% for the $p + p$ and 5.2% for the $d + \mathrm{Au}$ cross section as well as the MB-trigger-bias uncertainty of $\sim 3\%$ for the centrality-selected yields are not listed.

meson [p_T (GeV/c)]	π^0 [2]	π^0 [15]	η [3]	η [10]
(a) peak extraction	2.7(2.7)	2.0(2.0)	14(14)	6.0(6.0)
(b) geom. accept.	3.5(3.5)	3.5(3.5)	4.5(4.5)	4.5(4.5)
(c) π^0 reconstr. eff.	0.7(0.7)	4.0(4.0)	0.7(0.7)	3.6(3.6)
(d) energy scale	5.0(5.0)	11.4(11.4)	5.0(5.0)	9.4(9.4)
(e) merging corr.	...	5.9(2.1)	...	...
Total	6.7(6.7)	17.0(12.9)	15.5(15.5)	12.6(12.6)

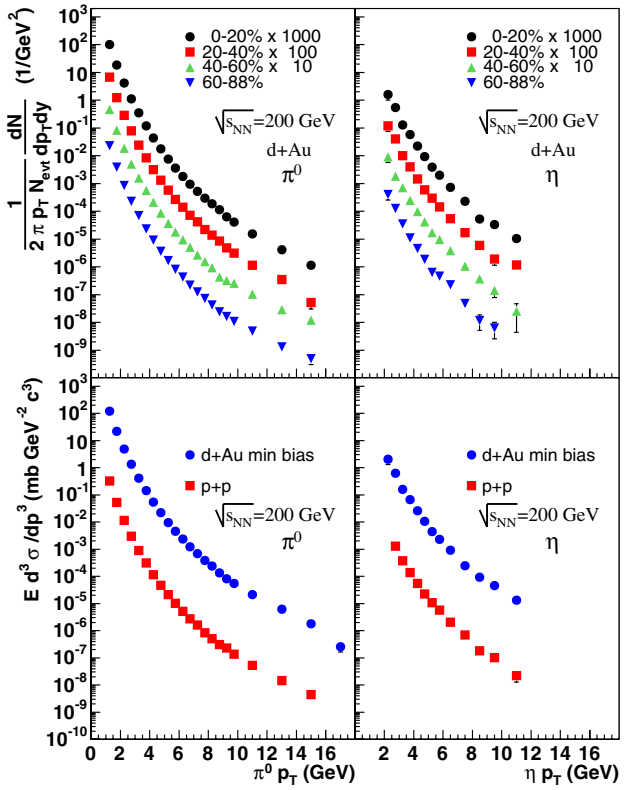

FIG. 1 (color online). Top: invariant yields at midrapidity for π^0 (left) and η (right) in $d + \mathrm{Au}$ collisions as a function of p_T for different selections of the centrality of the collision. Bottom: invariant cross section at midrapidity for π^0 (left) and η (right) in $p + p$ and $d + \mathrm{Au}$ collisions as a function of p_T.

invariant cross section in $p + p$ and $d + \mathrm{Au}$ collisions. The improved data set allows the study of π^0 (η) production up to 18(12) GeV/c, the highest p_T values measured for identified particles in $p + A$ ($d + A$) collisions. For the first time, the invariant cross section for π^0 and η in $d + \mathrm{Au}$ collisions has been measured at this energy. The π^0 result in $p + p$ agrees with the previous measurement at $\sqrt{s_{NN}} = 200$ GeV [23] within statistical uncertainties, and confirms the agreement with pQCD within the uncertainty of the calculation. Therefore, the $p + p$ cross section can be used as a well-understood reference for the production in $d + A$ and Au + Au collisions.

To quantify nuclear medium effects at high p_T, it is customary to use the *nuclear modification factor* which is given by the ratio of the invariant $d + \mathrm{Au}$ yield to the invariant $p + p$ cross section [13] scaled by $\langle T_{AB} \rangle$:

$$R_{AB}(p_T) = \frac{d^2 N_{AB}^{\pi^0}/dy dp_T}{\langle T_{AB} \rangle d^2 \sigma_{pp}^{\pi^0}/dy dp_T}. \quad (1)$$

The average nuclear overlap function $\langle T_{AB} \rangle$, averaged over the respective impact parameter range, is determined solely by the density distribution of the nucleons in the nuclei A and B and the impact parameter.

Figure 2 shows the nuclear modification factor $R_{dA}(p_T)$ for π^0 and η in $d + \mathrm{Au}$ collisions at $\sqrt{s_{NN}} = 200$ GeV for four different centrality selections and for minimum bias events. As the $p + p$ and $d + \mathrm{Au}$ measurements are both made in the same year, many of the systematic errors associated with detector performance are nearly identical, and the corresponding systematic errors in the comparison are negligible. Within systematic errors, $R_{dA}(p_T)$ for π^0 and η is ≈ 1 in all centrality bins, and only a weak p_T dependence can be seen. In order to check the absolute normalization systematics, we can also calculate $R_{dA}(p_T)$ using the inelastic cross section measured through photodissociation of the deuteron. This constitutes an important cross check. It replaces the systematic uncertainties of the BBC efficiency and $\langle T_{AB} \rangle$, which are determined by model calculations, by the uncertainty of the cross section measurement of similar size. The resulting $R_{dA}(p_T)$ is 9.8% larger than that obtained from the minimum bias yield, consistent within 1.5 σ.

Though very different in mass, η and π^0 show a similar, weak centrality dependence of $R_{dA}(p_T)$ over the measured p_T range. These results do not show the significant enhancement seen for protons where the proton R_{AA} is substantially larger than that of pions in the intermediate p_T (2 GeV/$c < p_T <$ 4 GeV/c) region [17]. The π^0 data exhibit small shape variations with centrality that may be due to initial-state effects including shadowing and multiple scattering. Possible Cronin enhancements in the intermediate p_T region due to initial-state multiple scattering or antishadowing are not more than 10% around 4 GeV/c. At low p_T ($p_T < 3$ GeV/c), the drop towards smaller R_{dA} is consistent with analogous measurements for charged pions [17] and is usually attributed to a change to a regime of soft physics (N_{part} scaling) at the smallest p_T values. At the largest p_T values measured ($p_T > 9$ GeV/c), the most central π^0 result hints at a small suppression, though this is only a ~1.7 sigma effect.

In conclusion, we have presented the first study of the centrality dependence of π^0 and η production at midrapidity in $d + \mathrm{Au}$ collisions at $\sqrt{s_{NN}} = 200$ GeV. Transverse momentum spectra up to $p_T = 18$ and 12 GeV/c have been measured for π^0 and η, respectively. The invariant yield per nucleon-nucleon collision is compared to that in $p + p$ collisions measured at the same $\sqrt{s_{NN}}$. The strong suppression observed for π^0 production at high p_T in central Au-Au collisions is not seen for $d + \mathrm{Au}$ in any centrality: Within systematic errors, $R_{dA}(p_T)$ is ≈ 1 in all centrality bins. A weak centrality dependence of the shape of R_{dA} versus p_T is seen, presumably due to initial-state effects. A possible Cronin enhancement is substantially smaller than the $R_{dA} \gtrsim 1.9$ that corresponds to results from lower energy measurements [7,25]. Within systematic errors, R_{dA} for π^0 and η agree well, giving no indication for cold nuclear matter effects having a mass dependence. Since nuclear modifications in $d + \mathrm{Au}$ are

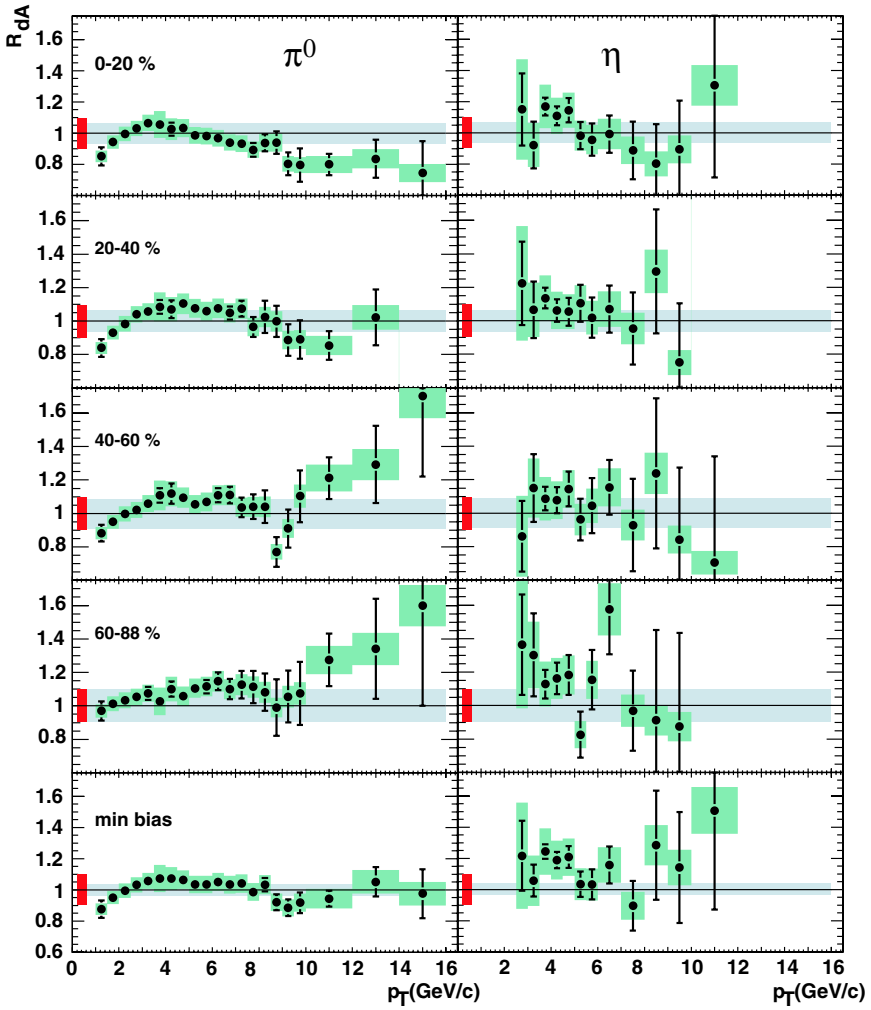

FIG. 2 (color online). Nuclear modification factor R_{dA} for π^0 and η in different centrality selections and min. bias data at midrapidity. The bands around the data points show systematic errors which can vary with p_T. The shaded bands around unity indicate the $\langle T_{AB} \rangle$ uncertainty, and the small bands on the left side of the data points indicate the normalization uncertainty due to the $p + p$ reference.

small even in the most central collisions where initial-state effects are expected to be largest, we conclude that initial-state effects in Au + Au must be small as well, and therefore the large suppression seen in Au + Au must be mostly due to medium effects.

We thank the staff of the Collider-Accelerator and Physics Departments at BNL for their vital contributions. We acknowledge support from the Department of Energy and NSF (U.S.A.), MEXT and JSPS (Japan), CNPq and FAPESP (Brazil), NSFC (China), IN2P3/CNRS, CEA, and ARMINES (France), BMBF, DAAD, and AvH (Germany), OTKA (Hungary), DAE and DST (India), ISF (Israel), KRF and KOSEF (Korea), RMIST, RAS, and RMAE (Russia), VR and KAW (Sweden), U.S. CRDF for the FSU, US-Hungarian NSF-OTKA-MTA, and US-Israel BSF.

*Deceased
†PHENIX Spokesperson: zajc@nevis.columbia.edu

[1] J. W. Harris and B. Müller, Annu. Rev. Nucl. Part. Sci. **46**, 71 (1996).
[2] K. Adcox *et al.* (PHENIX), Nucl. Phys. A **757**, 184 (2005).
[3] K. Adcox *et al.* (PHENIX), Phys. Rev. Lett. **88**, 022301 (2001).
[4] J. D. Bjorken, Fermilab, Report No. FERMILAB-PUB-82-059-THY, 1982.
[5] R. Baier, D. Schiff, and B. G. Zakharov, Ann. Rev. Nucl. Part. Sci. **50**, 37 (2000).
[6] S. S. Adler *et al.* (PHENIX), Phys. Rev. Lett. **91**, 072303 (2003).
[7] J. W. Cronin *et al.*, Phys. Rev. D **11**, 3105 (1975).
[8] I. Vitev, Phys. Lett. B **562**, 36 (2003).
[9] A. Accardi and M. Gyulassy, Phys. Lett. B **586**, 244 (2004).
[10] M. Arneodo, Phys. Rep. **240**, 301 (1994).
[11] D. Kharzeev, E. Levin, and L. McLerran, Phys. Lett. B **561**, 93 (2003).
[12] D. Kharzeev, Y. V. Kovchegov, and K. Tuchin, Phys. Rev. D **68**, 094013 (2003).
[13] S. S. Adler *et al.* (PHENIX), Phys. Rev. Lett. **91**, 072301 (2003).

[14] S. S. Adler *et al.* (PHENIX), Phys. Rev. C **69**, 034910 (2004).
[15] J. Adams *et al.* (STAR), Phys. Rev. Lett. **91**, 172302 (2003).
[16] S. S. Adler *et al.* (PHENIX), High p_T charged centrality dependence and h/π^0 ratio in d + Au collisions (to be published).
[17] S. S. Adler *et al.* (PHENIX), Phys. Rev. C **74**, 024904 (2006).
[18] S. S. Adler *et al.* (PHENIX), Phys. Rev. C **72**, 014903 (2005).
[19] R. C. Hwa and C. B. Yang, Phys. Rev. Lett. **93**, 082302 (2004).
[20] K. Adcox *et al.* (PHENIX), Nucl. Instrum. Methods Phys. Res., Sect. A **499**, 469 (2003).
[21] S. S. Adler (PHENIX), Phys. Rev. C **75**, 024909 (2007).
[22] S. N. White, AIP Conf. Proc. **792**, 527 (2005).
[23] S. S. Adler *et al.* (PHENIX), Phys. Rev. Lett. **91**, 241803 (2003).
[24] G. David *et al.*, IEEE Trans. Nucl. Sci. **47**, 1982 (2000).
[25] A. L. S. Angelis *et al.* (BCMOR), Phys. Lett. B **185**, 213 (1987).

Measurement of Direct Photon Production in $p + p$ Collisions at $\sqrt{s} = 200$ GeV

S. S. Adler,[5] S. Afanasiev,[20] C. Aidala,[10] N. N. Ajitanand,[44] Y. Akiba,[21,40] A. Al-Jamel,[35] J. Alexander,[44] K. Aoki,[25] L. Aphecetche,[46] R. Armendariz,[35] S. H. Aronson,[5] R. Averbeck,[45] T. C. Awes,[36] V. Babintsev,[17] A. Baldisseri,[11] K. N. Barish,[6] P. D. Barnes,[28] B. Bassalleck,[34] S. Bathe,[6,31] S. Batsouli,[10] V. Baublis,[39] F. Bauer,[6] A. Bazilevsky,[5,41] S. Belikov,[19,17] M. T. Bjorndal,[10] J. G. Boissevain,[28] H. Borel,[11] M. L. Brooks,[28] D. S. Brown,[35] N. Bruner,[34] D. Bucher,[31] H. Buesching,[5,31] V. Bumazhnov,[17] G. Bunce,[5,41] J. M. Burward-Hoy,[28,27] S. Butsyk,[45] X. Camard,[46] P. Chand,[4] W. C. Chang,[2] S. Chernichenko,[17] C. Y. Chi,[10] J. Chiba,[21] M. Chiu,[10] I. J. Choi,[53] R. K. Choudhury,[4] T. Chujo,[5] V. Cianciolo,[36] Y. Cobigo,[11] B. A. Cole,[10] M. P. Comets,[37] P. Constantin,[19] M. Csanád,[13] T. Csörgő,[22] J. P. Cussonneau,[46] D. d'Enterria,[10] K. Das,[14] G. David,[5] F. Deák,[13] H. Delagrange,[46] A. Denisov,[17] A. Deshpande,[41] E. J. Desmond,[5] A. Devismes,[45] O. Dietzsch,[42] J. L. Drachenberg,[1] O. Drapier,[26] A. Drees,[45] A. Durum,[17] D. Dutta,[4] V. Dzhordzhadze,[47] Y. V. Efremenko,[36] H. En'yo,[40,41] B. Espagnon,[37] S. Esumi,[49] D. E. Fields,[34,41] C. Finck,[46] F. Fleuret,[26] S. L. Fokin,[24] B. D. Fox,[41] Z. Fraenkel,[52] J. E. Frantz,[10] A. Franz,[5] A. D. Frawley,[14] Y. Fukao,[25,40,41] S.-Y. Fung,[6] S. Gadrat,[29] M. Germain,[46] A. Glenn,[47] M. Gonin,[26] J. Gosset,[11] Y. Goto,[40,41] R. Granier de Cassagnac,[26] N. Grau,[19] S. V. Greene,[50] M. Grosse Perdekamp,[18,41] H.-Å. Gustafsson,[30] T. Hachiya,[16] J. S. Haggerty,[5] H. Hamagaki,[8] A. G. Hansen,[28] E. P. Hartouni,[27] M. Harvey,[5] K. Hasuko,[40] R. Hayano,[8] X. He,[15] M. Heffner,[27] T. K. Hemmick,[45] J. M. Heuser,[40] P. Hidas,[22] H. Hiejima,[18] J. C. Hill,[19] R. Hobbs,[34] W. Holzmann,[44] K. Homma,[16] B. Hong,[23] A. Hoover,[35] T. Horaguchi,[40,41,48] T. Ichihara,[40,41] V. V. Ikonnikov,[24] K. Imai,[25,40] M. Inaba,[49] M. Inuzuka,[8] D. Isenhower,[1] L. Isenhower,[1] M. Ishihara,[40] M. Issah,[44] A. Isupov,[20] B. V. Jacak,[45] J. Jia,[45] O. Jinnouchi,[40,41] B. M. Johnson,[5] S. C. Johnson,[27] K. S. Joo,[32] D. Jouan,[37] F. Kajihara,[8] S. Kametani,[8,51] N. Kamihara,[40,48] M. Kaneta,[41] J. H. Kang,[53] K. Katou,[51] T. Kawabata,[8] A. V. Kazantsev,[24] S. Kelly,[9,10] B. Khachaturov,[52] A. Khanzadeev,[39] J. Kikuchi,[51] D. J. Kim,[53] E. Kim,[43] G.-B. Kim,[26] H. J. Kim,[53] E. Kinney,[9] A. Kiss,[13] E. Kistenev,[5] A. Kiyomichi,[40] C. Klein-Boesing,[31] H. Kobayashi,[41] L. Kochenda,[39] V. Kochetkov,[17] R. Kohara,[16] B. Komkov,[39] M. Konno,[49] D. Kotchetkov,[6] A. Kozlov,[52] P. J. Kroon,[5] C. H. Kuberg,[1,*] G. J. Kunde,[28] K. Kurita,[40] M. J. Kweon,[23] Y. Kwon,[53] G. S. Kyle,[35] R. Lacey,[44] J. G. Lajoie,[19] Y. Le Bornec,[37] A. Lebedev,[19,24] S. Leckey,[45] D. M. Lee,[28] M. J. Leitch,[28] M. A. L. Leite,[42] X. H. Li,[6] H. Lim,[43] A. Litvinenko,[20] M. X. Liu,[28] C. F. Maguire,[50] Y. I. Makdisi,[5] A. Malakhov,[20] V. I. Manko,[24] Y. Mao,[38,40] G. Martinez,[46] H. Masui,[49] F. Matathias,[45] T. Matsumoto,[8,51] M. C. McCain,[1] P. L. McGaughey,[28] Y. Miake,[49] T. E. Miller,[50] A. Milov,[45] S. Mioduszewski,[5] G. C. Mishra,[15] J. T. Mitchell,[5] A. K. Mohanty,[4] D. P. Morrison,[5] J. M. Moss,[28] D. Mukhopadhyay,[52] M. Muniruzzaman,[6] S. Nagamiya,[21] J. L. Nagle,[9,10] T. Nakamura,[16] J. Newby,[47] A. S. Nyanin,[24] J. Nystrand,[30] E. O'Brien,[5] C. A. Ogilvie,[19] H. Ohnishi,[40] I. D. Ojha,[3,50] H. Okada,[25,40] K. Okada,[40,41] A. Oskarsson,[30] I. Otterlund,[30] K. Oyama,[8] K. Ozawa,[8] D. Pal,[52] A. P. T. Palounek,[28] V. Pantuev,[45] V. Papavassiliou,[35] J. Park,[43] W. J. Park,[23] S. F. Pate,[35] H. Pei,[19] V. Penev,[20] J.-C. Peng,[18] H. Pereira,[11] V. Peresedov,[20] A. Pierson,[34] C. Pinkenburg,[5] R. P. Pisani,[5] M. L. Purschke,[5] A. K. Purwar,[45] J. M. Qualls,[1] J. Rak,[19] I. Ravinovich,[52] K. F. Read,[36,47] M. Reuter,[45] K. Reygers,[31] V. Riabov,[39] Y. Riabov,[39] G. Roche,[29] A. Romana,[26,*] M. Rosati,[19] S. S. E. Rosendahl,[30] P. Rosnet,[29] V. L. Rykov,[40] S. S. Ryu,[53] N. Saito,[25,40,41] T. Sakaguchi,[8,51] S. Sakai,[49] V. Samsonov,[39] L. Sanfratello,[34] R. Santo,[31] H. D. Sato,[25,40] S. Sato,[5,49] S. Sawada,[21] Y. Schutz,[46] V. Semenov,[17] R. Seto,[6] T. K. Shea,[5] I. Shein,[17] T.-A. Shibata,[40,48] K. Shigaki,[16] M. Shimomura,[49] A. Sickles,[45] C. L. Silva,[42] D. Silvermyr,[28] K. S. Sim,[23] A. Soldatov,[17] R. A. Soltz,[27] W. E. Sondheim,[28] S. P. Sorensen,[47] I. V. Sourikova,[5] F. Staley,[11] P. W. Stankus,[36] E. Stenlund,[30] M. Stepanov,[35] A. Ster,[22] S. P. Stoll,[5] T. Sugitate,[16] J. P. Sullivan,[28] S. Takagi,[49] E. M. Takagui,[42] A. Taketani,[40,41] K. H. Tanaka,[21] Y. Tanaka,[33] K. Tanida,[40] M. J. Tannenbaum,[5] A. Taranenko,[44] P. Tarján,[12] T. L. Thomas,[34] M. Togawa,[25,40] J. Tojo,[40] H. Torii,[25,41] R. S. Towell,[1] V-N. Tram,[26] I. Tserruya,[52] Y. Tsuchimoto,[16] H. Tydesjö,[30] N. Tyurin,[17] T. J. Uam,[32] J. Velkovska,[5] M. Velkovsky,[45] V. Veszprémi,[12] A. A. Vinogradov,[24] M. A. Volkov,[24] E. Vznuzdaev,[39] X. R. Wang,[15] Y. Watanabe,[40,41] S. N. White,[5] N. Willis,[37] F. K. Wohn,[19] C. L. Woody,[5] W. Xie,[6] A. Yanovich,[17] S. Yokkaichi,[40,41] G. R. Young,[36] I. E. Yushmanov,[24] W. A. Zajc,[10,†] O. Zaudtke,[31] C. Zhang,[10] S. Zhou,[7] J. Zimányi,[22,*] L. Zolin,[20] X. Zong,[19] and H. W. vanHecke[28]

(PHENIX Collaboration)

[1]*Abilene Christian University, Abilene, Texas 79699, USA*
[2]*Institute of Physics, Academia Sinica, Taipei 11529, Taiwan*
[3]*Department of Physics, Banaras Hindu University, Varanasi 221005, India*

[4]Bhabha Atomic Research Centre, Bombay 400 085, India
[5]Brookhaven National Laboratory, Upton, New York 11973-5000, USA
[6]University of California—Riverside, Riverside, California 92521, USA
[7]China Institute of Atomic Energy (CIAE), Beijing, People's Republic of China
[8]Center for Nuclear Study, Graduate School of Science, University of Tokyo, 7-3-1 Hongo, Bunkyo, Tokyo 113-0033, Japan
[9]University of Colorado, Boulder, Colorado 80309, USA
[10]Columbia University, New York, New York 10027, USA,
and Nevis Laboratories, Irvington, New York 10533, USA
[11]Dapnia, CEA Saclay, F-91191, Gif-sur-Yvette, France
[12]Debrecen University, H-4010 Debrecen, Egyetem tér 1, Hungary
[13]ELTE, Eötvös Loránd University, H-1117 Budapest, Pázmány P. s. 1/A, Hungary
[14]Florida State University, Tallahassee, Florida 32306, USA
[15]Georgia State University, Atlanta, Georgia 30303, USA
[16]Hiroshima University, Kagamiyama, Higashi-Hiroshima 739-8526, Japan
[17]IHEP Protvino, State Research Center of Russian Federation, Institute for High Energy Physics, Protvino 142281, Russia
[18]University of Illinois at Urbana—Champaign, Urbana, Illinois 61801, USA
[19]Iowa State University, Ames, Iowa 50011, USA
[20]Joint Institute for Nuclear Research, 141980 Dubna, Moscow Region, Russia
[21]KEK, High Energy Accelerator Research Organization, Tsukuba, Ibaraki 305-0801, Japan
[22]KFKI Research Institute for Particle and Nuclear Physics of the Hungarian Academy of Sciences (MTA KFKI RMKI), H-1525 Budapest 114, P.O. Box 49, Budapest, Hungary
[23]Korea University, Seoul 136-701, Korea
[24]Russian Research Center "Kurchatov Institute," Moscow, Russia
[25]Kyoto University, Kyoto 606-8502, Japan
[26]Laboratoire Leprince-Ringuet, Ecole Polytechnique, CNRS-IN2P3, Route de Saclay, F-91128 Palaiseau, France
[27]Lawrence Livermore National Laboratory, Livermore, California 94550, USA
[28]Los Alamos National Laboratory, Los Alamos, New Mexico 87545, USA
[29]LPC, Université Blaise Pascal, CNRS-IN2P3, Clermont-Fd, 63177 Aubiere Cedex, France
[30]Department of Physics, Lund University, Box 118, SE-221 00 Lund, Sweden
[31]Institut für Kernphysik, University of Muenster, D-48149 Muenster, Germany
[32]Myongji University, Yongin, Kyonggido 449-728, Korea
[33]Nagasaki Institute of Applied Science, Nagasaki-shi, Nagasaki 851-0193, Japan
[34]University of New Mexico, Albuquerque, New Mexico 87131, USA
[35]New Mexico State University, Las Cruces, New Mexico 88003, USA
[36]Oak Ridge National Laboratory, Oak Ridge, Tennessee 37831, USA
[37]IPN-Orsay, Universite Paris Sud, CNRS-IN2P3, BP1, F-91406 Orsay, France
[38]Peking University, Beijing, People's Republic of China
[39]PNPI, Petersburg Nuclear Physics Institute, Gatchina, Leningrad Region 188300, Russia
[40]RIKEN (The Institute of Physical and Chemical Research), Wako, Saitama 351-0198, Japan
[41]RIKEN BNL Research Center, Brookhaven National Laboratory, Upton, New York 11973-5000, USA
[42]Instituto de Física, Universidade de São Paulo, Caixa Postal 66318, São Paulo CEP05315-970, Brazil
[43]System Electronics Laboratory, Seoul National University, Seoul, Korea
[44]Chemistry Department, Stony Brook University, Stony Brook, SUNY, New York 11794-3400, USA
[45]Department of Physics and Astronomy, Stony Brook University, SUNY, Stony Brook, New York 11794, USA
[46]SUBATECH (Ecole des Mines de Nantes, CNRS-IN2P3, Université de Nantes), BP 20722-44307, Nantes, France
[47]University of Tennessee, Knoxville, Tennessee 37996, USA
[48]Department of Physics, Tokyo Institute of Technology, Oh-okayama, Meguro, Tokyo 152-8551, Japan
[49]Institute of Physics, University of Tsukuba, Tsukuba, Ibaraki 305, Japan
[50]Vanderbilt University, Nashville, Tennessee 37235, USA
[51]Advanced Research Institute for Science and Engineering, Waseda University, 17 Kikui-cho, Shinjuku-ku, Tokyo 162-0044, Japan
[52]Weizmann Institute, Rehovot 76100, Israel
[53]Yonsei University, IPAP, Seoul 120-749, Korea

(Received 18 September 2006; published 5 January 2007)

Cross sections for midrapidity production of direct photons in $p + p$ collisions at the Relativistic Heavy Ion Collider (RHIC) are reported for transverse momenta of $3 < p_T < 16$ GeV/c. Next-to-leading order perturbative QCD (pQCD) describes the data well for $p_T > 5$ GeV/c, where the uncertainties of the measurement and theory are comparable. We also report on the effect of requiring the photons to be isolated from parton jet energy. The observed fraction of isolated photons is well described by pQCD for $p_T > 7$ GeV/c.

DOI: 10.1103/PhysRevLett.98.012002 PACS numbers: 13.85.Qk, 25.75.Dw

The production of direct photons, i.e., photons not from hadronic decays, in hadron-hadron collisions has been recognized as providing direct access to the gluon distributions in the hadron, both unpolarized and polarized [1,2]. The process of direct-photon production is described, at high energy and high momentum transfer, by perturbative quantum chromodynamics (pQCD). Three parton-parton subprocesses dominate at lowest order: Compton scattering $g + q \rightarrow \gamma + q$, annihilation $q + \bar{q} \rightarrow \gamma + g$, and parton-parton hard scattering with the scattered quark or gluon fragmenting to a photon, where g (q) represent gluon (quark) states. At next-to-leading order (NLO), bremsstrahlung emission of photons from the quarks undergoing hard scattering also contributes to the direct-photon signal. The annihilation process is suppressed for $p + p$ collisions, due to the lower probability density of $\bar{q}$ vs g in the proton. In general, the fragmentation and bremsstrahlung processes will produce photons in the vicinity of parton jets. Therefore, a requirement that the photon be isolated from parton jet activity can emphasize the Compton graph. Here, only the gluon distribution is unknown, particularly for the polarized case, and direct-photon production therefore provides direct access to this (polarized) gluon distribution.

Comparisons of data to theory test our understanding of direct-photon production in hadron-hadron collisions. Previous experiments have shown significant disagreement between data and theory at fixed target energy, $\sqrt{s} <$ 40 GeV, and good agreement at collider energy, $\sqrt{s} >$ 60 GeV [3,4]. Results from the Relativistic Heavy Ion Collider (RHIC) for $p + p$ collisions cover intermediate energy and momentum transfer, overlapping CERN Intersecting Storage Rings, and Super anti-Proton Proton Synchrotron collider kinematics, and address the robustness of the pQCD prediction for direct-photon production. In addition, the comparison of the direct-photon rate using no isolation requirement, to the rate of observed photons that are isolated from parton jets, tests our understanding of the processes of parton fragmentation to photons and of the bremsstrahlung emission of photons from quarks in hard scattering.

Furthermore, direct-photon production in $p + p$ collisions provides a valuable baseline for the interpretation of direct-photon data from heavy ion ($A + A$) collisions. Jet-quenching models attribute the strong suppression of high-p_T hadrons in central $A + A$ collisions to energy loss of scattered quarks and gluons in the hot and dense medium created in these collisions [5]. Since photons interact with the medium only electromagnetically, they provide a monitor of the initial parton flux and therefore test a crucial assumption of these models.

In this Letter, we present cross sections for direct-photon production in $p + p$ collisions at $\sqrt{s} = 200$ GeV, from the 2003 run of RHIC, at midrapidity for $3 < p_T < 16$ GeV/c. An earlier measurement [6] from the 2002 run of RHIC covered a much smaller region of p_T. Unpolarized cross sections are reported, obtained by averaging over the spin states of the beams, with $<1\%$ residual polarization.

The data were collected by the PHENIX detector [7]. The primary detector for this measurement is an electromagnetic calorimeter (EMCal), consisting of two subsystems, a six sector lead-scintillator (PbSc), and a two sector lead glass (PbGl) detector, each located 5 m radially from the beam line. Each sector covers a range of $|\eta| < 0.35$ in pseudorapidity and 22.5° in azimuth. The EMCal has fine granularity. Each calorimeter tower covers $\Delta\eta \times \Delta\phi \sim 0.01 \times 0.01$, and a tower contains $\sim$80% of the photon energy hitting the center of the tower. Two photons from $\pi^0 \rightarrow \gamma\gamma$ decays are clearly resolved up to a π^0 p_T of 12 GeV/c, and a shower profile analysis extends the γ/π^0 discrimination to beyond 20 GeV/c. The energy calibration of each tower is obtained from minimum-ionizing tracks and from the reconstructed π^0 mass. The uncertainty on the energy scale is less than 1.5%.

Beam-beam counters (BBC) positioned at pseudorapidities $3.1 < |\eta| < 3.9$ provide a minimum bias (MB) trigger. Events with high p_T photons are selected by a level-1 trigger that requires a minimum energy deposit of 1.4 GeV in an overlapping tile of 4×4 towers of the EMCal in coincidence with the MB trigger. The MB trigger cross section is $\sigma_{\mathrm{BBC}} = (23.0 \pm 2.2)$ mb, about 50% of $\sigma^{pp}_{\mathrm{inel}}$. The efficiency bias due to the MB trigger in the 2003 run, $\epsilon_{\mathrm{bias}} = 0.79 \pm 0.02$, is determined from the ratio of the yield of high $p_T \pi^0$ with and without the MB trigger. An integrated luminosity ($\mathcal{L}$) of 240 nb^{-1} after a vertex cut of ± 30 cm is used in this analysis.

The first step in the analysis is to cluster the hit towers. If there are two tower energy maxima and at least one lower-energy tower between them, the cluster is split into two, with the energy of each tower divided between the two clusters according to electromagnetic shower profiles associated with the clusters. Photons are identified by a shower profile cut that was calibrated using test beam data, identified electrons, and decay photons from identified π^0. The cut rejects $\sim$50% of hadrons depositing $E >$ 3 GeV in the EMCal and accepts $\sim$98% of real photons. The charged particle veto of the photon sample is based on tracks in drift chambers 2 m from the beam line, and hits in the pad chamber (PC3) immediately in front of the EMCal. Loss of photons from conversions in material before the EMCal is estimated using a GEANT [8] simulation and confirmed by the observed fraction of identified π^0 photons vetoed. The conversion correction is 3% for the drift chamber veto and $\sim$8% for the PC3 veto. Remaining nonphoton background, including converting neutral had-

rons and albedo from the magnet yokes, is also estimated from the GEANT simulation at ~1%.

The experimental challenge in direct-photon measurements is the large photon background from decays of hadrons, primarily from $\pi^0 \to \gamma\gamma$ (~ 80% of the decays) and $\eta \to \gamma\gamma$ (~15%). We use two techniques described below to subtract the decay background: a π^0-tagging method and a cocktail subtraction method.

In the π^0-tagging method, a candidate photon is tagged as a π^0 decay photon if it forms a pair with another photon in the mass range $105 < M_{\gamma\gamma} < 165$ MeV ($M_{\pi^0} \pm 3\sigma$), with $E_\gamma > 150$ MeV. A fiducial region for direct-photon candidates excludes 10 towers (0.1 rad) from the edges of the EMCal, while partner photons are accepted over the entire detector, to improve the probability of observing both decay photons from the π^0.

This method overestimates the yield of photons from π^0 decays, γ_{π^0}, due to combinatorial background. A p_T dependent correction (~10%) is estimated from a fit to the π^0 sidebands, with ±3% uncertainty. The yield of direct photons, $\gamma_{\rm dir}$, is obtained from the inclusive photon yield, $\gamma_{\rm incl}$, using the equation

$$\gamma_{\rm dir} = \gamma_{\rm incl} - (1 + \delta^{\gamma}_{h/\pi^0})(1 + R^{\rm miss}_{\pi^0})\gamma_{\pi^0}, \qquad (1)$$

where $R^{\rm miss}_{\pi^0}$ is the correction for missing photon partners to π^0; $(1 + R^{\rm miss}_{\pi^0})\gamma_{\pi^0}$ represents the total contribution of photons from π^0 decays in each p_T^γ bin, and $\delta^{\gamma}_{h/\pi^0}$ is the fraction of photons from hadrons other than π^0.

To estimate $R^{\rm miss}_{\pi^0}$, a Monte Carlo simulation is used that includes the acceptance, energy resolution, and our measured π^0 spectrum [9] as input. Figure 1 shows $R^{\rm miss}_{\pi^0}$ from the simulation. The largest uncertainty is from the calibration of the EMCal at low energy. $\delta^{\gamma}_{h/\pi^0}$ is estimated by a

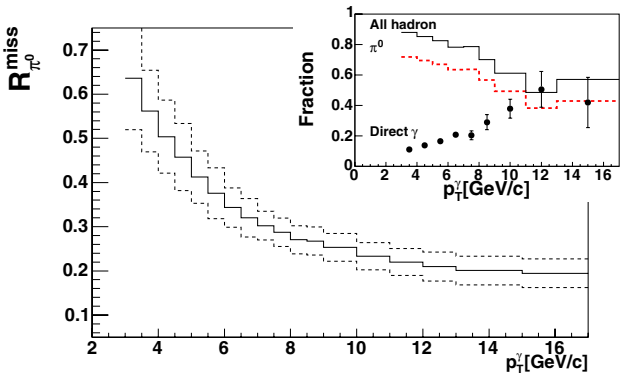

FIG. 1 (color online). Correction for missing photon partners to the π^0 ($R^{\rm miss}_{\pi^0}$) vs p_T^γ. Dashed lines show the systematic uncertainty. Inset: Different contributions to the inclusive photon spectrum. Solid (dashed) lines represent all hadronic (π^0) decay contributions. The data points show the remaining photon contributions.

simulation of hadron decays based on the η/π^0 [10] and ω/π^0 [11] ratios from our measurements: $\delta^{\gamma}_{h/\pi^0} \approx 0.24$, with $\delta^{\gamma}_{\eta/\pi^0} = 0.19$ and $\delta^{\gamma}_{\omega/\pi^0} = 0.05$. The contribution from other hadrons is less than 0.01. A small p_T dependence is assumed to follow m_T scaling [12]. The inset of Fig. 1 shows the fraction of photons from h, π^0, and $\gamma_{\rm dir}$ to $\gamma_{\rm incl}$. The direct-photon fraction ranges from 10% at low p_T^γ to 50% for $p_T^\gamma > 10$ GeV.

In the cocktail method [6,13], the spectrum of decay photons is simulated utilizing our measured π^0 spectrum and applying m_T scaling in order to account for other hadronic contributions. The effect of shower merging is also taken into account in the simulation. A double ratio $R_\gamma = (\gamma/\pi^0)^{\rm data}/(\gamma/\pi^0)^{\rm sim}$ is calculated for each p_T bin. $R_\gamma > 1$ indicates a direct-photon signal. The direct-photon yield is extracted as $\gamma_{\rm dir} = (1 - R_\gamma^{-1})\gamma_{\rm incl}$. Using the γ/π^0 ratio has the advantage that some systematic uncertainties cancel.

A summary of the systematic uncertainties is presented in Table I. Uncertainties of similar contributions are grouped together: global quantities (a), the inclusive photon yield (b), and the direct-photon background (c)–(e). The categories (a)–(d) apply to both analysis methods. Category (a) includes the uncertainties of the energy scale, luminosity, and geometrical acceptance. The main contribution to category (b) is the uncertainty of the nonphoton background estimation. The uncertainty of the charged particle veto is based on a study of the cluster vs track matching in the EMCal and the tracking detectors. The uncertainty in the neutral hadron contamination is estimated from identified charged hadrons. We assign the estimate of the albedo contribution as its uncertainty. Category (c) includes uncertainties of the correction for combinatorial background as estimated by different parametrizations of the background shape and the uncertainties of the π^0 reconstruction efficiency. Category (d) refers to the uncertainty of contributions from hadronic decays other than π^0's, derived from our measurement of the hadron production ratios. Finally, category (e) combines all remaining uncertainties separately for the two analysis

TABLE I. Relative systematic uncertainties of the direct-photon spectra.

p_T [GeV/c]	4.5–5	7.5–8	10–12
Signal fraction	9%	27%	49%
(a) Global	16.8%	14.9%	14.9%
(b) Inclusive photons	12.3%	4.7%	3.1%
(c) Photons from π^0	30.1%	10.7%	6.5%
(d) Other hadrons	21.4%	6.7%	3.8%
(e) Nonlinearity (+ remaining)			
(e_1) π^0 tagging	42.7%	6.8%	5.4%
(e_2) cocktail	69.5%	20.4%	13.4%
Total	71.6%	25.2%	19.8%

methods. Nonlinearity effects in the energy calibration affect the minimum energy cut in the π^0-tagging method (e_1) and distort the π^0 spectra in the cocktail method (e_2). After the individual calibration, a difference in the γ/π^0 ratio of PbGl and PbSc remains (5%–7%). This is used to assign a systematic uncertainty of the nonlinear part of the energy scale. Because of the small signal fraction at low p_T, this translates into the large relative uncertainty in the direct-photon spectra in Table I. In addition, the uncertainty of the shower profile analysis of the γ/π^0 discrimination at high p_T is included in this category. The two uncertainties (e_1, e_2) are combined by averaging the squared uncertainties, and then all uncertainties were added in quadrature.

The results from the π^0-tagging and cocktail method, obtained from independent analyses, agree within systematic uncertainties. We report an average of the results and uncertainties of the two methods giving equal weight to the two analysis methods.

The invariant cross section of direct-photon production is calculated by the following formula:

$$E\frac{d^3\sigma}{dp^3} = \frac{1}{\mathcal{L}}\frac{1}{2\pi p_T}\frac{\gamma_{\mathrm{dir}}}{\Delta p_T \Delta y}\frac{1}{\epsilon}\frac{1}{\epsilon_{\mathrm{bias}}}, \qquad (2)$$

where ϵ includes geometrical acceptance and the smearing effect from the energy resolution. The data points are plotted at the bin centers, with a correction to take into account the effect of finite bin sizes. The uncertainty of this correction is small compared to other systematic uncertainties.

Figure 2(a) shows the measured invariant cross section for midrapidity direct-photon production at $\sqrt{s} =$ 200 GeV. In addition, a NLO pQCD prediction [14–19], using CTEQ 6M parton distribution functions (PDF) [20] and the BFGII parton to photon fragmentation function (FF) [21], is shown with three theory scales (μ) as indicated. Figure 2(b) shows the fractional difference between the data and this calculation. The results are well described by pQCD.

The direct-photon sample includes photons from the Compton and annihilation subprocesses, which are expected to be isolated from parton jet activity. To measure the fraction of isolated photons, we apply an isolation requirement in the π^0-tagging method. Isolated photons are selected with less than 10% additional energy within a cone of radius $\Delta r = \sqrt{(\Delta\eta)^2 + (\Delta\phi)^2} = 0.5$ around the candidate photon direction. The cone energy is the sum of track momenta in the drift chamber and EMCal energy. In most cases the cone is larger than the PHENIX acceptance, and this is corrected for with a 0.08 increase in the photon isolation fraction in the theory predictions below [22].

Figure 3 presents the results of the isolation cut for photons from the π^0-tagging method. Solid circles show the fraction of isolated direct photons to all direct photons.

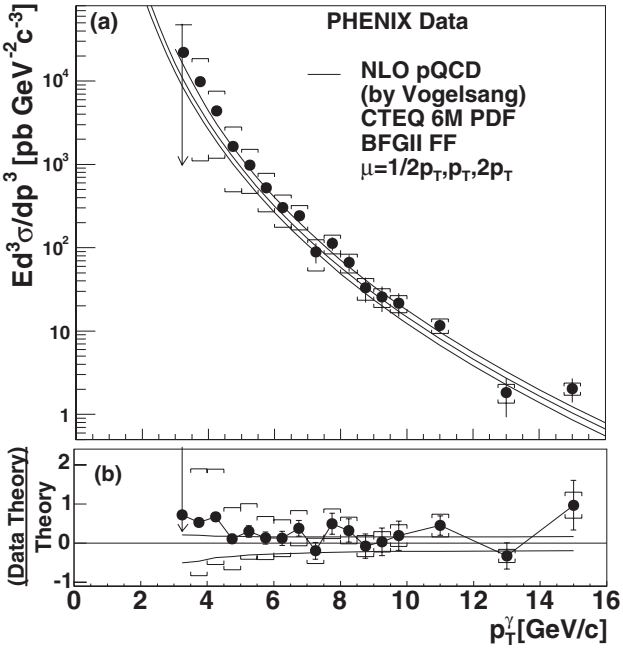

FIG. 2. (a) Direct-photon spectra with NLO pQCD calculations for three theory scales, μ. Brackets around data points show systematic errors. (b) Comparison to the NLO pQCD calculation for $\mu = p_T$, with upper and lower curves for $\mu = p_T/2$ and $2p_T$.

The curves are predictions from NLO pQCD, for the parton distribution and fragmentation functions as in Fig. 2, and for an additional parton to photon fragmentation function. The observed ratio is ~90% for $p_T^\gamma > 7$ GeV/c, and it is well described by pQCD. An additional loss of ~15%

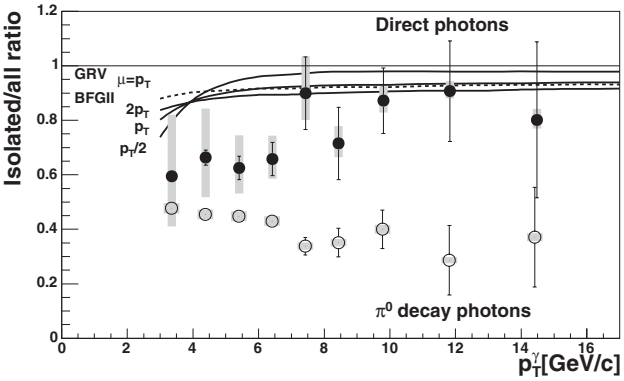

FIG. 3. Solid circles: Ratio of isolated direct photons to all direct photons from the π^0-tagging method. The statistical uncertainties are shown as black error bars and the systematic uncertainties are plotted as shaded bars. The solid and dashed curves are NLO pQCD calculations with three theory scales for BFGII [21] and one scale for GRV [25] parton to photon fragmentation functions. Open circles: Ratio of isolated photons from π^0 decays to all photons from π^0 decays.

($p_T^\gamma = 3$ GeV/c) to less than 5% (for $p_T^\gamma > 10$ GeV/c) due to the underlying event is estimated by a PYTHIA [23] simulation. Finally, for comparison, the open circles show the ratio of isolated photons from π^0 decays to all photons from π^0 decays. This indicates significantly less isolation than in the direct-photon sample.

In summary, invariant cross sections for direct-photon production at midrapidity have been measured up to $p_T = 16$ GeV/c in $\sqrt{s} = 200$ GeV $p + p$ collisions. The data are well described by NLO pQCD predictions for $p_T > 5$ GeV/c where the uncertainties of the measurement and theory are comparable. When these data are combined with fixed target and Tevatron collider data, these measurements demonstrate the robustness of the pQCD description of direct-photon production [24]. In addition, the ratio of isolated photons to all nonhadronic decay photons is well described by pQCD for $p_T > 7$ GeV/c.

Based on the comparison of high p_T direct-photon data from Au + Au collisions at RHIC with a $p + p$ reference from NLO pQCD, the origin of the observed suppression of high-p_T hadrons in central Au + Au collisions can be attributed to properties of the hot and dense matter created in the Au + Au collision [13]. The measurements presented here confirm this conclusion and put it on a firm experimental basis. Furthermore, the successful description of direct-photon production at RHIC is a necessary test for the extraction of the gluon polarization from direct-photon production in collisions of longitudinally polarized protons.

We thank the staff of the Collider-Accelerator and Physics Departments at BNL for their vital contributions. We thank Michel Fontannaz, Werner Vogelsang, and Monique Werlen for their interest and input. We acknowledge support from the Department of Energy and NSF (USA), MEXT and JSPS (Japan), CNPq and FAPESP (Brazil), NSFC (China), IN2P3/CNRS, CEA, and ARMINES (France), BMBF, DAAD, and AvH (Germany), OTKA (Hungary), DAE and DST (India), ISF (Israel), KRF and CHEP (Korea), RMIST, RAS, and RMAE (Russia), VR and KAW (Sweden), U.S. CRDF for the FSU, U.S.-Hungarian NSF-OTKA-MTA, and U.S.-Israel BSF.

*Deceased.
†PHENIX Spokesperson.
Electronic address: zajc@nevis.columbia.edu

[1] C. Papavasiliou, N. Mobed, and M. Svec, Phys. Rev. D **26**, 3284 (1982).
[2] E. L. Berger and J. Qiu, Phys. Rev. D **40**, 3128 (1989).
[3] W. Vogelsang and M. R. Whalley, J. Phys. G **23**, A1 (1997).
[4] P. Aurenche *et al.*, Eur. Phys. J. C **9**, 107 (1999).
[5] K. Adcox *et al.* (PHENIX Collaboration), Nucl. Phys. **A757**, 184 (2005).
[6] S. S. Adler *et al.* (PHENIX Collaboration), Phys. Rev. D **71**, 071102 (2005).
[7] K. Adcox *et al.* (PHENIX Collaboration), Nucl. Instrum. Methods Phys. Res., Sect. A **499**, 469 (2003).
[8] R. Brun *et al.*, GEANT 3.2.1, CERN Program Library Long Writeup (1994), http://wwwasdoc.web.cern.ch/wwwasdoc/pdfdir/geant.pdf.
[9] S. S. Adler *et al.* (PHENIX Collaboration), Phys. Rev. Lett. **91**, 241803 (2003).
[10] S. S. Adler *et al.* (PHENIX Collaboration), Phys. Rev. Lett. **96**, 202301 (2006).
[11] V. Ryabov *et al.* (PHENIX Collaboration), Nucl. Phys. **A774**, 735 (2006).
[12] K. Adcox *et al.* (PHENIX Collaboration), Phys. Rev. Lett. **88**, 192303 (2002).
[13] S. S. Adler *et al.* (PHENIX Collaboration), Phys. Rev. Lett. **94**, 232301 (2005).
[14] L. E. Gordon and W. Vogelsang, Phys. Rev. D **48**, 3136 (1993).
[15] L. E. Gordon and W. Vogelsang, Phys. Rev. D **50**, 1901 (1994).
[16] P. Aurenche *et al.*, Phys. Lett. **140B**, 87 (1984).
[17] P. Aurenche *et al.*, Nucl. Phys. **B297**, 661 (1988).
[18] H. Baer, J. Ohnemus, and J. F. Owens, Phys. Rev. D **42**, 61 (1990).
[19] H. Baer *et al.*, Phys. Lett. B **234**, 127 (1990).
[20] J. Pumplin *et al.*, J. High Energy Phys. 07 (2002) 012.
[21] L. Bourhis, M. Fontannaz, and J. P. Guillet, Eur. Phys. J. C **2**, 529 (1998).
[22] W. Vogelsang (private communication).
[23] T. Sjöstrand *et al.*, hep-ph/0308153 (Rick Field's tune A has been used).
[24] P. Aurenche, J. P. Guillet, E. Pilon, M. Werlen, and M. Fontannaz, Phys. Rev. D **73**, 094007 (2006).
[25] M. Gluck, E. Reya, and A. Vogt, Phys. Rev. D **48**, 116 (1993); **51**, 1427(E) (1995).

Detailed study of high-p_T neutral pion suppression and azimuthal anisotropy in Au+Au collisions at $\sqrt{s_{NN}} = 200$ GeV

S. S. Adler,[5] S. Afanasiev,[17] C. Aidala,[5] N. N. Ajitanand,[43] Y. Akiba,[20,38] J. Alexander,[43] R. Amirikas,[12] L. Aphecetche,[45] S. H. Aronson,[5] R. Averbeck,[44] T. C. Awes,[35] R. Azmoun,[44] V. Babinstev,[15] A. Baldisseri,[10] K. N. Barish,[6] P. D. Barnes,[27] B. Bassalleck,[33] S. Bathe,[30] S. Batsouli,[9] V. Baublis,[37] A. Bazilevsky,[39,15] S. Belikov,[16,15] Y. Berndnikov ,[40] S. Bhagavatula,[16] J. G. Boissevain,[27] H. Borel,[10] S. Borenstein,[25] M. L. Brooks,[27] D. S. Brown,[34] N. Bruner,[33] D. Bucher,[30] H. Buesching,[30] V. Bumazhnov,[15] G. Bunce,[5,39] J. M. Burward-Hoy,[26,44] S. Butsyk,[44] X. Camard,[45] J.-S. Chai,[18] P. Chand,[4] W. C. Chang,[2] S. Chernichenko,[15] C. Y. Chi,[9] J. Chiba,[20] M. Chiu,[9] I. J. Choi,[52] J. Choi,[19] R. K. Choudhury,[4] T. Chujo,[5] V. Cianciolo,[35] Y. Cobigo,[10] B. A. Cole,[9] P. Constantin,[16] D. d'Enterria,[45] G. David,[5] H. Delagrange,[45] A. Denisov,[15] A. Deshpande,[39] E. J. Desmond,[5] A. Devismes,[44] O. Dietzsch,[41] O. Drapier,[25] A. Drees,[44] K. A. Drees,[5] R. du Rietz,[29] A. Durum,[15] D. Dutta,[4] Y. V. Efremenko,[35] K. El Chenawi,[49] A. Enokizono,[14] H. En'yo,[38,39] S. Esumi,[48] L. Ewell,[5] D. E. Fields,[33,39] F. Fleuret,[25] S. L. Fokin,[23] B. D. Fox,[39] Z. Fraenkel,[51] J. E. Frantz,[9] A. Franz,[5] A. D. Frawley,[12] S.-Y. Fung,[6] S. Garpman,[29,*] T. K. Ghosh,[49] A. Glenn,[46] G. Gogiberidze,[46] M. Gonin,[25] J. Gosset,[10] Y. Goto,[39] R. Granier de Cassagnac,[25] N. Grau,[16] S. V. Greene,[49] M. Grosse Perdekamp,[39] W. Guryn,[5] H.-Å. Gustafsson,[29] T. Hachiya,[14] J. S. Haggerty,[5] H. Hamagaki,[8] A. G. Hansen,[27] E. P. Hartouni,[26] M. Harvey,[5] R. Hayano,[8] N. Hayashi,[38] X. He,[13] M. Heffner,[26] T. K. Hemmick,[44] J. M. Heuser,[44] M. Hibino,[50] J. C. Hill,[16] W. Holzmann,[43] K. Homma,[14] B. Hong,[22] A. Hoover,[34] T. Ichihara,[38,39] V. V. Ikonnikov,[23] K. Imai,[24,38] D. Isenhower,[1] M. Ishihara,[38] M. Issah,[43] A. Isupov,[17] B. V. Jacak,[44] W. Y. Jang,[22] Y. Jeong,[19] J. Jia,[44] O. Jinnouchi,[38] B. M. Johnson,[5] S. C. Johnson,[26] K. S. Joo,[31] D. Jouan,[36] S. Kametani,[8,50] N. Kamihara,[47,38] J. H. Kang,[52] S. S. Kapoor,[4] K. Katou,[50] S. Kelly,[9] B. Khachaturov,[51] A. Khanzadeev,[37] J. Kikuchi,[50] D. H. Kim,[31] D. J. Kim,[52] D. W. Kim,[19] E. Kim,[42] G.-B. Kim,[25] H. J. Kim,[52] E. Kistenev,[5] A. Kiyomichi,[48] K. Kiyoyama,[32] C. Klein-Boesing,[30] H. Kobayashi,[38,39] L. Kochenda,[37] V. Kochetkov,[15] D. Koehler,[33] T. Kohama,[14] M. Kopytine,[44] D. Kotchetkov,[6] A. Kozlov,[51] P. J. Kroon,[5] C. H. Kuberg,[1,27,*] K. Kurita,[39] Y. Kuroki,[48] M. J. Kweon,[22] Y. Kwon,[52] G. S. Kyle,[34] R. Lacey,[43] V. Ladygin,[17] J. G. Lajoie,[16] A. Lebedev,[16,23] S. Leckey,[44] D. M. Lee,[27] S. Lee,[19] M. J. Leitch,[27] X. H. Li,[6] H. Lim,[42] A. Litvinenko,[17] M. X. Liu,[27] Y. Liu,[36] C. F. Maguire,[49] Y. I. Makdisi,[5] A. Malakhov,[17] V. I. Manko,[23] Y. Mao,[7,38] G. Martinez,[45] M. D. Marx,[44] H. Masui,[48] F. Matathias,[44] T. Matsumoto,[8,50] P. L. McGaughey,[27] E. Melnikov,[15] F. Messer,[44] Y. Miake,[48] J. Milan,[43] T. E. Miller,[49] A. Milov,[44,51] S. Mioduszewski,[5] R. E. Mischke,[27] G. C. Mishra,[13] J. T. Mitchell,[5] A. K. Mohanty,[4] D. P. Morrison,[5] J. M. Moss,[27] F. Mühlbacher,[44] D. Mukhopadhyay,[51] M. Muniruzzaman,[6] J. Murata,[38,39] S. Nagamiya,[20] J. L. Nagle,[9] T. Nakamura,[14] B. K. Nandi,[6] M. Nara,[48] J. Newby,[46] P. Nilsson,[29] A. S. Nyanin,[23] J. Nystrand,[29] E. O'Brien,[5] C. A. Ogilvie,[16] H. Ohnishi,[5,38] I. D. Ojha,[49,3] K. Okada,[38] M. Ono,[48] V. Onuchin,[15] A. Oskarsson,[29] I. Otterlund,[29] K. Oyama,[8] K. Ozawa,[8] D. Pal,[51] A. P. T. Palounek,[27] V. Pantuev,[44] V. Papavassiliou,[34] J. Park,[42] A. Parmar,[33] S. F. Pate,[34] T. Peitzmann,[30] J.-C. Peng,[27] V. Peresedov,[17] C. Pinkenburg,[5] R. P. Pisani,[5] F. Plasil,[35] M. L. Purschke,[5] A. K. Purwar,[44] J. Rak,[16] I. Ravinovich,[51] K. F. Read,[35,46] M. Reuter,[44] K. Reygers,[30] V. Riabov,[37,40] Y. Riabov,[37] G. Roche,[28] A. Romana,[25,*] M. Rosati,[16] P. Rosnet,[28] S. S. Ryu,[52] M. E. Sadler,[1] N. Saito,[38,39] T. Sakaguchi,[8,50] M. Sakai,[32] S. Sakai,[48] V. Samsonov,[37] L. Sanfratello,[33] R. Santo,[30] H. D. Sato,[24,38] S. Sato,[5,48] S. Sawada,[20] Y. Schutz,[45] V. Semenov,[15] R. Seto,[6] M. R. Shaw,[1,27] T. K. Shea,[5] T.-A. Shibata,[47,38] K. Shigaki,[14,20] T. Shiina,[27] C. L. Silva,[41] D. Silvermyr,[27,29] K. S. Sim,[22] C. P. Singh,[3] V. Singh,[3] M. Sivertz,[5] A. Soldatov,[15] R. A. Soltz,[26] W. E. Sondheim,[27] S. P. Sorensen,[46] I. V. Sourikova,[5] F. Staley,[10] P. W. Stankus,[35] E. Stenlund,[29] M. Stepanov,[34] A. Ster,[21] S. P. Stoll,[5] T. Sugitate,[14] J. P. Sullivan,[27] E. M. Takagui,[41] A. Taketani,[38,39] M. Tamai,[50] K. H. Tanaka,[20] Y. Tanaka,[32] K. Tanida,[38] M. J. Tannenbaum,[5] P. Tarján,[11] J. D. Tepe,[1,27] T. L. Thomas,[33] J. Tojo,[24,38] H. Torii,[24,38] R. S. Towell,[1] I. Tserruya,[51] H. Tsuruoka,[48] S. K. Tuli,[3] H. Tydesjö,[29] N. Tyurin,[15] H. W. van Hecke,[27] J. Velkovska,[5,44] M. Velkovsky,[44] V. Veszprémi,[11] L. Villatte,[46] A. A. Vinogradov,[23] M. A. Volkov,[23] E. Vznuzdaev,[37] X. R. Wang,[13] Y. Watanabe,[38,39] S. N. White,[5] F. K. Wohn,[16] C. L. Woody,[5] W. Xie,[6] Y. Yang,[7] A. Yanovich,[15] S. Yokkaichi,[38,39] G. R. Young,[35] I. E. Yushmanov,[23] W. A. Zajc,[9,†] C. Zhang,[9] S. Zhou,[7] S. J. Zhou,[51] and L. Zolin[17]

(PHENIX Collaboration)

[1]*Abilene Christian University, Abilene, Texas 79699, USA*

[2]*Institute of Physics, Academia Sinica, Taipei 11529, Taiwan*

[3]*Department of Physics, Banaras Hindu University, Varanasi 221005, India*

[4]*Bhabha Atomic Research Centre, Bombay 400 085, India*

[5]*Brookhaven National Laboratory, Upton, New York 11973-5000, USA*

[6]*University of California - Riverside, Riverside, California 92521, USA*

[7]*China Institute of Atomic Energy (CIAE), Beijing, People's Republic of China*

[8]*Center for Nuclear Study, Graduate School of Science, University of Tokyo, 7-3-1 Hongo, Bunkyo, Tokyo 113-0033, Japan*

[9]*Columbia University, New York, New York 10027 and Nevis Laboratories, Irvington, New York 10533, USA*

[10]*Dapnia, CEA Saclay, F-91191, Gif-sur-Yvette, France*

[11]*Debrecen University, H-4010 Debrecen, Egyetem tér 1, Hungary*

[12]*Florida State University, Tallahassee, Florida 32306, USA*

[13]*Georgia State University, Atlanta, Georgia 30303, USA*

[14]*Hiroshima University, Kagamiyama, Higashi-Hiroshima 739-8526, Japan*

[15]*Institute for High Energy Physics (IHEP), Protvino, Russia*
[16]*Iowa State University, Ames, Iowa 50011, USA*
[17]*Joint Institute for Nuclear Research, 141980 Dubna, Moscow Region, Russia*
[18]*KAERI, Cyclotron Application Laboratory, Seoul, South Korea*
[19]*Kangnung National University, Kangnung 210-702, South Korea*
[20]*KEK, High Energy Accelerator Research Organization, Tsukuba-shi, Ibaraki-ken 305-0801, Japan*
[21]*KFKI Research Institute for Particle and Nuclear Physics (RMKI), H-1525 Budapest 114, POBox 49, Hungary*
[22]*Korea University, Seoul, 136-701, Korea*
[23]*Russian Research Center "Kurchatov Institute," Moscow, Russia*
[24]*Kyoto University, Kyoto 606-8502, Japan*
[25]*Laboratoire Leprince-Ringuet, Ecole Polytechnique, CNRS-IN2P3, Route de Saclay, F-91128, Palaiseau, France*
[26]*Lawrence Livermore National Laboratory, Livermore, California 94550, USA*
[27]*Los Alamos National Laboratory, Los Alamos, New Mexico 87545, USA*
[28]*LPC, Université Blaise Pascal, CNRS-IN2P3, Clermont-Fd, 63177 Aubiere Cedex, France*
[29]*Department of Physics, Lund University, Box 118, SE-221 00 Lund, Sweden*
[30]*Institut für Kernphysik, University of Muenster, D-48149 Muenster, Germany*
[31]*Myongji University, Yongin, Kyonggido 449-728, Korea*
[32]*Nagasaki Institute of Applied Science, Nagasaki-shi, Nagasaki 851-0193, Japan*
[33]*University of New Mexico, Albuquerque, New Mexico 87131, USA*
[34]*New Mexico State University, Las Cruces, New Mexico 88003, USA*
[35]*Oak Ridge National Laboratory, Oak Ridge, Tennessee 37831, USA*
[36]*IPN-Orsay, Universite Paris Sud, CNRS-IN2P3, BP1, F-91406, Orsay, France*
[37]*PNPI, Petersburg Nuclear Physics Institute, Gatchina, Russia*
[38]*RIKEN (The Institute of Physical and Chemical Research), Wako, Saitama 351-0198, JAPAN*
[39]*RIKEN BNL Research Center, Brookhaven National Laboratory, Upton, New York 11973-5000, USA*
[40]*St. Petersburg State Technical University, St. Petersburg, Russia*
[41]*Universidade de São Paulo, Instituto de Física, Caixa Postal 66318, São Paulo CEP05315-970, Brazil*
[42]*System Electronics Laboratory, Seoul National University, Seoul, South Korea*
[43]*Chemistry Department, Stony Brook University, SUNY, Stony Brook, New York 11794-3400, USA*
[44]*Department of Physics and Astronomy, Stony Brook University, SUNY, Stony Brook, New York 11794, USA*
[45]*SUBATECH (Ecole des Mines de Nantes, CNRS-IN2P3, Université de Nantes) BP 20722 - 44307, Nantes, France*
[46]*University of Tennessee, Knoxville, Tennessee 37996, USA*
[47]*Department of Physics, Tokyo Institute of Technology, Tokyo, 152-8551, Japan*
[48]*Institute of Physics, University of Tsukuba, Tsukuba, Ibaraki 305, Japan*
[49]*Vanderbilt University, Nashville, Tennessee 37235, USA*
[50]*Waseda University, Advanced Research Institute for Science and Engineering, 17 Kikui-cho, Shinjuku-ku, Tokyo 162-0044, Japan*
[51]*Weizmann Institute, Rehovot 76100, Israel*
[52]*Yonsei University, IPAP, Seoul 120-749, Korea*
(Received 7 November 2006; published 25 September 2007)

Measurements of neutral pion (π^0) production at midrapidity in $\sqrt{s_{NN}} = 200$ GeV Au+Au collisions as a function of transverse momentum, p_T, collision centrality, and angle with respect to reaction plane are presented. The data represent the final π^0 results from the PHENIX experiment for the first RHIC Au+Au run at design center-of-mass energy. They include additional data obtained using the PHENIX Level-2 trigger with more than a factor of 3 increase in statistics over previously published results for $p_T > 6$ GeV/c. We evaluate the suppression in the yield of high-p_T π^0's relative to pointlike scaling expectations using the nuclear modification factor $R_{\rm AA}$. We present the p_T dependence of $R_{\rm AA}$ for nine bins in collision centrality. We separately integrate $R_{\rm AA}$ over larger p_T bins to show more precisely the centrality dependence of the high-p_T suppression. We then evaluate the dependence of the high-p_T suppression on the emission angle $\Delta\phi$ of the pions with respect to event reaction plane for seven bins in collision centrality. We show that the yields of high-p_T π^0's vary strongly with $\Delta\phi$, consistent with prior measurements [1,2]. We show that this variation persists in the most peripheral bin accessible in this analysis. For the peripheral bins we observe no suppression for neutral pions produced aligned with the reaction plane, whereas the yield of π^0's produced perpendicular to the reaction plane is suppressed by a factor of $\sim$2. We analyze the combined centrality and $\Delta\phi$ dependence of the π^0 suppression in different p_T bins using different possible descriptions of parton energy loss dependence on jet path-length averages to determine whether a single geometric picture can explain the observed suppression pattern.

DOI: 10.1103/PhysRevC.76.034904 PACS number(s): 25.75.Dw

I. INTRODUCTION

High transverse momentum particles resulting from hard scatterings between incident partons have become one of the most effective tools for probing the properties of the medium created in ultra-relativistic heavy ion collisions at RHIC. Data from the four RHIC experiments have unequivocally established the phenomenon of high transverse momentum hadron suppression in Au+Au compared to (appropriately scaled) $p+p$ collisions [3–9], whereas the lack of similar suppression in d+Au collisions [9–12] provides strong evidence that the suppression is not due to modification of parton distributions in the incident nuclei. This suppression has been observed for a large variety of hadron species, at highest p_T for π^0 and most recently η [13], supporting further the notion that energy loss occurs at the parton level. Conversely, direct photon measurements by the PHENIX collaboration show that the yield of hard photons in Au+Au collisions is consistent with $p+p$ expectations scaled by the number of incoherent nucleon-nucleon collisions [14] and, thus, provide final confirmation that hard scattering processes occur at rates expected from pointlike processes. This observation makes definitive the conclusion that the suppression of high-p_T hadron production in Au+Au collisions is a final-state effect. Measurements of azimuthal angle correlations between hadron pairs resulting from fragmentation of hard-scattered partons into jets have provided additional confirmation of final-state medium effects on these partons [15].

Predictions of high-p_T suppression were made before the start of RHIC operation [16,17] and confirmation of these predictions may be considered one of the key successes of the RHIC program so far. The suppression of high-p_T single hadrons was predicted to result from the energy loss of hard-scattered quarks and gluons in the hot and dense quantum chromodynamics (QCD) medium created in ultrarelativistic heavy-ion collisions (see Refs. [18,19] and references therein). In the canonical models, medium-induced gluon bremsstrahlung is expected to dominate the energy loss process [16], and calculations of the high-p_T suppression factor incorporating this effect have been able to successfully describe the experimental measurements [20–22]; however, recent measurements of heavy quark suppression pose some questions to this canonical view. Nonetheless, from comparisons of the energy loss calculations with the experimental data, estimates of the initial net color charge density that is usually expressed in terms of a gluon rapidity density, dN_g/dy, have been obtained yielding $dN_g/dy \approx 1000$ and, assuming thermalization, estimates of the initial energy density have produced values in excess of $10\,\mathrm{GeV/fm}^3$ [23,24].

However, in spite of this success, there are still a number of outstanding issues with the interpretation of the Au+Au high-p_T single-hadron suppression. Because the properties of the medium created in heavy-ion collisions are not *a priori* known, the energy-loss calculations necessarily use the observed suppression to infer initial parton densities, usually through an intermediate parameter that appears in the energy loss calculations. Although the initial parton density obtained by such "tomographic" studies has to be consistent with the final (measured) total particle multiplicity, it is fair to acknowledge that the p_T dependence of the suppression (rather than its absolute magnitude) is a more discriminating observable to test the various energy loss models. For π^0 spectra, the suppression in central Au+Au collisions at $\sqrt{s_{NN}} = 200$ GeV is found to be approximately constant with p_T over the range, $3 < p_T < 10$ GeV/c. Although the different energy loss calculations can reproduce this p_T-independent suppression, the detailed explanation of the constancy is different in each model. The effects invoked to explain the p_T dependence of the observed Au+Au high-p_T suppression include finite-energy effects, absorption of energy from the medium, evolution from incoherent (Bethe-Heitler) to coherent (Landau-Pomeranchuk-Migdal or LPM) radiation with increasing parton energy [25], the p_T-dependent mixture of quark and gluon contributions to the hard-scattered parton spectrum, the increasingly larger exponent of the underlying (power-law) parton p_T spectra [22], and shadowing/EMC effect [26]. Although most calculations of the high-p_T suppression in Au+Au collisions account for shadowing/EMC modifications of the nuclear parton distributions and for the relative mixture of quarks and gluons in the hard-scattered parton spectra, finite-energy corrections, absorption of energy from the medium, and the description of the energy loss process itself differs from calculation to calculation. Clearly the central Au+Au single-particle spectra are not sufficient, by themselves, to validate or exclude any of the different energy loss models; we must use more "differential" probes of medium-induced energy loss to better understand the phenomenon.

A robust prediction of non-Abelian parton energy loss calculations is that the average energy loss as a function of the in-medium path length L shows a quadratic dependence $\propto L^2$ [27]. Such a behavior predicted for a *static* QCD medium turns into an effective $\propto L$ dependence in an expanding quark-gluon plasma (QGP) [28]. In principle, the centrality dependence of the high-p_T suppression [5,6,8] provides an effective test of energy-loss calculations because the length of the path of the partons in the medium will change between peripheral and central collisions. However, the energy loss calculations also have to account for changes in the initial properties of the medium with centrality and the extra flexibility in the description of the initial conditions means that the measured centrality dependence of the high-p_T suppression also does not stringently constrain energy loss models [29]. However, the path length of the parton in the medium can also be controlled by selecting high-p_T hadrons in different bins of azimuthal angle difference from the event-by-event determined reaction plane. Indeed, shortly after experimental observations of azimuthal anisotropy were reported [1,15], arguments were made that the high-p_T anisotropy in noncentral collisions was due to the spatial asymmetry of the medium and the resulting $\Delta\phi$ dependence of parton path lengths [30,31]. However, recent analyses have argued that the large azimuthal anisotropies at high p_T cannot be accounted for by energy loss alone—at least when realistic nuclear geometry is used to

*Deceased.
†PHENIX Spokesperson: zajc@nevis.columbia.edu

describe the spatial asymmetry of the initial state [29,32,33]. Some of these analyses were based on a picture of the energy loss process in which quarks or gluons that have emitted radiation effectively disappear from the steeply falling high-p_T spectrum because they are overwhelmed by partons of lower energy that escape from the medium losing little or no energy. In this picture, the medium effectively attenuates the high-p_T quarks and gluons and the high-p_T spectrum is dominated by partons originating near the surface—i.e., partons originating in the "corona" [29,32,33]. Then, the azimuthal anisotropy could be largely determined by the shape of the surface [32]. However, it has been separately argued that fluctuations in the number of emitted gluons may be large and such fluctuations may weaken the corona effect [28].

In this article we present measurements of π^0 production in $\sqrt{s_{NN}} = 200$ GeV Au+Au collisions from the PHENIX experiment at RHIC. These data, obtained during Run-2 operation of RHIC in 2002, include additional data obtained with the PHENIX Level-2 trigger, which improved the total statistics by a factor of $\sim$3 compared to the prior analysis in Ref. [6]. The analyses presented here have also benefited from advanced electromagnetic calorimeter calibrations and from improved understanding of the systematic errors in the π^0 measurement in course of the direct photon analysis presented in Ref. [14], where the π^0 decay photons provide the main source of background. With the improved statistics, the p_T reach of the data is extended to higher p_T, allowing us to test whether the suppression starts to diminish above 10 GeV/c in p_T. In addition, we extend the measurement of the centrality dependence of the suppression up to 8 GeV/c.

We present measurements of the dependence of the π^0 yield as a function of the angle $\Delta\phi$ of the π^0 with respect to the event reaction plane. By measuring the high-p_T hadron suppression as a function of $\Delta\phi$, for a given centrality bin, we can keep the properties of the medium fixed and vary only the average geometry of the jet propagation in the medium. By comparing different centrality bins we can, in principle, test how the initial properties of the medium affect the induced energy loss. Traditionally, measurements of the $\Delta\phi$ dependence of hadron yields have been analyzed in terms of the azimuthal asymmetry parameter, v_2, and we note that the data presented here were used to obtain measurements of π^0 v_2 for comparison to inclusive photon v_2 [34]. However, in this publication we focus not on v_2, but explicitly on the suppression as a function of $\Delta\phi$, expressed in terms of the $\Delta\phi$-dependent nuclear modification factor $R_{\rm AA}(\Delta\phi)$. Although the data presented this way contain, in principle, the same information as the combination of $\Delta\phi$-averaged $R_{\rm AA}$ and v_2, $R_{\rm AA}(\Delta\phi)$ provides a useful alternative way to evaluate the dependence of high-p_T suppression on geometry because it effectively combines $R_{\rm AA}(p_T)$ and v_2 into a single set of data. We analyze the combined $\Delta\phi$ and centrality dependence of the high-p_T suppression in the context of different path-length and density dependencies of the parton energy loss process to evaluate whether any geometric picture can simultaneously describe the centrality and $\Delta\phi$ dependence of the observed high p_T deficit.

II. EXPERIMENTAL DETAILS

The data presented in this article were obtained during Run-2 operation of the PHENIX experiment [35] at the Relativistic Heavy Ion Collider facility at Brookhaven National Laboratory [36]. The primary detectors used to obtain the presented results were the PHENIX central arm spectrometers, particularly the electromagnetic calorimeters [37], and the two beam-beam counters (BBC's) [38]. In addition, the PHENIX zero-degree calorimeters [39] were used for triggering and centrality determination.

Two-photon decays of neutral pions were measured in the PHENIX electromagnetic calorimeter, located at a radial distance of $\sim$5.1 m from the beam-line, which has a pseudo-rapidity acceptance of $-0.35 < \eta < 0.35$ and covers π radians in azimuth. The electromagnetic calorimeter is divided into eight sectors, with each sector covering the full pseudo-rapidity range and $\pi/8$ in azimuth. The calorimeter consists of two distinct parts using different technologies. A lead-scintillator sandwich calorimeter (PbSc) with 5 cm $\times$ 5 cm towers covers 3/4 (6 sectors) of the central arm acceptance. A lead-glass Čerenkov calorimeter (PbGl) with 4 cm $\times$ 4 cm towers covers the remaining 1/4 (2 sectors) of the central arm acceptance. The corresponding $\Delta\eta \times \Delta\phi$ acceptance of a single tower at $\eta = 0$ is 0.011^2 and 0.0075^2 for the PbSc and PbGl calorimeters, respectively.

The event reaction plane in Au+Au collisions was measured in the two BBC's. Each BBC consists of 64 hexagonal, quartz Čerenkov radiators closely packed around the beam pipe, in an approximately azimuthally symmetric configuration. The beam-beam counters, located 144 cm in each direction from the nominal center of the interaction diamond, are used to count charged particles produced in the pseudorapidity range $3.0 < |\eta| < 3.9$. The distribution of particles over the individual channels of the BBC's allows measurement of the azimuthal distribution, $dN_{\rm ch}/d\phi$, of charged particles within this pseudorapidity acceptance. The BBC's also provide measurement of the collision vertex position along the interaction diamond with a resolution of 0.6 cm [38].

The data presented here were obtained using the PHENIX minimum-bias Level-1 trigger, based on the BBC's and the PHENIX zero-degree calorimeters, that selects $92.2^{+2.5}_{-3.0}$% of the total Au+Au hadronic interaction cross section of 6.9 b [6]. For a subset of the data, events selected by the Level-1 trigger were subjected to software Level-2 trigger filtering after full assembly of events in the PHENIX event builder [40]. A software algorithm performed a crude reconstruction of electromagnetic clusters by summing the pedestal-subtracted and gain-calibrated energies of "tiles" made of adjacent 4 $\times$ 4 calorimeter towers groups. The tiles are allowed to overlap such that every possible such tile that can be constructed in each calorimeter is tested. One of the Level-2 triggers (LVL2A) selected events in which at least one cluster (tile) had energy >3.5 GeV. Another Level-2 trigger (LVL2B) selected events in the 50–92% centrality range (50% most peripheral events) with at least one cluster having energy >1.5 GeV.

The measurements presented in this article were obtained from 31.4 M minimum bias triggers and approximately

1.7 M Level-2 trigger selected events. Of the Level-2 triggered events, 743 K events were selected by the higher energy LVL2A trigger and the remainder were selected by the peripheral, lower-energy LVL2B trigger. Taking into account their rejection factors, the two triggers sampled the equivalent of 44.4×10^6 LVL2A and 28.7×10^6 LVL2B minimum-bias triggers. The difference is due to different online trigger pre-scale factors. Thus, the combined event sample contains approximately a factor of 2.5–3 (considering both triggers over all centralities) more π^0's above 6 GeV/c than previously published Run-2 π^0 measurements [6].

III. DATA ANALYSIS

A. Event selection and centrality

In the offline analysis, the timing difference measured between the two PHENIX BBC's is used to determine the position of the collision vertex along the beam axis and to select events with vertex position within 30 cm of the nominal center of the detector for subsequent analysis. The energies measured in the zero-degree calorimeters and the charged-particle multiplicity measured in the BBC's are used to determine the collision centrality [41]. For the π^0 spectrum measurements presented here the total measured centrality range (0–92.2%) is subdivided into nine bins: 0–10, 10–20, 20–30, 30–40, 40–50, 60–70, 70–80, 80–92.2%. For the reaction plane-dependent analysis, the most central and two most peripheral bins are excluded, the peripheral due to their large uncertainty in the reaction plane resolution, and the 0–10% bin simply because of its smaller intrinsic eccentricity. Additionally, we present also combined 0–20%, 20–60%, and 60–92% data sets for comparison with other PHENIX analyses of high p_T hadron production that use such centralities.

B. Reaction plane measurement

PHENIX has previously published measurements of elliptic flow using an event-by-event measured reaction plane [34,42,43], and the same technique is used for the analysis presented here. Each BBC detector consists of 128 quartz radiators placed in hexagonal, roughly concentric rings whose light is individually collected by photomultiplier tubes (PMT's). The calibrated charge from each radiator is converted into an estimate for the number of charged particles within the acceptance of each detector, N_i, using the measured single-particle peak centroid.

For the reaction plane measurement the measured N_i values are corrected such that the weight of the inner rings that have the fewest radiators covering the full azimuthal angle range is reduced. Then, in terms of the corrected N_i values, N_i^{adj}, the angle of the reaction plane Ψ is obtained from the formula

$$\tan(2\Psi) = \frac{\sum_i N_i^{\mathrm{adj}} \sin(2\phi_i) - \left\langle \sum_i N_i^{\mathrm{adj}} \sin(2\phi_i) \right\rangle}{\sum_i N_i^{\mathrm{adj}} \cos(2\phi_i) - \left\langle \sum_i N_i^{\mathrm{adj}} \cos(2\phi_i) \right\rangle}, \quad (1)$$

where ϕ_i represents the azimuthal angle of the center of a given radiator i. The subtraction of the average centroid position in Eq. (1) removes the bias in the reaction plane measurement resulting from nonzero angle of the colliding beams, nonuniformities in detector acceptance, and other similar effects. The average is taken over many events localized in time with the event in question. A final correction is applied to remove nonuniformities at the 20% level in the Ψ distribution.

TABLE I. Relative systematic uncertainty of the reaction plane resolution for the centrality bins shown in Fig. 1.

Centrality	Syst. error
0–10%	20.3%
10–20%	5.1%
20–30%	3.9%
30–40%	3.8%
40–50%	4.1%
50–60%	4.6%
60–70%	22.5%

Because the above-described procedure can also be applied individually to each BBC, we have a redundant measurement of the reaction plane in the north and in the south, and we exploit this to determine the resolution of the full reaction plane measurement using standard procedures [44]. The resolution of the reaction plane is directly measured from the quantity $\langle \cos 2(\Psi_1 - \Psi_2) \rangle$ where Ψ_1 and Ψ_2 are the reaction plane angles measured in each of the two beam-beam counters individually and the average is taken over events. Figure 1 and Table I show the variation of the resolution, usually determined as $\langle \cos 2(\Psi_{\mathrm{meas}} - \Psi_{\mathrm{true}}) \rangle = \sqrt{(2\langle \cos 2(\Psi_1 - \Psi_2) \rangle}$. The needed correction factors can be derived from this using Eq. (11) in Sec. III F, where the reaction plane corrections are described in more detail.

The systematic errors associated with the measurement of the reaction plane come dominantly from how well the resolution is known. The uncertainty on this quantity is also shown with Fig. 1 for all but the most peripheral centralities. This error is determined by observing comparison of the

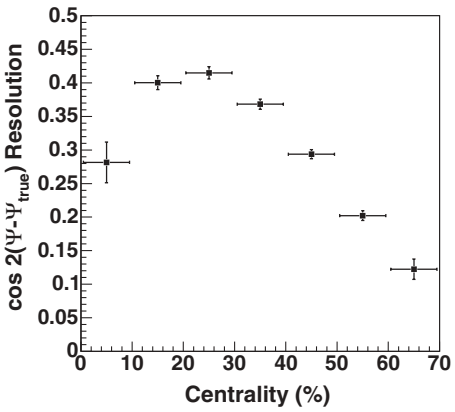

FIG. 1. Resolution of the reaction plane determined in the BBC versus centrality. As usual, the resolution is defined as the unitless quantity $\langle \cos 2(\Psi_{\mathrm{meas}} - \Psi_{\mathrm{true}}) \rangle$, equal to the inverse of the v_2 correction factor.

similarly calculated quantity $\langle \sin 2(\Psi_1 - \Psi_2)\rangle$ which should by definition be equal to zero. The value of $\langle \sin 2(\Psi_1 - \Psi_2)\rangle$ is found to be consistent with 0 for all centralities. The mean size of its fluctuations around 0 are compared to the size of the $\langle \cos 2(\Psi_1 - \Psi_2)\rangle$ to derive the systematic errors in the table. Because the value of $\langle \cos 2(\Psi_1 - \Psi_2)\rangle$ decreases dramatically in the lower multiplicity peripheral events, the relative size of the error increases. The size of this relative error is also cross checked by comparing it to the relative error on elliptic flow (v_2) measurements which is directly comparable since, as discussed in Sec. III F, the resolution correction for v_2 is a plain multiplicative factor. For the cross check, the v_2 error is derived by taking the difference of v_2 made with reaction planes from the BBC North and BBC South separately.

Because of the large rapidity gap between the PHENIX BBC's and the PHENIX Central Arm ($\Delta\eta > 2.7 - 4.0$), the measurements made in the BBC's are assumed to have no correlations (except collision geometry) with processes detected in the central arm that would affect the results presented in Sec. III F. Specifically, PYTHIA studies [45] indicate that any large rapidity-gap production correlated with jets (and thus the hard π^0's we study) detected in the central arm have a negligible effect on reaction plane determination even for the most peripheral events considered in this article. Further, we average both the North and South BBC, which are separated by $\Delta\eta > 6.0$, making potential effects of this nature especially unlikely.

C. Neutral pion detection

The detection of neutral pions is one of the major sources of information on identified particle production at high p_T at RHIC, and PHENIX has already published the results of a number of π^0 measurements in different colliding systems [3,6,10,46,47]. Here we will describe the technique for obtaining π^0 yields as a function of p_T and centrality, which is now well established within PHENIX.

Neutral pions are detected via their $\pi^0 \to \gamma + \gamma$ decay channel. Due to the relatively short mean lifetime of neutral pions of about 10^{-16} s, typical of electromagnetic decays, the pions decay close to the interaction point ($c\tau \approx 25$ nm). This makes the decay vertex well known and the pions can be reconstructed via an invariant mass analysis of photon pairs measured by the EMCal.

In the EMCal, hits or clusters are reconstructed by finding contiguous calorimeter towers with pulse heights above the ADC pedestal value. In order to obtain a cleaner sample of electromagnetic hits shower shape cuts are applied to select candidate photons and time-of-flight cuts are applied to reject slow hadrons. For the PbSc we require measured cluster times to be $t_{\rm clust} < L/c \pm 1.2$ ns, where L is the straight-line path from the collision vertex to the reconstructed cluster centroid. For the PbGl we require reconstructed clusters to have times, $t_{\rm clust} < L/c \pm 2$ ns; the difference is due to the intrinsic timing resolutions of the two calorimeter technologies.

The energy of each EMCal cluster is corrected for angular dependence and nonlinearity based on test beam results and simulation. The linearity corrections for both detector types are different with the PbGl showing a stronger dependence on the energy. The correction factors for a photon with a detected energy of 1 GeV (10 GeV) are 1 (0.95) for the PbSc and 1.05 (0.975) for the PbGl, respectively. The PbGl calorimeter also shows a stronger variation of the measured photon energy with the angle of incidence on the detector surface, at 20° the measured energy is reduced by 5% compared to perpendicular incidence (0°), whereas in the PbSc the effect is only of the order of 2%.

In a typical Au+Au central event the EMCal detects $\gtrsim$300 clusters corresponding to an occupancy of $\sim$10% and therefore a non-negligible probability of cluster overlaps. To minimize the effects of cluster overlaps in high multiplicity events, the energy of each cluster in the PbSc calorimeter is determined not only from the sum of all contiguous towers with deposited energy above a given threshold (15 MeV was our default value) but also, alternatively, "extrapolating" the measured "core energy" of the four to five central towers assuming a standard electromagnetic shower profile in an event with zero background. For this latter case, the *ecore* energy was computed from the experimentally measured center of gravity, central shower energy, and impact angle in the calorimeter using a parameterized shower profile function obtained from electromagnetic showers measured in the beam tests. Such an *ecore* energy represented an estimate of the true energy of a photon impinging on the PbSc unbiased by background contributions from other particles produced in the same event and depositing energy in the neighborhood of a given cluster. The use of *ecore* instead of the total cluster energy for photon reconstruction, helped to reduce considerably the effects of cluster overlaps in central Au+Au collisions.

For a photon pair originating from a π^0 decay the invariant mass

$$m_{\gamma\gamma} = \sqrt{\left(P_{\gamma_1} + P_{\gamma_2}\right)^2} = \sqrt{2E_1 \cdot E_2 \cdot (1 - \cos\theta_{12})} \qquad (2)$$

is identical to the π^0 rest mass. However, due to the finite energy and position resolution in the detection of the photon pair, the actual reconstructed value is smeared around a mean value, which can deviate from the nominal value. The reconstructed peak position is also influenced by the high multiplicity in a heavy-ion collision, where overlapping clusters can shift the measured energy of each photon.

With the invariant mass analysis, π^0's cannot be identified uniquely because all possible photon-photon combinations have to be considered. This leads to a large combinatorial background, which increases quadratically with the multiplicity. The π^0 yield is instead determined on a statistical basis, with the background contribution established via a *mixed event* technique as described below.

One possibility to reduce the combinatorial background is to make use of the phase-space distribution of the photons in a π^0 decay. For the $\pi^0 \to \gamma + \gamma$ decay, the two photons have minimum opening angle

$$\tan\theta_{12}/2 = \frac{m}{p}, \qquad (3)$$

where m is the π^0 mass and p its momentum, with $p \simeq p_T$ in the PHENIX central spectrometer. The angular distribution of

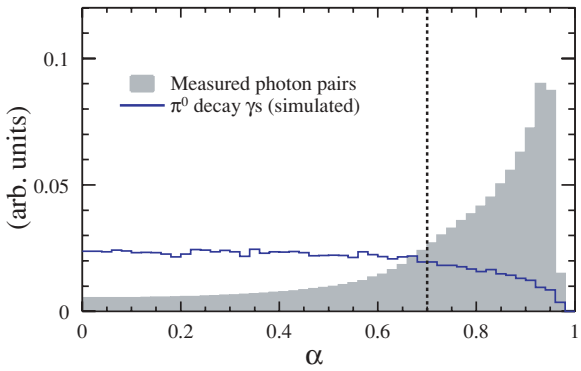

FIG. 2. (Color online) Asymmetry of photon pairs with $3\,\mathrm{GeV}/c \leqslant p_T < 5\,\mathrm{GeV}/c$ within the acceptance of one PbGl sector, for simulated single π^0s and measured within minimum bias events. An asymmetry cut used during the analysis is also shown. (Due to the limited acceptance of the detector, the distribution of the energy asymmetry shows a slight decrease toward $\alpha = 1$.)

the γ pair in the π^0 rest frame, $d\sigma/d\cos\theta^*$, is constant, which leads to a flat distribution in the measured energy asymmetry of the two photons from π^0 decay:

$$\alpha = \frac{|E_1 - E_2|}{E_1 + E_2} = \beta|\cos\theta^*|, \tag{4}$$

where $\beta = p/E \sim 1$ is the velocity of the π^0. However, high p_T combinatorial pairs are strongly peaked near $\alpha = 1$ because of the steeply falling spectrum of single photon candidates. This is illustrated in Fig. 2, where the asymmetry distribution for photons from π^0s in a simulation is compared to the measured asymmetry for photon candidate pairs in real Au+Au collisions. In two independent analyses, asymmetry cuts of $\alpha < 0.7$ and $\alpha < 0.8$ were employed, other values were used as a cross-check and to verify the energy scale (see below).

Pairs of candidate photon clusters within the PbGl and the PbSc calorimeter that satisfy the asymmetry cut are considered candidate π^0's. Figure 3 shows example invariant mass distributions for π^0 candidates with $3.0 < p_T < 3.5$ GeV/c in Au+Au collisions for two different bins of collision centrality. The background under the clear π^0 mass peak in these figures is due to combinatorial mixing of photons from two different decaying π^0's or from pairs containing one or two nonphoton clusters that nonetheless pass the above-described cuts.

Such a combinatorial background can be determined by a so-called *mixed event* technique. It is a widely used method to determine the combinatorial background of combined particle properties, e.g., the invariant mass of a photon pair. The basic idea is to compare the result obtained by combining particles within one event to the result for particle combinations from different events, which are *a priori* not correlated.

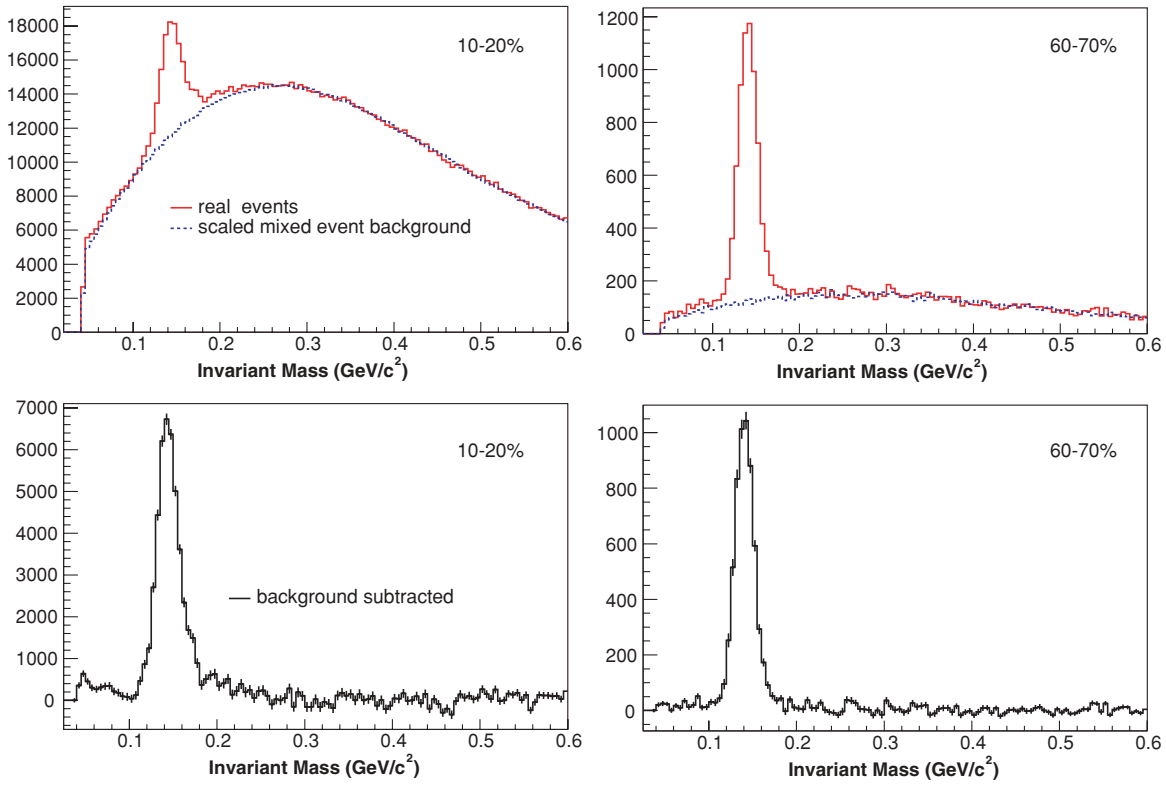

FIG. 3. (Color online) Invariant mass distributions of pairs of electromagnetic clusters passing photon selection cuts for pair transverse momenta satisfying $3.0 < p_T < 3.5$ GeV/c. (Top panels) $m_{\gamma\gamma}$ distributions in Au+Au events compared to a normalized mixed-event sample representing the combinatoric background. (Bottom panels) The $m_{\gamma\gamma}$ distributions after subtraction of the combinatoric background. (Left) 10–20% centrality bin; (right) 60–70% centrality bin.

In the case of the π^0 invariant mass, the mixed event distribution is determined by combining one photon candidate from the current event with all photon candidates from previous events stored in a buffer. The number of previous events used for the pair combinations determines the statistical error of the background, which can be made small by increasing the buffer size. In this analysis, the buffer is varied from ~3 to 10 previous events depending on centrality due to the centrality-dependent multiplicity.

To describe the combinatorial background correctly it is essential that the events used for mixing have similar properties as the real event. Different event classes for collision vertex, centrality, and reaction plane are employed. Also events are chosen for mixing so that they are not biased toward a certain reaction. This is because triggered samples, even from the high-p_{T} photon trigger, contain biases, e.g., in momenta and centrality distributions, which do not accurately represent the dominant uncorrelated background. For this reason only minimum bias events are used for mixing with both the trigger and minimum bias data sets.

For the photons used in the event mixing the same criteria are applied as for the pair combinations from one event, such as PID cuts, cuts on bad modules, and the asymmetry cut. Other properties valid *a priori* for the real photon pairs, e.g., a minimum distance that allows to distinguish them, have to be considered in addition. In the analysis a minimum distance cut of a least 8 cm is required for each photon pair combination, within one event and for mixed events, respectively.

For a given p_T bin the mixed-event background is normalized to the same-event invariant mass distribution outside the range of the π^0 peak by scaling the mixed-event background with a function $f(m_{\mathrm{inv}})$. This scaling function is determined by fitting the ratio of the same-event and mixed-event invariant mass distribution for p_T bins up to 3 GeV/c with a linear function. This is needed because at low p_T correlations in the real-event background due to overlapping clusters cannot be reproduced by the mixed-event technique. For the p_T bins above 3 GeV/c, a constant is used. To cross-check the result, the linear and the constant scaling function are also determined over the complete invariant mass region, including the π^0 peak, which is taken into account by an additional Gaussian in the fit function (e.g., a linear plus a Gaussian function).

The determination of the scaling function for large pair-p_T is limited by statistics in the real event sample and does not lead to stable results. Instead a constant scaling factor is used if the ratio of the invariant mass distribution shows bins with zero entries in the fit region. The scaling factor is determined by integrating the real and the mixed invariant mass distributions in the range with the peak region excluded.

The scaled mixed-event background is subtracted from the same-event distribution to produce a statistical measure of the true π^0 yield. The result of such a subtraction procedure is shown in the bottom plots of Fig. 3. The raw π^0 yield is obtained in each p_T bin by integrating the subtracted invariant mass distribution in a range around the peak mean (m_{π^0}) of ± 3 times the Gaussian width (σ_{π^0}) of the π^0 peak. Values of the mean and σ_{π^0}, can be seen in Fig. 4. Varying the size

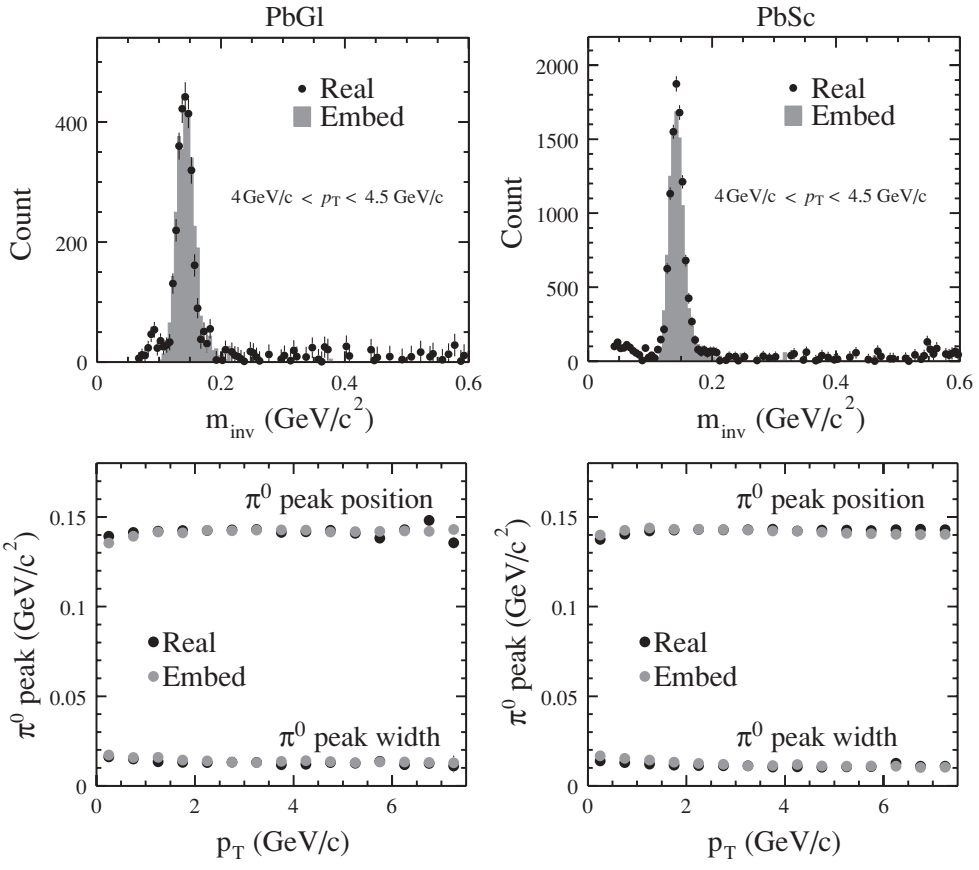

FIG. 4. Comparison of the π^0 peak position in real events (MB) measured with the PbGl and the PbSc with the results obtained for embedded π^0s. The p_T dependence of the peak position and width is due to calorimeter energy resolution as discussed in the text.

of the integration window results in slightly different results, which contributes to the overall systematic uncertainty of the measurement, discussed in Sec. III D4.

Residual differences between the mixed background and the foreground are still apparent in some p_T bins, especially below $\sim$2 GeV/c. Cluster merging, cluster splitting (fluctuations in the two-dimensional $\phi - z$ energy profile cause multiple local maxima that are incorrectly separated into distinct clusters), antineutron annihilation, and even second-order residual physics correlations such as three and multibody decays, flow, HBT, etc., can all cause such differences. These remaining differences are compensated by the shape of the scaling function. In addition, as a systematic check, the shape of the remaining background after subtraction is also fit with various low order polynomial functions and potential contributions to the peak yield are considered in the determination of the total systematic error from the peak extraction procedure.

The values of the peak width and mean are extracted in one initial analysis of the invariant mass distribution in which a p_T-dependent parameterization is determined for different centralities. The use of predefined values for the position and spread of the π^0 peak has the advantage that even in p_T regions where no fit to the subtracted invariant mass distribution is possible, the integration region is well defined just by extrapolation from low p_T.

D. π^0 spectrum measurement

For the reaction-plane independent π^0 spectrum measurement in a given centrality class *cent*, the aforementioned analysis is applied in $\Delta p_T = 0.5$ GeV/c bins for $p_T >$ 1 GeV/c. We cease attempting to extract π^0 yields at high p_T when the number of pairs within the selected (background-subtracted) π^0 mass window falls below 4 counts. We then correct the resulting raw π^0 spectrum for the geometric acceptance $a_{\Delta y}(p_T)$, the overall detection efficiency $\varepsilon_{\text{cent}}(p_T)$, which accounts for the cluster cut efficiency, the π^0 mass cut efficiency, for losses due to cluster overlaps in high multiplicity events, for cuts on bad modules and for the calorimeter energy and position resolution. In addition a correction for conversion losses (c_{conv}) in the material of the PHENIX central arms and for the branching ratio of the two photon decay ($c_{\gamma\gamma}$) is applied:

$$\frac{1}{2\pi p_T}\frac{d^2N^{\pi^0}_{\text{cent}}}{dp_T\,dy} \equiv \frac{1}{2\pi p_T N^{\text{event}}_{\text{cent}}} \times \frac{1}{a_{\Delta y}(p_T)\varepsilon_{\text{cent}}(p_T)c_{\text{conv}}c_{\gamma\gamma}} \times \frac{N^{\pi^0}_{\text{cent}}(\Delta p_T)}{\Delta p_T\,\Delta y}. \quad (5)$$

1. Acceptance and detector efficiency

The geometric acceptance of the EMCal for the $\pi^0 \to \gamma\gamma$ decay is evaluated using a Monte Carlo (MC) program that generates π^0s in a rapidity interval Δy with the same vertex distribution and rapidity distribution as observed in real events and contains the complete geometry information of the EMCal. The π^0 decay is calculated via JETSET routines that are part of the PYTHIA event generator [48]. For each π^0 it is verified that both decay photons hit the detector. The resulting p_T distribution of accepted π^0s is divided by the transverse-momentum distribution of the generated π^0s and provides the geometrical acceptance of the PbSc and PbGl, respectively.

The detection efficiency is determined using GEANT to simulate the complete response of the calorimeter to single π^0 decays. The data from each simulated π^0 is then embedded into real Au+Au events by adding the EMCal tower information of the simulated π^0 to the tower information of the real event and recalculating the EMCal clusters. The efficiency for detecting the embedded π^0 is then again determined by comparing the input p_T spectrum to the reconstructed p_T spectrum of the embedded π^0's. Using this technique we determine "efficiency" corrections that account for the energy resolution and position resolution of the calorimeter, as well as for the losses due to overlapping clusters in a real event environment. In addition, the embedding allows for a precise determination of the effect of edge cuts and bad modules. Though these effects can be in principle considered as acceptance corrections, they depend not only on the geometry but also on the energy deposition of an electromagnetic shower in the different calorimeter towers.

In the embedding procedure the effects of photon conversions are also included, as the GEANT simulation considers the material budget in front of the EMCal and the information for decay-photon conversions is retained. The final conversion correction, which is factorized from the rest of the efficiency for book-keeping purposes, is evaluated by comparing the π^0 yield with and without including conversions in the simulation. The final conversion correction, constant with p_T depends on the photon PID cuts and material in front of each individual sector and ranges from 6 to 8% in PbGl and 9 to 10% in PbSc. Comparing this to the sheer probability of a π^0 having at least one photon which converts, 21% PbGl and 14% PbSc, we see that a large portion of these π^0 are still reconstructable.

For the embedding, the input π^0 spectrum is weighted to match a fit function (see below, at the end of Sec. III D3) which is fit to the measured π^0 spectrum so that the correct folding of the π^0 spectrum with the resolution is obtained. This procedure is iterated, with the fit of the p_T dependence of the input weights adjusted as the estimate of the efficiency correction improves, until the procedure converges within the nearly p_T-independent statistical error of the embedded sample, approximately 3%.

Figure 4 compares the invariant-mass peak after background subtraction in the real data and the invariant mass peak of the embedded π^0 for the two different detector types in minimum bias events. The measured π^0 peak position is shifted from the nominal value of approximately 134.98 MeV due to the finite energy resolution of the detector in combination with the steeply falling spectrum and due to the additional effect of overlapping clusters. As illustrated the effects are well reproduced by the embedded π^0's.

2. Trigger efficiency

The efficiency of the Level-2 trigger is separately evaluated by processing recorded minimum-bias events with the Level-2

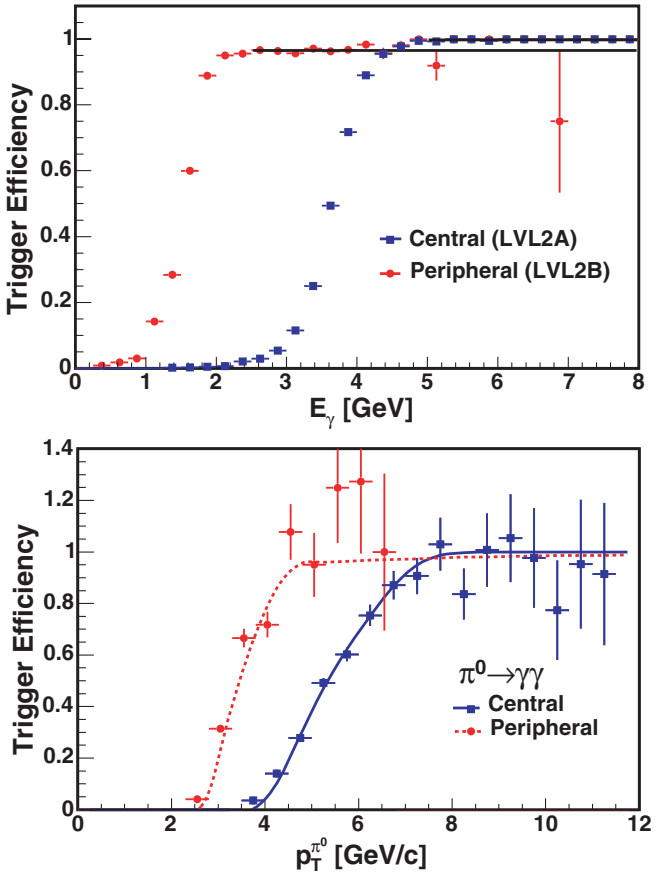

FIG. 5. (Color online) (Upper) Measured efficiency of single clusters of LVL2A (blue) and LVL2B (red) triggers as discussed in the text. The black lines are constant value fits to the plateau efficiency, greater than 99.7 (95%) for LVL2A (LVL2B). (Lower) Efficiency for neutral pion detection of the triggers as a function of π^0 p_T, calculated (solid curves) based on the efficiencies in (upper) and, as a cross-check (data points), compared to ratio of per equivalent minimum-bias event yields in the full trigger sample with the same in the true minimum bias sample. Because the latter is the ratio of two separate data samples, independent statistical fluctuations, as well as ∼8% systematic effects in the yield extraction (discussed Sec. III D4) in either sample can cause this measured ratio to be greater than 100%.

trigger and evaluating the efficiency for the trigger to select events containing a high p_T cluster. This analysis shows complete (100%) efficiency for the LVL2A trigger at momenta well above the trigger threshold of 3.5 GeV/c (95% above 1.5 GeV/c for LVL2B) for obtaining clusters that also pass all offline cluster cuts. This is demonstrated in Fig. 5 (upper). The "plateau" values are determined from fitting the region above the turn-on also shown.

The related trigger efficiency of reconstructed π^0's is calculated from a fast MC simulation based on these measured single cluster efficiencies. The calculation is performed both by using a integrated Gaussian fit to the single cluster efficiency and by directly using the finely binned histogram and constant plateau fit. Both methods give consistent results. The result for the latter method is shown in Fig. 5 (lower), solid curves. The calculation is cross-checked, as demonstrated by the data

TABLE II. Corrections in the PbGl and PbSc to the raw π^0 yield in central collisions (0–10%) and with TOF and shower shape cut applied. The main part of the efficiency loss in PbGl is due to the effect of bad module and edge cuts which is approximately 40% at high p_T for the PbGl and 20% for the PbSc, respectively.

p_T	PbGl		PbSc	
	3.25 GeV/c	8.5 GeV/c	3.25 GeV/c	8.5 GeV/c
$a_{\Delta y}$	0.068	0.080	0.216	0.246
ε	0.351	0.358	0.455	0.515
c_{conv}	0.93	0.93	0.90	0.90
$c_{\gamma\gamma}$	0.98798			

points in Fig. 5 (lower), which show the ratio of the yield from the two Level-2 trigger samples per *equivalent* number of minimum bias events to the same from the true minimum bias sample itself. We combine the yields obtained in the minimum bias event sample and the LVL2A (LVL2B) trigger sample above a cutoff of 6.5 GeV/c (3.5 GeV/c) where the trigger reaches efficiencies greater than 0.4 such that the correction factor is not allowed to be large. A conservative error of 3% is assigned to the efficiency calculations, resulting in a total error of ∼3–5%, based on the three studies: (1) comparisons of the data shown in Fig. 5, (2) comparisons of the two calculational methods, and (3) a study of the yields in the subsample of minimum bias events that also fired the triggers, similar to (1).

3. *Other corrections*

The calculated corrections are applied to the raw π^0 yield as given by Eq. (5). Table II shows the corrections in central collisions for two different bins in transverse momentum and for the PbGl and PbSc, respectively. As discussed above the effect of the cut on bad modules is included in the efficiency correction, due to its dependence on the depth of the electromagnetic shower.

Following the usual PHENIX procedure of modifying the quoted yield values for each finite sized p_T bin such that the measurement corresponds to p_T value at the bin center instead of the average p_T of the bin [49] (thereby facilitating taking ratios of spectra from different collision systems), a final correction is applied to the *yield* of each data point. Using a continuous function that is fit to the data points, values for the invariant yields at the centers of the chosen p_T bins are scaled by the ratio of the fit value at the fit's average p_T to the fit value at the bin center. This is an iterative procedure similar to the final efficiency correction described in Sec. III D1 above, with a smaller convergence criteria of <0.1% of the previous correction. The fit function is empirically determined and several functional forms were found to give similar performance (e.g., see Fig. 6 below) and negligible differences in the resulting corrections. All the functional forms either explicitly contain or implicitly converge quickly to, a pure power law form (const/p_T^n) above $p_T \sim 4$ GeV/c.

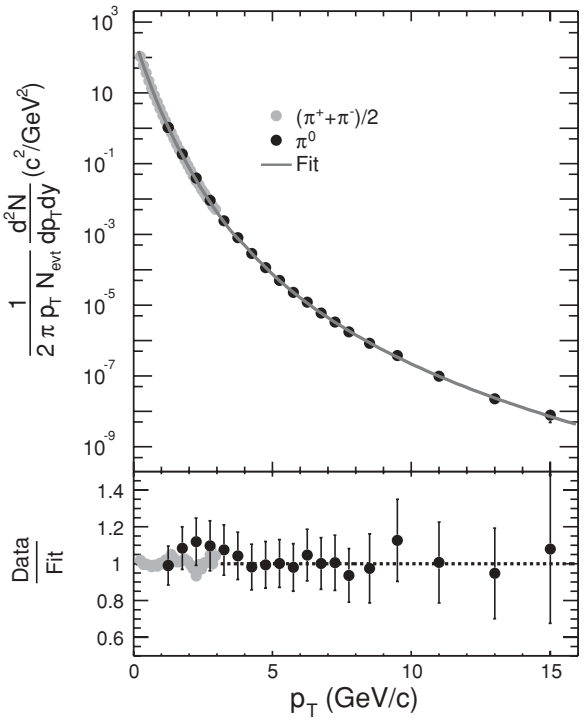

FIG. 6. Comparison of the combined π^0 result to the measurement of charged pions within the PHENIX experiment in minimum bias events. The fit (see previous Sec. III D3) considers the averaged result of the π^+ and π^- measurement [7] below $p_T = 3\,\mathrm{GeV}/c$ and the π^0 data above.

The spectral shape is discussed further under Secs. IV A and IV B.

4. Systematic errors

Each correction of the raw yield following Eq. (5) is afflicted with its own uncertainty, but already the determination of the π^0 raw yield itself is sensitive to the method of extraction. In particular it is sensitive to the choice of the fit function for the background scaling and the extraction window. In principle, both should be taken into account by the detector efficiency, but in the efficiency calculation no background subtraction is necessary. For this reason the systematic error of the peak extraction method is determined in two steps: first via the comparison of the raw yield obtained with two different fits for the background scaling, and second through the comparison of the fully corrected spectra for different sizes of the extraction window, for the real data as well as for the efficiency calculation.

The systematic error introduced by the efficiency calculation is estimated by comparing the fully corrected spectra for different PID criteria as well as for different additional smearing. The smearing (or energy resolution in the simulation) is changed in a way that a clear disagreement between the measured π^0 peak width and the peak width from the embedding is observed.

Apart from the uncertainty of the efficiency, the main contribution to the systematic error is the determination of the absolute energy scale. Based on the comparison of the π^0 peak positions in the data to the expectation from simulation the energy scale can only be determined or confirmed with limited accuracy, $\Delta(E)/E = 1.6\%$ in the PbSc and, because of the smaller acceptance, $\Delta(E)/E = 2\%$ in the PbGl.

The additional contributions to the systematic error that have not been discussed in detail involve the uncertainty of the conversion correction (2.9%) and of the acceptance calculation (2.5%) both due to small uncertainties in detector material and alignment. Table III provides a final overview of the various contributions to the total error of the π^0 measurement in the PbSc and the PbGl, respectively.

The most important cross-check of the final result is the comparison of the result for the two different detector types PbGl and PbSc, which is shown for peripheral events in Fig. 7. A good agreement within the errors is seen and similar consistency is found in all centralities. Because they represent essentially independent measurements, the two

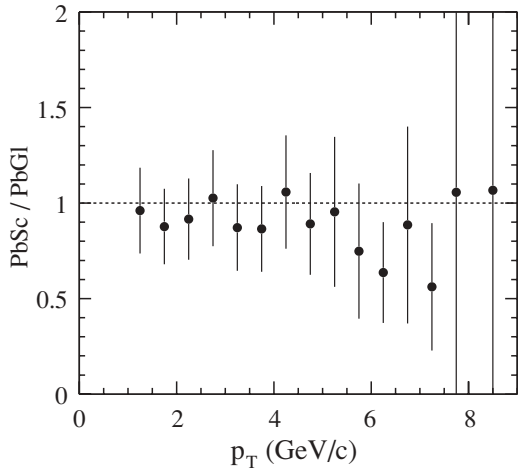

FIG. 7. Comparison of fully corrected spectra for the PbGl and the PbSc for peripheral events. Similar consistency is observed for all centralities. The error bars represent the statistical and systematic uncertainties.

TABLE III. Summary of the dominant sources of systematic errors on the π^0 yields extracted independently with the PbGl and PbSc electromagnetic calorimeters in central events for different p_T. For comparison the statistical uncertainty is also shown.

p_T (GeV/c)	PbGl		PbSc	
	3.25	8.5	3.25	8.5
Yield extraction	8.7%	6.%	9.8%	7.3%
Efficiency	11.4%	11.4%	11.4%	11.4%
Acceptance	2.5%	2.5%	2.5%	2.5%
Conversions	2.9%	2.9%	2.9%	2.9%
Level-2 data	—	—	—	3%
Energy scale	13.8%	14.1%	10.5%	11.2%
Total syst.	20.5%	19.3%	18.8%	18.7%
Statistical	10.6%	50%	8.1%	26.6%

results are averaged and the total error of the combined result is reduced using a standard weighted least-squares method also described in Ref. [50]. An additional cross-check of the final result based on isospin symmetry is provided by the measurement of charged pions in the central arm [7], this is shown for minimum-bias collisions in Fig. 6. The neutral pion measurement smoothly extends the result for charged pions to larger transverse momenta.

E. $R_{AA}(p_T)$ measurement

Using the invariant yields obtained from the above-described analysis and the separately measured invariant cross section for π^0 production in $p+p$ collisions [46], we calculate the nuclear modification factor, R_{AA}, according to

$$R_{AA}(p_T) = \frac{\left(1/N_{AA}^{evt}\right) d^2N_{AA}^{\pi^0}/dp_T\,dy}{\langle T_{AA}\rangle \times d^2\sigma_{pp}^{\pi^0}/dp_T\,dy}, \tag{6}$$

where $\langle T_{AA}\rangle$ is the average Glauber nuclear overlap function for the centrality bin under consideration

$$\langle T_{AA}\rangle \equiv \frac{\int T_{AA}(\mathbf{b})\,d\mathbf{b}}{\int \left(1 - e^{-\sigma_{pp}^{inel} T_{AA}(\mathbf{b})}\right) d\mathbf{b}}, \tag{7}$$

from which the corresponding average number of nucleon-nucleon collisions, $\langle N_{coll}\rangle = \sigma_{pp}^{inel}\langle T_{AA}\rangle$, can be easily obtained [51].

F. $R_{AA}(\Delta\phi)$ measurement

The measurement of the raw π^0 yield with respect to the event reaction plane, $\Delta\phi = \phi(\pi^0) - \Psi$, proceeds as described in Sec. III D for the p_T spectrum except that we measure the yields as a simultaneous function of both p_T and $\Delta\phi$. Because the beam-beam counters have 2π acceptance, PHENIX can measure the π^0 yields with uniform acceptance over $0 < \Delta\phi < 2\pi$ even though the electromagnetic calorimeters have only 1π nominal azimuthal acceptance. Because the measurement of Ψ is ambiguous with respect to a 180° rotation of the reaction plane, and because we expect the π^0 yields to be symmetric with respect to reflection around $\Delta\phi = 0$, we measure the π^0 yields in six bins of $|\Delta\phi|$ over the range $0 < |\Delta\phi| < \pi/2$. For each p_T bin we evaluate the ratio,

$$R(\Delta\phi_i, p_T) = \frac{\Delta N(\Delta\phi_i, p_T)}{\sum_{i=1}^{6} \Delta N(\Delta\phi_i, p_T)}, \tag{8}$$

where $N(\Delta\phi_i, p_T)$ is the measured number of π^0's in a given $(\Delta\phi, p_T)$ bin, $\Delta\phi_i$ representing one orientation of $\Delta\phi$. Because the PHENIX central arm acceptance is effectively constant as a function of $\Delta\phi$ and we do not expect any azimuthal dependence of our π^0 efficiency corrections, $R(\Delta\phi_i, p_T)$ can be written as:

$$R(\Delta\phi_i, p_T) = R_{AA}(\Delta\phi_i, p_T)/R_{AA}(p_T). \tag{9}$$

Using the measured $R_{AA}(p_T)$ values we can directly convert the $R(\Delta\phi, p_T)$ to $R_{AA}(\Delta\phi, p_T)$ without having to apply acceptance and efficiency corrections to the reaction-plane dependent yields. These corrections are already included in the $R_{AA}(p_T)$ values as described above.

However, before applying this procedure we must first correct the $R(\Delta\phi, p_T)$ values for the finite resolution of the reaction plane measurement. One goal of our measurement is to determine $R_{AA}(\Delta\phi, p_T)$ without assuming any particular functional dependence on $\Delta\phi$. For purposes of correcting for reaction plane resolution, we take advantage of the fact that the observed π^0 yields and hence the nuclear modification vary with $\Delta\phi$ to first order as

$$R^{raw}(\Delta\phi, p_T) \approx R_0\left[1 + 2v_2^{raw}\cos(2\Delta\phi)\right], \tag{10}$$

ignoring the much smaller higher-order harmonics such as v_4 terms. The superscript "raw" denotes the values not corrected for the reaction plane resolution. This resolution reduces v_2 by the factor $\sqrt{2\langle\cos 2(\Psi_1 - \Psi_2)\rangle}$ [44], which is given by the independent measurement of Ψ in the two BBC's shown previously in Fig 1. For each p_T bin in a given centrality class we fit the $R(\Delta\phi, p_T)$ values to the functional form in Eq. (10) and then correct each measured $R(\Delta\phi, p_T)$ value according to

$$R^{corr}(\Delta\phi, p_T) = R^{raw}(\Delta\phi, p_T)\left[\frac{1 + v_2^{corr}\cos(2\Delta\phi)}{1 + v_2^{raw}\cos(2\Delta\phi)}\right], \tag{11}$$

with $v_2^{corr} = v_2^{raw}/\sqrt{2\langle\cos 2(\Psi_1 - \Psi_2)\rangle}$. We estimate the systematic error in the reaction plane resolution correction by propagating the centrality dependent uncertainties in $\sqrt{2\langle\cos 2(\Psi_1 - \Psi_2)\rangle} = \langle\cos 2(\Psi_{meas} - \Psi_{true})\rangle$ from Table I. Of course, the above-described correction only strictly applies if $R_{AA}(\Delta\phi)$ is well described by the functional form in Eq. (10). Although we do observe some departure from this harmonic form in the data, the differences are typically below 5% so our correction will not introduce a large error.

IV. RESULTS

A. π^0 transverse-momentum spectra and nuclear modification factors

The π^0 invariant yields obtained using the procedure described in Sec. III D are presented in Fig. 8 as a function of p_T for the nine chosen centrality bins. With the increased statistics included in this analysis, we have extended the p_T range of the previous PHENIX measurement by at least 2 GeV/c for all centrality bins. The p_T range of the central bin has been extended from 10 to 14 GeV/c. Where the spectra overlap, the results shown here are consistent with the previously published results within systematic errors. The errors shown on the points in Fig. 8 include statistical errors and point-to-point varying systematic errors. The appendix tabulates the π^0 spectra plotted in Fig. 8 (centralities: 0–10, 10–20, . . . , 70–80, 80–92%) plus the combined spectra for centralities 0–20, 20–60, and 60–92%, which are used for

comparison to other neutral meson measurements [13]. The spectra in Fig. 8 depart from the exponential-like shape above 3 GeV/c, which is consistent with the expectation that high-p_T hadron production is dominated by hard-scattering processes that produce a power-law p_T spectrum [52] for hadrons resulting from quark and gluon fragmentation.

In previous publications, we have established the suppression of high-p_T π^0 production in Au+Au collisions [3,6]. This suppression cannot be easily seen given the large range of invariant yield covered by Fig. 8.

To evaluate the suppression of high-p_T π^0's, we show in Fig. 9 the p_T dependence of the π^0 nuclear modification factor, $R_{\rm AA}(p_T)$, for the nine individual bins of collision centrality and for the full minimum-bias centrality range 0–92.2%. We make use of the PHENIX Run3 $p+p$ baseline π^0 data. [47]. The error bars on the data in Fig. 9 include contributions from statistical errors in the Au+Au and $p+p$ measurements and from the systematic errors that do not cancel between the measurements. The separate band shown in each panel indicates p_T-independent errors on the $R_{\rm AA}$ measurement resulting from uncertainties in estimating $T_{\rm AA}(x, y)$ and systematic errors on the normalization of the Au+Au and $p+p$ measurements that do not cancel. As in previously published articles (e.g., Refs. [4,5,7]), a factor of ∼5 high p_T π^0 suppression in the most central Au+Au collisions, $R_{\rm AA} \approx 0.2$, is observed, with the suppression approximately p_T independent for $p_T > 5$ GeV/c. The suppression at high p_T decreases in more peripheral collisions such that the two most peripheral bins have $R_{\rm AA}$ values consistent with unity for $p_T > 3$ GeV/c.

B. Suppression via spectrum shift

The suppression of high-p_T particles as shown above was determined by comparison of the semi-inclusive measured yields as a function of centrality in Au+Au collisions at $\sqrt{s_{NN}} = 200$ GeV to the $\langle T_{\rm AA}\rangle$ scaled p_T spectrum from $p+p$ collisions [53]. A direct comparison of the 0–10% centrality Au+Au spectrum to the scaled $p+p$ spectrum is shown in Fig. 10 as a log-log plot to emphasize the pure power law

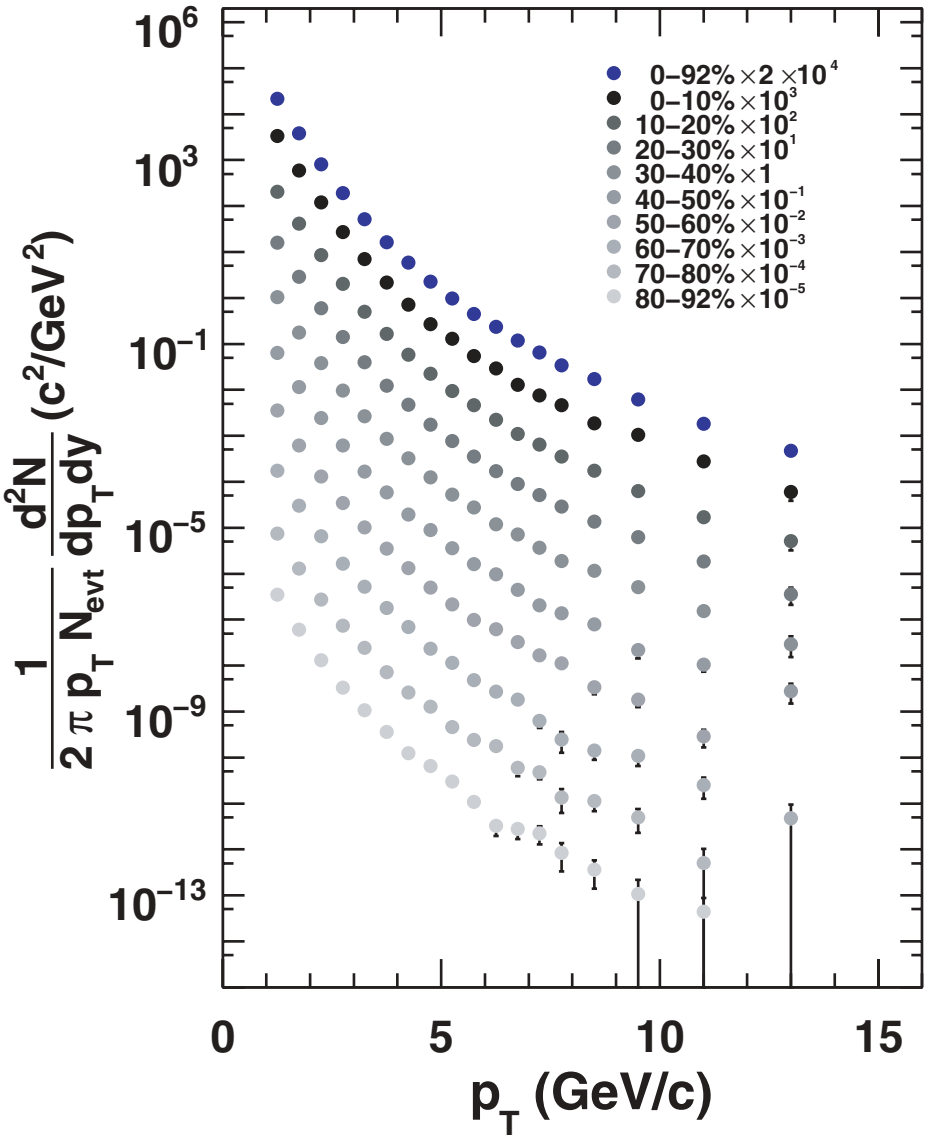

FIG. 8. (Color online) Neutral pion invariant yields as a function of p_T measured in minimum bias and nine centrality classes in Au+Au collisions at $\sqrt{s_{NN}} = 200$ GeV. Spectra for different centralities are scaled for clarity. Errors are total errors, full systematic, and statistical added in quadrature.

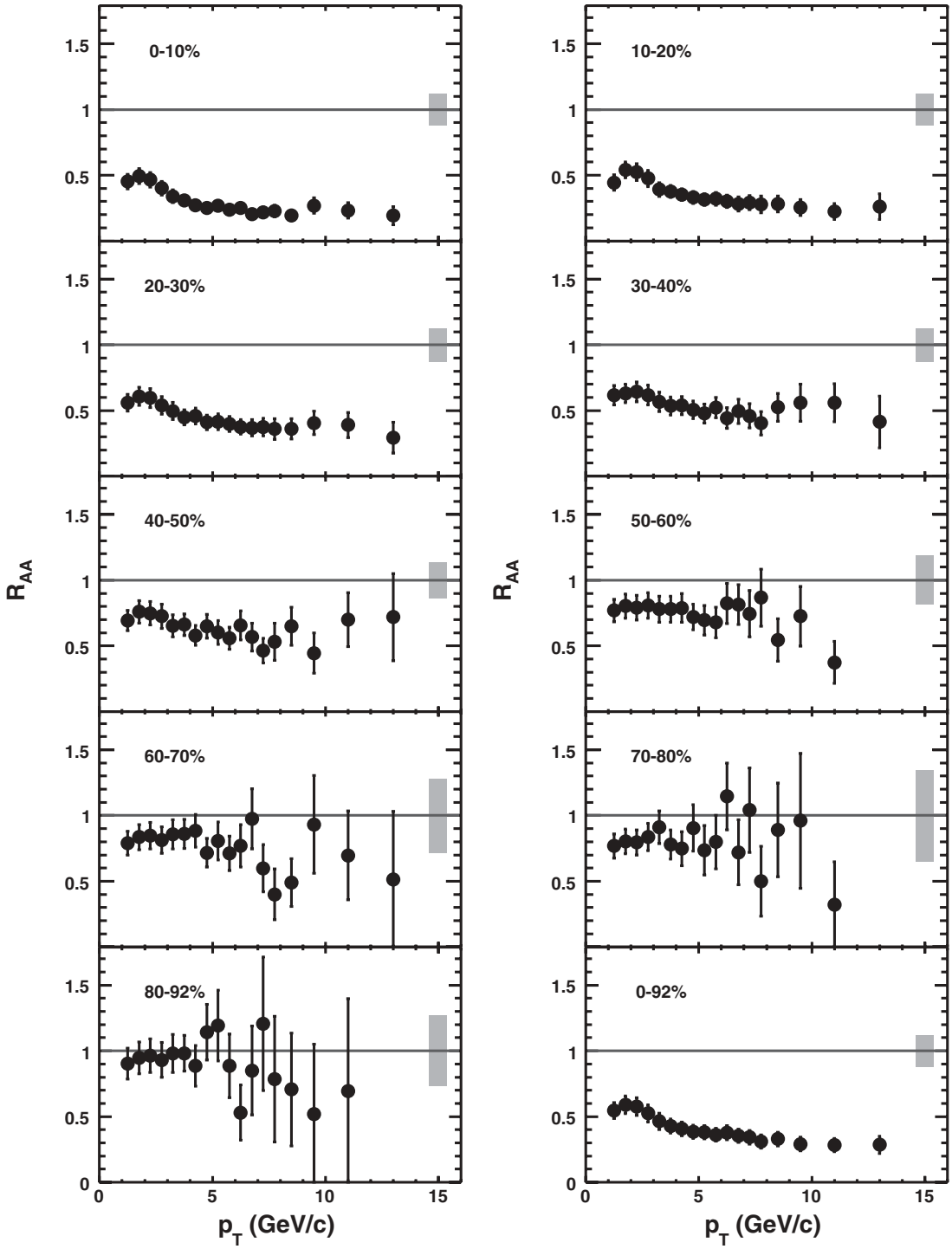

FIG. 9. Nuclear modification factor R_{AA} for neutral pions as a function of p_T for different centralities. The shaded error band around unity indicates the uncertainty in scaling factor T_{AA} and an overall scale uncertainty in the $p+p$ reference.

dependence of the data for $p_T > 3$ GeV/c. The suppression is commonly expressed by taking R_{AA} the ratio of the point-like scaled semi-inclusive yield to the reference distribution [Eq. (6)].

As illustrated in Fig. 10, instead of viewing the suppression in the nuclear modification factor as "vertical" reduction of the Au + Au yields, it can equally well be taken as a "horizontal" shift in the $\langle T_{\mathrm{AA}}\rangle$ scaled Au+Au spectrum, such that

$$\frac{\left(1/N_{\mathrm{AA}}^{\mathrm{evt}}\right)d^2N_{\mathrm{AA}}(p_T)/dp_T dy}{\langle T_{\mathrm{AA}}\rangle} = \frac{d^2\sigma_{pp}[p'_T{=}p_T{+}S(p_T)]}{dp'_T dy} \times [1 + dS(p_T)/dp_T], \quad (12)$$

where the last term in parenthesis is the Jacobian, dp'_T/dp_T.

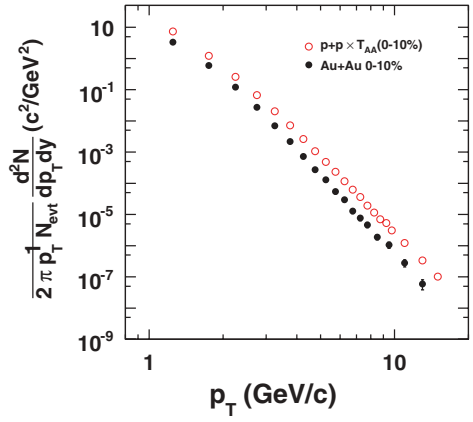

FIG. 10. (Color online) Log-log plot of central Au+Au and scaled $p+p$ π^0 p_T distributions.

Furthermore, owing to the pure power law of the $p+p$ reference spectrum, $Ed^3\sigma/dp^3 \propto p_T^{-n}$ with $n = 8.10 \pm 0.05$ above $p_T \approx 4$ GeV/c, the relative shift of the spectra—assumed to be the result of energy loss for the Au+Au spectrum—is easily related to the equivalent ratio, $R_{\rm AA}(p_T)$:

$$R_{\rm AA}(p_T) = \frac{[p_T + S(p_T)]^{-n+1}}{{p_T}^{-n+1}}[1 + dS(p_T)/dp_T] \qquad (13)$$

$$= [1 + S(p_T)/p_T]^{-n+1}[1 + dS(p_T)/dp_T]$$

where the exponent is $n-1$ because the relevant shift is in the $d\sigma/dp_T$ spectrum rather than in $d\sigma/p_T\,dp_T$. The fact that the Au+Au and reference $p+p$ p_T spectra are parallel in Fig. 10 provides a graphical illustration that the fractional p_T shift in the spectrum, $S(p_T)/pt = S_0$, is a constant for all $p_T > 3$ GeV/c, which also results in a constant ratio of the spectra, $R_{\rm AA}(p_T)$. For the constant fractional shift, the Jacobian is simply $dS(p_T)/dp_T = S_0$ and Eq. (13) becomes:

$$R_{\rm AA}(p_T) = (1 + S_0)^{-n+2}, \qquad (14)$$

$$R_{\rm AA}(p_T)^{1/(n-2)} = \frac{1}{1 + S_0}. \qquad (15)$$

The effective fractional energy loss, $S_{\rm loss}$, is related to the fractional shift in the measured spectrum, S_0. The hadrons that would have been produced in the reference $p+p$ spectrum at transverse momentum $p_T + S(p_T) = (1 + S_0)p_T$, were detected with transverse momentum, p_T, implying a fractional energy loss:

$$S_{\rm loss} = 1 - 1/(1 + S_0) = 1 - R_{\rm AA}(p_T)^{1/(n-2)}. \qquad (16)$$

The fractional energy loss $S_{\rm loss}$ as a function of centrality expressed as $N_{\rm part}$ is shown in Fig. 11 for two different p_T ranges, $3 < p_T < 5$ GeV/c and $5 < p_T < 7$ GeV/c. There appears to be a small decrease of $S_{\rm loss}$ with increasing p_T, but the main observation from Fig. 11 is that $S_{\rm loss}$ increases approximately like $N_{\rm part}^{2/3}$, as suggested by GLV [54] and PQM [55].

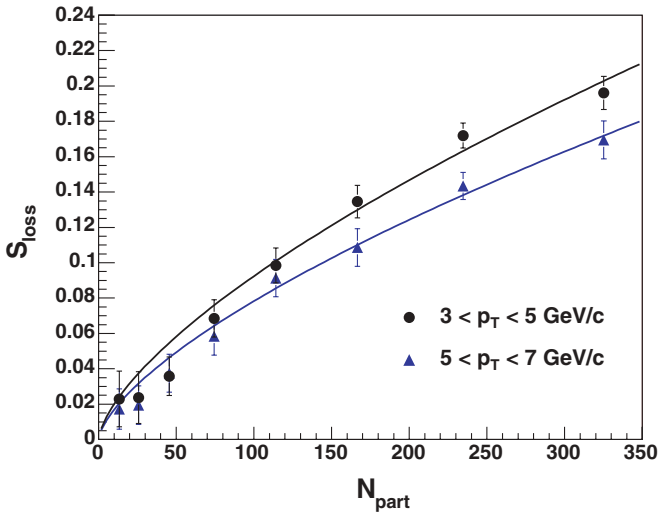

FIG. 11. (Color online) Fractional energy loss $S_{\rm loss}$ obtained from Eq. (16) versus centrality given by $N_{\rm part}$. The lines are fits of the form $\propto N_{\rm part}^{2/3}$ for each p_T range.

It is important to realize that the effective fractional energy loss, $S_{\rm loss}$ estimated from the shift in the p_T spectrum, is actually less than the real average energy loss at a given p_T, i.e., the observed particles have p_T closer to the original value than to the average. The effect is similar to that of "trigger bias" [56] where, due to the steeply falling spectrum, the $\langle z \rangle$ of detected single inclusive particles is much larger than the $\langle z \rangle$ of jet fragmentation, where $z = \vec{p}_{\pi^0} \cdot \vec{p}_{\rm jet}/p_{\rm jet}^2$. Similarly for a given observed p_T, the events at larger p_T' with larger energy loss are lost under the events with smaller p_T' with smaller energy loss.

It should be noted that fluctuations due to the variation of the path length and densities traversed by different partons also contribute to the difference between the true $S_{\rm loss}$ ($S_{\rm loss}^{\rm true}$) and that which is observed ($S_{\rm loss}^{\rm obs}$). However, as long as the dependencies of the induced energy loss on path length and parton energy approximately factorize, these fluctuations will also produce a p_T-independent reduction in $S_{\rm loss}^{\rm obs}$ compared to $S_{\rm loss}^{\rm true}$.

C. Angle dependence of high p_T suppression

To try to separate the effects of the density of the medium and path length traversed, we study the dependence of the π^0 yield with respect to the reaction plane. For a given centrality, variation of $\Delta\phi$ gives a variation of the path length traversed for fixed initial conditions, whereas varying the centrality allows determination of the effect of varying the initial conditions.

Figures 12 and 13 show the nuclear modification factor $R_{\rm AA}$ as a function of $\Delta\phi$ integrated over $3\,{\rm GeV}/c < p_T < 5\,{\rm GeV}/c$ and $5\,{\rm GeV}/c < p_T < 8\,{\rm GeV}/c$, respectively. For all centralities (eccentricities) considered, there is almost a factor of 2 more suppression out-of-plane ($\Delta\phi = \pi/2$) than in-plane ($\Delta\phi = 0$), something that is immediately apparent in viewing the data in this fashion—explicitly displaying information that is implicit only in $R_{\rm AA}$, v_2, or the combination thereof.

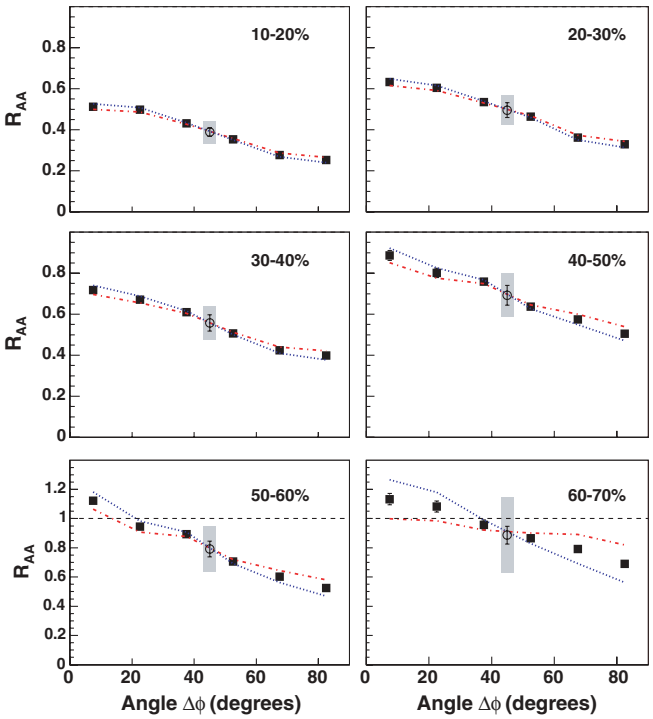

FIG. 12. (Color online) R_{AA} versus $\Delta\phi$ for π^0 yields integrated over $3 < p_T < 5$ GeV/c. Most statistical errors are smaller than the size of the points. The lines following the data points show the bin-to-bin errors resulting from the uncertainty in the reaction plane resolution correction (Fig. 1) and from bin-to-bin uncertainties in the R_{AA} values. The shaded band indicates the overall R_{AA} uncertainty.

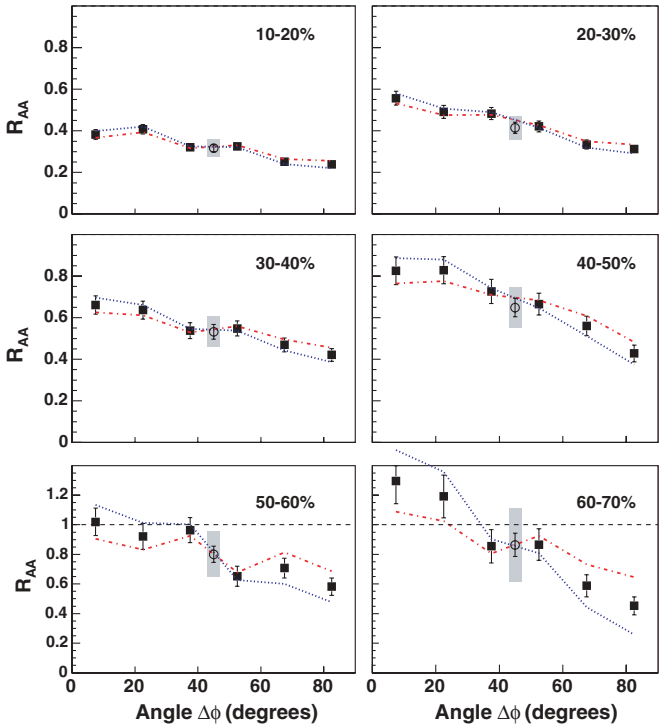

FIG. 13. (Color online) R_{AA} versus $\Delta\phi$ for π^0 yields integrated over $5 < p_T < 8$ GeV/c. The error lines and band are the same as in Fig. 12.

Strikingly, in contradiction to the data the variation in R_{AA} with respect to the reaction plane expected by parton energy loss models [29,57] should be much smaller for the more peripheral bins than for the central bins. As a result, the suppression vanishes (and perhaps an enhancement is observed) for smaller $\Delta\phi$ in the peripheral bins, corresponding to small path length traversed in the medium. Although collective elliptic flow effects, usually not included in those models, are known to boost in-plane (compared to out-of-plane) particle production [2,42], it is unclear how such collective effects can still play such an important role at the high-p_T bins considered. This may point to the possible need for a formation time before suppression can occur [58] and which could also explain why attempts to describe the azimuthal asymmetry v_2 solely in terms of purely geometrical energy loss have failed. Figures 14 and 15 give the angular dependence in terms of the fractional energy loss $S_{\rm loss}$, and provide essentially the same information as shown in the plots of $R_{AA}(\Delta\phi)$ in Figs. 12 and 13. Once again we see a large variation in energy loss as a function of angle. All the measurements of R_{AA} or equivalently $S_{\rm loss}$ vs. reaction plane and centrality, provide new constraints to models of jet quenching. To better understand the implications of the results shown in these figures, we will attempt in the next section to find a common geometric description of the angle and centrality dependences in terms of an estimated path length of the parton in the medium.

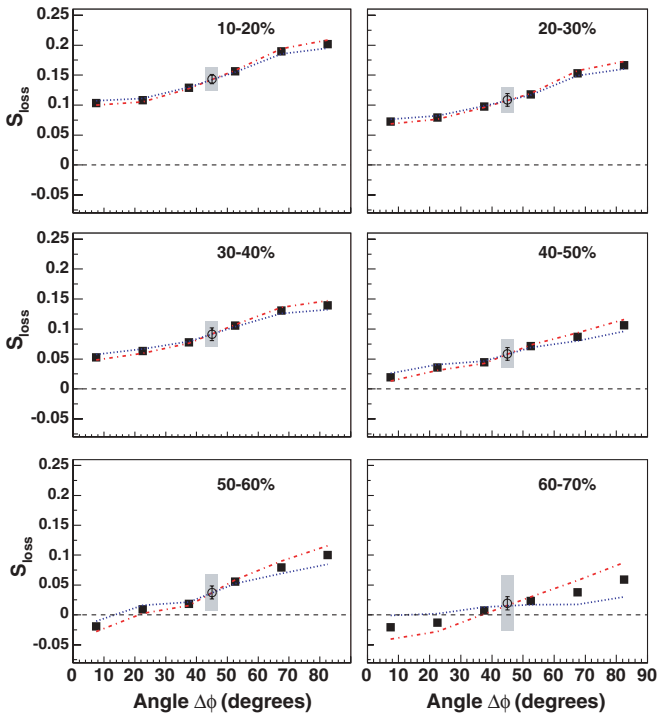

FIG. 14. (Color online) $S_{\rm loss}$ versus $\Delta\phi$ for π^0 yields integrated over $3 < p_T < 5$ GeV/c. The statistical errors are smaller than the size of the points. The lines following the data points show the bin-to-bin errors resulting from the uncertainty in the reaction plane resolution correction (Fig. 1) and from bin-to-bin uncertainties in the $S_{\rm loss}$ values. The shaded band indicates the overall $S_{\rm loss}$ uncertainty.

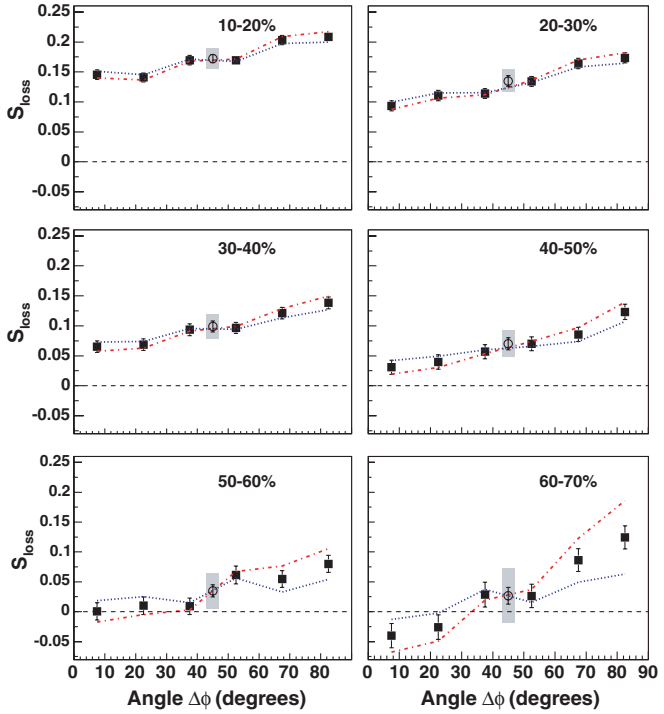

FIG. 15. (Color online) $S_{\rm loss}$ versus $\Delta\phi$ for π^0 yields integrated over $5 < p_T < 8$ GeV/c. The error lines and band are the same as in Fig. 14.

D. Path-length dependence of energy loss

To analyze the path-length dependence of parton energy loss using the data presented here we will use different methods for estimating the path lengths of partons in the medium as a function of centrality and $\Delta\phi$. The "standard" approach would be to evaluate a length-weighted integral of the participant charge density in the medium along the parton path. We will adopt such an approach, described by the parameter L_{xy} defined below, but we will also consider two other simplified approaches that may help indicate which physics is most relevant in determining the observed suppression. We first consider, simply, L_ε, the distance from the edge to the center of the elliptical overlap zone of the Au+Au collision to represent the average path length of a parton in the medium. Then we try to weight the path length (or length-squared) traversed by a parton from the center of the ellipse by the participant density in the transverse plane: $\rho L(\Delta\phi)$ $[\rho L^2(\Delta\phi)]$. Finally, we do the same path-length weighting for partons produced across the overlap ellipse, with hard-scattering production points weighted by $T_{\rm AA}(x, y)$: ρL_{xy} (ρL_{xy}^2). It is obvious that such a $\Delta\phi$-dependent analysis is not possible from just a simple combination of $R_{\rm AA}$ and v_2.

In detail, the three approaches considered here are as follows:

(i) The simplest picture for the angular dependence of the energy loss in noncentral collisions is that it is due to the asymmetric shape of the overlap region of the colliding nuclei. Taking this idea to its extreme, only the simplest length scale, the length of the overlap region in a particular direction, matters.

To evaluate this length, we first estimated the root-mean-square radius and eccentricity of an ellipse approximating the shape of the overlap region from the transverse distribution of the participant density calculated using standard Glauber Monte Carlo techniques in which all variations of impact parameter, etc., for a given centrality class are taken account in the quoted errors of the geometrical quanties [51]. Only the errors on the averages are considered; for instance, the fluctuations in the event-by-event participant eccentricity are taken into account in the quoted error of the centrality averaged ε. We then estimated the path length, L_ε, of partons emitted at a given angle $\Delta\phi$ by evaluating the distance from the center of ellipse to the edge. For each centrality, the value of L_ε is calculated as a function of $\Delta\phi$:

$$L_\varepsilon = \frac{b\sqrt{1+\varepsilon}}{\sqrt{1+\varepsilon\cos(2\Delta\phi)}}, \tag{17}$$

where $b = \sqrt{\langle x^2\rangle}$, the root-mean-square semiminor axis (conventionally taken in the x direction) and $\varepsilon = (\langle y^2\rangle - \langle x^2\rangle)/(\langle y^2\rangle + \langle x^2\rangle)$ are taken from the Monte Carlo Glauber calculation. The errors on b and ε are propagated through Eq. (17) for the error on L_ε. A plot of L_ε as a function of centrality and $\Delta\phi$ is shown in Fig. 16.

As described previously in Section III F, the effect and associated uncertainties of reaction plane resolution are

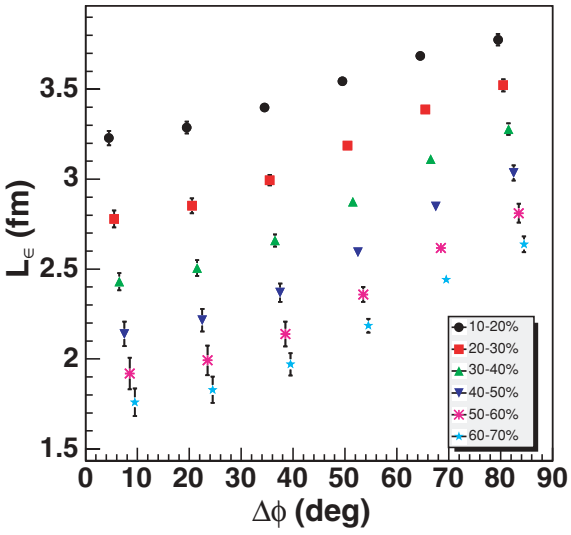

FIG. 16. (Color online) Simple geometrical length estimator L_ε with uncertainties plotted *vs.* angle with respect to reaction plane, plotted for the six centralities considered as indicated in the legend. The angle with respect to reaction plane, $\Delta\phi$, is for the center of the bins (7.5°, 22.5°, 37.5°, 52.5°, 67.5°, and 82.5°), the same for all centralities. For visual clarity a centrality dependent offset is introduced.

taken into account (i.e., corrected for) in the values and quoted errors of $R_{AA}(\Delta\phi)$. Thus detector effects of reaction plane resolution should not be considered in the evaluation of L_ε.

(ii) Although the participant density is used to evaluate the dimensions of the ellipse, the above analysis ignores the dependence of participant density on position in the transverse plane. Thus as a natural extension of the simple length scale in (i), for another analysis of the dependence of energy loss on $\Delta\phi$, we assume that the color-charge density in the medium is proportional to participant density (see Refs. [29,59]) and evaluate ρL, the integral of this density along the path length of the particle. This quantity is proportional to the opacity of the medium ($n = L/\lambda$) divided by some undetermined cross section. Although the integral in principle extends to infinity the participant density naturally cuts off the integral outside the collision zone.

$$\rho L = \int_0^\infty dr\ \rho_{\text{part}}(r, \Delta\phi). \tag{18}$$

To account for the possible role of LPM coherence in the energy loss process, we evaluate a similar quantity, including an extra factor of r in the integrand.

$$\rho L^2 = \int_0^\infty dr\ r\rho_{\text{part}}(r, \Delta\phi). \tag{19}$$

We note that a Bjorken $1/\tau$ expansion of the medium would approximately cancel one power of r in the above expressions. Then, ρL, might represent LPM energy

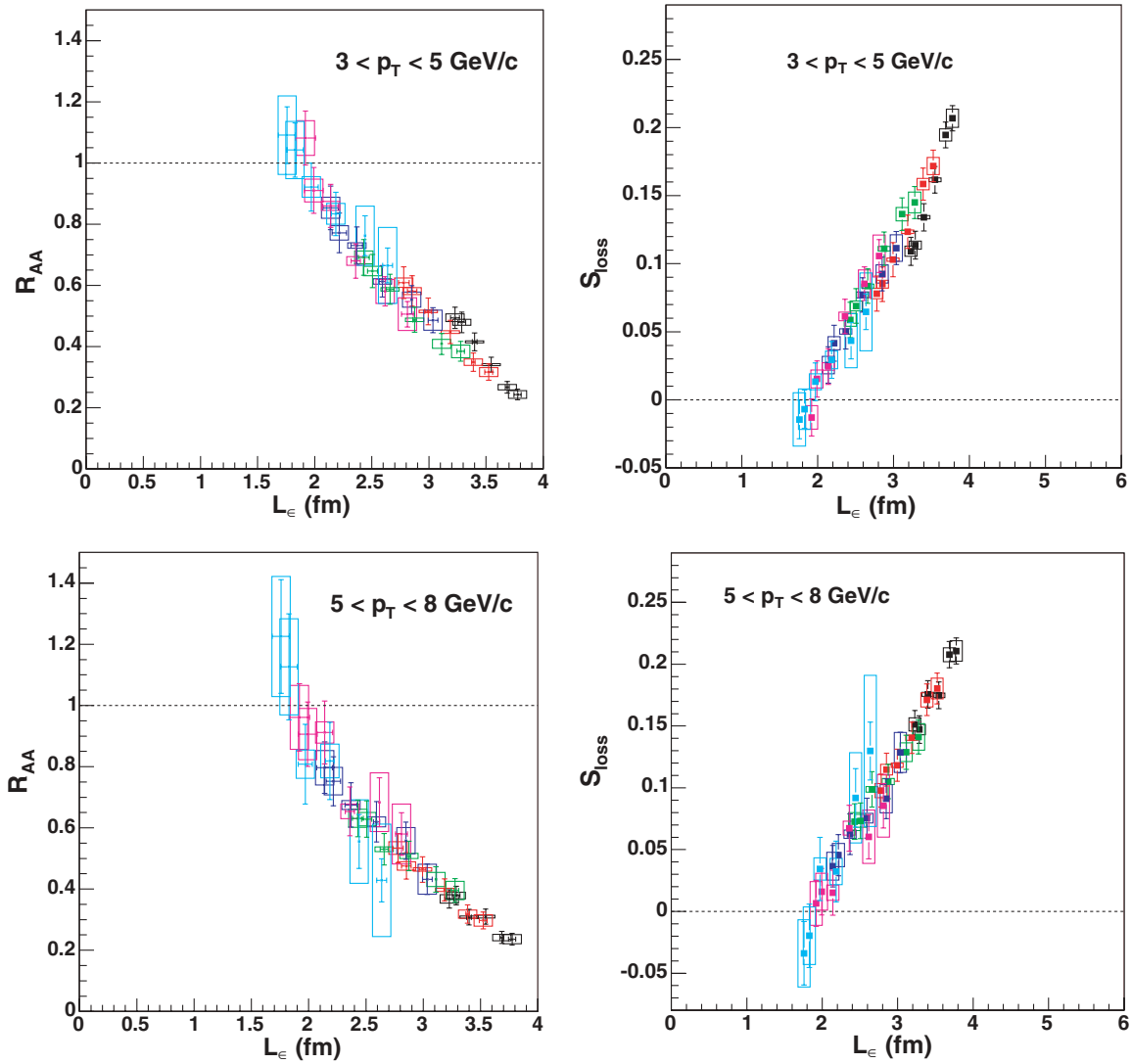

FIG. 17. (Color online) R_{AA} and S_{loss} versus L_ε whose definition is explained in the text. Each data point represents a centrality bin and $\Delta\phi$ (azimuth defined *w.r.t.* the reaction plane) bin combination. The six centrality bins are denoted by different colors as follows: cyan, 60–70%; mauve, 50–60%; blue, 40–50%; green, 30–40%; red, 20–30%; black, 0–10%. Within each centrality group, the six different data points correspond to the same $\Delta\phi$ bins as in Figs. 12–15. The height of the bars around each data point represent the systematic error in $R_{AA}(\Delta\phi)$ (S_{loss}) corresponding to L_ε.

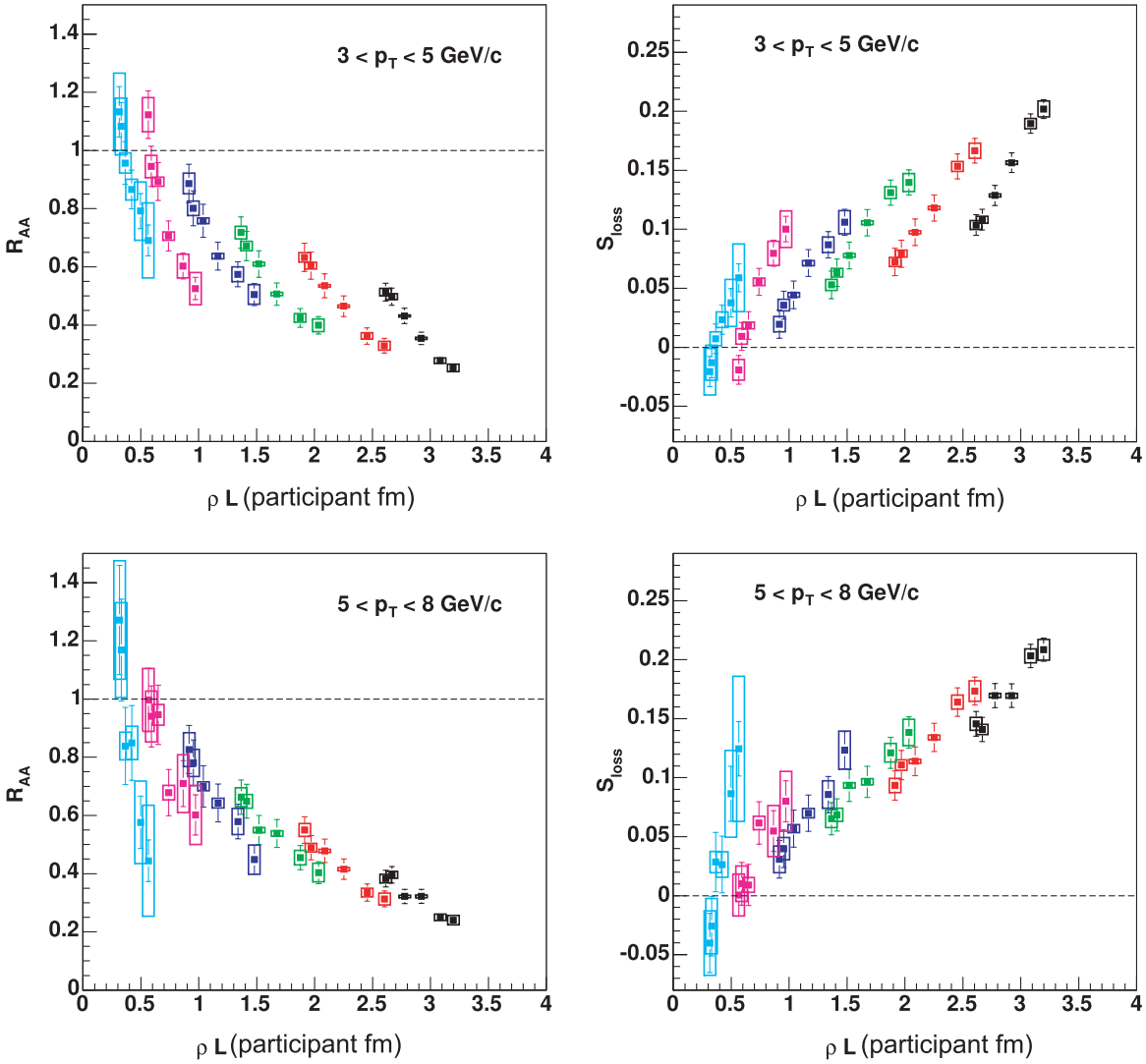

FIG. 18. (Color online) $R_{\rm AA}$ and $S_{\rm loss}$ versus ρL, the participant density-weighted path length. The units of ρL are (nucleon) participants times fm. Colors/data points as in Fig. 17.

loss in the presence of one-dimensional expansion. In the above integrals we assume all jets originate at the center of the collision region similar to our assumption for L_ε.

(iii) A final refinement on our geometrical calculation evaluates integrals like those in Eq. (18) for jet production points distributed over the collision region to better account for geometric fluctuations. We are using a Monte Carlo algorithm to sample jet production points (x_0, y_0) according to $T_{\rm AA}(x, y)$ weighting and $\Delta\phi$ angles from a uniform distribution. For each jet, we evaluate the integral of the color-charge density (assumed $\propto$ participant density as above) along the path of the parton out of the medium,

$$\rho L_{xy} = \int_0^\infty dl\ \rho_{\rm part}(x_0 + l\cos\Delta\phi,\, y_0 + l\sin\Delta\phi). \tag{20}$$

The above Monte Carlo sampling yields a distribution of ρL_{xy} values for each centrality. The larger values of ρL_{xy} correspond to larger energy loss, which means these jets will have smaller contribution to the observed yield. To take this into account, a weighting factor is applied when evaluating $\langle \rho L_{xy}\rangle$. We assume that the energy loss can be represented by our empirical energy loss, $S_{\rm loss}$ which we take to be proportional to ρL_{xy} but with an undetermined multiplicative constant, κ. We determine this constant in each centrality bin by relating $S_{\rm loss}$ to $R_{\rm AA}$ using Eq. (16) and then evaluating the survival probability of each jet through

$$P_{\rm surv}(\rho L_{xy}) = 1 - (\kappa \rho L_{xy})^{(n-2)} \tag{21}$$

and requiring that the resulting suppression summed over all sampled jets agrees with the measured $\Delta\phi$-integrated $R_{\rm AA}$ for that centrality bin. This determines the constant $\kappa(N_{\rm part})$ and allows us to

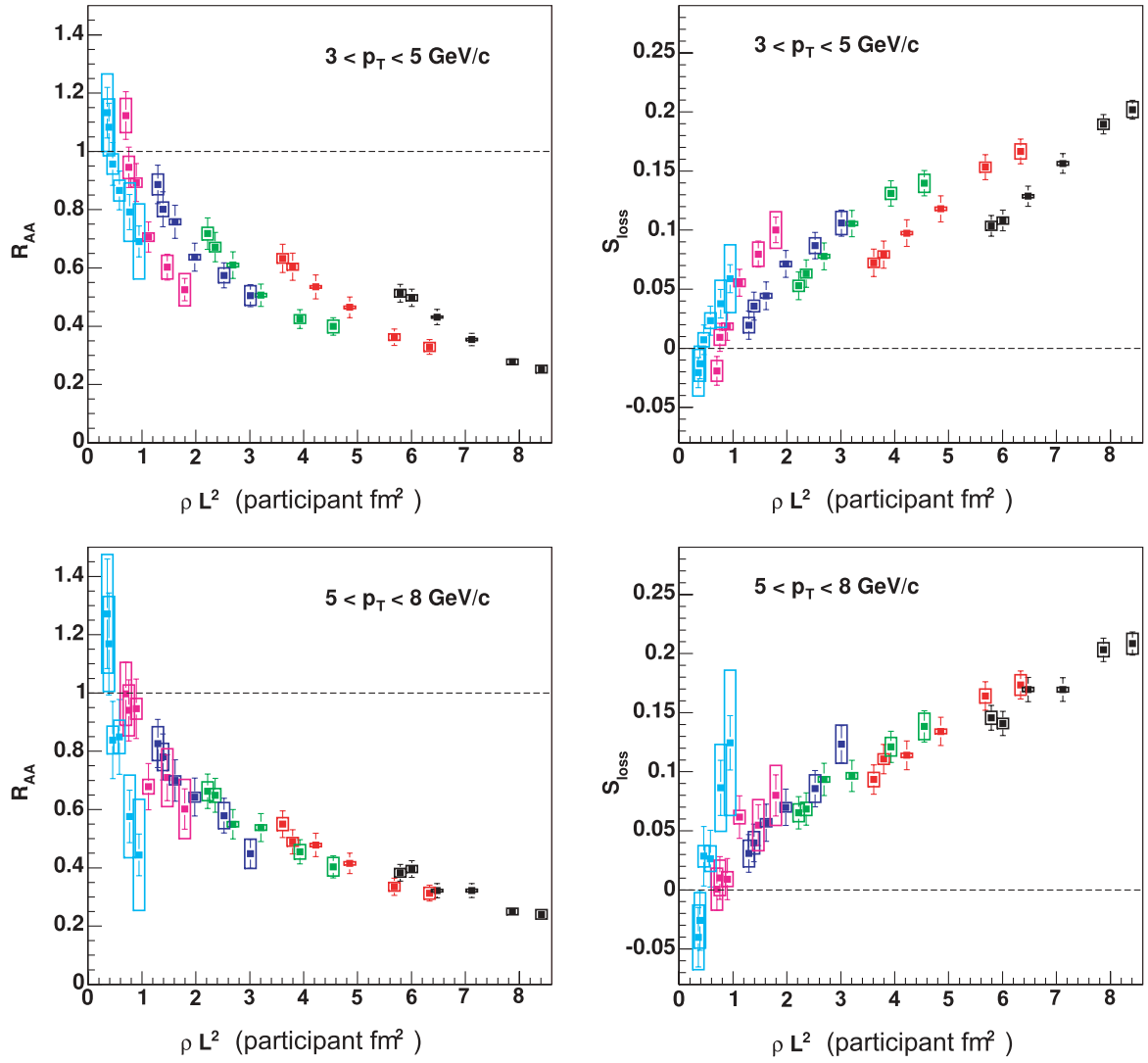

FIG. 19. (Color online) R_{AA} and S_{loss} versus ρL^2, the density-weighted path length squared. The units of ρL^2 are (nucleon) participants times fm squared. Colors/data points as in Fig. 17.

evaluate a survival probability weighted average for ρL_{xy}.

We now evaluate how well the three above-described treatments of the geometry of the parton propagation in the medium perform in providing a consistent description of the $\Delta\phi$ *and* centrality dependence of π^0 suppression.

The plots shown in Figs. 17–21 illustrate the path-length and path-density line-integral dependence of suppression using our empirical estimators. The integral of the ρ_{part} density (i.e., its normalization) is commonly called the "number of participants" N_{part}. The systematic error, mostly from N_{part}, in the estimators due to the uncertainty of the overlap geometry parameter in a centrality class is approximately 10–20%, decreasing with centrality and is not included in the figures. This uncertainty is derived by propagating the impact parameter and eccentricity uncertainties from the PHENIX Glauber MC itself [1,41].

From Figs. 17–21 it is evident that the individual centrality bins exhibit roughly parallel linear dependencies of the variables vs ρL_{xy}, etc. For the $3 < p_T < 5$ GeV/c bin these slopes are such that the curves are disjoint due to the steeper value of the slopes in each centrality group (each color in the plots) compared to the bin-to-bin trend. For the higher $5 < p_T < 8$ GeV/c bin, the slopes in the individual centralities flatten such that they follow the bin-to-bin trend much better. These are meant to be qualitative statements. We defer further quantitative tests, e.g., statistical tests, to subsequent data sets (e.g., the larger PHENIX 2004–2005 Run4 data set) with which we can improve statistical precision.

In this spirit, we note several other interesting qualitative dependencies:

(i) R_{AA} is universal as a function of L_ε for all centrality classes and both p_T ranges.

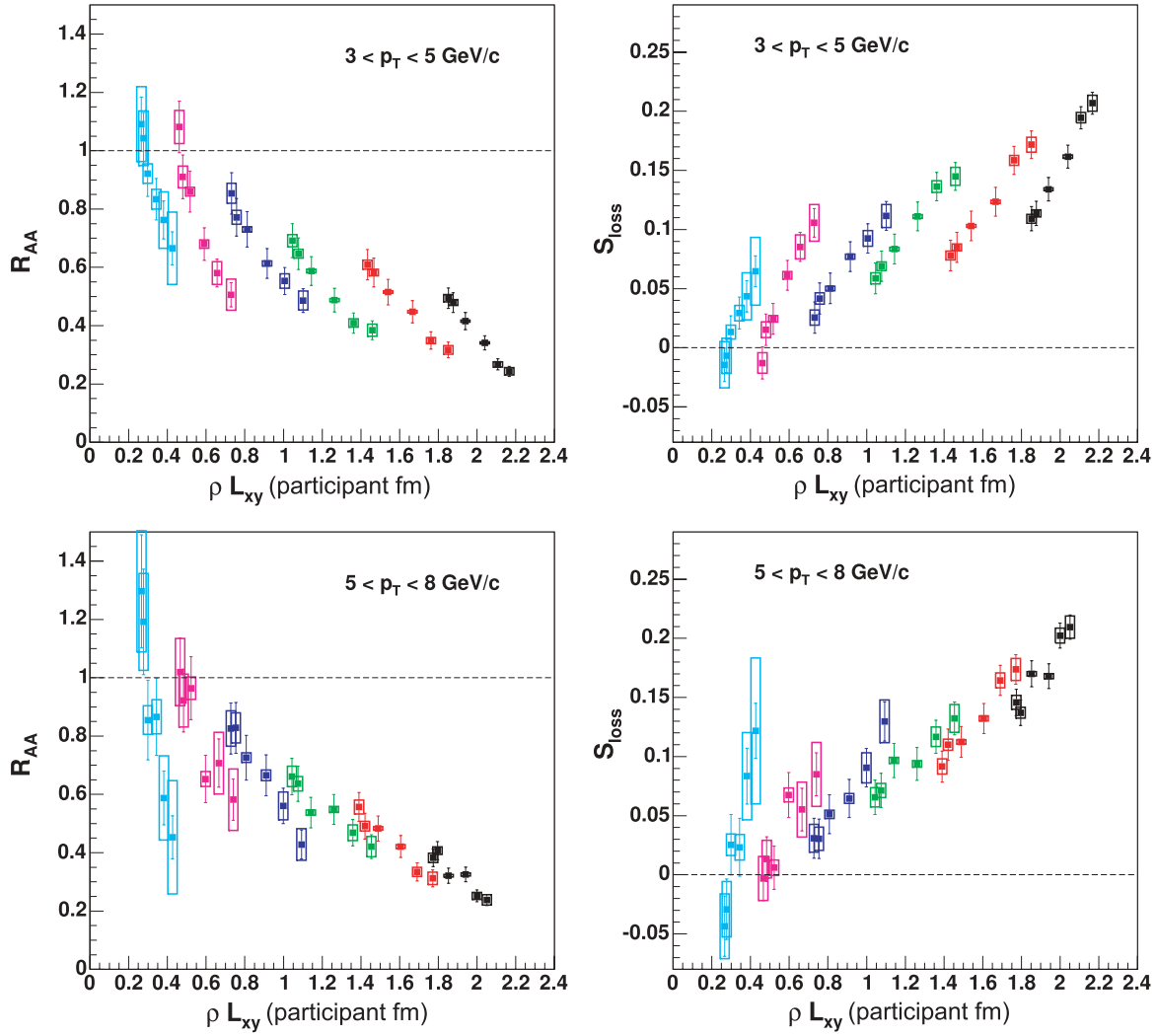

FIG. 20. (Color online) $R_{\rm AA}$ and $S_{\rm loss}$ versus ρL_{xy} whose definition is explained in the text. The units of ρL_{xy} are (nucleon) participants times fm. Colors/data points as in Fig. 17.

(ii) $S_{\rm loss}$ is universal and is a linear function of L_ε for all centrality classes and both p_T ranges.

(iii) Within our errors, we see no suppression $R_{\rm AA} \approx 1$, hence no apparent fractional energy loss $S_{\rm loss}$ for $L_\varepsilon \leqslant 2$ fm.

(iv) Neither $R_{\rm AA}$ nor $S_{\rm loss}$ is universal as a function of ρL, ρL^2, or ρL_{xy} for $3 < p_T < 5$ GeV/c.

(v) For the higher $5 < p_T < 8$ GeV/c p_T bin, $S_{\rm loss}$ ($R_{\rm AA}$) approaches universality as a function of ρL^2, ρL, and ρL_{xy} (possibly to a lesser extent for the latter two) but does not achieve the level of universality found for L_ε. The largest deviations from universality in these quantities are toward the longer axis (perpendicular to the event plane) in the more peripheral events. The dependence of $S_{\rm loss}$ is reasonably linear as a function of ρL but tends to level off at larger values of ρL^2.

(vi) When ρL is normalized by the central density $\rho_{\rm part}(0, 0) = \rho_{\rm cent}$, then $S_{\rm loss}$ ($R_{\rm AA}$) become universal in the quantities $\rho L/\rho_{\rm cent}$ for both p_T ranges with a linear dependence. The universality appears to become more exact in the higher p_T range. A similar improvement (not shown) of the qualitative universality for ρL^2 and ρL_{xy} is also observed when these quantities are scaled in the same way by $\rho_{\rm cent}$. The fact that scaling by $\rho_{\rm cent}$ improves the universality suggests that simple geometry may be more important than the details of the participant density.

The most important of these observations is the absence of suppression for the same value of $L_\varepsilon \leqslant 2$ fm for both p_T ranges, $3 \leqslant p_T \leqslant 5$ GeV/c and $5 \leqslant p_T \leqslant 8$ GeV/c. This may suggest a "formation time effect" (see Ref. [58], also considering mechanisms suggested in Ref. [60]) or some other type of emission zone which has generally not been taken into account in parton energy-loss models. The level of universal scaling with this simple geometric quantity is surprising.

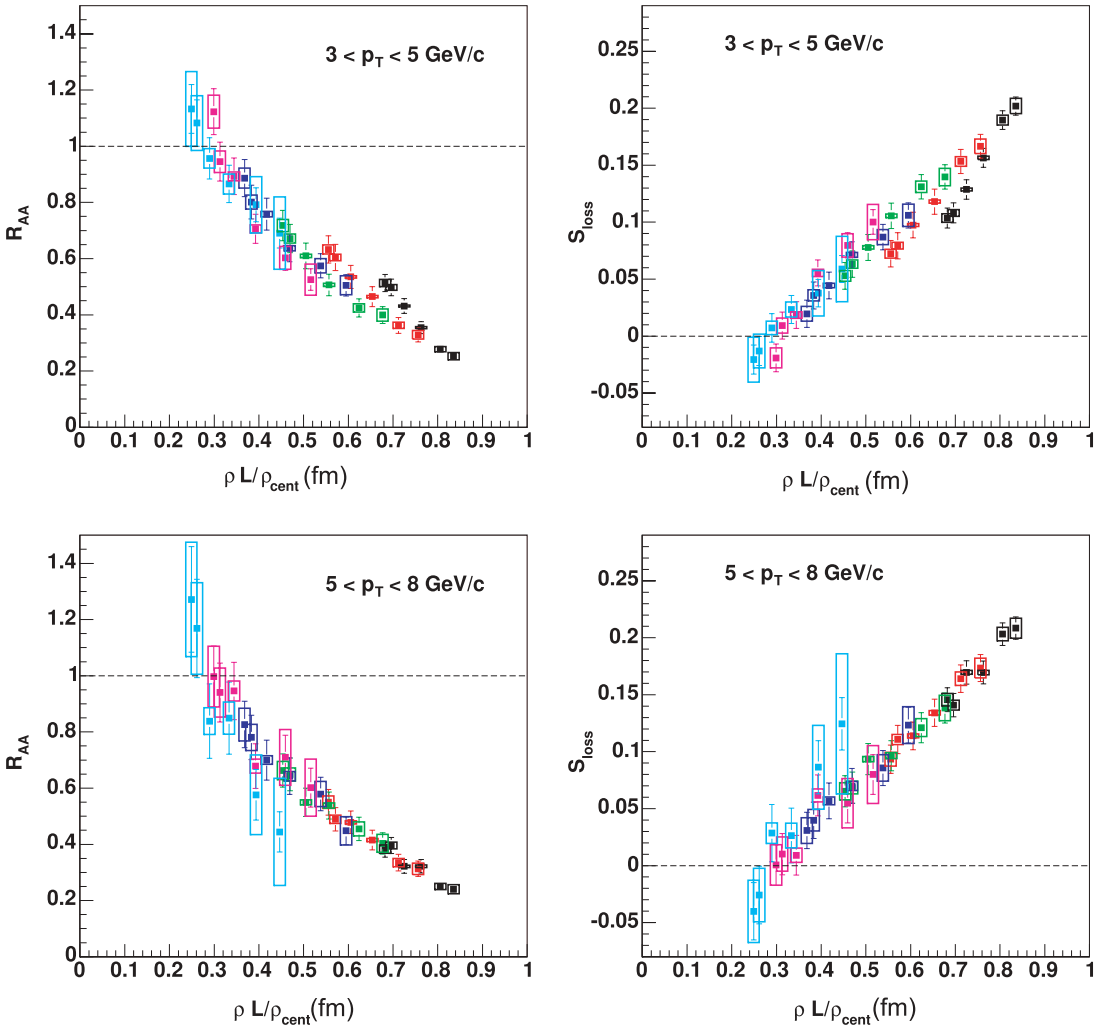

FIG. 21. (Color online) R_{AA} and S_{loss} versus ρL normalized by the most central ($b_x = b_y = 0$) density ρ_{cent}. Colors/data points as in Fig. 17.

V. SUMMARY AND CONCLUSIONS

We have presented a detailed analysis of high-p_T neutral pion suppression as a function of transverse momentum, centrality, and angle with respect to reaction plane in Au+Au collisions at $\sqrt{s_{NN}} = 200$ GeV. The π^0 yields have been measured in the range $p_T \approx 1$–14 GeV/c in nine centrality bins and compared to the π^0 differential cross sections measured in $p+p$. The ratio of Au+Au over $p+p$ spectra (scaled by the number of equivalent nucleon-nucleon scatterings) is reduced more and more for larger centralities. The resulting suppression factor is, however, independent of p_T above $p_T \approx 4$ GeV/c for all centralities. This observation can be interpreted as an indication of a constant effective fractional energy loss, fixed S_{loss} "p_T shift," in the Au+Au compared to the $p+p$ yields. The dependence of S_{loss} in the centrality as given by the number of participating nucleons N_{part} follows an approximately $N_{\mathrm{part}}^{2/3}$ law as predicted by parton energy loss models.

To constrain the "jet quenching" models with more differential observables, we have experimentally tested the path-length (L) dependence of the energy loss by exploiting the spatial azimuthal asymmetry of the system produced in noncentral nuclear collisions. Due to the characteristic almondlike shape of the overlapping matter produced in $A+A$ reactions with finite impact parameter, partons traversing the produced medium along the direction perpendicular to the reaction plane ("out-of-plane") will comparatively go through more matter than those going parallel to it ("in-plane") and therefore are expected to lose more energy.

We have studied the suppression pattern along different $\Delta\phi$ trajectories with respect to the reaction plane determined with the beam-beam counters at high rapidities. The measured $R_{\mathrm{AA}}(\Delta\phi)$ curves show clearly a factor of $\sim$2 more suppression out-of-plane ($\Delta\phi = \pi/2$) than in-plane ($\Delta\phi = 0$) for all the centralities (eccentricities) considered. Theoretical calculations of parton energy loss in an azimuthally asymmetric medium predict a significantly smaller difference between the suppression patterns for partons emitted at $\Delta\phi = 0$ and $\Delta\phi = \pi/2$ [29,32,33]. The discrepancy is stronger for more peripheral centralities (with correspondingly larger eccentricities) and challenges the underlying in-medium path-length

dependence of non-Abelian parton energy loss. Although elliptic flow effects are responsible for extra boost of in-plane (compared to out-of-plane) pions, it is unclear how such collective effects persist up to p_T values as high as $\sim$8 GeV/c. We have analyzed the observed reaction-plane and centrality dependence of the nuclear modification factor with three different versions of a Monte Carlo model with an increasing level of refinement in the description of the azimuthal propagation of the parton in the medium. For all three approaches we observe that the π^0 suppression tends to vanish for values of the path-length $L \approx 2$ fm in the two p_T ranges considered, $3 \leqslant p_T \leqslant 5$ GeV/c and $5 \leqslant p_T \leqslant 8$ GeV/c. Such a result suggests either a formation time effect or a surface emission zone that results in a p_T-independent suppression and puts additional constraints to parton energy-loss models.

ACKNOWLEDGMENTS

We thank the staff of the Collider-Accelerator and Physics Departments at Brookhaven National Laboratory and the staff of the other PHENIX participating institutions for their vital contributions. We acknowledge support from the Department of Energy, Office of Science, Nuclear Physics Division, the National Science Foundation, Abilene Christian University Research Council, Research Foundation of SUNY, and Dean of the College of Arts and Sciences, Vanderbilt University (U.S.A), Ministry of Education, Culture, Sports, Science, and Technology and the Japan Society for the Promotion of Science (Japan), Conselho Nacional de Desenvolvimento Científico e Tecnológico and Fundação de Amparo à Pesquisa do Estado de S̃ao Paulo (Brazil), Natural Science Foundation of China (People's Republic of China), Centre National de la Recherche Scientifique, Commissariat à l'Énergie Atomique, and Institut National de Physique Nucléaire et de Physique des Particules, (France), Bundesministerium für Bildung und Forschung, Deutscher Akademischer Austausch Dienst, and Alexander von Humboldt Stiftung (Germany), Hungarian National Science Fund, OTKA (Hungary), Department of Atomic Energy and Department of Science and Technology (India), Israel Science Foundation (Israel), Korea Research Foundation and Korea Science and Engineering Foundation (Korea), Russian Ministry of Industry, Science and Tekhnologies, Russian Academy of Science, Russian Ministry of Atomic Energy (Russia), VR and the Wallenberg Foundation (Sweden), the U.S. Civilian Research and Development Foundation for the Independent States of the Former Soviet Union, the US-Hungarian NSF-OTKA-MTA, the US-Israel Binational Science Foundation, and the 5th European Union TMR Marie-Curie Programme.

APPENDIX: DATA TABLES OF AU + AU $\rightarrow \pi^0 + X$ p_T SPECTRA

Tables IV–XVI show numerical data in the same units as plotted in the figures: p_T (GeV/c) and invariant yield (c^2/GeV^2).

TABLE IV. Final combined PbSc+PbGl π^0 invariant yields vs. p_T for centrality 0–10%.

p_T	Yield	Stat. error	%	Sys. error	%
1.25	3.314	2.518×10^{-2}	0.76	4.026×10^{-1}	12.15
1.75	5.981×10^{-1}	4.946×10^{-3}	0.83	6.784×10^{-2}	11.34
2.25	1.208×10^{-1}	1.253×10^{-3}	1.04	1.447×10^{-2}	11.98
2.75	2.718×10^{-2}	3.744×10^{-4}	1.38	3.521×10^{-3}	12.96
3.25	6.970×10^{-3}	1.270×10^{-4}	1.82	9.751×10^{-4}	13.99
3.75	2.158×10^{-3}	4.713×10^{-5}	2.18	2.686×10^{-4}	12.44
4.25	7.185×10^{-4}	2.133×10^{-5}	2.97	9.349×10^{-5}	13.01
4.75	2.715×10^{-4}	1.063×10^{-5}	3.92	3.575×10^{-5}	13.17
5.25	1.288×10^{-4}	5.931×10^{-6}	4.61	1.702×10^{-5}	13.21
5.75	5.417×10^{-5}	2.606×10^{-6}	4.81	7.731×10^{-6}	14.27
6.25	2.940×10^{-5}	1.560×10^{-6}	5.31	4.106×10^{-6}	13.97
6.75	1.280×10^{-5}	9.501×10^{-7}	7.43	1.922×10^{-6}	15.02
7.25	7.641×10^{-6}	6.459×10^{-7}	8.45	1.241×10^{-6}	16.24
7.75	4.630×10^{-6}	4.668×10^{-7}	10.08	7.508×10^{-7}	16.22
8.50	1.883×10^{-6}	1.809×10^{-7}	9.61	3.033×10^{-7}	16.11
9.50	1.057×10^{-6}	1.276×10^{-7}	12.07	1.952×10^{-7}	18.47
11.00	2.777×10^{-7}	4.274×10^{-8}	15.39	5.664×10^{-8}	20.39
13.00	5.941×10^{-8}	1.704×10^{-8}	28.87	1.222×10^{-8}	20.57

TABLE V. Final combined PbSc+PbGl π^0 invariant yields vs. p_T for centrality 10–20%.

p_T	Yield	Stat. error	%	Sys. error	%
1.25	2.054	1.461×10^{-2}	0.71	2.655×10^{-1}	12.93
1.75	4.137×10^{-1}	2.933×10^{-3}	0.71	4.616×10^{-2}	11.16
2.25	8.576×10^{-2}	7.654×10^{-4}	0.89	1.039×10^{-2}	12.11
2.75	2.028×10^{-2}	2.305×10^{-4}	1.14	2.612×10^{-3}	12.88
3.25	5.057×10^{-3}	7.980×10^{-5}	1.58	6.778×10^{-4}	13.40
3.75	1.665×10^{-3}	3.170×10^{-5}	1.90	1.995×10^{-4}	11.98
4.25	5.859×10^{-4}	1.511×10^{-5}	2.58	7.301×10^{-5}	12.46
4.75	2.253×10^{-4}	7.948×10^{-6}	3.53	3.003×10^{-5}	13.33
5.25	9.486×10^{-5}	4.369×10^{-6}	4.61	1.246×10^{-5}	13.14
5.75	4.651×10^{-5}	2.087×10^{-6}	4.49	6.696×10^{-6}	14.40
6.25	2.224×10^{-5}	1.249×10^{-6}	5.62	3.252×10^{-6}	14.62
6.75	1.109×10^{-5}	8.621×10^{-7}	7.78	1.899×10^{-6}	17.13
7.25	6.455×10^{-6}	5.485×10^{-7}	8.50	1.091×10^{-6}	16.90
7.75	3.568×10^{-6}	3.999×10^{-7}	11.21	7.173×10^{-7}	20.10
8.50	1.724×10^{-6}	1.718×10^{-7}	9.96	3.279×10^{-7}	19.01
9.50	6.318×10^{-7}	9.789×10^{-8}	15.49	1.144×10^{-7}	18.11
11.00	1.701×10^{-7}	3.347×10^{-8}	19.68	3.147×10^{-8}	18.51
13.00	5.093×10^{-8}	1.610×10^{-8}	31.62	9.747×10^{-9}	19.14

TABLE VI. Final combined PbSc+PbGl π^0 invariant yields vs. p_T for centrality 20–30%.

p_T	Yield	Stat. error	%	Sys. error	%
1.25	1.601	9.668×10^{-3}	0.60	1.852×10^{-1}	11.57
1.75	2.879×10^{-1}	1.911×10^{-3}	0.66	3.260×10^{-2}	11.32
2.25	6.045×10^{-2}	5.117×10^{-4}	0.85	7.416×10^{-3}	12.27
2.75	1.429×10^{-2}	1.537×10^{-4}	1.08	1.761×10^{-3}	12.32
3.25	3.983×10^{-3}	5.534×10^{-5}	1.39	5.192×10^{-4}	13.04
3.75	1.233×10^{-3}	2.340×10^{-5}	1.90	1.546×10^{-4}	12.53
4.25	4.749×10^{-4}	1.158×10^{-5}	2.44	6.115×10^{-5}	12.88
4.75	1.732×10^{-4}	5.898×10^{-6}	3.41	2.258×10^{-5}	13.04
5.25	7.761×10^{-5}	3.503×10^{-6}	4.51	1.074×10^{-5}	13.84
5.75	3.573×10^{-5}	1.627×10^{-6}	4.55	4.870×10^{-6}	13.63
6.25	1.714×10^{-5}	9.568×10^{-7}	5.58	2.389×10^{-6}	13.94
6.75	9.015×10^{-6}	6.625×10^{-7}	7.35	1.384×10^{-6}	15.36
7.25	5.146×10^{-6}	4.423×10^{-7}	8.59	8.214×10^{-7}	15.96
7.75	2.878×10^{-6}	3.267×10^{-7}	11.35	5.465×10^{-7}	18.99
8.50	1.363×10^{-6}	1.452×10^{-7}	10.65	2.517×10^{-7}	18.46
9.50	6.216×10^{-7}	8.347×10^{-8}	13.43	1.088×10^{-7}	17.50
11.00	1.825×10^{-7}	2.972×10^{-8}	16.28	3.299×10^{-8}	18.08
13.00	3.552×10^{-8}	1.267×10^{-8}	35.68	6.852×10^{-9}	19.29

TABLE VII. Final combined PbSc+PbGl π^0 invariant yields vs. p_T for centrality 30–40%.

p_T	Yield	Stat. error	%	Sys. error	%
1.25	1.040	5.648×10^{-3}	0.54	1.244×10^{-1}	11.96
1.75	1.754×10^{-1}	1.100×10^{-3}	0.63	2.001×10^{-2}	11.41
2.25	3.833×10^{-2}	3.102×10^{-4}	0.81	4.567×10^{-3}	11.91
2.75	9.610×10^{-3}	9.930×10^{-5}	1.03	1.175×10^{-3}	12.23
3.25	2.670×10^{-3}	3.764×10^{-5}	1.41	3.512×10^{-4}	13.15
3.75	8.612×10^{-4}	1.667×10^{-5}	1.94	1.097×10^{-4}	12.74
4.25	3.270×10^{-4}	8.158×10^{-6}	2.49	4.185×10^{-5}	12.80
4.75	1.252×10^{-4}	4.421×10^{-6}	3.53	1.619×10^{-5}	12.94
5.25	5.266×10^{-5}	2.822×10^{-6}	5.36	7.394×10^{-6}	14.04
5.75	2.761×10^{-5}	1.348×10^{-6}	4.88	3.839×10^{-6}	13.90
6.25	1.189×10^{-5}	8.138×10^{-7}	6.85	1.949×10^{-6}	16.39
6.75	7.115×10^{-6}	5.804×10^{-7}	8.16	1.198×10^{-6}	16.84
7.25	3.705×10^{-6}	3.972×10^{-7}	10.72	6.264×10^{-7}	16.91
7.75	1.898×10^{-6}	2.549×10^{-7}	13.42	3.307×10^{-7}	17.42
8.50	1.168×10^{-6}	1.301×10^{-7}	11.13	1.967×10^{-7}	16.83
9.50	5.043×10^{-7}	8.312×10^{-8}	16.48	9.634×10^{-8}	19.10
11.00	1.541×10^{-7}	2.748×10^{-8}	17.83	2.910×10^{-8}	18.89
13.00	2.941×10^{-8}	1.278×10^{-8}	33.46	5.621×10^{-9}	19.11

TABLE VIII. Final combined PbSc+PbGl π^0 invariant yields vs. p_T for centrality 40–50%.

p_T	Yield	Stat. error	%	Sys. error	%
1.25	6.389×10^{-1}	3.367×10^{-3}	0.53	7.216×10^{-2}	11.29
1.75	1.156×10^{-1}	6.789×10^{-4}	0.59	1.315×10^{-2}	11.37
2.25	2.442×10^{-2}	1.926×10^{-4}	0.79	2.911×10^{-3}	11.92
2.75	6.172×10^{-3}	6.521×10^{-5}	1.06	7.890×10^{-4}	12.78
3.25	1.682×10^{-3}	2.455×10^{-5}	1.46	2.194×10^{-4}	13.04
3.75	5.822×10^{-4}	1.161×10^{-5}	1.99	7.179×10^{-5}	12.33
4.25	1.927×10^{-4}	6.113×10^{-6}	3.17	2.480×10^{-5}	12.87
4.75	8.818×10^{-5}	3.476×10^{-6}	3.94	1.169×10^{-5}	13.26
5.25	3.627×10^{-5}	2.166×10^{-6}	5.97	4.995×10^{-6}	13.77
5.75	1.611×10^{-5}	9.656×10^{-7}	5.99	2.261×10^{-6}	14.04
6.25	9.635×10^{-6}	6.880×10^{-7}	7.14	1.490×10^{-6}	15.47
6.75	4.467×10^{-6}	4.278×10^{-7}	9.58	7.232×10^{-7}	16.19
7.25	2.044×10^{-6}	2.585×10^{-7}	12.65	3.197×10^{-7}	15.64
7.75	1.363×10^{-6}	2.198×10^{-7}	16.13	2.882×10^{-7}	21.15
8.50	7.878×10^{-7}	1.056×10^{-7}	13.41	1.409×10^{-7}	17.88
9.50	2.197×10^{-7}	5.630×10^{-8}	25.62	4.969×10^{-8}	22.61
11.00	1.053×10^{-7}	2.280×10^{-8}	21.66	2.116×10^{-8}	20.10
13.00	2.792×10^{-8}	1.140×10^{-8}	40.82	6.121×10^{-9}	21.92

TABLE IX. Final combined PbSc+PbGl π^0 invariant yields vs. p_T for centrality 50–60%. For points with no errors given, data value represents 90% confidence level upper limit.

p_T	Yield	Stat. error	%	Sys. error	%
1.25	3.593×10^{-1}	1.941×10^{-3}	0.54	4.022×10^{-2}	11.19
1.75	6.197×10^{-2}	4.018×10^{-4}	0.65	7.069×10^{-3}	11.41
2.25	1.309×10^{-2}	1.175×10^{-4}	0.90	1.553×10^{-3}	11.87
2.75	3.479×10^{-3}	4.211×10^{-5}	1.21	4.205×10^{-4}	12.09
3.25	1.019×10^{-3}	1.695×10^{-5}	1.66	1.291×10^{-4}	12.67
3.75	3.480×10^{-4}	8.518×10^{-6}	2.45	4.380×10^{-5}	12.59
4.25	1.329×10^{-4}	4.558×10^{-6}	3.43	1.763×10^{-5}	13.26
4.75	4.959×10^{-5}	2.434×10^{-6}	4.91	6.310×10^{-6}	12.73
5.25	2.125×10^{-5}	1.585×10^{-6}	7.46	3.032×10^{-6}	14.27
5.75	9.917×10^{-6}	7.569×10^{-7}	7.63	1.540×10^{-6}	15.52
6.25	6.127×10^{-6}	5.471×10^{-7}	8.93	9.978×10^{-7}	16.29
6.75	3.246×10^{-6}	3.392×10^{-7}	10.45	4.965×10^{-7}	15.30
7.25	1.664×10^{-6}	2.449×10^{-7}	14.72	3.102×10^{-7}	18.65
7.75	1.129×10^{-6}	1.886×10^{-7}	16.70	2.114×10^{-7}	18.72
8.50	3.362×10^{-7}	7.419×10^{-8}	22.07	6.694×10^{-8}	19.91
9.50	1.817×10^{-7}	4.619×10^{-8}	25.42	3.329×10^{-8}	18.32
11.00	2.858×10^{-8}	1.112×10^{-8}	38.89	4.803×10^{-9}	16.81
13.00	2.311×10^{-8}	—	—	—	—

TABLE X. Final combined PbSc+PbGl π^0 invariant yields vs. p_T for centrality 60–70%.

p_T	Yield	Stat. error	%	Sys. error	%
1.25	1.731×10^{-1}	1.121×10^{-3}	0.65	1.985×10^{-2}	11.47
1.75	3.022×10^{-2}	2.288×10^{-4}	0.76	3.425×10^{-3}	11.33
2.25	6.567×10^{-3}	7.011×10^{-5}	1.07	7.773×10^{-4}	11.84
2.75	1.644×10^{-3}	2.565×10^{-5}	1.56	2.057×10^{-4}	12.51
3.25	5.255×10^{-4}	1.158×10^{-5}	2.20	6.682×10^{-5}	12.72
3.75	1.801×10^{-4}	6.044×10^{-6}	3.36	2.259×10^{-5}	12.54
4.25	6.986×10^{-5}	3.184×10^{-6}	4.56	9.254×10^{-6}	13.25
4.75	2.312×10^{-5}	1.631×10^{-6}	7.06	3.101×10^{-6}	13.41
5.25	1.156×10^{-5}	1.145×10^{-6}	9.90	1.720×10^{-6}	14.87
5.75	4.884×10^{-6}	5.045×10^{-7}	10.33	7.560×10^{-7}	15.48
6.25	2.690×10^{-6}	3.650×10^{-7}	13.57	4.303×10^{-7}	16.00
6.75	1.822×10^{-6}	2.658×10^{-7}	14.58	3.369×10^{-7}	18.48
7.25	6.281×10^{-7}	1.480×10^{-7}	23.57	1.178×10^{-7}	18.76
7.75	2.446×10^{-7}	1.082×10^{-7}	44.22	4.632×10^{-8}	18.94
8.50	1.417×10^{-7}	4.482×10^{-8}	31.62	2.707×10^{-8}	19.10
9.50	1.094×10^{-7}	3.843×10^{-8}	35.14	2.106×10^{-8}	19.26
11.00	2.492×10^{-8}	1.114×10^{-8}	44.72	4.816×10^{-9}	19.33
13.00	4.728×10^{-9}	4.728×10^{-9}	100.00	9.226×10^{-10}	19.51

TABLE XI. Final combined PbSc+PbGl π^0 invariant yields vs. p_T for centrality 70–80%.

p_T	Yield	Stat. error	%	Sys. error	%
1.25	7.416×10^{-2}	5.166×10^{-4}	0.70	8.842×10^{-3}	11.92
1.75	1.282×10^{-2}	1.189×10^{-4}	0.93	1.496×10^{-3}	11.67
2.25	2.721×10^{-3}	3.774×10^{-5}	1.39	3.245×10^{-4}	11.92
2.75	7.455×10^{-4}	1.514×10^{-5}	2.03	9.131×10^{-5}	12.25
3.25	2.461×10^{-4}	7.508×10^{-6}	3.05	3.248×10^{-5}	13.20
3.75	7.200×10^{-5}	3.689×10^{-6}	5.12	9.687×10^{-6}	13.46
4.25	2.609×10^{-5}	2.071×10^{-6}	7.94	4.034×10^{-6}	15.46
4.75	1.288×10^{-5}	1.308×10^{-6}	10.15	2.161×10^{-6}	16.78
5.25	4.650×10^{-6}	7.727×10^{-7}	16.62	9.050×10^{-7}	19.46
5.75	2.416×10^{-6}	3.897×10^{-7}	16.13	4.736×10^{-7}	19.60
6.25	1.763×10^{-6}	2.713×10^{-7}	15.39	2.795×10^{-7}	15.85
6.75	5.945×10^{-7}	1.651×10^{-7}	27.77	1.221×10^{-7}	20.53
7.25	4.817×10^{-7}	1.245×10^{-7}	25.84	8.088×10^{-8}	16.79
7.75	1.344×10^{-7}	6.718×10^{-8}	50.00	2.545×10^{-8}	18.94
8.50	1.135×10^{-7}	4.012×10^{-8}	35.36	2.167×10^{-8}	19.10
9.50	4.968×10^{-8}	2.484×10^{-8}	50.00	9.568×10^{-9}	19.26
11.00	5.060×10^{-9}	5.060×10^{-9}	100.00	9.778×10^{-10}	19.33

TABLE XII. Final combined PbSc+PbGl π^0 invariant yields vs. p_T for centrality 80–92%.

p_T	Yield	Stat. error	%	Sys. error	%
1.25	3.494×10^{-2}	6.093×10^{-4}	1.74	4.504×10^{-3}	12.89
1.75	6.037×10^{-3}	1.291×10^{-4}	2.14	7.607×10^{-4}	12.60
2.25	1.319×10^{-3}	3.628×10^{-5}	2.75	1.701×10^{-4}	12.89
2.75	3.321×10^{-4}	1.243×10^{-5}	3.74	4.570×10^{-5}	13.76
3.25	1.059×10^{-4}	5.281×10^{-6}	4.99	1.483×10^{-5}	14.01
3.75	3.625×10^{-5}	2.408×10^{-6}	6.64	4.455×10^{-6}	12.29
4.25	1.233×10^{-5}	1.293×10^{-6}	10.48	1.730×10^{-6}	14.03
4.75	6.501×10^{-6}	7.988×10^{-7}	12.29	9.044×10^{-7}	13.91
5.25	3.018×10^{-6}	5.360×10^{-7}	17.76	4.224×10^{-7}	13.99
5.75	1.072×10^{-6}	2.315×10^{-7}	21.60	1.815×10^{-7}	16.94
6.25	3.265×10^{-7}	1.154×10^{-7}	35.36	5.945×10^{-8}	18.21
6.75	2.805×10^{-7}	9.918×10^{-8}	35.36	5.185×10^{-8}	18.48
7.25	2.231×10^{-7}	8.434×10^{-8}	37.80	4.187×10^{-8}	18.76
7.75	8.467×10^{-8}	4.888×10^{-8}	57.74	1.604×10^{-8}	18.94
8.50	3.602×10^{-8}	2.080×10^{-8}	57.74	6.880×10^{-9}	19.10
9.50	1.077×10^{-8}	1.077×10^{-8}	100.00	2.074×10^{-9}	19.26
11.00	4.375×10^{-9}	4.375×10^{-9}	100.00	8.455×10^{-10}	19.32

TABLE XIII. Final combined PbSc+PbGl π^0 invariant yields vs. p_T for centrality 0–92%.

p_T	Yield	Stat. error	%	Sys. error	%
1.25	1.078	3.333×10^{-3}	0.31	1.205×10^{-1}	11.17
1.75	1.928×10^{-1}	6.847×10^{-4}	0.36	2.171×10^{-2}	11.26
2.25	4.038×10^{-2}	1.742×10^{-4}	0.43	4.822×10^{-3}	11.94
2.75	9.578×10^{-3}	5.293×10^{-5}	0.55	1.202×10^{-3}	12.55
3.25	2.564×10^{-3}	1.858×10^{-5}	0.72	3.375×10^{-4}	13.17
3.75	8.115×10^{-4}	7.353×10^{-6}	0.91	1.013×10^{-4}	12.48
4.25	2.906×10^{-4}	3.475×10^{-6}	1.20	3.729×10^{-5}	12.84
4.75	1.121×10^{-4}	1.806×10^{-6}	1.61	1.466×10^{-5}	13.08
5.25	4.924×10^{-5}	1.031×10^{-6}	2.09	6.494×10^{-6}	13.19
5.75	2.240×10^{-5}	4.723×10^{-7}	2.11	3.012×10^{-6}	13.45
6.25	1.190×10^{-5}	2.909×10^{-7}	2.44	1.647×10^{-6}	13.83
6.75	5.970×10^{-6}	1.943×10^{-7}	3.25	8.494×10^{-7}	14.23
7.25	3.246×10^{-6}	1.273×10^{-7}	3.92	4.758×10^{-7}	14.65
7.75	1.715×10^{-6}	9.049×10^{-8}	5.28	2.658×10^{-7}	15.49
8.50	8.583×10^{-7}	3.892×10^{-8}	4.53	1.285×10^{-7}	14.98
9.50	3.078×10^{-7}	2.351×10^{-8}	7.64	5.041×10^{-8}	16.38
11.00	9.178×10^{-8}	7.770×10^{-9}	8.47	1.417×10^{-8}	15.44
13.00	2.380×10^{-8}	3.856×10^{-9}	16.20	3.816×10^{-9}	16.03

TABLE XIV. π^0 spectrum for combined centralities: 0–20%

p_T	Yield	Stat. error	%	Sys. error	%
1.25	2.684	1.455×10^{-2}	0.54	3.106×10^{-1}	11.58
1.75	5.059×10^{-1}	2.875×10^{-3}	0.57	5.131×10^{-2}	10.14
2.25	1.033×10^{-1}	7.343×10^{-4}	0.71	1.137×10^{-2}	11.01
2.75	2.373×10^{-2}	2.198×10^{-4}	0.93	2.837×10^{-3}	11.96
3.25	6.014×10^{-3}	7.501×10^{-5}	1.25	7.693×10^{-4}	12.79
3.75	1.912×10^{-3}	2.840×10^{-5}	1.49	2.137×10^{-4}	11.18
4.25	6.522×10^{-4}	1.307×10^{-5}	2.00	7.660×10^{-5}	11.74
4.75	2.484×10^{-4}	6.637×10^{-6}	2.67	3.055×10^{-5}	12.30
5.25	1.118×10^{-4}	3.683×10^{-6}	3.29	1.368×10^{-5}	12.23
5.75	5.034×10^{-5}	1.670×10^{-6}	3.32	6.775×10^{-6}	13.46
6.25	2.582×10^{-5}	9.994×10^{-7}	3.87	3.466×10^{-6}	13.43
6.75	1.194×10^{-5}	6.415×10^{-7}	5.37	1.825×10^{-6}	15.29
7.25	7.048×10^{-6}	4.237×10^{-7}	6.01	1.115×10^{-6}	15.82
7.75	4.099×10^{-6}	3.073×10^{-7}	7.50	7.159×10^{-7}	17.46
8.50	1.804×10^{-6}	1.247×10^{-7}	6.92	3.037×10^{-7}	16.84
9.50	8.445×10^{-7}	8.042×10^{-8}	9.52	1.491×10^{-7}	17.65
11.00	2.239×10^{-7}	2.714×10^{-8}	12.12	4.219×10^{-8}	18.84
13.00	5.517×10^{-8}	1.011×10^{-8}	18.32	1.044×10^{-8}	18.93

TABLE XV. π^0 spectrum for combined centralities: 20–60%

p_T	Yield	Stat. error	%	Sys. error	%
1.25	9.097×10^{-1}	2.963×10^{-3}	0.33	9.041×10^{-2}	9.94
1.75	1.602×10^{-1}	5.854×10^{-4}	0.37	1.570×10^{-2}	9.80
2.25	3.407×10^{-2}	1.599×10^{-4}	0.47	3.579×10^{-3}	10.51
2.75	8.386×10^{-3}	4.969×10^{-5}	0.59	9.138×10^{-4}	10.90
3.25	2.339×10^{-3}	1.832×10^{-5}	0.78	2.711×10^{-4}	11.59
3.75	7.562×10^{-4}	8.034×10^{-6}	1.06	8.387×10^{-5}	11.09
4.25	2.819×10^{-4}	4.021×10^{-6}	1.43	3.259×10^{-5}	11.56
4.75	1.090×10^{-4}	2.126×10^{-6}	1.95	1.263×10^{-5}	11.58
5.25	4.695×10^{-5}	1.310×10^{-6}	2.79	5.959×10^{-6}	12.69
5.75	2.234×10^{-5}	6.107×10^{-7}	2.73	2.907×10^{-6}	13.01
6.25	1.120×10^{-5}	3.833×10^{-7}	3.42	1.605×10^{-6}	14.33
6.75	5.961×10^{-6}	2.591×10^{-7}	4.35	8.809×10^{-7}	14.78
7.25	3.140×10^{-6}	1.732×10^{-7}	5.52	4.937×10^{-7}	15.73
7.75	1.817×10^{-6}	1.264×10^{-7}	6.96	3.292×10^{-7}	18.12
8.50	9.139×10^{-7}	5.846×10^{-8}	6.40	1.581×10^{-7}	17.30
9.50	3.818×10^{-7}	3.462×10^{-8}	9.07	7.055×10^{-8}	18.48
11.00	1.176×10^{-7}	1.194×10^{-8}	10.15	2.061×10^{-8}	17.52
13.00	2.899×10^{-8}	6.031×10^{-9}	20.80	4.497×10^{-9}	15.51

TABLE XVI. π^0 spectrum for combined centralities: 60–92%

p_T	Yield	Stat. error	%	Sys. error	%
1.25	9.037×10^{-2}	4.484×10^{-4}	0.50	9.891×10^{-3}	10.94
1.75	1.571×10^{-2}	9.400×10^{-5}	0.60	1.680×10^{-3}	10.69
2.25	3.397×10^{-3}	2.836×10^{-5}	0.83	3.765×10^{-4}	11.08
2.75	8.712×10^{-4}	1.041×10^{-5}	1.19	1.025×10^{-4}	11.76
3.25	2.808×10^{-4}	4.746×10^{-6}	1.69	3.442×10^{-5}	12.26
3.75	9.236×10^{-5}	2.390×10^{-6}	2.59	1.073×10^{-5}	11.61
4.25	3.461×10^{-5}	1.282×10^{-6}	3.70	4.593×10^{-6}	13.27
4.75	1.369×10^{-5}	7.188×10^{-7}	5.25	1.857×10^{-6}	13.57
5.25	6.198×10^{-6}	4.761×10^{-7}	7.68	9.308×10^{-7}	15.02
5.75	2.683×10^{-6}	2.173×10^{-7}	8.10	4.415×10^{-7}	16.46
6.25	1.514×10^{-6}	1.486×10^{-7}	9.81	2.414×10^{-7}	15.94
6.75	8.605×10^{-7}	1.046×10^{-7}	12.16	1.589×10^{-7}	18.46
7.25	4.305×10^{-7}	6.822×10^{-8}	15.85	7.426×10^{-8}	17.25
7.75	1.502×10^{-7}	4.381×10^{-8}	29.17	2.719×10^{-8}	18.10
8.50	9.326×10^{-8}	2.035×10^{-8}	21.82	1.706×10^{-8}	18.29
9.50	5.374×10^{-8}	1.486×10^{-8}	27.65	9.997×10^{-9}	18.60
11.00	1.101×10^{-8}	4.162×10^{-9}	37.80	2.062×10^{-9}	18.73
13.00	1.478×10^{-9}	1.478×10^{-9}	100.00	2.883×10^{-10}	19.51

[1] K. Adcox *et al.* (PHENIX), Phys. Rev. Lett. **89**, 212301 (2002).
[2] K. H. Ackermann *et al.* (STAR), Phys. Rev. Lett. **86**, 402 (2001).
[3] K. Adcox *et al.* (PHENIX), Phys. Rev. Lett. **88**, 022301 (2002).
[4] K. Adcox *et al.* (PHENIX), Phys. Lett. **B561**, 82 (2003).
[5] J. Adams *et al.* (STAR), Phys. Rev. Lett. **91**, 172302 (2003).
[6] S. S. Adler *et al.* (PHENIX), Phys. Rev. Lett. **91**, 072301 (2003).
[7] S. S. Adler *et al.* (PHENIX), Phys. Rev. C **69**, 034910 (2004).
[8] B. B. Back *et al.* (PHOBOS), Phys. Lett. **B578**, 297 (2004).
[9] I. Arsene *et al.* (BRAHMS), Phys. Rev. Lett. **91**, 072305 (2003).
[10] S. S. Adler *et al.* (PHENIX), Phys. Rev. Lett. **91**, 072303 (2003).
[11] J. Adams *et al.* (STAR), Phys. Rev. Lett. **91**, 072304 (2003).
[12] B. B. Back *et al.* (PHOBOS), Phys. Rev. Lett. **91**, 072302 (2003).
[13] S. S. Adler *et al.* (PHENIX), Phys. Rev. Lett. **96**, 202301 (2006).
[14] S. S. Adler *et al.* (PHENIX), Phys. Rev. Lett. **94**, 232301 (2005).
[15] C. Adler *et al.* (STAR), Phys. Rev. Lett. **90**, 032301 (2003).
[16] X.-N. Wang and M. Gyulassy, Phys. Rev. Lett. **68**, 1480 (1992).
[17] S. A. Bass *et al.*, Nucl. Phys. **A661**, 205 (1999).
[18] M. Gyulassy, I. Vitev, X.-N. Wang, and B.-W. Zhang, *Quark Gluon Plasma*, Vol. 3 (World Scientific, Singapore, 2003).
[19] A. Kovner and U. A. Wiedemann, *Quark Gluon Plasma*, Vol. 3 (World Scientific, Singapore, 2003).
[20] I. Vitev and M. Gyulassy, Phys. Rev. Lett. **89**, 252301 (2002).
[21] E. Wang and X.-N. Wang, Phys. Rev. Lett. **89**, 162301 (2002).
[22] K. J. Eskola, H. Honkanen, C. A. Salgado, and U. A. Wiedemann, Nucl. Phys. **A747**, 511 (2005).
[23] M. Gyulassy and L. McLerran, Nucl. Phys. **A750**, 30 (2005).
[24] X.-N. Wang, Nucl. Phys. **A750**, 98 (2005).
[25] P. Aurenche, F. Gelis, and H. Zaraket, Phys. Rev. D **62**, 096012 (2000).
[26] M. Arneodo, Phys. Rep. **240**, 301 (1994).
[27] R. Baier, D. Schiff, and B. G. Zakharov, Annu. Rev. Nucl. Part. Sci. **50**, 37 (2000).
[28] M. Gyulassy, P. Levai, and I. Vitev, Phys. Lett. **B538**, 282 (2002).
[29] A. Drees, H. Feng, and J. Jia, Phys. Rev. C **71**, 034909 (2005).
[30] M. Gyulassy, I. Vitev, and X. N. Wang, Phys. Rev. Lett. **86**, 2537 (2001).
[31] M. Gyulassy, I. Vitev, X.-N. Wang, and P. Huovinen, Phys. Lett. **B526**, 301 (2002).

[32] E. V. Shuryak, Phys. Rev. C **66**, 027902 (2002).
[33] B. Muller, Phys. Rev. C **67**, 061901(R) (2003).
[34] S. S. Adler *et al.* (PHENIX), Phys. Rev. Lett. **96**, 032302 (2006).
[35] K. Adcox *et al.* (PHENIX), Nucl. Instrum. Methods A **499**, 469 (2003).
[36] H. Hahn *et al.*, Nucl. Instrum. Methods A **499**, 245 (2003).
[37] L. Aphecetche *et al.* (PHENIX), Nucl. Instrum. Methods A **499**, 521 (2003).
[38] M. Allen *et al.* (PHENIX), Nucl. Instrum. Methods A **499**, 549 (2003).
[39] C. Adler *et al.*, Nucl. Instrum. Methods A **470**, 488 (2001).
[40] S. S. Adler *et al.* (PHENIX), Nucl. Instrum. Methods A **499**, 560 (2003).
[41] K. Adcox *et al.* (PHENIX), Phys. Rev. Lett. **86**, 3500 (2001).
[42] S. S. Adler *et al.* (PHENIX), Phys. Rev. Lett. **91**, 182301 (2003).
[43] S. S. Adler *et al.* (PHENIX), Phys. Rev. C **72**, 024901 (2005).
[44] A. M. Poskanzer and S. A. Voloshin, Phys. Rev. C **58**, 1671 (1998).
[45] J. Jia *et al.* (PHENIX), Nucl. Phys. **A783**, 501c (2007).
[46] S. S. Adler *et al.* (PHENIX), Phys. Rev. Lett. **91**, 241803 (2003).
[47] S. S. Adler *et al.* (PHENIX), Phys. Rev. Lett. **93**, 202002 (2004).
[48] T. Sjostrand *et al.*, Comput. Phys. Commun. **135**, 238 (2001).
[49] G. D. Lafferty and T. R. Wyatt, Nucl. Instrum. Methods A **355**, 541 (1995).
[50] S. Eidelman *et al.* (Particle Data Group), Phys. Lett. **B592**, 1 (2004).
[51] M. L. Miller, K. Reygers, S. J. Sanders, and P. Steinberg, to appear in Annu. Rev. Nucl. Part. Sci. **57**, 205 (2007).
[52] K. Adcox *et al.* (PHENIX Collaboration), Nucl. Phys. **A757**, 184 (2005).
[53] S. S. Adler *et al.* (PHENIX), Phys. Rev. Lett. **98**, 172302 (2007).
[54] I. Vitev, Phys. Lett. **B639**, 38 (2006).
[55] A. Dainese, C. Loizides, and G. Paic, Acta Phys. Hung. **A27**, 245 (2006).
[56] M. Jacob and P. V. Landshoff, Phys. Rep. **48**, 285 (1978).
[57] A. Dainese, C. Loizides, and G. Paic, Eur. Phys. J. C **38**, 461 (2005).
[58] V. S. Pantuev, JETP Lett. **85**, 104 (2005).
[59] A. Adil and M. Gyulassy, Phys. Rev. C **72**, 034907 (2005).
[60] E. V. Shuryak and I. Zahed, Phys. Rev. C **70**, 021901(R) (2004).

Onset of π^0 Suppression Studied in Cu + Cu Collisions at $\sqrt{s_{NN}} = 22.4$, 62.4, and 200 GeV

A. Adare,[12] S. Afanasiev,[26] C. Aidala,[13,37] N. N. Ajitanand,[54] Y. Akiba,[48,49] H. Al-Bataineh,[43] J. Alexander,[54] K. Aoki,[31,48] L. Aphecetche,[56] R. Armendariz,[43] S. H. Aronson,[7] J. Asai,[48,49] E. T. Atomssa,[32] R. Averbeck,[55] T. C. Awes,[44] B. Azmoun,[7] V. Babintsev,[22] M. Bai,[6] G. Baksay,[18] L. Baksay,[18] A. Baldisseri,[15] K. N. Barish,[8] P. D. Barnes,[34] B. Bassalleck,[42] A. T. Basye,[1] S. Bathe,[8] S. Batsouli,[44] V. Baublis,[47] C. Baumann,[38] A. Bazilevsky,[7] S. Belikov,[7] R. Bennett,[55] A. Berdnikov,[51] Y. Berdnikov,[51] A. A. Bickley,[12] J. G. Boissevain,[34] H. Borel,[15] K. Boyle,[55] M. L. Brooks,[34] H. Buesching,[7] V. Bumazhnov,[22] G. Bunce,[7,49] S. Butsyk,[34,55] C. M. Camacho,[34] S. Campbell,[55] B. S. Chang,[63] W. C. Chang,[2] J.-L. Charvet,[15] S. Chernichenko,[22] J. Chiba,[27] C. Y. Chi,[13] M. Chiu,[23] I. J. Choi,[63] R. K. Choudhury,[4] T. Chujo,[59,60] P. Chung,[54] A. Churyn,[22] V. Cianciolo,[44] Z. Citron,[55] C. R. Cleven,[20] B. A. Cole,[13] M. P. Comets,[45] P. Constantin,[34] M. Csanád,[17] T. Csörgő,[28] T. Dahms,[55] S. Dairaku,[31,48] K. Das,[19] G. David,[7] M. B. Deaton,[1] K. Dehmelt,[18] H. Delagrange,[56] A. Denisov,[22] D. d'Enterria,[13,32] A. Deshpande,[49,55] E. J. Desmond,[7] O. Dietzsch,[52] A. Dion,[55] M. Donadelli,[52] O. Drapier,[32] A. Drees,[55] K. A. Drees,[6] A. K. Dubey,[62] A. Durum,[22] D. Dutta,[4] V. Dzhordzhadze,[8] Y. V. Efremenko,[44] J. Egdemir,[55] F. Ellinghaus,[12] W. S. Emam,[8] T. Engelmore,[13] A. Enokizono,[33] H. En'yo,[48,49] S. Esumi,[59] K. O. Eyser,[8] B. Fadem,[39] D. E. Fields,[42,49] M. Finger, Jr.,[9,26] M. Finger,[9,26] F. Fleuret,[32] S. L. Fokin,[30] Z. Fraenkel,[62,*] J. E. Frantz,[55] A. Franz,[7] A. D. Frawley,[19] K. Fujiwara,[48] Y. Fukao,[31,48] T. Fusayasu,[41] S. Gadrat,[35] I. Garishvili,[57] A. Glenn,[12] H. Gong,[55] M. Gonin,[32] J. Gosset,[15] Y. Goto,[48,49] R. Granier de Cassagnac,[32] N. Grau,[13,25] S. V. Greene,[60] M. Grosse Perdekamp,[23,49] T. Gunji,[11] H.-Å. Gustafsson,[36] T. Hachiya,[21] A. Hadj Henni,[56] C. Haegemann,[42] J. S. Haggerty,[7] H. Hamagaki,[11] R. Han,[46] H. Harada,[21] E. P. Hartouni,[33] K. Haruna,[21] E. Haslum,[36] R. Hayano,[11] M. Heffner,[33] T. K. Hemmick,[55] T. Hester,[8] X. He,[20] H. Hiejima,[23] J. C. Hill,[25] R. Hobbs,[42] M. Hohlmann,[18] W. Holzmann,[54] K. Homma,[21] B. Hong,[29] T. Horaguchi,[11,48,58] D. Hornback,[57] S. Huang,[60] T. Ichihara,[48,49] R. Ichimiya,[48] Y. Ikeda,[59] K. Imai,[31,48] J. Imrek,[16] M. Inaba,[59] Y. Inoue,[50,48] D. Isenhower,[1] L. Isenhower,[1] M. Ishihara,[48] T. Isobe,[11] M. Issah,[54] A. Isupov,[26] D. Ivanischev,[47] B. V. Jacak,[55,+] J. Jia,[13] J. Jin,[13] O. Jinnouchi,[49] B. M. Johnson,[7] K. S. Joo,[40] D. Jouan,[45] F. Kajihara,[11] S. Kametani,[11,48,61] N. Kamihara,[48,49] J. Kamin,[55] M. Kaneta,[49] J. H. Kang,[63] H. Kanou,[48,58] J. Kapustinsky,[34] D. Kawall,[37,49] A. V. Kazantsev,[30] T. Kempel,[25] A. Khanzadeev,[47] K. M. Kijima,[21] J. Kikuchi,[61] B. I. Kim,[29] D. H. Kim,[40] D. J. Kim,[63] E. Kim,[53] S. H. Kim,[63] E. Kinney,[12] K. Kiriluk,[12] A. Kiss,[17] E. Kistenev,[7] A. Kiyomichi,[48] J. Klay,[33] C. Klein-Boesing,[38] L. Kochenda,[47] V. Kochetkov,[22] B. Komkov,[47] M. Konno,[59] J. Koster,[23] D. Kotchetkov,[8] A. Kozlov,[62] A. Král,[14] A. Kravitz,[13] J. Kubart,[9,24] G. J. Kunde,[34] N. Kurihara,[11] K. Kurita,[50,48] M. Kurosawa,[48] M. J. Kweon,[29] Y. Kwon,[57,63] G. S. Kyle,[43] R. Lacey,[54] Y.-S. Lai,[13] Y. S. Lai,[13] J. G. Lajoie,[25] D. Layton,[23] A. Lebedev,[25] D. M. Lee,[34] K. B. Lee,[29] M. K. Lee,[63] T. Lee,[53] M. J. Leitch,[34] M. A. L. Leite,[52] B. Lenzi,[52] P. Liebing,[49] T. Liška,[14] A. Litvinenko,[26] H. Liu,[43] M. X. Liu,[34] X. Li,[10] B. Love,[60] D. Lynch,[7] C. F. Maguire,[60] Y. I. Makdisi,[6,7] A. Malakhov,[26] M. D. Malik,[42] V. I. Manko,[30] E. Mannel,[13] Y. Mao,[46,48] L. Mašek,[9,24] H. Masui,[59] F. Matathias,[13] M. McCumber,[55] P. L. McGaughey,[34] N. Means,[55] B. Meredith,[23] Y. Miake,[59] P. Mikeš,[9,24] K. Miki,[59] T. E. Miller,[60] A. Milov,[7,55] S. Mioduszewski,[7] M. Mishra,[3] J. T. Mitchell,[7] M. Mitrovski,[54] A. K. Mohanty,[4] Y. Morino,[11] A. Morreale,[8] D. P. Morrison,[7] T. V. Moukhanova,[30] D. Mukhopadhyay,[60] J. Murata,[50,48] S. Nagamiya,[27] Y. Nagata,[59] J. L. Nagle,[12] M. Naglis,[62] M. I. Nagy,[17] I. Nakagawa,[48,49] Y. Nakamiya,[21] T. Nakamura,[21] K. Nakano,[48,58] J. Newby,[33] M. Nguyen,[55] T. Niita,[59] B. E. Norman,[34] R. Nouicer,[5] A. S. Nyanin,[30] E. O'Brien,[7] S. X. Oda,[11] C. A. Ogilvie,[25] H. Ohnishi,[48] H. Okada,[31,48] K. Okada,[49] M. Oka,[59] O. O. Omiwade,[1] Y. Onuki,[48] A. Oskarsson,[36] M. Ouchida,[21] K. Ozawa,[11] R. Pak,[5,7] D. Pal,[60] A. P. T. Palounek,[34] V. Pantuev,[55] V. Papavassiliou,[43] J. Park,[53] W. J. Park,[29] S. F. Pate,[43] H. Pei,[25] J.-C. Peng,[23] H. Pereira,[15] V. Peresedov,[26] D. Yu. Peressounko,[30] C. Pinkenburg,[7] M. L. Purschke,[7] A. K. Purwar,[34] H. Qu,[20] J. Rak,[42] A. Rakotozafindrabe,[32] I. Ravinovich,[62] K. F. Read,[44,57] S. Rembeczki,[18] M. Reuter,[55] K. Reygers,[38] V. Riabov,[47] Y. Riabov,[47] D. Roach,[60] G. Roche,[35] S. D. Rolnick,[8] A. Romana,[32,*] M. Rosati,[25] S. S. E. Rosendahl,[36] P. Rosnet,[35] P. Rukoyatkin,[26] P. Ružička,[24] V. L. Rykov,[48] B. Sahlmueller,[38] N. Saito,[31,48,49] T. Sakaguchi,[7] S. Sakai,[59] K. Sakashita,[48,58] H. Sakata,[21] V. Samsonov,[47] S. Sato,[27] T. Sato,[59] S. Sawada,[27] K. Sedgwick,[8] J. Seele,[12] R. Seidl,[23] A. Yu. Semenov,[25] V. Semenov,[22] R. Seto,[8] D. Sharma,[62] I. Shein,[22] A. Shevel,[47,54] T.-A. Shibata,[48,58] K. Shigaki,[21] M. Shimomura,[59] K. Shoji,[31,48] P. Shukla,[4] A. Sickles,[7,55] C. L. Silva,[52] D. Silvermyr,[44] C. Silvestre,[15] K. S. Sim,[29] B. K. Singh,[3] C. P. Singh,[3] V. Singh,[3] S. Skutnik,[25] M. Slunečka,[9,26] A. Soldatov,[22] R. A. Soltz,[33] W. E. Sondheim,[34] S. P. Sorensen,[57] I. V. Sourikova,[7] F. Staley,[15] P. W. Stankus,[44] E. Stenlund,[36] M. Stepanov,[43] A. Ster,[28] S. P. Stoll,[7] T. Sugitate,[21] C. Suire,[45] A. Sukhanov,[5] J. Sziklai,[28] T. Tabaru,[49] S. Takagi,[59] E. M. Takagui,[52] A. Taketani,[48,49] R. Tanabe,[59] Y. Tanaka,[41] K. Tanida,[48,49] M. J. Tannenbaum,[7] A. Taranenko,[54] P. Tarján,[16] H. Themann,[55] T. L. Thomas,[42]

M. Togawa,[31,48] A. Toia,[55] J. Tojo,[48] L. Tomášek,[24] Y. Tomita,[59] H. Torii,[21,48] R. S. Towell,[1] V-N. Tram,[32] I. Tserruya,[62] Y. Tsuchimoto,[21] C. Vale,[25] H. Valle,[60] H. W. vanHecke,[34] A. Veicht,[23] J. Velkovska,[60] R. Vertesi,[16] A. A. Vinogradov,[30] M. Virius,[14] V. Vrba,[24] E. Vznuzdaev,[47] M. Wagner,[31,48] D. Walker,[55] X. R. Wang,[43] Y. Watanabe,[48,49] F. Wei,[25] J. Wessels,[38] S. N. White,[7] D. Winter,[13] C. L. Woody,[7] M. Wysocki,[12] W. Xie,[49] Y. L. Yamaguchi,[61] K. Yamaura,[21] R. Yang,[23] A. Yanovich,[22] Z. Yasin,[8] J. Ying,[20] S. Yokkaichi,[48,49] G. R. Young,[44] I. Younus,[42] I. E. Yushmanov,[30] W. A. Zajc,[13] O. Zaudtke,[38] C. Zhang,[44] S. Zhou,[10] J. Zimányi,[28,*] and L. Zolin[26]

(PHENIX Collaboration)

[1]*Abilene Christian University, Abilene, Texas 79699, USA*
[2]*Institute of Physics, Academia Sinica, Taipei 11529, Taiwan*
[3]*Department of Physics, Banaras Hindu University, Varanasi 221005, India*
[4]*Bhabha Atomic Research Centre, Bombay 400 085, India*
[5]*Chemistry Department, Brookhaven National Laboratory, Upton, New York 11973-5000, USA*
[6]*Collider-Accelerator Department, Brookhaven National Laboratory, Upton, New York 11973-5000, USA*
[7]*Physics Department, Brookhaven National Laboratory, Upton, New York 11973-5000, USA*
[8]*University of California–Riverside, Riverside, California 92521, USA*
[9]*Charles University, Ovocný trh 5, Praha 1, 116 36, Prague, Czech Republic*
[10]*China Institute of Atomic Energy (CIAE), Beijing, People's Republic of China*
[11]*Center for Nuclear Study, Graduate School of Science, University of Tokyo, 7-3-1 Hongo, Bunkyo, Tokyo 113-0033, Japan*
[12]*University of Colorado, Boulder, Colorado 80309, USA*
[13]*Columbia University, New York, New York 10027, USA and Nevis Laboratories, Irvington, New York 10533, USA*
[14]*Czech Technical University, Zikova 4, 166 36 Prague 6, Czech Republic*
[15]*Dapnia, CEA Saclay, F-91191, Gif-sur-Yvette, France*
[16]*Debrecen University, H-4010 Debrecen, Egyetem tér 1, Hungary*
[17]*ELTE, Eötvös Loránd University, H-1117 Budapest, Pázmány P. s. 1/A, Hungary*
[18]*Florida Institute of Technology, Melbourne, Florida 32901, USA*
[19]*Florida State University, Tallahassee, Florida 32306, USA*
[20]*Georgia State University, Atlanta, Georgia 30303, USA*
[21]*Hiroshima University, Kagamiyama, Higashi-Hiroshima 739-8526, Japan*
[22]*IHEP Protvino, State Research Center of Russian Federation, Institute for High Energy Physics, Protvino, 142281, Russia*
[23]*University of Illinois at Urbana-Champaign, Urbana, Illinois 61801, USA*
[24]*Institute of Physics, Academy of Sciences of the Czech Republic, Na Slovance 2, 182 21 Prague 8, Czech Republic*
[25]*Iowa State University, Ames, Iowa 50011, USA*
[26]*Joint Institute for Nuclear Research, 141980 Dubna, Moscow Region, Russia*
[27]*KEK, High Energy Accelerator Research Organization, Tsukuba, Ibaraki 305-0801, Japan*
[28]*KFKI Research Institute for Particle and Nuclear Physics of the Hungarian Academy of Sciences (MTA KFKI RMKI), H-1525 Budapest 114, PO Box 49, Budapest, Hungary*
[29]*Korea University, Seoul, 136-701, Korea*
[30]*Russian Research Center "Kurchatov Institute," Moscow, Russia*
[31]*Kyoto University, Kyoto 606-8502, Japan*
[32]*Laboratoire Leprince-Ringuet, Ecole Polytechnique, CNRS-IN2P3, Route de Saclay, F-91128, Palaiseau, France*
[33]*Lawrence Livermore National Laboratory, Livermore, California 94550, USA*
[34]*Los Alamos National Laboratory, Los Alamos, New Mexico 87545, USA*
[35]*LPC, Université Blaise Pascal, CNRS-IN2P3, Clermont-Fd, 63177 Aubiere Cedex, France*
[36]*Department of Physics, Lund University, Box 118, SE-221 00 Lund, Sweden*
[37]*Department of Physics, University of Massachusetts, Amherst, Massachusetts 01003-9337, USA*
[38]*Institut für Kernphysik, University of Muenster, D-48149 Muenster, Germany*
[39]*Muhlenberg College, Allentown, Pennsylvania 18104-5586, USA*
[40]*Myongji University, Yongin, Kyonggido 449-728, Korea*
[41]*Nagasaki Institute of Applied Science, Nagasaki-shi, Nagasaki 851-0193, Japan*
[42]*University of New Mexico, Albuquerque, New Mexico 87131, USA*
[43]*New Mexico State University, Las Cruces, New Mexico 88003, USA*
[44]*Oak Ridge National Laboratory, Oak Ridge, Tennessee 37831, USA*
[45]*IPN-Orsay, Universite Paris Sud, CNRS-IN2P3, BP1, F-91406, Orsay, France*
[46]*Peking University, Beijing, People's Republic of China*
[47]*PNPI, Petersburg Nuclear Physics Institute, Gatchina, Leningrad region, 188300, Russia*
[48]*RIKEN, The Institute of Physical and Chemical Research, Wako, Saitama 351-0198, Japan*
[49]*RIKEN BNL Research Center, Brookhaven National Laboratory, Upton, New York 11973-5000, USA*

[50]Physics Department, Rikkyo University, 3-34-1 Nishi-Ikebukuro, Toshima, Tokyo 171-8501, Japan
[51]Saint Petersburg State Polytechnic University, St. Petersburg, Russia
[52]Universidade de São Paulo, Instituto de Física, Caixa Postal 66318, São Paulo CEP05315-970, Brazil
[53]System Electronics Laboratory, Seoul National University, Seoul, Korea
[54]Chemistry Department, Stony Brook University, SUNY, Stony Brook, New York 11794-3400, USA
[55]Department of Physics and Astronomy, Stony Brook University, SUNY, Stony Brook, New York 11794, USA
[56]SUBATECH (Ecole des Mines de Nantes, CNRS-IN2P3, Université de Nantes) BP 20722 - 44307, Nantes, France
[57]University of Tennessee, Knoxville, Tennessee 37996, USA
[58]Department of Physics, Tokyo Institute of Technology, Oh-okayama, Meguro, Tokyo 152-8551, Japan
[59]Institute of Physics, University of Tsukuba, Tsukuba, Ibaraki 305, Japan
[60]Vanderbilt University, Nashville, Tennessee 37235, USA
[61]Waseda University, Advanced Research Institute for Science and Engineering, 17 Kikui-cho, Shinjuku-ku, Tokyo 162-0044, Japan
[62]Weizmann Institute, Rehovot 76100, Israel
[63]Yonsei University, IPAP, Seoul 120-749, Korea
(Received 30 January 2008; published 15 October 2008)

Neutral pion transverse momentum (p_T) spectra at midrapidity ($|y| \lesssim 0.35$) were measured in Cu + Cu collisions at $\sqrt{s_{NN}} = 22.4$, 62.4, and 200 GeV. Relative to π^0 yields in $p + p$ collisions scaled by the number of inelastic nucleon-nucleon collisions ($N_{\rm coll}$) the π^0 yields for $p_T \gtrsim 2$ GeV/c in central Cu + Cu collisions are suppressed at 62.4 and 200 GeV whereas an enhancement is observed at 22.4 GeV. A comparison with a jet-quenching model suggests that final state parton energy loss dominates in central Cu + Cu collisions at 62.4 and 200 GeV, while the enhancement at 22.4 GeV is consistent with nuclear modifications in the initial state alone.

DOI: 10.1103/PhysRevLett.101.162301 PACS numbers: 25.75.Dw

The measurement of particle yields at high transverse momentum ($p_T \gtrsim 2$ GeV/c) has played a key role in characterizing the medium created in nucleus-nucleus collisions at the Relativistic Heavy Ion Collider (RHIC) [1,2]. Hadrons produced at sufficiently high p_T result from the interaction of quarks and gluons with high momentum transfer (''hard scattering'') which can be described by perturbative quantum chromodynamics (pQCD). These hadrons are produced as particle jets in the fragmentation of the scattered partons. A scattered parton propagating through a medium with high color-charge density such as a quark-gluon plasma loses energy (''jet quenching'') resulting in hadron yields at high p_T being suppressed [3]. Such a suppression was indeed observed in central Au + Au collisions at $\sqrt{s_{NN}} = 130$ and 200 GeV at RHIC, providing evidence for large color-charge densities in these systems [4–6]. This Letter presents results on the onset of π^0 suppression in Cu + Cu collisions as a function of $\sqrt{s_{NN}}$.

Characteristic properties of the suppression of hadrons at high p_T, e.g., the dependence on p_T and centrality, were studied in detail in Au + Au collisions at $\sqrt{s_{NN}} =$ 200 GeV [5]. However, the energy dependence of hadron production in $A + A$ collisions as predicted by jet-quenching models [7–9] is not well constrained by measurements. Work in this direction was presented in [10–13]. To study the energy dependence of jet quenching it is desirable to measure identified particles in the same colliding system over a large $\sqrt{s_{NN}}$ range and to compare to $p + p$ reference data measured in the same experimental setup. Identified particles provide an advantage over unidentified hadrons in that the interpretation is not complicated by the different contributions from baryons and mesons. The study of Cu + Cu collisions is particularly useful because hadron suppression in Au + Au collisions is observed for rather peripheral collisions with a number of participating nucleons of $N_{\rm part} \sim 50$–100 [5]. This $N_{\rm part}$ range can be studied with reduced uncertainties in $N_{\rm coll}$ with the smaller ^{63}Cu nucleus.

A critical parameter in jet-quenching models is the initial color-charge density of the medium. By studying Cu + Cu collisions in the range $\sqrt{s_{NN}} \sim 20$–200 GeV this parameter can be varied with essentially no change in transverse size and shape of the reaction zone. Moreover, the enhancement of hadron yields due to multiple soft scattering of the incoming partons (''nuclear k_T'' or ''Cronin enhancement'') is expected to increase towards smaller $\sqrt{s_{NN}}$ [8], thus the interplay between this enhancement and the suppression due to parton energy loss can be studied.

In this Letter we present π^0 yields for Cu + Cu collisions at $\sqrt{s_{NN}} = 22.4$, 62.4, and 200 GeV. Reference data for $p + p$ collisions at $\sqrt{s} = 62.4$ and 200 GeV were taken with the same experiment [14,15]. At $\sqrt{s_{NN}} = 22.4$ GeV a $p + p$ reference was obtained from a parametrization of the world's data on pion production [16].

Neutral pions were measured via their $\pi^0 \to \gamma\gamma$ decay branch with the electromagnetic calorimeter (EMCal) of the PHENIX experiment [17]. The EMCal comprises two calorimeter types: 6 sectors of a lead scintillator sampling calorimeter (PbSc) and 2 sectors of a lead glass Cherenkov calorimeter (PbGl). Each sector is located ~5 m from the beam line and subtends $|\eta| < 0.35$ in pseudorapidity and

$\Delta\varphi = 22.5°$ in azimuth. Owing to the PbSc (PbGl) granularity of $\Delta\eta \times \Delta\varphi = 0.011 \times 0.011$ (0.008×0.008) the probability that the two photon showers from a π^0 decay result in partially overlapping clusters is negligible up to a π^0 p_T of 12 GeV/c (15 GeV/c). The energy calibration of the EMCal was corroborated by the position of the π^0 invariant mass peak, the energy deposited by minimum ionizing charged particles traversing the EMCal (PbSc), and the correlation between the measured momenta of electron and positron tracks identified by the ring-imaging Cherenkov detector and the associated energy deposited in the EMCal. These studies showed that the accuracy of the energy measurement was better than 1.5%.

The total number of analyzed Cu + Cu events for the three energies is shown in Table I. The minimum bias (MB) trigger for all reaction systems was provided by beam-beam counters (BBCs) located at $3.0 \lesssim |\eta| \lesssim 3.9$. The reaction vertex along the beam axis, determined from the arrival time differences in the BBCs, was required to be in the range $|z| \leq 30$ cm. An additional high-p_T trigger was employed in Cu + Cu at $\sqrt{s_{NN}} = 200$ GeV. This trigger was based on the analog energy signal measured in overlapping 4×4 towers of the EMCal in coincidence with the MB trigger condition. It reached an efficiency plateau for photon energies $E \gtrsim 4$ GeV.

The centrality selection in Cu + Cu at $\sqrt{s_{NN}} = 200$ GeV and $\sqrt{s_{NN}} = 62$ GeV was based on the charge signal of the BBCs which is proportional to the charged-particle multiplicity. The BBC trigger efficiency ($\varepsilon_{\text{trig}}$) for these systems was determined with the aid of the HIJING event generator and a full GEANT simulation of the BBC response (see Table I). At $\sqrt{s_{NN}} = 22.4$ GeV centrality classes were defined based on the charged-particle multiplicity N_{PC1} measured with the pad chamber (PC1) detector ($|\eta| < 0.35$). The measured N_{PC1} distribution was accurately reproduced in a Glauber Monte Carlo calculation [18] and centrality classes were determined by identical cuts on the measured and simulated PC1 multiplicities. In the Glauber calculation N_{PC1} was assumed to scale with N_{part}^{α} and multiplicity fluctuations were described with a negative binomial distribution. Varying α and the negative binomial distribution parameters, the measured N_{PC1} distribution could be reproduced with $\varepsilon_{\text{trig}}$ values between 0.75 and 0.90. Possible autocorrelations between N_{PC1} and the π^0 yield resulting from measuring these quantities in the same pseudorapidity range were studied with HIJING and found to be negligible. Results of the Glauber calculations for $\sqrt{s_{NN}} = 22.4$, 62.4, and 200 GeV are shown in Table II.

Neutral pion yields were measured on a statistical basis by calculating the invariant mass of all photon pairs in a given event and counting those within the π^0 mass range. The background of combinatorial pairs was calculated by pairing photon hits from different events. Only photon pairs with an energy asymmetry $|E_1 - E_2|/(E_1 + E_2) < 0.7$ were accepted. The raw π^0 yields were corrected for the geometrical acceptance and reconstruction efficiency. The latter takes into account the loss of π^0's due to photon identification cuts, the energy asymmetry cut, inactive detector areas, and photon conversions. Moreover, it corrects the distortion of the π^0 spectrum which results from the finite energy resolution in conjunction with the steeply falling spectra and shower overlap effects. The reconstruction efficiency was determined in a Monte Carlo simulation and is typically on the order of $\varepsilon_{\pi^0} \approx 0.7$–$0.8$. For Cu + Cu at $\sqrt{s_{NN}} = 200$ GeV the transition between the minimum bias and the high-p_T sample occurs at $p_T = 8$ GeV/c. The final spectra were calculated as the weighted average of the PbSc and PbGl results, which agree within 15%, a deviation well covered by the uncertainties.

The main systematic uncertainties of the π^0 spectra result from the π^0 peak extraction, the reconstruction efficiency, and the EMCal energy calibration. For $p_T \gtrsim 2$ GeV/c the peak extraction uncertainty is ~4% for all systems, approximately independent of p_T. The uncertainty in the reconstruction efficiency was estimated to be ~15% for the three Cu + Cu analyses. The uncertainty in the EMCal energy scale of 1.5% translates into an uncer-

TABLE I. Cu + Cu data sets presented with the number of analyzed events. For the data taken with the high-p_T trigger, the number of equivalent minimum bias events is given. At 22.4 GeV the given $\varepsilon_{\text{trig}}$ range indicates the uncertainty.

$\sqrt{s_{NN}}$ (GeV)	$\varepsilon_{\text{trig}}$	$N_{\text{evt}}^{\text{MB}}$	$N_{\text{evt}}^{\text{high}-p_T}$ ($N_{\text{evt}}^{\text{sampled}}$)
22.4	75%–90%	5.8×10^6	···
62.4	(88 ± 4)%	192×10^6	···
200	(94 ± 2)%	794×10^6	15.5×10^6 (4720×10^6)

TABLE II. Glauber Monte Carlo calculations for Cu + Cu collisions at 22.4, 62.4, and 200 GeV using inelastic cross sections of 32.3, 35.6, and 42 mb, respectively. The N_{coll} systematic uncertainty at 62.4 and 200 GeV is ~12%, almost independent of N_{coll}. At 22.4 GeV the relative uncertainty of N_{coll} can be parametrized as $0.094 + 0.173e^{-0.0272N_{\text{coll}}}$.

	22.4 GeV		62.4 GeV		200 GeV	
	$\langle N_{\text{part}} \rangle$	$\langle N_{\text{coll}} \rangle$	$\langle N_{\text{part}} \rangle$	$\langle N_{\text{coll}} \rangle$	$\langle N_{\text{part}} \rangle$	$\langle N_{\text{coll}} \rangle$
0%–10%	92.2	140.7	93.3	152.3	98.2	182.7
10%–20%	67.8	93.3	71.1	105.5	73.6	121.1
20%–30%	48.3	59.7	51.3	67.8	53.0	76.1
30%–40%	34.1	38.0	36.2	42.6	37.3	47.1
40%–50%	23.1	22.9	24.9	26.2	25.4	28.1
50%–60%	15.5	13.9	16.1	15.0	16.7	16.2
60%–70%	···	···	···	···	10.4	9.0
70%–80%	···	···	···	···	6.4	4.9
80%–94%	···	···	···	···	3.6	2.4
60%–88%	···	···	7.0	5.5	···	···

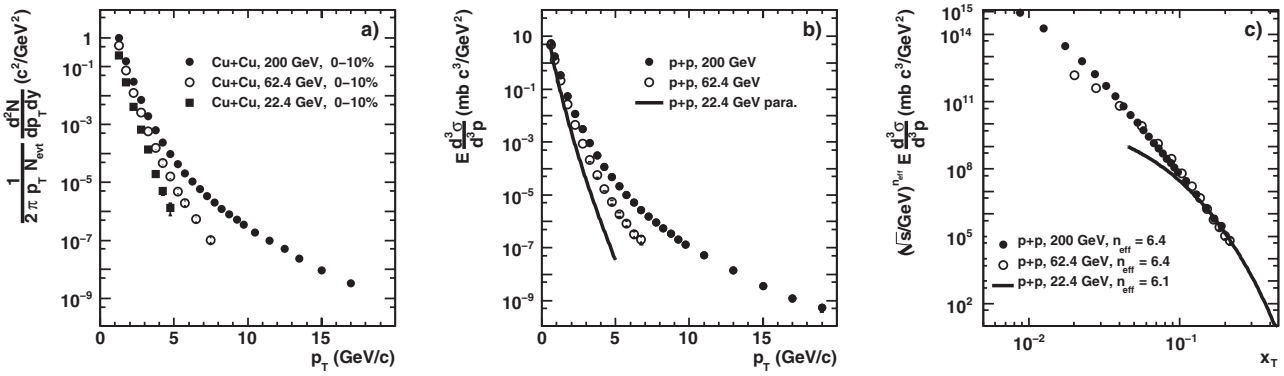

FIG. 1. For $\sqrt{s_{NN}} = 22.4$, 62.4, and 200 GeV are plotted (a) invariant π^0 yields in central Cu + Cu collisions, (b) invariant π^0 cross sections in $p + p$ collisions [14–16], and (c) the $p + p$ data plotted as a function of $x_T = 2p_T/\sqrt{s}$, which exhibit an approximate x_T scaling. The error bars represent the quadratic sum of the statistical and total systematic uncertainties.

tainty in the yields that increases from ~8% at $p_T = 3$ GeV/c to 15% at $p_T = 6$ GeV/c. The part of the spectra in Cu + Cu at 200 GeV measured with the high-p_T trigger is subject to an additional uncertainty of 10% related to the trigger efficiency.

PHENIX has not yet acquired a $p + p$ data set at $\sqrt{s} = 22.4$ GeV. In [16] the world's data on charged and neutral pion production for $21.7 \le \sqrt{s} \le 23.8$ GeV were scaled to $\sqrt{s} = 22.4$ GeV and fit with $Ed^3\sigma/d^3p = A(1 + p_T/p_0)^n(1 - 2p_T/\sqrt{s})^m$ where $A = 174.4$ mb GeV$^{-2}c^3$, $p_0 = 2.59$ GeV/c, $n = -17.43$, $m = 6.15$. The scaling correction was determined with a next-to-leading-order pQCD calculation. The correction is largest for $\sqrt{s} = 23.8$ GeV and reduces these spectra by ~30%. The systematic uncertainty of the fit increases from ~12% at $p_T = 1.5$ GeV/c to ~23% at $p_T = 4.0$ GeV/c [16].

The π^0 p_T spectra for $p + p$ and central Cu + Cu collisions (0%–10% of $\sigma_{\text{inel}}^{\text{Cu+Cu}}$) at $\sqrt{s_{NN}} = 22.4$, 62.4 [14], and 200 GeV [6] are shown in Figs. 1(a) and 1(b). At sufficiently high p_T where pion production in $p + p$ collisions is dominated by fragmentation of jets, QCD predicts a scaling law $\sqrt{s}^{n_{\text{eff}}(x_T,\sqrt{s})} Ed^3\sigma/d^3p = G(x_T)$ with a universal function $G(x_T)$ where $x_T = 2p_T/\sqrt{s}$ [19]. Figure 1(c) shows that such a scaling in x_T is indeed observed for $p + p$ collisions at 22.4, 62.4, and 200 GeV, consistent with previous observations [20]. The x_T values at which the universal curve $G(x_T)$ is reached indicate that particle production is dominated by hard processes for $p_T \gtrsim 2$ GeV/c.

Nuclear effects on high-p_T π^0 production can be quantified with the nuclear modification factor

$$R_{AA}(p_T) = \frac{(1/N_{AA}^{\text{evt}})d^2N_{AA}/dp_Tdy}{\langle T_{AA}\rangle d^2\sigma_{pp}/dp_Tdy}, \qquad (1)$$

where $\langle T_{AA}\rangle = \langle N_{\text{coll}}\rangle/\sigma_{pp}^{\text{inel}}$. Figure 2 shows $R_{AA}(p_T)$ for the 0%–10% most central Cu + Cu collisions. The suppression at 62.4 GeV ($R_{AA} \approx 0.6$ for $p_T \gtrsim 3$ GeV/c) and 200 GeV ($R_{AA} \approx 0.5$–0.6 for $p_T \gtrsim 3$ GeV/c) is consistent with expectations from parton energy loss. The $R_{AA} > 1$ in Cu + Cu at 22.4 GeV is similar to the enhancement by a factor ~1.5 (at $p_T \approx 3$ GeV/c) observed in p + W relative to p + Be collisions at $\sqrt{s_{NN}} = 19.4$ and 23.8 GeV [21]. For similar N_{part} values the R_{AA} in Cu + Cu at 22.4 GeV agrees with the R_{AA} in Pb + Pb collisions at 17.3 GeV [12].

For $p_T \gtrsim 3$ GeV/c the measured R_{AA} values at 62.4 and 200 GeV are consistent with a numerically evaluated parton energy-loss model described in [22,23]; see Fig. 2. This calculation takes into account shadowing from coherent final state interactions in nuclei [24], Cronin enhancement

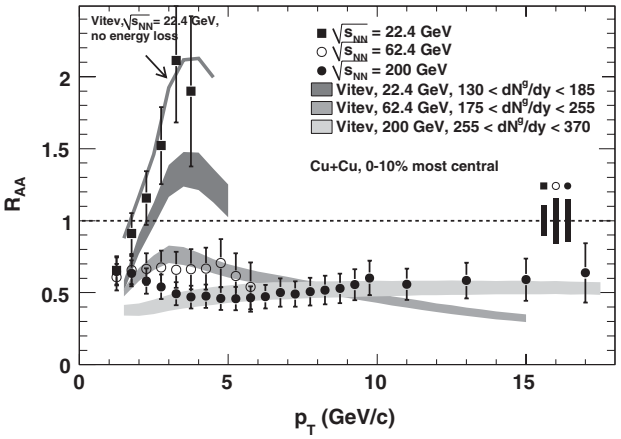

FIG. 2. Measured π^0 R_{AA} are compared to a jet quenching calculation [22,23]. The error bars (here and in Fig. 3) represent the quadratic sum of the statistical and the point-to-point uncorrelated and correlated systematic uncertainties. For $\sqrt{s_{NN}} = 22.4$ GeV the error bars also include the systematic error of the fit of the $p + p$ spectra. The boxes around unity indicate uncertainties related to $\langle N_{\text{coll}}\rangle$ and absolute normalization. The bands for the calculation correspond to the assumed range of the initial gluon density dN^g/dy.

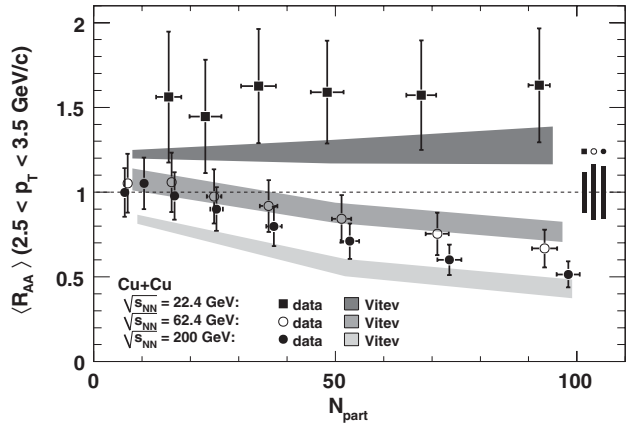

FIG. 3. The average R_{AA} in the interval $2.5 < p_T < 3.5$ GeV/c as a function of centrality for Cu + Cu collisions at $\sqrt{s_{NN}} =$ 22.4, 62.4, and 200 GeV. The shaded bands represent jet-quenching calculations at three discrete centralities ($N_{\rm part} \sim$ 10, 50, 100) [22,23]. The boxes around unity represent the normalization and $\langle N_{\rm coll} \rangle$ uncertainties for a typical $N_{\rm coll}$ uncertainty of 12%.

[25], initial state parton energy loss in cold nuclear matter [26], and final state parton energy loss in dense partonic matter [9,22,23]. The Cronin enhancement measured in $p + A$ collisions is described well by this model [25]. The initial gluon rapidity density dN^g/dy which characterizes the medium was not fit to the R_{AA} values, but instead was constrained by measured charged-particle multiplicities and the assumption of parton-hadron duality ($dN^g/dy = \kappa d\eta/dy dN_{ch}/d\eta$ with $\kappa = 3/2 \pm 30\%$ and $d\eta/dy \equiv 1.2$ at all energies) [22,23]. The average fractional energy losses $\Delta E/E$ for a quark (gluon) with $E =$ 6 GeV corresponding to the dN^g/dy ranges in Fig. 2 are 0.13–0.19 (0.29–0.42), 0.16–0.20 (0.35–0.44), 0.20–0.28 (0.44–0.63) in central Cu + Cu collisions at 22.4, 62.4, and 200 GeV, respectively [23]. For Cu + Cu at $\sqrt{s_{NN}} =$ 22.4 GeV the calculation is also shown without final state parton energy loss. The measurement is consistent with this calculation but does not rule out a scenario with parton energy loss.

Figure 3 shows that the π^0 suppression in the range $2.5 < p_T < 3.5$ GeV/c increases towards more central Cu + Cu collisions for $\sqrt{s_{NN}} = 62.4$, 200 GeV. On the other hand, R_{AA} at $\sqrt{s_{NN}} = 22.4$ GeV remains approximately constant as a function of $N_{\rm part}$, suggesting either that the Cronin enhancement depends only weakly on centrality or that in this energy range parton energy loss is offset by the larger effect of Cronin enhancement.

In conclusion, high-p_T π^0 yields in central Cu + Cu collisions at 62.4 and 200 GeV are suppressed, suggesting that parton energy loss is significant, while at 22.4 GeV the π^0 yields for $p_T \gtrsim 2$ GeV/c are not suppressed. The R_{AA} measured in central Cu + Cu at 22.4 GeV is consistent with Cronin enhancement alone but does not rule out parton energy-loss effects. These measurements provide a unique constraint for jet-quenching models and demonstrate that parton energy loss starts to prevail over the Cronin enhancement between $\sqrt{s_{NN}} = 22.4$ and 62.4 GeV.

We thank the staff of the Collider-Accelerator and Physics Departments at BNL for their vital contributions. We thank Ivan Vitev for providing the jet-quenching calculations. We acknowledge support from the Office of Nuclear Physics in DOE Office of Science, NSF, and a sponsored research grant from Renaissance Technologies (U.S.), MEXT and JSPS (Japan), CNPq and FAPESP (Brazil), NSFC (China), MSMT (Czech Republic), IN2P3/CNRS, and CEA (France), BMBF, DAAD, and AvH (Germany), OTKA (Hungary), DAE (India), ISF (Israel), KRF and KOSEF (Korea), MES, RAS, and FAAE (Russia), VR and KAW (Sweden), U.S. CRDF for the FSU, U.S.-Hungary Fulbright, and U.S.-Israel BSF.

*Deceased.
+PHENIX Spokesperson.
jacak@skipper.physics.sunysb.edu.

[1] K. Adcox *et al.*, Nucl. Phys. **A757**, 184 (2005).
[2] A. Adare *et al.*, Phys. Rev. C **77**, 064907 (2008).
[3] M. Gyulassy and M. Plumer, Phys. Lett. B **243**, 432 (1990).
[4] K. Adcox *et al.*, Phys. Rev. Lett. **88**, 022301 (2001).
[5] S. S. Adler *et al.*, Phys. Rev. Lett. **91**, 072301 (2003).
[6] J. Adams *et al.*, Phys. Rev. Lett. **91**, 172302 (2003).
[7] X.-N. Wang, Phys. Rev. C **61**, 064910 (2000).
[8] I. Vitev and M. Gyulassy, Phys. Rev. Lett. **89**, 252301 (2002).
[9] I. Vitev, Phys. Lett. B **606**, 303 (2005).
[10] B. Alver *et al.*, Phys. Rev. Lett. **96**, 212301 (2006).
[11] B. I. Abelev *et al.*, Phys. Lett. B **655**, 104 (2007).
[12] M. M. Aggarwal *et al.*, Phys. Rev. Lett. **100**, 242301 (2008).
[13] C. Alt *et al.*, Phys. Rev. C **77**, 034906 (2008).
[14] A. Adare *et al.* (to be published).
[15] A. Adare *et al.*, Phys. Rev. D **76**, 051106 (2007).
[16] F. Arleo and D. d'Enterria, arXiv:0807.1252.
[17] L. Aphecetche *et al.*, Nucl. Instrum. Methods Phys. Res., Sect. A **499**, 521 (2003).
[18] M. L. Miller, K. Reygers, S. J. Sanders, and P. Steinberg, Annu. Rev. Nucl. Part. Sci. **57**, 205 (2007).
[19] R. F. Cahalan, K. A. Geer, J. B. Kogut, and L. Susskind, Phys. Rev. D **11**, 1199 (1975).
[20] S. S. Adler *et al.*, Phys. Rev. C **69**, 034910 (2004).
[21] D. Antreasyan *et al.*, Phys. Rev. D **19**, 764 (1979).
[22] I. Vitev, Phys. Lett. B **639**, 38 (2006).
[23] I. Vitev (private communication).
[24] J.-w. Qiu and I. Vitev, Phys. Lett. B **632**, 507 (2006).
[25] I. Vitev, Phys. Lett. B **562**, 36 (2003).
[26] I. Vitev, Phys. Rev. C **75**, 064906 (2007).

Suppression Pattern of Neutral Pions at High Transverse Momentum in Au + Au Collisions at $\sqrt{s_{NN}} = 200$ GeV and Constraints on Medium Transport Coefficients

A. Adare,[8] S. Afanasiev,[22] C. Aidala,[9] N. N. Ajitanand,[49] Y. Akiba,[43,44] H. Al-Bataineh,[38] J. Alexander,[49] A. Al-Jamel,[38] K. Aoki,[28,43] L. Aphecetche,[51] R. Armendariz,[38] S. H. Aronson,[3] J. Asai,[44] E. T. Atomssa,[29] R. Averbeck,[50] T. C. Awes,[39] B. Azmoun,[3] V. Babintsev,[18] G. Baksay,[14] L. Baksay,[14] A. Baldisseri,[11] K. N. Barish,[4] P. D. Barnes,[31] B. Bassalleck,[37] S. Bathe,[4] S. Batsouli,[9,39] V. Baublis,[42] F. Bauer,[4] A. Bazilevsky,[3] S. Belikov,[3,21,*] R. Bennett,[50] Y. Berdnikov,[46] A. A. Bickley,[8] M. T. Bjorndal,[9] J. G. Boissevain,[31] H. Borel,[11] K. Boyle,[50] M. L. Brooks,[31] D. S. Brown,[38] D. Bucher,[34] H. Buesching,[3] V. Bumazhnov,[18] G. Bunce,[3,44] J. M. Burward-Hoy,[31] S. Butsyk,[31,50] S. Campbell,[50] J.-S. Chai,[23] B. S. Chang,[58] J.-L. Charvet,[11] S. Chernichenko,[18] J. Chiba,[24] C. Y. Chi,[9] M. Chiu,[9,19] I. J. Choi,[58] T. Chujo,[55] P. Chung,[49] A. Churyn,[18] V. Cianciolo,[39] C. R. Cleven,[16] Y. Cobigo,[11] B. A. Cole,[9] M. P. Comets,[40] P. Constantin,[21,31] M. Csanád,[13] T. Csörgő,[25] T. Dahms,[50] K. Das,[15] G. David,[3] M. B. Deaton,[1] K. Dehmelt,[14] H. Delagrange,[51] A. Denisov,[18] D. d'Enterria,[9] A. Deshpande,[44,50] E. J. Desmond,[3] O. Dietzsch,[47] A. Dion,[50] M. Donadelli,[47] J. L. Drachenberg,[1] O. Drapier,[29] A. Drees,[50] A. K. Dubey,[57] A. Durum,[18] V. Dzhordzhadze,[4,52] Y. V. Efremenko,[39] J. Egdemir,[50] F. Ellinghaus,[8] W. S. Emam,[4] A. Enokizono,[17,30] H. En'yo,[43,44] B. Espagnon,[40] S. Esumi,[54] K. O. Eyser,[4] D. E. Fields,[37,44] M. Finger,[5,22] M. Finger, Jr.,[5,22] F. Fleuret,[29] S. L. Fokin,[27] B. Forestier,[32] Z. Fraenkel,[57,*] J. E. Frantz,[9,50] A. Franz,[3] A. D. Frawley,[15] K. Fujiwara,[43] Y. Fukao,[28,43] S.-Y. Fung,[4] T. Fusayasu,[36] S. Gadrat,[32] I. Garishvili,[52] F. Gastineau,[51] M. Germain,[51] A. Glenn,[8,52] H. Gong,[50] M. Gonin,[29] J. Gosset,[11] Y. Goto,[43,44] R. Granier de Cassagnac,[29] N. Grau,[21] S. V. Greene,[55] M. Grosse Perdekamp,[19,44] T. Gunji,[7] H.-Å. Gustafsson,[33] T. Hachiya,[17,43] A. Hadj Henni,[51] C. Haegemann,[37] J. S. Haggerty,[3] M. N. Hagiwara,[1] H. Hamagaki,[7] R. Han,[41] H. Harada,[17] E. P. Hartouni,[30] K. Haruna,[17] M. Harvey,[3] E. Haslum,[33] K. Hasuko,[43] R. Hayano,[7] M. Heffner,[30] T. K. Hemmick,[50] T. Hester,[4] J. M. Heuser,[43] X. He,[16] H. Hiejima,[19] J. C. Hill,[21] R. Hobbs,[37] M. Hohlmann,[14] M. Holmes,[55] W. Holzmann,[49] K. Homma,[17] B. Hong,[26] T. Horaguchi,[43,53] D. Hornback,[52] M. G. Hur,[23] T. Ichihara,[43,44] K. Imai,[28,43] J. Imrek,[12] M. Inaba,[54] Y. Inoue,[45,43] D. Isenhower,[1] L. Isenhower,[1] M. Ishihara,[43] T. Isobe,[7] M. Issah,[49] A. Isupov,[22] B. V. Jacak,[50,+] J. Jia,[9] J. Jin,[9] O. Jinnouchi,[44] B. M. Johnson,[3] K. S. Joo,[35] D. Jouan,[40] F. Kajihara,[7,43] S. Kametani,[7,56] N. Kamihara,[43,53] J. Kamin,[50] M. Kaneta,[44] J. H. Kang,[58] H. Kanou,[43,53] T. Kawagishi,[54] D. Kawall,[44] A. V. Kazantsev,[27] S. Kelly,[8] A. Khanzadeev,[42] J. Kikuchi,[56] D. H. Kim,[35] D. J. Kim,[58] E. Kim,[48] Y.-S. Kim,[23] E. Kinney,[8] A. Kiss,[13] E. Kistenev,[3] A. Kiyomichi,[43] J. Klay,[30] C. Klein-Boesing,[34] L. Kochenda,[42] V. Kochetkov,[18] B. Komkov,[42] M. Konno,[54] D. Kotchetkov,[4] A. Kozlov,[57] A. Král,[10] A. Kravitz,[9] P. J. Kroon,[3] J. Kubart,[5,20] G. J. Kunde,[31] N. Kurihara,[7] K. Kurita,[45,43] M. J. Kweon,[26] Y. Kwon,[52,58] G. S. Kyle,[38] R. Lacey,[49] Y.-S. Lai,[9] J. G. Lajoie,[21] A. Lebedev,[21] Y. Le Bornec,[40] S. Leckey,[50] D. M. Lee,[31] M. K. Lee,[58] T. Lee,[48] M. J. Leitch,[31] M. A. L. Leite,[47] B. Lenzi,[47] H. Lim,[48] T. Liška,[10] A. Litvinenko,[22] M. X. Liu,[31] X. Li,[6] X. H. Li,[4] B. Love,[55] D. Lynch,[3] C. F. Maguire,[55] Y. I. Makdisi,[3] A. Malakhov,[22] M. D. Malik,[37] V. I. Manko,[27] Y. Mao,[41,43] L. Mašek,[5,20] H. Masui,[54] F. Matathias,[9,50] M. C. McCain,[19] M. McCumber,[50] P. L. McGaughey,[31] Y. Miake,[54] P. Mikeš,[5,20] K. Miki,[54] T. E. Miller,[55] A. Milov,[50] S. Mioduszewski,[3] G. C. Mishra,[16] M. Mishra,[2] J. T. Mitchell,[3] M. Mitrovski,[49] A. Morreale,[4] D. P. Morrison,[3] J. M. Moss,[31] T. V. Moukhanova,[27] D. Mukhopadhyay,[55] J. Murata,[45,43] S. Nagamiya,[24] Y. Nagata,[54] J. L. Nagle,[8] M. Naglis,[57] I. Nakagawa,[43,44] Y. Nakamiya,[17] T. Nakamura,[17] K. Nakano,[43,53] J. Newby,[30] M. Nguyen,[50] B. E. Norman,[31] A. S. Nyanin,[27] J. Nystrand,[33] E. O'Brien,[3] S. X. Oda,[7] C. A. Ogilvie,[21] H. Ohnishi,[43] I. D. Ojha,[55] H. Okada,[28,43] K. Okada,[44] M. Oka,[54] O. O. Omiwade,[1] A. Oskarsson,[33] I. Otterlund,[33] M. Ouchida,[17] K. Ozawa,[7] R. Pak,[3] D. Pal,[55] A. P. T. Palounek,[31] V. Pantuev,[50] V. Papavassiliou,[38] J. Park,[48] W. J. Park,[26] S. F. Pate,[38] H. Pei,[21] J.-C. Peng,[19] H. Pereira,[11] V. Peresedov,[22] D. Yu. Peressounko,[27] C. Pinkenburg,[3] R. P. Pisani,[3] M. L. Purschke,[3] A. K. Purwar,[31,50] H. Qu,[16] J. Rak,[21,37] A. Rakotozafindrabe,[29] I. Ravinovich,[57] K. F. Read,[39,52] S. Rembeczki,[14] M. Reuter,[50] K. Reygers,[34] V. Riabov,[42] Y. Riabov,[42] G. Roche,[32] A. Romana,[29,*] M. Rosati,[21] S. S. E. Rosendahl,[33] P. Rosnet,[32] P. Rukoyatkin,[22] V. L. Rykov,[43] S. S. Ryu,[58] B. Sahlmueller,[34] N. Saito,[28,43,44] T. Sakaguchi,[3,7,56] S. Sakai,[54] H. Sakata,[17] V. Samsonov,[42] H. D. Sato,[28,43] S. Sato,[3,24,54] S. Sawada,[24] J. Seele,[8] R. Seidl,[19] V. Semenov,[18] R. Seto,[4] D. Sharma,[57] T. K. Shea,[3] I. Shein,[18] A. Shevel,[42,49] T.-A. Shibata,[43,53] K. Shigaki,[17] M. Shimomura,[54] T. Shohjoh,[54] K. Shoji,[28,43] A. Sickles,[50] C. L. Silva,[47] D. Silvermyr,[39] C. Silvestre,[11] K. S. Sim,[26] C. P. Singh,[2] V. Singh,[2] S. Skutnik,[21] M. Slunečka,[5,22] W. C. Smith,[1] A. Soldatov,[18] R. A. Soltz,[30] W. E. Sondheim,[31] S. P. Sorensen,[52] I. V. Sourikova,[3] F. Staley,[11] P. W. Stankus,[39] E. Stenlund,[33] M. Stepanov,[38] A. Ster,[25] S. P. Stoll,[3] T. Sugitate,[17] C. Suire,[40] J. P. Sullivan,[31] J. Sziklai,[25] T. Tabaru,[44] S. Takagi,[54] E. M. Takagui,[47] A. Taketani,[43,44] K. H. Tanaka,[24] Y. Tanaka,[36] K. Tanida,[43,44] M. J. Tannenbaum,[3] A. Taranenko,[49] P. Tarján,[12] T. L. Thomas,[37]

M. Togawa,[28,43] A. Toia,[50] J. Tojo,[43] L. Tomášek,[20] H. Torii,[43] R. S. Towell,[1] V-N. Tram,[29] I. Tserruya,[57] Y. Tsuchimoto,[17,43] S. K. Tuli,[2] H. Tydesjö,[33] N. Tyurin,[18] C. Vale,[21] H. Valle,[55] H. W. van Hecke,[31] J. Velkovska,[55] R. Vertesi,[12] A. A. Vinogradov,[27] M. Virius,[10] V. Vrba,[20] E. Vznuzdaev,[42] M. Wagner,[28,43] D. Walker,[50] X. R. Wang,[38] Y. Watanabe,[43,44] J. Wessels,[34] S. N. White,[3] N. Willis,[40] D. Winter,[9] C. L. Woody,[3] M. Wysocki,[8] W. Xie,[4,44] Y. L. Yamaguchi,[56] A. Yanovich,[18] Z. Yasin,[4] J. Ying,[16] S. Yokkaichi,[43,44] G. R. Young,[39] I. Younus,[37] I. E. Yushmanov,[27] W. A. Zajc,[9] O. Zaudtke,[34] C. Zhang,[9,39] S. Zhou,[6] J. Zimányi,[25,*] and L. Zolin[22]

(PHENIX Collaboration)

[1]*Abilene Christian University, Abilene, Texas 79699, USA*
[2]*Department of Physics, Banaras Hindu University, Varanasi 221005, India*
[3]*Brookhaven National Laboratory, Upton, New York 11973-5000, USA*
[4]*University of California-Riverside, Riverside, California 92521, USA*
[5]*Charles University, Ovocný trh 5, Praha 1, 116 36, Prague, Czech Republic*
[6]*China Institute of Atomic Energy (CIAE), Beijing, People's Republic of China*
[7]*Center for Nuclear Study, Graduate School of Science, University of Tokyo, 7-3-1 Hongo, Bunkyo, Tokyo 113-0033, Japan*
[8]*University of Colorado, Boulder, Colorado 80309, USA*
[9]*Columbia University, New York, New York 10027 and Nevis Laboratories, Irvington, New York 10533, USA*
[10]*Czech Technical University, Zikova 4, 166 36 Prague 6, Czech Republic*
[11]*Dapnia, CEA Saclay, F-91191, Gif-sur-Yvette, France*
[12]*Debrecen University, H-4010 Debrecen, Egyetem tér 1, Hungary*
[13]*ELTE, Eötvös Loránd University, H-1117 Budapest, Pázmány P. s. 1/A, Hungary*
[14]*Florida Institute of Technology, Melbourne, Florida 32901, USA*
[15]*Florida State University, Tallahassee, Florida 32306, USA*
[16]*Georgia State University, Atlanta, Georgia 30303, USA*
[17]*Hiroshima University, Kagamiyama, Higashi-Hiroshima 739-8526, Japan*
[18]*IHEP Protvino, State Research Center of Russian Federation, Institute for High Energy Physics, Protvino, 142281, Russia*
[19]*University of Illinois at Urbana-Champaign, Urbana, Illinois 61801, USA*
[20]*Institute of Physics, Academy of Sciences of the Czech Republic, Na Slovance 2, 182 21 Prague 8, Czech Republic*
[21]*Iowa State University, Ames, Iowa 50011, USA*
[22]*Joint Institute for Nuclear Research, 141980 Dubna, Moscow Region, Russia*
[23]*KAERI, Cyclotron Application Laboratory, Seoul, Korea*
[24]*KEK, High Energy Accelerator Research Organization, Tsukuba, Ibaraki 305-0801, Japan*
[25]*KFKI Research Institute for Particle and Nuclear Physics of the Hungarian Academy of Sciences (MTA KFKI RMKI), H-1525 Budapest 114, POBox 49, Budapest, Hungary*
[26]*Korea University, Seoul, 136-701, Korea*
[27]*Russian Research Center "Kurchatov Institute", Moscow, Russia*
[28]*Kyoto University, Kyoto 606-8502, Japan*
[29]*Laboratoire Leprince-Ringuet, Ecole Polytechnique, CNRS-IN2P3, Route de Saclay, F-91128, Palaiseau, France*
[30]*Lawrence Livermore National Laboratory, Livermore, California 94550, USA*
[31]*Los Alamos National Laboratory, Los Alamos, New Mexico 87545, USA*
[32]*LPC, Université Blaise Pascal, CNRS-IN2P3, Clermont-Fd, 63177 Aubiere Cedex, France*
[33]*Department of Physics, Lund University, Box 118, SE-221 00 Lund, Sweden*
[34]*Institut für Kernphysik, University of Muenster, D-48149 Muenster, Germany*
[35]*Myongji University, Yongin, Kyonggido 449-728, Korea*
[36]*Nagasaki Institute of Applied Science, Nagasaki-shi, Nagasaki 851-0193, Japan*
[37]*University of New Mexico, Albuquerque, New Mexico 87131, USA*
[38]*New Mexico State University, Las Cruces, New Mexico 88003, USA*
[39]*Oak Ridge National Laboratory, Oak Ridge, Tennessee 37831, USA*
[40]*IPN-Orsay, Universite Paris Sud, CNRS-IN2P3, BP1, F-91406, Orsay, France*
[41]*Peking University, Beijing, People's Republic of China*
[42]*PNPI, Petersburg Nuclear Physics Institute, Gatchina, Leningrad region, 188300, Russia*
[43]*RIKEN, The Institute of Physical and Chemical Research, Wako, Saitama 351-0198, Japan*
[44]*RIKEN BNL Research Center, Brookhaven National Laboratory, Upton, New York 11973-5000, USA*
[45]*Physics Department, Rikkyo University, 3-34-1 Nishi-Ikebukuro, Toshima, Tokyo 171-8501, Japan*
[46]*Saint Petersburg State Polytechnic University, St. Petersburg, Russia*
[47]*Universidade de São Paulo, Instituto de Física, Caixa Postal 66318, São Paulo CEP05315-970, Brazil*
[48]*System Electronics Laboratory, Seoul National University, Seoul, Korea*
[49]*Chemistry Department, Stony Brook University, SUNY, Stony Brook, New York 11794-3400, USA*

[50]Department of Physics and Astronomy, Stony Brook University, SUNY, Stony Brook, New York 11794, USA
[51]SUBATECH (Ecole des Mines de Nantes, CNRS-IN2P3, Université de Nantes) BP 20722-44307, Nantes, France
[52]University of Tennessee, Knoxville, Tennessee 37996, USA
[53]Department of Physics, Tokyo Institute of Technology, Oh-okayama, Meguro, Tokyo 152-8551, Japan
[54]Institute of Physics, University of Tsukuba, Tsukuba, Ibaraki 305, Japan
[55]Vanderbilt University, Nashville, Tennessee 37235, USA
[56]Waseda University, Advanced Research Institute for Science and Engineering, 17 Kikui-cho, Shinjuku-ku, Tokyo 162-0044, Japan
[57]Weizmann Institute, Rehovot 76100, Israel
[58]Yonsei University, IPAP, Seoul 120-749, Korea
(Received 25 January 2008; published 3 December 2008)

For Au + Au collisions at 200 GeV, we measure neutral pion production with good statistics for transverse momentum, p_T, up to 20 GeV/c. A fivefold suppression is found, which is essentially constant for $5 < p_T < 20$ GeV/c. Experimental uncertainties are small enough to constrain any model-dependent parametrization for the transport coefficient of the medium, e.g., $\langle \hat{q} \rangle$ in the parton quenching model. The spectral shape is similar for all collision classes, and the suppression does not saturate in Au + Au collisions.

DOI: 10.1103/PhysRevLett.101.232301 PACS numbers: 25.75.Dw

Large transverse momentum (p_T) hadrons originate primarily from the fragmentation of hard scattered quarks or gluons. In high energy $p + p$ collisions, this is well described in the framework of perturbative QCD [1]. In ultrarelativistic heavy ion collisions, such hard scatterings occur in the early phase of the reaction, and the transiting partons serve as probes of the strongly interacting medium produced in the collisions. Lattice QCD predicts a phase transition to a plasma of deconfined quarks and gluons, which induces gluon radiation from the scattered parton and depletes hadron production at high p_T (''jet quenching'') [2,3]. The measurements in Au + Au collisions at Relativistic Heavy Ion Collider (RHIC) showed suppressed hadron yields in central collisions [4] as predicted [5,6], and motivated advanced theoretical studies of radiative energy loss.

All energy loss models must incorporate the space-time evolution of the medium, as it is not static, and the initial distribution of the partons throughout the medium. Models generally also include an input parameter for the medium density and/or the coupling. Different assumptions in the various models lead to similar descriptions of the π^0 suppression with different model-dependent parameters [7,8]. For instance, the Parton Quenching model (PQM) is a Monte Carlo program using the quenching weights from Baier-Dokshitzer-Mueller-Peigne-Schiff (BDMPS) [5] that combines the coupling strength with the color-charge density to create a single transport coefficient, often referred to as $\langle \hat{q} \rangle$ [9,10], which gives the $\langle p_T^2 \rangle$ transferred from the medium to the parton per mean free path.

Establishing the magnitude, p_T and centrality dependence of the suppression pattern up to the highest possible p_T is crucial to constrain the theoretical models and separate contributions of initial and final state effects from the energy loss mechanism. As neutral pions can be identified up to very high p_T, their suppression and its centrality (average pathlength) dependence puts important constraints on the energy loss. Whereas di-hadron suppression at high p_T may be somewhat more sensitive to medium opacity [11] than single hadron suppression, such improvement is contingent upon theoretical and experimental, statistical and systematic uncertainties.

This Letter reports on the measurement of π^0s up to $p_T = 20$ GeV/c in Au + Au collisions at $\sqrt{s_{NN}} = 200$ GeV at RHIC, using the high statistics data taken in 2004. The results are used to extract the $\langle \hat{q} \rangle$ parameter of the PQM model for the most central collisions.

The analysis used 1.03×10^9 minimum bias events taken by the PHENIX experiment [12]. Collision centrality was determined from the correlation between the number of charged particles detected in the Beam-Beam Counters (BBC, $3.0 < |\eta| < 3.9$) and the energy measured in the Zero Degree Calorimeters (ZDC). A Glauber model Monte Carlo program with a simulation of the BBC and ZDC responses was used to estimate the average number of participating nucleons ($\langle N_{\mathrm{part}} \rangle$) and binary nucleon-nucleon collisions ($\langle N_{\mathrm{coll}} \rangle$) for each centrality bin [13].

Neutral pions were measured in the $\pi^0 \to \gamma\gamma$ decay channel with the photons reconstructed in the Electromagnetic Calorimeter (EMCal) located in the two central arms of PHENIX ($|\eta| \leq 0.35$). The EMCal [14] consists of two subsystems: six sectors of lead-scintillator sandwich calorimeter (PbSc) and two sectors of lead-glass Čerenkov calorimeter (PbGl) at the radial distance of about 5 m. The fine segmentation of the EMCal ($\delta\phi \times \delta\eta \sim 0.01 \times 0.01$ for PbSc and $\sim 0.008 \times 0.008$ for PbGl) ensures that the two photons from a $\pi^0 \to \gamma\gamma$ decay are well resolved up to $p_T^{\pi^0} \approx 12$ (PbSc) and 16 (PbGl) GeV/c. Data from the two subsystems were analyzed separately, and the fully corrected results were combined.

Details of the analysis including extraction of the raw π^0 yield, correction for acceptance, detector response, reconstruction efficiency have been described elsewhere [15,16]. In this analysis, the higher p_T range required an additional

TABLE I. Summary of the systematic uncertainties on the π^0 yield extracted independently with the PbSc (PbGl) electromagnetic calorimeters. The last row is the total systematic uncertainty on the combined spectra.

p_T (GeV/c)	2	6	10	16
uncertainty source	PbSc (PbGl)			
yield extraction (%)	3.0 (4.1)	3.0 (4.1)	3.0 (4.1)	3.0 (4.1)
PID efficiency (%)	3.5 (3.9)	3.5 (3.5)	3.5 (3.7)	3.5 (3.9)
Energy scale (%)	6.7 (9.0)	8.0 (9.2)	8.0 (8.2)	8.0 (12.3)
Acceptance (%)	1.5 (4.1)	1.5 (4.1)	1.5 (4.1)	1.5 (4.1)
π^0 merging (%)	$\cdots$ ($\cdots$)	$\cdots$ ($\cdots$)	4.4 ($\cdots$)	28 (4.8)
Conversion (%)	3.0 (2.5)	3.0 (2.5)	3.0 (2.5)	3.0 (2.5)
off-vertex π^0 (%)	1.5 (1.5)	1.5 (1.5)	1.5 (1.5)	1.5 (1.5)
Total (%)	8.7 (12)	9.8 (11)	11 (11)	30 (15)
PbSc and PbGl combined: Total (%)	7.0	7.5	7.6	14

correction for losses in the observed (raw) π^0s due to "cluster merging."

With increasing $p_T^{\pi^0}$, the minimum opening angle of the two photons decreases, and eventually they will be reconstructed as a single cluster. Such "merging" reaches 50% of the total raw yield at $p_T = 14$ GeV/c in the PbSc and at $p_T = 18$ GeV/c in the PbGl. Merged clusters were rejected by various shower profile cuts, and the loss was determined by simulated π^0s embedded into real events and analyzed with the same cuts. The systematic uncertainties were estimated by comparing π^0 yields in the PbSc extracted in bins of asymmetry $|E_{\gamma_1} - E_{\gamma_2}|/(E_{\gamma_1} + E_{\gamma_2})$ and also by comparing yields in the PbSc and PbGl.

We considered two sources of π^0s not coming from the vertex (off-vertex π^0): those produced by hadrons interacting with detector material (instrumental background) and feed-down products from weak decay of higher mass hadrons (physics background). Based upon simulations both types of background were found to be negligible ($< 1\%$ at $p_T > 2.0$ GeV/c) except for π^0s from K^0_S decay ($\approx 3\%$ of π^0 yield for $p_T > 1$ GeV/c), which has been subtracted from the data. Finally, the yields were corrected to the center of the p_T bins using the local slope.

The main sources of systematic uncertainties are yield extraction, efficiency corrections, energy scale, and merging, none of which exhibits a significant centrality dependence. The PbSc and PbGl have quite different systematics with all but one of them (off-vertex π^0) uncorrelated. Therefore, when combining their results, the total error is reduced in the weighted average of the two independent measurements. The final systematic uncertainties (1 standard deviation) on the spectra are shown in Table I.

The top panel of Fig. 1 shows the π^0 invariant yield for all centralities and minimum bias, combined from the independent PbSc and PbGl measurements which now extend to $p_T \sim 20$ GeV/c, 6 GeV/c higher than those published earlier [15]. In the overlap region, the results are consistent with the ones in [15] while the errors are reduced by a factor of 2 to 2.5. The bottom panel shows the consistency of the PbSc and PbGl results. The spectra are similar at all centralities: when fitting $p_T > 5$ GeV/c with a power-law function ($\propto p_T^{-n}$), the exponents vary from $n = 8.00 \pm 0.12$ in 0–5% to $n = 8.06 \pm 0.08$ in the 80–92% (most peripheral) bin. Note that $n = 8.22 \pm 0.09$ in $p + p$ collisions. The errors are combined statistical errors and systematic uncertainties.

To quantify the comparison of spectra in heavy ion and $p + p$ collisions, the nuclear modification factor

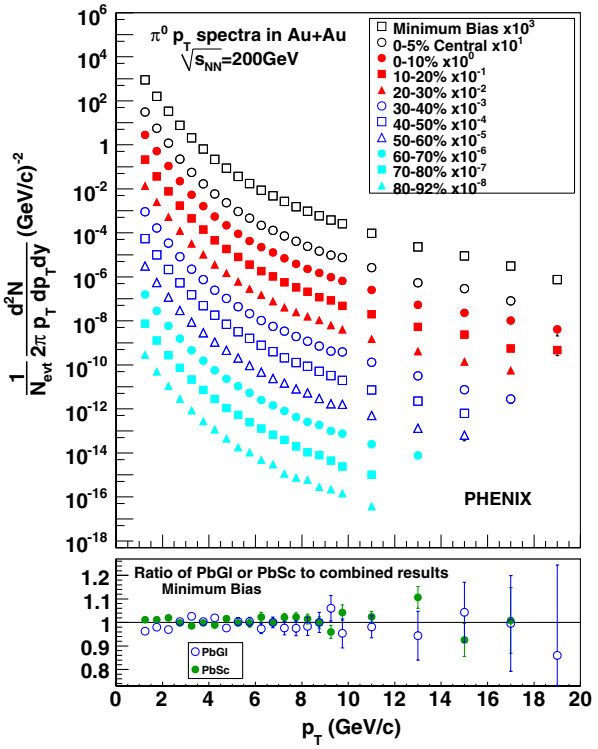

FIG. 1 (color online). Top: π^0 invariant yields for all centralities and minimum bias. Bottom: ratios of the (separately analyzed) PbSc and PbGl yields to the combined minimum bias invariant yield, which is shown in the top panel.

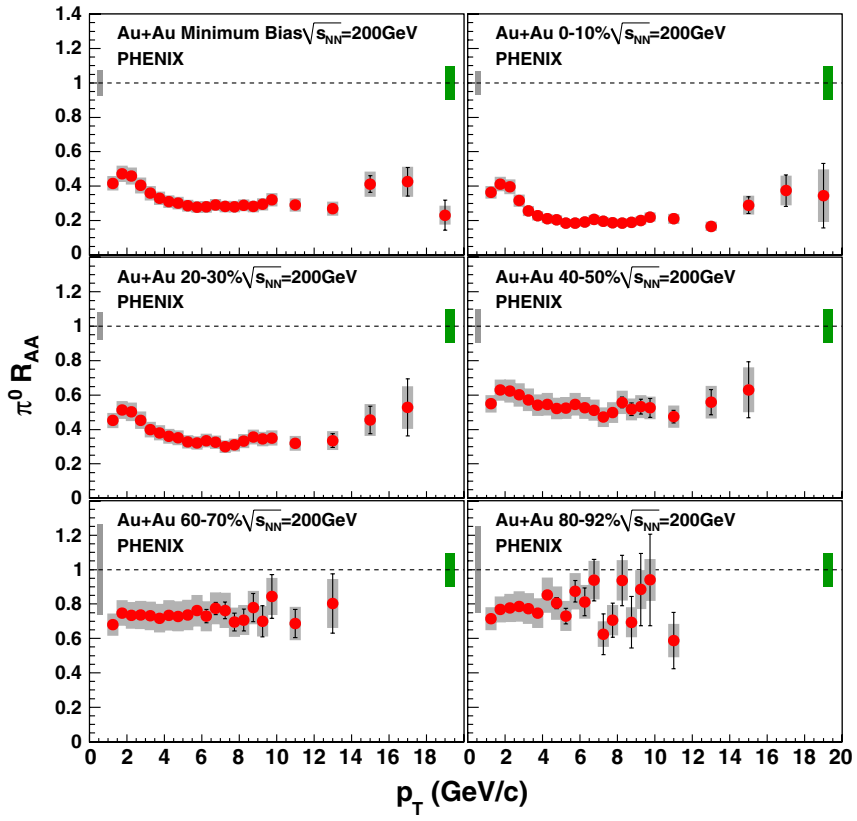

FIG. 2 (color online). Nuclear modification factor (R_{AA}) for π^0s. Error bars are statistical and p_T-uncorrelated errors, boxes around the points indicate p_T-correlated errors. Single box around $R_{AA} = 1$ on the left is the error due to N_{coll}, whereas the single box on the right is the overall normalization error of the $p + p$ reference spectrum.

$$R_{AA} = \frac{1/N_{evt} d^2N/dydp_T}{\langle T_{AB}\rangle d^2\sigma_{pp}/dydp_T} \quad (1)$$

is used, where σ_{pp} is the production cross section of the particle in $p + p$ collisions, and $\langle T_{AB}\rangle$ is the nuclear thickness function averaged over a range of impact parameters for the given centrality, calculated within a Glauber model [13]. Figures 2 and 3 show R_{AA} for π^0 at different centralities. The reference $p + p$ yield was obtained from the 2005 (Run-5) RHIC $p + p$ measurement [17].

R_{AA} reaches ~0.2 in 0–10% centrality at $p_T > 5$ GeV/c with very little (if any) p_T dependence. This trend is compatible with most current energy loss models but not with a semiopaque medium assumption, where R_{AA} would decrease with increasing p_T [7]. While its magnitude changes, the suppression pattern itself is remarkably similar at all centralities suggesting that the bulk R_{AA} (integrated over azimuth) is sensitive only to the N_{part} but not to the specific geometry. Consequently, study of the p_T-integrated R_{AA} vs centrality is instructive.

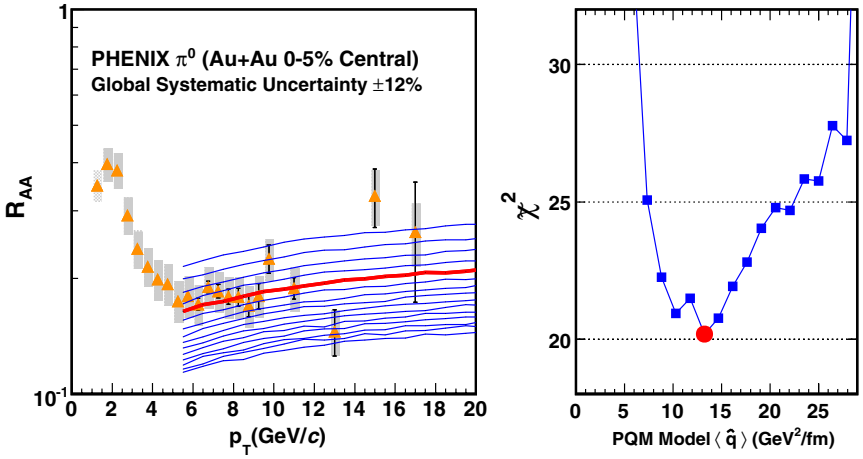

FIG. 3 (color online). Left: π^0 R_{AA} for the most central (0–5%) Au + Au collisions and PQM model calculations for different values of $\langle\hat{q}\rangle$. Right: $\tilde{\chi}^2(\epsilon_b, \epsilon_c, p)$ distribution for the corresponding values of $\langle\hat{q}\rangle$. The bold (red) curve in the left panel and the round (red) point in the right panel are the best fit values.

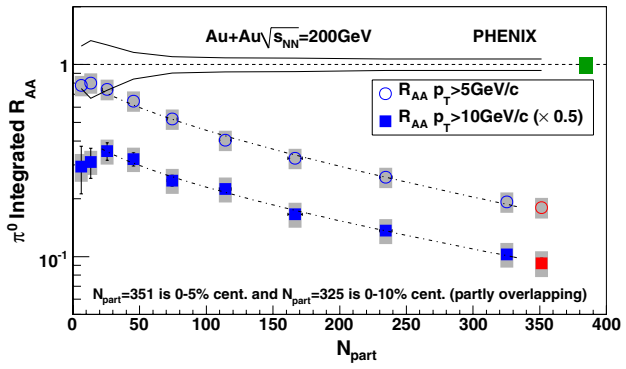

FIG. 4 (color online). Integrated nuclear modification factor (R_{AA}) for π^0 as a function of collision centrality expressed in terms of N_{part}. The error bars/bands are the same as in Fig. 2. The two lines at unity show the errors on $\langle N_{\mathrm{coll}}\rangle$. The last two points correspond to partially overlapping centrality bins. The dashed lines show the fit explained in the text.

Figure 4 shows R_{AA} for π^0s integrated above $p_T > 5$ GeV/c, and $p_T > 10$ GeV/c, as a function of centrality. The last two points indicate overlapping 0–10% and 0–5% bins. In both cases, the suppression increases monotonically with N_{part} without any sign of saturation, suggesting that larger colliding systems (such as $U + U$ planned at RHIC) should exhibit even more suppression.

The common power-law behavior ($\propto p_T^{-n}$) in $p + p$ and Au + Au allows the suppression to be reinterpreted as a fractional energy loss $S_{\mathrm{loss}} = 1 - R_{\mathrm{AA}}^{1/(n-2)}$ where n is the power-law exponent, and we found that $S_{\mathrm{loss}} \propto N_{\mathrm{part}}^a$ [15,18]. Fitting the integrated R_{AA} with a function $R_{\mathrm{AA}} = (1 - S_0 N_{\mathrm{part}}^a)^{n-2}$, where n is fixed as 8.1, gives $a = 0.57 \pm 0.13$ for $N_{\mathrm{part}} > 20$ for $p_T > 5$ GeV/c, and $a = 0.55 \pm 0.14$ for $p_T > 10$ GeV/c. The fit does not take errors on $p + p$ luminosity into account. The Gyulassy-Levai-Vitev (GLV) [6] and PQM [10] models predict that $a \approx 2/3$, which is consistent with the data. The fitted values of S_0 are $(9.0 \pm 6.1) \times 10^{-3}$ and $(9.4 \pm 7.3) \times 10^{-3}$ for $p_T > 5$ GeV/c and $p_T > 10$ GeV/c, respectively. The fits are shown as dashed lines in Fig. 4.

We use the highest centrality (0–5%) R_{AA} data as shown in Fig. 3 to constrain the PQM model parameter $\langle\hat{q}\rangle$. This must be done with careful consideration of the various, partially coupled error sources, leading to necessary refinement beyond a naive least square analysis. We calculate

$$\tilde{\chi}^2(\epsilon_b, \epsilon_c, p) = \left(\sum_{i=1}^{n} \frac{[y_i + \epsilon_b \sigma_{b_i} + \epsilon_c y_i \sigma_c - \mu_i(p)]^2}{\tilde{\sigma}_i^2}\right) + \epsilon_b^2 + \epsilon_c^2, \quad (2)$$

using theory curves $\mu_i(p)$ with different values of the input parameter p, i.e., $\langle\hat{q}\rangle$ in the PQM model. p_T-uncorrelated, statistical ⊕ systematic errors are σ_i, p_T-correlated errors are σ_{b_i} (boxes on Figs. 2 and 3), while uniform fractional shifts of all points are given by σ_c. All the measured values y_i are allowed to shift by the same fraction, ϵ_b, of their systematic error σ_{b_i} from the nominal values. The ϵ_c is a similar correlated fraction of σ_c, and $\tilde{\sigma}_i = \sigma_i(y_i + \epsilon_b \sigma_{b_i} + \epsilon_c y_i \sigma_c)/y_i$ is the point-to-point random error scaled by the multiplicative shift, so that the fractional error is unchanged by the shift, which is true for the present measurement. The best fit, $\tilde{\chi}^2_{\mathrm{min}}$, the minimum of $\tilde{\chi}^2(\epsilon_b, \epsilon_c, p)$ by variation of ϵ_b, ϵ_c, and p, is found by standard methods. Further details are given in [16]. The right panel of Fig. 3 shows the minima of $\tilde{\chi}^2(\epsilon_b, \epsilon_c, p)$ by varying ϵ_b and ϵ_c for a wide range of values of the PQM model transport coefficient, $\langle\hat{q}\rangle$. Our data constrain $\langle\hat{q}\rangle$ as $13.2\ ^{+2.1}_{-3.2}$ and $^{+6.3}_{-5.2}$ GeV^2/fm at the 1 and 2 standard deviation levels. These constraints include only the experimental uncertainties and do not account for the large model-dependent differences in the quenching scenario and description of the medium. Extracting fundamental model-independent properties of the medium from the present data requires resolution of ambiguities and open questions in the models themselves, which also will have to account simultaneously for the p_T and centrality (average path-length) dependence. This work demonstrates the power of data for pion production in constraining the energy loss of partons. The large $\langle\hat{q}\rangle$ suggests that the matter consists of strongly coupled partons.

The $R_{\mathrm{AA}}(p_T)$ for 0–5% was fitted with a simple linear function in the entire $p_T > 5$ GeV/c range as well: the slope of the fit is $0.0017\ ^{+0.0035}_{-0.0039}$ and $^{+0.0070}_{-0.0076}$ c/GeV at the 1 and 2 standard deviation levels [16]. The fact that R_{AA} as well as the power (n) for all spectra from $p + p$ to Au + Au are essentially constant proves that the dominant term in energy loss is proportional to p_T.

In summary, PHENIX has measured neutral pions in Au + Au collisions at $\sqrt{s_{NN}} = 200$ GeV at mid rapidity in the transverse momentum range of $1 < p_T < 20$ GeV/c, analyzing high statistics data taken in 2004. The shape of the spectra is similar for all centralities, as is the shape of $R_{\mathrm{AA}}(p_T)$ at $p_T > 5$ GeV/c. In central collisions, the yield is suppressed by a factor of ~5 at 5 GeV/c compared to the binary scaled $p + p$ reference, and the suppression prevails with little or no change up to 20 GeV/c. The integrated R_{AA} vs centrality does not saturate at this nuclear size; also, the predicted $S_{\mathrm{loss}} \propto N_{\mathrm{part}}^{2/3}$ [6,10] is consistent with our data. In this picture, the energy loss increases with p_T. Using the 0–5% (most central) R_{AA}, we find that the transport coefficient $\langle\hat{q}\rangle$ of the PQM model is constrained to $13.2\ ^{+2.1}_{-3.2}$ ($^{+6.3}_{-5.2}$) GeV^2/fm at the one (two) σ level. The experimental evidence for a high transport coefficient, derived with remarkable accuracy due to high quality data and sophisticated new analysis, as presented here and in [16], reveals a totally nontrivial feature of the dense QCD medium created at RHIC. The shape of the spectra and the suppression pattern

indicate that the dominant term in energy loss is proportional to p_T.

We thank the staff of the Collider-Accelerator and Physics Departments at BNL for their vital contributions. We acknowledge support from the Office of Nuclear Physics in DOE Office of Science and NSF (USA), MEXT and JSPS (Japan), CNPq and FAPESP (Brazil), NSFC (China), MSMT (Czech Republic), IN2P3/CNRS, and CEA (France), BMBF, DAAD, and AvH (Germany), OTKA (Hungary), DAE (India), ISF (Israel), KRF and KOSEF (Korea), MES, RAS, and FAAE (Russia), VR and KAW (Sweden), U.S. CRDF for the FSU, US-Hungarian NSF-OTKA-MTA, and US-Israel BSF.

*Deceased

+PHENIX Spokesperson:
jacak@skipper.physics.sunysb.edu

[1] D. de Florian and W. Vogelsang, Phys. Rev. D **71**, 114004 (2005).
[2] M. Gyulassy and M. Plumer, Phys. Lett. B **243**, 432 (1990).
[3] X.-N. Wang and M. Gyulassy, Phys. Rev. Lett. **68**, 1480 (1992).
[4] K. Adcox *et al.*, Phys. Rev. Lett. **88**, 022301 (2001).
[5] R. Baier, Y. L. Dokshitzer, A. H. Mueller, S. Peigne, and D. Schiff, Nucl. Phys. B **484**, 265 (1997).
[6] M. Gyulassy, P. Levai, and I. Vitev, Phys. Rev. Lett. **85**, 5535 (2000).
[7] T. Renk, Phys. Rev. C **74**, 034906 (2006).
[8] R. Baier and D. Schiff, J. High Energy Phys. 09 (2006) 059.
[9] A. Dainese, C. Loizides, and G. Paic, Eur. Phys. J. C **38**, 461 (2005).
[10] C. Loizides, Eur. Phys. J. C **49**, 339 (2007).
[11] H. Zhang, J. F. Owens, E. Wang, and X.-N. Wang, Phys. Rev. Lett. **98**, 212301 (2007).
[12] K. Adcox *et al.*, Nucl. Instrum. Methods Phys. Res., Sect. A **499**, 469 (2003).
[13] M. L. Miller, K. Reygers, S. J. Sanders, and P. Steinberg, Annu. Rev. Nucl. Part. Sci. **57**, 205 (2007).
[14] L. Aphecetche *et al.*, Nucl. Instrum. Methods Phys. Res., Sect. A **499**, 521 (2003).
[15] S. S. Adler *et al.*, Phys. Rev. C **76**, 034904 (2007).
[16] A. Adare *et al.*, Phys. Rev. C **77**, 064907 (2008).
[17] A. Adare, Phys. Rev. D **76**, 051106 (2007).
[18] K. Adcox *et al.* (PHENIX), Nucl. Phys. A **757**, 184 (2005).

Observation of direct-photon collective flow in Au+Au collisions at $\sqrt{s_{NN}} = 200$ GeV

A. Adare,[11] S. Afanasiev,[27] C. Aidala,[40] N.N. Ajitanand,[57] Y. Akiba,[51,52] H. Al-Bataineh,[46] J. Alexander,[57] K. Aoki,[33,51] Y. Aramaki,[10] E.T. Atomssa,[34] R. Averbeck,[58] T.C. Awes,[47] B. Azmoun,[5] V. Babintsev,[22] M. Bai,[4] G. Baksay,[18] L. Baksay,[18] K.N. Barish,[6] B. Bassalleck,[45] A.T. Basye,[1] S. Bathe,[6] V. Baublis,[50] C. Baumann,[41] A. Bazilevsky,[5] S. Belikov,[5,*] R. Belmont,[62] R. Bennett,[58] A. Berdnikov,[54] Y. Berdnikov,[54] A.A. Bickley,[11] J.S. Bok,[65] K. Boyle,[58] M.L. Brooks,[36] H. Buesching,[5] V. Bumazhnov,[22] G. Bunce,[5,52] S. Butsyk,[36] C.M. Camacho,[36] S. Campbell,[58] C.-H. Chen,[58] C.Y. Chi,[12] M. Chiu,[5] I.J. Choi,[65] R.K. Choudhury,[3] P. Christiansen,[38] T. Chujo,[61] P. Chung,[57] O. Chvala,[6] V. Cianciolo,[47] Z. Citron,[58] B.A. Cole,[12] M. Connors,[58] P. Constantin,[36] M. Csanád,[16] T. Csörgő,[30] T. Dahms,[58] S. Dairaku,[33,51] I. Danchev,[62] K. Das,[19] A. Datta,[40] G. David,[5] A. Denisov,[22] A. Deshpande,[52,58] E.J. Desmond,[5] O. Dietzsch,[55] A. Dion,[58] M. Donadelli,[55] O. Drapier,[34] A. Drees,[58] K.A. Drees,[4] J.M. Durham,[58] A. Durum,[22] D. Dutta,[3] S. Edwards,[19] Y.V. Efremenko,[47] F. Ellinghaus,[11] T. Engelmore,[12] A. Enokizono,[35] H. En'yo,[51,52] S. Esumi,[61] B. Fadem,[42] D.E. Fields,[45] M. Finger,[7] M. Finger, Jr.,[7] F. Fleuret,[34] S.L. Fokin,[32] Z. Fraenkel,[64,*] J.E. Frantz,[58] A. Franz,[5] A.D. Frawley,[19] K. Fujiwara,[51] Y. Fukao,[51] T. Fusayasu,[44] I. Garishvili,[59] A. Glenn,[11] H. Gong,[58] M. Gonin,[34] Y. Goto,[51,52] R. Granier de Cassagnac,[34] N. Grau,[12] S.V. Greene,[62] M. Grosse Perdekamp,[23,52] T. Gunji,[10] H.-Å. Gustafsson,[38,*] J.S. Haggerty,[5] K.I. Hahn,[17] H. Hamagaki,[10] J. Hamblen,[59] R. Han,[49] J. Hanks,[12] E.P. Hartouni,[35] E. Haslum,[38] R. Hayano,[10] X. He,[20] M. Heffner,[35] T.K. Hemmick,[58] T. Hester,[6] J.C. Hill,[26] M. Hohlmann,[18] W. Holzmann,[12] K. Homma,[21] B. Hong,[31] T. Horaguchi,[21] D. Hornback,[59] S. Huang,[62] T. Ichihara,[51,52] R. Ichimiya,[51] J. Ide,[42] Y. Ikeda,[61] K. Imai,[33,51] M. Inaba,[61] D. Isenhower,[1] M. Ishihara,[51] T. Isobe,[10] M. Issah,[62] A. Isupov,[27] D. Ivanischev,[50] B.V. Jacak,[58,†] J. Jia,[5,57] J. Jin,[12] B.M. Johnson,[5] K.S. Joo,[43] D. Jouan,[48] D.S. Jumper,[1] F. Kajihara,[10] S. Kametani,[51] N. Kamihara,[52] J. Kamin,[58] J.H. Kang,[65] J. Kapustinsky,[36] K. Karatsu,[33] D. Kawall,[40,52] M. Kawashima,[53,51] A.V. Kazantsev,[32] T. Kempel,[26] A. Khanzadeev,[50] K.M. Kijima,[21] B.I. Kim,[31] D.H. Kim,[43] D.J. Kim,[28] E. Kim,[56] E.J. Kim,[8] S.H. Kim,[65] Y.J. Kim,[23] E. Kinney,[11] K. Kiriluk,[11] Á. Kiss,[16] E. Kistenev,[5] C. Klein-Boesing,[41] L. Kochenda,[50] B. Komkov,[50] M. Konno,[61] J. Koster,[23] D. Kotchetkov,[45] A. Kozlov,[64] A. Král,[13] A. Kravitz,[12] G.J. Kunde,[36] K. Kurita,[53,51] M. Kurosawa,[51] Y. Kwon,[65] G.S. Kyle,[46] R. Lacey,[57] Y.S. Lai,[12] J.G. Lajoie,[26] A. Lebedev,[26] D.M. Lee,[36] J. Lee,[17] K. Lee,[56] K.B. Lee,[31] K.S. Lee,[31] M.J. Leitch,[36] M.A.L. Leite,[55] E. Leitner,[62] B. Lenzi,[55] X. Li,[9] P. Liebing,[52] L.A. Linden Levy,[11] T. Liška,[13] A. Litvinenko,[27] H. Liu,[36,46] M.X. Liu,[36] B. Love,[62] R. Luechtenborg,[41] D. Lynch,[5] C.F. Maguire,[62] Y.I. Makdisi,[4] A. Malakhov,[27] M.D. Malik,[45] V.I. Manko,[32] E. Mannel,[12] Y. Mao,[49,51] H. Masui,[61] F. Matathias,[12] M. McCumber,[58] P.L. McGaughey,[36] N. Means,[58] B. Meredith,[23] Y. Miake,[61] A.C. Mignerey,[39] P. Mikeš,[7,25] K. Miki,[61] A. Milov,[5] M. Mishra,[2] J.T. Mitchell,[5] A.K. Mohanty,[3] Y. Morino,[10] A. Morreale,[6] D.P. Morrison,[5] T.V. Moukhanova,[32] J. Murata,[53,51] S. Nagamiya,[29] J.L. Nagle,[11] M. Naglis,[64] M.I. Nagy,[16] I. Nakagawa,[51,52] Y. Nakamiya,[21] T. Nakamura,[21,29] K. Nakano,[51,60] J. Newby,[35] M. Nguyen,[58] R. Nouicer,[5] A.S. Nyanin,[32] E. O'Brien,[5] S.X. Oda,[10] C.A. Ogilvie,[26] M. Oka,[61] K. Okada,[52] Y. Onuki,[51] A. Oskarsson,[38] M. Ouchida,[21] K. Ozawa,[10] R. Pak,[5] V. Pantuev,[24,58] V. Papavassiliou,[46] I.H. Park,[17] J. Park,[56] S.K. Park,[31] W.J. Park,[31] S.F. Pate,[46] H. Pei,[26] J.-C. Peng,[23] H. Pereira,[14] V. Peresedov,[27] D.Yu. Peressounko,[32] C. Pinkenburg,[5] R.P. Pisani,[5] M. Proissl,[58] M.L. Purschke,[5] A.K. Purwar,[36] H. Qu,[20] J. Rak,[28] A. Rakotozafindrabe,[34] I. Ravinovich,[64] K.F. Read,[47,59] K. Reygers,[41] V. Riabov,[50] Y. Riabov,[50] E. Richardson,[39] D. Roach,[62] G. Roche,[37] S.D. Rolnick,[6] M. Rosati,[26] C.A. Rosen,[11] S.S.E. Rosendahl,[38] P. Rosnet,[37] P. Rukoyatkin,[27] P. Ružička,[25] B. Sahlmueller,[41] N. Saito,[29] T. Sakaguchi,[5] K. Sakashita,[51,60] V. Samsonov,[50] S. Sano,[10,63] T. Sato,[61] S. Sawada,[29] K. Sedgwick,[6] J. Seele,[11] R. Seidl,[23] A.Yu. Semenov,[26] R. Seto,[6] D. Sharma,[64] I. Shein,[22] T.-A. Shibata,[51,60] K. Shigaki,[21] M. Shimomura,[61] K. Shoji,[33,51] P. Shukla,[3] A. Sickles,[5] C.L. Silva,[55] D. Silvermyr,[47] C. Silvestre,[14] K.S. Sim,[31] B.K. Singh,[2] C.P. Singh,[2] V. Singh,[2] M. Slunečka,[7] R.A. Soltz,[35] W.E. Sondheim,[36] S.P. Sorensen,[59] I.V. Sourikova,[5] N.A. Sparks,[1] P.W. Stankus,[47] E. Stenlund,[38] S.P. Stoll,[5] T. Sugitate,[21] A. Sukhanov,[5] J. Sziklai,[30] E.M. Takagui,[55] A. Taketani,[51,52] R. Tanabe,[61] Y. Tanaka,[44] K. Tanida,[33,51,52] M.J. Tannenbaum,[5] S. Tarafdar,[2] A. Taranenko,[57] P. Tarján,[15] H. Themann,[58] T.L. Thomas,[45] M. Togawa,[33,51] A. Toia,[58] L. Tomášek,[25] H. Torii,[21] R.S. Towell,[1] I. Tserruya,[64] Y. Tsuchimoto,[21] C. Vale,[5,26] H. Valle,[62] H.W. van Hecke,[36] E. Vazquez-Zambrano,[12] A. Veicht,[23] J. Velkovska,[62] R. Vértesi,[15,30] A.A. Vinogradov,[32] M. Virius,[13] V. Vrba,[25] E. Vznuzdaev,[50] X.R. Wang,[46] D. Watanabe,[21] K. Watanabe,[61] Y. Watanabe,[51,52] F. Wei,[26] R. Wei,[57] J. Wessels,[41] S.N. White,[5] D. Winter,[12] J.P. Wood,[1] C.L. Woody,[5] R.M. Wright,[1] M. Wysocki,[11] W. Xie,[52] Y.L. Yamaguchi,[10] K. Yamaura,[21] R. Yang,[23] A. Yanovich,[22] J. Ying,[20] S. Yokkaichi,[51,52]

Z. You,[49] G.R. Young,[47] I. Younus,[45] I.E. Yushmanov,[32] W.A. Zajc,[12] C. Zhang,[47] S. Zhou,[9] and L. Zolin[27]
(PHENIX Collaboration)

[1]*Abilene Christian University, Abilene, Texas 79699, USA*
[2]*Department of Physics, Banaras Hindu University, Varanasi 221005, India*
[3]*Bhabha Atomic Research Centre, Bombay 400 085, India*
[4]*Collider-Accelerator Department, Brookhaven National Laboratory, Upton, New York 11973-5000, USA*
[5]*Physics Department, Brookhaven National Laboratory, Upton, New York 11973-5000, USA*
[6]*University of California - Riverside, Riverside, California 92521, USA*
[7]*Charles University, Ovocný trh 5, Praha 1, 116 36, Prague, Czech Republic*
[8]*Chonbuk National University, Jeonju, 561-756, Korea*
[9]*Science and Technology on Nuclear Data Laboratory, China Institute of Atomic Energy, Beijing 102413, P. R. China*
[10]*Center for Nuclear Study, Graduate School of Science, University of Tokyo, 7-3-1 Hongo, Bunkyo, Tokyo 113-0033, Japan*
[11]*University of Colorado, Boulder, Colorado 80309, USA*
[12]*Columbia University, New York, New York 10027 and Nevis Laboratories, Irvington, New York 10533, USA*
[13]*Czech Technical University, Zikova 4, 166 36 Prague 6, Czech Republic*
[14]*Dapnia, CEA Saclay, F-91191, Gif-sur-Yvette, France*
[15]*Debrecen University, H-4010 Debrecen, Egyetem tér 1, Hungary*
[16]*ELTE, Eötvös Loránd University, H - 1117 Budapest, Pázmány P. s. 1/A, Hungary*
[17]*Ewha Womans University, Seoul 120-750, Korea*
[18]*Florida Institute of Technology, Melbourne, Florida 32901, USA*
[19]*Florida State University, Tallahassee, Florida 32306, USA*
[20]*Georgia State University, Atlanta, Georgia 30303, USA*
[21]*Hiroshima University, Kagamiyama, Higashi-Hiroshima 739-8526, Japan*
[22]*IHEP Protvino, State Research Center of Russian Federation, Institute for High Energy Physics, Protvino, 142281, Russia*
[23]*University of Illinois at Urbana-Champaign, Urbana, Illinois 61801, USA*
[24]*Institute for Nuclear Research of the Russian Academy of Sciences, prospekt 60-letiya Oktyabrya 7a, Moscow 117312, Russia*
[25]*Institute of Physics, Academy of Sciences of the Czech Republic, Na Slovance 2, 182 21 Prague 8, Czech Republic*
[26]*Iowa State University, Ames, Iowa 50011, USA*
[27]*Joint Institute for Nuclear Research, 141980 Dubna, Moscow Region, Russia*
[28]*Helsinki Institute of Physics and University of Jyväskylä, P.O.Box 35, FI-40014 Jyväskylä, Finland*
[29]*KEK, High Energy Accelerator Research Organization, Tsukuba, Ibaraki 305-0801, Japan*
[30]*KFKI Research Institute for Particle and Nuclear Physics of the Hungarian Academy of Sciences (MTA KFKI RMKI), H-1525 Budapest 114, POBox 49, Budapest, Hungary*
[31]*Korea University, Seoul, 136-701, Korea*
[32]*Russian Research Center "Kurchatov Institute", Moscow, 123098 Russia*
[33]*Kyoto University, Kyoto 606-8502, Japan*
[34]*Laboratoire Leprince-Ringuet, Ecole Polytechnique, CNRS-IN2P3, Route de Saclay, F-91128, Palaiseau, France*
[35]*Lawrence Livermore National Laboratory, Livermore, California 94550, USA*
[36]*Los Alamos National Laboratory, Los Alamos, New Mexico 87545, USA*
[37]*LPC, Université Blaise Pascal, CNRS-IN2P3, Clermont-Fd, 63177 Aubiere Cedex, France*
[38]*Department of Physics, Lund University, Box 118, SE-221 00 Lund, Sweden*
[39]*University of Maryland, College Park, Maryland 20742, USA*
[40]*Department of Physics, University of Massachusetts, Amherst, Massachusetts 01003-9337, USA*
[41]*Institut fur Kernphysik, University of Muenster, D-48149 Muenster, Germany*
[42]*Muhlenberg College, Allentown, Pennsylvania 18104-5586, USA*
[43]*Myongji University, Yongin, Kyonggido 449-728, Korea*
[44]*Nagasaki Institute of Applied Science, Nagasaki-shi, Nagasaki 851-0193, Japan*
[45]*University of New Mexico, Albuquerque, New Mexico 87131, USA*
[46]*New Mexico State University, Las Cruces, New Mexico 88003, USA*
[47]*Oak Ridge National Laboratory, Oak Ridge, Tennessee 37831, USA*
[48]*IPN-Orsay, Universite Paris Sud, CNRS-IN2P3, BP1, F-91406, Orsay, France*
[49]*Peking University, Beijing 100871, P. R. China*
[50]*PNPI, Petersburg Nuclear Physics Institute, Gatchina, Leningrad region 188300, Russia*
[51]*RIKEN Nishina Center for Accelerator-Based Science, Wako, Saitama 351-0198, Japan*
[52]*RIKEN BNL Research Center, Brookhaven National Laboratory, Upton, New York 11973-5000, USA*
[53]*Physics Department, Rikkyo University, 3-34-1 Nishi-Ikebukuro, Toshima, Tokyo 171-8501, Japan*
[54]*Saint Petersburg State Polytechnic University, St. Petersburg, 195251 Russia*
[55]*Universidade de São Paulo, Instituto de Física, Caixa Postal 66318, São Paulo CEP05315-970, Brazil*
[56]*Seoul National University, Seoul, Korea*
[57]*Chemistry Department, Stony Brook University, SUNY, Stony Brook, New York 11794-3400, USA*
[58]*Department of Physics and Astronomy, Stony Brook University, SUNY, Stony Brook, New York 11794-3400, USA*
[59]*University of Tennessee, Knoxville, Tennessee 37996, USA*
[60]*Department of Physics, Tokyo Institute of Technology, Oh-okayama, Meguro, Tokyo 152-8551, Japan*

[61] Institute of Physics, University of Tsukuba, Tsukuba, Ibaraki 305, Japan
[62] Vanderbilt University, Nashville, Tennessee 37235, USA
[63] Waseda University, Advanced Research Institute for Science and Engineering, 17 Kikui-cho, Shinjuku-ku, Tokyo 162-0044, Japan
[64] Weizmann Institute, Rehovot 76100, Israel
[65] Yonsei University, IPAP, Seoul 120-749, Korea
(Dated: August 23, 2011)

The second Fourier component v_2 of the azimuthal anisotropy with respect to the reaction plane was measured for direct photons at midrapidity and transverse momentum (p_T) of 1–13 GeV/c in Au+Au collisions at $\sqrt{s_{NN}} = 200$ GeV. Previous measurements of this quantity for hadrons with $p_T < 6$ GeV/c indicate that the medium behaves like a nearly perfect fluid, while for $p_T > 6$ GeV/c a reduced anisotropy is interpreted in terms of a path-length dependence for parton energy loss. In this measurement with the PHENIX detector at the Relativistic Heavy Ion Collider we find that for $p_T > 4$ GeV/c the anisotropy for direct photons is consistent with zero, as expected if the dominant source of direct photons is initial hard scattering. However, in the $p_T < 4$ GeV/c region dominated by thermal photons, we find a substantial direct photon v_2 comparable to that of hadrons, whereas model calculations for thermal photons in this kinematic region significantly underpredict the observed v_2.

PACS numbers: 25.75.Dw

Direct photons are produced in various processes during the entire space-time history of relativistic heavy ion collisions and, due to their small coupling, can leave the collision region without appreciable further interaction. This makes them a sensitive and direct probe of all stages of the collision, including initial hard scattering, formation and evolution of the strongly interacting partonic medium, its transition to hadronic matter, and final decoupling [1, 2]. The transverse momentum (p_T) ranges populated by various production mechanisms overlap. However, azimuthal asymmetries tied to the event-by-event collision geometry provide useful additional information and a means to distinguish between sources of direct photons. In this paper we consider the second Fourier component (v_2, often referred to as elliptic flow) of the event-by-event photon distribution in azimuth with respect to the reaction plane for minimum bias and selected centralities in Au+Au collisions.

At higher p_T (> 4 GeV/c) there are four fundamental sources of direct photons, characterized by different v_2 [2, 3]. Photons from initial hard scattering (predominantly from $qg \to q\gamma$ "gluon Compton scattering") are isotropic and so $v_2 = 0$. Jet fragmentation photons have positive v_2 since the energy loss of the originating parton is smaller in the reaction plane [4]. Jet-conversion photons where a hard scattered quark interacts with a thermal gluon in the medium and converts into a photon with almost equal p_T have negative v_2 [3], because the average pathlength of the parton in the medium (proportional to the conversion probability) is larger out of the reaction plane than within. Finally, Bremsstrahlung photons are also emitted preferentially in the direction where the medium is thicker, leading to a negative v_2 [3]. Note that in this picture the azimuthal asymmetry of high p_T photon production – while expressed in terms of v_2– reflects the pure geometry of the medium, not its dynamics: it depends on the pathlength, not on the boost from the hydrodynamic pressure gradients.

The picture is quite different in the low p_T range ($1 < p_T < 4$ GeV/c) dominated by thermal photons, as first measured in [5], where bulk dynamics (expansion) plays an important role since it influences both the rate and azimuthal asymmetries of photon production [3, 6]. It is now established that collectivity – which already exists in the partonic phase (strongly interacting Quark-Gluon Plasma, sQGP) – persists after transition into the hadronic phase and the resulting azimuthal asymmetries in particle production can be described by near-ideal hydrodynamics. The expectation is that thermal radiation from both the sQGP and the hadronic phase will inherit the collective motion of the medium, i.e. will have a bona fide elliptic flow, positive v_2 at low p_T [7]. The low p_T behavior of direct photon v_2 puts constraints on the viscosity of the sQGP [6].

The PHENIX experiment has published the invariant yield as a function of p_T for direct photons both via real photons and internal conversions of nearly real virtual photons [5, 8]. In the $1 < p_T < 4$ GeV/c region, a substantial excess of direct photons was observed relative to scaling of $p+p$ yields and has been interpreted in terms of thermal photon emission from the hot medium. An early attempt to infer v_2 of direct photons from a π^0 and inclusive photon v_2 measurement performed in a limited p_T range has been published in [9]. In this Letter we present measurements by the PHENIX experiment [10] of v_2 of π^0 and inclusive photons in a much extended transverse momentum (p_T) range (up to 13 GeV/c) in $\sqrt{s_{NN}} = 200$ GeV Au+Au collisions. Also, at low p_T the fraction R_γ of direct over inclusive photons is now measured with much higher precision [5] than before [8], therefore, for the first time a meaningful extraction of the direct photon v_2 itself is possible.

Data were taken in the 2007 run of the Relativistic Heavy Ion Collider at Brookhaven National Laboratory. The analyzed sample includes $\sim 3.0 \times 10^9$ minimum bias Au+Au collisions. Events were triggered by the Beam-Beam Counters (BBC), as described in [11], which comprise two arrays of Čerenkov counters covering $3.1 < |\eta| < 3.9$ and 2π in azimuth in both beam directions (North and South). Event centrality was determined by the charge sum in the BBC.

The event-by-event reaction plane (RP) has been determined by two detectors, the first being the BBC itself. The RP resolution (effectively a dilution factor with which the observed v_2 is normalized to obtain the true v_2) is defined as $\sigma_{\rm RP} =< \cos[2(\Psi^{\rm true} - \Psi^{\rm RP})] >$ and it is established by comparing event-by-event the RPs obtained separately in the North and South detectors. The resolution is highest in the 20-30% centrality bin where it reaches a value of 0.4. For the 2007 data taking period, a dedicated reaction plane detector (RXN) [12] was installed covering $1.0 < |\eta| < 2.8$ and the full azimuth. The RXN is a highly segmented lead-scintillator sampling detector providing much better measurement ($\sigma_{\rm RP} \sim 0.7$) than the BBC, but it is closer to the central $|\eta| < 0.35$ pseudorapidity region where v_2 is measured, making it more sensitive to jet bias in those (rare) events where a high p_T particle is observed. The $0.7/0.4 = 1.75$ improvement on the reaction plane resolution results is a 1.75-fold improvement on point-by-point uncertainty.

Inclusive photons were measured in the PHENIX electromagnetic calorimeter [13]. Particles were identified (PID) and hadrons were rejected by a shower shape cut and a veto on charged particles using the Pad Chambers [14]. The remaining sample is collected for each p_T range in histograms binned according to $\Phi - \Psi^{\rm RP}$ where $\Psi^{\rm RP}$ is the azimuth of the event-by-event reaction plane and established independently by the BBC and RXN. These distributions are then fit for each p_T range with $N_0\ [1 + 2\ v_2\ \cos\{2(\Phi - \Psi^{\rm RP})\}]$ to extract the raw $v_2^{\gamma,{\rm meas}}$ coefficient for inclusive photons. As a cross-check of the fit value, another $v_2^{\gamma,{\rm meas}}$ is also calculated from the average cosine of the particles with respect to the reaction plane. While the PID eliminates virtually all hadrons above 6 GeV deposited energy (which might come from hadrons of *any* p_T above 6 GeV/c), a significant fraction of hadrons (up to 20% below 2 GeV deposited energy) survive the photon identification cuts. Since hadrons are known to have a large v_2 value, the observed $v_2^{\rm obs}$ of inclusive photons is obtained after correcting for hadrons as

$$v_2^{\gamma,{\rm obs}} = \frac{v_2^{\gamma,{\rm meas}} - (N^{\rm hadr}/N^{\rm meas}) v_2^{\rm hadr}}{1 - N^{\rm hadr}/N^{\rm meas}},$$

where $v_2^{\rm hadr}$ is the elliptic flow of hadrons and $N^{\rm hadr}/N^{\rm meas}$ is the fraction of hadrons in the sample surviving the PID cuts, as estimated from GEANT simulations (20% at 2 GeV, 10% at 4 GeV and negligible above 6 GeV deposited energy). Finally the true $v_2^{\gamma,{\rm inc}}$ for inclusive photons is obtained by dividing by the reaction plane resolution $v_2^{\gamma,{\rm inc}} = v_2^{\gamma,{\rm obs}}/\sigma_{\rm RP}$.

A large fraction of inclusive photons comes from hadron decays, predominantly from π^0 ($\sim$80%) and η ($\sim$15%), with a small fraction coming from ρ, ω and η' decays, but only the π^0 v_2 is directly measured. The measurement of neutral pions and their v_2 is described in detail in [4, 15]. We assume that η, ω, etc. follow the same KE_T scaling observed in hadrons [16] where $KE_T = m_T - m$, Thus, $v_2^{\rm hadr}(p_T)$ can be calculated for all hadrons from $v_2^{\pi^0}(p_T)$. For this we assume m_T-scaling of hadron p_T spectra and establish a "hadron cocktail" using the measured yield ratios, similar to the one in [5]. This cocktail is the input of a Monte Carlo simulation to calculate the total $v_2^{\gamma,{\rm bg}}$ due to photons from hadron decays. The direct photon $v_2^{\gamma,{\rm dir}}$ is then obtained using the $R_\gamma(p_T)$ "direct photon excess ratio" as

$$v_2^{\gamma,{\rm dir}} = \frac{R_\gamma(p_T) v_2^{\gamma,{\rm inc}} - v_2^{\gamma,{\rm bg}}}{R_\gamma(p_T) - 1},$$

where $R_\gamma(p_T) = N^{\rm inc}(p_T)/N^{bg}(p_T)$ with $N^{\rm inc} = N^{\rm meas} - N^{\rm hadr}$, the number of inclusive photons, while $N^{bg}(p_T)$ is the number of photons attributed to hadron decay. Values of $R_\gamma(p_T)$ above 5 GeV/c are taken from the real photon measurement with the PHENIX electromagnetic calorimeter [8], and below that from the more accurate, but p_T-range limited internal conversion measurement of direct photons [5].

TABLE I: Systematic uncertainties ($\delta x/x$) contributing to the direct photon $v_2^{\gamma,{\rm dir}}$ measurement for minimum-bias collisions over two p_T ranges.

Contributing via	Source	p_T range 1-3 GeV/c	p_T range 10-16 GeV/c	Type
$v_2^{\gamma,{\rm inc}}$	remaining hadrons	2.2%	N/A	B
	v_2 extraction method	0.4%	0.6%	B
$v_2^{\pi^0}$	particle ID	3.7%	6.0%	B
	normalization	0.4%	7.2%	B
	shower merging	N/A	4.0%	B
subtraction	R_γ	3.1%	22%	B
common	reaction plane	6.3%	6.3%	C

Sources of systematic uncertainties for representative p_T values are listed in Table I along with their characterization: type A means point-by-point uncertainties which are uncorrelated with p_T, type B means uncertainties that are correlated (with p_T) and type C is the overall normalization uncertainty, moving all points by the same fraction up or down. Since the v_2 measurement is a relative one (the azimuthal anisotropy is fit without the need to know the absolute normalization), the π^0 and

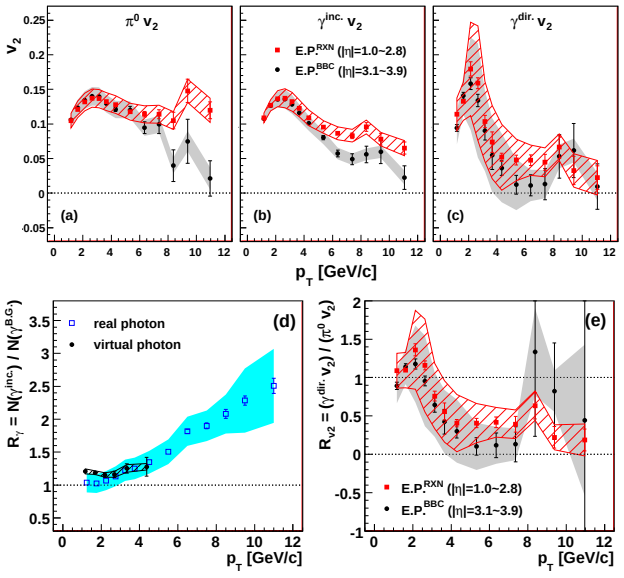

FIG. 1: (Color online) (a,b,c) v_2 in minimum bias collisions, using two different reaction plane detectors: (solid black circles) BBC and (solid red squares) RXN for (a) π^0, (b) inclusive photon, and (c) direct photon. (d) direct photon fraction R_γ for (solid black circles) virtual photons [5] and (open blue squares) real photons [8] and (e) ratio of direct photon to π^0 v_2 for (solid black circles) BBC and (solid red squares) RXN. The vertical error bars on each data point indicate statistical uncertainties and shaded (gray and cyan) and hatched (red) areas around the data points indicate sizes of systematic uncertainties.

inclusive photon v_2 measurements are largely immune to energy scale uncertainties which are typically the dominant source of uncertainty in an absolute (invariant yield) measurement. The uncertainties on v_2 are dominated by the common uncertainty on determining $\sigma_{\rm RP}$ and by uncertainties on particle identification. Uncertainties from absolute yields enter indirectly via the hadron cocktail (normalization) and more directly at higher p_T (where the real photon measurement is used) by the $R_\gamma(p_T)$ needed to establish the direct photon v_2. Note that due to the way $v_2^{\gamma,\rm dir}$ is calculated, once R_γ is large, its relative error contributes to the error on $v_2^{\gamma,\rm dir}$ less and less.

Figure 1 shows steps of the analysis using the minimum bias sample, as well as the differences between results obtained with BBC and RXN. The first v_2 of π^0 and inclusive photons ($v_2^{\pi^0}$,$v_2^{\gamma,inc}$) are measured, as described above (panels (a) and (b)). Then, using the $v_2^{\gamma,bg}$ of photons from hadronic decays and the R_γ direct photon excess ratio, we derive the $v_2^{\gamma,dir}$ of direct photons (panel (c)). Panel (d) shows the $R_\gamma(p_T)$ values from the direct photon invariant yield measurements using internal conversion [5] and real [8] photons, with their respective uncertainties. Panel (e) shows the ratio of $v_2^{\gamma,dir}/v_2^{\pi^0}$. We observe substantial direct photon flow in the low p_T region (c), commensurate with the hadron flow itself (e). However, in contrast to hadrons, the direct photon v_2 rapidly decreases with p_T; and starting with 5 GeV/c and above, it is consistent with zero (c). The rapid transition from high direct photon flow at 3 GeV/c to zero flow at 5 GeV/c is also demonstrated on panel (e), since the π^0 v_2 changes little in this region [4].

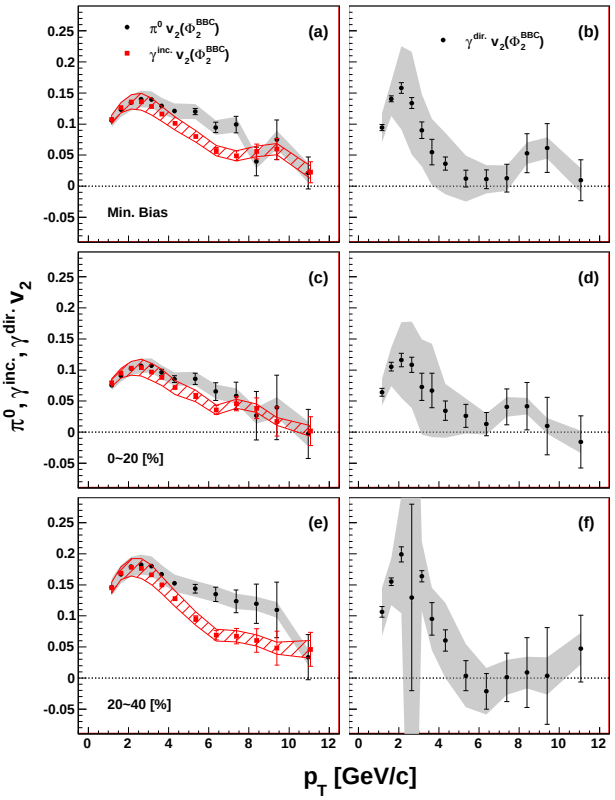

FIG. 2: (Color online) (a,c,e) Centrality dependence of v_2 for (solid black circles) π^0, (solid red squares) inclusive photons, and (b,d,f) (solid black circles) direct photons measured with the BBC detector for (a,b) minimum bias (c,d) 0-20% centrality, and (e,f) 20-40% centrality. For (b,d,f) the direct photon fraction is taken from [5] up to 4 GeV/c and from [8] for higher p_T. The vertical error bars on each data point indicate statistical uncertainties and the shaded (gray) and hatched (red) areas around the data points indicate sizes of systematic uncertainties.

A major issue in any azimuthal asymmetry measurement is the potential bias from where in pseudorapidity the (event-by-event) reaction plane is measured. At low p_T– where multiplicities are high and particle production is dominated by the bulk with genuine hydrodynamic behavior – there is no difference between the flow derived with BBC and RXN. However, at higher p_T we observe that the v_2 values using BBC and RXN diverge, particularly for π^0 (panel (a) in Fig. 1), less for inclusive photons. For direct photons (panel (c)) the two results are apparently consistent within their *total* errors, including the

error $\delta R_\gamma/R_\gamma$ (see Table I) but it should be noted that R_γ is a common correction factor in the v_2 measurements with both reaction plane detectors.

Event substructure not related to bulk properties and expansion – most notably jets – can bias the reaction plane measurement, particularly at higher p_T and lower multiplicity. Observation of a high p_T particle practically guarantees the presence of a jet, which in turn modifies the event structure over a large η range. The bias on the true event plane (with the bulk as its origin) is stronger if the overall multiplicity is small and if the η gap between the central arm (where v_2 is measured) and the reaction plane detector is reduced. The bias in Fig. 1 is largest for π^0, since high p_T hadrons are always jet fragments. Inclusive photons are a mixture of hadron decay photons, inheriting the bias seen in π^0 and the mostly unbiased direct photons, therefore, the difference between BBC and RXN is smaller. Finally, the bias is smallest (but nonzero) for direct photons, of which only a relatively small fraction (jet fragmentation photons) exhibit bias.

Figure 2 shows v_2 for minimum bias and two centralities as a function of transverse momentum for π^0, inclusive and direct photons. For reaction plane determination the BBC is used because it is farthest from midrapidity where v_2 is measured. Despite the fact that there is a significant direct (thermal) photon yield at low p_T [5], the π^0 and inclusive photon v_2 is virtually identical there. Note that the surprisingly large inclusive photon v_2 is confirmed by the (so far preliminary) results with a completely different analysis technique [17]. For direct photons at low p_T we observe a pronounced positive v_2 signal, increasing with decreasing centrality and comparable to the π^0 flow, but then rapidly going toward zero at 5-6 GeV/c. Qualitatively this shape agrees with the prediction for very early thermalization times, 0.2-0.4 fm/c in [18], 0.2 fm/c and vanishing viscosity in [7], but both models severely underestimate the magnitude of the v_2. The model in [19] combines somewhat later thermalization time (0.6 fm/c) with partial chemical equilibrium in the hadronic phase, reproducing the shape, but missing the magnitude of the observed v_2 at low p_T. While such large direct photon v_2 in principle could be attributed to a dominant production mechanism at the later stage when bulk flow is already developed, simultaneously explaining the large values of v_2 at ~2 GeV/c and its vanishing above 5 GeV/c remains a challenge to current theories.

Figure 3 shows the high p_T integrated v_2 ($p_T >$ 6 GeV/c) for π^0 and photons (inclusive and direct) as a function of centrality. The low $N_{\rm part}$ behavior is strongly influenced by the location in pseudorapidity of the reaction plane detector. The π^0 v_2 is comparable to other hadrons and is higher than the inclusive photon v_2, which is diluted by direct photons. The two direct photon v_2 measurements (panel (c)) are consistent with zero (and each other) at all centralities within their total systematic errors. While zero v_2 would be expected if initial hard scattering is the dominant (sole considered) source of photons, it should be pointed out that the typical contribution from jet-conversion only would be $v_2 \sim -0.02$ and from fragmentation $v_2 \leq 0.01$ weighted with the fraction of photons coming from these specific processes [3, 7]. Currently the experiment is not sensitive to their negative/positive contributions to v_2.

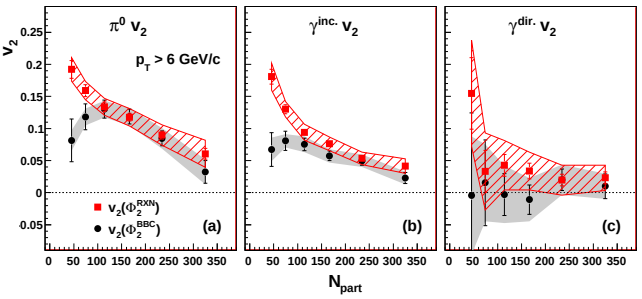

FIG. 3: High p_T ($p_T >$ 6 GeV/c) integrated v_2 vs $N_{\rm part}$ for (a) π^0, (b) inclusive photon, and (c) direct photon. Results are shown with both reaction plane detectors: (solid black circles) BBC and (solid red squares) RXN. Each point represents a 10% wide centrality bin from 60–0%. The vertical error bars on each data point indicate statistical uncertainties and the shaded (gray) and hatched (red) areas around the data points indicate sizes of systematic uncertainties.

In conclusion, PHENIX has measured v_2 of π^0, inclusive and direct photons in the $1 < p_T < 13$ GeV/c range for minimum bias and selected centralities in $\sqrt{s_{NN}} =$ 200 GeV Au+Au collisions. At higher p_T ($>$ 6 GeV/c) the direct photon v_2 is consistent with zero at all centralities, as expected if the dominant source of photon production is initial hard scattering. However, the experimental uncertainties are currently about a factor of 2 higher than the predicted (small) positive and negative contributions from fragmentation and jet conversion photons, respectively. In the thermal region ($p_T < 4$ GeV/c), a positive direct photon v_2 is observed which is comparable in magnitude to the π^0 v_2 and consistent with early thermalization times and low viscosity, but its magnitude is much larger than current theories predict.

We thank the staff of the Collider-Accelerator and Physics Departments at Brookhaven National Laboratory and the staff of the other PHENIX participating institutions for their vital contributions. We acknowledge support from the Office of Nuclear Physics in the Office of Science of the Department of Energy, the National Science Foundation, Abilene Christian University Research Council, Research Foundation of SUNY, and Dean of the College of Arts and Sciences, Vanderbilt University (U.S.A), Ministry of Education, Culture, Sports, Science, and Technology and the Japan Society for the Promotion of Science (Japan), Conselho Nacional de Desenvolvimento Científico e Tecnológico and Fundação de

Amparo à Pesquisa do Estado de São Paulo (Brazil), Natural Science Foundation of China (P. R. China), Ministry of Education, Youth and Sports (Czech Republic), Centre National de la Recherche Scientifique, Commissariat à l'Énergie Atomique, and Institut National de Physique Nucléaire et de Physique des Particules (France), Ministry of Industry, Science and Tekhnologies, Bundesministerium für Bildung und Forschung, Deutscher Akademischer Austausch Dienst, and Alexander von Humboldt Stiftung (Germany), Hungarian National Science Fund, OTKA (Hungary), Department of Atomic Energy and Department of Science and Technology (India), Israel Science Foundation (Israel), National Research Foundation and WCU program of the Ministry Education Science and Technology (Korea), Ministry of Education and Science, Russian Academy of Sciences, Federal Agency of Atomic Energy (Russia), VR and the Wallenberg Foundation (Sweden), the U.S. Civilian Research and Development Foundation for the Independent States of the Former Soviet Union, the US-Hungarian Fulbright Foundation for Educational Exchange, and the US-Israel Binational Science Foundation.

* Deceased
† PHENIX Spokesperson: jacak@skipper.physics.sunysb.edu

[1] S. Turbide, R. Rapp, and C. Gale, Phys. Rev. C **69**, 014903 (2004).
[2] W. Liu and R. J. Fries, Phys. Rev. C **77**, 054902 (2008).
[3] S. Turbide, C. Gale, and R. J. Fries, Phys.Rev.Lett. **96**, 032303 (2006).
[4] S. Afanasiev et al. (PHENIX Collaboration), Phys. Rev. C **80**, 054907 (2009).
[5] A. Adare et al. (PHENIX Collaboration), Phys. Rev. Lett. **104**, 132301 (2010).
[6] K. Dusling, Nucl. Phys. **A389**, 70 (2010).
[7] C. Gale, arXiv:0904.2184 [hep-ph] (2009).
[8] S. S. Adler et al. (PHENIX Collaboration), Phys. Rev. Lett. **94**, 232301 (2005).
[9] S. S. Adler et al. (PHENIX Collaboration), Phys. Rev. Lett. **96**, 032302 (2006).
[10] K. Adcox et al., Nucl. Instrum. Meth. **A499**, 469 (2003).
[11] M. Allen et al. (PHENIX Collaboration), Nucl. Instrum. Meth. **A499**, 549 (2003), ISSN 0168-9002.
[12] E. Richardson et al. (PHENIX Collaboration), Nucl.Instr. Meth. **A636**, 99 (2011).
[13] L. Aphecetche et al. (PHENIX Collaboration), Nucl. Instrum. Meth. **A499**, 521 (2003).
[14] K. Adcox et al. (PHENIX Collaboration), Nucl. Instrum. Meth. **A499**, 489 (2003).
[15] A. Adare et al. (PHENIX Collaboration), Phys. Rev. Lett. **105**, 142301 (2010).
[16] A. Adare et al. (PHENIX Collaboration), Phys. Rev. Lett. **98**, 162301 (2007).
[17] R. Petti, arXiv:1107.5379 [nucl-ex] (2011).
[18] R. Chatterjee and D. K. Srivastava, Phys. Rev. C **79**, 021901(R) (2009).
[19] F.-M. Liu, T. Hirano, K. Werner, and Y. Zhu, Phys. Rev. C **80**, 034905 (2009).

Published for SISSA by Springer

Received: *January 11, 2012*
Accepted: *February 20, 2012*
Published: *March 16, 2012*

Measurement of event background fluctuations for charged particle jet reconstruction in Pb-Pb collisions at $\sqrt{s_{\rm NN}} = 2.76$ TeV

The ALICE collaboration

Abstract: The effect of event background fluctuations on charged particle jet reconstruction in Pb-Pb collisions at $\sqrt{s_{\rm NN}} = 2.76$ TeV has been measured with the ALICE experiment. The main sources of non-statistical fluctuations are characterized based purely on experimental data with an unbiased method, as well as by using single high $p_{\rm t}$ particles and simulated jets embedded into real Pb-Pb events and reconstructed with the anti-$k_{\rm t}$ jet finder. The influence of a low transverse momentum cut-off on particles used in the jet reconstruction is quantified by varying the minimum track $p_{\rm t}$ between 0.15 GeV/c and 2 GeV/c. For embedded jets reconstructed from charged particles with $p_{\rm t} > 0.15$ GeV/c, the uncertainty in the reconstructed jet transverse momentum due to the heavy-ion background is measured to be 11.3 GeV/c (standard deviation) for the 10% most central Pb-Pb collisions, slightly larger than the value of 11.0 GeV/c measured using the unbiased method. For a higher particle transverse momentum threshold of 2 GeV/c, which will generate a stronger bias towards hard fragmentation in the jet finding process, the standard deviation of the fluctuations in the reconstructed jet transverse momentum is reduced to 4.8-5.0 GeV/c for the 10% most central events. A non-Gaussian tail of the momentum uncertainty is observed and its impact on the reconstructed jet spectrum is evaluated for varying particle momentum thresholds, by folding the measured fluctuations with steeply falling spectra.

Keywords: Heavy Ions

ArXiv ePrint: 1201.2423

doi:10.1007/JHEP03(2012)053

JHEP03(2012)053

Contents

JHEP03(2012)053

1 Introduction

High energy heavy-ion collisions explore strongly interacting matter under extreme conditions of energy density, where lattice QCD predicts a phase transition to a new state of matter above a critical value of about $1\,\mathrm{GeV/fm^3}$ [1]. In this new state, called the Quark-Gluon Plasma (QGP), quarks and gluons rather than hadrons are expected to be the dominant degrees of freedom over length scales larger than that of a nucleon. Experiments studying the collision of heavy nuclei at high energy at both the Relativistic Heavy Ion Collider (RHIC) [2–5], and recently at the Large Hadron Collider (LHC) [6–9], have made several key observations that point to the formation of a hot, dense and strongly coupled system, possibly the QGP.

Hard (large momentum transfer Q^2) probes are well calibrated tools to study the properties of the matter created in such collisions. The scattered partons generated in a hard momentum exchange are created in the initial stages of the heavy-ion collision, with production rates that are calculable using perturbative QCD, which can be compared to the same measurements in proton-proton collisions. The scattered partons then propagate through the medium, where their fragmentation into observed jets of hadrons is expected to be modified relative to the vacuum case by interactions with the medium (*jet quenching*) [10, 11]. This modification of parton fragmentation provides sensitive observables to study properties of the created matter.

Jet quenching has been observed at RHIC [12–15] and at the LHC [16] via the measurement of high p_{t} hadron inclusive production and correlations, which are observed to be strongly suppressed in central A–A collisions compared to a scaled pp reference. These high

p_{t} hadron observables have been the major tool for measuring the energy loss of hard scattered partons and thereby the properties of the medium, but they provide only indirect and biased information on the parton evolution in the medium. The aim of full jet reconstruction is to measure jet modifications due to energy loss in an unbiased way [17, 18]. Already first measurements of reconstructed jets in heavy-ion collisions at the LHC showed an energy imbalance between back-to-back dijets, which is attributed to jet quenching [9, 19].

Jet reconstruction in the complex environment of a heavy-ion collision requires a quantitative understanding of background-induced fluctuations of the measured jet signal and the effects of the underlying heavy-ion event on the jet finding process itself. Here, region-to-region background fluctuations are the main source of jet energy or momentum uncertainty and can have a large impact on jet structure observables, such as the fraction of energy inside the jet core or the shape of the jet, and will distort the measured jet energy balance even in the absence of medium effects [20].

In this paper the measurement of jet transverse momentum fluctuations due to the background in heavy-ion collisions is reported and its sources are identified, based on jet reconstruction using charged particles with varying minimum track p_{t}. For this purpose three methods are employed to probe the measured Pb-Pb events: fixed area (*rigid*) cones placed randomly in the acceptance, the simulation of high-p_{t} single tracks or full jets from pp collisions. Rigid cones enable the identification of contributions to the fluctuations in an unbiased fashion, while single tracks and embedded jets explore the interplay between the jet finding process, the underlying event, and the jet fragmentation pattern.

2 Detector Description and Track Selection

The data presented here were collected by the ALICE experiment [21] in the first Pb-Pb run of the LHC in November 2010, at a collision energy of $\sqrt{s_{\mathrm{NN}}} = 2.76\,\mathrm{TeV}$. This analysis is based on minimum-bias events, triggered by two forward VZERO counters and the Silicon Pixel Detector (SPD) [22]. A description of the minimum-bias trigger can be found in [6]. The VZERO trigger counters are forward scintillator detectors covering a pseudo-rapidity range of $2.8 < \eta < 5.1$ (V0A) and $-3.7 < \eta < -1.7$ (V0C). The sum of VZERO amplitudes is also used as a measure of event centrality [23]. The SPD consists of two silicon pixel layers at a radial distance to the beam line of $r = 3.9$ cm and $r = 7.6$ cm.

To ensure a uniform track acceptance in pseudo-rapidity η, only events whose primary vertex lies within $\pm 8\,\mathrm{cm}$ from the center of the detector along the beam line are used, resulting in 13.3 M minimum-bias Pb-Pb events for this analysis.

Charged particle tracking is carried out using the Time Projection Chamber (TPC) [24] and the Inner Tracking System (ITS) [22], located in the central barrel of the ALICE experiment within a 0.5 T solenoidal magnetic field and covering the full azimuth within pseudo-rapidity $|\eta| < 0.9$. The ITS consists of six cylindrical layers of silicon detectors, with distances from the beam-axis between $r = 3.9\,\mathrm{cm}$ and $r = 43\,\mathrm{cm}$. The ITS layers measure track points close to the primary vertex, with the two innermost layers (SPD) providing a precise measurement of the primary vertex position. The TPC, a cylindrical drift detector

JHEP03(2012)053

surrounding the ITS, is the main tracking detector in ALICE. The TPC inner radius is 85 cm and the outer radius is 247 cm, with longitudinal coverage $-250 < z < 250$ cm. It provides a uniformly high tracking efficiency for charged particles. The high precision of the ITS and the large radial lever arm of the TPC provide a good momentum resolution for combined (*global*) tracks.

For this dataset the ITS has significantly non-uniform efficiency as a function of azimuthal angle ϕ and pseudo-rapidity η. In order to obtain high and uniform tracking efficiency together with good momentum resolution, two different track populations are utilized: (i) tracks containing at least one space-point reconstructed in one of the two innermost layers of the ITS (78% of all accepted tracks), and (ii) accepted tracks that lack the position information close to the beam-line. Here, the primary vertex is added to the fit of the track which modifies the reconstructed curvature of the charged track in the magnetic field. Since the majority of the tracks originates from the primary vertex this constraint improves the momentum resolution. Both track types have transverse momentum resolution of $\sigma(p_{\mathrm{t}})/p_{\mathrm{t}} \approx 1\%$ at $1\,\mathrm{GeV}/c$. For the majority of tracks the resolution at $p_{\mathrm{t}} = 50\,\mathrm{GeV}/c$ is $\sigma(p_{\mathrm{t}})/p_{\mathrm{t}} \approx 10\%$, only tracks having fewer than three reconstructed space points in the ITS (about 6% of the total population) have a resolution at $50\,\mathrm{GeV}/c$ of $\sigma(p_{\mathrm{t}})/p_{\mathrm{t}} \approx 20\%$.

Tracks are accepted for $p_{\mathrm{t}} > 0.15\,\mathrm{GeV}/c$ and $|\eta| < 0.9$. The tracking efficiency at $p_{\mathrm{t}} = 0.15\,\mathrm{GeV}/c$ is 50%, increasing to 90% at $1\,\mathrm{GeV}/c$ and above. Tracks with measured $p_{\mathrm{t}} > 100\,\mathrm{GeV}/c$ are accepted at the tracking stage, but jets containing them are rejected from the analysis to reduce the influence of fake tracks and limited tracking resolution at very high p_{t}.

3 Jet Reconstruction and Background Subtraction

Charged particle jet reconstruction and estimation of the background employ the sequential recombination algorithms anti-k_{t} and k_{t} from the FastJet package [25]. The clustering starts with the list of tracks that satisfy the quality, acceptance, and p_{t}-cuts, with no pre-clustering or grouping of tracks. A list of jet candidates (anti-k_{t}) or clusters (k_{t}) is generated, with direction and transverse momentum given by the p_{t}-weighted average of (η, ϕ) of the individual constituents and the scalar sum of their p_{t}, respectively. The distance parameter that determines the terminating condition for the clustering is chosen as $R = 0.4$, which is a common value for reconstruction of jets in heavy-ion collisions [9, 18, 26]. As proposed in [27], the clusters found by the k_{t} algorithm are used to estimate the event-wise background p_{t}-density per unit area, ρ, defined as the median value of the ratio $p_{\mathrm{t}}^{\mathrm{rec}}/A^{\mathrm{rec}}$ for all considered k_{t}-clusters. A^{rec} is the area of the reconstructed cluster in the (η, ϕ)-plane calculated by the active ghost area method of FastJet [28], with a ghost area of 0.005. To minimize the influence of the track acceptance interval on ρ, only reconstructed clusters with $|\eta| < 0.5$ have been used. In addition, the two clusters with the largest $p_{\mathrm{t}}^{\mathrm{rec}}$ (leading) in the full acceptance of $|\eta| < 0.9$ are excluded from the calculation of the median to further reduce the influence of true jets on the background estimate [29]. The jet population reconstructed by the anti-k_{t} algorithm is used as signal jets. Their p_{t}

JHEP03(2012)053

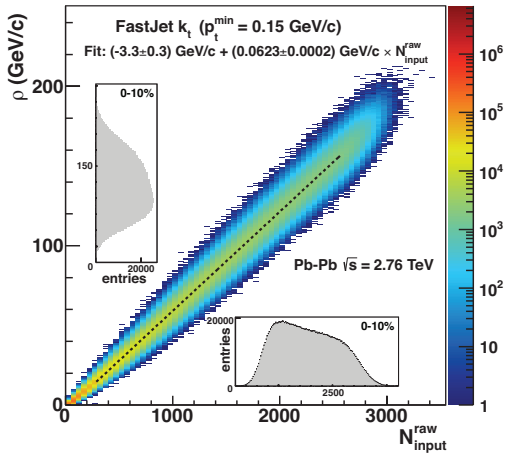

Figure 1. Dependence of charged particle background p_{t} density ρ on uncorrected multiplicity of tracks used for jet finding ($|\eta| < 0.9$). The dotted line is a linear fit to the centroids in each multiplicity bin. The insets show the projected distributions of ρ and raw multiplicity for the 10% most central events.

is corrected for the background p_{t}-density in each event using the jet area $A^{\mathrm{jet,rec}}$ with $p_{\mathrm{t}}^{\mathrm{jet}} = p_{\mathrm{t}}^{\mathrm{jet,rec}} - \rho \cdot A^{\mathrm{jet,rec}}$. Signal jets are only considered for $|\eta| < 0.5$.

The average transverse momentum of tracks $\langle p_{\mathrm{t}} \rangle$ and the total charged multiplicity are global observables that are closely related to the value of ρ, though the determination of ρ uses varying phase-space intervals (with typical areas in the (η, ϕ)-plane of πR^2) and suppresses hard jet contributions by using the median of the distribution. Figure 1 shows the correlation between ρ and the uncorrected multiplicity of tracks with $|\eta| < 0.9$. The linear increase corresponds to an uncorrected $\langle p_{\mathrm{t}} \rangle$ of about $0.7\,\mathrm{GeV}/c$ per accepted charged track. Both $\langle p_{\mathrm{t}} \rangle$ and multiplicity, and thus also the background p_{t} density, strongly depend on the minimum p_{t} threshold ($p_{\mathrm{t}}^{\mathrm{min}}$) applied for tracks used as input to the jet finding. To minimize the bias on jet fragmentation, a value of $p_{\mathrm{t}}^{\mathrm{min}} = 0.15\,\mathrm{GeV}/c$ is preferred. In addition, $p_{\mathrm{t}}^{\mathrm{min}} = 1$ and $2\,\mathrm{GeV}/c$ are investigated to facilitate comparisons to other experiments and to Monte-Carlo generators in a region of constant and high tracking efficiency. The mean ρ over all events and its standard deviation is given for different $p_{\mathrm{t}}^{\mathrm{min}}$ and two centralities in table 1. As expected, the mean background p_{t} density decreases for larger $p_{\mathrm{t}}^{\mathrm{min}}$, for central collisions and $p_{\mathrm{t}}^{\mathrm{min}} = 2\,\mathrm{GeV}/c$ it is reduced by an order of magnitude. As one can see in the insets of figure 1 and the standard deviation in table 1, the spread of ρ for the 10% most central events is considerable, underlining the importance of the event-by-event background subtraction.

4 Sources of Background Fluctuations

To study the sources of background fluctuations in an unbiased way that is not influenced by a particular choice of jet finder, a single rigid cone with radius $R = 0.4$ is placed in each reconstructed event at random ϕ and η, with centroid lying within $|\eta| < 0.5$. The

JHEP03(2012)053

$p_{\mathrm{t}}^{\mathrm{min}}$ (GeV/c)	$\langle\rho\rangle$ (GeV/c)	$\sigma(\rho)$ (GeV/c)
0-10%		
0.15	138.32 ± 0.02	18.51 ± 0.01
1.00	59.30 ± 0.01	9.27 ± 0.01
2.00	12.28 ± 0.01	3.29 ± 0.01
50-60%		
0.15	12.05 ± 0.01	3.41 ± 0.01
1.00	4.82 ± 0.01	1.77 ± 0.01
2.00	4.41 ± 0.05	0.92 ± 0.04

Table 1. Average and standard deviation of the event-wise charged particle p_{t} density ρ for three choices of minimum particle p_{t} and two centrality bins. The quoted uncertainties are purely statistical.

background fluctuations are characterized by calculating the difference of the scalar sum of all track p_{t} in the cone and the expected background:

$$\delta p_{\mathrm{t}} = \sum_i p_{\mathrm{t,i}} - A \cdot \rho, \tag{4.1}$$

where $A = \pi R^2$.

The rigid random cone (RC) area and position are not influenced by the event, so that it provides a sampling of the event structure at the typical scale of a jet, but independent of biases induced by the choice of a particular jet finding algorithm. The RC measurements will be compared to the embedding of jet-like objects, that is directly relevant to the measurement of the inclusive jet spectrum with a specific choice of jet finder.

To characterize the δp_{t} distribution the standard deviation, $\sigma(\delta p_{\mathrm{t}})$, is utilized. In addition, a Gaussian distribution with mean $\mu^{\mathrm{l.h.s.}}$ and standard deviation $\sigma^{\mathrm{l.h.s.}}$ is iteratively fit to the distribution within $[\mu^{\mathrm{l.h.s.}} - 3\sigma^{\mathrm{l.h.s.}}, \mu^{\mathrm{l.h.s.}} + 0.5\sigma^{\mathrm{l.h.s.}}]$, i.e. to the left-hand-side. The $\sigma^{\mathrm{l.h.s.}}$ of the fit provides the lower limit on the magnitude of the fluctuations and is used to characterize shape differences between the positive and negative tails of the distribution, by extrapolating the Gaussian distribution to positive δp_{t}.

Various sources contribute to background fluctuations in a heavy-ion event, including: (i) random, uncorrelated (Poissonian) fluctuations of particle number and momentum; (ii) region-to-region correlated variations of the momentum density, induced by detector effects, e.g. a non-uniform efficiency, and by the heavy-ion collision itself, e.g. by variation of the eccentricity of the nuclear overlap for collisions with finite impact parameter.

The measured δp_{t} distribution for random cones in the 10% most central Pb-Pb events is shown in figure 2. The distribution is peaked near zero, illustrating the agreement of the background estimate via k_{t}-clusters and that due to random sampling of the event. The distribution exhibits an asymmetric shape with a tail to the right-hand-side of the distribution, which is also reflected in the difference between the standard deviation of

JHEP03(2012)053

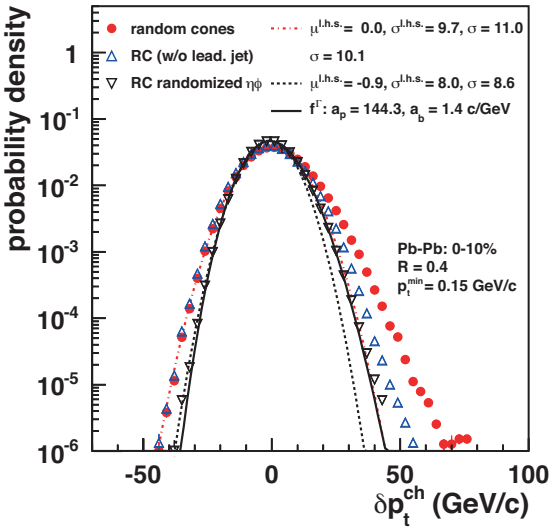

Figure 2. δp_{t} of random cones in the 10% most central Pb-Pb events for the three types of random cone probes with $p_{\mathrm{t}}^{\mathrm{min}} = 0.15\,\mathrm{GeV}/c$. A Gaussian fit to the left-hand-side and its extrapolation to positive δp_{t} are shown for measured Pb-Pb events and for randomized Pb-Pb events ($\mu^{\mathrm{l.h.s.}}$ and $\sigma^{\mathrm{l.h.s.}}$ in GeV/c). The solid line is a fit to the δp_{t} distribution for the randomized events with a Γ distribution shifted to zero (equation (4.2)) as approximation for the shape in case of independent particle emission.

the full distribution of $\sigma(\delta p_{\mathrm{t}}) = 11.0\,\mathrm{GeV}/c$ and the Gaussian width of the left-hand-side $\sigma^{\mathrm{l.h.s.}}(\delta p_{\mathrm{t}}) = 9.6\,\mathrm{GeV}/c$.

To further differentiate random and correlated sources of fluctuations, three variations of the random cone method are employed: (i) sampling of measured Pb-Pb events, (ii) sampling of measured Pb-Pb events, but avoiding overlap with the leading jet candidate in the event after background subtraction by requiring a distance $D = 1.0$ in (η, ϕ) between the random cone direction and the jet axis, and (iii) sampling of Pb-Pb events in which the (η,ϕ) direction of the tracks has been randomized within the acceptance, which destroys all correlations in the event. Figure 2 shows that when avoiding the leading jet candidate to suppress upward fluctuations, e.g. due to a hard process, the tail to the right-hand-side is already significantly reduced.

Note that, even for the case of purely statistical fluctuations, the distribution is not expected to be symmetric or to follow a Gaussian shape on the right-hand-side, since the shapes of the underlying single particle p_{t} and multiplicity distributions are not Gaussian. In the case of uncorrelated particle emission a Γ-distribution provides a more accurate description of the event-wise $\langle p_{\mathrm{t}} \rangle$ fluctuations [30]. This also holds for δp_{t} distributions, which are similar to a measurement of $\langle p_{\mathrm{t}} \rangle$ fluctuations in a limited interval of phase space. Taking into account the subtraction of the average background the functional form of the probability distribution of δp_{t} for independent particle emission can be written:

$$f^{\Gamma}(\delta p_{\mathrm{t}}) = A \cdot a_b/\Gamma(a_p) \cdot (a_b \delta p_{\mathrm{t}} + a_p)^{a_p - 1} \cdot e^{-(a_b \delta p_{\mathrm{t}} + a_p)}. \tag{4.2}$$

JHEP03(2012)053

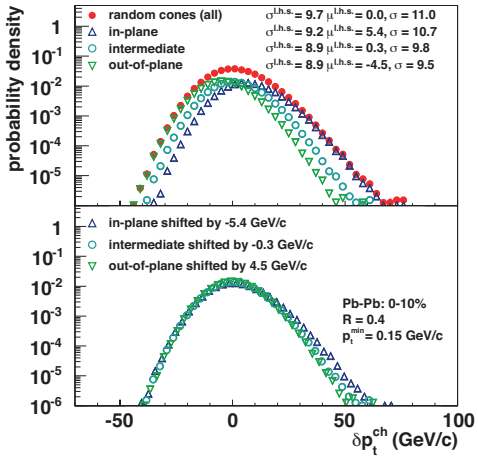

Figure 3. δp_{t} distribution for random cones, averaged over the full azimuth and separated for three bins of random cone azimuthal orientations with respect to the measured event plane. In the bottom panel the distributions have been shifted to zero using the mean of the left-hand-side Gaussian fit ($\mu^{\mathrm{l.h.s.}}$).

This corresponds to a Γ-distribution with mean shifted from a_p/a_b to zero and standard deviation $\sigma = \sqrt{a_p}/a_b$. As seen in figure 2 this functional form provides a good approximation of the δp_{t} distribution for randomized events, corresponding to uncorrelated emission. In this case the distribution is also narrower on the left-hand-side. This points to the presence of correlated region-to-region fluctuations in addition to purely statistical fluctuations and those expected from hard processes.

One source of region-to-region variation in the background p_{t} density is the initial anisotropy of the nuclear overlap for finite impact parameter collisions, which translates via the collective expansion of the medium into an anisotropy in momentum space [7, 31] with respect to the symmetry plane of the collision. The event plane direction can be calculated using the azimuthal distribution of all accepted tracks within each event, which is dominated by soft particle production. The final state hadron azimuthal distribution with respect to the reaction plane of the event, is characterized by a Fourier expansion where the leading term is the second moment, called elliptic flow v_2. In addition to the geometry driven even harmonics (mainly v_2), odd flow components (e.g. v_3) driven by intial state fluctuations can modify the azimuthal distribution within the event [32].

To explore the effect on background fluctuations of azimuthal orientation relative to the reaction plane, the δp_{t} distribution from random cone sampling is studied as a function of the azimuthal orientation of the cone axis, ϕ, relative to the reconstructed event plane orientation, ψ_{RP}. Three bins are chosen; the out-of-plane orientation where the azimuthal angle between the reconstructed event plane and the cone axis is $> 60°$, the in-plane orientation where this angle is $< 30°$, and the intermediate orientation where the angle is between 30 and 60°. The distributions of δp_{t} for random cones averaged over the full azimuth and for the three different orientations are shown in figure 3. It can be seen

JHEP03(2012)053

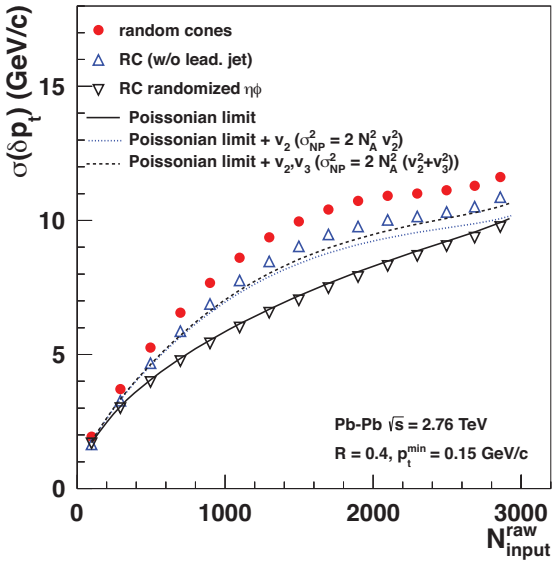

Figure 4. Dependence of the standard deviation of the δp_{t} distributions on uncorrected charged particle multiplicity, compared to the limit derived from the measured track p_{t} spectrum (equation (4.3)) and from additional elliptic and triangular flow contributions (equation (4.4)). $R = 0.4$, $p_{\mathrm{t}}^{\mathrm{min}} = 0.15\,\mathrm{GeV}/c$.

that, for out-of-plane cones, the most probable background p_{t} density is smaller by almost $5\,\mathrm{GeV}/c$ relative to the azimuthally averaged estimate of ρ, with opposite effect in-plane. This shift scales with the average flow and the background p_{t} density for a given centrality ($\propto\ v_2 \cdot \rho$), and is seen to be sizable in central events, though discrimination of the event plane orientations is limited by finite event-plane resolution [33] and possible biases due to hard jets. The decreasing width of left-hand-side Gaussian is qualitatively consistent with the expectation from reduced particle number fluctuations out-of-plane compared to in-plane. For a visual comparison of their shape, the distributions have been shifted such that the centroid of the left-hand-side Gaussian fit is zero (see figure 3). Notably, the left-hand-side of the distribution appears similar for all orientations of the random cones to the event-plane. The random cones distributed in-plane show a more pronounced tail to the right-hand-side, compared to out-of-plane. This may point to a dependence of the jet spectrum on the orientation relative to the reaction plane, though further systematic studies are needed to assess biases in the event plane determination due to jet production and possible auto-correlations. For the measurement of the inclusive jet spectrum the correction via an event-plane dependent ρ will reduce the influence of even flow components on the average reconstructed jet momentum, but its systematic precision is limited by the finite event-plane resolution.

The width of the δp_{t} distribution due to purely random fluctuations can be estimated from the measured single particle p_{t} spectrum via [18]:

$$\sigma(\delta p_{\mathrm{t}}) = \sqrt{N_{\mathrm{A}} \cdot \sigma^2(p_{\mathrm{t}}) + N_{\mathrm{A}} \cdot \langle p_{\mathrm{t}} \rangle^2}. \tag{4.3}$$

JHEP03(2012)053

Here, $N_{\rm A}$ is the expected number of tracks in the cone area A for a given event centrality or multiplicity class, $\langle p_{\rm t}\rangle$ the average $p_{\rm t}$ and $\sigma(p_{\rm t})$ the standard deviation of the track $p_{\rm t}$ spectrum. Local variations of the average multiplicity, $\langle p_{\rm t}\rangle$, or $\sigma(p_{\rm t})$, lead to additional fluctuations. These region-to-region variations can be induced e.g. by (mini-)jets, where the particle $p_{\rm t}$ spectrum is considerably harder than for the global event average, and by collective flow. Uncorrelated non-Poissonian (NP) fluctuations can be added to equation (4.3) knowing their standard deviation, e.g. for additional region-to-region variation of the average multiplicity:

$$\sigma(\delta p_{\rm t}) = \sqrt{N_{\rm A}\cdot\sigma^2(p_{\rm t}) + \left(N_{\rm A} + \sigma^2_{\rm NP}(N_{\rm A})\right)\cdot\langle p_{\rm t}\rangle^2}. \tag{4.4}$$

Figure 4 shows the comparison of the multiplicity dependence of $\sigma(\delta p_{\rm t})$ for the three different types of random cones. The distribution of purely statistical fluctuations given by equation (4.3) well describes the randomized events. Also shown are two parameterizations following equation (4.4). Additional multiplicity fluctuations due to elliptic flow are approximated from the $p_{\rm t}$-integrated v_2 values measured by ALICE for different centralities [7] as $\sigma^2_{\rm NP}(N_{\rm A}) \approx 2v_2^2N_{\rm A}^2$. This approximate inclusion of v_2-effects accounts qualitatively for the larger fluctuations in mid central collisions compared to the randomized events and the deviation from a $\sqrt{N}$-increase. The random cone sampling with an anti-bias on the leading jet has, by construction, a reduced standard deviation and is close to the parameterization of elliptic flow. Taking into account also region-to-region fluctuations from triangular flow, v_3, is of particular importance in central events where it reaches a similar magnitude as v_2 [32]. The contribution of v_3 can be added in quadrature ($\sigma^2_{\rm NP}(N_{\rm A}) \approx 2N_{\rm A}^2(v_2^2+v_3^2)$) since the second and the third harmonic are not correlated via a common plane of symmetry [32], for simplicity v_3 has been approximated by a constant value of $v_3 = 2.4\%$. As expected, the inclusion of v_3 can account partially for the difference to the randomized event in the most central events. In the comparison one has to consider that in practice the contribution from hard processes to the right-hand-side tail cannot be cleanly separated from (soft) upward multiplicity fluctuations induced by flow. In addition, the approximate description of flow effects following equation (4.4) does not take into account any flow-correlated changes of $\langle p_{\rm t}\rangle$ and $\sigma(p_{\rm t})$.

The track reconstruction efficiency affects the total multiplicity and the shape of the measured $p_{\rm t}$-spectrum at low $p_{\rm t}$. Using equation (4.3), the change of the uncorrelated fluctuations due to finite efficiency can be estimated from the efficiency corrected $p_{\rm t}$-spectrum in each centrality bin. This procedure suggests that, for $p_{\rm t}^{\rm min}$= 0.15 GeV/c, there is an increase of the standard deviation by 5.4-6.0%, depending on centrality. The complete correction requires the knowledge of all correlations within the heavy-ion event and is beyond the scope of the present study.

5 Background Fluctuations in Jet Reconstruction

The measured jet spectrum in heavy-ion collisions is affected over the entire $p_{\rm t}$ range by background fluctuations, especially due to the large and asymmetric tail towards positive $\delta p_{\rm t}$. For the measurement of the inclusive jet cross section, background fluctuations can

JHEP03(2012)053

only be corrected on a statistical basis via unfolding. Such background fluctuations are evaluated using embedding and reconstruction of a probe with identical jet algorithm and parameters as those applied to the data analysis, to account for the jet-finder-specific response to the heavy-ion background.

In the present study, two probes are embedded into the Pb-Pb events measured by ALICE: (i) single high-p_{t} tracks at various p_{t}, and (ii) pp jet events generated using PYTHIA [34] followed by a detailed simulation of the full detector response. Jet candidates are reconstructed from the event using the anti-k_{t} algorithm with $R = 0.4$ and matched to the embedded probe, by either finding the single track in it, or by requiring that the p_{t} of the embedded tracks within the reconstructed jet sum up to at least 50% of the original probe jet transverse momentum ($p_{\mathrm{t}}^{\mathrm{probe}}$). The difference between the reconstructed, background subtracted jet and the embedded probe is then given, similar to equation (4.1), by [29, 35]:

$$\delta p_{\mathrm{t}} = p_{\mathrm{t}}^{\mathrm{jet,rec}} - A^{\mathrm{jet,rec}} \cdot \rho - p_{\mathrm{t}}^{\mathrm{probe}}. \tag{5.1}$$

The response may depend on the jet finder, its settings, and the properties of the embedded probe, such as $p_{\mathrm{t}}^{\mathrm{probe}}$, area, and fragmentation pattern. In particular the insensitivity to the latter is essential for a robust and unbiased reconstruction of jets in heavy-ion collisions, where the fragmentation pattern is potentially modified relative to that in pp collisions, and is indeed the observable of interest.

The δp_{t} distributions measured for each of the methods are shown in figure 5. Here, the focus is on high $p_{\mathrm{t}}^{\mathrm{probe}}$ ($> 60\,\mathrm{GeV}/c$), where the efficiency of matching the embedded probe to the reconstructed jet approaches unity. The results are very similar to the random cone method, including the presence of an asymmetric tail to the right-hand-side of the distribution. The standard deviations, however, show a small increase compared to the random cone method, which is largest for jet embedding (see table 2). The increase may be due to sensitivity of the jet finder to back-reaction, e.g. the stability of the probe area and jet direction after embedding. The single particle embedding can be considered as extreme fragmentation leading to rather rigid cones with stable area πR^2, while in the case of true pp-jets the probe and reconstructed area may differ, depending on the fragmentation pattern. In addition the finite jet area resolution due to the size of the ghost area has to be taken into account [29]. With a ghost area of 0.005 a compromise between reasonable jet area resolution and computing time and memory consumption was chosen. In the case of track embedding at high p_{t}, the jet area resolution fully accounts for the difference of $200\,\mathrm{MeV}/c$ observed in the standard deviation.

The broadening of the δp_{t} distribution for jets with $p_{\mathrm{t}}^{\mathrm{min}} = 0.15\,\mathrm{GeV}/c$, as seen in figure 5, has been investigated more closely. The additional left-hand-side structure is caused by probe jets with large area ($A^{\mathrm{probe}} > 0.6$) that are split in the heavy-ion event into two separate objects of smaller size. Jets with a large area ($A > 0.6$) are only formed by the anti-k_{t} algorithm in exceptional cases, where there are two hard cores at distance close to R [36]. It is also seen in figure 5 that, with increasing $p_{\mathrm{t}}^{\mathrm{min}}$, the deviations on the left-hand-side in the case of jet embedding become more pronounced, suggesting that the jet-splitting is an effect of hard fragmentation.

JHEP03(2012)053

In the determination of δp_{t} fluctuations as described above, the probes have been embedded into an event population recorded with a minimum-bias trigger. However, the requirement of a hard process biases the population towards more central (small impact parameter) collisions, due to nuclear geometry. Correction of this effect for centrality bins of 10% width, generates a negligible increase of the fluctuations ($< 0.1\,\mathrm{GeV}/c$).

The full centrality dependence of the fluctuations is given via the standard deviation of the distributions and for different $p_{\mathrm{t}}^{\mathrm{min}}$ cuts in table 3.

The increase of the $p_{\mathrm{t}}^{\mathrm{min}}$ cut on the input tracks for jet finding reduces the background fluctuations, due to the smaller influence of statistical and soft region-to-region fluctuations. This is observed in figure 5 when the $p_{\mathrm{t}}^{\mathrm{min}}$ is varied from 0.15 to $2\,\mathrm{GeV}/c$. A $p_{\mathrm{t}}^{\mathrm{min}}$ of $2\,\mathrm{GeV}/c$ reduces the standard deviation by more than a factor of two compared to $0.15\,\mathrm{GeV}/c$. Soft region-to-region fluctuations that dominate the left-hand-side of the distribution are reduced by a factor of three (see table 2). A high $p_{\mathrm{t}}^{\mathrm{min}}$ significantly reduces the impact of fluctuations in the jet spectrum (see table 4). However, it may also introduce a bias in the jet reconstruction towards hard fragmentation.

To estimate the influence of the observed fluctuations on the jet measurement, a power law spectrum starting at $p_{\mathrm{t}} = 4\,\mathrm{GeV}/c$ has been folded with a Gaussian of width $\sigma^{\mathrm{Gauss}} = 11\,\mathrm{GeV}/c$ ($5\,\mathrm{GeV}/c$) and with the measured δp_{t} distributions for $p_{\mathrm{t}}^{\mathrm{min}} = 0.15\,\mathrm{GeV}/c$ ($2\,\mathrm{GeV}/c$). The yield increase relative to the unsmeared spectrum in one high p_{t}-bin for the most central collisions is given in table 4. For the different probes, they agree within the uncertainties given by the statistical fluctuations in the tails of the δp_{t}-distributions; about a factor of ten increase for $p_{\mathrm{t}}^{\mathrm{min}} = 0.15\,\mathrm{GeV}/c$ and a 30% effect for $p_{\mathrm{t}}^{\mathrm{min}} = 2\,\mathrm{GeV}/c$. Minor differences in the standard deviation as well as the left-hand-side differences have no sizable effect on the spectral shape after folding. The difference between smearing with the full δp_{t} and with a Gaussian distribution illustrates the strong influence of the right-hand-side tail, which must be taken into account in the analysis of background fluctuation effects on jet reconstruction. The extracted values naturally depend on the choice of the input spectrum, so, in addition to the power law, a jet spectrum for pp collisions at $\sqrt{s_{\mathrm{NN}}} = 2.76\,\mathrm{TeV}$ extracted from PYTHIA simulations has been used. These studies indicate that the increase of yield due to background fluctuations falls below 50% for reconstructed charged jets in the region of $p_{\mathrm{t}} \approx 100 \pm 15\,\mathrm{GeV}/c$ ($60 \pm 10\,\mathrm{GeV}/c$) for $p_{\mathrm{t}}^{\mathrm{min}} = 0.15\,\mathrm{GeV}/c$ ($2\,\mathrm{GeV}/c$). Repeating the exercise with a Gaussian smearing of a $\sigma^{\mathrm{Gauss}} = 11\,\mathrm{GeV}/c$ and with the δp_{t} distribution of random cones avoiding the leading jet for $p_{\mathrm{t}}^{\mathrm{min}} = 0.15\,\mathrm{GeV}/c$ leads, as expected, to a reduced influence of the tail. Here, the relative yield increase falls below 50% in the range of $p_{\mathrm{t}} \approx 75 \pm 10\,\mathrm{GeV}/c$. The employed input spectra do not consider the geometrical limitation on the number of jets that can be reconstructed within the acceptance for a single event [37]. This effect also limits the extraction of jet spectra at lower p_{t} via unfolding.

6 Summary

The first detailed study of event background fluctuations for jet reconstruction using charged particles in Pb-Pb collisions at the LHC has been presented. The standard devia-

JHEP03(2012)053

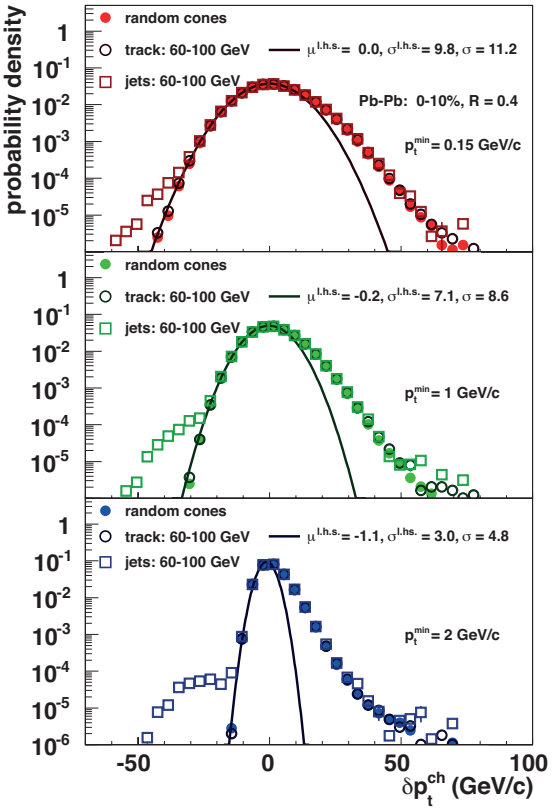

Figure 5. δp_{t} distribution of charged particles for jet reconstruction with the three methods in the 10% most central Pb-Pb events for $p_{\mathrm{t}}^{\mathrm{min}} = 0.15\,\mathrm{GeV}/c$, $1\,\mathrm{GeV}/c$, and $2\,\mathrm{GeV}/c$.

tion of the fluctuations in the 10% most central events is $\sigma = (10.98 \pm 0.01)$ GeV/c within a rigid cone of $R = 0.4$ and for a low p_{t} cut-off of $0.15\,\mathrm{GeV}/c$. It has been shown that the non-statistical sources of fluctuations are driven in part by the anisotropy of the particles emitted from the collision (elliptic and triangular flow). The variation of multiplicity in different orientations with respect to the event plane, induces shifts in the background-subtracted jet p_{t} even for central Pb-Pb-collisions.

The anti-k_{t} jet finder response for charged particle jet reconstruction has a modest dependence on the method used to characterize the fluctuations. For embedded, simulated pp-jets the standard deviation increases to $(11.34 \pm 0.02)\,\mathrm{GeV}/c$. In addition, certain rare fragmentation patterns in pp are likely to be split in the heavy-ion environment leading to minor effects in the background response. The observed differences between the two types of embedded probes (namely single tracks and pp jets) do not indicate a strong sensitivity of the reconstructed anti-k_{t} jet spectrum on fragmentation. The case of a strong broadening of the jet due to medium effects has not been considered here.

The use of reconstructed charged particles down to $p_{\mathrm{t}}^{\mathrm{min}} = 0.15\,\mathrm{GeV}/c$ allows a comparison of the impact of background fluctuations with a minimal bias on hard fragmentation in jet finding to the case with increased bias ($p_{\mathrm{t}}^{\mathrm{min}} \geq 1\,\mathrm{GeV}/c$). The observed reduc-

JHEP03(2012)053

	σ (GeV/c)	$\sigma^{\text{l.h.s.}}$ (GeV/c)	$\mu^{\text{l.h.s.}}$ (GeV/c)
$p_{\text{t}}^{\text{min}} = 0.15\,\text{GeV}/c$			
random cones	10.98 ± 0.01	9.65 ± 0.02	-0.04 ± 0.03
track emb.	11.19 ± 0.01	9.80 ± 0.02	0.00 ± 0.03
jet emb.	11.34 ± 0.02	9.93 ± 0.06	0.06 ± 0.09
$p_{\text{t}}^{\text{min}} = 1\,\text{GeV}/c$			
random cones	8.50 ± 0.01	7.08 ± 0.01	-0.22 ± 0.02
track emb.	8.61 ± 0.01	7.11 ± 0.01	-0.25 ± 0.02
jet emb.	8.78 ± 0.02	7.25 ± 0.04	-0.08 ± 0.08
$p_{\text{t}}^{\text{min}} = 2\,\text{GeV}/c$			
random cones	4.82 ± 0.01	3.41 ± 0.01	-0.01 ± 0.01
track emb.	4.88 ± 0.01	3.05 ± 0.01	-0.92 ± 0.01
jet emb.	5.03 ± 0.01	3.52 ± 0.01	0.01 ± 0.02

Table 2. Background fluctuations in central events. Comparison of the Gaussian fit to the left-hand-side of the δp_{t}-distributions and the standard deviation in central Pb-Pb collisions for the three different methods and for the three $p_{\text{t}}^{\text{min}}$-cuts. The quoted uncertainties are purely statistical.

	$p_{\text{t}}^{\text{min}}$ (GeV/c)		
	0.15	1.0	2.0
Centrality Class	$\sigma(\delta p_{\text{t}})$ (GeV/c)		
0-10%	11.19 ± 0.01	8.61 ± 0.01	4.88 ± 0.01
10-20%	10.19 ± 0.01	7.67 ± 0.01	4.29 ± 0.01
20-30%	8.46 ± 0.01	6.35 ± 0.01	3.58 ± 0.01
30-40%	6.51 ± 0.01	4.93 ± 0.01	2.68 ± 0.01
40-50%	4.71 ± 0.01	3.63 ± 0.01	1.95 ± 0.01
50-60%	3.28 ± 0.01	2.61 ± 0.01	1.41 ± 0.01
60-70%	2.22 ± 0.01	1.70 ± 0.01	0.95 ± 0.01
70-80%	1.48 ± 0.01	1.01 ± 0.01	0.62 ± 0.01

Table 3. Centrality dependence of fluctuations. Standard deviation of δp_{t} distributions and statistical uncertainty for different centrality bins and $p_{\text{t}}^{\text{min}}$ cuts using the track embedding probe.

tion of the standard deviation to $\sigma = (4.82 \pm 0.01)\,\text{GeV}/c$ for the unbiased sampling and $p_{\text{t}}^{\text{min}} = 2\,\text{GeV}/c$ is driven by the smaller number fluctuations and the reduced influence of soft region-to-region fluctuations.

The asymmetric shape of the δp_{t} distribution with a tail towards positive fluctuations has a large impact on the jet measurement, compared to purely Gaussian fluctuations, though the role of signal jets contributing to the tail has to be considered. Using different assumptions on the shape of the true jet spectrum it is found that for $p_{\text{t}}^{\text{min}} = 0.15\,\text{GeV}/c$ fluctuations can have a large influence on the charged jet yield for transverse momenta up to $100 \pm 15\,\text{GeV}/c$.

JHEP03(2012)053

$f(p_{\mathrm{t}})$ folded with	relative yield for $p_{\mathrm{t}} = 60 - 68\,\mathrm{GeV}/c$		
δp_{t}	RC	tracks	jets
$p_{\mathrm{t}}^{\mathrm{min}} = 0.15\,\mathrm{GeV}/c$	9.8 ± 1.7	11.4 ± 1.1	10.9 ± 3.4
$p_{\mathrm{t}}^{\mathrm{min}} = 2\,\mathrm{GeV}/c$	1.30 ± 0.02	1.31 ± 0.02	1.65 ± 0.25
Gauss			
$\sigma = 11\,\mathrm{GeV}/c$	1.82 ± 0.04		
$\sigma = 5\,\mathrm{GeV}/c$	1.05 ± 0.01		

Table 4. Yield modification for power law spectrum. Relative yield in the bin $p_{\mathrm{t}} = 60 - 68\,\mathrm{GeV}/c$ for a power law spectrum ($f(p_{\mathrm{t}}) = 0.7/(0.7 + p_{\mathrm{t}}^5)$ and $p_{\mathrm{t}} > 4\,\mathrm{GeV}/c$), folded with the different δp_{t} distributions for 0-10% centrality and with a Gaussian, where the width is similar to the standard deviation of the δp_{t} distributions.

Acknowledgments

The ALICE collaboration would like to thank all its engineers and technicians for their invaluable contributions to the construction of the experiment and the CERN accelerator teams for the outstanding performance of the LHC complex.

The ALICE collaboration acknowledges the following funding agencies for their support in building and running the ALICE detector: Calouste Gulbenkian Foundation from Lisbon and Swiss Fonds Kidagan, Armenia; Conselho Nacional de Desenvolvimento Científico e Tecnológico (CNPq), Financiadora de Estudos e Projetos (FINEP), Fundação de Amparo à Pesquisa do Estado de São Paulo (FAPESP); National Natural Science Foundation of China (NSFC), the Chinese Ministry of Education (CMOE) and the Ministry of Science and Technology of China (MSTC); Ministry of Education and Youth of the Czech Republic; Danish Natural Science Research Council, the Carlsberg Foundation and the Danish National Research Foundation; The European Research Council under the European Community's Seventh Framework Programme; Helsinki Institute of Physics and the Academy of Finland; French CNRS-IN2P3, the 'Region Pays de Loire', 'Region Alsace', 'Region Auvergne' and CEA, France; German BMBF and the Helmholtz Association; General Secretariat for Research and Technology, Ministry of Development, Greece; Hungarian OTKA and National Office for Research and Technology (NKTH); Department of Atomic Energy and Department of Science and Technology of the Government of India; Istituto Nazionale di Fisica Nucleare (INFN) of Italy; MEXT Grant-in-Aid for Specially Promoted Research, Japan; Joint Institute for Nuclear Research, Dubna; National Research Foundation of Korea (NRF); CONACYT, DGAPA, México, ALFA-EC and the HELEN Program (High-Energy physics Latin-American-European Network); Stichting voor Fundamenteel Onderzoek der Materie (FOM) and the Nederlandse Organisatie voor Wetenschappelijk Onderzoek (NWO), Netherlands; Research Council of Norway (NFR); Polish Ministry of Science and Higher Education; National Authority for Scientific Research - NASR (Autoritatea Naţională pentru Cercetare Ştiinţifică - ANCS); Federal Agency of Science of the Ministry of Education and Science of Russian Federation, International Science and Technology Center, Russian Academy of Sciences, Russian Federal Agency of Atomic Energy,

JHEP03(2012)053

Russian Federal Agency for Science and Innovations and CERN-INTAS; Ministry of Education of Slovakia; Department of Science and Technology, South Africa; CIEMAT, EELA, Ministerio de Educación y Ciencia of Spain, Xunta de Galicia (Consellería de Educación), CEADEN, Cubaenergía, Cuba, and IAEA (International Atomic Energy Agency); Swedish Reseach Council (VR) and Knut & Alice Wallenberg Foundation (KAW); Ukraine Ministry of Education and Science; United Kingdom Science and Technology Facilities Council (STFC); The United States Department of Energy, the United States National Science Foundation, the State of Texas, and the State of Ohio.

JHEP03(2012)053

References

[1] F. Karsch and E. Laermann, *Thermodynamics and in-medium hadron properties from lattice QCD*, in *Quark-gluon plasma 3*, Rudolph C. Hwa ed., WorldScientific, Singapore (2003) 1.

[2] STAR collaboration, J. Adams et al., *Experimental and theoretical challenges in the search for the quark gluon plasma: the STAR collaboration's critical assessment of the evidence from RHIC collisions*, *Nucl. Phys.* **A 757** (2005) 102 [nucl-ex/0501009] [INSPIRE].

[3] PHENIX collaboration, K. Adcox et al., *Formation of dense partonic matter in relativistic nucleus-nucleus collisions at RHIC: experimental evaluation by the PHENIX collaboration*, *Nucl. Phys.* **A 757** (2005) 184 [nucl-ex/0410003] [INSPIRE].

[4] BRAHMS collaboration, I. Arsene et al., *Quark gluon plasma and color glass condensate at RHIC? the perspective from the BRAHMS experiment*, *Nucl. Phys.* **A 757** (2005) 1 [nucl-ex/0410020] [INSPIRE].

[5] B. Back, M. Baker, M. Ballintijn, D. Barton, B. Becker, et al., *The PHOBOS perspective on discoveries at RHIC*, *Nucl. Phys.* **A 757** (2005) 28 [nucl-ex/0410022] [INSPIRE].

[6] ALICE collaboration, B. Abelev et al., *Charged-particle multiplicity density at mid-rapidity in central Pb-Pb collisions at* $\sqrt{s_{NN}} = 2.76$ *TeV*, *Phys. Rev. Lett.* **105** (2010) 252301 [arXiv:1011.3916] [INSPIRE].

[7] The ALICE collaboration, K. Aamodt et al., *Elliptic flow of charged particles in Pb-Pb collisions at 2.76 TeV*, *Phys. Rev. Lett.* **105** (2010) 252302 [arXiv:1011.3914] [INSPIRE].

[8] CMS collaboration, S. Chatrchyan et al., *Dependence on pseudorapidity and centrality of charged hadron production in Pb-Pb collisions at a nucleon-nucleon centre-of-mass energy of 2.76 TeV*, *JHEP* **08** (2011) 141 [arXiv:1107.4800] [INSPIRE].

[9] ATLAS collaboration, G. Aad et al., *Observation of a centrality-dependent dijet asymmetry in lead-lead collisions at* $\sqrt{s_{NN}}$ *2.76 TeV with the ATLAS detector at the LHC*, *Phys. Rev. Lett.* **105** (2010) 252303 [arXiv:1011.6182] [INSPIRE].

[10] M. Gyulassy and M. Plumer, *Jet quenching in dense matter*, *Phys. Lett.* **B 243** (1990) 432 [INSPIRE].

[11] R. Baier, Y.L. Dokshitzer, A.H. Mueller, S. Peigne and D. Schiff, *Radiative energy loss and* p_T *broadening of high-energy partons in nuclei*, *Nucl. Phys.* **B 484** (1997) 265 [hep-ph/9608322] [INSPIRE].

[12] PHENIX collaboration, K. Adcox et al., *Suppression of hadrons with large transverse momentum in central Au+Au collisions at* $\sqrt{s_{NN}} = 130\,GeV$, *Phys. Rev. Lett.* **88** (2002) 022301 [nucl-ex/0109003] [INSPIRE].

[13] PHENIX collaboration, S. Adler et al., *Suppressed* π^0 *production at large transverse momentum in central Au+ Au collisions at* $\sqrt{s_{NN}} = 200\,GeV$, *Phys. Rev. Lett.* **91** (2003) 072301 [nucl-ex/0304022] [INSPIRE].

[14] STAR collaboration, J. Adams et al., *Transverse momentum and collision energy dependence of high* p_T *hadron suppression in Au+Au collisions at ultrarelativistic energies*, *Phys. Rev. Lett.* **91** (2003) 172302 [nucl-ex/0305015] [INSPIRE].

[15] STAR collaboration, J. Adams et al., *Evidence from* $D + Au$ *measurements for final state suppression of high* p_T *hadrons in Au+Au collisions at RHIC*, *Phys. Rev. Lett.* **91** (2003) 072304 [nucl-ex/0306024] [INSPIRE].

[16] ALICE collaboration, K. Aamodt and C. Loizides, *Suppression of charged particle production at large transverse momentum in central Pb-Pb collisions at* $\sqrt{s_{NN}} = 2.76\,TeV$, *Phys. Lett.* **B 696** (2011) 30 [arXiv:1012.1004] [INSPIRE].

[17] C.A. Salgado and U.A. Wiedemann, *Medium modification of jet shapes and jet multiplicities*, *Phys. Rev. Lett.* **93** (2004) 042301 [hep-ph/0310079] [INSPIRE].

[18] ALICE collaboration, B. Alessandro et al., *ALICE: physics performance report, volume II*, *J. Phys.* **G 32** (2006) 1295.

[19] CMS collaboration, S. Chatrchyan et al., *Observation and studies of jet quenching in PbPb collisions at nucleon-nucleon center-of-mass energy = 2.76 TeV*, *Phys. Rev.* **C 84** (2011) 024906 [arXiv:1102.1957] [INSPIRE].

[20] M. Cacciari, G.P. Salam and G. Soyez, *Fluctuations and asymmetric jet events in Pb-Pb collisions at the LHC*, *Eur. Phys. J.* **C 71** (2011) 1692 [arXiv:1101.2878] [INSPIRE].

[21] ALICE collaboration, K. Aamodt et al., *The ALICE experiment at the CERN LHC*, 2008 *JINST* **3** S08002 [INSPIRE].

[22] ALICE collaboration, K. Aamodt et al., *Alignment of the ALICE inner tracking system with cosmic-ray tracks*, 2010 *JINST* **5** P03003 [arXiv:1001.0502] [INSPIRE].

[23] ALICE collaboration, K. Aamodt et al., *Centrality dependence of the charged-particle multiplicity density at mid-rapidity in Pb-Pb collisions at* $\sqrt{s_{NN}} = 2.76\,TeV$, *Phys. Rev. Lett.* **106** (2011) 032301 [arXiv:1012.1657] [INSPIRE].

[24] J. Alme, Y. Andres, H. Appelshauser, S. Bablok, N. Bialas, et al., *The ALICE TPC, a large 3-dimensional tracking device with fast readout for ultra-high multiplicity events*, *Nucl. Instrum. Meth.* **A 622** (2010) 316 [arXiv:1001.1950] [INSPIRE].

[25] M. Cacciari and G.P. Salam, *Dispelling the* N^3 *myth for the* k_t *jet-finder*, *Phys. Lett.* **B 641** (2006) 57 [hep-ph/0512210] [INSPIRE].

[26] STAR collaboration, S. Salur, *First direct measurement of jets in* $\sqrt{S_{NN}} = 200\,GeV$ *heavy ion collisions by STAR*, *Eur. Phys. J.* **C 61** (2009) 761 [arXiv:0809.1609] [INSPIRE].

[27] M. Cacciari and G.P. Salam, *Pileup subtraction using jet areas*, *Phys. Lett.* **B 659** (2008) 119 [arXiv:0707.1378] [INSPIRE].

[28] M. Cacciari, G.P. Salam and G. Soyez, *The catchment area of jets*, *JHEP* **04** (2008) 005 [arXiv:0802.1188] [INSPIRE].

JHEP03(2012)053

[29] M. Cacciari, J. Rojo, G.P. Salam and G. Soyez, *Jet reconstruction in heavy ion collisions*, *Eur. Phys. J.* **C 71** (2011) 1539 [arXiv:1010.1759] [INSPIRE].

[30] M. Tannenbaum, *The distribution function of the event-by-event average p_T for statistically independent emission*, *Phys. Lett.* **B 498** (2001) 29 [INSPIRE].

[31] J.-Y. Ollitrault, *Anisotropy as a signature of transverse collective flow*, *Phys. Rev.* **D 46** (1992) 229 [INSPIRE].

[32] ALICE collaboration, C. Loizides, *Higher harmonic anisotropic flow measurements of charged particles in Pb-Pb collisions at $\sqrt{s_{NN}} = 2.76$ TeV*, *Phys. Rev. Lett.* **107** (2011) 032301 [arXiv:1105.3865] [INSPIRE].

[33] J. Bielcikova, S. Esumi, K. Filimonov, S. Voloshin and J. Wurm, *Elliptic flow contribution to two particle correlations at different orientations to the reaction plane*, *Phys. Rev.* **C 69** (2004) 021901 [nucl-ex/0311007] [INSPIRE].

[34] T. Sjöstrand, S. Mrenna and P.Z. Skands, *PYTHIA 6.4 physics and manual*, *JHEP* **05** (2006) 026 [hep-ph/0603175] [INSPIRE].

[35] P. Jacobs, *Background fluctuations in heavy ion jet reconstruction*, *Nucl. Phys.* **A 855** (2011) 299 [arXiv:1012.2406].

[36] M. Cacciari, G.P. Salam and G. Soyez, *The $\bar{k}_t$ jet clustering algorithm*, *JHEP* **04** (2008) 063 [arXiv:0802.1189] [INSPIRE].

[37] Gabriel de Barros. *Inclusive distribution of fully reconstructed jets in heavy ion collisions at RHIC: status report*, proceedings for *PANIC 2011*, to appear in AIP conference series (2011).

JHEP03(2012)053

The ALICE collaboration

B. Abelev[70] , J. Adam[35] , D. Adamová[75] , A.M. Adare[122] , M.M. Aggarwal[79] , G. Aglieri Rinella[31] , A.G. Agocs[61] , A. Agostinelli[20] , S. Aguilar Salazar[57] , Z. Ahammed[118] , N. Ahmad[15] , A. Ahmad Masoodi[15] , S.U. Ahn[65,38] , A. Akindinov[47] , D. Aleksandrov[90] , B. Alessandro[96] , R. Alfaro Molina[57] , A. Alici[97,31,10] , A. Alkin[3] , E. Almaráz Aviña[57] , T. Alt[37] , V. Altini[29,31] , S. Altinpinar[16] , I. Altsybeev[119] , C. Andrei[72] , A. Andronic[87] , V. Anguelov[84] , J. Anielski[55] , C. Anson[17] , T. Antičić[88] , F. Antinori[101] , P. Antonioli[97] , L. Aphecetche[103] , H. Appelshäuser[53] , N. Arbor[66] , S. Arcelli[20] , A. Arend[53] , N. Armesto[14] , R. Arnaldi[96] , T. Aronsson[122] , I.C. Arsene[87] , M. Arslandok[53] , A. Asryan[119] , A. Augustinus[31] , R. Averbeck[87] , T.C. Awes[76] , J. Äystö[39] , M.D. Azmi[15] , M. Bach[37] , A. Badalà[98] , Y.W. Baek[65,38] , R. Bailhache[53] , R. Bala[96] , R. Baldini Ferroli[10] , A. Baldisseri[13] , A. Baldit[65] , F. Baltasar Dos Santos Pedrosa[31] , J. Bán[48] , R.C. Baral[49] , R. Barbera[25] , F. Barile[29] , G.G. Barnaföldi[61] , L.S. Barnby[92] , V. Barret[65] , J. Bartke[106] , M. Basile[20] , N. Bastid[65] , B. Bathen[55] , G. Batigne[103] , B. Batyunya[60] , C. Baumann[53] , I.G. Bearden[73] , H. Beck[53] , I. Belikov[59] , F. Bellini[20] , R. Bellwied[112] , E. Belmont-Moreno[57] , S. Beole[27] , I. Berceanu[72] , A. Bercuci[72] , Y. Berdnikov[77] , D. Berenyi[61] , C. Bergmann[55] , D. Berzano[96] , L. Betev[31] , A. Bhasin[82] , A.K. Bhati[79] , N. Bianchi[67] , L. Bianchi[27] , C. Bianchin[23] , J. Bielčík[35] , J. Bielčíková[75] , A. Bilandzic[74] , F. Blanco[112] , F. Blanco[8] , D. Blau[90] , C. Blume[53] , M. Boccioli[31] , N. Bock[17] , A. Bogdanov[71] , H. Bøggild[73] , M. Bogolyubsky[44] , L. Boldizsár[61] , M. Bombara[36] , J. Book[53] , H. Borel[13] , A. Borissov[121] , S. Bose[91] , F. Bossú[31,27] , M. Botje[74] , S. Böttger[52] , B. Boyer[43] , P. Braun-Munzinger[87] , M. Bregant[103] , T. Breitner[52] , M. Broz[34] , R. Brun[31] , E. Bruna[122,27,96] , G.E. Bruno[29] , D. Budnikov[89] , H. Buesching[53] , S. Bufalino[27,96] , K. Bugaiev[3] , O. Busch[84] , Z. Buthelezi[81] , D. Caballero Orduna[122] , D. Caffarri[23] , X. Cai[41] , H. Caines[122] , E. Calvo Villar[93] , P. Camerini[21] , V. Canoa Roman[9,2] , G. Cara Romeo[97] , F. Carena[31] , W. Carena[31] , N. Carlin Filho[109] , F. Carminati[31] , C.A. Carrillo Montoya[31] , A. Casanova Díaz[67] , M. Caselle[31] , J. Castillo Castellanos[13] , J.F. Castillo Hernandez[87] , E.A.R. Casula[22] , V. Catanescu[72] , C. Cavicchioli[31] , J. Cepila[35] , P. Cerello[96] , B. Chang[39,125] , S. Chapeland[31] , J.L. Charvet[13] , S. Chattopadhyay[91] , S. Chattopadhyay[118] , M. Cherney[78] , C. Cheshkov[31,111] , B. Cheynis[111] , E. Chiavassa[96] , V. Chibante Barroso[31] , D.D. Chinellato[110] , P. Chochula[31] , M. Chojnacki[46] , P. Christakoglou[74,46] , C.H. Christensen[73] , P. Christiansen[30] , T. Chujo[116] , S.U. Chung[86] , C. Cicalo[94] , L. Cifarelli[20,31] , F. Cindolo[97] , J. Cleymans[81] , F. Coccetti[10] , J.-P. Coffin[59] , F. Colamaria[29] , D. Colella[29] , G. Conesa Balbastre[66] , Z. Conesa del Valle[31,59] , P. Constantin[84] , G. Contin[21] , J.G. Contreras[9] , T.M. Cormier[121] , Y. Corrales Morales[27] , P. Cortese[28] , I. Cortés Maldonado[2] , M.R. Cosentino[69,110] , F. Costa[31] , M.E. Cotallo[8] , E. Crescio[9] , P. Crochet[65] , E. Cruz Alaniz[57] , E. Cuautle[56] , L. Cunqueiro[67] , A. Dainese[23,101] , H.H. Dalsgaard[73] , A. Danu[51] , K. Das[91] , D. Das[91] , I. Das[91,43] , A. Dash[49,110] , S. Dash[42,96] , S. De[118] , A. De Azevedo Moregula[67] , G.O.V. de Barros[109] , A. De Caro[26,10] , G. de Cataldo[95] , J. de Cuveland[37] , A. De Falco[22] , D. De Gruttola[26] ,

JHEP03(2012)053

H. Delagrange[103] , E. Del Castillo Sanchez[31] , A. Deloff[102] , V. Demanov[89] , N. De Marco[96] , E. Dénes[61] , S. De Pasquale[26] , A. Deppman[109] , G. D Erasmo[29] , R. de Rooij[46] , D. Di Bari[29] , T. Dietel[55] , C. Di Giglio[29] , S. Di Liberto[100] , A. Di Mauro[31] , P. Di Nezza[67] , R. Divià[31] , Ø. Djuvsland[16] , A. Dobrin[121 ,30] , T. Dobrowolski[102] , I. Domínguez[56] , B. Dönigus[87] , O. Dordic[19] , O. Driga[103] , A.K. Dubey[118] , L. Ducroux[111] , P. Dupieux[65] , A.K. Dutta Majumdar[91] , M.R. Dutta Majumdar[118] , D. Elia[95] , D. Emschermann[55] , H. Engel[52] , H.A. Erdal[33] , B. Espagnon[43] , M. Estienne[103] , S. Esumi[116] , D. Evans[92] , G. Eyyubova[19] , D. Fabris[23 ,101] , J. Faivre[66] , D. Falchieri[20] , A. Fantoni[67] , M. Fasel[87] , R. Fearick[81] , A. Fedunov[60] , D. Fehlker[16] , L. Feldkamp[55] , D. Felea[51] , G. Feofilov[119] , A. Fernández Téllez[2] , A. Ferretti[27] , R. Ferretti[28] , J. Figiel[106] , M.A.S. Figueredo[109] , S. Filchagin[89] , R. Fini[95] , D. Finogeev[45] , F.M. Fionda[29] , E.M. Fiore[29] , M. Floris[31] , S. Foertsch[81] , P. Foka[87] , S. Fokin[90] , E. Fragiacomo[99] , M. Fragkiadakis[80] , U. Frankenfeld[87] , U. Fuchs[31] , C. Furget[66] , M. Fusco Girard[26] , J.J. Gaardhøje[73] , M. Gagliardi[27] , A. Gago[93] , M. Gallio[27] , D.R. Gangadharan[17] , P. Ganoti[76] , C. Garabatos[87] , E. Garcia-Solis[11] , I. Garishvili[70] , J. Gerhard[37] , M. Germain[103] , C. Geuna[13] , A. Gheata[31] , M. Gheata[31] , B. Ghidini[29] , P. Ghosh[118] , P. Gianotti[67] , M.R. Girard[120] , P. Giubellino[31] , E. Gladysz-Dziadus[106] , P. Glässel[84] , R. Gomez[108] , E.G. Ferreiro[14] , L.H. González-Trueba[57] , P. González-Zamora[8] , S. Gorbunov[37] , A. Goswami[83] , S. Gotovac[104] , V. Grabski[57] , L.K. Graczykowski[120] , R. Grajcarek[84] , A. Grelli[46] , C. Grigoras[31] , A. Grigoras[31] , V. Grigoriev[71] , S. Grigoryan[60] , A. Grigoryan[123] , B. Grinyov[3] , N. Grion[99] , P. Gros[30] , J.F. Grosse-Oetringhaus[31] , J.-Y. Grossiord[111] , R. Grosso[31] , F. Guber[45] , R. Guernane[66] , C. Guerra Gutierrez[93] , B. Guerzoni[20] , M. Guilbaud[111] , K. Gulbrandsen[73] , T. Gunji[115] , A. Gupta[82] , R. Gupta[82] , H. Gutbrod[87] , Ø. Haaland[16] , C. Hadjidakis[43] , M. Haiduc[51] , H. Hamagaki[115] , G. Hamar[61] , B.H. Han[18] , L.D. Hanratty[92] , A. Hansen[73] , Z. Harmanova[36] , J.W. Harris[122] , M. Hartig[53] , D. Hasegan[51] , D. Hatzifotiadou[97] , A. Hayrapetyan[31 ,123] , S.T. Heckel[53] , M. Heide[55] , H. Helstrup[33] , A. Herghelegiu[72] , G. Herrera Corral[9] , N. Herrmann[84] , K.F. Hetland[33] , B. Hicks[122] , P.T. Hille[122] , B. Hippolyte[59] , T. Horaguchi[116] , Y. Hori[115] , P. Hristov[31] , I. Hřivnáčová[43] , M. Huang[16] , S. Huber[87] , T.J. Humanic[17] , D.S. Hwang[18] , R. Ichou[65] , R. Ilkaev[89] , I. Ilkiv[102] , M. Inaba[116] , E. Incani[22] , G.M. Innocenti[27] , P.G. Innocenti[31] , M. Ippolitov[90] , M. Irfan[15] , C. Ivan[87] , A. Ivanov[119] , V. Ivanov[77] , M. Ivanov[87] , O. Ivanytskyi[3] , A. Jachołkowski[31] , P. M. Jacobs[69] , L. Jancurová[60] , H.J. Jang[64] , S. Jangal[59] , R. Janik[34] , M.A. Janik[120] , P.H.S.Y. Jayarathna[112] , S. Jena[42] , R.T. Jimenez Bustamante[56] , L. Jirden[31] , P.G. Jones[92] , H. Jung[38] , W. Jung[38] , A. Jusko[92] , A.B. Kaidalov[47] , V. Kakoyan[123] , S. Kalcher[37] , P. Kaliňák[48] , M. Kalisky[55] , T. Kalliokoski[39] , A. Kalweit[54] , K. Kanaki[16] , J.H. Kang[125] , V. Kaplin[71] , A. Karasu Uysal[31 ,124] , O. Karavichev[45] , T. Karavicheva[45] , E. Karpechev[45] , A. Kazantsev[90] , U. Kebschull[63 ,52] , R. Keidel[126] , P. Khan[91] , M.M. Khan[15] , S.A. Khan[118] , A. Khanzadeev[77] , Y. Kharlov[44] , B. Kileng[33] , D.J. Kim[39] , D.W. Kim[38] , J.H. Kim[18] , J.S. Kim[38] , M. Kim[125] , S.H. Kim[38] , S. Kim[18] , T. Kim[125] , B. Kim[125] , S. Kirsch[37 ,31] , I. Kisel[37] , S. Kiselev[47] , A. Kisiel[31 ,120] , J.L. Klay[5] , J. Klein[84] ,

JHEP03(2012)053

C. Klein-Bösing[55] , M. Kliemant[53] , A. Kluge[31] , M.L. Knichel[87] , K. Koch[84] , M.K. Köhler[87] , A. Kolojvari[119] , V. Kondratiev[119] , N. Kondratyeva[71] , A. Konevskikh[45] , A. Korneev[89] , C. Kottachchi Kankanamge Don[121] , R. Kour[92] , M. Kowalski[106] , S. Kox[66] , G. Koyithatta Meethaleveedu[42] , J. Kral[39] , I. Králik[48] , F. Kramer[53] , I. Kraus[87] , T. Krawutschke[84] ,[32] , M. Krelina[35] , M. Kretz[37] , M. Krivda[92] ,[48] , F. Krizek[39] , M. Krus[35] , E. Kryshen[77] , M. Krzewicki[74] ,[87] , Y. Kucheriaev[90] , C. Kuhn[59] , P.G. Kuijer[74] , P. Kurashvili[102] , A. Kurepin[45] , A.B. Kurepin[45] , A. Kuryakin[89] , V. Kushpil[75] , S. Kushpil[75] , H. Kvaerno[19] , M.J. Kweon[84] , Y. Kwon[125] , P. Ladrón de Guevara[56] , I. Lakomov[43] ,[119] , R. Langoy[16] , C. Lara[52] , A. Lardeux[103] , P. La Rocca[25] , C. Lazzeroni[92] , R. Lea[21] , Y. Le Bornec[43] , K.S. Lee[38] , S.C. Lee[38] , F. Lefèvre[103] , J. Lehnert[53] , L. Leistam[31] , M. Lenhardt[103] , V. Lenti[95] , H. León[57] , I. León Monzón[108] , H. León Vargas[53] , P. Lévai[61] , X. Li[12] , J. Lien[16] , R. Lietava[92] , S. Lindal[19] , V. Lindenstruth[37] , C. Lippmann[87] ,[31] , M.A. Lisa[17] , L. Liu[16] , P.I. Loenne[16] , V.R. Loggins[121] , V. Loginov[71] , S. Lohn[31] , D. Lohner[84] , C. Loizides[69] , K.K. Loo[39] , X. Lopez[65] , E. López Torres[7] , G. Løvhøiden[19] , X.-G. Lu[84] , P. Luettig[53] , M. Lunardon[23] , J. Luo[41] , G. Luparello[46] , L. Luquin[103] , C. Luzzi[31] , K. Ma[41] , R. Ma[122] , D.M. Madagodahettige-Don[112] , A. Maevskaya[45] , M. Mager[54] ,[31] , D.P. Mahapatra[49] , A. Maire[59] , M. Malaev[77] , I. Maldonado Cervantes[56] , L. Malinina[60] ,[,ii], D. Mal'Kevich[47] , P. Malzacher[87] , A. Mamonov[89] , L. Manceau[96] , L. Mangotra[82] , V. Manko[90] , F. Manso[65] , V. Manzari[95] , Y. Mao[66] ,[41] , M. Marchisone[65] ,[27] , J. Mareš[50] , G.V. Margagliotti[21] ,[99] , A. Margotti[97] , A. Marín[87] , C. Markert[107] , I. Martashvili[114] , P. Martinengo[31] , M.I. Martínez[2] , A. Martínez Davalos[57] , G. Martínez García[103] , Y. Martynov[3] , A. Mas[103] , S. Masciocchi[87] , M. Masera[27] , A. Masoni[94] , L. Massacrier[111] ,[103] , M. Mastromarco[95] , A. Mastroserio[29] ,[31] , Z.L. Matthews[92] , A. Matyja[103] , D. Mayani[56] , C. Mayer[106] , J. Mazer[114] , M.A. Mazzoni[100] , F. Meddi[24] , A. Menchaca-Rocha[57] , J. Mercado Pérez[84] , M. Meres[34] , Y. Miake[116] , A. Michalon[59] , L. Milano[27] , J. Milosevic[19] ,[,1] , A. Mischke[46] , A.N. Mishra[83] , D. Miśkowiec[87] ,[31] , C. Mitu[51] , J. Mlynarz[121] , B. Mohanty[118] , A.K. Mohanty[31] , L. Molnar[31] , L. Montaño Zetina[9] , M. Monteno[96] , E. Montes[8] , T. Moon[125] , M. Morando[23] , D.A. Moreira De Godoy[109] , S. Moretto[23] , A. Morsch[31] , V. Muccifora[67] , E. Mudnic[104] , S. Muhuri[118] , H. Müller[31] , M.G. Munhoz[109] , L. Musa[31] , A. Musso[96] , B.K. Nandi[42] , R. Nania[97] , E. Nappi[95] , C. Nattrass[114] , N.P. Naumov[89] , S. Navin[92] , T.K. Nayak[118] , S. Nazarenko[89] , G. Nazarov[89] , A. Nedosekin[47] , M. Nicassio[29] , B.S. Nielsen[73] , T. Niida[116] , S. Nikolaev[90] , V. Nikolic[88] , S. Nikulin[90] , V. Nikulin[77] , B.S. Nilsen[78] , M.S. Nilsson[19] , F. Noferini[97] ,[10] , P. Nomokonov[60] , G. Nooren[46] , N. Novitzky[39] , A. Nyanin[90] , A. Nyatha[42] , C. Nygaard[73] , J. Nystrand[16] , A. Ochirov[119] , H. Oeschler[54] ,[31] , S. Oh[122] , S.K. Oh[38] , J. Oleniacz[120] , C. Oppedisano[96] , A. Ortiz Velasquez[56] , G. Ortona[31] ,[27] , A. Oskarsson[30] , P. Ostrowski[120] , I. Otterlund[30] , J. Otwinowski[87] , K. Oyama[84] , K. Ozawa[115] , Y. Pachmayer[84] , M. Pachr[35] , F. Padilla[27] , P. Pagano[26] , G. Paić[56] , F. Painke[37] , C. Pajares[14] , S.K. Pal[118] , S. Pal[13] , A. Palaha[92] , A. Palmeri[98] , V. Papikyan[123] , G.S. Pappalardo[98] , W.J. Park[87] , A. Passfeld[55] , B. Pastirčák[48] , D.I. Patalakha[44] , V. Paticchio[95] , A. Pavlinov[121] , T. Pawlak[120] , T. Peitzmann[46] ,

JHEP03(2012)053

M. Perales[11] , E. Pereira De Oliveira Filho[109] , D. Peresunko[90] , C.E. Pérez Lara[74] , E. Perez Lezama[56] , D. Perini[31] , D. Perrino[29] , W. Peryt[120] , A. Pesci[97] , V. Peskov[31,56] , Y. Pestov[4] , V. Petráček[35] , M. Petran[35] , M. Petris[72] , P. Petrov[92] , M. Petrovici[72] , C. Petta[25] , S. Piano[99] , A. Piccotti[96] , M. Pikna[34] , P. Pillot[103] , O. Pinazza[31] , L. Pinsky[112] , N. Pitz[53] , F. Piuz[31] , D.B. Piyarathna[112] , M. Płoskoń[69] , J. Pluta[120] , T. Pocheptsov[60,19] , S. Pochybova[61] , P.L.M. Podesta-Lerma[108] , M.G. Poghosyan[31,27] , K. Polák[50] , B. Polichtchouk[44] , A. Pop[72] , S. Porteboeuf-Houssais[65] , V. Pospíšil[35] , B. Potukuchi[82] , S.K. Prasad[121] , R. Preghenella[97,10] , F. Prino[96] , C.A. Pruneau[121] , I. Pshenichnov[45] , S. Puchagin[89] , G. Puddu[22] , A. Pulvirenti[25,31] , V. Punin[89] , M. Putiš[36] , J. Putschke[121,122] , E. Quercigh[31] , H. Qvigstad[19] , A. Rachevski[99] , A. Rademakers[31] , S. Radomski[84] , T.S. Räihä[39] , J. Rak[39] , A. Rakotozafindrabe[13] , L. Ramello[28] , A. Ramírez Reyes[9] , S. Raniwala[83] , R. Raniwala[83] , S.S. Räsänen[39] , B.T. Rascanu[53] , D. Rathee[79] , K.F. Read[114] , J.S. Real[66] , K. Redlich[102,58] , P. Reichelt[53] , M. Reicher[46] , R. Renfordt[53] , A.R. Reolon[67] , A. Reshetin[45] , F. Rettig[37] , J.-P. Revol[31] , K. Reygers[84] , L. Riccati[96] , R.A. Ricci[68] , T. Richert[30] , M. Richter[19] , P. Riedler[31] , W. Riegler[31] , F. Riggi[25,98] , M. Rodríguez Cahuantzi[2] , K. Røed[16] , D. Rohr[37] , D. Röhrich[16] , R. Romita[87] , F. Ronchetti[67] , P. Rosnet[65] , S. Rossegger[31] , A. Rossi[23] , F. Roukoutakis[80] , P. Roy[91] , C. Roy[59] , A.J. Rubio Montero[8] , R. Rui[21] , E. Ryabinkin[90] , A. Rybicki[106] , S. Sadovsky[44] , K. Šafařík[31] , P.K. Sahu[49] , J. Saini[118] , H. Sakaguchi[40] , S. Sakai[69] , D. Sakata[116] , C.A. Salgado[14] , J. Salzwedel[17] , S. Sambyal[82] , V. Samsonov[77] , X. Sanchez Castro[56,59] , L. Šándor[48] , A. Sandoval[57] , M. Sano[116] , S. Sano[115] , R. Santo[55] , R. Santoro[95,31] , J. Sarkamo[39] , E. Scapparone[97] , F. Scarlassara[23] , R.P. Scharenberg[85] , C. Schiaua[72] , R. Schicker[84] , C. Schmidt[87] , H.R. Schmidt[87,117] , S. Schreiner[31] , S. Schuchmann[53] , J. Schukraft[31] , Y. Schutz[31,103] , K. Schwarz[87] , K. Schweda[87,84] , G. Scioli[20] , E. Scomparin[96] , P.A. Scott[92] , R. Scott[114] , G. Segato[23] , I. Selyuzhenkov[87] , S. Senyukov[28,59] , J. Seo[86] , S. Serci[22] , E. Serradilla[8,57] , A. Sevcenco[51] , I. Sgura[95] , A. Shabetai[103] , G. Shabratova[60] , R. Shahoyan[31] , N. Sharma[79] , S. Sharma[82] , K. Shigaki[40] , M. Shimomura[116] , K. Shtejer[7] , Y. Sibiriak[90] , M. Siciliano[27] , E. Sicking[31] , S. Siddhanta[94] , T. Siemiarczuk[102] , D. Silvermyr[76] , G. Simonetti[29,31] , R. Singaraju[118] , R. Singh[82] , S. Singha[118] , T. Sinha[91] , B.C. Sinha[118] , B. Sitar[34] , M. Sitta[28] , T.B. Skaali[19] , K. Skjerdal[16] , R. Smakal[35] , N. Smirnov[122] , R. Snellings[46] , C. Søgaard[73] , R. Soltz[70] , H. Son[18] , M. Song[125] , J. Song[86] , C. Soos[31] , F. Soramel[23] , I. Sputowska[106] , M. Spyropoulou-Stassinaki[80] , B.K. Srivastava[85] , J. Stachel[84] , I. Stan[51] , I. Stan[51] , G. Stefanek[102] , G. Stefanini[31] , T. Steinbeck[37] , M. Steinpreis[17] , E. Stenlund[30] , G. Steyn[81] , D. Stocco[103] , M. Stolpovskiy[44] , K. Strabykin[89] , P. Strmen[34] , A.A.P. Suaide[109] , M.A. Subieta Vásquez[27] , T. Sugitate[40] , C. Suire[43] , M. Sukhorukov[89] , R. Sultanov[47] , M. Šumbera[75] , T. Susa[88] , A. Szanto de Toledo[109] , I. Szarka[34] , A. Szostak[16] , C. Tagridis[80] , J. Takahashi[110] , J.D. Tapia Takaki[43] , A. Tauro[31] , G. Tejeda Muñoz[2] , A. Telesca[31] , C. Terrevoli[29] , J. Thäder[87] , D. Thomas[46] , J.H. Thomas[87] , R. Tieulent[111] , A.R. Timmins[112] , D. Tlusty[35] , A. Toia[37,31] , H. Torii[40,115] , L. Toscano[96] , F. Tosello[96] , T. Traczyk[120] , D. Truesdale[17] , W.H. Trzaska[39] , T. Tsuji[115] , A. Tumkin[89] , R. Turrisi[101] , T.S. Tveter[19] , J. Ulery[53] ,

JHEP03(2012)053

K. Ullaland[16], J. Ulrich[63,52], A. Uras[111], J. Urbán[36], G.M. Urciuoli[100], G.L. Usai[22], M. Vajzer[35,75], M. Vala[60,48], L. Valencia Palomo[43], S. Vallero[84], N. van der Kolk[74], P. Vande Vyvre[31], M. van Leeuwen[46], L. Vannucci[68], A. Vargas[2], R. Varma[42], M. Vasileiou[80], A. Vasiliev[90], V. Vechernin[119], M. Veldhoen[46], M. Venaruzzo[21], E. Vercellin[27], S. Vergara[2], D.C. Vernekohl[55], R. Vernet[6], M. Verweij[46], L. Vickovic[104], G. Viesti[23], O. Vikhlyantsev[89], Z. Vilakazi[81], O. Villalobos Baillie[92], A. Vinogradov[90], Y. Vinogradov[89], L. Vinogradov[119], T. Virgili[26], Y.P. Viyogi[118], A. Vodopyanov[60], S. Voloshin[121], K. Voloshin[47], G. Volpe[29,31], B. von Haller[31], D. Vranic[87], G. Øvrebekk[16], J. Vrláková[36], B. Vulpescu[65], A. Vyushin[89], B. Wagner[16], V. Wagner[35], R. Wan[59,41], Y. Wang[84], M. Wang[41], D. Wang[41], Y. Wang[41], K. Watanabe[116], J.P. Wessels[31,55], U. Westerhoff[55], J. Wiechula[84,117], J. Wikne[19], M. Wilde[55], G. Wilk[102], A. Wilk[55], M.C.S. Williams[97], B. Windelband[84], L. Xaplanteris Karampatsos[107], H. Yang[13], S. Yang[16], S. Yasnopolskiy[90], J. Yi[86], Z. Yin[41], H. Yokoyama[116], I.-K. Yoo[86], J. Yoon[125], W. Yu[53], X. Yuan[41], I. Yushmanov[90], C. Zach[35], C. Zampolli[97,31], S. Zaporozhets[60], A. Zarochentsev[119], P. Závada[50], N. Zaviyalov[89], H. Zbroszczyk[120], P. Zelnicek[31,52], I.S. Zgura[51], M. Zhalov[77], X. Zhang[65,41], F. Zhou[41], D. Zhou[41], Y. Zhou[46], X. Zhu[41], A. Zichichi[20,10], A. Zimmermann[84], G. Zinovjev[3], Y. Zoccarato[111], M. Zynovyev[3]

[i] Deceased

[ii] Also at: M.V.Lomonosov Moscow State University, D.V.Skobeltsyn Institute of Nuclear Physics, Moscow, Russia

[1] Also at: "Vinča" Institute of Nuclear Sciences, Belgrade, Serbia

[2] Benemérita Universidad Autónoma de Puebla, Puebla, Mexico

[3] Bogolyubov Institute for Theoretical Physics, Kiev, Ukraine

[4] Budker Institute for Nuclear Physics, Novosibirsk, Russia

[5] California Polytechnic State University, San Luis Obispo, California, United States

[6] Centre de Calcul de l'IN2P3, Villeurbanne, France

[7] Centro de Aplicaciones Tecnológicas y Desarrollo Nuclear (CEADEN), Havana, Cuba

[8] Centro de Investigaciones Energéticas Medioambientales y Tecnológicas (CIEMAT), Madrid, Spain

[9] Centro de Investigación y de Estudios Avanzados (CINVESTAV), Mexico City and Mérida, Mexico

[10] Centro Fermi – Centro Studi e Ricerche e Museo Storico della Fisica "Enrico Fermi", Rome, Italy

[11] Chicago State University, Chicago, United States

[12] China Institute of Atomic Energy, Beijing, China

[13] Commissariat à l'Energie Atomique, IRFU, Saclay, France

[14] Departamento de Física de Partículas and IGFAE, Universidad de Santiago de Compostela, Santiago de Compostela, Spain

[15] Department of Physics Aligarh Muslim University, Aligarh, India

[16] Department of Physics and Technology, University of Bergen, Bergen, Norway

[17] Department of Physics, Ohio State University, Columbus, Ohio, United States

JHEP03(2012)053

[18] Department of Physics, Sejong University, Seoul, South Korea
[19] Department of Physics, University of Oslo, Oslo, Norway
[20] Dipartimento di Fisica dell'Università and Sezione INFN, Bologna, Italy
[21] Dipartimento di Fisica dell'Università and Sezione INFN, Trieste, Italy
[22] Dipartimento di Fisica dell'Università and Sezione INFN, Cagliari, Italy
[23] Dipartimento di Fisica dell'Università and Sezione INFN, Padova, Italy
[24] Dipartimento di Fisica dell'Università 'La Sapienza' and Sezione INFN, Rome, Italy
[25] Dipartimento di Fisica e Astronomia dell'Università and Sezione INFN, Catania, Italy
[26] Dipartimento di Fisica 'E.R. Caianiello' dell'Università and Gruppo Collegato INFN, Salerno, Italy
[27] Dipartimento di Fisica Sperimentale dell'Università and Sezione INFN, Turin, Italy
[28] Dipartimento di Scienze e Tecnologie Avanzate dell'Università del Piemonte Orientale and Gruppo Collegato INFN, Alessandria, Italy
[29] Dipartimento Interateneo di Fisica 'M. Merlin' and Sezione INFN, Bari, Italy
[30] Division of Experimental High Energy Physics, University of Lund, Lund, Sweden
[31] European Organization for Nuclear Research (CERN), Geneva, Switzerland
[32] Fachhochschule Köln, Köln, Germany
[33] Faculty of Engineering, Bergen University College, Bergen, Norway
[34] Faculty of Mathematics, Physics and Informatics, Comenius University, Bratislava, Slovakia
[35] Faculty of Nuclear Sciences and Physical Engineering, Czech Technical University in Prague, Prague, Czech Republic
[36] Faculty of Science, P.J. Šafárik University, Košice, Slovakia
[37] Frankfurt Institute for Advanced Studies, Johann Wolfgang Goethe-Universität Frankfurt, Frankfurt, Germany
[38] Gangneung-Wonju National University, Gangneung, South Korea
[39] Helsinki Institute of Physics (HIP) and University of Jyväskylä, Jyväskylä, Finland
[40] Hiroshima University, Hiroshima, Japan
[41] Hua-Zhong Normal University, Wuhan, China
[42] Indian Institute of Technology, Mumbai, India
[43] Institut de Physique Nucléaire d'Orsay (IPNO), Université Paris-Sud, CNRS-IN2P3, Orsay, France
[44] Institute for High Energy Physics, Protvino, Russia
[45] Institute for Nuclear Research, Academy of Sciences, Moscow, Russia
[46] Nikhef, National Institute for Subatomic Physics and Institute for Subatomic Physics of Utrecht University, Utrecht, Netherlands
[47] Institute for Theoretical and Experimental Physics, Moscow, Russia
[48] Institute of Experimental Physics, Slovak Academy of Sciences, Košice, Slovakia
[49] Institute of Physics, Bhubaneswar, India
[50] Institute of Physics, Academy of Sciences of the Czech Republic, Prague, Czech Republic
[51] Institute of Space Sciences (ISS), Bucharest, Romania
[52] Institut für Informatik, Johann Wolfgang Goethe-Universität Frankfurt, Frankfurt, Germany
[53] Institut für Kernphysik, Johann Wolfgang Goethe-Universität Frankfurt, Frankfurt, Germany
[54] Institut für Kernphysik, Technische Universität Darmstadt, Darmstadt, Germany
[55] Institut für Kernphysik, Westfälische Wilhelms-Universität Münster, Münster, Germany
[56] Instituto de Ciencias Nucleares, Universidad Nacional Autónoma de México, Mexico City,

JHEP03(2012)053

Mexico
[57] Instituto de Física, Universidad Nacional Autónoma de México, Mexico City, Mexico
[58] Institut of Theoretical Physics, University of Wroclaw
[59] Institut Pluridisciplinaire Hubert Curien (IPHC), Université de Strasbourg, CNRS-IN2P3, Strasbourg, France
[60] Joint Institute for Nuclear Research (JINR), Dubna, Russia
[61] KFKI Research Institute for Particle and Nuclear Physics, Hungarian Academy of Sciences, Budapest, Hungary
[62] Kharkiv Institute of Physics and Technology (KIPT), National Academy of Sciences of Ukraine (NASU), Kharkov, Ukraine
[63] Kirchhoff-Institut für Physik, Ruprecht-Karls-Universität Heidelberg, Heidelberg, Germany
[64] Korea Institute of Science and Technology Information
[65] Laboratoire de Physique Corpusculaire (LPC), Clermont Université, Université Blaise Pascal, CNRS–IN2P3, Clermont-Ferrand, France
[66] Laboratoire de Physique Subatomique et de Cosmologie (LPSC), Université Joseph Fourier, CNRS-IN2P3, Institut Polytechnique de Grenoble, Grenoble, France
[67] Laboratori Nazionali di Frascati, INFN, Frascati, Italy
[68] Laboratori Nazionali di Legnaro, INFN, Legnaro, Italy
[69] Lawrence Berkeley National Laboratory, Berkeley, California, United States
[70] Lawrence Livermore National Laboratory, Livermore, California, United States
[71] Moscow Engineering Physics Institute, Moscow, Russia
[72] National Institute for Physics and Nuclear Engineering, Bucharest, Romania
[73] Niels Bohr Institute, University of Copenhagen, Copenhagen, Denmark
[74] Nikhef, National Institute for Subatomic Physics, Amsterdam, Netherlands
[75] Nuclear Physics Institute, Academy of Sciences of the Czech Republic, Řež u Prahy, Czech Republic
[76] Oak Ridge National Laboratory, Oak Ridge, Tennessee, United States
[77] Petersburg Nuclear Physics Institute, Gatchina, Russia
[78] Physics Department, Creighton University, Omaha, Nebraska, United States
[79] Physics Department, Panjab University, Chandigarh, India
[80] Physics Department, University of Athens, Athens, Greece
[81] Physics Department, University of Cape Town, iThemba LABS, Cape Town, South Africa
[82] Physics Department, University of Jammu, Jammu, India
[83] Physics Department, University of Rajasthan, Jaipur, India
[84] Physikalisches Institut, Ruprecht-Karls-Universität Heidelberg, Heidelberg, Germany
[85] Purdue University, West Lafayette, Indiana, United States
[86] Pusan National University, Pusan, South Korea
[87] Research Division and ExtreMe Matter Institute EMMI, GSI Helmholtzzentrum für Schwerionenforschung, Darmstadt, Germany
[88] Rudjer Bošković Institute, Zagreb, Croatia
[89] Russian Federal Nuclear Center (VNIIEF), Sarov, Russia
[90] Russian Research Centre Kurchatov Institute, Moscow, Russia
[91] Saha Institute of Nuclear Physics, Kolkata, India
[92] School of Physics and Astronomy, University of Birmingham, Birmingham, United Kingdom
[93] Sección Física, Departamento de Ciencias, Pontificia Universidad Católica del Perú, Lima,

JHEP03(2012)053

Peru
[94] Sezione INFN, Cagliari, Italy
[95] Sezione INFN, Bari, Italy
[96] Sezione INFN, Turin, Italy
[97] Sezione INFN, Bologna, Italy
[98] Sezione INFN, Catania, Italy
[99] Sezione INFN, Trieste, Italy
[100] Sezione INFN, Rome, Italy
[101] Sezione INFN, Padova, Italy
[102] Soltan Institute for Nuclear Studies, Warsaw, Poland
[103] SUBATECH, Ecole des Mines de Nantes, Université de Nantes, CNRS-IN2P3, Nantes, France
[104] Technical University of Split FESB, Split, Croatia
[105] test institute
[106] The Henryk Niewodniczanski Institute of Nuclear Physics, Polish Academy of Sciences, Cracow, Poland
[107] The University of Texas at Austin, Physics Department, Austin, TX, United States
[108] Universidad Autónoma de Sinaloa, Culiacán, Mexico
[109] Universidade de São Paulo (USP), São Paulo, Brazil
[110] Universidade Estadual de Campinas (UNICAMP), Campinas, Brazil
[111] Université de Lyon, Université Lyon 1, CNRS/IN2P3, IPN-Lyon, Villeurbanne, France
[112] University of Houston, Houston, Texas, United States
[113] University of Technology and Austrian Academy of Sciences, Vienna, Austria
[114] University of Tennessee, Knoxville, Tennessee, United States
[115] University of Tokyo, Tokyo, Japan
[116] University of Tsukuba, Tsukuba, Japan
[117] Eberhard Karls Universität Tübingen, Tübingen, Germany
[118] Variable Energy Cyclotron Centre, Kolkata, India
[119] V. Fock Institute for Physics, St. Petersburg State University, St. Petersburg, Russia
[120] Warsaw University of Technology, Warsaw, Poland
[121] Wayne State University, Detroit, Michigan, United States
[122] Yale University, New Haven, Connecticut, United States
[123] Yerevan Physics Institute, Yerevan, Armenia
[124] Yildiz Technical University, Istanbul, Turkey
[125] Yonsei University, Seoul, South Korea
[126] Zentrum für Technologietransfer und Telekommunikation (ZTT), Fachhochschule Worms, Worms, Germany

JHEP03(2012)053

Measurement of Direct Photons in pp and Pb-Pb Collisions with ALICE

Martin Wilde (for the ALICE Collaboration)[1]

Institut für Kernphysik, Westfälische Wilhelms-Universität Münster, Münster, Germany

Abstract

The measurement of the direct photon transverse momentum spectrum in Pb-Pb collisions at $\sqrt{s_{NN}}$ = 2.76 TeV with data taken by the ALICE experiment is presented. The measurement shows a clear direct-photon signal for 0-40% most central collisions below 4 GeV/c that can not be described by next-to-leading-order perturbative QCD (NLO pQCD) calculations. Above this value of p_{T} the result is in agreement with pQCD predictions. The low p_{T} signal is expected to have thermal photon contributions. The inverse slope parameter of an exponential fit is extracted as $T_{\mathrm{LHC}} = 304 \pm 51^{\mathrm{syst+stat}}$ MeV. For a baseline measurement the analysis is performed for proton-proton collisions at $\sqrt{s}$ = 7 TeV and for peripheral (40-80%) Pb-Pb collisions. Both results show no low p_{T} direct-photon signal and are in agreement with pQCD calculations.

1. Introduction

Direct-photon production in hadronic collisions can be understood as a superposition of different production sources. In pp collisions, leading order pQCD processes, quark-gluon compton-scattering and quark-anti-quark annihilation are the main components of direct-photon production at high p_{T}. The second source is photons produced in yet fragmentation [1]. In heavy-ion collisions these prompt photons should be enhanced by the larger number of binary collisions. They may be modified by isospin effects and nuclear shadowing. Fragmentation photons are affected by jet quenching; saturation effects may lead to further modifications for both sources [2, 3].

In addition, final-state production mechanisms have to be considered in heavy-ion collisions. In the QGP phase, photons should be produced by the scattering of hard partons traversing the medium with thermalized partons, as well as by the scattering of thermalized partons. In the hot hadronic gas, produced after hadronization, direct photons should emerge from the scattering of the thermalized hadrons within the gas [2, 3, 4]. The thermalized nature of the production medium (QGP and hadron gas) should be reflected in the p_{T} distribution of the produced thermal photons.

The measurement of direct photons in pp collision is an important test for the validation of pQCD. In heavy-ion collisions a thermal photon signal is expected. From this signal an average temperature can be extracted. The comparison to pp pQCD results at higher p_{T} tests the binary scaling behavior of initial hard scatterings.

[1] A list of members of the ALICE Collaboration and acknowledgements can be found at the end of this issue.

2. Analysis Method

For both analyzed systems (Pb-Pb at $\sqrt{s_{NN}} = 2.76\,\text{TeV}$, pp at $\sqrt{s} = 7\,\text{TeV}$) the same analysis method is used. The Pb-Pb analysis is divided into two bins of centrality (central: 0-40%, peripheral: 40-80%). The direct-photon signal is extracted via the subtraction method (see e.g. [5]):

$$\gamma_{\text{direct}} = \gamma_{\text{inc}} - \gamma_{\text{decay}} = (1 - \frac{\gamma_{\text{decay}}}{\gamma_{\text{inc}}}) \cdot \gamma_{\text{inc}}. \tag{1}$$

The method is based on the measurement of the inclusive photon yield via the reconstruction of their conversion products. For this purpose a secondary vertex finder is used. The algorithm combines oppositely charged tracks with a large impact parameter. If a pair is accepted the conversion point and the momentum of the photon is calculated. The algorithm is generally used to identify weakly decaying particles like Λ or K^0_s.

To optimize the signal to background ratio and to exclude other sources of secondary vertices beside photons (combinatorial background, Λ, K^0_s, etc.), several photon selection criteria comparable to the criteria used in [7] are applied.

The extracted raw photon spectrum is corrected for purity, reconstruction efficiency and conversion probability of photons in the detector estimated from MC simulations.

The decay photon spectrum, γ_{decay}, is obtained by a cocktail calculation. The calculation is based on yield parametrizations of mesons with photon decay branches. The main source of decay photons ($\sim 80\%$) is $\pi^0 \to \gamma\gamma$. The second largest contribution ($\sim 18\%$) is the decay of the η meson ($\eta \to \gamma\gamma$). In the analyzed pp collisions both meson yields, π^0 and η, are measured [7]. In Pb-Pb only the π^0 yield is known [8]. In both cases additional sources of decay photons from unknown meson yields (η, η', ω, ϕ and ρ_0) are obtained from m_T-scaling [9].

To minimize the systematic uncertainties the ratio $\frac{\gamma_{\text{decay}}}{\gamma_{\text{inc}}}$ used in formula (1) is calculated via:

$$\frac{\gamma_{\text{inc}}}{\gamma_{\text{decay}}} = \frac{\gamma_{\text{inc}}}{\pi^0} \Big/ \frac{\gamma_{\text{decay}}}{\pi^0_{\text{param}}}. \tag{2}$$

The method guarantees an exact cancellation of all normalization factors used in the spectra. Further uncertainties are canceled due to the fact that the π^0 extraction is based on the same set of photon candidates as the inclusive photon yield [5, 6].

3. Results

Figure 1 shows the invariant cross section of inclusive photons produced in pp collisions at $\sqrt{s} = 7\,\text{TeV}$. It is calculated as:

$$E\frac{\mathrm{d}^3\sigma}{\mathrm{d}p^3} = \frac{1}{2\pi}\frac{\sigma_{MB_{OR}}}{N_{\text{events}}}\frac{1}{p_{\text{T}}}\frac{\mathcal{P}}{C\mathcal{E}}\frac{N^\gamma}{\Delta y \Delta p_{\text{T}}}. \tag{3}$$

In the formula, $\mathcal{P}$, C and $\mathcal{E}$ are the purity, the conversion probability and the efficiency. They are obtained from MC. $\sigma_{MB_{OR}}$ is the interaction cross section for the MBOR trigger that is used for the pp collisions ($\sigma_{MB_{OR}} = 62.2 \pm 2.2\,\text{mb}$ (syst)). N_{events} is the number of MBOR events that were collected and N^γ represents the number of photon candidates. In Fig. 2, the invariant inclusive photon yields for both centralities in Pb-Pb are presented.

In Fig. 3 the double ratio (Eq. (2)) for pp collisions at $\sqrt{s} = 7\,\text{TeV}$ is shown. Over the measured p_{T} range, the result is consistent with no direct-photon signal. The systematic uncertainties

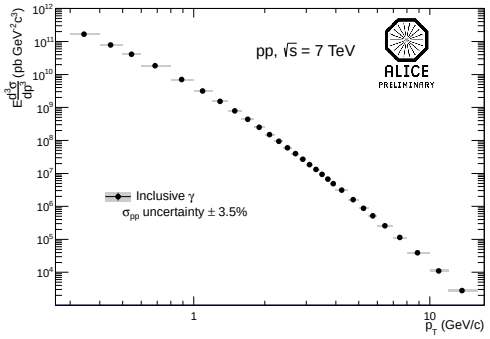

Figure 1: Invariant cross section of inclusive photons in pp collisions at $\sqrt{s} = 7\,\mathrm{TeV}$

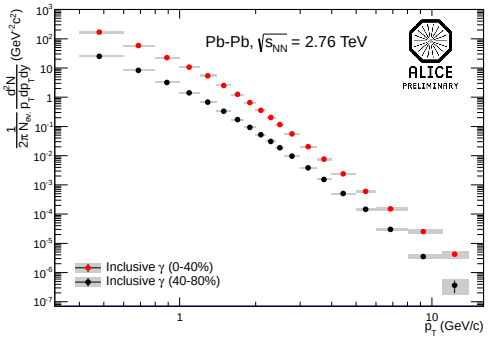

Figure 2: (color online) Invariant yield of inclusive photons in Pb-Pb collisions at $\sqrt{s_{NN}} = 2.76\,\mathrm{TeV}$ for 0-40% and 40-80% centrality

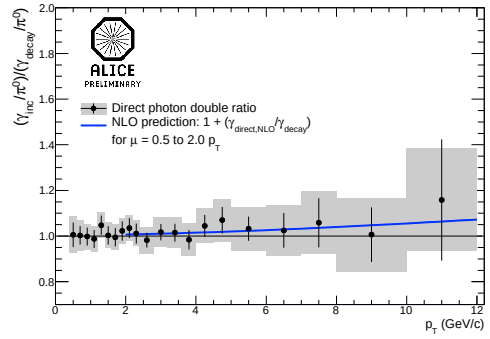

Figure 3: (color online) Direct-photon double ratio in pp collisions at $\sqrt{s} = 7\,\mathrm{TeV}$ with NLO pQCD predictions

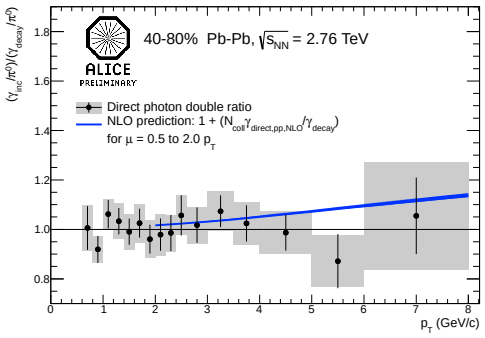

Figure 4: (color online) Direct-photon double ratio in Pb-Pb collisions at $\sqrt{s_{NN}} = 2.76\,\mathrm{TeV}$ for 40-80% centrality with NLO pQCD predictions

are too large to make a statement about the production of direct photons. A similar result for peripheral Pb-Pb collisions is presented in Fig. 4. Both measurements are compared to NLO pQCD predictions for direct photons in pp collisions ($\gamma_{\mathrm{direct,NLO}}$ in Eq. 4) [10]. These predictions are reformulated via

$$\mathcal{R}_{\mathrm{NLO}} = 1 + \left(N_{\mathrm{coll}} \cdot \frac{\gamma_{\mathrm{direct,NLO}}}{\gamma_{\mathrm{decay}}} \right) \tag{4}$$

to be comparable to a double ratio. N_{coll} is the average number of binary collisions from a Glauber Monte Carlo calculation (0-40%: $N_{\mathrm{coll}} = 825$, 40-80%: $N_{\mathrm{coll}} = 78$) [11]. In pp it is set to one. Both measurements, pp and peripheral Pb-Pb are in agreement with the NLO results, represented by a blue band.

The situation changes in central Pb-Pb collisions, as shown in Fig. 5. The double ratio shows a clear signal over the whole range of p_{T}. Below $4\,\mathrm{GeV/c}$ the direct-photon signal should contain a significant part of photons produced from a thermalized medium. Jet-photon conversions are also expected to contribute in this region. From the double ratio the direct-photon yield is

extracted using Eq. (1) and shown in Fig. 6. Fig. 6 also shows a direct-photon NLO calculation for pp at $\sqrt{s} = 2.76\,\mathrm{TeV}$ scaled by N_{coll} [10] and an exponential fit to the low momentum part of the spectrum. The inverse slope parameter of the exponential for $0.8\,\mathrm{GeV/c} < p_{\mathrm{T}} < 2.2\,\mathrm{GeV/c}$ is extracted as:

$$T_{\mathrm{LHC}} = 304 \pm 51^{\mathrm{syst+stat}}\,\mathrm{MeV}. \tag{5}$$

In a similar analysis, PHENIX measures an inverse slope parameter of $T_{\mathrm{RHIC}} = 221 \pm 19^{\mathrm{stat}} \pm 19^{\mathrm{syst}}$ MeV for 0-20% Au-Au collisions at $\sqrt{s_{NN}} = 200\,\mathrm{GeV}$. In hydrodynamic models describing the PHENIX data, the inverse slope of 220 MeV indicates an initial temperature of the QGP above the critical temperature T_C for the transition to the QGP [12, 13]. The ALICE result shows an expected increase in the extracted temperature. This is the first measurement of a direct-photon signal at low p_{T} with real photons.

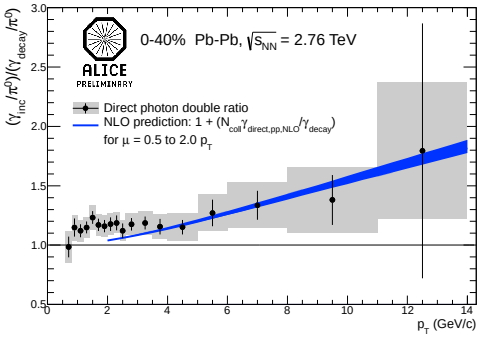

Figure 5: (color online) Direct-photon double ratio in Pb-Pb collisions at $\sqrt{s_{NN}} = 2.76\,\mathrm{TeV}$ for 0-40% centrality with NLO pQCD predictions

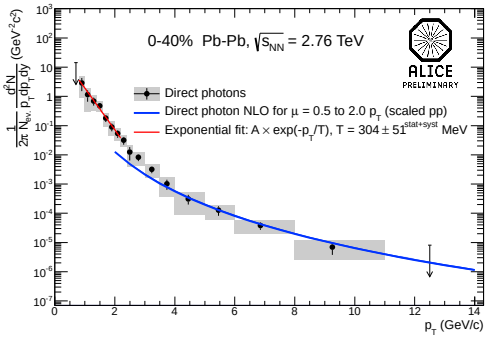

Figure 6: (color online) Direct-photon invariant yield in Pb-Pb collisions at $\sqrt{s_{NN}} = 2.76\,\mathrm{TeV}$ for 0-40% centrality with NLO pQCD predictions and exponential fit

References

References

[1] Tomasz Pietrycki, Antoni Szczurek 2006 Int.J.Mod.Phys. A22 (2007) 541-545 (arXiv:hep-ph/0608190)
[2] Fu-Ming Liu, Klaus Werner 2009 J. Phys. G: Nucl. Part. Phys. 36 035101 (arXiv:0712.3619)
[3] Thomas Peitzmann, Markus H. Thoma 2002
[4] Charles Gale 2009 Landolt-Boernstein Volume 1-23A (arXiv:0904.2184)
[5] WA98 Collaboration 2000 (arXiv:nucl-ex/0006007)
[6] The STAR Collaboration 2009 Phys. Rev. C (arXiv:0912.3838)
[7] The ALICE Collaboration 2012 Phys. Lett. B 717, 162 (arXiv:1205.5724)
[8] Dimitry Peresunko, These Proceedings
[9] P. K. Khandai, P. Shukla, V. Singh 2011 Phys. Rev. C (arXiv:1110.3929)
[10] Werner Vogelsang 2010 Private Comunication
[11] The ALICE Collaboration 2010 Phys.Rev.Let (arXiv:1011.3916)
[12] PHENIX Collaboration 2005 Phys.Rev.Lett.94:232301 (arXiv:nucl-ex/0503003)
[13] PHENIX Collaboration 2010 Phys.Rev.Lett.104:132301 (arXiv:0804.4168)

Results on Jet Spectra and Structure from ALICE

Andreas Morsch (for the ALICE Collaboration)[1]

CERN, 1211 Geneva 23, Switzerland

Abstract

Full jet reconstruction in ALICE uses the combined information from charged and neutral particles. Essentially all jet constituents can be measured with large efficiency down to very low transverse momenta ($p_T > 150\,\mathrm{MeV}/c$). This has the advantage to introduce a minimum bias on the jet fragmentation, in particular for low jet momenta and in the presence of quenching. In this article, we present preliminary results from reconstruction of charged jets in Pb–Pb collisions at $\sqrt{s_{\mathrm{NN}}} = 2.76\,\mathrm{TeV}$. The inclusive charged jet spectrum, the jet nuclear modification factors (R_{AA}, R_{CP}), the ratio of spectra measured with different resolution parameters and hadron-jet correlations are discussed. For pp data at the same center of mass energy, the inclusive spectrum of fully reconstructed jets and its resolution parameter dependence are reported.

1. Introduction

The analysis of hadronic jets in heavy-ion collisions represents a formidable tool to study the properties of the Quark-Gluon Plasma. Jets emerge from high-p_T quarks and gluons produced in hard scatterings during the very early phase of the reaction. The partons traverse the medium losing energy through elastic scattering and gluon radiation, a process in general called jet quenching [1]. Comparing heavy ion collisions to more elementary collisions like pp the prominent experimentally observable effects of jet quenching are the decrease of the jet yield, energy imbalance of di-jet events, and the modification of the fragmentation function and the angular distribution of energy with respect to the jet axis.

At the LHC, rates are high at transverse energies where jets can be reconstructed above the fluctuations of the background energy contribution from the underlying event. In particular, for jet transverse energies $E_{\mathrm{T}} > 100\,\mathrm{GeV}$ the influence of the underlying event is relatively small allowing for robust jet measurements [2, 3]. However, the measurements of the suppression of single particle production R_{AA} show that quenching effects are strongest for intermediate transverse momenta ($R_{\mathrm{AA}} < 0.2$ for $4 < p_T < 20\,\mathrm{GeV}/c$ corresponding to parton p_T in the range $\approx 6 - 30\,\mathrm{GeV}/c$) [4]. The objective of ALICE is to access this p_T region introducing the smallest possible bias on the jet fragmentation by measuring jet fragments down to low p_T ($> 150\,\mathrm{MeV}/c$). The key elements of this analysis are the detailed measurement of the underlying event fluctuations (published in Ref. [5]), the development of robust deconvolution procedures for spectra measured with low constituent p_T cuts [6] and the suppression of fake jets (random combination of uncorrelated particles) at low p_T [7].

[1] A list of members of the ALICE Collaboration and acknowledgements can be found at the end of this issue.

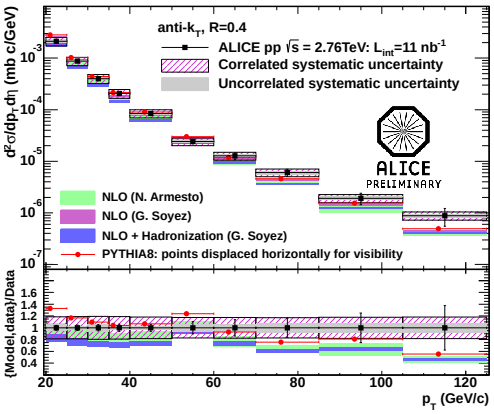

Figure 1: Differential cross section of fully reconstructed jets in pp collisions at $\sqrt{s}$ = 2.76 TeV compared to NLO pQCD [11, 12] and PYTHIA8 [13].

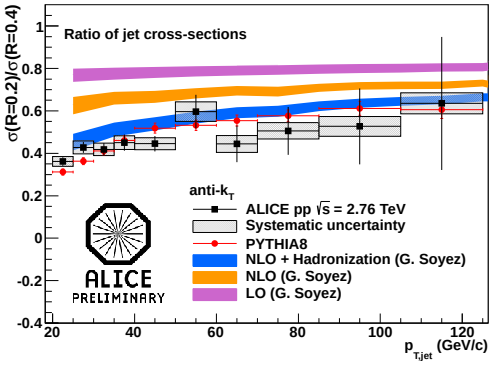

Figure 2: Ratio of jet cross sections reconstructed with $R = 0.2$ and $R = 0.4$ in pp collisions at $\sqrt{s}$ = 2.76 TeV compared NLO pQCD [11, 12] and PYTHIA8 [13].

2. Jet Reconstruction in ALICE

In ALICE, full jet reconstruction uses the combined information from charged and neutral particle measurements. Charged particle momentum vectors are measured with the central tracking detectors, the Time Projection Chamber (TPC) and the Inner Tracking System (ITS) covering the full azimuth and $|\eta| < 0.9$. Energy and direction of neutral particles are measured with the Pb-scintillator sampling ElectroMagnetic Calorimeter (EMCal), covering $1/3$ of the azimuth and $|\eta| < 0.7$. A detailed description of the ALICE experiment is given in Ref. [8].

For jet reconstruction the anti-k_T algorithm from the FastJet package [9] with resolution parameters R varying between 0.2 and 0.4 is used. The jet 4-momentum vector is calculated using the boost invariant p_T recombination scheme. Analysis with charged jets using only tracking information and fully reconstructed jets including EMCal information have been performed. The input for charged jets are tracks with $p_T > 150\,\mathrm{MeV}/c$. The input for fully reconstructed jets is the charged jet input adding the EMCal cluster energy with E_T above $150\,\mathrm{MeV}/c$ after correcting for charged particle energy contributions. These jets are required to be fully contained in the EMCal acceptance.

Jet-by-jet we correct for the energy contribution from charged particles to the energy measured with EMCAL and the contribution from the underlying event. The sum of momenta of charged tracks matching the EMCal clusters from the cluster energy is subtracted resetting negative values to zero:

$$E_\mathrm{clus}^\mathrm{corr} = E_\mathrm{clus}^\mathrm{raw} - c \cdot \sum p^\mathrm{matched};\ E_\mathrm{clus}^\mathrm{corr} > 0 \qquad (1)$$

The nominal value of c is unity and is varied over a wide range to estimate the systematic uncertainty of this procedure.

In Pb–Pb collisions, one has also to subtract the contribution of the Underlying Event (UE) from the reconstructed jet p_T. The summed p_T from the background is calculated as the product of mean momentum density ρ and the jet area A^Jet, where ρ is determined using the k_T -algorithm [10] via: $\rho = \mathrm{median}(\frac{p_\mathrm{T}^\mathrm{Jet}}{A^\mathrm{Jet}})$. Further corrections can only be applied on the raw spectrum bin-by-bin or using unfolding techniques. These corrections comprise the unmeasured p_T from neutrons

and K^0_L, as well as the tracking efficiency and the corresponding jet-by-jet fluctuations of these quantities. In Pb–Pb collisions, we also correct for the smearing of the spectra induced by the UE energy fluctuations. This smearing is quantified by δp_T, the difference between the UE corrected summed p_T and the true jet p_T: $\delta p_T = (p_T^{rec} - \rho A^{Jet}) - p_T^{true}$.

A data-driven method to determine the distribution of δp_T consists of embedding different objects into measured Pb–Pb collisions [5]. These objects can be single high-p_T tracks, jets or random cones. An advantage of the anti-k_T algorithm is, that the distribution does not depend significantly on the embedded object. The distribution is almost Gaussian with enhanced tails towards positive differences, owing to the pile-up of jets in the same jet area. For a resolution parameter $R = 0.2$ the width (σ) of the Gaussian amounts to 6.2 GeV/c (4.5 GeV/c) summing neutral and charged p_T (for charged particles only).

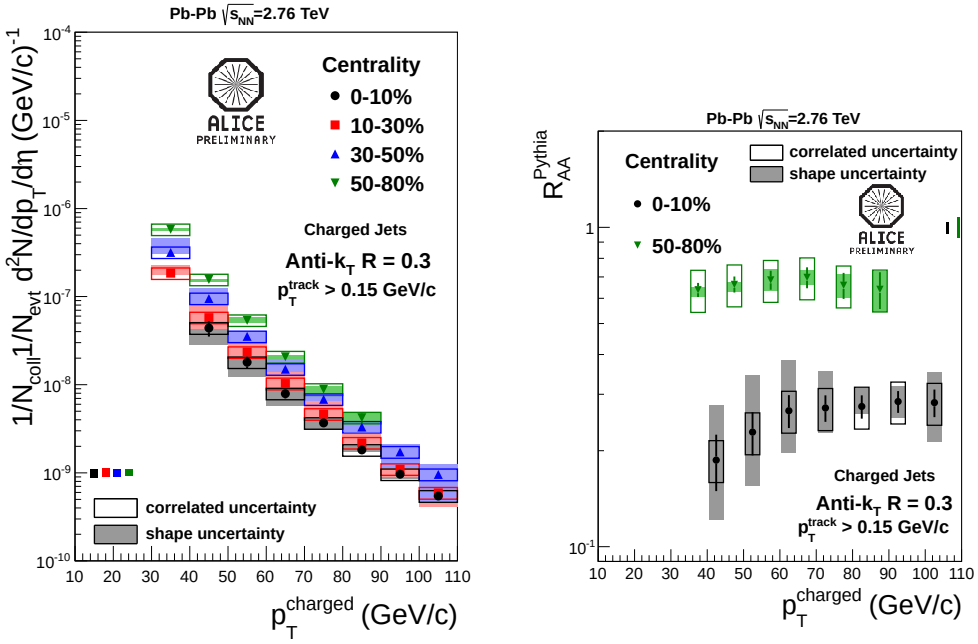

Figure 3: Left: Corrected jet spectrum with charged tracks for jet radius $R = 0.3$. Right: Nuclear modification factor for charged jets reconstructed in central and peripheral Pb–Pb collisions. The pp reference is obtained from PYTHIA simulation at the same $\sqrt{s}$.

3. Jet Spectra in pp at $\sqrt{s} = 2.76$ TeV

In March 2011, a short pp reference run at the Pb–Pb energy of 2.76 TeV was taken integrating 20 nb^{-1} of rare triggers. This was the first running period in which the EMCal was fully installed allowing us to perform measurements with fully reconstructed jets up to 120 GeV/c from 11 nb^{-1} of these data. Fig. 1 shows the jet p_T spectrum reconstructed with a resolution parameter of $R = 0.4$. The jet energy scale uncertainty amounts to 4% and it is mainly due to uncertainties in the missing neutral energy, the tracking efficiency and energy double-counting.

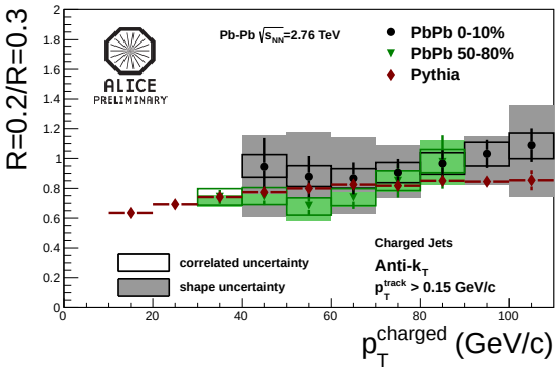

Figure 4: Ratio of reconstructed charged jets with different cone radii in central and peripheral Pb–Pb collisions at $\sqrt{s_{\rm NN}}$ = 2.76 TeV compared to PYTHIA (unquenched).

The jet p_T resolution $\Delta p_T / p_T$ amounts to 20% and is dominated by the jet energy scale fluctuations, tracking and EMCal resolutions. Efficiency and resolution effects on the jet spectrum were taken into account by applying a bin-by-bin correction. The measured spectrum is compared to NLO pQCD calculations [11, 12] and PYTHIA8 [13]. A good agreement is observed. The measurement itself represents an important reference for our Pb–Pb measurements.

Ratios of differential cross-sections measured with different R provide information on the energy distribution within the jet area (jet shape). Note that for jets reconstructed with the anti-k_T algorithm, R is to a good approximation the radius of a circular jet area. Fig. 2 shows the measured ratio for $R = 0.2$ and 0.4. Due to the fact that higher p_T jets are more collimated, the ratio rises with $p_T^{\rm Jet}$; in agreement with the pQCD and PYTHIA8 calculations.

4. Jet Suppression in Pb–Pb

Measurements of jet spectra in Pb–Pb collisions were obtained from a sample of $3 \cdot 10^7$ minimum bias events at $\sqrt{s_{\rm NN}} = 2.76$ TeV collected in November 2010. Since the electromagnetic calorimeter was only fully installed in the beginning of 2011, jet reconstruction was performed using charged particle information only.

Fig. 3 (left) shows the charged jet yields as a function of p_T normalized by the number of collisions (resolution parameters $R = 0.3$) for four centrality classes. The influence of detector effects and background fluctuations were corrected for by applying a regularized unfolding procedure with χ^2 minimization. The systematic uncertainties are dominated by the choice of the unfolding parameters (4%) and the jet energy scale corrections (4 – 10%).

Comparing the spectra for different centrality classes a sizable suppression increasing with centrality can be observed. In order to study the modifications of the Pb–Pb spectra with respect to an incoherent superposition of binary nucleon–nucleon collisions, the nuclear modification factor $R_{\rm AA}^{\rm Jet}$ was calculated and is shown in Fig. 3 (right). As a reference we use the spectra from pp collisions at the same centre-of-mass energy simulated by the PYTHIA MC [13]. The results for the highest centrality bin (0-10%) and the lowest one (50-80%) for $R = 0.2$ are shown. A strong nuclear suppression qualitatively and quantitatively similar to the $R_{\rm AA}$ of inclusive hadrons is observed in the most central collisions.